Dissertation zur Erlangung des Doktorgrades der Fakultät für Chemie und Pharmazie der Ludwig-Maximilians-Universität München

Synthetic Iron(IV)-oxido Complexes as Biomimetics for Ten-Eleven Translocation Methyl Cytosine Dioxygenases

A Comprehensive Study on the Reactivity Towards Natural and Artificial Substrates and on the Iron Chemistry Behind

Annika Menke, geb. Steinmetz

aus

Heidelberg, Deutschland

2024

Erklärung

Diese Dissertation wurde im Sinne von §7 der Promotionsordnung der Ludwig-Maximilians-Universität von Frau Prof. Dr. Lena J. Daumann betreut.

Eidesstattliche Versicherung

Diese Dissertation wurde eigenständig und ohne unerlaubte Hilfe erarbeitet.

München, den 03.05.2024

_____

Annika Menke

Dissertation eingereicht am 03.05.2024

1. Gutachterin Prof. Dr. Lena J. Daumann

2. Gutachter Prof. Dr. Konstantin Karaghiosoff

Mündliche Prüfung am 14.06.2024

für meine Familie

Haben Sie den Mut, mit Ihrem Kopf zu denken.

Marie Curie

DANKSAGUNG

Zuerst möchte ich mich bei meiner Betreuerin Prof. Dr. Lena Daumann vom Department für Chemie und Pharmazie der LMU München für die Möglichkeit bedanken, dass ich mein Promotionsstudium in ihrem Arbeitskreis durchführen durfte. Ich schätze sehr wie Du sowohl wissenschaftlich als auch menschlich Deine Mitarbeiter:innen unterstützt und man jederzeit mit Fragen aller Art zu Dir kommen kann. Besonders betonen möchte ich meinen Dank für die Freiheiten, die Du mir gegeben hast bezüglich flexibler Arbeitszeiten und spontanem Homeoffice aufgrund all der Herausforderungen, vor die man als Eltern gestellt wird. Ohne Deine fortwährende Unterstützung und Dein Verständnis wäre es mir nicht möglich gewesen diesen gewagten Spagat zwischen Studium und Familie erfolgreich zu meistern.

Ich bedanke mich außerdem bei Prof. Dr. Konstantin Karaghiosoff als Zweitgutachter meine Arbeit zu evaluieren und zu bewerten. Ebenso danke ich den weiteren Mitgliedern meiner Prüfungskommission für ihre Zeit und ihr Interesse an meiner Arbeit.

Des Weiteren bedanke ich mich bei dem gesamten Arbeitskreis bestehend aus den Ehemaligen, derzeitigen Mitgliedern, Masteranden, Arbeitskolleg:innen und gleichzeitig Freunden Henning, Berenice, Niko, Violeta, Helena, Tri, Rachel, Sophie, Ioana, Doreen, Mikey, Philippe, David, Jan und Laura. Ich habe mich in der hilfsbereiten und fröhlichen Arbeitsatmosphäre sehr wohl gefühlt – egal ob bei fachlichen Diskussionen, gemeinsamen Cola-Pausen, leckerem Kuchen, Regenbogen-Schauen, Schokolade & Eis und nicht zu vergessen bei den vielen lustigen Spieleabenden! Ihr seid mir in dieser Zeit alle sehr ans Herz gewachsen. Besonderer Dank gilt Violeta, Helena, Doreen und Ioana, die sich Zeit genommen haben Teile meiner Arbeit korrekturzulesen und mir wertvolles Feedback geben konnten sowie allen lieben und hilfsbereiten Menschen, die mit mir das Labor geteilt haben. Liebe Ioana, dir möchte ich besonders danken, dass du mich nicht alleine gelassen hast und weiter tapfer mit mir die Stellung an der LMU hälst.

Meinen Forschungspraktikant:innen Maya, Abdullah, Jan, Domenic, Antonia und Matthias sowie meinen Hiwi-Kräften Ksenija, Doreen, Sophie, Tobi und Domenic danke ich für ihr Interesse an meinem Projekt, ihre Beiträge und Ideen zu meiner Arbeit, die vielen Kuchen und für eine schöne unterhaltsame Zeit im Labor.

Ein großer Dank geht auch an die finanzielle Unterstützung des Mentoring Programms der LMU, das mir Fortbildungen, Reisen und die Anstellung von Hiwi-Kräften ermöglicht hat sowie an den SFB1309 für fachlichen Austausch. Besonders hervorheben möchte ich den Einsatz von Birgit Carell, die es mir unter anderem auch ermöglicht hat, meine Kinder zu Konferenzen mitnehmen zu können.

Außerdem bedanke ich mich bei allen Kooperationspartnern, die mit mir und für mich Messungen durchgeführt haben. Ein herzliches Dankeschön geht an Jonathan Gutenthaler-Tietze für seine Begutachtung meiner vielen Kristallproben. Trotz zahlreicher Fehlordnungen und streuschwacher Kristalle war er immer motiviert dabei mit mir herauszufinden, was nun schon wieder Unerwartetes kristallisiert ist. Fabian Zott und Kuangjie Liu vom AK Zipse danke ich für die Berechnungen der Bindungsdissoziationsenergien und die Bereitstellung von synthetisierten Substraten für gemeinsame Kooperationen. Des Weiteren bedanke ich mich für die Zusammenarbeit mit dem AK Ivanović-Burmazović (LMU München): Laura Senft für die Messung und Simulation von Massenspektren, Andreas Squarcina für die Durchführung und Auswertung von Cyclovoltammetrie-Experimenten und Julian Oppelt für erste stopped-flow UV-vis Spektren. Thomas Josephy aus dem AK Comba (Heidelberg) danke ich für die herzliche Aufnahme in Heidelberg und den Einsatz bei weiteren stopped-flow UV-vis Messungen. Mein Dank geht auch an den AK Meyer (Göttingen) für zahlreiche Charakterisierungen meiner Eisenkomplexe durch Mößbauer Spektroskopie, durchgeführt von Jan Kruse sowie Messungen magnetischer Suszeptibilität von Serhiy Demeshko. Hanife Sahin (AK Carell) danke ich für die Quantifizierung meiner Produkte aus Oligonukleotid- und DNA-Reaktionen und Pascal Giehr für wertvolle Diskussionen und Tipps bezüglich biochemischer Arbeitspraktiken.

Ebenso bedanke ich mich bei der Analytik Abteilung der LMU: Bei Brigitte Breitenstein für die Aufnahme von NMR Spektren (und die Bereitschaft jederzeit meine Extrawünsche hierbei zu erfüllen), bei Peter Meyer für die Durchführung von Kristallstrukturanalysen und bei Werner Spahl für die Messung hochaufgelöster Massenspektren.

Zuletzt möchte ich meiner Familie danken: Meinen Eltern Christiane und Andreas, meinen zwei Schwestern Leonie und Ida und meinen Großeltern Edith, Jürgen und Helga. Ihr habt den Grundstein für den Weg gelegt, den ich gegangen bin und ohne Eure bedingungslose Unterstützung in allen Bereichen wäre ich heute nicht wo ich nun bin. Ich weiß, dass Ihr immer für mich da seid. Danke!

Lieber Jan, Dir danke ich vor allem für die Zeit, die wir als kleine Familie zusammen verbracht haben. Außerdem kann es natürlich nie schaden, einen exzellenten organischen Chemiker im Hause zu haben, der einen mit seinem weisen Rat beiseite steht. Sei es bei ChemDraw-Unterstützung oder Berechnung „komplizierter“ Ansätze – Du hattest immer ein offenes Ohr für meine Probleme verschiedenster Art und nicht selten sogar eine passende Lösung für mich. Ich danke Dir für dein Verständnis in stressigen Zeiten und Dein stetiges Aufbauen und Aufwärmen. Zum Glück bist Du nicht nur ein toller Chemiker, sondern auch ein wundervoller Vater, sodass ich unsere zwei Jungs immer in allerbesten Händen wusste, wenn ich mal etwas mehr Zeit auf der Arbeit verbracht habe. Ich freue mich auf eine weitere wunderschöne Zeit gemeinsam als Familie!

Lieber Joni, lieber Beni, Ihr habt einen ganz besonderen Dank verdient! Mit Euch habe ich gelernt im Labor zügig und konzentriert zu arbeiten, um dann nachmittags noch eine tolle Zeit mit Euch verbringen zu können! Ihr habt es geschafft, mich die Probleme des Arbeitsalltags für einen Moment vergessen zu lassen und mich mit tollen Kunstwerken, gemütlichen Lesezeiten und wildem Toben zu überraschen. Danke für Euer Verständnis, wenn das Labor auch mal spät abends oder am Wochenende gerufen hat. Auch wenn meine Arbeit manchmal sehr einnehmend war, habe ich mich immer über die Zeit gefreut, die wir zusammen verbracht haben!

DISCLOSURE OF PARTICIPATION

The following people mentioned underneath contributed in the practical laboratory work of this thesis, as part of their research internships or as laboratory assistant under my supervision.

Ksenija Arslanova (laboratory assistant) assisted in the synthesis of *iso*cytosine derivatives (section III.2.1).

Doreen Reuter (laboratory assistant) contributed in ligand syntheses and the synthesis of *iso*cytosine derivatives (section III.2.1).

Maya Isabel Brown (research internship) synthesized ribonucleosides and tested their reactivity towards the iron(IV)-oxido complex (see section III.1.1).

Abdullah Sandhu (research internship) investigated stability tests and background reactions of the iron(IV)-oxido complex and assisted in reactivity measurements of the iron(IV)-oxido complex with different substrates (see section III.1.1 and IV).

Sophie Falkai (laboratory assistant) provided different ligands and iron complexes and assisted in the characterization of new iron complexes as well as in the investigation of their reactivity towards different substrates (see section IV.1.1 and IV.1.2).

Jan Philip Prohaska (research internship) contributed in the synthesis of a new ligand system and the corresponding iron complexes and tested their reactivity on different substrates (see section IV.1.1 and IV.1.2).

Tobias Frederick Walter (laboratory assistant) helped in the first steps of the synthesis of 6-aza-5-formylcytosine (see section 0).

Domenic Georg Mayer (research internship and laboratory assistant) contributed in developing a synthesis route for the compound 6-aza-5-formylcytosine and performed some reactions of iron(IV)-oxido complexes with different substrates (see section 0).

Antonia Goldhammer (research internship) assisted in the synthesis of new iron(II) complexes and investigated their spin crossover properties (see section IV.2).

Matthias Loibl (research internship) contributed in the synthesis of some 6-aza-cytosine derivatives and tested their reactivity towards iron(IV)-oxido complexes (see section 0).

ABSTRACT

Iron enzymes are ubiquitous in nature and perform a high number of different important biochemical transformations. Ten-eleven translocation 5-methylcytosine dioxygenase (TET) belongs to the family of iron(II)/α-ketoglutarate-dependent enzymes and is involved in the process of removing the methyl group from the epigenetic marker 5-methylcytosine. This is accomplished by successively oxidizing the methyl group obtaining the respective species 5-hydoxymethylcytosine, 5-formylcytosine and 5-carboxycytosine which is subsequently removed *via* base excision repair. The active species in this enzymatic catalysis is believed to consist of an *in situ* generated iron(IV)-oxido moiety that abstracts a hydrogen atom from the substrate. The resulting iron(III)-hydroxido species recombines with the carbon-centered radical to form the hydroxylated product.

Previous results from our group showed that the synthetic iron(IV)-oxido complex $[Fe^{IV}\mathbf{L1}(O)]^{2+}$ was able to also oxidize 5-methylcytosine to its natural metabolites. This was tested on the nucleobase, deoxyribonucleoside and short oligonucleotide.

In this work, the ability of $[Fe^{IV}\mathbf{L1}(O)]^{2+}$ to act as functional model for TET enzymes was further established. The conversion of the ribonucleoside 5-methylribocytidine to its natural metabolites was demonstrated (section III.1.1) and the reactivity of 5-methylcytosine-containing oligonucleotides extended (section III.1.2). Compared to the former studies, the overall oxidation of 5-methylcytidine in oligonucleotides was increased and depending on the reaction conditions, selective accumulation of 5-formyldeoxycytidine was achieved. First reactions between 5-methylcytosine-containing single-stranded DNA and $[Fe^{IV}\mathbf{L1}(O)]^{2+}$ showed small conversion (section III.1.3).

In a cooperation with the group of Prof. Zipse, the reactivity of various natural and artificial methylated nucleobases with $[Fe^{IV}\mathbf{L1}(O)]^{2+}$ was investigated (section III.2). The experimentally determined reaction rates could be correlated to the calculated bond dissociation energies of the substrates. This correlation was further exploited to get insights

into mechanistic details of the enzymatic catalysis. Until now, it is unclear whether oxidation of 5-formylcytidine occurs through the aldehyde or the corresponding hydrate form (section 0). To address this question, the synthesis of several target structures containing specific amounts of hydrate was attempted. First reactivity studies were performed and further investigations are currently ongoing. Hopefully, the observed reactivities will allow suggestions for the enzymatic oxidation mechanism.

In addition to substrate reactivity studies, the iron chemistry in this system was also further examined. An iron(II)/iron(IV) comproportionation reaction was identified as important side reaction forming an iron(III)-hydroxido species (section IV.1). Two additional ligands were introduced affording new iron complexes (iron(IV)-oxido species $[Fe^{IV}\mathbf{L2}/\mathbf{L3}(O)]^{2+}$ and mononuclear iron(III)-hydroxido complexes $[Fe^{III}\mathbf{L1}/\mathbf{L2}(OH)]^{2+}$ for example) that were thoroughly characterized and their reactivity compared.

To investigate spin crossover properties of iron(II) complexes in this system, a variety of iron(II) complexes within the pentapyridyl ligand family and different co-ligands (acetonitrile, water and methanol) were synthesized and characterized (section IV.2). Spin crossover behavior of the obtained species was studied with temperature-dependent ^{1}H NMR and UV-vis spectroscopy.

TABLE OF CONTENTS

I. INTRODUCTION

Deoxyribonucleic acid (DNA) is the basis for information about function, development and reproduction of all biological organisms and viruses. It is composed of the four natural nucleobases adenine (A), thymine (T), guanine (G) and cytosine (C) which are connected through a phosphate-2'-deoxyribose backbone to form a natural polymer. Most commonly, this polynucleotide of a specific sequence is aligned antiparallelly with a second DNA strand forming a double-helix. Size complementary and hydrogen bonding of the well-defined base pairs stabilize the double-stranded DNA (A:T and G:C, see Figure 1).[1]

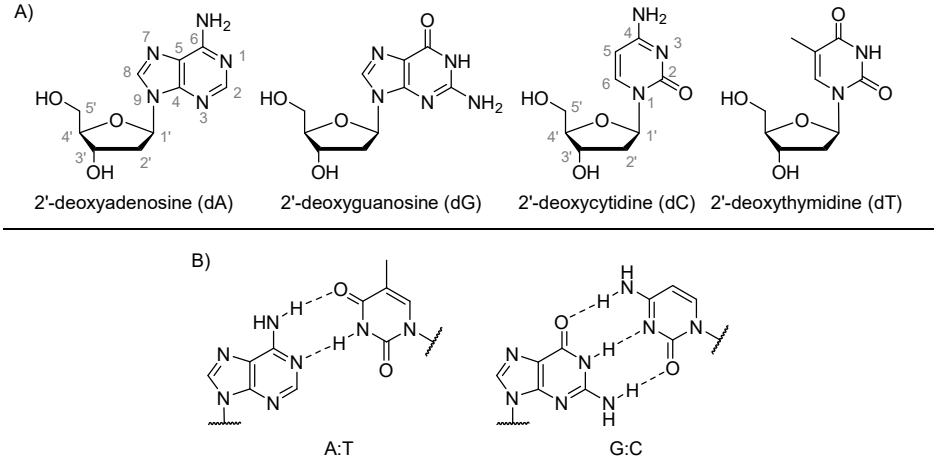

Figure 1: A) Representation of the four natural nucleosides in DNA and B) base pairing in DNA. The nucleobase is abbreviated with one letter (e.g. A) whereas for the corresponding deoxynucleoside, the prefix 'd' (e.g. dA) is used.

In eukaryotic cells, this double-stranded DNA (dsDNA) is coiled around histone proteins that, together with additional DNA binding proteins, form a compact deoxyribonucleoprotein complex known as chromatin (Figure 2). According to the central dogma of molecular biology, the genetic sequence of the DNA is decoded unidirectionally into proteins.[2-3] To achieve this so-called gene expression, two main processes are needed. During transcription, the DNA strands are separated and a new complementary strand (ribonucleic acid, RNA) is generated from a specific DNA area (gene). In the following translation step, this RNA is converted into the corresponding protein.

Epigenetic processes involved in the regulation of gene expression

However, the study of these mechanisms referred to as genetics could not explain questions such as cell differentiation. In 1996, the increasing knowledge about gene expression and the understanding that all cells of an organism carry the same DNA formed the updated definition of the term of epigenetics as "the study of mitotically and/or meiotically heritable changes in gene function that cannot be explained by changes in DNA sequence".[4] Epigenetics is today still understood as the study of heritable changes of the phenotype that are not associated with changes in the sequence of the DNA bases but with chemical modifications of DNA or of the structural and regulatory proteins bound to it.[4-6]

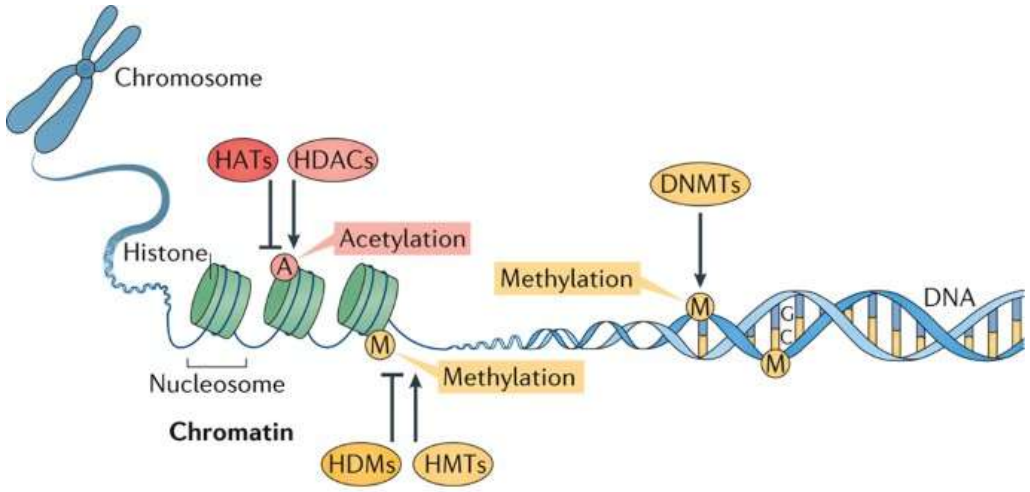

Figure 2: Representation of the chromatin structure including DNA and histones as well as epigenetic modifications. HATs= histone acetyltransferases, HDACs = histone deacetylases, DNMTs = DNA methyltransferases, HDMs = histone demethylases, HMTs = histone methyltransferases. Figure taken from reference.[7]

Gene expression is controlled by epigenetic processes mainly consisting in chromatin remodeling[8-9], histone modifications[10-12] or DNA modifications which alter the chromatin structure (Figure 2).

Histones are a class of structural and regulatory proteins interacting with DNA forming a unit of DNA coiled around a histone which is called nucleosome. Their modifications – so-called epigenetic marks – play a critical role in chromatin packing and they occur on the highly basic histone tail including methylation, acetylation, phosphorylation, ubiquitylation, and SUMOylation. These epigenetic modifications modulate the affinity of

chromatin-binding proteins by changing the accessibility to specific genes. For example, acetylation of histone tails forms "relaxed" accessible chromatin regions which result in actively transcribed genes. Deacetylation of histone tails in contrast leads to densely packed chromatin regions and transcription repression.

Epigenetic DNA modification

In addition to the chromatin structure, also specific epigenetic modification pattern directly on the DNA define active or inactive states of gene expression. These modifications can for example prevent interactions or recruit specific readers and therefore affect the accessibility of genomic regions for regulatory proteins such as transcription factors or activators.[13-16]

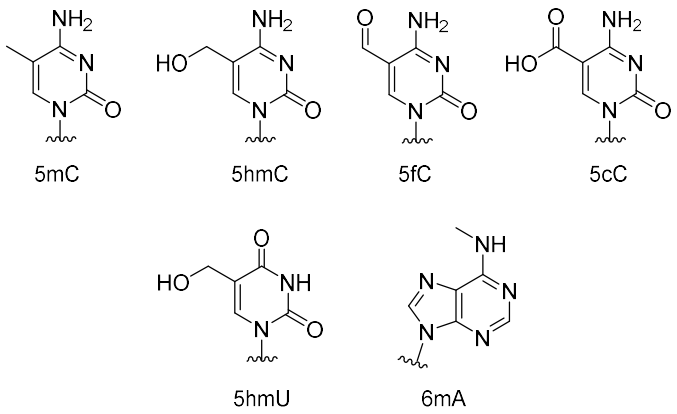

Chart 1: Selected DNA modifications. 5mC = 5-methylcytosine, 5hmC = 5-hydroxymethylcytosine, 5fC = 5-formylcytosine, 5cC = 5-carboxycytosine, 5hmU = 5-hydroxyuracil, 6mA = 6-methyladenine.

The most prominent epigenetic modification is 5-methylcytosine (5mC, see Chart 1), where the natural nucleobase cytosine is chemically modified by attaching a methyl group to its 5-position. Due to its relatively high abundance (about 4% of the cytosine residues in the human genome), 5mC is also referred to as the "fifth base". In mammals, the 5mC modification occurs almost exclusively in GC- and CpG-rich sequences termed CpG islands.[17] The 5mC modifications are attached symmetrically on CpG dinucleotides so that the methylation mark is present on both DNA strands and the methylation pattern can be propagated in DNA replication. More than 80% of the CpG dinucleotides are methylated in the human genome, whereas active regulatory elements such as promoters and enhancers

display local gaps.[18-20] DNA methylation in promotor regions induces transcription repression; this process is also described as "gene silencing".[19-20] Mechanistically, this repression of gene expression can be achieved by hindering the binding of transcriptional proteins to the genes or by inducing the binding of specific 5mC-binding proteins that can recruit additional proteins such as chromatin remodeling proteins or and histone deacetylase resulting in a dense chromatin structure.[21-24]

To achieve a dynamic epigenetic process, active removal of the methylation mark is required. This is accomplished by enzymes called ten-eleven-translocation (TET) enzymes which oxidize the methyl group of 5mC successively to 5-hydroxymethylcytosine (5hmC), 5-formylcytosine (5fC) and 5-carboxycytosine (5cC) as shown in Scheme 1. These modified nucleobases are then proposed to be either directly demodified or removed by base excision repair (BER).[25-28]

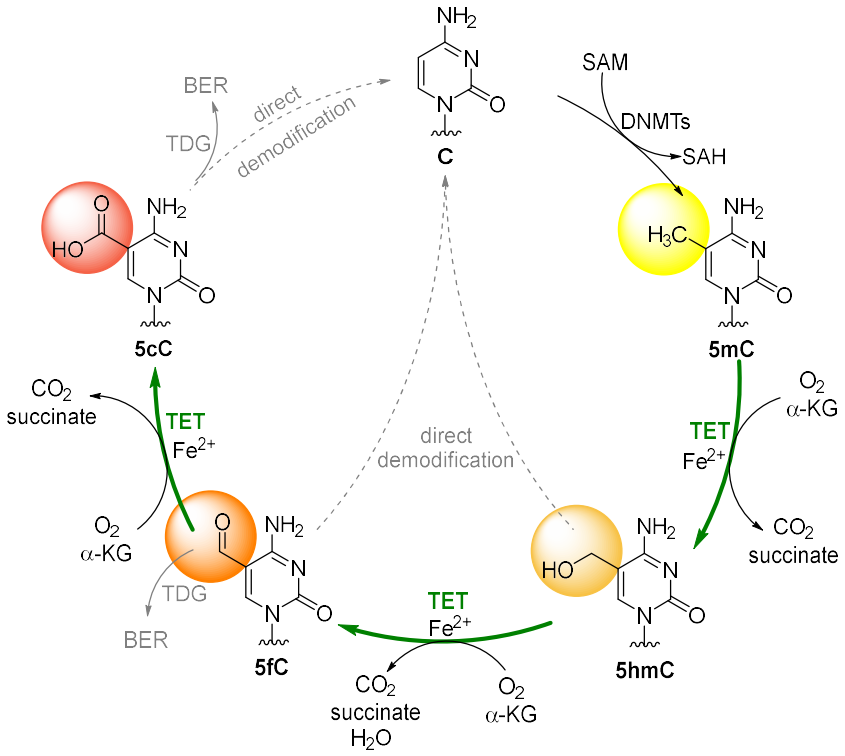

Scheme 1: Methylation and demethylation pathway of cytosine in DNA.[29-30] SAM = *S*-adenosyl methionine, DNMTs = DNA methyl transferases, SAH = *S*-adenosyl homocysteine, TET = ten eleven translocation methyl cytosine dioxygenase, TDG = thymine DNA glycosylase, BER = base excision repair.

The oxidation products 5hmC, 5fC and 5cC are intermediates of the demethylation process, however, 5hmC is believed to play a significant role as independent epigenetic mark. This modification was first discovered in 1972[31] but it took more than 40 years until its biological significance was addressed.[32] As 5hmC can also be found as relatively stable modification at promotor regions and actively described genes it is suggested to act in recruiting epigenetic regulation proteins and support activated transcription.[33-37]

Recently, it was discovered that TET enzymes also oxidize thymine to 5-hydroxymethyluracil (5hmU, see Chart 1). This modification is suggested to promote active demethylation by recruiting repair factors.[38] Additionally, 5hmU can also be generated by occasional deamination of 5hmC which subsequently can be removed by BER mechanisms. Deamination of 5mC in contrast results in thymine which is a natural DNA nucleobase and not recognized by BER. This mutation in DNA sequence is supposed to play a significant role in cancer development.[39-41]

1 Ten Eleven Translocation Methyl Cytosine Dioxygenase (TET)

A crucial role in the active demethylation process (Scheme 1) is played by TET enzymes, which belong to the superfamily of α-KG/iron(II)-dependent dioxygenases. A broad summary of investigations on this enzyme family is given in this section.

The following publication[42] presents a review discussing a variety of analytical methods employed in the investigation of α-KG/iron(II)-dependent dioxygenases to study changes in the active site and the overall enzyme structure upon substrate, cofactor and inhibitor addition. The focus is set especially on the human homologues AlkBH of *Escherichia coli*, EcAlkB and TET enzymes. Of special interest for this work are the sections about enzyme mechanism including the active species in this process, roles in epigenetic processes and the overview of nucleobase modifications functioning as substrates for α-KG/iron(II)-dependent enzymes.

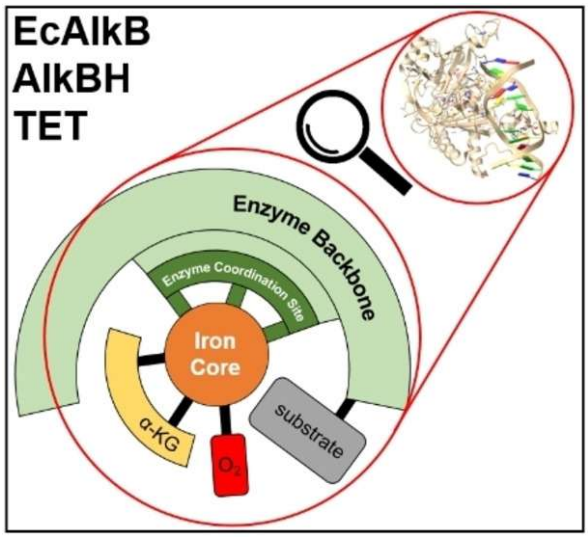

Title

Spectroscopic and *in vitro* Investigations of Fe^{2+}/α-Ketoglutarate-Dependent Enzymes Involved in Nucleic Acid Repair and Modification

Authors

David Schmidl, Niko S. W. Lindlar né Jonasson, Annika Menke, Sabine Schneider and Lena J. Daumann*

Author contribution

All authors were involved in literature search, review and writing of this manuscript.

Licence

The manuscript is available at

https://doi.org/10.1002/cbic.202100605

ChemBioChem

Review
doi.org/10.1002/cbic.202100605

Chemistry Europe
European Chemical Societies Publishing

www.chembiochem.org

Spectroscopic and *in vitro* Investigations of Fe^{2+}/α-Ketoglutarate-Dependent Enzymes Involved in Nucleic Acid Repair and Modification

David Schmidl,[a] Niko S. W. Lindlar né Jonasson,[a] Annika Menke,[a] Sabine Schneider,[a] and Lena J. Daumann*[a]

The activation of molecular oxygen for the highly selective functionalization and repair of DNA and RNA nucleobases is achieved by α-ketoglutarate (α-KG)/iron-dependent dioxygenases. Of special interest are the human homologues AlkBH of *Escherichia coli* EcAlkB and ten-eleven translocation (TET) enzymes. These enzymes are involved in demethylation or dealkylation of DNA and RNA, although additional physiological functions are continuously being found. Given their importance, studying enzyme-substrate interactions, turnover and kinetic parameters is pivotal for the understanding of the mode of action of these enzymes. Diverse analytical methods, including X-ray crystallography, UV/Vis absorption, electron paramagnetic resonance (EPR), circular dichroism (CD) and nuclear magnetic resonance (NMR) spectroscopy have been employed to study the changes in the active site and the overall enzyme structure upon substrate, cofactor, and inhibitor addition. Several methods are now available to assess the activity of these enzymes. By discussing limitations and possibilities of these techniques for EcAlkB, AlkBH and TET we aim to give a comprehensive synopsis from a bioinorganic point-of-view, addressing researchers from different disciplines working in the highly interdisciplinary and rapidly evolving field of epigenetic processes and DNA/RNA repair and modification.

1. Introduction

In 1955 Hayaishi and Mason independently reported the existence of enzymes that use molecular oxygen (O_2) to activate C–H bonds.[1] Remarkably, no potentially damaging reactive oxygen species (ROS) are formed during this process, which has raised interest in how the delicate task to activate molecular oxygen is handled in biology. Over the past 60 years, numerous enzymes with transition metal ion centers (Fe and Cu in particular) capable of controlled oxygen activation have been discovered. One important class, the non-heme iron enzymes such as the α-ketoglutarate- (α-KG) and Fe^{2+}-dependent dioxygenases form a large superfamily and some members have been found to be pivotal for the modification and repair of biomolecules such as RNA and DNA. Two of the most investigated subfamilies to be discussed are the AlkB subfamily, particularly the bacterial EcAlkB and the nine homologues known in humans (AlkBH1-9), as well as the ten-eleven translocation (TET) enzyme subfamily with its three variants (TET1-3). All these enzymes are mostly involved in demethylation or dealkylation of proteins, DNA and/or RNA, although more physiological functions have been, and will potentially be, revealed. Included in this review are only such AlkB homologues that act on RNA/DNA substrates. As the active site structure is strongly conserved among EcAlkB, AlkBH and TET, their reaction mechanisms are generally believed to be very similar, despite their large substrate scope. To study the mode of action and molecular recognition mechanisms of these enzymes, diverse analytical methods, including X-ray crystallography, UV/Vis and NMR spectroscopy or HPLC-MS techniques, have been employed. In this review, we provide an outline of important strategies used *in vitro* and summarize to what extent an insight into enzymatic structure and activity can be gained by their application. By discussing available data and conclusions for EcAlkB, AlkBH and TET we provide an extensive overview from a bioinorganic perspective, including aspects from the different interdisciplinary research areas addressing this rapidly evolving field of epigenetic processes and nucleic acid repair. In the present article, enzymes that incorporate both atoms of molecular dioxygen into organic molecules (either the substrate or α-KG) are referred to as "dioxygenases" and only their primary substrate beside α-KG is mentioned (α-KG is sometimes referred to as co-substrate, however, in this review, it will be considered a co-factor, in addition to Fe^{2+}, to highlight the differences in substrates of the discussed enzymes). In contrast, enzymes which incorporate one oxygen atom into an organic substrate and the other atom is released as water are referred to as monooxygenases.

[a] D. Schmidl, N. S. W. Lindlar né Jonasson, A. Menke, Dr. S. Schneider, Prof. Dr. L. J. Daumann
Department Chemie
Ludwig-Maximilians-Universität München
Butenandtstraße 5–13, 81377 München (Germany)
E-mail: lena.daumann@lmu.de

1.1. Consensus mechanism of Fe^{2+}/α-KG-dependent enzymes

For the superfamily of Fe^{2+}/α-KG-dependent enzymes, a consensus mechanism has been formulated based on the work on bacterial taurine dioxygenase (TauD).[2] Variations of this mechanism, for example regarding the substrate and cofactor addition sequence, have been described.[3] Due to the lack of mechanistic data on the herein discussed EcAlkB, ALkBH, and TET enzymes, we present a summary of this consensus mechanism here, even though differences between the mechanisms of TauD on the one hand and EcAlkB/AlkBH/TET on the other hand are possible.

In this commonly accepted mechanism, the iron core is always coordinated by the so-called facial triad consisting of two histidine and one carboxylic acid (aspartate or glutamate) residues on one face of the coordination sphere, which is completed by three water ligands (Scheme 1, structure **I**). Subsequent coordination by α-KG replaces two water molecules (**II**). The last aqua ligand is displaced by uptake of a substrate R–H (**III**), which does not usually coordinate to the metal center, but rather is held close to the active site by the enzyme backbone. The free coordination site is then filled by molecular oxygen, which leads to the formation of a proposed iron(III)-superoxido species **IV** (in this article, the IUPAC nomenclature oxido, hydroxido, superoxido, etc., will be used in contrast to the more common, but outdated, terms oxo, hydroxo, superoxo, etc.). These observations were mainly made *via* UV/Vis,[4] electron paramagnetic resonance (EPR),[5] and Mößbauer spectroscopy, often in combination with stopped-flow freeze-quench techniques. In addition, comparison of circular dichroism (CD) and magnetic circular dichroism (MCD) spectra collected from TauD with spectra of synthetic inorganic coordination compounds has given insight into the coordination chemistry of these enzymes.[6] The order of steps from **I** to **IV** is subject to some debate, as shown by a recent study by Solomon and co-workers on the coordination sequence in deacetoxycephalosporin C synthase (DAOCS, another enzyme of the Fe^{2+}/α-KG superfamily).[3a] The superoxide in **IV** is proposed to react with the ketone carbon atom in α-KG to form the bridged peroxido species **V**. Loss of carbon dioxide generates the trigonal bipyramidal active iron(IV)-oxido species **VI**, which was first directly characterized in 2003 by Price and co-workers.[5] The nature of this compound was discovered by rapid freeze-quenching and subsequent Mößbauer measurements, and later by extended X-ray absorption fine structure (EXAFS) and resonance Raman studies.[2d,7] The iron(IV)-oxido species **VI** abstracts a hydrogen atom from the substrate resulting in the iron(III)-hydroxido species **VII** and a carbon-centered, organic radical $R^{\bullet}$.[4–5,8] In addition, Proshlyakov *et al.* used time-resolved Raman spectroscopy in conjunction with

David Schmidl received his B.Sc. and M.Sc. in Chemistry from the Ludwig-Maximilians-Universität (LMU) in Munich. After working with Prof. Theodor Agapie at California Institute of Technology (Pasadena) and in the chemical industry, he joined the laboratory of Prof. Lena J. Daumann at LMU in 2019 to work on a functional TET enzyme model complex and DNA cytosine modifications. He has been pursuing his Ph.D. degree at the University of Cambridge since October 2020, under the supervision of Prof. Sir Shankar Balasubramanian, exploring the chemical biology of the epigenome.

Niko S. W. Lindlar né Jonasson studied chemistry at the University of Heidelberg, Germany, at the Ludwig-Maximilians-University Munich, Germany, at Leopold-Franzens-University Innsbruck, Austria, and Harvard University, USA. He recently finished his Ph.D. on the use of functional model complexes for the study of iron(II)/α-keto acid dependent enzymes in the group of Prof. Lena Daumann at Ludwig-Maximilians-University, Germany.

Annika Menke completed her B.Sc. in a transnational chemistry program (Regio Chimica) at the Albert-Ludwig University of Freiburg and université de l'Haute Alsace Mulhouse, and prepared her Bachelor's thesis in the group of Prof. Weber. She conducted research internships in the groups of Prof. Newman at the university of Ottawa, Prof. Carell, and Prof. Daumann at the LMU before she began her Master's thesis followed by her Ph.D. in the group of Prof. Daumann working on TET model complexes and their reactivity in epigenetics.

Sabine Schneider studied biology at the Ludwig-Maximilians University in Munich and conducted her Ph.D. at the University of Nottingham (UK). Following her postdoctoral work at the LMU, she started her independent research group at the Technical University Munich in 2010. In 2018 she became a Heisenberg fellow (DFG) and moved to the LMU Munich in 2019. Her research group uses molecular and chemical biology, biochemistry, and structural biology to investigate the molecular mechanism and function of structured nucleic acids and enzymes.

Lena Daumann studied chemistry at the University of Heidelberg and conducted her Ph.D. at the University of Queensland (Australia). Following postdoctoral stays at UC Berkeley and in Heidelberg she began her independent career at the LMU Munich in 2016. Her bioinorganic research group works on elucidating the role of lanthanides for bacteria as well as on iron enzymes and small biomimetic complexes that play a role in epigenetics and DNA repair.

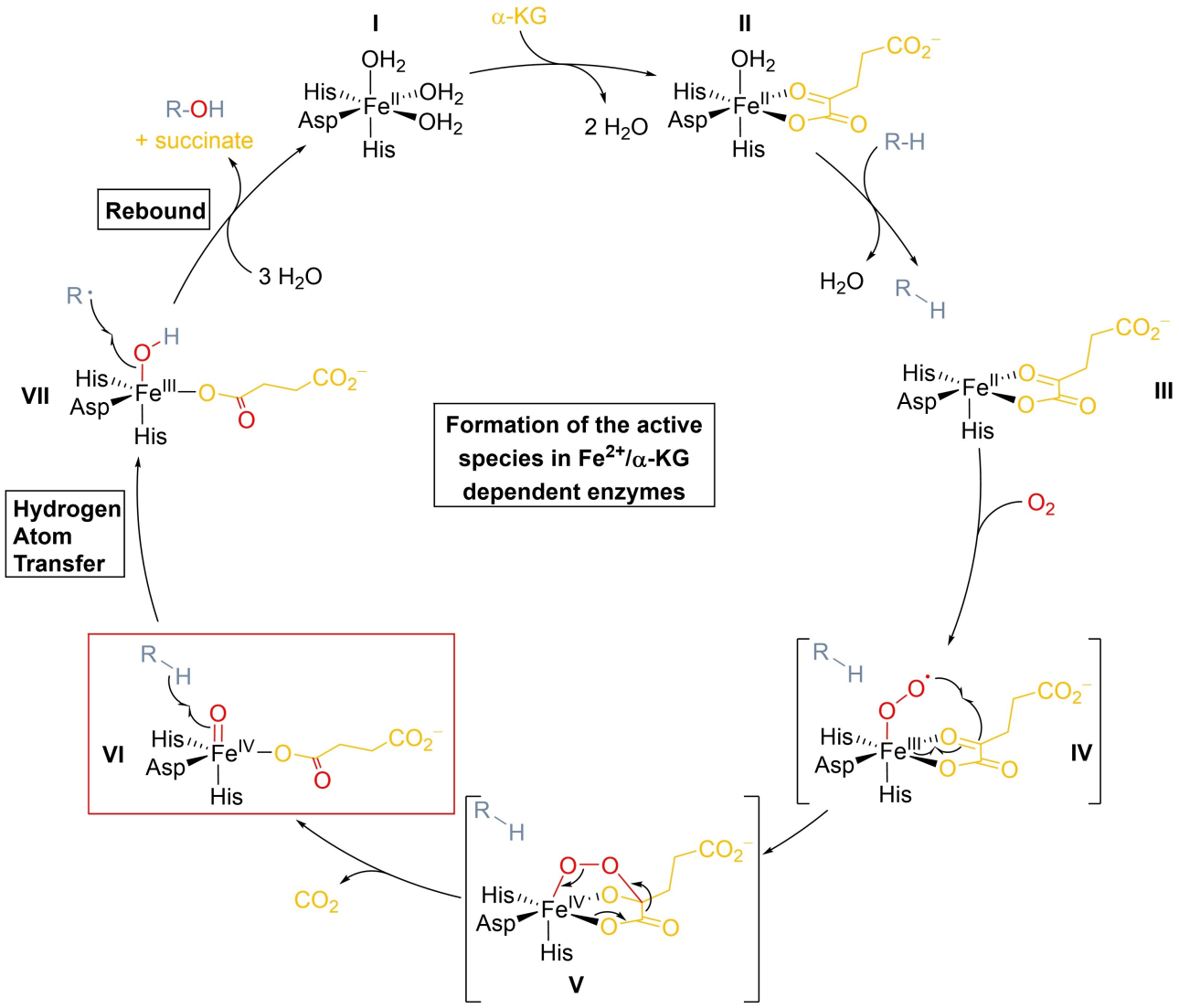

Scheme 1. Consensus mechanism of an Fe^{2+}/α-KG-dependent dioxygenase, the active species **VI** is highlighted in a red rectangle.[2] Species **IV** and **V** have not been observed directly but are often proposed as intermediates,[12] however, this is still a matter of discussion. R–H = substrate, R–OH = product.

stable isotope replacement ($^{16}O/^{18}O$ and $^{1}H/^{2}H$) to identify and characterize the iron species present during enzymatic catalysis. The authors detected the iron(IV)-oxido species **VI**, the iron(III)-hydroxido species **VII** as well as small amounts of a species consisting of the hydroxylated product coordinated to iron via the product's alcohol moiety.[9] The aforementioned hydrogen atom transfer (HAT) step from intermediate **VI** to **VII** is often, though not necessarily always, rate-limiting, which has been demonstrated in kinetic isotope effect (KIE) studies.[5,10] These two species finally react in a rebound-type reaction to produce the product R–OH and succinate, as well as regenerating the resting state **I**.

In a kinetic investigation of the enzyme factor inhibiting hypoxia inducible factors (FIHs), Knapp *et al.* studied the activation mechanism of such iron(II)/α-KG dependent enzymes. Here, the authors found that whereas the mechanism itself is similar, the rate-limiting step is the formation of the bridged peroxido species instead of the reaction with the substrate, which is to be expected, as FIHs are responsible for the sensing of oxygen.[11] This serves as an example that the mechanisms of different enzymes may show remarkable similarities in general but still differ in detail. Therefore, the presented mechanism should be viewed with caution and mechanistic work on EcAlkB, AlkBH and TET enzymes should be conducted.

1.2. Role in epigenetic processes, DNA repair and disease

The field of Fe^{2+}/α-KG-dependent enzymes has seen considerable advances in the last decade and of increasing interest are the AlkBH and TET enzymes. These enzymes play important roles in gene regulation, epigenetic transformations and DNA repair, since they act on a wide range of alkylated nucleobases in DNA and RNA context. Table 1 presents an overview of the relevant enzymes and those involved in epigenetic processes. A

Table 1. Overview of discussed enzymes in this review with selected substrates and function. Please note for enzymes for which modified nucleobases in RNA as well as DNA were reported as substrates, only the modified base with non-superscript position descriptor is indicated, without differentiation between DNA or RNA. If only RNA is acted on, the modification position is indicated as superscript in line with the most commonly used nomenclature. However, TET-enzymes were shown to predominantly act on modified C in DNA, which is therefore indicated by using dC.

Enzyme	Selected substrates	Product	Function	References
EcAlkB	*N*-alkylated bases in DNA (ss preferred over ds) and RNA	Natural bases	DNA repair	[14, 20]
	1mA	A		
	3mC	C		
	3mT	T		
	1mG	G		
	6mA	A		
AlkBH1	*N*-alkylated bases in ssDNA, mRNA and tRNA, alkylated histones, abasic sites in DNA	Natural bases and proteins	RNA repair Histone dioxygenase Hydroxylase AP lyase[a]	[14, 20a, 20b, 21]
	3mC	C		
	1mA	A		
	6mA	A		
	5mC	5fC		
	Methylated histone H2A	Histone H2A		
AlkBH2	*N*-alkylated bases in dsDNA and tRNA	Natural bases	DNA repair	[14, 20a, 20b, 20e, 22]
	3mC	C		
	1mA	A		
AlkBH3	Alkylated bases in ss DNA, ss RNA, tRNA, mRNA		Cell-type-dependent DNA repair Hydroxylation	[14, 20a, 20b, 20e, 20h, 22a, 22b, 23]
	3mC	C		
	1mA	A		
AlkBH5	mRNA m^6A	Natural bases A	RNA demethylation	[14, 20a, 20b, 24]
AlkBH8	tRNA		Translation, tRNA hypermodification	[14, 20a, 20b, 25]
	cm^5U	mcm^5U, (*S*)-$mchm^5U$		
AlkBH9[b]	mRNA (ss preferred over ds) m^6A	Natural bases A	RNA demethylation	[14, 20a, 20b, 26]
TET1,2,3	Methylated bases in DNA	Oxidizes bases in DNA	Regulation of epigenetically relevant DNA modifications	[27]
	5mdC	5hmdC, 5fdC, 5cadC		

[a] Activity independent from Fe^{2+} and α-KG. [b] Also referred to as FTO (fat mass and obesity-associated protein).

summary of selected natural and *in vitro* used substrates and products, together with commonly used abbreviations, can be found in Scheme 2. Due to the direct interconnection of gene expression (alkylated substrates) and primary metabolic pathways (dioxygen and α-KG co-substrates), these enzymes are often found to be involved in diseases. In addition, DNA hypermethylation of tumor suppressor gene promoters seems to be connected to hypoxia in tumors and a decreased function of TET enzymes in these tissues.[13] For individual mammalian AlkBH and TET enzymes, it has been shown that their loss-of-function as well as their aberrant expression and activities has an influence on various disease phenotypes, such as obesity, severe sensitivity to inflammation, multiple malformations, infertility and cancer.[14] This emphasizes the vital importance of these enzymes. Certain Fe^{2+}/α-KG-dependent enzymes, such as AlkBH1, are located in mitochondria next to enzymes that participate in the tricarboxylic acid (TCA) cycle, the source of their essential cofactor α-KG and their coproduct succinate. In the presence of oxygen, healthy cells utilize oxidative phosphorylation and the TCA cycle as controlled sources of basic metabolites and energy. In contrast, cancer cells adapt their metabolism to maximal cell growth through faster ATP production and redistribution of carbons towards nucleotide, protein and fatty acid synthesis by switching to high rates of glycolysis (= Warburg effect), even in the presence of oxygen.[15] Consequently, mutations in genes related to the TCA cycle have been associated with tumorigenesis, and cancer cells show altered concentrations of metabolites as well as accumulation of so-called oncometabolites.[16] For example, a mutation in the gene responsible for expressing isocitrate dehydrogenase leads to the generation of the novel oncometabolite 2-hydroxyglutarate (2-HG).[17] Due to the structural similarity between 2-HG and

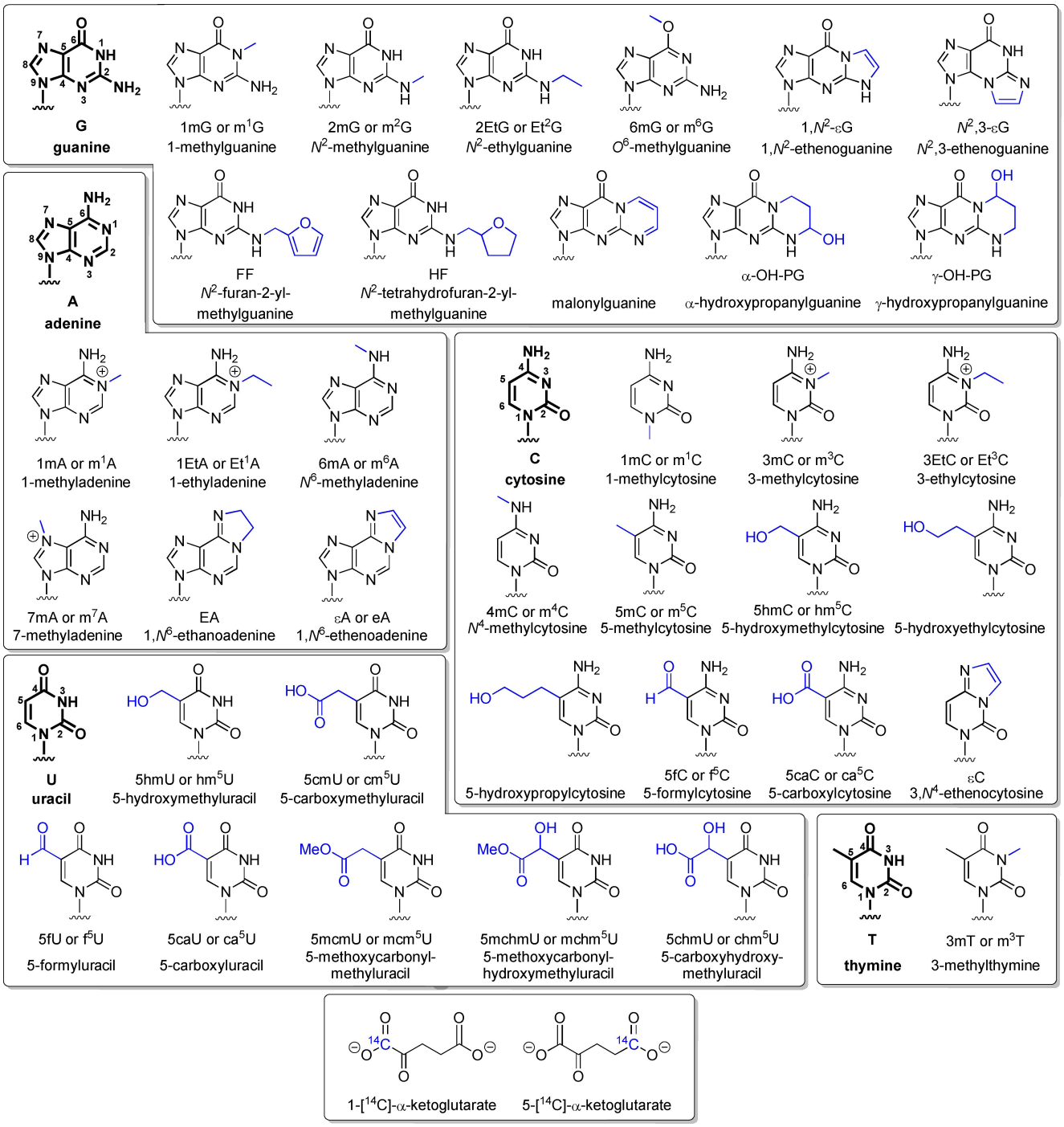

Scheme 2. Overview of nucleobase substrates and products for Fe^{2+}/α-KG dependent enzymes discussed herein. Please note, to enhance readability we did not differentiate between DNA and RNA. In addition, not all of these substrates necessarily represent the natural substrates of the mentioned enzymes.

α-KG, 2-HG is a competitive inhibitor of Fe^{2+}/α-KG-dependent dioxygenases, such as TET enzymes and methyl-lysine demethylases.[16b,18] Thus, the inhibitory effect of oncometabolites on enzymes important for modulation of the epigenome and epitranscriptome directly links metabolic dysfunction to altered gene expression and oncogenesis.[19]

2. Structural Studies and Substrate Interactions

A variety of techniques are used to study the (*in vitro*) structure and function of the enzymes relevant for this review. This includes a detailed analysis of their backbone (backbone here refers to any structure of the enzyme excluding the metal binding site/enzyme coordination site or the co-factors) structure, their active sites/enzyme coordination site and the

nature of enzyme-substrate interactions. Figure 1 gives an overview of a simplified enzyme-cofactor-substrate complex, consisting of the enzyme backbone, the enzyme's coordination site (the so-called facial triad), the Fe central atom, the co-factor α-KG (or succinate after oxidation of the iron center), dioxygen and the respective substrate or product. This review discusses the most important spectroscopic and spectrometric methods used to study the various parts of the enzyme-cofactor-substrate complex as well as the reactivity and kinetic properties of the aforementioned enzymes. The main focus lies on spectroscopic investigation of the enzyme backbone and active site as well as on techniques which assess enzyme reactivity by tracking the fate of substrates and/or products. It should be noted that there are more aspects contributing to a complete picture of the function of the enzyme in question than covered by this article. For instance, point mutations or deletion variants are very commonly included in activity studies to give indication for the function of particular amino acid residues. Also, hydrazines have recently been introduced as novel, versatile nucleophilic *in situ* probes for the study of (among others) AlkBH and related enzymes by activity-based protein profiling (ABPP).[28] While there are examples of these methods briefly introduced in several of the following sections where appropriate, this frequent element is not described as a technique in the context of this review in detail. Further, the mutual dependence between detailed *in vitro* investigation of an enzyme and experiments *in vivo* (*e.g.*, by gene deletion studies to learn about its physiological function) is not addressed as *in vivo* studies are beyond the scope of this article.

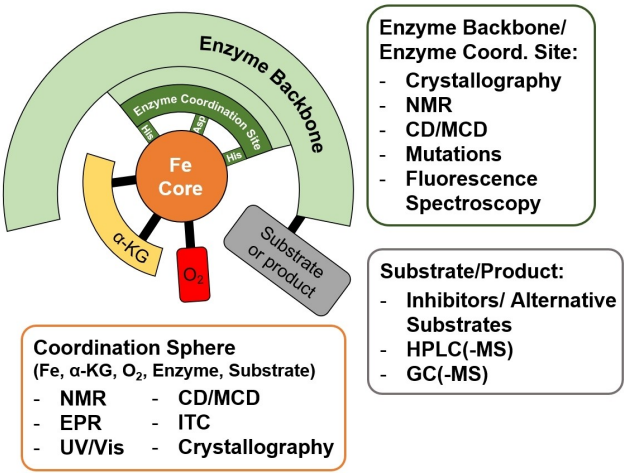

Figure 1. Overview of the methods used for the study of EcAlkB, AlkBH and TET discussed in this study. "Enzyme backbone" here refers to any structure of the enzyme excluding the metal binding site/enzyme coordination site or the co-factors).

2.1. Crystal structures

Structure-function relationship of Fe^{2+}/α-KG dependent enzymes

Despite the low overall sequence identity of α-KG-dependent enzymes (10–30%, between members of the AlkB-family and less than 10% between AlkB and TET enzymes), they consistently share the "jelly-roll" folding topology of the catalytic domain, made up of eight β-strands arranged in two four-stranded sheets (Figure 2A).[29] In addition, they have a minimal conserved binding motif for Fe^{2+} and α-KG in common, comprising of Asp-X_x–His–X_y–His–X_z–Arg, which enables the catalytic reaction (Figure 2B, Scheme 1).

Crystal structures of EcAlkB (Figure 2B),[30] as well as eukaryotic AlkBH1,[31] AlkBH2,[30e,32] AlkBH3,[33] AlkBH5,[20d,34] AlkBH8,[35] AlkBH9,[36] TET1,[37] TET2[38] and the CXXC-domain of TET3[39] are available, some of them in complex with their substrate. Their differences in sequence, structural elements and accessory domains account for their remarkably large diversity in substrates and biological roles. Here, the binding interface (width of the cleft) and loop regions control access to the active site and determine the nature of the substrate the enzymes act on, such as dsDNA, ssDNA or RNA. Recently, a detailed review on the sequence and structural evolution of the AlkBH-family in respect to their substrate scope was published.[40] By substituting Fe^{2+} and α-KG with Mn^{2+} and/or N-oxalylglycine (N–Ox), the latter being an broad-spectrum inhibitor of α-KG-dependent oxygenases,[41] which occupy the same binding sites but do not allow substrate turnover, enables the elucidation of a structural snap-shot of substrate recognition by the oxygenases.[21d,34c,42] The first step in recognition of nucleobases with altered chemical structure (i.e. methylation, oxidatively damaged, etc.) in DNA or RNA by the dioxygenases occurs, as for most nucleic acid-binding proteins, by detection of changes in the local flexibility of the nucleic acid duplex, in duplex formation and in the stability of base pairing, which are induced by the altered nucleobase structures.[43] For example, m^6A in RNA impedes RNA-duplex formation,[44] while 5mdC rigidifies the DNA backbone[45] and increases base pair stacking.[46] Substrate specificity is then further governed by molecular recognition through the residues lining the dioxygenase active site. For instance, EcAlkB has a broad substrate specificity and demethylates the predominant lesions 1-methyladenine (1mdA) and 3-methylcytosine (3mdC), as well as larger adducts, such as 1-ethyladenine and etheno-adducts in DNA.[20d,29a] Additionally, EcAlkB can use RNA as a substrate.[20i] There are about 30 X-ray crystal structures of EcAlkB alone and in complex with DNA containing various methylated or damaged nucleobases in the Protein Data Bank (PDB), providing insight into the enzyme's recognition mechanism.[30a–d,h] EcAlkB achieves this promiscuity by predominantly forming non-nucleobase-specific π-stacking interactions with the nucleobase through sandwiching it between Trp69 and His131 (Figure 2C). In contrast, TET1, TET2 and AlkBH9 act precisely on 5mdC, 5hmdC and m^6A in DNA and RNA, respectively, by forming base-specific interactions as shown by the structures of their

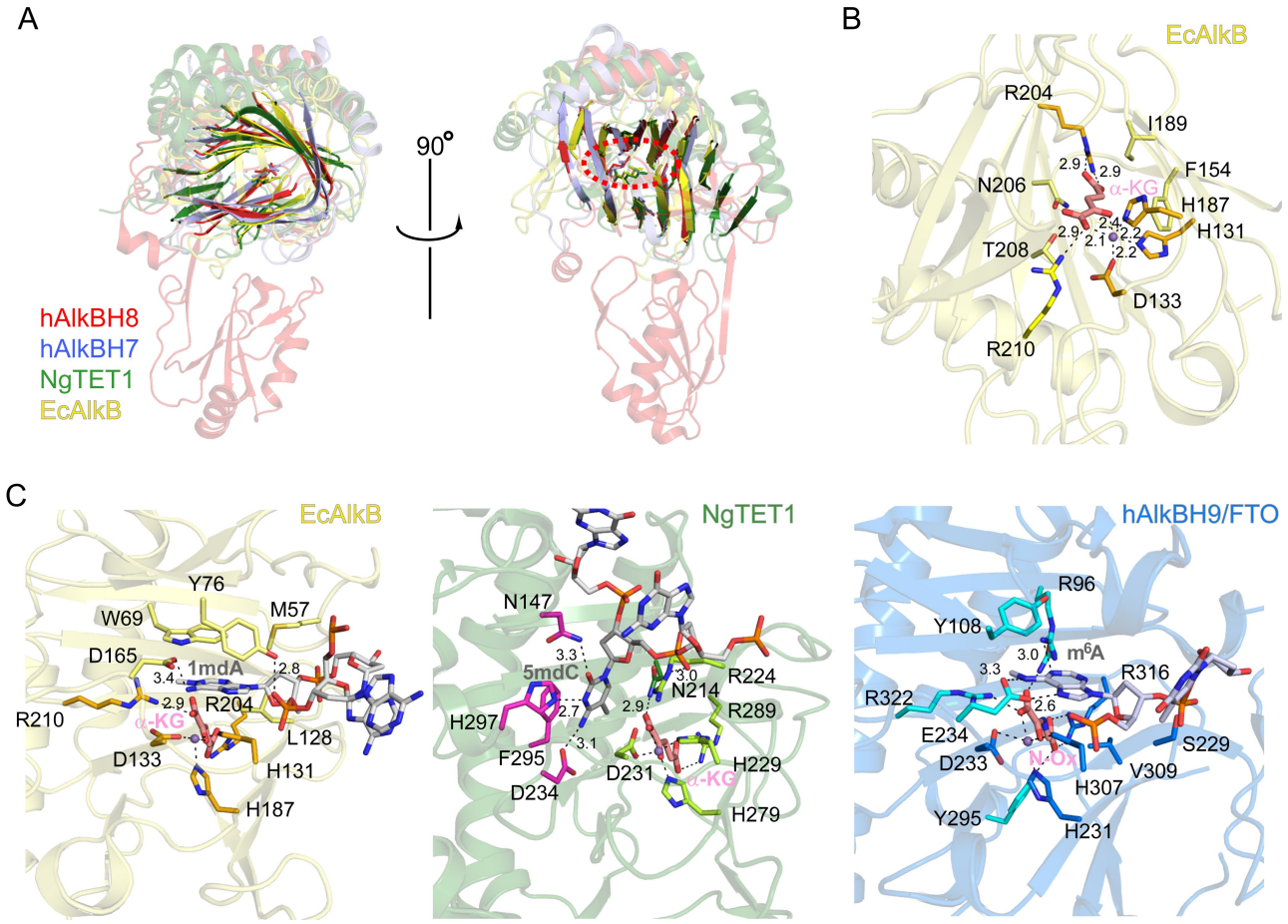

Figure 2. Structural comparison of Fe^{2+}/α-KG-dependent enzymes. **A** Superposition of hAlkBH8 (red, PDB code 3THT, *Homo sapiens*), hAlkBH7 (blue, PDB code 4QKD, *Homo sapiens*), NgTET1 (green, PDB code 5CG9, amoeba *Naegleria gruberi*) and EcAlkB (yellow, PDB code 3BIE, *E. coli*) displayed as transparent ribbon, with the jelly-roll folding topology and α-KG binding site highlighted. α-KG is shown as stick-model. **B** Structure of the EcAlkB active site (PDB code 3BIE), with residues coordinating Mn^{2+} and α-KG depicted as stick model. Amino acids coordinating α-KG and the metal ion which are conserved across species are highlighted in golden. **C** Substrate recognition by NgTET1 (green, PDB code 5CG9), EcAlkB (yellow, PDB code 3BIE) and hAlkBH9 (blue, PDB code 5ZMD, *H. sapiens*) in complex with their respective substrates. Active site residues are depicted as stick models, with the residues involved in substrate and α-KG/N–Ox recognition highlighted by color. Metal ions (Mn^{2+} or Fe^{2+}) are drawn as purple spheres. Hydrogen bond distances are shown in Å. (N–Ox = N-oxalylglycine; 5mdC = 5-methyl deoxycytosine; 1mdA = N^1-methyl-deoxyadenine; m^6A = N^6-methyl-adenine).

substrate complexes (Figure 2C).[36g,37a,38b] All TET enzymes have the ability to catalyze the oxidation of 5mdC to 5hmdC, 5fdC and ultimately 5cadC in DNA. However, they exhibit not only differences in their large unstructured *N*-terminal domains, but also possess a distinct spatial-temporal cellular distribution during development and cellular differentiation.[47] In addition to the variability and flexibility of loops and domains in the different Fe^{2+}/α-KG-dependent dioxygenases, which determine the substrate scope, alteration in active site dynamics through interaction with the cofactor α-KG or byproduct succinate impacts on substrate binding and product release. NMR-spectroscopic analysis of EcAlkB revealed that the active site in the EcAlkB-Fe^{2+}-α-KG complex is more rigid than the EcAlkB-Fe^{2+}-succinate complex, indicated by an observable sharpening of the resonances and higher resolution spectrum.[48] In line with this observation, EcAlkB enters a catalytically competent folded state only when in complex with Fe^{2+} and α-KG.[49] The use of NMR spectroscopy to gain more insight into the dynamics of Fe^{2+}/α-KG-dependent enzymes is described in more detail in the next section.

2.2. Structural and active site studies in solution

2.2.1. NMR spectroscopy

NMR spectroscopy has been widely utilized to investigate protein dynamics in the presence of substrates and cofactors. In general, proteins that are studied by NMR are smaller than ~30kDa, albeit due to recent technical advances data on larger monomeric proteins and protein complex have been reported. Here also the required isotope labelling of the protein in order to unambiguously assign NMR signals provides additional challenges for structure determination.[50] A study of EcAlkB dynamics and how the binding of cofactor α-KG or the byproduct succinate is altered in the presence of substrate

which results in different dynamic properties of these complexes, was reported by Matthews and co-workers.[48] Initially, they found that between 0.5 and 1.5 ppm the EcAlkB–Fe-α-KG complex exhibited sharper resonances and better resolved NMR spectra than the EcAlkB–Fe-succinate counterpart (Figure 3). The same trend was observed with Co^{2+} as the central metal ion. The authors concluded that the α-KG-bound form is more rigid than the succinate-bound form and this was proposed to be an important feature for effective product release. $^{1}H–^{15}N$–HSQC was used for backbone assignment and proved useful in the case of the α-KG-bound complex. ^{1}H-spectrum pseudo-contact shifts verified the presence of high-spin Fe^{2+} in the active site. In contrast, some very broad, nearly undetectable peaks confirmed the increased dynamic motion of the succinate-bound complex. Within the detected signals, 25 peaks with different shifts indicating different chemical environment were found (Figure 3, right).

Comparison of the shifted signals with the crystal structure revealed that the observed amino acids are all close to α-KG. In the crystal structure, no channel for α-KG/succinate exchange is observed, thus dynamic flexibility and conformational change upon α-KG-succinate conversion is essential and allows for the efficient dissociation of the products. A follow-up study, already mentioned in section 2.1, by Bleijlevens, Matthews and co-workers confirmed that only with both Fe^{2+} and α-KG bound to EcAlkB, the protein enters a catalytically competent folded state.[49] Figure 4A shows the sharp ^{1}H resonances of holo-EcAlkB around −1 ppm indicating a well-folded protein. The

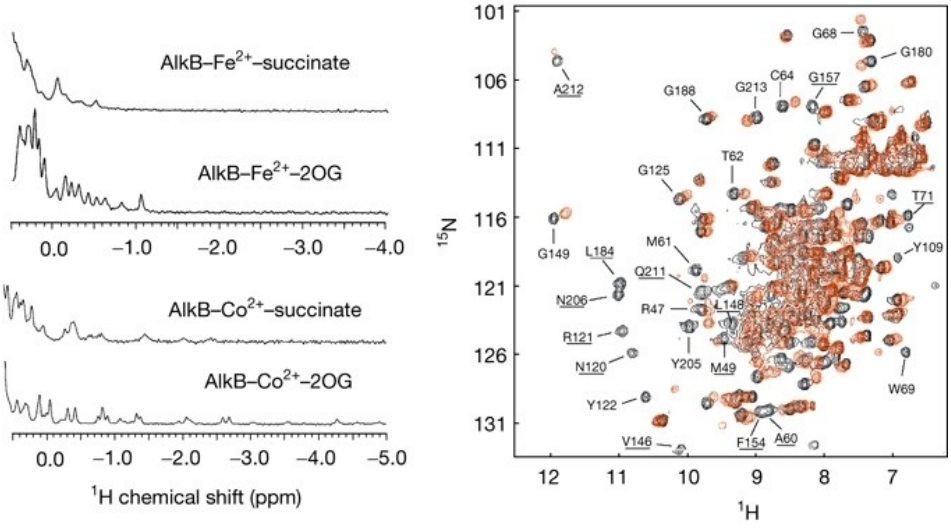

Figure 3. Copyright © 2008, European Molecular Biology Organization.[48] Left: ^{1}H NMR of EcAlkB–Fe/Co complexes with either succinate or α-KG bound. Right: $^{1}H–^{15}N$ HSQC of EcAlkB/Fe^{2+}/α-KG (black) and EcAlkB/Fe^{2+}/succinate (red).

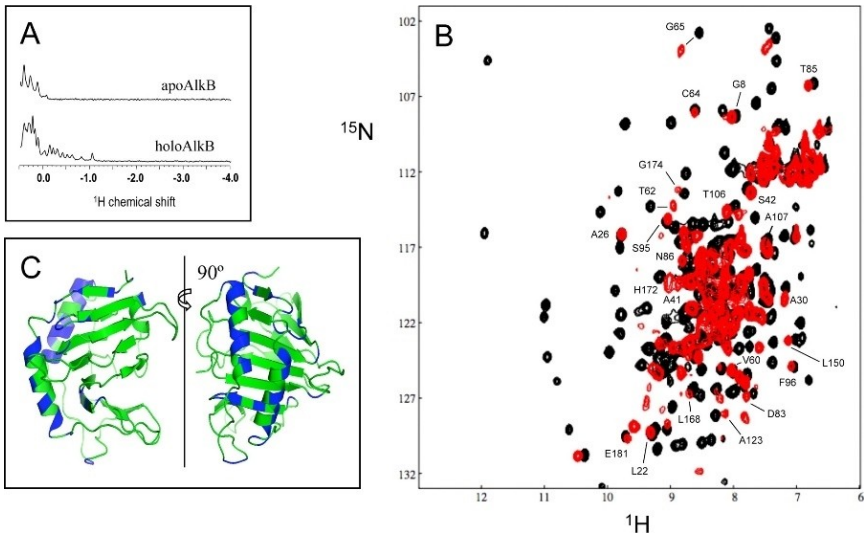

Figure 4. Copyright © 2012, American Chemical Society.[49] Changes of EcAlkB folding can be monitored by NMR. **A** ^{1}H NMR spectra of apo-EcAlkB and holo-EcAlkB (EcAlkB/Fe^{2+}/α-KG). **B** $^{1}H–^{15}N$ NMR spectra of apo-EcAlkB (red) and holo-EcAlkB (black). **C** Holo-EcAlkB (PDB 2FD8, active site and substrate omitted) with the position of tentatively assigned residues that are affected by cofactor binding highlighted in blue.

marked differences in folding between apo- and holo-EcAlkB became even more obvious in a $^{1}H–^{15}N$ NMR experiment (Figure 4B). The location of the residues mainly affected by Fe^{2+} and α-KG binding are mapped in blue onto the ribbon diagram of the structure (Figure 4C).

In a complementary study, the Hunt group studied binding dynamics of [^{13}C]-methionine-enriched EcAlkB to a DNA substrate in the presence of Zn^{2+} (to avoid paramagnetic shifting) and α-KG/succinate.[51] While they propose that apo-EcAlkB adopts a defined conformation rather than a globule-like structure (termed 'open' conformation), their ^{1}H, ^{13}C and $^{1}H–^{13}C$ correlation spectra indicate that addition of the co-factors modulates one distinct transition from the 'open' to a more rigid 'closed' conformation which also includes binding interaction with the DNA substrate. Not only Fe^{2+}, Co^{2+} and Zn^{2+}, can be used to reconstitute EcAlkB, NMR spectroscopy also revealed a properly folded protein after Cu^{2+} binding.[52] This is particularly advantageous to study the distinct properties of the EcAlkB active site, when bound to Cu^{2+} using Electron Paramagnetic Resonance (EPR) spectroscopy.

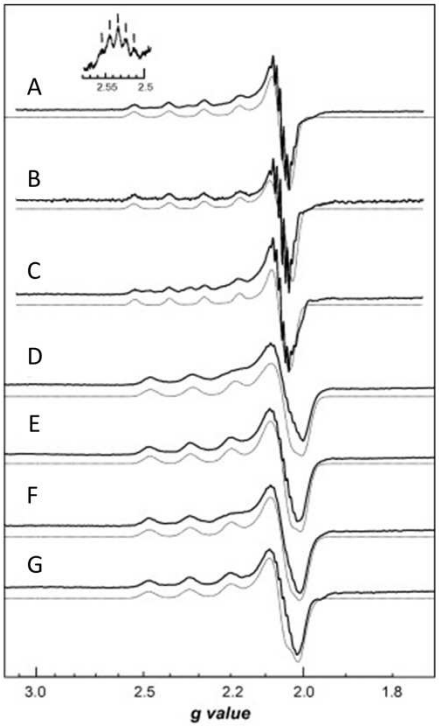

Figure 5. Copyright © 2007 Elsevier[52] **A** EcAlkB–Cu^{2+}-α-KG, **B** EcAlkB–Cu^{2+}-α-KG-imidazole, **C** EcAlkB–Cu^{2+}-α-KG-meDNA, **D** EcAlkB–Cu^{2+}, **E** EcAlkB–Cu-imidazole, **F** EcAlkB–Cu^{2+}-succinate, **G** EcAlkB–Cu^{2+}-succinate-imidazole. Solid lines correspond to recorded spectra and grey lines represent corresponding simulations. Conditions: 20 mM Tris-HCl, pH 7.6.

2.2.2. EPR spectroscopy

EPR spectroscopy can be useful to gain insight into the changes in geometry and coordination sphere around the metal ion in the presence or absence of substrate and cofactors. In EPR, the effect of ligands on the central metals' unpaired electron(s) can be measured and used to deduce structural and electronic information. However, the native metal ion of the enzymes in question, Fe^{2+} (d^6, high spin), is very difficult to observe with this method due to it generating complicated spectra as a result of spin-orbit coupling as well as hyperfine coupling.[53] In addition, the allowed EPR transitions in Fe^{2+} ions occur at very high magnetic fields which typically lie outside the range of common spectrometers. Hence, researchers have substituted it for the excellent EPR probe Cu^{2+} to enable active site analysis of Fe^{2+}/α-KG-dependent dioxygenases. Matthews *et al.* investigated the active site coordination environment in EcAlkB and classified the metal coordination site as a so-called type 2 copper site, i.e. the metal is bound by three to four amino acid residues of which at least one is His,[54] based on EPR data.[52] Although copper binding yields an inactive protein and this metal typically exhibits a lower coordination number than observed with ferrous ions, the authors showed *via* NMR and CD spectroscopy that the secondary and tertiary structure of EcAlkB with Cu^{2+} is identical to the native EcAlkB containing Fe^{2+}. Several different geometries[55] have been reported for copper centers bound to proteins such as octahedral or square pyramidal geometries that were observed in the crystal structure of the iron transporter lactoferrin binding Co^{2+} instead of Fe^{2+}.[56] Figure 5 shows the X-band EPR spectra of different EcAlkB–Cu^{2+}-substrate combinations, recorded at 20 K. The EcAlkB–Cu^{2+}–α-KG complex produced an axial spectrum ($g_x = g_y = 2.06$) with parameters indicative of a type 2 copper site ($g_z = 2.334$, $A_z = 145$ G). Furthermore, following the work of Peisach and Blumberg, who derived correlation plots of g_z and A_z and grouped areas representing the varying oxygen and nitrogen coordination environments of the copper centers, the parameters of EcAlkB were shown to be characteristic for a mixture of oxygen and nitrogen donors.[52,57] Nitrogen coordination was further confirmed by the superhyperfine coupling pattern of the high field g_z line. Here, the five-line pattern (intensities 1:2:3:2:1) indicates a coupling to two $I = 1$ nuclei (^{14}N) in the *xy*-plane, consistent with coordination by two histidine residues in the active site. Interestingly, the addition of imidazole (Figure 5B), DNA (not shown) and methylated DNA (Figure 5C) to EcAlkB–Cu^{2+}-α-KG complex did not result in notable changes in the spectra. Hence, substrate binding does not occur near the active site metal, consistent with X-ray structural data. However, when the cofactor α-KG is absent or replaced by succinate, the active site gains enough flexibility and is able to bind imidazole. This example study demonstrates how EPR spectroscopy can yield structural and dynamic information about the interaction of active site residues with the substrates, albeit in frozen solution and with the replacement of the native metal ion by copper(II).

2.2.3. Fluorescence spectroscopy

Steady-state and time-resolved fluorescence can be used to examine changes in local protein dynamics and folding *via*

tryptophan reporters. EcAlkB contains four tryptophan residues which show a fluorescence maximum at 343 nm, with the fluorescence intensity depending on the micro environment, which can therefore be exploited for this purpose.

Addition of Fe^{2+} to EcAlkB causes quenching of the Trp-fluorescence, which is reduced even further when both Fe^{2+} and N–Ox (this inhibitor was used instead of α-KG to avoid background activity of the enzyme) are added (Figure 6A).[49] This observation was attributed to an increased ordering of the holo-EcAlkB enzyme tertiary structure. Furthermore, the fluorescence anisotropy was largest when both Fe^{2+} and N–Ox were added (Figure 6B), reflecting lower mobility of the Trp-side chains. This finding also points to a decreased flexibility of the tryptophan-bearing domains in the fully assembled enzyme. Analogously, EcAlkB affinity towards other metal cations such as Co^{2+} and Ni^{2+}[58] as well as the conformational changes of the respective enzyme domain upon binding of α-KG[51] were tracked and the fate of the nucleotide recognition lid when accommodating a DNA substrate was analyzed.[51,58] Trp-fluorescence is further amenable to investigate the thermal stability of these enzymes.[49] The behavior of EcAlkB apo-protein upon heating (Figure 6C) is perplexing because the fluorescence intensity decreases continuously with temperatures above 10 °C. This observation could indicate a higher stability of the protein complex which seemed to undergo a two-stage unfolding process. Yang, He and co-workers used these alterations in Trp-fluorescence to study the interaction of AlkBH2 with different substrates to probe how the enzyme senses base pair stability in duplex DNA.[30e] Information about the kinetics of (co-)substrate binding can be accessible through combining fluorescence spectroscopy, which works on a very small time scale, with the Stopped-Flow technique. This way, Fedorova *et al.* were able to propose a kinetic model for the conformational behavior of EcAlkB upon metal and DNA binding, based on the temporal course of the Trp fluorescence signal.[58] This spectroscopic approach has been extended to track the fluorescence of 2-aminopurine, which had been placed 3′ to the 1mdA lesion to be repaired by EcAlkB in DNA, and to measure Förster Resonance Energy Transfer (FRET) when an oligonucleotide modified with a 5′-Fluorescein Amidite (FAM) fluorophore and a 3′-Black Hole Quencher 1 (BHQ1) quencher was employed.[59] This allowed for approaching EcAlkB protein dynamics from multiple angles.

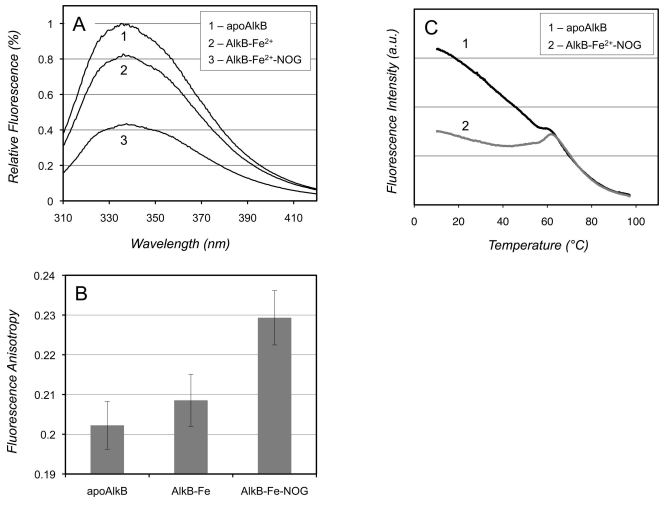

Figure 6. Copyright © 2012, American Chemical Society, taken from reference.[49] **A** Typical steady-state fluorescence of tryptophan residues in apo-EcAlkB and EcAlkB–Fe^{2+} with (holo-EcAlkB) and without N–Ox. **B** Fluorescence anisotropy. **C** Thermal denaturation curves. Conditions: EcAlkB 7 μM, Fe^{2+} 10 μM, N–Ox 1 mM in 20 mM Tris-HCl, pH 7.6. EcAlkB 1 μM in 20 mM Tris-HCl containing 150 mM NaCl, pH 7.6, 20 °C.

Besides through mere quenching of fluorescence, the structural dynamics of a protein upon substrate binding can also be assessed *via* monitoring of the polarization of the emitted light.[60] While freely rotating fluorophores, such as a fluorescent label (fluorescein, carboxyfluorescein) at the 5′-end of a DNA strand in solution, commonly show barely polarized or non-polarized emission when excited with polarized light, restriction of rotational freedom through binding to a protein can result in retained polarization of fluorescence. This behavior is exploited in Fluorescence Anisotropy (FA) spectroscopy which has been applied in various studies of biomolecule interactions (and even live-cell imaging) and can provide information about structural, kinetic and thermodynamic properties of DNA-protein interaction when monomer and complex differ significantly in size. FA spectroscopy, in combination with point variant experiments, helped Holland and Hollis determine two different binding conformations ('searching' and 'repair') of EcAlkB when screening a DNA strand for methylation damage.[30a] Hunt and co-workers added evidence (through both FA and Trp-fluorescence quenching experiments) that EcAlkB preferentially binds alkylated DNA rather than non-alkylated DNA as a result of a conformational change from the 'open' to the 'closed' state induced by metal/co-substrate binding.[51] Apart from the generally very thoroughly studied EcAlkB enzyme, two of its human homologues were subjected to FA spectroscopy to elucidate their binding behavior towards their primary substrates. Multiple variants of AlkBH8, which usually act on modified uracil in some tRNAs, were provided with synthetic RNA strands and their binding affinities to those substrates appeared to be dependent on both the RNA recognition motif close to the *N*-terminus and an additional *N*-terminal α-helix domain, even though with rather low sequence specificity.[35] Jia *et al.*, on the other hand, utilized FA spectroscopy in their structural study of AlkBH9 with its main substrate m^6A in mRNA, to screen for AlkBH9 variants suitable for crystallization which would exhibit increased binding affinity to 6mdA-containing DNA instead of RNA without significant impact on demethylation efficiency.[36g] They identified a Gln86Lys/Gln306Lys variant with 16-fold increased binding affinity compared to the wild type enzyme, which allowed for more facile crystallization and enabled them to structurally characterize the preference of AlkBH9 for binding of m^6A in the 5′-cap motif of mRNA. FAM-labelled DNA samples have been used to explore the binding affinity of 5mdC, 5hmdC, 5fdC or C-containing DNA and TET2. The fluorescence polarization measurements showed that the affinity for all four substrates was similar and was further unaffected by the presence of Fe^{2+}/Mn^{2+} and N–Ox/α-KG.[38b]

2.2.4. Isothermal titration calorimetry (ITC)

ITC is a method that can be used to monitor the thermodynamics of metal and substrate binding events to proteins as well as to obtain equilibrium constants and even kinetic information on substrate turnover.[61] In the previously mentioned study by Matthews and co-workers,[48] the binding affinity of EcAlkB to a DNA substrate at different stages of the oxidative catalytic cycle was assessed (Figure 7). Figure 7A shows the results for binding of methylated T(1mdA)T to EcAlkB–Fe^{2+}-α-KG representing the situation at the pre-chemistry stage. After oxidative catalysis, the co-substrate has been oxidatively decarboxylated to succinate impacting on DNA binding which was modelled by titrating T(1mdA)T to EcAlkB–Fe^{2+}-succinate (Figure 7B). The situation after oxidative demethylation of the DNA substrate was investigated with an unmethylated DNA pentamer binding to EcAlkB–Fe^{2+}-succinate (Figure 7C). The authors had shown by NMR and CD spectroscopy (see Sections 2.2.1 and 2.2.5) that the succinate-containing holoenzyme exhibited higher conformational flexibility than the α-KG-containing complex. This is also reflected by the ITC data, as the methylated trimer was bound more strongly by EcAlkB–Fe^{2+}-α-KG than by EcAlkB–Fe^{2+}-succinate. Notably, biphasic isotherms were obtained in both cases (discernable from the presence of a saddle point in the curves and the derivability of two K_d values from them). This was attributed to two different EcAlkB species of which one might have undergone auto-oxidation with a different affinity for substrate. Upon dealkylation of the substrate, the binding affinity to the now unmethylated DNA drops dramatically (as reflected in the higher K_d value in Figure 7C) hinting to further increased flexibility as a prerequisite for substrate release. It should be noted, though, that the unmethylated substrate is of a different length and sequence (TTdCTT) than the substrate in the first two cases (T(1mdA)T), so that potential sequence biases were not accounted for.

The DNA binding properties of TET enzymes have also been tested by ITC. As the DNA-binding CXXC domain of TET enzymes lacks a sequence motif which determines the properties of other CXXC-containing enzymes,[62] Shi *et al.* examined the *Xenopus* TET3 CXXC domain (as well as the human version) *via* ITC.[39b] Indeed, while preferring CpG-containing sequences, TET3 CXXC also binds to non-CpG oligonucleotides with similar specificity as long as one dC or dG is present. This distinguishes it from, *e.g.*, CFP1 or MLL which exhibit strict dependence on CpG dinucleotides.[62] They further identified an unmodified cytosine as indispensable for TET3 CXXC binding.[39b] These ITC data provided a principle foundation for a subsequent analysis of the genome-wide TET3 CXXC binding profile (in HEK293T cells) by other, DNA sequencing-based, techniques, demonstrating that simplified *in vitro* assays can help elucidate biological observations. Isothermal Titration Calorimetry further showed that mammalian TET3 had high binding affinity to 5cadC compared to unmodified dC in a dC(xdC)dG context, while binding to 5mdC, 5hmdC and 5fdC was markedly reduced.[39a] ITC can even be useful in screening for (non-DNA) high-affinity inhibitors of such enzymes, as exemplified by Yu and co-workers who established a small-molecule inhibitor for TET2 which was consequently employed to investigate the role of TET2 in somatic cell reprogramming.[63]

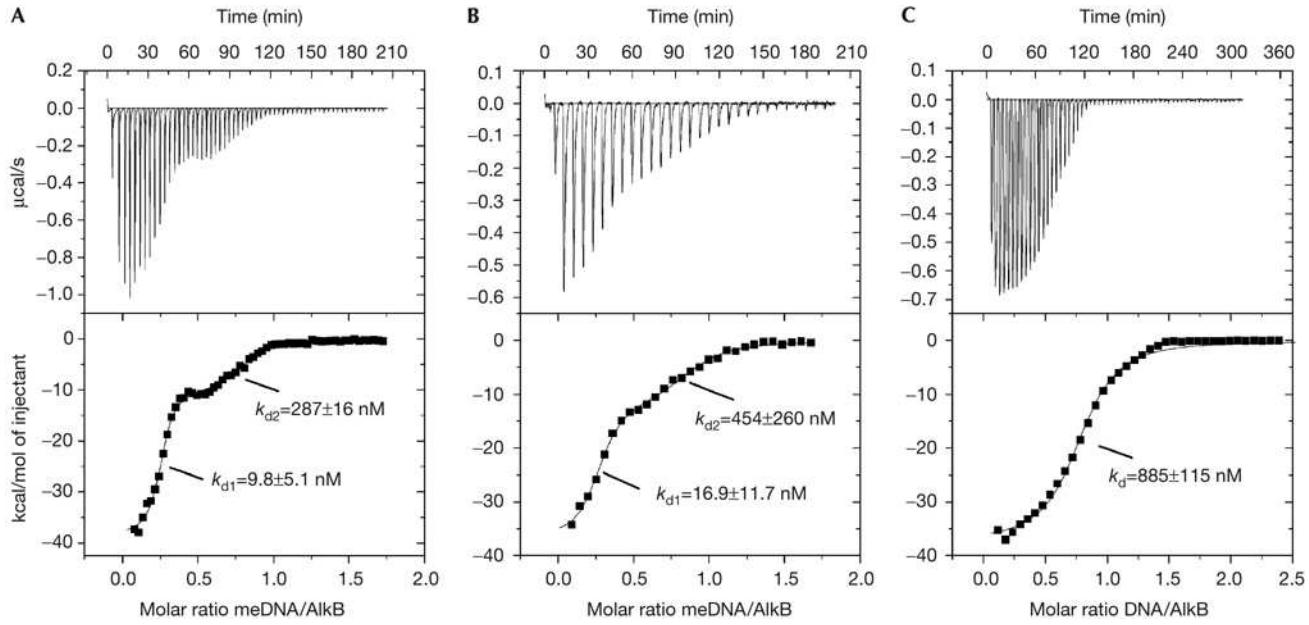

Figure 7. Copyright © 2008, European Molecular Biology Organization.[48] Isothermal calorimetric titrations (ITC), top: calorimetric titration profiles, bottom: fit of heat absorbed per mole of titrant versus DNA/EcAlkB ratio. **A** Binding of T(1mdA)T to EcAlkB–Fe^{2+}-α-KG. **B** Binding of T(1mdA)T to EcAlkB–Fe^{2+}-succinate. **C** Binding of unmethylated DNA (here: TTdCTT) to EcAlkB–Fe^{2+}-succinate.[48]

2.2.5. CD spectroscopy

Circular Dichroism (CD) spectroscopy is an excellent method to determine correct folding of proteins and secondary structure traits, to investigate interactions of proteins with substrates and to monitor concomitant conformational changes as well as the impact of temperature, denaturants and additives.[64] Ideal for this method are inorganic buffer systems such as phosphate, but HEPES (2-[4-(2-hydroxyethyl)piperazin-1-yl]ethane-1-sulfonic acid) and Tris (tris(hydroxymethyl)aminomethane) have likewise been used successfully in CD spectroscopy. Matthews and co-workers reported the CD spectra of EcAlkB in the presence of α-KG (here labelled as 2OG) and succinate.[48] To stabilize the native metal ion Fe^{2+}, ascorbate is usually included, however this additive possesses an intense CD signal in the near UV-region obscuring the EcAlkB signature. For an excellent discussion on the role of ascorbate for α-KG/Fe-dependent oxygenases please see reference.[65] Due to the observed auto-oxidation of the EcAlkB–Fe^{2+} species in the presence of O_2, metal ion substitution with Co^{2+} was consequently explored. Hunt *et al.* had previously demonstrated that the active site structures of Fe^{2+} and Co^{2+}-substituted EcAlkB are nearly identical, hence no major structural changes upon metal addition are expected.[30c] Besides Co^{2+}, Cu^{2+} is also suitable for reconstitution of the active site without distinct changes in the secondary and tertiary structures, while yielding an inactive, but stable enzyme for structural investigations.[52] Spectral fitting of the CD spectra in Figure 8 showed that EcAlkB mostly consists of β-sheets (39%) and only $<10\%$ α-helices, and revealed that no significant structural changes upon α-KG or succinate binding were induced.[48]

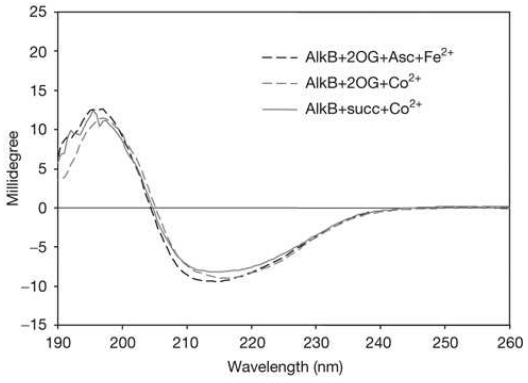

Figure 8. Copyright © 2008, European Molecular Biology Organization. CD spectra of EcAlkB in the presence of different cofactors and metal ions.[48] Conditions: 20 °C, 1 mm path length, 12.5 μM EcAlkB, 1 mM Ascorbate, 1 mM Tris-HCl pH 7.6. Background signals from buffer and cofactors were subtracted from the spectra.

Several years later, the same group reported a comparison of apo-EcAlkB and holo-EcAlkB in the presence of different cofactors.[49] Consistent with previous reports, CD-spectroscopic analysis demonstrated predominant β-sheet contribution, in accordance with the structural motifs found in the crystal structure. Interestingly, both the maximum (195 nm) and minimum (210 nm) intensify upon metal binding, possibly because the metal binds to two residues that are part of a β-barrel and thus stabilize the structures. The nature of the metal (Fe, Co) had little influence and the addition of α-KG did not alter the spectra significantly (Figure 9A). Absorbance in Near UV is commonly caused by disulfide bridges and aromatic residues. EcAlkB does not contain any disulfide bridges, however, aromatic residues are integrated into the protein structure in unique ways upon folding, hence, they can be used to probe a proteins tertiary structure. The spectrum of holo-EcAlkB is markedly different in the near-UV region, pointing towards variation between apo-EcAlkB and holo-EcAlkB tertiary structure (Figure 9B). Hunt *et al.* reported another study on the folding behavior of wild type and mutant EcAlkB variants dependent on the presence of viable co-factors.[51] Through following protein denaturation upon heating, thermodynamic stabilization of the holo-enzyme by ligand binding was observed, further supported by NMR and FA spectroscopy experiments.

At the time of writing, we were unaware that magnetic circular dichroism (MCD) or variable-temperature, variable-field (VTVH) MCD spectroscopy had been applied to any of the relevant enzymes discussed in this review. In particular, local modifications of the iron coordination site, such as changes in coordination number during cofactor and substrate binding,

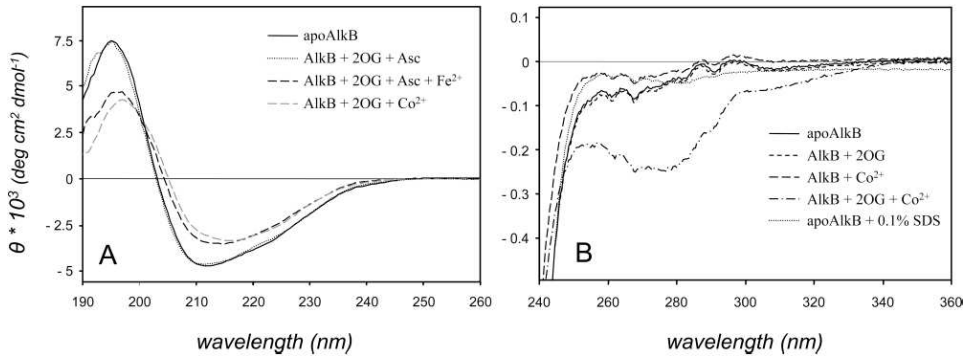

Figure 9. Copyright © 2012, American Chemical Society, taken from reference.[49] **A** Far-UV spectra and **B** Near-UV spectra. Conditions: Far-UV CD spectra = 1 mm path length quartz cuvette, 20 °C, 12.5 μM EcAlkB (0.3 mg/mL) in 1 mM Tris-HCl, pH 7.6. Near-UV CD spectra = 4 mm path length quartz cuvette, 10 °C, 1 mg/mL EcAlkB in 20 mM Tris-HCl, pH 7.6. Spectra corrected for background signals.

can be elucidated with these methods.[66] A possible question that could be addressed with MCD would be how readily a catalytically competent active center is formed in the presence of a certain substrate, which in turn could help with assigning native functionality. In addition to CD and MCD spectroscopy, UV/Vis spectroscopy is widely utilized in the concerned area of research and some examples are given in the next paragraph.

2.2.6. UV/Vis spectroscopy

UV/Vis absorption spectroscopy is, except for the spectroscopically silent metals Cu^{+} and Zn^{2+} (full d-shell, d^{10}), widely used in bioinorganic chemistry to investigate the characteristic features of metalloproteins. In 2002 Sedgwick, Hausinger and co-workers confirmed for the first time experimentally that EcAlkB is an Fe^{2+}/α-KG-dependent enzyme, partly based on the observation of a weak Metal-to-Ligand-Charge-Transfer (MLCT) band around 500 nm, reflecting charge transfer from Fe^{2+} to α-KG.[20d] This type of MLCT is a characteristic feature of Fe^{2+}/α-KG-dependent dioxygenases.[4] The authors compared the difference spectra of anaerobic apo-EcAlkB with α-KG in the presence and absence of iron and also noted that the absorption maximum of 500 nm was slightly shifted compared to other members of the Fe^{2+}/α-KG enzyme family (530 nm).[20d] Previously reported UV/Vis signatures of EcAlkB were at $\lambda_{max} = 560$ nm[67] or described as broad band around 450–500 nm.[20d] The difference in absorption maxima was attributed on whether iron was already present from purification or added to the purified apoenzyme.[67] Once oxygen is introduced into these systems (in the absence of substrate), self-hydroxylation of the enzymes can be observed (also referred to as uncoupled decarboxylation). In TauD and EcAlkB this is reflected by a band around 550 nm (oxidation of a tyrosine residue)[68] and 595 nm (tryptophan oxidation),[69] respectively. These spectral changes are most likely due to Ligand-to-Metal-Charge-Transfer (LMCT) from Trp–OH to Fe^{3+}.[70] This unwanted self-hydroxylation can be avoided by handling the enzyme under strictly anaerobic conditions, especially in the absence of a suitable substrate. For EcAlkB UV/Vis absorption spectroscopy was also used to examine substrate binding and/or the ability to form a catalytically competent active center. Mishina, Chen and He investigated the impact of ssDNA binding on EcAlkB.[67] They observed that the Fe^{2+}-α-KG MLCT band at 560 nm broadened and shifted to 551 nm upon addition of ssDNA and attributed this to a geometry change around the iron center upon substrate binding. For TET2 the absorbance decay of the Fe^{IV}-oxido species was monitored in the presence of different substrates with stopped flow absorption spectroscopy. For this, an anaerobic solution of TET2 and $Fe(NH_4)_2(SO_4)_2$ was mixed rapidly with a solution (that had been previously exposed to air and hence contained O_2) of α-KG and dsDNA bearing either 5mdC, 5hmdC or 5fdC. The emergence and decay of species **VI** (see Scheme 3, Figure 10) was then monitored at 318 nm. For 5hmdC and 5fdC containing substrates, the intensity of the signal in the beginning was larger than for 5mdC. Thus, the catalytically active Fe^{IV}-oxido species (species **VI**) accumulated when 5hmdC or 5fdC were present, before it was consumed by reaction with the substrate. The decay of this species was also slower for those two substrates than for 5mdC. The authors concluded that the substrate influences the reaction time and that the substrate preference in TET2 is caused not by altering the formation of the Fe^{IV}-oxido species but acts through the changes in the hydrogen abstraction step, which is the rate determining step.[38b]

2.2.7. Surface plasmon resonance (SPR) spectroscopy

Albeit surface plasmon resonance (SPR) spectroscopy (Biacore) has to our knowledge so far not been reported to be used for the characterization of AlkB-family oxygenases, SPR spectroscopy allows the *in situ* real-time and label-free detection of biomolecular interactions, which could be utilized for their functional investigation. Here the target molecule (i.e. protein or nucleic acid fragment) is immobilized on a prepared gold sensor surface and a solution with the potential interaction partner is applied through flow cells. Alteration of the mass on the sensor surface impacts on the intensity of the reflected, incident polarized light beam at a specific angle (=resonance

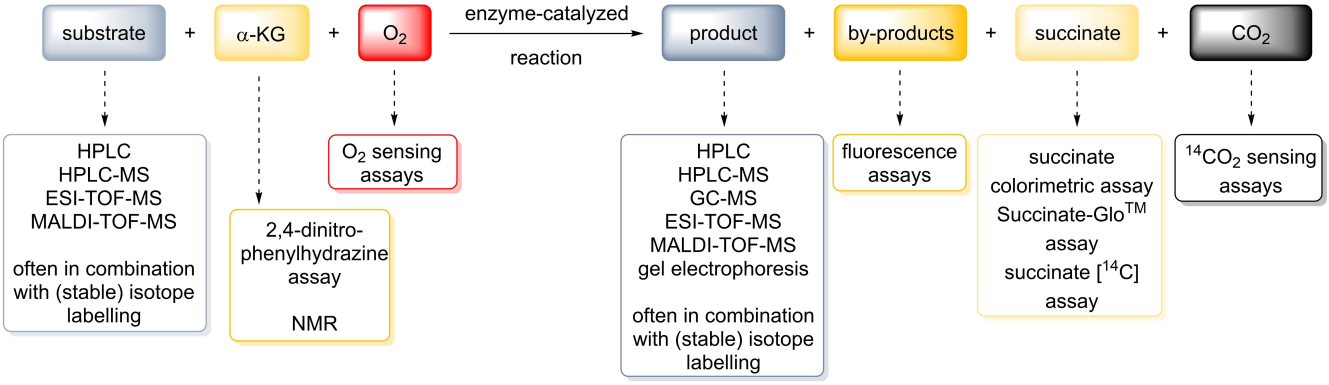

Scheme 3. Different possibilities to monitor activity of Fe^{2+}/α-KG-dependent enzymes. "Substrate" here refers only to the nucleic acid substrate, not α-KG or O_2. Similarly, "product" refers only to the nucleic acid product. Any other products are considered "byproducts".

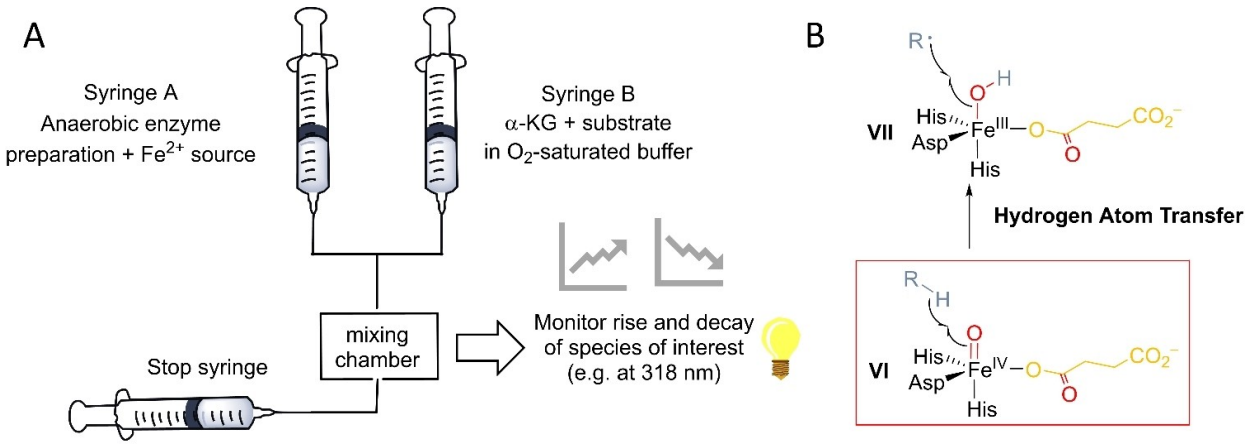

Figure 10. Stopped-flow with UV-Vis detection can be used to gain information how different substrates affect the formation and consumption of reactive species. A. Example of stopped flow setup. B. Formation of species **VI** as well as its decay can be monitored with stopped flow. In the case of TET2, it was reported that with 5mdC-containing DNA the decay was faster than for 5hmdC or 5fdC containing DNA, but the emergence of species **VI** was similar for all three. Thus, the hydrogen atom transfer step is likely the one that causes the observed substrate preference in TET2.

angle), from which information about binding affinity, dissociation and association rate constants and thermodynamic parameters, such as entropy, enthalpy, and activation energy can be deduced.[71] Luo, Hu and co-workers used this technique to assess the interaction of TET2 with 5mdC-, 5hmdC- and 5fdC-containing DNA.[38b] The authors used biotinylated DNA (26 base pairs including the cytosine modification of interest) that was immobilized on a streptavidin-chip to monitor the kinetics of association and dissociation of TET2 to the three DNA substrates. Since no significant differences were observed, they concluded that the DNA-binding affinity to TET2 is comparable between the substrates and that this is not the source of substrate preference for 5mdC-containing DNA.

3. Kinetic Investigations using Different Assay Methods

Over the past decades multiple assays have been developed that give insight into the kinetics and substrate turnover of Fe^{2+}/α-KG-dependent enzymes that play a role in epigenetics and DNA repair, based on measurements of substrates and products of the enzymatic reaction. For nucleic acid substrates, the utilization of substrates and generation of products can be directly monitored by HPLC and different mass spectrometry (MS) methods (Scheme 3). Oxygen consumption can likewise be followed as well as the formation of CO_2 byproduct after the active species has been generated. Popular assays also rely on the emergence of succinate as byproduct of the C–H activation reaction and thus provide an indirect analysis of substrate turnover. For those enzymes eliminating alkyl groups from their substrates, the small molecules which are released might serve as activity indicators as well. Typically, combinations of these approaches are employed to obtain a broad image of enzyme activity. In the following text, the different methods are critically discussed.

3.1. Direct analysis of enzyme-specific substrates and products

A common practice for the study of enzymes is the analysis of the substrate or product after enzymatic treatment by a variety of techniques. In particular liquid, but also gas chromatography (both stand-alone and coupled with mass spectrometry) are widely used methods to determine substrate consumption and/or product formation. GC or HPLC and GC- or HPLC-MS analysis allow for the investigation of both *in vitro* and *in vivo* systems, if the samples are prepared accordingly.[22b,72] Various excellent descriptions of analytical procedures can be found in the literature.

For example, HPLC analysis of reaction products using isotopically labelled substrates in combination with measuring of the radioactivity in the sample can be used to track the demethylation activity of EcAlkB or related enzymes. Here, the methyl (or more general alkyl) group on oligonucleotides is [^{14}C]-labelled and the radioactive activity in the supernatant analyzed by scintillation counting, giving detailed information on the activity of the studied enzymes. In 2003 Hausinger, Sedgwick and co-workers applied this combined procedure to show for the first time that EcAlkB demethylates 1mdA and 3mdC in DNA directly to dA and dC.[20d] They used the potent methylating agent [^{14}C]-methyl iodide to methylate oligonucleotides (poly(dA) and poly(dC)) in combination with wt-EcAlkB or some EcAlkB variants. Following the enzymatic reaction, the nucleobases were digested and analyzed by HPLC, and the radioactivity in the supernatant determined by scintillation counting of the collected fractions. This was complemented by measuring the radioactivity of the ethanolic supernatants containing the eliminated formaldehyde. The study found that,

while 3mdA and 7mdA had also formed, they were not demethylated by EcAlkB. In a similar way, Krokan *et al.* tracked the fate of [^{3}H]-methylated DNA and RNA substrates to study EcAlkB, hAlkBH2 and hAlkBH3.[22b] However, they focused their experiments on the detection of nucleosides and concluded, among others, that hAlkBH2 is more active on dsDNA than on ssDNA and that EcAlkB is involved in RNA repair. Kizaki and Sugiyama used HPLC to study TET activity on a hexameric substrate comprising only guanine, cytosine and 5mdC. They reported that, under *in vitro* conditions (55.4 μM CGmCGCG; 7.29 μM mTET1 active domain 1376–2039; 37 °C; 40 min) 5mdC is quickly converted to 5hmdC, already reaching its maximum level after only a few minutes incubation time. 5hmdC is further transformed to 5fdC, which reaches steady levels in a dynamic equilibrium after 10 min incubation, as it is continuously produced from 5hmdC, but also consumed to form 5cadC.[72a]

Currently, mostly MS-based techniques are applied, as the instruments are sensitive (detection limits down to a low femtomole range) and allow to detect epigenetic modified bases in a nucleic acid sample directly. For example, in 2019 Carell *et al.* published a protocol on the quantification of non-canonical natural DNA nucleosides, where they describe a short (14 min/sample) method in which DNA is extracted and digested, the sample diluted with isotopically labeled internal standards (^{13}C and/or ^{15}N) that have similar chromatographic and fragmentation properties, followed by LC-MS quantification of the nucleosides.[73] By now this method has been adapted and used by several groups, for instance to determine the influence of epigenetics on cancer or to generally study the turnover of genomic methylcytosine in pluripotent cells.[72b,74] This method has also been used to detect levels of 5mdC, 5fdC and 5cadC after oxidation of a 5mdC containing oligomer by a TET biomimetic.[75] An excellent review was published on the detection, structure and function of modified DNA bases by Balasubramanian *et al.* in 2019, which dives into this topic in greater detail.[76]

In addition to HPLC analysis, gas chromatography has been utilized for the detection of DNA fragments. In 2015, Sowers *et al.* used a combination of HPLC separation and GC-MS analysis (detection limit also in the low femtomole range) to determine the amounts of cytosine modifications (probably as a result of TET activity) in rodent brain cells.[77] While HPLC(-MS) can be used to detect both nucleoside and nucleobase substrates, GC-MS requires the digestion of DNA to the nucleobases since (derivatized) nucleosides are not stable under the conditions of GC-MS. Derivatization of nucleobases with for example *N*,*O*-bis(trimethylsilyl)trifluoroacetamide (BSTFA) in acetonitrile and subsequent detection as well as quantification has been reported for a range of epigenetically relevant cytosine derivatives as well as for artificial DNA bases.[78]

Not only single nucleosides or nucleobases can be processed with HPLC, DNA oligomers can also serve as analytes. In 2009, Yu and Hunt published their results on EcAlkB activity on trimeric (TmdCT or TmdAT or TεdAT) or pentameric (3mdC or 1mdA in different combinations with C/T/A, as well as 1mdG, 3mT and εA) substrates.[79] They found that 3mdC and 1mdA lesions were repaired three orders of magnitude faster than εA in the trimer, whereas repair activity on 1mdG and 3mT was decreased 10.000-fold compared to 1mdA or 3mdC. Similarly, Maciejewska and co-workers performed another in-detail study of EcAlkB activity on different randomly methylated pentamers containing 3mdC, εdA, εdC, hydroxyethyl C (HEC), or hydroxypropyl C (HPC).[20g] In an HPLC-based assay, they optimized the pH as well as the Fe^{2+} and α-KG concentrations and calculated the rate constants for repair efficiency for each of these substrates. The authors observed the pH optimum for oxidation to consistently be one unit below the pK_a of the substrate in all cases, indicating that cationic protonated substrates are preferred. Interestingly, the Fe^{2+} dependence was found to be inversely correlated to the pH, with higher optimum Fe^{2+} concentration at lower pH values. In contrast, no significant dependence for the α-KG concentration was detected.

In addition to chromatographic separation and subsequent quantification of substrates and reaction products, stand-alone MS analysis played a critical role in assessing enzyme activity.[20f,80] Essigmann *et al.* used a variety of MS methods (MALDI-TOF-MS, ESI-TOF-MS or Q-TOF-MS) without prior digestion to elucidate the scope of nucleic acid lesions that can be removed by EcAlkB *in vitro* as well as the kinetics of the repair reactions. By tracking the −4 charge state of an 16mer ssDNA oligonucleotide, they identified a variety of modifications EcAlkB is able to act upon, which include, among others, 1mdA, etheno-A, 6mdA (with an intermediate described in EcAlkB hydroxylation studies for the first time), 2mdG, 2etdG, furyl-G, THF-G, "α-hydroxypropanyl"-G, "γ-hydroxypropanyl"-G and "malonyl"-G (Scheme 2). These mainly toxicologically interesting alkylated nucleobases either are lesions found to be formed in the presence of metabolic side products and external chemicals, or served as substrate models for more complex lesions found *in vivo (*especially furyl-G and THF-G). Moreover, they were able to observe some intermediates of the repair mechanism and corroborated parts of their findings *via* GC-MS experiments.

Moreover, upon incubation of hAlkBH1 with oligomeric DNA substrates and subsequent analysis of the reaction products by gel electrophoresis by Hausinger and co-workers, revealed that hAlkBH1 is also able to cleave non-methylated DNA oligomers.[81] The authors found that this AP-lyase activity is neither dependent on Fe^{2+} nor α-KG, nor serves ascorbate as an activator as had been observed for the demethylation activity of hAlkBH1.[21h] In addition, ssDNA-cleavage by AlkBH1 was also found to be unaffected by the presence of EDTA, Mg^{2+}, Mn^{2+} or Zn^{2+} and by incorporating THF as an abasic-site analogue into their substrates, Hausinger and team were able to show that hAlkBH1 cleaved the 3′-position of abasic sites.[81] Cleavage of specific DNA sequences by restriction enzymes and glycosylases followed by gel-electrophoretic analysis can be a useful low-effort tool to investigate enzymatic modification of nucleobases. The main requirement is, however, that such a DNA-cleaving protein (as described above for hAlkBH1, this can also be the examined enzyme itself) is available which is able to hydrolyze a DNA strand in the presence of either the substrate or product base of the enzyme in question. For example, a *Bacillus subtilis* alkyl adenine DNA glycosylase was used by O'Brien *et al.* to study EcAlkB kinetics on 1mdA and εdA which

are both excised by the glycosylase initiating a DNA strand break under basic conditions.[82] Analysis of the fragmented and unfragmented oligonucleotides (carrying a fluorescent marker) on a gel allowed for a simple read-out of EcAlkB activity. It should be noted that they found rapidly decreasing instantaneous reaction rates in their steady-state kinetic assays which they attributed to potential self-inactivation of EcAlkB upon DNA binding. This might originate from self-hydroxylation at Trp178 and might be a potential cause for variable and inaccurate (hence not reproducible) kinetic parameters dependent on the time-scale of the measurement. To prevent this, the authors also performed steady-state experiments with 1mdA and εdA-containing DNA fragments in direct competition to each other, as well as single-turnover experiments. However, these approaches do not provide the same information as conventional steady-state kinetic assays and should rather be seen as complementary experiments.

3.2. Direct analysis of co-substrates and byproducts

Besides relying on the detection of the nucleic acid substrates or products, a variety of approaches are available which exploit the conversion of the co-substrates, α-KG and O_2, to the co-products succinate and carbon dioxide, specific substrate-independent hallmarks of the Fe^{2+}/α-KG-dependent dioxygenase catalyzed reactions. Moreover, the AlkB dealkylase families produce further co-products, primarily formaldehyde or its homologues. Hence, this class of enzymes provides a diverse number of targets for activity studies, which are often combined to give a full picture of the enzymatic properties. Although the fates of α-KG or its oxidation products are commonly tracked when investigating Fe^{2+}/α-KG-dependent dioxygenases, such as deacetoxycephalosporin C synthase, prolyl hydroxylase and TauD,[83] the AlkB- and TET family enzymes have not been analyzed in detail *via* one of these strategies so far. Indeed, α-KG has not yet been a considerable factor of interest in kinetic studies, although α-KG turnover (or succinate formation) can be easily monitored with ^{1}H-NMR spectroscopy.[84] Nevertheless, the formation of either carbon dioxide or succinate has been followed in a series of assays. In both cases, quantitative radioactivity measurements are typically undertaken after supplementing a mixture of approximately 10% [^{14}C]-labelled α-KG in unlabeled α-KG. Isotopic labelling of the 1-carbon enables $^{14}CO_2$ production monitoring[83b] (after capturing with hydroxides), whereas 5-[^{14}C]-α-KG application allows for observation of 1-[^{14}C]-succinate.[85] It is noteworthy, however, that a recent study has found that α-KG can, albeit slowly, be decarboxylated non-enzymatically in the presence of anti-oxidants like ascorbate or dithiothreitol, which are commonly used in activity studies of Fe^{2+}/α-KG-dependent (di)oxygenases.[86] This was attributed to the formation of hydrogen peroxide from the anti-oxidant and dioxygen, which might then mediate α-KG decarboxylation. In light of this, it might be worth performing assays tracking succinate or CO_2 formation with additional controls, especially when high concentrations of anti-oxidant or long reaction times (*e.g.*, for inhibition studies or for investigation of variants with reduced activity) are required, to ensure the robustness of the acquired data. Unrelated to ascorbate/dithiothreitol, but along the line of commonly added (anti-oxidant) additives that may interact with metalloenzymes, Rodríguez-Maciá, Birrell and team have recently shown that for hydrogenases, the addition of the often-used reductant sodium dithionite influences the mechanism and thus spectroscopic features of this iron enzyme.[87] However, it should be noted that for the Fe^{2+}/α-KG-dependent oxygenase TfdA (2,4-dichlorophenoxyacetate/α-KG dioxygenase) it was reported that addition of dithionite remediated the effects of self-hydroxylation to some extent.[70] Recently, Haigis and co-workers have established a colorimetric α-KG detection assay for the prolyl hydroxylases domain protein family.[88] The α-KG consumption assay, relying on the derivatization of α-KG with 2,4-dinitrophenylhydrazine (2,4-DNPH, Scheme 5) in the presence of concentrated base (Scheme 4), could also find use for the enzymes described in Table 1. Succinate does not form the colored product. However, it should be considered that 2,4-DNPH might react with formaldehyde, which can be a reaction product by AlkB-family dioxygenases (e.g. from 6mA demethylation).

3.2.1. Carbon dioxide production assays

Based on $^{14}CO_2$ quantification, hAlkBH1 was described as a histone demethylase, which regulates the methylation status of histone H2A, by Larsen and co-workers.[21a] Pollard *et al.* assessed the activity of hAlkBH5 towards a variety of methylated ssDNA substrates by this technique.[89] They first confirmed that hAlkBH5 is a Fe^{2+}/α-KG-dependent dioxygenase by identifying one of their characteristic activity features: the so-

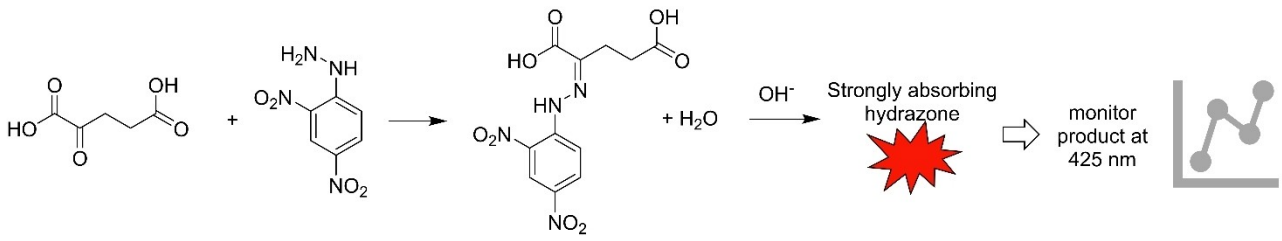

Scheme 4. Assay based on capturing α-KG with 2,4-DNPH and subsequent treatment with base to yield a colored hydrazone product which can be quantified using UV-Vis absorption spectroscopy.

called uncoupled decarboxylation reaction,[90] which describes the oxidation of α-KG followed by elimination of CO_2 in the absence of a substrate. This reaction was found to be dependent on the presence of Fe^{2+} and the cofactor ascorbate, as expected for a Fe^{2+}/α-KG-dependent dioxygenase.[89] Analogously, the Fe^{2+} and ascorbate dependent decarboxylation activity of hAlkBH1 was demonstrated by Krokan *et al.*[21h] Pollard and team further measured $^{14}CO_2$ production to gain information on the dioxygen dependence of the hAlkBH5 uncoupled decarboxylation, which is strongly impaired under anaerobic conditions.[89] They linked this *in vitro* behavior to the upregulation of hAlkBH5 under hypoxia *in vivo* and proposed a specific function for AlkBH5 in hypoxic cells. However, no significant increase in CO_2 production in the presence of methylated oligonucleotide substrates was found and the authors concluded that hAlkBH5 does not function as DNA demethylase.[89]

Other family-members whose activity was examined by analyzing the $^{14}CO_2$ capture method were AlkBH2 and AlkBH3 (for their functionality in substrate recognition)[91] and the three TET proteins.[92]

3.2.2. Succinate production assays

In 1990, an activity assay based on the formation of 1-[^{14}C]-succinate was developed by Kaule and Günzler for the investigation of prolyl 4-hydroxylase, which applies to any kind of Fe^{2+}/α-KG-dependent dioxygenase.[85a] Since the radioactively labelled oxidation co-product is not volatile, capture is not required and it can be quantified *via* scintillation counting. However, unreacted 5-[^{14}C]-α-KG must be removed beforehand, for instance, through precipitation as a hydrazone.[83a,93] This methodology was used to investigate several viral AlkB homologues which show activity against methylated nucleobases, especially in RNA context.[93] Krokan and co-workers reported hAlkBH1 to act on methylated adenines and cytosines in both mitochondrial DNA and RNA.[21h] Further, a lack of succinate release, in combination with other methods, implicated a lack of DNA demethylase activity in the case of a yeast AlkBH1[94] (even though it showed weak DNA lyase activity as found for hAlkBH1 by Hausinger *et al.*[81]). Analogous to the $^{14}CO_2$ assay, 1-[^{14}C]-succinate accumulation can be utilized to detect uncoupled decarboxylation. This approach was chosen by Andersson *et al.*, who investigated the general activity of AlkBH4, the substrate of which has not yet been identified.[95] Besides, different succinate-sensing strategies are (commercially) available, including colorimetric, coupled enzymatic assays.[83d,96]

3.2.3. Dioxygen consumption assays

Molecular oxygen is the second essential co-substrate of Fe^{2+}/α-KG-dependent dioxygenases. Consequently, oxygen levels have been shown to modulate TET reactivity in tissues and hypoxia is known as an important factor in epigenetic regulation and disease.[97] Surprisingly, O_2-levels in assays of epigenetically relevant enzymes are rarely controlled nor monitored *in vitro*, but have been reported for other Fe^{2+}/α-KG-dependent enzymes and related non-heme enzymes (for example, by monitoring the decrease of atmospheric dioxygen levels).[66b,98] Depending on the assay design, this is likely to be due either to the necessity to initially prepare the reaction mixture under strictly oxygen-free conditions, or because the concentration is difficult to control without specialized equipment (*e.g.* oxygen electrode). For example, Sedgwich, Hausinger *et al.* monitored the consumption of oxygen by EcAlkB in the presence of 1mdA- or 3mdC-containing DNA-substrates potentiometrically, when they first characterized the enzyme's mode of action in detail.[20d] Using a Clark-type electrode[99] as an oxygen sensor, they showed that EcAlkB uses up significant amounts of dioxygen, if a suitable substrate is available, and that these amounts are stoichiometrically related to substrate oxidation. Since availability of dioxygen impacts on the activity of Fe^{2+}/α-KG-dependent dioxygenases both *in vitro* and *in vivo*, these enzymes are commonly referred to as "physiological oxygen sensors" and contribute to metabolic changes under hypoxia.[100] Proteins as tightly connected to epigenetic processes as AlkB and TET family enzymes might be critical players in the cellular response to hypoxia as well as in disease and cancer development. The diminishing activity of hAlkBH5 with decreasing dioxygen concentration *in vitro*, demonstrated by Pollard and co-workers, and its consequent upregulation under such conditions *in vivo* provide some evidence for this connection.[89] TET1 and TET2 kinetics were measured more thoroughly with respect to O_2 availability by Koivunen *et al.*[92] Here Michaelis-Menten analysis revealed a K_M around 30 μM in both cases. In contrast, for the proline-4-hydroxylases which modify the hypoxia-inducible transcription factors (HIF-P4Hs) and initiate the cellular hypoxia response through being inhibited at dropping oxygen levels, a $K_M = 230–250$ μM was reported.[101] Thus, it was concluded that TET enzymes remain active even under hypoxic stress.[92] However, additional comparable studies providing detailed insight into those enzymes' behavior during dioxygen deficiency are required.

A remarkable, very different oxygen-sensing approach to measuring TET2 kinetics was developed by Dai, Zhang and co-workers in 2018, which is based on the luminescence of a Cu^+-containing metal-organic framework (MOF, Figure 11).[102] Here the MOF MLCT phosphorescence is quenched by interaction with triplet state molecules, such as dioxygen in its ground state. Due to the high porosity of the MOF, the luminescence intensity changes reversibly upon alteration of the dioxygen concentration (more rapidly than the enzymatic O_2 consumption rate) and this heterogeneous sensor does not interfere with the enzymatic reaction. Hence, it represents a versatile tool for the kinetic investigation of Fe^{2+}/α-KG-dependent dioxygenases allowing for real-time, continuous monitoring. Based on this method, the authors were able to identify lag, linear and non-linear phases of the TET-mediated 5mdC oxidation process. The real-time nature of the assay allowed for relatively accurate determination of reaction velocity in comparison to other more common methods (LC-MS/MS, $^{14}CO_2$ radioisotope assay, global

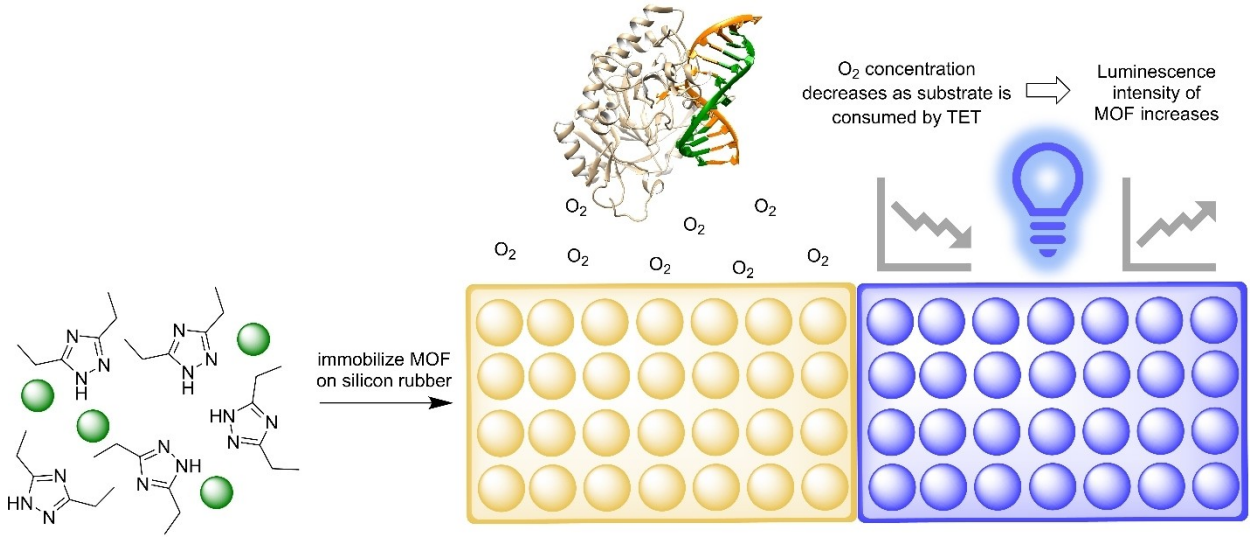

Figure 11. Real-time continuous monitoring of TET activity by means of an MOF-based O_2 sensor. After assembly of the MOF from the starting materials (green spheres represent copper ions) on silicone rubber (golden plate) the system exhibits little luminescence due to the quenching by O_2. As oxygen is consumed during the enzymatic reaction (structural representation of TET is shown as an example, green and orange represent opposite strands of DNA in the substrate), the MOF becomes luminescent (blue plate).

5hmdC quantification), which can only provide average values and are snapshots at certain time points in addition to being more time-consuming. Due to differences in the methods used, distinct K_M and k_{cat} values for TET2 towards 5mdC in ssDNA were reported and compared to previous studies,[13,38b,92] which also confirmed the finding that TET enzymes only show low sensitivity against O_2 concentration changes.[92]

3.2.4. Assays based on co-product elimination from the main substrate

As already mentioned above, the AlkB enzyme family produces small organic molecules as side products. Most often, this is formaldehyde (in the case of methylated bases), but more complex aldehydes can be eliminated as well, depending on the structure of the alkyl modification (see Scheme 2). These side products provide viable and reasonably convenient pathways to study enzyme activity. Firstly, short alkyl groups, and especially methyl groups, can easily be artificially introduced into DNA substrates, which is particularly interesting for isotopic and radioactive labelling strategies (see above). Secondly, the highly electrophilic reactivity of aldehydes towards a variety of functionalities, such as amines, hydroxylamines or hydrazines can be exploited in chemical capture approaches. Thirdly, a series of enzymes are known that process the cytotoxin formaldehyde and can be employed for coupled enzymatic assays. Formaldehyde can also be tracked when a ^{13}C-labelled methyl group is incorporated in the substrate. This was demonstrated by Schofield with histone demethylase JMJD2E and labelled tri- and dimethylated peptides and using 1D ^{13}C heteronuclear single quantum coherence (HSQC) NMR spectroscopy.[84b]

When DNA substrates are artificially (hyper)methylated, radioactive [^{14}C]- or [^{3}H]-containing methyl groups can be introduced *via* common methylation agents such as methyl iodide, dimethyl sulphate or methyl nitrosourea. Upon demethylase treatment, they are eliminated as radioactively labelled formaldehyde, which can be quantified by scintillation counting after DNA precipitation. This approach was utilized by Sedgwick, Hausinger *et al.*, in combination with other strategies, to test EcAlkB activity against randomly [^{14}C]-methylated poly(dA) and poly(dC) oligonucleotides.[20d] In a comparative study of EcAlkB and its human homologues hAlkBH1, hAlkBH2 and hAlkBH3, [^{14}C]-methyl groups were introduced as well.[22a] While hAlkBH1 appeared active on neither 1mdA nor 3mdC, hAlkBH2 and hAlkBH3 repaired both lesions in single-stranded and double-stranded DNA, although with different substrate preference. Another group proposed that hAlkBH2 prefers dsDNA, whereas hAlkBH3 rather requires ssDNA or even RNA,[22b] based on [^{3}H]-radioactivity measurements. Subsequently, it was shown that the substrate specificity of hAlkBH2 is dependent on the Mg^{2+} concentration.[20e] EcAlkB, hAlkBH2 and hAlkBH3 were also tested for their demethylation reactivity towards 3mT.[20h] Later, Krokan and co-workers reported that hAlkBH1 acts even as 3mdC and m^3C demethylase in mitochondrial DNA and RNA.[21h] In conjunction with the 1-[^{14}C]-succinate method, radioactive formaldehyde monitoring provided access to the activities of several viral AlkB homologues.[93] An assay measuring depletion of a tritiated substrate was further utilized in a detailed study on the structure and function of wildtype hAlkBH3.[33]

When aldehydes react with hydroxylamines or hydrazines, oximes and hydrazones, respectively, are virtually quantitatively formed. This chemical behavior was exploited by Sedgwick, Hausinger *et al.* when they subjected unlabeled hypermethylated poly(dA) and poly(dC) oligonucleotides to EcAlkB

treatment.[20d] Their protocol involved the capture of formaldehyde with (pentafluorophenyl)hydrazine (Scheme 5) and quantification of this adduct *via* GC-MS analysis. The chemical derivatization approach can also be merged with other strategies. This is exemplified by Sedgwick *et al.* who studied EcAlkB activity on 1mdA, 3mdC and 1-ethyldA by condensation of [^{14}C]-formaldehyde or [^{14}C]-acetaldehyde with 2,4-DNPH (Scheme 5), followed by HPLC analysis and scintillation counting.[22a] Another common reagent for derivatization prior to GC-MS analysis is *O*-(pentafluorobenzyl)hydroxylamine (Scheme 5) that has been applied in a kinetic investigation of EcAlkB DNA repair.[80b] Even though not an elimination product, aldehyde reactivity towards hydrazines has further been made use of in an *in vitro* study on whether iterative TET1 oxidation of cytosine 5-substituents occurs in a consecutive or rather a distributive manner.[103] Therefore, a chemical probe reagent containing an aldehyde-sensitive hydrazine moiety, to react with the TET intermediate 5fdC, and a fluorescent pyrene function was utilized (2-hydrazineyl-*N*-(pyren-1-yl)acetamide, Scheme 5).

The high reactivity against *N*-nucleophiles makes formaldehyde a potent cytotoxin. Since several metabolic pathways yield formaldehyde as byproduct, many organisms possess formaldehyde dehydrogenases (FDHs), rendering it harmless by oxidation.[104] The redox co-factor NAD^+ is simultaneously reduced to NADH which shows fluorescence at around 460 nm.[105] Thus, kinetic assays coupling nucleic acid demethylase activity to formaldehyde oxidation are viable, which was, for instance, exploited by Sedgwick, Hausinger *et al.*[20d] Roy and Bhagwat later achieved advancement in terms of sensitivity of that assay.[106] They exchanged the redox co-factor NAD^+ by 3-acetylpyridine adenine dinucleotide ($APAD^+$) and reached a 30 times higher extinction coefficient with a slight shift of excitation and luminescence wavelengths (363 nm and 482 nm, respectively), which allows working with sub-nanomole amounts of methylated substrate. With this assay, they investigated Michaelis-Menten kinetics of EcAlkB towards 1mdA

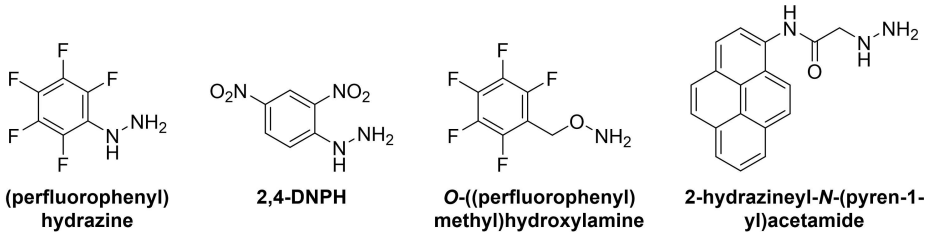

Scheme 5. Different hydrazines and hydroxylamines that have been used to capture formaldehyde or derivatize other molecules of interest with aldehyde functional groups such as 5fC. The abbreviation of 2,4-dinitrophenylhydrazine (2,4-DNPH) is indicated as this structure was mentioned regularly in this text.

Table 2. Summary of methods discussed in section 2 of this review with selected accessible features of the system of interest.

Characterization method	Type of information gained	Advantages/disadvantages/comments
X-ray crystallography	Molecular structural details of substrate recognition	Applicable for resting state (inhibitor might be needed); requires crystals; sometimes *in crystallo* reactions possible to track intermediate species
NMR spectroscopy	Changes in flexibility/rigidity of entire protein upon substrate and co-factor or product binding and release	Size limitation for protein; isotope labelling often necessary
EPR spectroscopy	Coordination environment of metal in the active site (*e.g.* Number of N-donor atoms bound to metal), geometry	Fe^{2+} difficult to observe without highly specialized equipment, thus Cu^{2+} often used instead
Fluorescence spectroscopy	Local protein dynamics, folding and substrate binding	Fluorescent labels or antenna features need to be present on enzyme or substrate; thermodynamic and kinetic information (combined with stopped flow) accessible
Isothermal titration calorimetry	Thermodynamics of metal and substrate binding to protein, binding constants, and kinetics of substrate turnover	No labels necessary
CD spectroscopy	Thermal stability of protein, changes in secondary and tertiary structure upon substrate or co-factor binding	Additives (*e.g.* buffer, or ascorbate) can obscure signal
UV/Vis spectroscopy	Information on active site features (binding of α-KG to Fe^{2+}) by *e.g.* monitoring MLCT absorption bands	Kinetic information (combined with stopped flow) on rise and decay of certain intermediates accessible.
SPR spectroscopy	Real-time and label-free detection of biomolecular interactions to determine thermodynamic and kinetic parameters	Tag or label on protein or substrate for immobilization necessary; interaction can be studied under changing conditions

and 3mdC and obtained markedly distinct values than from previous studies,[20e,107] that they attributed to differences in DNA substrate sequence and secondary structure formation. They additionally noticed that Tris can serve as substrate for FDH and is thus an unsuitable buffer component for this type of assay. Further, it should be noted that Tris can react with formaldehyde itself in a Schiff base reaction.[108]

4. Conclusion

The study of DNA and RNA repair and modification mechanisms, both in and outside of epigenetics context, has seen remarkable progress in the last years. The collective effort of researchers across a broad range of disciplines, from biochemistry to inorganic chemistry, has led to a fair understanding of the mode of action of EcAlkB, AlkBH, TET and many other enzymes. However, these studies often apply a limited number of specific methods which has created "white spots" on the map of enzymatic DNA modification and repair. In addition, detailed mechanistic understanding has mostly been extrapolated from TauD (using Mössbauer and MCD among other methods). By collecting a comprehensive overview on used methods (Table 2) as well as the most recent information in this review, we hope to address this and give researchers in the field the opportunity to learn about available spectroscopic methods and assay setups that would be complementary and useful for their studies. One problem is the multitude of techniques that make it difficult to directly compare *e.g.* kinetic parameters from different studies. In addition, one recognized major pitfall in working with isolated Fe^{2+}/α-KG-dependent enzymes is their notorious ability to autoxidize and self-hydroxylate in the presence of molecular dioxygen but absence of substrate. Since *in vivo* tissue oxygen levels are generally low, better regulated and controlled, it stands to question how kinetic parameters determined *in vitro* reflect the *in vivo* situation. Thus, these results should always be interpreted with caution.

Author contributions

All authors were involved in literature search, review and writing of this manuscript.

Acknowledgements

The authors thank Angie Kirchner, Karina Betuker and Katie Fisher for proofreading. A grant from the Deutsche Forschungsgemeinschaft (DFG, German Research Foundation) – SFB 1309-325871075 is gratefully acknowledged. N.S.W.J. acknowledges financial support by the Studienstiftung des Deutschen Volkes and the Joachim Herz Stiftung. Open Access funding enabled and organized by Projekt DEAL.

Conflict of Interest

The authors declare no conflict of interest.

Keywords: AlkBH · DNA methylation · epigenetics · spectroscopy · TET enzymes

[1] a) O. Hayaishi, M. Katagiri, S. Rothberg, *J. Am. Chem. Soc.* **1955**, *77*, 5450–5451; b) H. S. Mason, W. L. Fowlks, E. Peterson, *J. Am. Chem. Soc.* **1955**, *77*, 2914–2915.
[2] a) H. Hanauske-Abel, V. Günzler, *J. Theor. Biol.* **1982**, *94*, 421–455; b) J. C. Price, E. W. Barr, B. Tirupati, J. M. Bollinger, C. Krebs, *Biochemistry* **2003**, *42*, 7497–7508; c) J. C. Price, E. W. Barr, T. E. Glass, C. Krebs, J. M. Bollinger, *J. Am. Chem. Soc.* **2003**, *125*, 13008–13009; d) D. A. Proshlyakov, T. F. Henshaw, G. R. Monterosso, M. J. Ryle, R. P. Hausinger, *J. Am. Chem. Soc.* **2004**, *126*, 1022–1023; e) J. C. Price, E. W. Barr, L. M. Hoffart, C. Krebs, J. M. Bollinger, *Biochemistry* **2005**, *44*, 8138–8147.
[3] a) S. Goudarzi, S. R. Iyer, J. T. Babicz, J. J. Yan, G. H. J. Peters, H. E. M. Christensen, B. Hedman, K. O. Hodgson, E. I. Solomon, *Proc. Natl. Acad. Sci. USA* **2020**, *117*, 5152–5159; b) E. I. Solomon, K. M. Light, L. V. Liu, M. Srnec, S. D. Wong, *Acc. Chem. Res.* **2013**, *46*, 2725–2739.
[4] M. J. Ryle, R. Padmakumar, R. P. Hausinger, *Biochemistry* **1999**, *38*, 15278–15286.
[5] J. C. Price, E. W. Barr, B. Tirupati, J. M. Bollinger Jr., C. Krebs, *Biochemistry* **2003**, *42*, 7497–7508.
[6] D. A. Proshlyakov, J. McCracken, R. P. Hausinger, *J. Biol. Inorg. Chem.* **2017**, *22*, 367–379.
[7] P. J. Riggs-Gelasco, J. C. Price, R. B. Guyer, J. H. Brehm, E. W. Barr, J. M. Bollinger, C. Krebs, *J. Am. Chem. Soc.* **2004**, *126*, 8108–8109.
[8] E. L. Hegg, L. Que Jr., *Eur. J. Biochem.* **1997**, *250*, 625–629.
[9] P. K. Grzyska, E. H. Appelman, R. P. Hausinger, D. A. Proshlyakov, *Proc. Natl. Acad. Sci. USA* **2010**, *107*, 3982–3987.
[10] S. Sinnecker, N. Svensen, E. W. Barr, S. Ye, J. M. Bollinger, F. Neese, C. Krebs, *J. Am. Chem. Soc.* **2007**, *129*, 6168–6179.
[11] J. A. Hangasky, H. Gandhi, M. A. Valliere, N. E. Ostrom, M. J. Knapp, *Biochemistry* **2014**, *53*, 8077–8084.
[12] a) C. W. John, G. M. Swain, R. P. Hausinger, D. A. Proshlyakov, *J. Phys. Chem.* **2019**, *123*, 7785–7793; b) S. D. Wong, M. Srnec, M. L. Matthews, L. V. Liu, Y. Kwak, K. Park, C. B. Bell III, E. E. Alp, J. Zhao, Y. Yoda, *Nature* **2013**, *499*, 320–323.
[13] B. Thienpont, J. Steinbacher, H. Zhao, F. D'Anna, A. Kuchnio, A. Ploumakis, B. Ghesquière, L. Van Dyck, B. Boeckx, L. Schoonjans, E. Hermans, F. Amant, V. N. Kristensen, K. P. Koh, M. Mazzone, M. L. Coleman, T. Carell, P. Carmeliet, D. Lambrechts, *Nature* **2016**, *537*, 63–68.
[14] R. Ougland, T. Rognes, A. Klungland, E. Larsen, *J. Mol. Cell Biol.* **2015**, *7*, 494–504.
[15] M. G. Vander Heiden, L. C. Cantley, C. B. Thompson, *Science* **2009**, *324*, 1029–1033.
[16] a) S. Nowicki, E. Gottlieb, *FEBS J.* **2015**, *282*, 2796–2805; b) M. Yang, T. Soga, P. J. Pollard, *J. Clin. Invest.* **2013**, *123*, 3652–3658.
[17] L. Dang, D. W. White, S. Gross, B. D. Bennett, M. A. Bittinger, E. M. Driggers, V. R. Fantin, H. G. Jang, S. Jin, M. C. Keenan, K. M. Marks, R. M. Prins, P. S. Ward, K. E. Yen, L. M. Liau, J. D. Rabinowitz, L. C. Cantley, C. B. Thompson, M. G. Vander Heiden, S. M. Su, *Nature* **2009**, *462*, 739–744.
[18] W. Xu, H. Yang, Y. Liu, Y. Yang, P. Wang, S. H. Kim, S. Ito, C. Yang, P. Wang, M. T. Xiao, L. X. Liu, W. Q. Jiang, J. Liu, J. Y. Zhang, B. Wang, S. Frye, Y. Zhang, Y. H. Xu, Q. Y. Lei, K. L. Guan, S. M. Zhao, Y. Xiong, *Cancer Cell* **2011**, *19*, 17–30.
[19] a) I. Martinez-Reyes, N. S. Chandel, *Nat. Commun.* **2020**, *11*, 102; b) H. Yang, H. Lin, H. Xu, L. Zhang, L. Cheng, B. Wen, J. Shou, K. Guan, Y. Xiong, D. Ye, *Cell Res.* **2014**, *24*, 1017–1020.
[20] a) V. Koliadenko, T. Wilanowski, *Free Radical Biol. Med.* **2020**, *146*, 1–15; b) T. Sun, R. Wu, L. Ming, *Biomed. Pharmacother.* **2019**, *112*, 108613; c) P. Ø Falnes, R. F. Johansen, E. Seeberg, *Nature* **2002**, *419*, 178–182; d) S. C. Trewick, T. F. Henshaw, R. P. Hausinger, T. Lindahl, B. Sedgwick, *Nature* **2002**, *419*, 174–178; e) P. Ø Falnes, M. Bjørås, P. A. Aas, O. Sundheim, E. Seeberg, *Nucleic Acids Res.* **2004**, *32*, 3456–3461; f) P. V. Afonine, R. W. Grosse-Kunstleve, N. Echols, J. J. Headd, N. W. Moriarty,

M. Mustyakimov, T. C. Terwilliger, A. Urzhumtsev, P. H. Zwart, P. D. Adams, *Acta Crystallogr. Sect. D* **2012**, *68*, 352–367; g) A. M. Maciejewska, J. Poznański, Z. Kaczmarska, B. Krowisz, J. Nieminuszczy, A. Polkowska-Nowakowska, E. Grzesiuk, J. T. Kuśmierek, *J. Biol. Chem.* **2013**, *288*, 432–441; h) P. Koivisto, P. Robins, T. Lindahl, B. Sedgwick, *J. Biol. Chem.* **2004**, *279*, 40470–40474; i) R. Ougland, C. M. Zhang, A. Liiv, R. F. Johansen, E. Seeberg, Y. M. Hou, J. Remme, P. O. Falnes, *Mol. Cell* **2004**, *16*, 107–116.

[21] a) R. Ougland, D. Lando, I. Jonson, J. A. Dahl, M. N. Moen, L. M. Nordstrand, T. Rognes, J. T. Lee, A. Klungland, T. Kouzarides, *Stem Cells* **2012**, *30*, 2672–2682; b) R. Ougland, I. Jonson, M. N. Moen, G. Nesse, G. Asker, A. Klungland, E. Larsen, *Cell. Physiol. Biochem.* **2016**, *38*, 173–184; c) T. P. Wu, T. Wang, M. G. Seetin, Y. Lai, S. Zhu, K. Lin, Y. Liu, S. D. Byrum, S. G. Mackintosh, M. Zhong, *Nature* **2016**, *532*, 329–333; d) M. Zhang, S. Yang, R. Nelakanti, W. Zhao, G. Liu, Z. Li, X. Liu, T. Wu, A. Xiao, H. Li, *Cell Res.* **2020**, *30*, 197–210; e) F. Liu, W. Clark, G. Luo, X. Wang, Y. Fu, J. Wei, X. Wang, Z. Hao, Q. Dai, G. Zheng, *Cell* **2016**, *167*, 816–828; f) A. R. Walker, P. Silvestrov, T. A. Müller, R. H. Podolsky, G. Dyson, R. P. Hausinger, G. A. Cisneros, *PLoS Comput. Biol.* **2017**, *13*, e1005345; g) T. A. Müller, M. M. Andrzejak, R. P. Hausinger, *Biochem. J.* **2013**, *452*, 509–518; h) M. P. Westbye, E. Feyzi, P. A. Aas, C. B. Vågbø, V. A. Talstad, B. Kavli, L. Hagen, O. Sundheim, M. Akbari, N.-B. Liabakk, G. Slupphaug, M. Otterlei, H. E. Krokan, *J. Biol. Chem.* **2008**, *283*, 25046–25056; i) S. Haag, K. E. Sloan, N. Ranjan, A. S. Warda, J. Kretschmer, C. Blessing, B. Hübner, J. Seikowski, S. Dennerlein, P. Rehling, *EMBO J.* **2016**, *35*, 2104–2119.

[22] a) T. Duncan, S. C. Trewick, P. Koivisto, P. A. Bates, T. Lindahl, B. Sedgwick, *Proc. Natl. Acad. Sci. USA* **2002**, *99*, 16660–16665; b) P. A. Aas, M. Otterlei, P. Ø Falnes, C. B. Vågbø, F. Skorpen, M. Akbari, O. Sundheim, M. Bjørås, G. Slupphaug, E. Seeberg, H. E. Krokan, *Nature* **2003**, *421*, 859–863; c) J. Ringvoll, L. M. Nordstrand, C. B. Vågbø, V. Talstad, K. Reite, P. A. Aas, K. H. Lauritzen, N. B. Liabakk, A. Bjørk, R. W. Doughty, *EMBO J.* **2006**, *25*, 2189–2198; d) K. Bian, S. A. Lenz, Q. Tang, F. Chen, R. Qi, M. Jost, C. L. Drennan, J. M. Essigmann, S. D. Wetmore, D. Li, *Nucleic Acids Res.* **2019**, *47*, 5522–5529; e) Z. Chen, M. Qi, B. Shen, G. Luo, Y. Wu, J. Li, Z. Lu, Z. Zheng, Q. Dai, H. Wang, *Nucleic Acids Res.* **2019**, *47*, 2533–2545.

[23] a) Y. Ueda, I. Ooshio, Y. Fusamae, K. Kitae, M. Kawaguchi, K. Jingushi, H. Hase, K. Harada, K. Hirata, K. Tsujikawa, *Sci. Rep.* **2017**, *7*, 42271; b) S. Dango, N. Mosammaparast, M. E. Sowa, L.-J. Xiong, F. Wu, K. Park, M. Rubin, S. Gygi, J. W. Harper, Y. Shi, *Mol. Cell* **2011**, *44*, 373–384; c) X. Li, X. Xiong, K. Wang, L. Wang, X. Shu, S. Ma, C. Yi, *Nat. Chem. Biol.* **2016**, *12*, 311–316; d) N. Tsao, J. R. Brickner, R. Rodell, A. Ganguly, M. Wood, C. Oyeniran, T. Ahmad, H. Sun, A. Bacolla, L. Zhang, *Mol. Cell* **2021**, *81*, 4228–4242, e4228.

[24] a) V. Rajecka, T. Skalicky, S. Vanacova, *Biochim. Biophys. Acta* **2019**, *1862*, 343–355; b) J. Wang, J. Wang, Q. Gu, Y. Ma, Y. Yang, J. Zhu, Q. a Zhang, *Cancer Cell Int.* **2020**, *20*, 1–7; c) S. Zhang, B. S. Zhao, A. Zhou, K. Lin, S. Zheng, Z. Lu, Y. Chen, E. P. Sulman, K. Xie, O. Bögler, *Cancer Cell* **2017**, *31*, 591–606, e596; d) G. Zheng, J. A. Dahl, Y. Niu, P. Fedorcsak, C.-M. Huang, C. J. Li, C. B. Vågbø, Y. Shi, W.-L. Wang, S.-H. Song, *Mol. Cell* **2013**, *49*, 18–29; e) J. D. Toh, S. W. Crossley, K. J. Bruemmer, J. G. Eva, D. He, D. A. Iovan, C. J. Chang, *Proc. Natl. Acad. Sci. USA* **2020**, *117*, 25284–25292.

[25] a) Y. Fu, Q. Dai, W. Zhang, J. Ren, T. Pan, C. He, *Angew. Chem. Int. Ed.* **2010**, *49*, 8885–8888; *Angew. Chem.* **2010**, *122*, 9069–9072; b) E. Van den Born, C. B. Vågbø, L. Songe-Møller, V. Leihne, G. F. Lien, G. Leszczynska, A. Malkiewicz, H. E. Krokan, F. Kirpekar, A. Klungland, *Nat. Commun.* **2011**, *2*, 1–7; c) L. Songe-Møller, E. van den Born, V. Leihne, C. B. Vågbø, T. Kristoffersen, H. E. Krokan, F. Kirpekar, P. Ø Falnes, A. Klungland, *Mol. Cell. Biochem.* **2010**, *30*, 1814–1827.

[26] a) M. Bartosovic, H. C. Molares, P. Gregorova, D. Hrossova, G. Kudla, S. Vanacova, *Nucleic Acids Res.* **2017**, *45*, 11356–11370; b) G. Jia, Y. Fu, X. Zhao, Q. Dai, G. Zheng, Y. Yang, C. Yi, T. Lindahl, T. Pan, Y.-G. Yang, C. He, *Nat. Chem. Biol.* **2011**, *7*, 885–887; c) G. Jia, C.-G. Yang, S. Yang, X. Jian, C. Yi, Z. Zhou, C. He, *FEBS Lett.* **2008**, *582*, 3313–3319; d) Z. Li, H. Weng, R. Su, X. Weng, Z. Zuo, C. Li, H. Huang, S. Nachtergaele, L. Dong, C. Hu, X. Qin, L. Tang, Y. Wang, G.-M. Hong, H. Huang, X. Wang, P. Chen, S. Gurbuxani, S. Arnovitz, Y. Li, S. Li, J. Strong, M. B. Neilly, R. A. Larson, X. Jiang, P. Zhang, J. Jin, C. He, J. Chen, *Cancer Cell* **2017**, *31*, 127–141.

[27] a) S. Ito, L. Shen, Q. Dai, S. C. Wu, L. B. Collins, J. A. Swenberg, C. He, Y. Zhang, *Science* **2011**, *333*, 1300–1303; b) M. Tahiliani, K. P. Koh, Y. Shen, W. A. Pastor, H. Bandukwala, Y. Brudno, S. Agarwal, L. M. Iyer, D. R. Liu, L. Aravind, A. Rao, *Science* **2009**, *324*, 930–935; c) Y.-F. He, B.-Z. Li, Z. Li, P. Liu, Y. Wang, Q. Tang, J. Ding, Y. Jia, Z. Chen, L. Li, Y. Sun, X. Li, Q. Dai, C.-X. Song, K. Zhang, C. He, G.-L. Xu, *Science* **2011**, *333*, 1303–1307; d) J. Lan, N. Rajan, M. Bizet, A. Penning, N. K. Singh, D. Guallar, E. Calonne, A. L. Greci, E. Bonvin, R. Deplus, P. J. Hsu, S. Nachtergaele, C. Ma, R. Song, A. Fuentes-Iglesias, B. Hassabi, P. Putmans, F. Mies, G. Menschaert, J. J. L. Wong, M. Fidalgo, B. Yuan, F. Fuks, *Nat. Commun.* **2020**, *11*, 1–15.

[28] Z. Lin, X. Wang, K. A. Bustin, K. Shishikura, N. R. McKnight, L. He, R. M. Suciu, K. Hu, X. Han, M. Ahmadi, *ACS Cent. Sci.* **2021**, *7*, 1524–1534.

[29] a) B. I. Fedeles, V. Singh, J. C. Delaney, D. Li, J. M. Essigmann, *J. Biol. Chem.* **2015**, *290*, 20734–20742; b) L. F. Wu, S. Meng, G. L. Tang, *Biochim. Biophys. Acta Proteins Proteomics* **2016**, *1864*, 453–470.

[30] a) P. J. Holland, T. Hollis, *PLoS One* **2010**, *5*, e8680; b) C. Yi, G. Jia, G. Hou, Q. Dai, W. Zhang, G. Zheng, X. Jian, C. G. Yang, Q. Cui, C. He, *Nature* **2010**, *468*, 330–333; c) B. Yu, W. C. Edstrom, J. Benach, Y. Hamuro, P. C. Weber, B. R. Gibney, J. F. Hunt, *Nature* **2006**, *439*, 879–884; d) B. Yu, J. F. Hunt, *Proc. Natl. Acad. Sci. USA* **2009**, *106*, 14315–14320; e) C. Yi, B. Chen, B. Qi, W. Zhang, G. Jia, L. Zhang, C. J. Li, A. R. Dinner, C.-G. Yang, C. He, *Nat. Struct. Mol. Biol.* **2012**, *19*, 671–676; f) E. C. Woon, M. Demetriades, E. A. Bagg, W. Aik, S. M. Krylova, J. H. Ma, M. Chan, L. J. Walport, D. W. Wegman, K. N. Dack, M. A. McDonough, S. N. Krylov, C. J. Schofield, *J. Med. Chem.* **2012**, *55*, 2173–2184; g) R. J. Hopkinson, A. Tumber, C. Yapp, R. Chowdhury, W. Aik, K. H. Che, X. S. Li, J. B. L. Kristensen, O. N. F. King, M. C. Chan, K. K. Yeoh, H. Choi, L. J. Walport, C. C. Thinnes, J. T. Bush, C. Lejeune, A. M. Rydzik, N. R. Rose, E. A. Bagg, M. A. McDonough, T. Krojer, W. W. Yue, S. S. Ng, L. Olsen, P. E. Brennan, U. Oppermann, S. Muller-Knapp, R. J. Klose, P. J. Ratcliffe, C. J. Schofield, A. Kawamura, *Chem. Sci.* **2013**, *4*, 3110–3117; h) C. Zhu, C. Yi, *Angew. Chem. Int. Ed. Engl.* **2014**, *53*, 3659–3662; i) Q. Li, Y. Huang, X. Liu, J. Gan, H. Chen, C. G. Yang, *J. Biol. Chem.* **2016**, *291*, 11083–11093.

[31] L. F. Tian, Y. P. Liu, L. Chen, Q. Tang, W. Wu, W. Sun, Z. Chen, X. X. Yan, *Cell Res.* **2020**, *30*, 272–275.

[32] a) C. G. Yang, C. Yi, E. M. Duguid, C. T. Sullivan, X. Jian, P. A. Rice, C. He, *Nature* **2008**, *452*, 961–965; b) L. Lu, C. Yi, X. Jian, G. Zheng, C. He, *Nucleic Acids Res.* **2010**, *38*, 4415–4425.

[33] O. Sundheim, C. B. Vagbo, M. Bjoras, M. M. Sousa, V. Talstad, P. A. Aas, F. Drablos, H. E. Krokan, J. A. Tainer, G. Slupphaug, *EMBO J.* **2006**, *25*, 3389–3397.

[34] a) W. Aik, J. S. Scotti, H. Choi, L. Gong, M. Demetriades, C. J. Schofield, M. A. McDonough, *Nucleic Acids Res.* **2014**, *42*, 4741–4754; b) W. Chen, L. Zhang, G. Zheng, Y. Fu, Q. Ji, F. Liu, H. Chen, C. He, *FEBS Lett.* **2014**, *588*, 892–898; c) C. Feng, Y. Liu, G. Wang, Z. Deng, Q. Zhang, W. Wu, Y. Tong, C. Cheng, Z. Chen, *J. Biol. Chem.* **2014**, *289*, 11571–11583.

[35] C. Pastore, I. Topalidou, F. Forouhar, A. C. Yan, M. Levy, J. F. Hunt, *J. Biol. Chem.* **2012**, *287*, 2130–2143.

[36] a) W. Aik, M. Demetriades, M. K. Hamdan, E. A. Bagg, K. K. Yeoh, C. Lejeune, Z. Zhang, M. A. McDonough, C. J. Schofield, *J. Med. Chem.* **2013**, *56*, 3680–3688; b) Z. Han, T. Niu, J. Chang, X. Lei, M. Zhao, Q. Wang, W. Cheng, J. Wang, Y. Feng, J. Chai, *Nature* **2010**, *464*, 1205–1209; c) Y. Huang, J. Yan, Q. Li, J. Li, S. Gong, H. Zhou, J. Gan, H. Jiang, G. F. Jia, C. Luo, C. G. Yang, *Nucleic Acids Res.* **2015**, *43*, 373–384; d) S. Peng, W. Xiao, D. Ju, B. Sun, N. Hou, Q. Liu, Y. Wang, H. Zhao, C. Gao, S. Zhang, R. Cao, P. Li, H. Huang, Y. Ma, Y. Wang, W. Lai, Z. Ma, W. Zhang, S. Huang, H. Wang, Z. Zhang, L. Zhao, T. Cai, Y. L. Zhao, F. Wang, Y. Nie, G. Zhi, Y. G. Yang, E. E. Zhang, N. Huang, *Sci. Transl. Med.* **2019**, *11*, eaau7116; e) J. D. W. Toh, L. Sun, L. Z. M. Lau, J. Tan, J. J. A. Low, C. W. Q. Tang, E. J. Y. Cheong, M. J. H. Tan, Y. Chen, W. Hong, Y. G. Gao, E. C. Y. Woon, *Chem. Sci.* **2015**, *6*, 112–122; f) T. Wang, T. Hong, Y. Huang, H. Su, F. Wu, Y. Chen, L. Wei, W. Huang, X. Hua, Y. Xia, J. Xu, J. Gan, B. Yuan, Y. Feng, X. Zhang, C. G. Yang, X. Zhou, *J. Am. Chem. Soc.* **2015**, *137*, 13736–13739; g) X. Zhang, L. H. Wei, Y. Wang, Y. Xiao, J. Liu, W. Zhang, N. Yan, G. Amu, X. Tang, L. Zhang, G. Jia, *Proc. Natl. Acad. Sci. USA* **2019**, *116*, 2919–2924.

[37] a) H. Hashimoto, J. E. Pais, N. Dai, I. R. Correa Jr., X. Zhang, Y. Zheng, X. Cheng, *Nucleic Acids Res.* **2015**, *43*, 10713–10721; b) H. Hashimoto, J. E. Pais, X. Zhang, L. Saleh, Z. Q. Fu, N. Dai, I. R. Correa Jr., Y. Zheng, X. Cheng, *Nature* **2014**, *506*, 391–395.

[38] a) L. Hu, Z. Li, J. Cheng, Q. Rao, W. Gong, M. Liu, Y. G. Shi, J. Zhu, P. Wang, Y. Xu, *Cell* **2013**, *155*, 1545–1555; b) L. Hu, J. Lu, J. Cheng, Q. Rao, Z. Li, H. Hou, Z. Lou, L. Zhang, W. Li, W. Gong, M. Liu, C. Sun, X. Yin, J. Li, X. Tan, P. Wang, Y. Wang, D. Fang, Q. Cui, P. Yang, C. He, H. Jiang, C. Luo, Y. Xu, *Nature* **2015**, *527*, 118–122.

[39] a) S. G. Jin, Z. M. Zhang, T. L. Dunwell, M. R. Harter, X. Wu, J. Johnson, Z. Li, J. Liu, P. E. Szabo, Q. Lu, G. L. Xu, J. Song, G. P. Pfeifer, *Cell Rep.*

2016, *14*, 493–505; b) Y. Xu, C. Xu, A. Kato, W. Tempel, J. G. Abreu, C. Bian, Y. Hu, D. Hu, B. Zhao, T. Cerovina, J. Diao, F. Wu, H. H. He, Q. Cui, E. Clark, C. Ma, A. Barbara, G. J. Veenstra, G. Xu, U. B. Kaiser, X. S. Liu, S. P. Sugrue, X. He, J. Min, Y. Kato, Y. G. Shi, *Cell* **2012**, *151*, 1200–1213.
[40] B. Xu, D. Liu, Z. Wang, R. Tian, Y. Zuo, *Cell. Mol. Life Sci.* **2020**.
[41] K. Al-Qahtani, B. Jabeen, R. Sekirnik, N. Riaz, T. D. W. Claridge, C. J. Schofield, J. S. O. McCullagh, *Phytochemistry* **2015**, *117*, 456–461.
[42] G. Wang, Q. He, C. Feng, Y. Liu, Z. Deng, X. Qi, W. Wu, P. Mei, Z. Chen, *J. Biol. Chem.* **2014**, *289*, 27924–27936.
[43] S. Harteis, S. Schneider, *Int. J. Mol. Sci.* **2014**, *15*, 12335–12363.
[44] a) N. Liu, Q. Dai, G. Zheng, C. He, M. Parisien, T. Pan, *Nature* **2015**, *518*, 560–564; b) C. Roost, S. R. Lynch, P. J. Batista, K. Qu, H. Y. Chang, E. T. Kool, *J. Am. Chem. Soc.* **2015**, *137*, 2107–2115.
[45] C. Rauch, M. Trieb, B. Wellenzohn, M. Loferer, A. Voegele, F. R. Wibowo, K. R. Liedl, *J. Am. Chem. Soc.* **2003**, *125*, 14990–14991.
[46] C. Acosta-Silva, V. Branchadell, J. Bertran, A. Oliva, *J. Phys. Chem. B* **2010**, *114*, 10217–10227.
[47] C. B. Mulholland, F. R. Traube, E. Ugur, E. Parsa, E. M. Eckl, M. Schonung, M. Modic, M. D. Bartoschek, P. Stolz, J. Ryan, T. Carell, H. Leonhardt, S. Bultmann, *Sci. Rep.* **2020**, *10*, 12066.
[48] B. Bleijlevens, T. Shivarattan, E. Flashman, Y. Yang, P. J. Simpson, P. Koivisto, B. Sedgwick, C. J. Schofield, S. J. Matthews, *EMBO Rep.* **2008**, *9*, 872–877.
[49] B. Bleijlevens, T. Shivarattan, K. S. van den Boom, A. de Haan, G. van der Zwan, P. J. Simpson, S. J. Matthews, *Biochemistry* **2012**, *51*, 3334–3341.
[50] D. P. Frueh, A. C. Goodrich, S. H. Mishra, S. R. Nichols, *Curr. Opin. Struct. Biol.* **2013**, *23*, 734–739.
[51] B. Ergel, M. L. Gill, L. Brown, B. Yu, A. G. Palmer, J. F. Hunt, *J. Biol. Chem.* **2014**, *289*, 29584–29601.
[52] B. Bleijlevens, T. Shivarattan, B. Sedgwick, S. E. J. Rigby, S. J. Matthews, *J. Inorg. Biochem.* **2007**, *101*, 1043–1048.
[53] J. Krzystek, A. Ozarowski, J. Telser, *Coord. Chem. Rev.* **2006**, *250*, 2308–2324.
[54] I. S. MacPherson, M. E. P. Murphy, *Cell. Mol. Life Sci.* **2007**, *64*, 2887–2899.
[55] M. M. Harding, *Acta Crystallogr. Sect. D* **2004**, *60*, 849–859.
[56] C. A. Smith, B. F. Anderson, H. M. Baker, E. N. Baker, *Biochemistry* **1992**, *31*, 4527–4533.
[57] J. Peisach, W. E. Blumberg, *Arch. Biochem. Biophys.* **1974**, *165*, 691–708.
[58] L. Kanazhevskaya, D. Smyshlyaev, I. Alekseeva, O. Fedorova, *Russ. J. Bioorg. Chem.* **2019**, *45*, 630–640.
[59] L. Y. Kanazhevskaya, I. V. Alekseeva, O. S. Fedorova, *Molecules* **2019**, *24*, 4576.
[60] C. C. Gradinaru, D. O. Marushchak, M. Samim, U. J. Krull, *Analyst* **2010**, *135*, 452–459.
[61] a) D. E. Wilcox, *Inorg. Chim. Acta* **2008**, *361*, 857–867; b) M. W. Freyer, E. A. Lewis, *Methods Cell Biol.* **2008**, *84*, 79–113; c) N. J. Buurma, I. Haq, *Methods* **2007**, *42*, 162–172.
[62] a) M. D. Allen, C. G. Grummitt, C. Hilcenko, S. Y. Min, L. M. Tonkin, C. M. Johnson, S. M. Freund, M. Bycroft, A. J. Warren, *EMBO J.* **2006**, *25*, 4503–4512; b) C. Xu, C. Bian, R. Lam, A. Dong, J. Min, *Nat. Commun.* **2011**, *2*, 1–8.
[63] A. K. Singh, B. Zhao, X. Liu, X. Wang, H. Li, H. Qin, X. Wu, Y. Ma, D. Horne, X. Yu, *Proc. Natl. Acad. Sci. USA* **2020**, *117*, 3621–3626.
[64] N. J. Greenfield, *Nat. Protoc.* **2006**, *1*, 2876–2890.
[65] R. P. Hausinger, *Crit. Rev. Biochem. Mol. Biol.* **2004**, *39*, 21–68.
[66] a) M. L. Neidig, C. D. Brown, K. M. Light, D. G. Fujimori, E. M. Nolan, J. C. Price, E. W. Barr, J. M. Bollinger Jr., C. Krebs, C. T. Walsh, E. I. Solomon, *J. Am. Chem. Soc.* **2007**, *129*, 14224–14231; b) S. R. Iyer, V. D. Chaplin, M. J. Knapp, E. I. Solomon, *J. Am. Chem. Soc.* **2018**, *140*, 11777–11783.
[67] Y. Mishina, L. X. Chen, C. He, *J. Am. Chem. Soc.* **2004**, *126*, 16930–16936.
[68] M. J. Ryle, A. Liu, R. B. Muthukumaran, R. Y. N. Ho, K. D. Koehntop, J. McCracken, L. Que, R. P. Hausinger, *Biochemistry* **2003**, *42*, 1854–1862.
[69] T. F. Henshaw, M. Feig, R. P. Hausinger, *J. Inorg. Biochem.* **2004**, *98*, 856–861.
[70] A. Liu, R. Y. N. Ho, L. Que, M. J. Ryle, B. S. Phinney, R. P. Hausinger, *J. Am. Chem. Soc.* **2001**, *123*, 5126–5127.
[71] R. Bakhtiar, *J. Chem. Educ.* **2013**, *90*, 203–209.
[72] a) S. Kizaki, H. Sugiyama, *Org. Biomol. Chem.* **2014**, *12*, 104–107; b) F. Spada, S. Schiffers, A. Kirchner, Y. Zhang, G. Arista, O. Kosmatchev, E. Korytiakova, R. Rahimoff, C. Ebert, T. Carell, *Nat. Chem. Biol.* **2020**, *16*, 1411–1419.
[73] F. R. Traube, S. Schiffers, K. Iwan, S. Kellner, F. Spada, M. Müller, T. Carell, *Nat. Protoc.* **2019**, *14*, 283–312.
[74] a) M. G. Krokidis, M. Louka, E. K. Efthimiadou, S.-K. Zervou, K. Papadopoulos, A. Hiskia, C. Ferreri, C. Chatgilialoglu, *Cancers* **2019**, *11*, 480; b) J.-B. Alberge, F. Magrangeas, M. Wagner, S. Denié, C. Guérin-Charbonnel, L. Campion, M. Attal, H. Avet-Loiseau, T. Carell, P. Moreau, S. Minvielle, A. A. Sérandour, *Clin. Epigenet.* **2020**, *12*, 163.
[75] D. Schmidl, N. S. W. Jonasson, E. Korytiaková, T. Carell, L. J. Daumann, *Angew. Chem. Int. Ed.* **2021**, *60*, 21457–21463.
[76] A. Hofer, Z. J. Liu, S. Balasubramanian, *J. Am. Chem. Soc.* **2019**, *141*, 6420–6429.
[77] J. P. Patel, M. L. Sowers, J. L. Herring, J. A. Theruvathu, M. R. Emmett, B. E. Hawkins, K. Zhang, D. S. DeWitt, D. S. Prough, L. C. Sowers, *Chem. Res. Toxicol.* **2015**, *28*, 2352–2363.
[78] a) N. S. W. Jonasson, R. Janßen, A. Menke, F. L. Zott, H. Zipse, L. J. Daumann, *ChemBioChem* **2021**, *22*, 3333–3340; b) N. S. W. Jonasson, L. J. Daumann, *Chem. Eur. J.* **2019**, *25*, 12091–12097.
[79] B. Yu, J. F. Hunt, *Proc. Natl. Acad. Sci. USA* **2009**, *106*, 14315–14320.
[80] a) V. Singh, B. I. Fedeles, D. Li, J. C. Delaney, I. D. Kozekov, A. Kozekova, L. J. Marnett, C. J. Rizzo, J. M. Essigmann, *Chem. Res. Toxicol.* **2014**, *27*, 1619–1631; b) J. C. Delaney, L. Smeester, C. Wong, L. E. Frick, K. Taghizadeh, J. S. Wishnok, C. L. Drennan, L. D. Samson, J. M. Essigmann, *Nat. Struct. Mol. Biol.* **2005**, *12*, 855–860; c) L. E. Frick, J. C. Delaney, C. Wong, C. L. Drennan, J. M. Essigmann, *Proc. Natl. Acad. Sci. USA* **2007**, *104*, 755–760; d) D. Li, J. C. Delaney, C. M. Page, A. S. Chen, C. Wong, C. L. Drennan, J. M. Essigmann, *J. Nucleic Acids* **2010**, *2010*, 369434; e) D. Li, B. I. Fedeles, N. Shrivastav, J. C. Delaney, X. Yang, C. Wong, C. L. Drennan, J. M. Essigmann, *Chem. Res. Toxicol.* **2013**, *26*, 1182–1187.
[81] T. A. Müller, K. Meek, R. P. Hausinger, *DNA Repair* **2010**, *9*, 58–65.
[82] M. R. Baldwin, S. J. Admiraal, P. J. O'Brien, *J. Biol. Chem.* **2020**, *295*, 7317–7326.
[83] a) J. J. Hutton, A. L. Tappel, S. Udenfriend, *Arch. Biochem. Biophys.* **1967**, *118*, 231–240; b) R. E. Rhoads, S. Udenfriend, *Proc. Natl. Acad. Sci. USA* **1968**, *60*, 1473–1478; c) L. A. McNeill, L. Bethge, K. S. Hewitson, C. J. Schofield, *Anal. Biochem.* **2005**, *336*, 125–131; d) L. Luo, M. B. Pappalardi, P. J. Tummino, R. A. Copeland, M. E. Fraser, P. K. Grzyska, R. P. Hausinger, *Anal. Biochem.* **2006**, *353*, 69–74; e) H.-J. Lee, M. D. Lloyd, K. Harlos, C. J. Schofield, *Biochem. Biophys. Res. Commun.* **2000**, *267*, 445–448.
[84] a) E. Flashman, L. M. Hoffart, R. B. Hamed, J. M. Bollinger Jr., C. Krebs, C. J. Schofield, *FEBS J.* **2010**, *277*, 4089–4099; b) R. J. Hopkinson, R. B. Hamed, N. R. Rose, T. D. Claridge, C. J. Schofield, *ChemBioChem* **2010**, *11*, 506–510.
[85] a) G. Kaule, V. Günzler, *Anal. Biochem.* **1990**, *184*, 291–297; b) C. J. Cunliffe, T. J. Franklin, R. M. Gaskell, *Biochem. J.* **1986**, *240*, 617–619.
[86] A. Khan, C. J. Schofield, T. D. Claridge, *ChemBioChem* **2020**, *21*, 2898.
[87] M. A. Martini, O. Rüdiger, N. Breuer, B. Nöring, S. DeBeer, P. Rodríguez-Maciá, J. A. Birrell, *J. Am. Chem. Soc.* **2021**, *143*, 18159–18171.
[88] S. J. Wong, A. E. Ringel, W. Yuan, J. A. Paulo, H. Yoon, M. A. Currie, M. C. Haigis, *J. Biol. Chem.* **2021**, *296*, 100397.
[89] A. Thalhammer, Z. Bencokova, R. Poole, C. Loenarz, J. Adam, L. O'Flaherty, J. Schödel, D. Mole, K. Giaslakiotis, C. J. Schofield, E. M. Hammond, P. J. Ratcliffe, P. J. Pollard, *PLoS One* **2011**, *6*, e16210.
[90] a) L. Tuderman, R. Myllylä, K. I. Kivirikko, *Eur. J. Biochem.* **1977**, *80*, 341–348; b) D. F. Counts, G. J. Cardinale, S. Udenfriend, *Proc. Natl. Acad. Sci. USA* **1978**, *75*, 2145–2149.
[91] V. T. Monsen, O. Sundheim, P. A. Aas, M. P. Westbye, M. M. Sousa, G. Slupphaug, H. E. Krokan, *Nucleic Acids Res.* **2010**, *38*, 6447–6455.
[92] T. Laukka, C. J. Mariani, T. Ihantola, J. Z. Cao, J. Hokkanen, W. G. Kaelin, L. A. Godley, P. Koivunen, *J. Biol. Chem.* **2016**, *291*, 4256–4265.
[93] E. van den Born, M. V. Omelchenko, A. Bekkelund, V. Leihne, E. V. Koonin, V. V. Dolja, P. Ø Falnes, *Nucleic Acids Res.* **2008**, *36*, 5451–5461.
[94] H. Korvald, P. Ø Falnes, J. K. Laerdahl, M. Bjørås, I. Alseth, *DNA Repair* **2012**, *11*, 453–462.
[95] L. G. Bjørnstad, G. Zoppellaro, A. B. Tomter, P. Ø. Falnes, K. K. Andersson, *Biochem. J.* **2011**, *434*, 391–398.
[96] A. B. F. Valle, A. D. Panek, J. R. Mattoon, *Anal. Biochem.* **1978**, *91*, 583–599.
[97] a) S. Burr, A. Caldwell, M. Chong, M. Beretta, S. Metcalf, M. Hancock, M. Arno, S. Balu, V. L. Kropf, R. K. Mistry, A. M. Shah, G. E. Mann, A. C. Brewer, *Nucleic Acids Res.* **2017**, *46*, 1210–1226; b) P. Prickaerts, M. E. Adriaens, T. v d Beucken, E. Koch, L. Dubois, V. E. H. Dahlmans, C. Gits, C. T. A. Evelo, M. Chan-Seng-Yue, B. G. Wouters, J. W. Voncken, *Epigenetics Chromatin* **2016**, *9*, 46; c) D. Camuzi, Í. S. S. de Amorim, L. F.

Ribeiro Pinto, L. Oliveira Trivilin, A. L. Mencalha, S. C. Soares Lima, *Cells* **2019**, *8*, 300.
[98] D. D. Shah, J. A. Conrad, B. Heinz, J. M. Brownlee, G. R. Moran, *Biochemistry* **2011**, *50*, 7694–7704.
[99] L. C. Clark JR, R. Wolf, D. Granger, Z. Taylor, *J. Appl. Physiol.* **1953**, *6*, 189–193.
[100] A. Ozer, R. K. Bruick, *Nat. Chem. Biol.* **2007**, *3*, 144–153.
[101] M. Hirsilä, P. Koivunen, V. Günzler, K. I. Kivirikko, J. Myllyharju, *J. Biol. Chem.* **2003**, *278*, 30772–30780.
[102] Y. Xu, S.-Y. Liu, J. Li, L. Zhang, D. Chen, J.-P. Zhang, Y. Xu, Z. Dai, X. Zou, *Anal. Chem.* **2018**, *90*, 9330–9337.
[103] L. Xu, Y. C. Chen, J. Chong, A. Fin, L. S. McCoy, J. Xu, C. Zhang, D. Wang, *Angew. Chem.* **2014**, *126*, 11405–11409; *Angew. Chem. Int. Ed.* **2014**, *53*, 11223–11227.
[104] H. Reingruber, L. B. Pontel, *Curr. Opin. Toxicol.* **2018**, *9*, 28–34.
[105] a) B. Chance, *Science* **1954**, *120*, 767–775; b) B. Chance, B. Thorell, *Nature* **1959**, *184*, 931–934.
[106] T. W. Roy, A. S. Bhagwat, *Nucleic Acids Res.* **2007**, *35*, e147–e147.
[107] P. Koivisto, T. Duncan, T. Lindahl, B. Sedgwick, *J. Biol. Chem.* **2003**, *278*, 44348–44354.
[108] B. Jahn, N. S. W. Jonasson, H. Hu, H. Singer, A. Pol, N. M. Good, H. J. M. O. den Camp, N. C. Martinez-Gomez, L. J. Daumann, *J. Biol. Inorg. Chem.* **2020**, *25*, 199–212.

Manuscript received: November 2, 2021
Revised manuscript received: January 14, 2022
Accepted manuscript online: January 18, 2022

2 Synthetic Iron Complexes Modeling Enzymatic Processes

Metalloenzymes are a family of enzymes that contain metal ions in their active site. They are ubiquitous in nature, making about one-third of all enzymes known so far.[43-44] Metalloenzymes perform various reactions and depending on their specific function, these enzymes are divided into different groups. Examples include oxygenases[45-47] that transfer oxygen from molecular oxygen to substrates, hydrogenases[48-51] facilitating uptake of molecular hydrogen and/or catalyzing proton reduction and halogenases[52-53] that halogenate substrates amongst others. The metal cation displays a distinctive role in the enzyme and acts for instance as redox partner or Lewis acid, facilitating the catalyzed reaction.

Many monooxygenases and dioxygenases involve high-valent metal-oxido species as reaction intermediate. In iron-containing oxygenases, different structural appearances for this intermediate can be found (Chart 2).[54-55] In heme enzymes such as cytochrome P450, reactions including olefin epoxidation and alkane hydroxylation are believed to proceed *via* high-valent iron(IV)-oxido porphyrin π-cation radicals.[56-57] Rieske dioxygenases catalyze the *cis*-dihydroxylation of arene C=C double bonds. Their active center displays a combination of a non-heme mononuclear iron center responsible for oxygen activation and ferredoxin containing [2Fe-2S] Rieske iron-sulfur clusters.[58-62] As described in the previous section for α-ketoglutarate-dependent enzymes, also the family of enzymes containing mononuclear iron centers plays a significant role. Enzymatic reactions such as hydroxylation, halogenation, desaturation, formation of heterocycling rings as well as stereoinversion can be catalyzed.[63-66] So-called soluble methane monooxygenases (sMMO) present a (bis(μ-oxo)diiron(IV) intermediate and catalyze the hydroxylation of methane.[67-71]

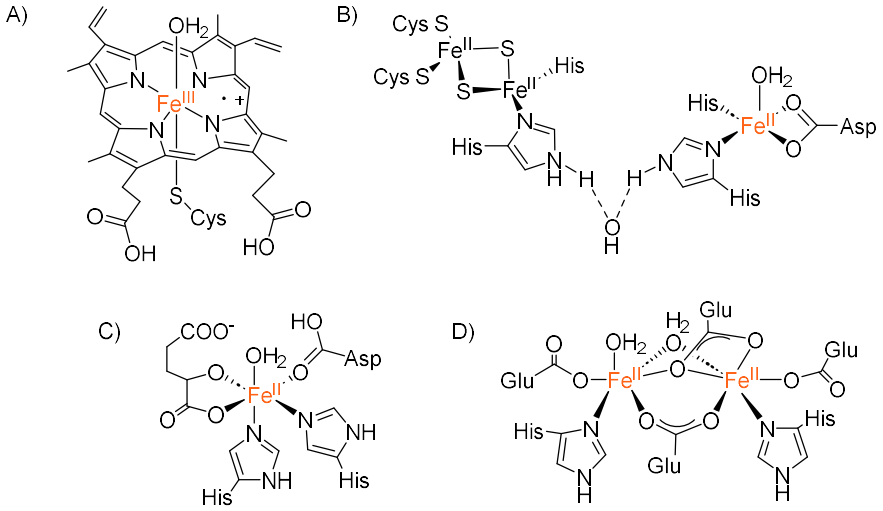

Chart 2: Representation of the active site in its resting state of selected enzymes involving high-valent iron-oxo intermediates. A) Cytochrome P450, B) Rieske dioxygenase, C) taurine dioxygenase, D) soluble methane monooxygenase.

The chemistry performed by metalloenzymes is rich and contains highly desired transformations that are still hard to achieve in synthetic chemistry. Moreover, in contrast to many synthetic catalysts, nature often uses cheap, abundant and non-toxic transition metals such as iron, copper or manganese for these catalytic transformations. Therefore, the development of synthetic model complexes mimicking the structural solutions provided by nature, opens the door for performing a variety of desired reactions. Furthermore, the study of processes such as complex-substrate interactions for instance on a small molecule level instead of the complicate enzymes can provide more mechanistic insights and illuminate the nature and chemical properties of the intermediates in enzymatic catalyses. Open questions focusing on the high selectivity and specificity of these enzymatic processes can also be approached by the investigation of synthetic model complexes. It is therefore not surprising that research afforded a wide field of enzyme mimics which have been thoroughly characterized and investigated concerning their reactivities towards various substrates. A selection of synthetic iron(IV)-oxido complexes is shown in Chart 3.

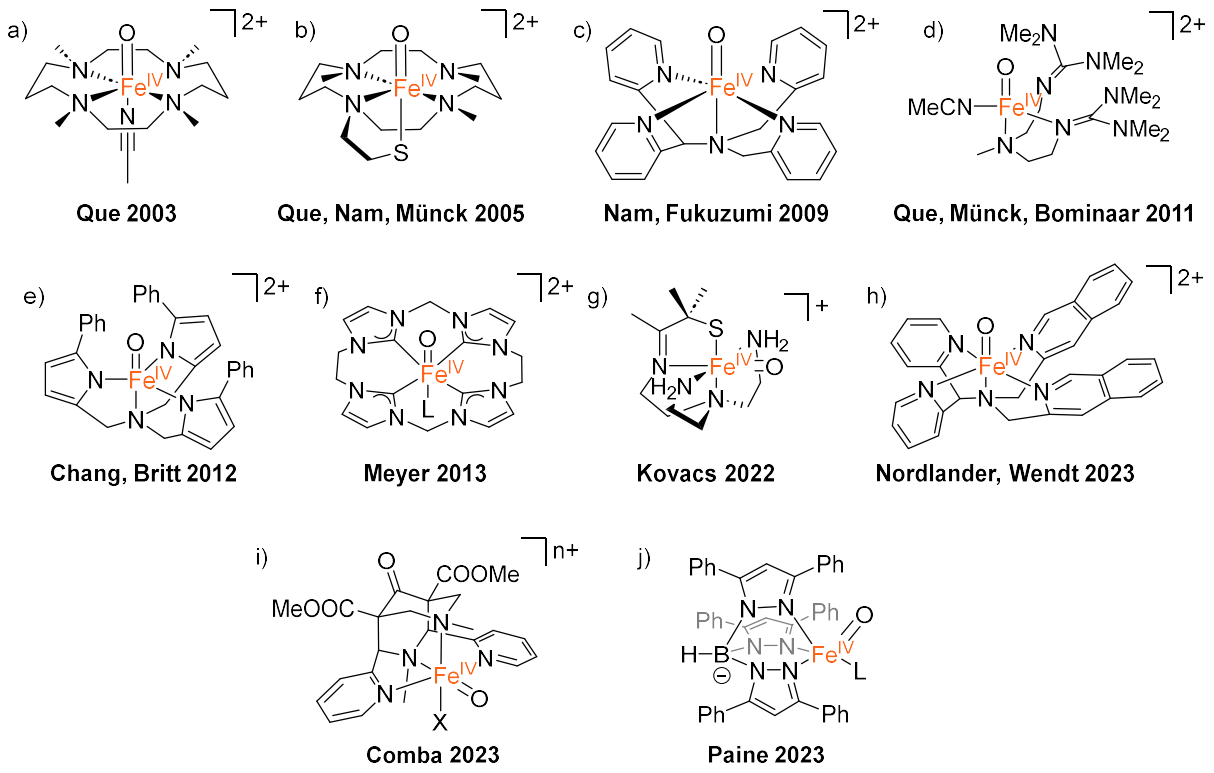

Chart 3: Structural representation of selected synthetic iron(IV)-oxido complexes. a),[72] b),[73] c),[74] d),[75] e),[76] f),[77] g),[78] h),[79] i),[80] j).[81]

Although the first synthetic high-valent iron(IV)-oxido complex modelling reactivity of heme enzymes was already reported in 1979,[82] it took more than twenty more years until the first non-heme iron(IV)-oxido complex could be isolated and characterized. This was achieved in 2003 by the groups of Que, Nam and Münck who also provided a crystal structure of this compound.[72] Since then, the amount of reported iron(IV)-oxido species increased strongly counting nowadays more than a hundred complexes.[77, 83-88] Predominantly, polydentate ligands with N-donors such as amines, N-heterocycles, pyridines, quinolines or benzimidazoles are employed. With the different ligands providing different electronic properties and influencing the thermal stability of the complexes, a range of half-lifes ($t_{½}$, required time to reduce a quantity of compound to half of its initial value) from seconds to days has been reported for these species. The majority of the presented iron(IV)-oxido complexes is present in the S = 1 low spin state, however, few examples of S = 2 high spin complexes can be found.[75-76, 83, 89]

The relevance of these complexes and prevalent dynamics in the current research community is reflected by the still increasing number of reported structures. In addition to thorough studies on existing complex systems, several new iron(IV)-oxido compounds have been presented only recently.[80, 90] The group of Kovacs proposed the formation of an iron(IV)-oxido complex from a dinuclear μ-O_2-bridged iron(III) species which could be confirmed by crystallization of the assumed reactive compound at -80 °C.[78] Another interesting example is presented by the group of Paine last year.[81] The authors use iron(II) complexes with a monoanionic tris(pyrazole) borate-based ligand system in combination with the coordination of α-hydroxy acids. Inspired by nature using α-hydroxy acids such as α-ketoglutarate as cofactors, this acid was anticipated to facilitate dioxygen reduction. Indeed, oxidative decarboxylation of the coordinated α-hydroxy acids was observed in the presence of dioxygen and dependent on the reaction conditions (presence of Lewis acids or protic acids), the authors were able to perform epoxidations, *cis*-dihydroxylations of alkenes or hydroxylation and halogenation of C-H bonds. However, it has to be noted that the authors assume the formation of an iron(IV)-oxido complex as active species but have not been able to trap this intermediate.

The iron(IV)-oxido species ($[Fe^{IV}Py_5Me_2(O)]^{2+}$ = $[Fe^{IV}\mathbf{L1}(O)]^{2+}$) first presented by the group of Chang in 2015[91] is of special interest for this work since fundamental parts of this theses are based on their results. The properties and reactivity of this complex will therefore be elaborated in more detail.

The generation of the high-valent iron-oxo species is often accomplished through the corresponding iron(II) precursor which is oxidized by reagents such as hydrogen peroxide, cerium(IV) compounds, ozone or peracids amongst others. Some examples can be found where molecular dioxygen is sufficient as oxidant[81, 92] and there exist also studies on the formation of iron(IV)-oxido species by using singlet oxygen.[93] The generation of the complex $[Fe^{IV}\mathbf{L1}(O)]^{2+}$ was achieved in two different procedures (Scheme 2).

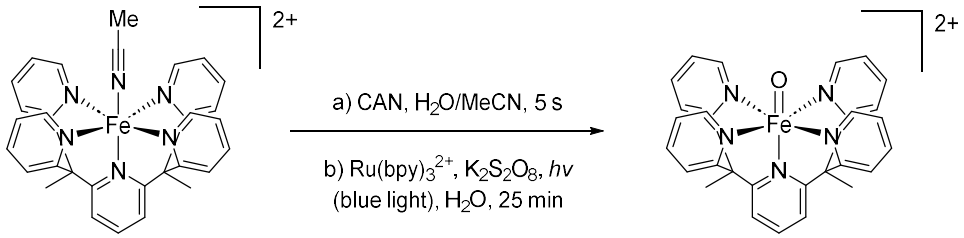

Scheme 2: a) Chemical or b) photochemical oxidation of the iron(II) precursor resulting in an iron(IV)-oxido complex.[91]

In an oxidation reaction of the iron(II) precursor with cerium(IV) ammonium nitrate (CAN) in a water/acetonitrile mixture, the resulting complex $[Fe^{IV}\mathbf{L1}(O)][Ce(NO_3)_6]$ could be isolated as a solid that was even stable at ambient conditions for a few days. In the photochemical oxidation reaction however, the iron(IV)-oxido species was only observed in solution. For this purpose, the iron(II) precursor was irradiated with a blue fluorescence light bulb in the presence of $[Ru(bpy)_3]^{2+}$ as photosensitizer and $K_2S_2O_8$ as terminal electron acceptor. In both processes, the solvent water acts as oxygen atom donor which could be confirmed by experiments performed in $^{18}OH_2$ and subsequent mass spectrometric analysis.

The oxidative reactivity of the formed iron(IV)-oxido complex was tested on different substrates containing hydrocarbon, alcohol or alkene moieties. The investigated compounds could be converted into alcohol, aldehyde and epoxide species, respectively, and the resulting products identified *via* ^{1}H NMR spectroscopy.

Previous work from the Daumann group

The iron(IV)-oxido complex developed by the group of Chang[91] was chosen in our group to investigate its potential ability to act as a model complex for TET enzymes (Fe(II)/α-KG-depentent enzymes with a high-valent iron-oxo intermediate as active species, compare section I.1 and Scheme 3a). Its exceptional stability in water at room temperature and ambient conditions attracted noticeable attention reflecting nearly physiological conditions. Furthermore, the complex proved to possess suitable oxidative properties required for the conversion of hydrocarbon or alcohol functional groups. Together with

the ease of synthesis, this complex seemed to have the features of a perfect candidate for mimicking enzymatic reactivity of TET enzymes.

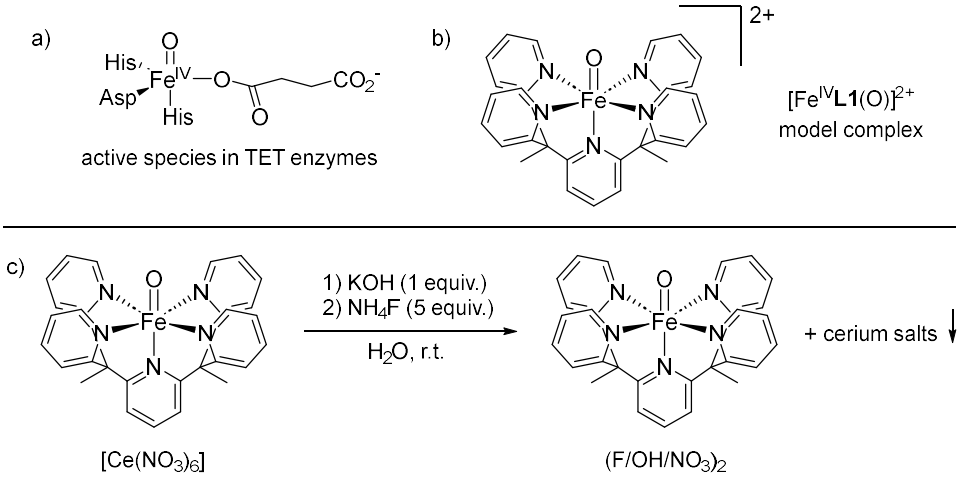

Scheme 3: a) Representation of the active species in TET enzymes. b) Structure of the synthetic iron(IV)-oxido complex. Anion exchange reaction for removal of the cerium(IV) nitrate counterion.[94]

In the work of Chang and coworkers, substrate oxidation reactivity studies are performed with the photochemically generated iron(IV)-oxido species.[91] To perform the investigations with the isolated iron(IV)-oxido solid, the cerium(IV) nitrate counterion present from the synthesis pathway needed to be removed in order to exclude unwanted oxidation of the substrates by this counterion. This was achieved by Lindlar *et al*. through precipitation of cerium salts with ammonium fluoride in water; the resulting $[Fe^{IV}\mathbf{L1}(O)]^{2+}$-containing supernatant was used as such *in situ* for further investigations (Scheme 3c).[94] The successful removal of the cerium counterion was confirmed by determination of the cerium content with ICP-MS measurement after the anion exchange. However, the actual species responsible for substrate oxidation can not clearly be identified in this process as a combination of possible anions in the reaction mixture (nitrate, hydroxide or fluoride) is assumed for the final compound.

To use $[Fe^{IV}\mathbf{L1}(O)]^{2+}$ as functional model for TET enzymes, 5-methylcytosine (5mC) was chosen as a substrate functioning as simple model for natural substrates of TET enzymes which consist of 5mC-containing genomic DNA. It was shown that indeed $[Fe^{IV}\mathbf{L1}(O)]^{2+}$ was capable of oxidizing 5mC to its natural metabolites 5-hydroxymethyl cytosine (5hmC),

5-formylcytosine (5fC) and 5-carboxycytosine (5cC) (Scheme 4a). The reaction products could be identified after separation of the iron species through silica filtration in its TMS-derivatized form *via* GC-MS measurements.[94]

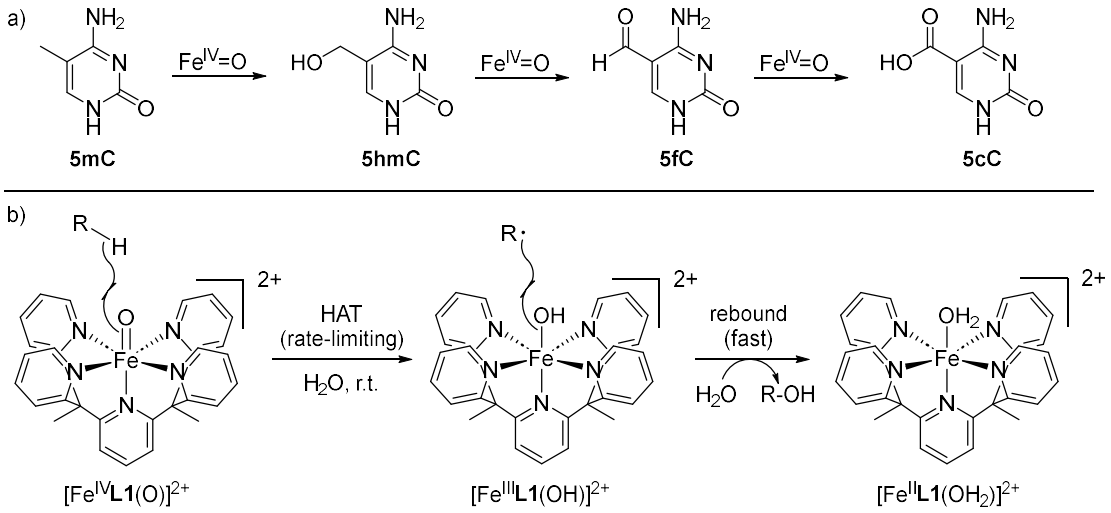

Scheme 4: a) Reaction of $[Fe^{IV}\mathbf{L1}(O)]^{2+}$ with the substrate 5-methylcytosine (5mC) and the successively formed reaction products 5-hydroxymethyl cytosine (5hmC), 5-formylcytosine (5fC) and 5-carboxycytosine (5cC). b) Proposed reaction mechanism of $[Fe^{IV}\mathbf{L1}(O)]^{2+}$ with 5mC.[94]

Analogous reactions with the deuterated species d_3-5mC revealed a large kinetic isotope effect suggesting a C-H bond cleavage as rate-determining step. Based on this observation, reaction mechanism was proposed consisting of a hydrogen atom transfer from the substrate to form an iron(III)-hydroxido species and the substrate radical as intermediate which subsequently react in a fast rebound reaction to release the hydroxylated substrate as well as an iron(II) species (Scheme 4b). As expected from this mechanism, substrates with lower bond dissociation energies (BDEs) react faster with the iron species (BDE(5mC): 90.39 kcal mol^{-1}; BDE(5hmC): 86.20 kcal mol^{-1}[95]). In the enzymatic process in contrast, the observed reaction rates do not follow the trends of the BDEs,[95] highlighting the importance of a secondary coordination sphere and a specific network of hydrogen bonds in the enzyme.

Further studies of this system to slowly approach the natural substrate of TET enzymes have been performed by Schmidl, Lindlar and Korytiaková.[96] Instead of the simple nucleobase, they employed the nucleoside 5mdC as substrate and a reaction with the

iron(IV)-oxido complex equally showed conversion into the expected derivatives. Despite of the rather complex substrate structure including the sugar moiety with several reactive C-H bonds, only one minor side reaction was detected leading to the corresponding nucleobase and a 2'-deoxyribono-γ-lactone. The products including side products in reactions with nucleosides have been identified and quantified using HPLC-MS methods with the corresponding synthesized reference samples.

In the same work, the authors also tested the reactivity of the iron(IV)-oxido complex towards a small 5mdC-containing oligonucleotide (5'-CCUUAACC5mdCG-3'). This complicated substrate containing the sugar backbone and phosphate groups as well as probable steric hindrance of the methyl group reacted fast with $[Fe^{IV}\mathbf{L1}(O)]^{2+}$. Notably, also in this reaction the expected reaction products could be identified *via* UHPLC-MS/MS measurements after digestion of the oligonucleotide into corresponding nucleosides. About 7% of the detected cytosine derivatives correspond to a mixture of oxidation products, the remaining part displays unreacted 5mdC. To confirm the intactness of the oligonucleotide strand after reaction with the iron(IV)-oxido complex, MALDI measurements were performed. From these experiments, the authors state that side reactions take place at the end of the strands such as loss of a cytidine-3'-phosphate or guanine fragment but no internal strand-breaks occurred. These promising results confirm the ability of the synthetic $[Fe^{IV}\mathbf{L1}(O)]^{2+}$ compound to act as a good model complex mimicking the reactivity of TET enzymes even with complex substrates.[96]

Very recently, another synthetic model complex for TET enzymes was presented by Manna and coworkers.[97] The authors employ the previously reported Fe^{III}TAML complex[98-99] and generated the reactive iron-oxido species *in situ* in the reaction mixture by the usage of H_2O_2 as oxidant.

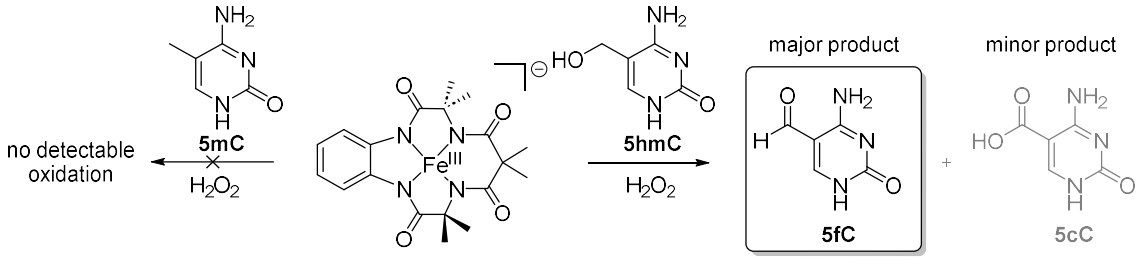

Scheme 5: Reactivity of the Fe^{III}TAML complex towards 5mC and 5hmC in the presence of H_2O_2 in phosphate buffer.[97]

Under the applied reaction conditions, this complex selectively oxidizes 5hmC to 5fC and only traces of 5cC could be detected. 5mC in contrast was not oxidized even when higher Fe^{III}TAML and H_2O_2 concentration were employed. It seems that simply the bond dissociation energies (BDEs) of the substrates are responsible for this selectivity with 5hmC having the lowest BDE in this series (see appendix section VII.3, Table 22 for important BDE values). The authors use HPLC chromatography for quantification of their reaction products. The reactive iron species however, has not been trapped in this study.

II. Motivation and Aim

Previous studies in our group showed that the synthetic iron(IV)-oxido complex $[Fe^{IV}\mathbf{L1}(O)]^{2+}$ can act as a functional model for TET enzymes. The DNA modification 5-methylcytosine (5mC) was used as a model substrate as nucleobase, nucleoside or short oligonucleotide and oxidation with $[Fe^{IV}\mathbf{L1}(O)]^{2+}$ afforded the natural oxidized derivatives. ***Based on these findings, the main goal of this work was to further understand the established model system and expand it by new substrates as well as additional ligands. Moreover, this work focused on the application of the synthetic iron(IV)-oxido complex as substitute for the natural enzyme and incorporate reactivity studies that allow for mechanistic conclusions concerning the enzymatic oxidation process.***

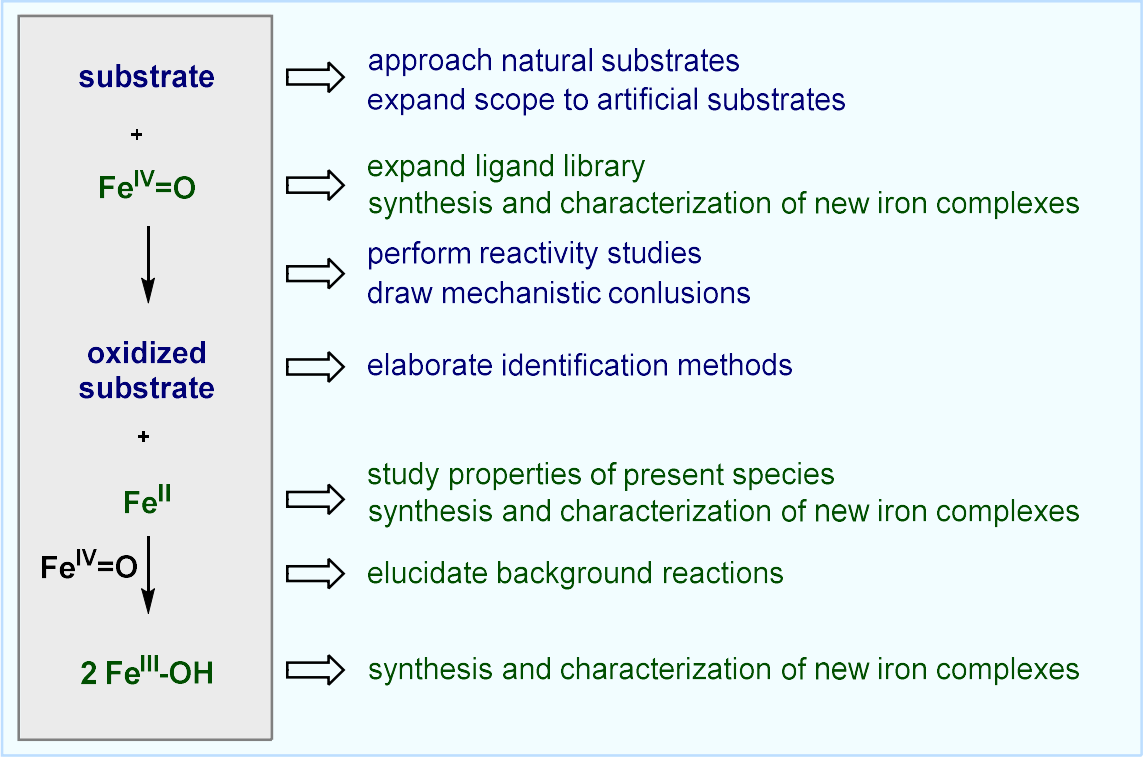

Figure 3: Graphical representation of the determined goals for this work, based on a substrate oxidation reaction performed by an iron(IV)-oxido complex serving as functional model for TET enzymes.

To further understand the established model system, background reactions in the illustrated substrate oxidation reaction (Figure 3) should be identified and the properties of all species present in the reaction mixture investigated. The substrate scope should be broadened towards the more complex, natural substrates of TET enzymes (DNA and RNA) and could therefore move the system closer to the natural process. Sequencing processes are an example of applications employing the natural enzyme in combination with its natural substrates. Therefore, the possibility of substituting the enzyme by the synthetic iron(IV)-oxido complex should be tested. Reactivity studies with further (artificial) substrates should give insight into the mechanism of substrate oxidation reactions or even into the mechanism of the enzymatic oxidation process.

The expansion of the established ligand systems allows for the synthesis and characterization of new iron complexes. Comparison of the reactivities of the different complexes should give insights into their specific properties and can eventually be exploited to achieve specific substrate oxidation products.

III. Iron(IV)-oxido Complexes as Model for TET Enzymes

The development of synthetic model complexes for enzymatic processes provides important mechanistic insights and information about intermediates in complicated enzymatic processes. Furthermore, its reactivity can be exploited to achieve difficult reactions performed in enzymatic catalysis. This chapter shows how a synthetic iron(IV)-oxido complex is established as model for the active site of TET enzymes. Its reactivity towards natural substrates is investigated with the goal of potentially substitute the enzyme in processes like sequencing applications. To broaden the scope of substrates, also artificial nucleobases were included in a reactivity study with the iron(IV)-oxido complex. Furthermore, the reactivity of the iron(IV)-oxido complex should be exploited to get mechanistic insights into the oxidation of 5fdC in the enzyme.

1 Approaching Natural Substrates of TET Enzymes

To further establish the synthetic iron(IV)-oxido complex as a suitable model for the active site of TET enzymes, the approach towards natural substrates is discussed in this chapter. However, if a similar reactivity is confirmed, the model complex can be tested as substitute for processes employing the enzyme. A large field with numerous processes including oxidation steps performed by TET enzymes consists of sequencing applications. In the following, a short overview is given about the current status of sequencing possibilities focusing on the detection of cytosine modifications.

The ability to determine the primary DNA code of entire genomes of organisms based on DNA sequencing technologies describes a milestone in research.[100-102] Until now, this research field is vastly improving and expanding. Only a couple of years ago the Human Genome Project could be accomplished after decades of work.[103-104] Since 1997, the so-called Sanger sequencing by synthesis (SBS) has become the standard sequencing method

and still is widely employed.[105-106] In this technology, fluorescently or radioactively labeled chain-terminating nucleotides (ddNTPs) terminate the DNA strand after incorporation by a DNA polymerase. After separation of the strands according to their lengths, the incorporated ddNTPs can be detected with the help of automated sequencing machines and allow the identification of the full DNA sequences. In the past few years, a new technology became popular which is called next-generation sequencing (NGS), performing high-throughput DNA sequencing.[101, 107] However, all these techniques lack the ability of accurately detect the epigenetically important DNA modification 5mC and its oxidized derivatives. To overcome this limitation, a variety of different procedures has been established. A selection of methods is presented in Figure 4, showing the chemical or enzymatic treatment of the native DNA containing cytosine modifications as well as the resulting readout from the sequencing technology.

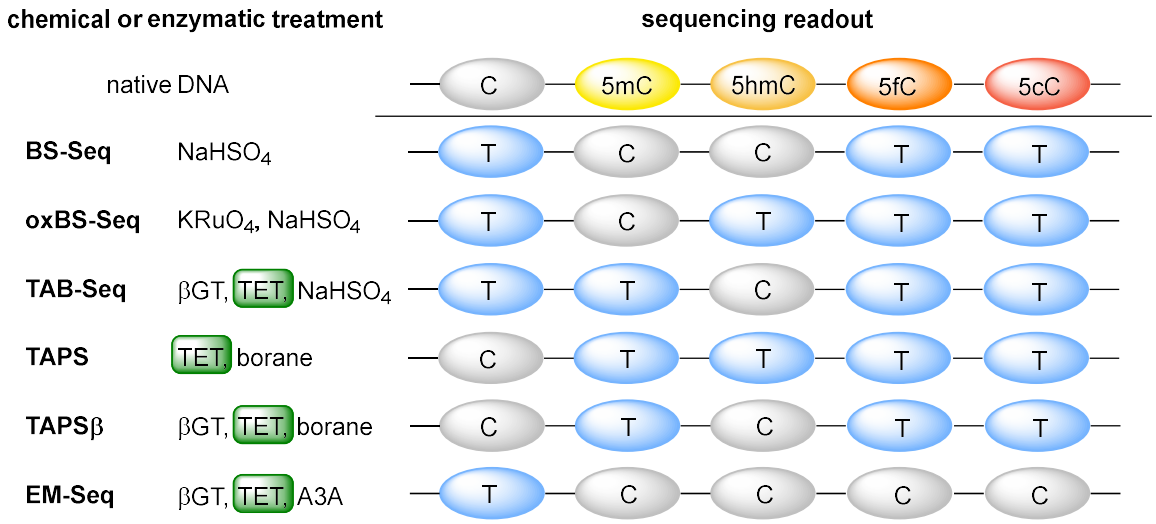

Figure 4: Overview of various currently applied sequencing methods with sample treatment and sequence readout for cytosine modifications. BS-Seq = bisulfate sequencing, oxBS-Seq = oxidative bisulfate sequencing, TAB-Seq = TET-assisted bisulfate sequencing, TAPS = TET-assisted pyridine borane sequencing, TAPSβ = TAPS with βGT protection sequencing, βGT = β-glycosyltransferase, EM-Seq = enzymatic methylation sequencing, A3A = APOBEC3A, an AID/APOBEC deaminase. Involvement of TET enzyme within sequencing procedure is highlighted in green.

Sequencing of cytosine modifications is classically performed by the bisulfate approach (BS-Seq[108]) where DNA samples are treated with sodium bisulfite under acidic conditions. This results in a deamination of cytosine generating uracil (Figure 5A) which in the sequencing process is read as thymine. 5mC does not react with bisulfite and 5hmC is transformed into

cytosine methylene sulfonate. Both nucleobases are not deaminated within the sulfonation procedure. For this reason, discrimination between 5mC and 5hmC is not possible.

This method has been expanded by the development of oxidative bisulfate sequencing (oxBS-Seq[109]) where the sample is treated with the chemical oxidant $KRuO_4$. This leads to selective oxidation of 5hmC whereas 5mC remains unchanged. After subsequent bisulfate treatment, the resulting read can be subtracted from a classic BS-Seq read enabling the determination of 5hmC amount present in the sample.

Furthermore, there are various approaches using TET enzymes for the oxidation of the cytosine modifications. One example, TET-assisted bisulfate sequencing (TAB-Seq[110]), is explained more detailed in Figure 5C. 5hmC is converted selectively to 5gmC by treatment with glucosyltransferase βGT and UDP-glucose (Figure 5B). In contrast to 5mC, it is therefore protected from oxidation by TET in the next step. Subsequent bisulfite treatment deaminates all cytosines and modifications except of the modified 5hmC.

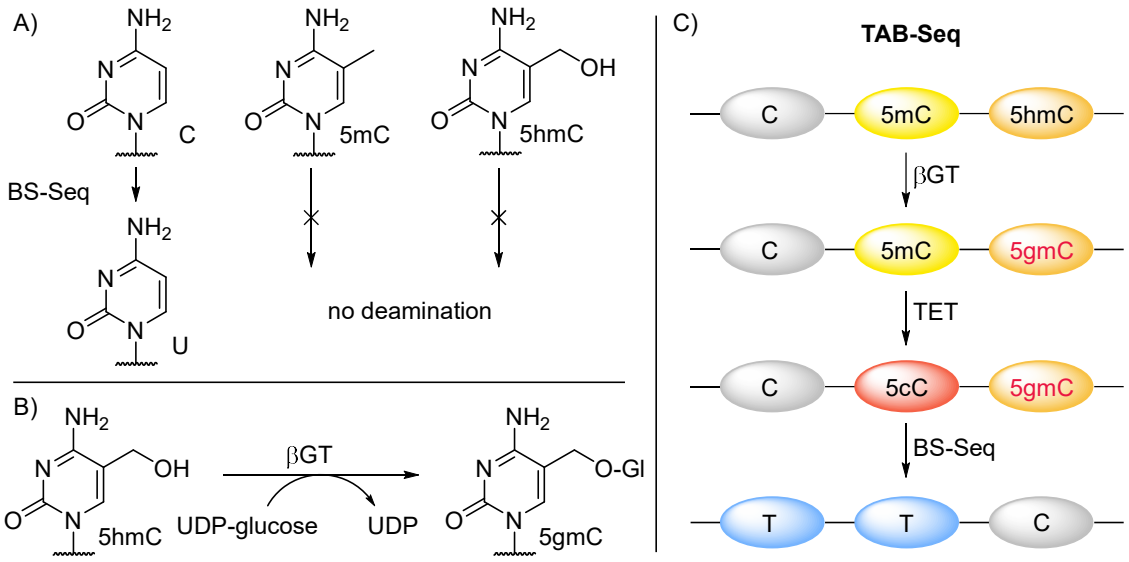

Figure 5: A) Within a bisulfate treatment cytosine is deaminated generating uracil whereas no deamination occurs with 5mC and 5hmC. B) Transfer of glucose from UDP-glucose to 5hmC generating 5gmC, catalyzed by glucosyltransferase βGT. C) Procedure applied in the TAB-Seq approach.[110] BS-Seq = bisulfate sequencing, UDP = uridine diphosphate, 5gmC = β-glycosyl-5-hydroxymethylcytosine, βGT = β-glucosyltransferase.

To avoid bisulfate treatment which is highly destructive for the DNA sample, non-destructive enzymatic approaches gain more and more popularity. In the enzymatic

methylation sequencing (EM-Seq[111]) deamination is achieved with an AID/APOBEC deaminase. This approach also uses TET enzymes for the oxidation of 5mC.

However, these techniques only allow indirect detection of cytosine modifications as they need to be compared with the results from a parallel BS-Seq experiment. Moreover, harsh chemical treatments are necessary and the usage of TET enzymes can also be challenging. With the growing importance of DNA modifications, researchers found promising alternative technologies. In the third generation sequencing (TGS) approach, native DNA samples can be sequenced directly without the need for prior amplification steps.[112-113] Two different technologies are available currently and consist of single molecules real-time sequencing (SMRT-Seq[114-115]) as well as oxford nanopore technology (ONT-Seq[116]). In ONT-Seq procedures, single-stranded native DNA or RNA travels through pores in electro-resistant membranes formed by small proteins. The thereby occurring electric current is measured and can be translated into the corresponding nucleobases with the aid of computational tools. The presence of cytosine modifications alters the detected signal and can be distinguished from the canonical nucleobases. With this method, cytosine modifications can therefore be detected in a single sequencing experiment without the need of further treatment. However, instead of distinguishing the specific modifications rather the totality of cytosine modifications is detected and only a differentiation between canonical and non-canonical cytosines is possible.

The necessity of TET enzymes within the sequencing procedures involves some tedious features such as sensitivity towards sample impurities and the presence of oxygen[110-111, 117-118] that could be overcome by a biomimetic substitute. The enzyme needs to be expressed and purified which takes about 9-10 working days, some procedures require even two different TET modifications (for example mTET1 and NgTET[111, 118]). Furthermore, TET activity is not reliable and has to be tested after purification in an activity assay which takes 4-5 more working days. Additionally, all enzyme samples have to be stored at -80 °C.

In contrast, all precursors of the iron(IV)-oxido complex $[Fe^{IV}\mathbf{L1}(O)]^{2+}$ are easily prepared from rather cheap starting materials within a week and can be stored at room temperature

for months. *In situ* preparation of $[Fe^{IV}\mathbf{L1}(O)]^{2+}$ from the corresponding iron(II) precursor takes about two hours.

It was therefore envisioned to further elaborate the synthetic iron(IV)-oxido complex as functional model for TET enzymes and investigate its activity towards more challenging substrates slowly approaching native DNA or RNA. As a long-term goal, this reactivity could eventually be exploited to substitute the need of TET enzymes in sequencing procedures by its synthetic counterpart. Furthermore, first sequencing experiments employing the ONT-Seq technology were anticipated together with the group of Pascal Giehr.

1.1 Investigations on the Reactivity of the Iron(IV)-oxido Complex Towards Ribonucleoside Substrates

In the process of increasing complexity of the studied substrates, not only DNA but also RNA samples were anticipated to be investigated. To start with more simple molecules it was decided to react the ribonucleoside 5mrC (5-metylribocytidine) with the iron(IV)-oxido complex (Scheme 6). These studies are based on the experiments described by Schmidl *et al.*[96] in which the reaction of the corresponding deoxynucleosides with the iron(IV)-oxido compound has been performed.

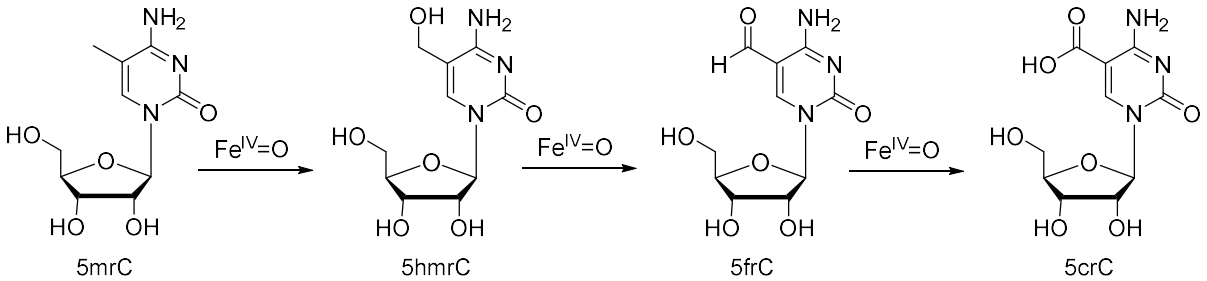

Scheme 6: Successive oxidation of the ribonucleoside 5mrC by the complex $[Fe^{IV}\mathbf{L1}(O)]^{2+}$ yielding 5hmrC, 5frC and 5crC.

Synthesis of reference samples

In order to identify the formed products from a reaction of 5mrC with $[Fe^{IV}\mathbf{L1}(O)]^{2+}$, the expected oxidation products 5hmrC, 5frC and 5crC needed to be present as reference samples. 5frC and 5crC were synthesized as described in Scheme 7 and the remaining compounds were provided by David Schmidl during his master thesis in our group.

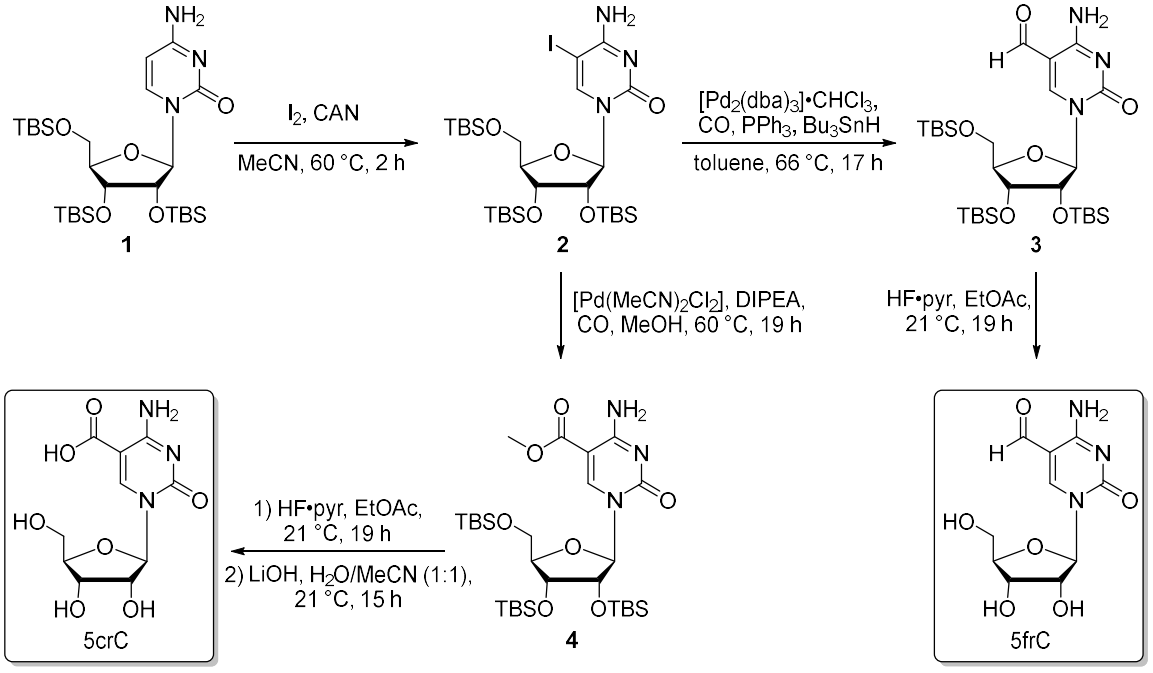

Scheme 7: Synthetic route towards the desired reference compounds 5frC and 5crC. TBS: *tert*-butyl dimethyl silyl, CAN: cerium(IV) ammonium nitrate, pyr: pyridine, DIPEA: di*iso*propyl ethyl amine.

The silylated cytidine **1** was transformed to the corresponding 5-iodocytidine precursor **2** by oxidative iodination with iodine and cerium(IV) ammonium nitrate (CAN). Palladium-catalyzed cross coupling of this compound in the presence of tributyltin hydride and carbon monoxide followed by a deprotection step yielded 5frC. If the reaction was carried out under basic conditions in methanol, the corresponding methoxycarbonylated species **4** could be obtained. Ester saponification with lithium hydroxide and deprotection afforded compound 5crC.

*Reaction of $[Fe^{IV}$**L1**$(O)]^{2+}$ with 5mrC as substrate*

In the reaction of 5mrC with $[Fe^{IV}$**L1**$(O)]^{2+}$, the reaction products should be identified with analytic high-performance liquid chromatography (HPLC) measurements. For this purpose, an HPLC method was developed where all potential compounds present in the reaction mixture (cytidine as well as cytosine derivatives) showed baseline-separated retention times. The resulting chromatogram is presented in Figure 6. More detailed information about the method parameters can be found in the appendix, Table 17.

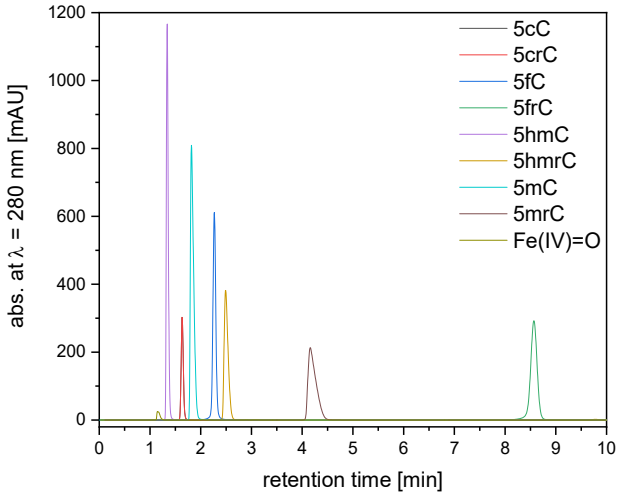

Figure 6: HPLC-chromatogram from the measurement of the reference samples. Conditions: c = 0.3 mg mL^{-1}, 30 °C, H_2O.

In order to quantify the formed reaction products, a dilution series of a mixture of all compounds (5mrC, 5hmrC, 5frC, 5crC, 5mC, 5hmC, 5fC, 5cC) was prepared (eight different concentrations ranging from 0.0012 to 0.099 mg mL^{-1}) and subjected to analytical HPLC measurements. From these measurements, calibration curves could be obtained.

The reaction of $[Fe^{IV}$**L1**$(O)]^{2+}$ with 5mrC was carried out in water under ambient conditions over a range of 70 min. Every 5 min, a sample was taken from the reaction mixture, the iron species separated from the mixture by filtration through silica to stop the reaction and the filtrate lyophilized. The resuspended residue was subjected to analytical HPLC and the resulting absorption peaks compared to the reference measurements. The obtained HPLC chromatograms are shown in Figure 7.

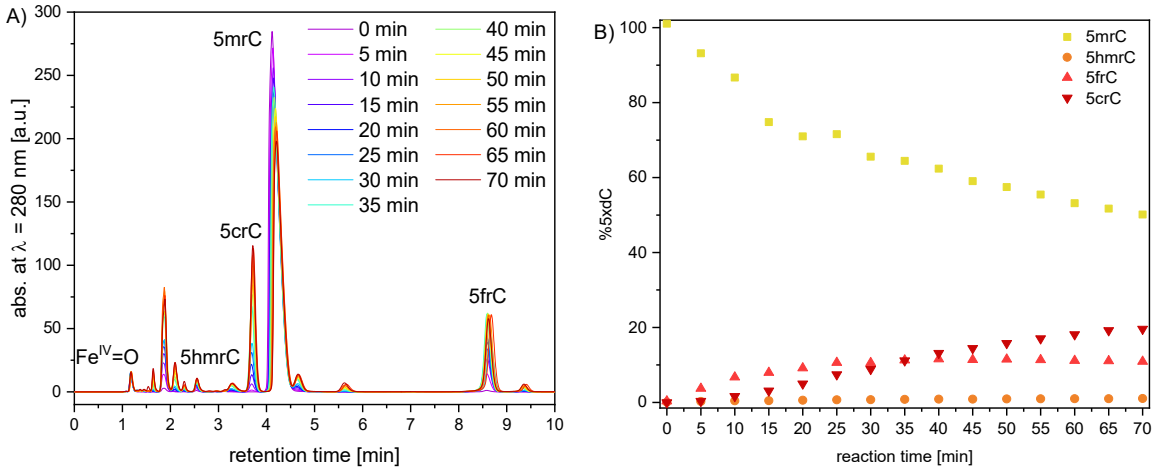

Figure 7: A) HPLC chromatograms of the obtained mixtures from a reaction of 5mrC with $[Fe^{IV}\mathbf{L1}(O)]^{2+}$ at different reaction times. B) Species distribution of cytidine derivatives over time. Condition: [5mrC] = 1 mM, $[Fe^{IV}=O]$ = 5 mM, H_2O, 25 °C.

All four ribocytidine derivatives could be detected in the HPLC chromatogram and were assigned by comparison with the retention times of the corresponding references. As expected, the amount of 5mrC starting material decreasing over time and a mixture of oxidation products formed. The amount of 5hmrC stayed very low over the entire investigated time frame, suggesting a fast transformation into the subsequent oxidation product 5frC. The amount of 5frC in contrast accumulated slightly in the beginning and then decreases minimally. Considering all oxidation products, the main species present at the end after a continuous increase is 5crC. These observations are perfectly in line with those made by Schmidl *et al.* for the reaction of $[Fe^{IV}\mathbf{L1}(O)]^{2+}$ with the corresponding deoxyribonucleoside 5mdC.[96]

The uncomplete consumption of starting material can be attributed to insufficient equivalents of iron complex present in the reaction mixture. Five equivalents of $[Fe^{IV}\mathbf{L1}(O)]^{2+}$ have been employed, however, at a later stage of this work it was found out that two equivalents were needed for the oxidation of one substrate due to a comproportionation side reaction of the formed iron(II) species with a second iron(IV)-oxido complex (refer to section IV.1.1 for more detailed information).

Furthermore, not only the formation of the oxidized nucleosides was observed but additionally also the corresponding nucleobases could be detected in the HPLC

chromatogram. Similar to the observations made by Schmidl *et al*. it is assumed here that oxidation occurs at the *C1*-position at the sugar moiety followed by the cleavage of the *N*-glycosidic bond (Scheme 8). This would lead to the formation of the corresponding nucleoside and a ribose γ-lactone. Another possibility would be the simple hydrolysis of the *N*-glycosidic bond resulting in ribonic acid. Further mass spectrometric analysis of side products could give more insights into the mechanism of the occurring side reactions.

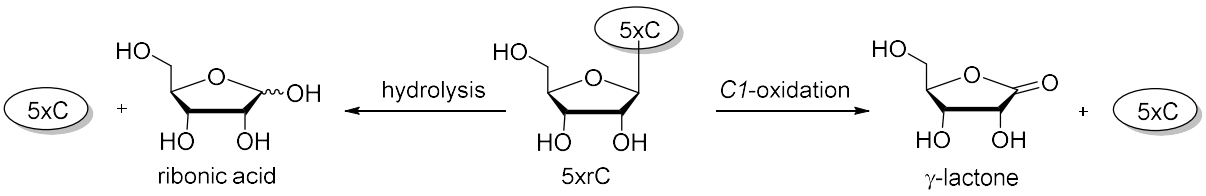

Scheme 8: Possible side reactions occurring in the oxidation of 5mrC with $[Fe^{IV}\mathbf{L1}(O)]^{2+}$ forming the cytosine nucleobases and ribonic acid (hydrolysis) or γ-lactone (C1-oxidation). The abbreviation 5xC stands for the cytosine modification 5mC including all oxidized derivatives.

To conclude, it could be shown that comparable to the corresponding deoxycytidine, also the ribonucleoside 5mrC can be oxidized to its natural metabolites 5hmrC, 5frC and 5crC within a reaction with $[Fe^{IV}\mathbf{L1}(O)]^{2+}$. Despite of many reactive sites in the sugar moiety of the nucleoside, preferably the anticipated reaction site is transformed and side reactions resulting in the cleavage of the *N*-glycosidic bond are only observed in small amounts.

1.2 Investigations on the Reactivity of the Iron(IV)-oxido Complex Towards Short Oligonucleotide Substrates

To further increase substrate complexity to slowly approach genomic DNA as natural substrate for TET enzymes, the next step from nucleobases and nucleosides was focused now on short oligonucleotides. Their reaction with the complex $[Fe^{IV}\mathbf{L1}(O)]^{2+}$ was first tested by Lindlar and Korytiaková *et al*. on a single stranded 5mdC-containing 10mer DNA oligonucleotide (compare introduction, section 0).[96] They showed about 7% conversion of the 5mdC nucleoside in the strand into the corresponding oxidation products. It was now anticipated to reproduce these experiments and increase the rate of conversion by

screening different reaction conditions. An overview of all oligonucleotide sequences used in this work is given in the appendix (section VII.1).

Reproducing previous experiments

To confirm the reproducibility of previous measurements, the 10mer oligonucleotide **oligo1**

5'- CCUUAACC[5mdC]G -3' (**oligo1**)

was reacted with $[Fe^{IV}\mathbf{L1}(O)]^{2+}$ under the same conditions as previously reported.[96] In this procedure, the reaction mixture was filtered over silica to be separated from the iron species. Subsequent digestion into nucleosides followed by ultra-high performance liquid chromatography tandem mass spectrometry (UHPLC-MS/MS) analysis for nucleoside quantification was performed by Hanife Sahin from the Carell group. Samples from the reaction mixture were taken over time to get more insight into the product distribution and the end of the reaction. Additionally, the study was expanded by a second ligand system (compare section IV.1.1 for details on synthesis, characterization and properties thereof) to investigate whether a different ligand environment has an impact on reaction outcome in terms of reaction rate, yield and product distribution. Exactly the same samples were taken in a reaction of $[Fe^{IV}\mathbf{L2}(O)]^{2+}$ with **oligo1**. Figure 8 shows the results of the reactions of **oligo1** with the two different iron(IV)-oxido complexes over time.

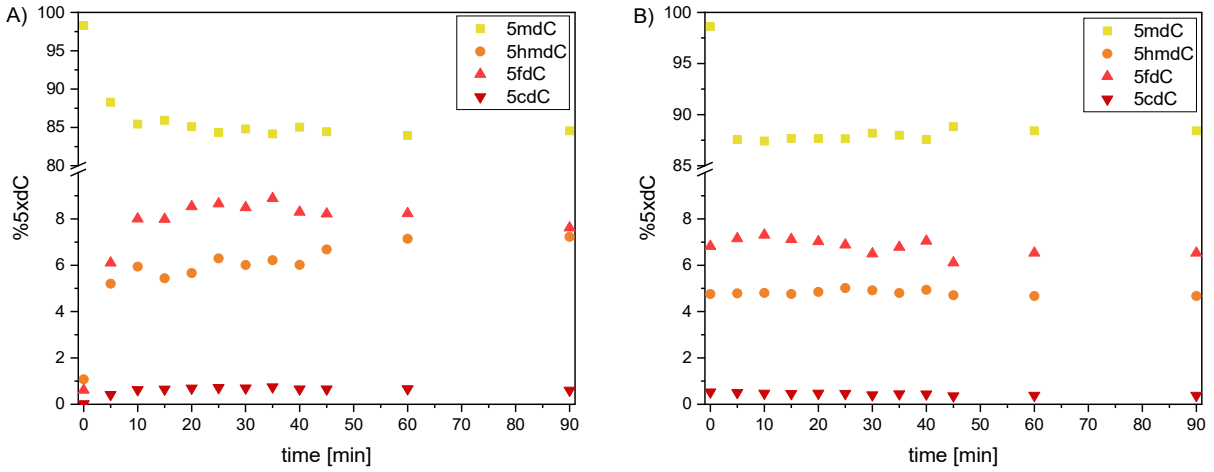

Figure 8: Amounts of 5xdC within the reaction of A) $[Fe^{IV}\mathbf{L1}(O)]^{2+}$ and B) $[Fe^{IV}\mathbf{L2}(O)]^{2+}$ with **oligo1** over time. Conditions: [**oligo1**] = 0.125 mM, $[Fe^{IV}{=}O]$ = 0.5 mM, H_2O, 25 °C. Quantification was performed by Hanife Sahin (Carell group, LMU Munich).

The results obtained in Figure 8A are in accordance with previous measurements.[96] Comparing the two ligand systems it can be stated that the reaction of **oligo1** with $[Fe^{IV}\mathbf{L2}(O)]^{2+}$ occurs significantly faster than with $[Fe^{IV}\mathbf{L1}(O)]^{2+}$ as the reaction seems to be completed after five minutes. However, the overall conversion of 5mdC starting material is lower in the reaction with $[Fe^{IV}\mathbf{L1}(O)]^{2+}$. Presumably, the higher reactivity of $[Fe^{IV}\mathbf{L1}(O)]^{2+}$ also leads to a higher amount of side reactions. Table 1 summarizes the obtained product distribution at the end of the reaction (after 90 min).

Table 1: Amount of 5xdC in a reaction of **oligo1** with $[Fe^{IV}\mathbf{L1}(O)]^{2+}$ and $[Fe^{IV}\mathbf{L2}(O)]^{2+}$ after 90 min reaction time.

	5mdC	5hmdC	5fdC	5cdC
$[Fe^{IV}\mathbf{L1}(O)]^{2+}$	84.56	7.23	7.62	0.60
$[Fe^{IV}\mathbf{L2}(O)]^{2+}$	88.42	4.67	6.53	0.38

Variation of reaction conditions

With this overview on the reactivity over time as a starting point, different reaction conditions (Table 2) were tested in order to affect the reaction outcome such as product distribution or overall yield. Changes in reaction temperature, concentration and equivalents of $[Fe^{IV}\mathbf{L1}(O)]^{2+}$/$[Fe^{IV}\mathbf{L2}(O)]^{2+}$ were tested. Samples were taken from the reaction mixture in certain time intervals (see section VI.3 for exact description).

Table 2: Conditions applied in the reaction of **oligo1** with $[Fe^{IV}\mathbf{L1}(O)]^{2+}$ and $[Fe^{IV}\mathbf{L2}(O)]^{2+}$. Ref is the reference sample with the starting conditions from the experiment shown in Figure 8, changes in conditions are highlighted in grey.

exp.	[oligo1]	temperature	equiv. Fe^{IV}=O
ref.	0.125 mM	25 °C	4 equiv.
1	0.125 mM	4 °C	4 equiv.
2	0.125 mM	40 °C	4 equiv.
3	0.05 mM	25 °C	4 equiv.
4	0.5 mM	25 °C	4 equiv.
5	0.125 mM	25 °C	6 equiv.
6	0.125 mM	25 °C	8 equiv.

The results of all different experiments can be found in the appendix (see section VII.6, Table 23). Figure 9 presents experiment 5 as example, showing the amounts of 5xdC over time.

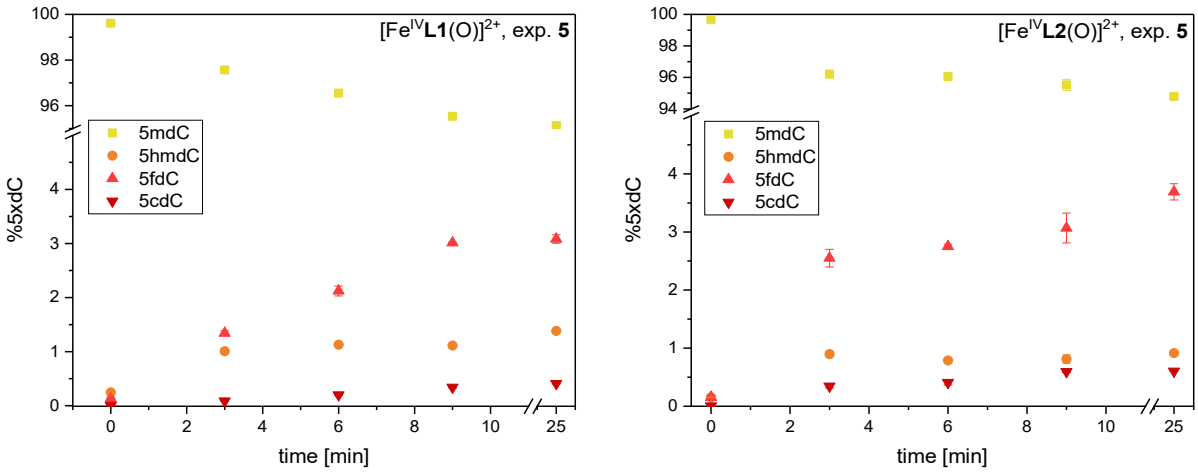

Figure 9: Amounts of 5xdC over time in a reaction of **oligo1** with $[Fe^{IV}\mathbf{L1}(O)]^{2+}$ (left) and $[Fe^{IV}\mathbf{L2}(O)]^{2+}$ (right). Conditions: [**oligo1**] = 0.125 mM, $[Fe^{IV}=O]$ = 0.75 mM, H_2O, 25 °C. Quantification was performed by Hanife Sahin (Carell group, LMU Munich).

Interestingly, the two iron(IV)-oxido complexes $[Fe^{IV}\mathbf{L1}(O)]^{2+}$ and $[Fe^{IV}\mathbf{L2}(O)]^{2+}$ show slightly different reactivity in terms of distribution of the oxidation products. The amount of formed 5hmdC is lower in the reaction with $[Fe^{IV}\mathbf{L2}(O)]^{2+}$, whereas the amount of 5fdC is higher compared to the reaction with $[Fe^{IV}\mathbf{L1}(O)]^{2+}$. This leads to a larger "gap" between

the two species 5hmdC and 5fdC in the reaction with $[Fe^{IV}\mathbf{L2}(O)]^{2+}$ which might be exploited in the future for specific enrichment of 5fdC for example.

To get an overall overview of the results of all the reactions described in Table 2, the amounts of 5xdC at the end of reaction were plotted for all experiments and for both iron(IV)-oxido species (Figure 10).

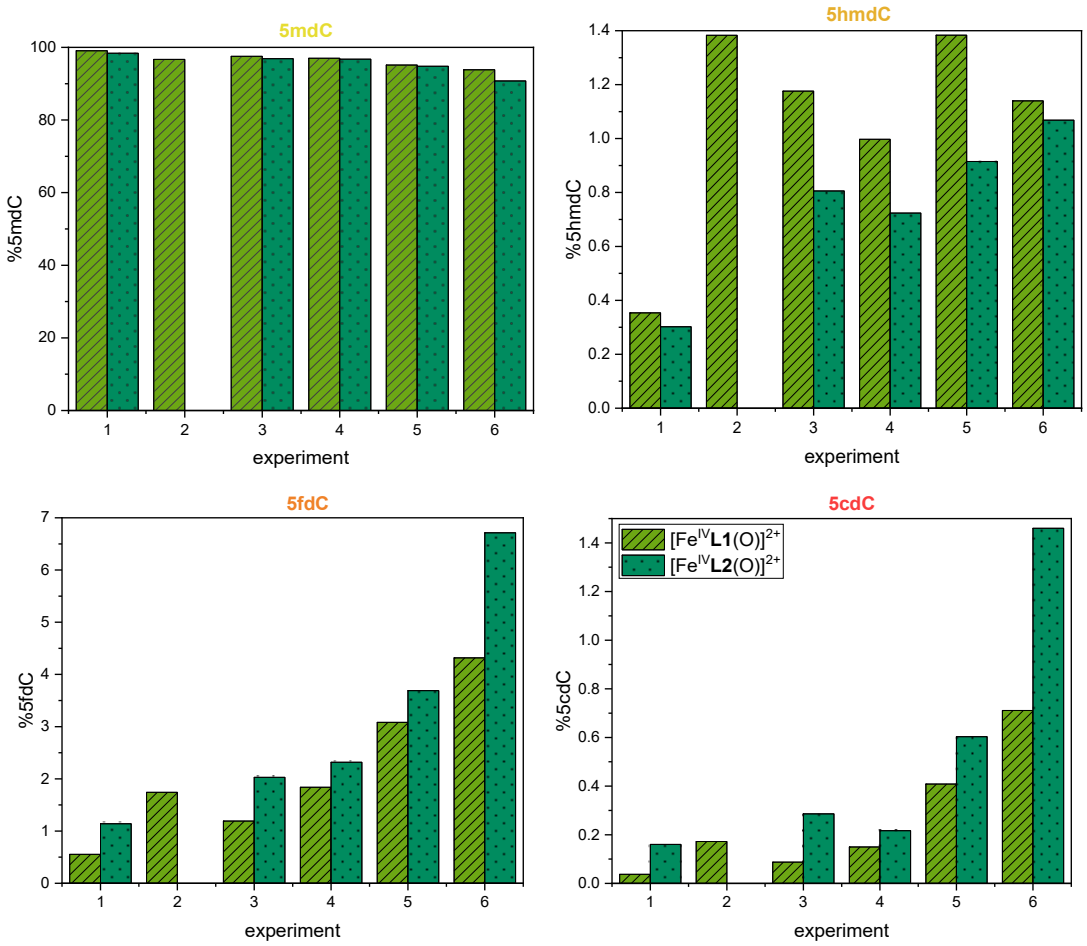

Figure 10: Amounts of 5xdC at the end of reaction of the different experiments (conditions see Table 2), shown for the two different iron(IV)-oxido species $[Fe^{IV}\mathbf{L1}(O)]^{2+}$ and $[Fe^{IV}\mathbf{L2}(O)]^{2+}$. Quantification was performed by Hanife Sahin (Carell group, LMU Munich).

Looking at the 5mdC consumption, it can be stated that surprisingly the reaction with $[Fe^{IV}\mathbf{L2}(O)]^{2+}$ leads to higher conversion of 5mdC. Comparing these values with previous results (Table 1: faster reaction with $[Fe^{IV}\mathbf{L2}(O)]^{2+}$, higher conversion with $[Fe^{IV}\mathbf{L1}(O)]^{2+}$), it can be concluded that probably impurity or decomposition of $[Fe^{IV}\mathbf{L1}(O)]^{2+}$ caused a reduced performance in the experiments. To avoid or better recognize such variations in

performance, it was decided to always include a reference measurement at the beginning and at the end of the experimental setup with known reactivities (see 'ref.' in Table 2).

Nevertheless, the interesting features about different product distribution depending on the iron(IV)-oxido species already mentioned above are clearly visible in this representation. The amount of 5hmdC is higher in the reaction with $[Fe^{IV}\mathbf{L1}(O)]^{2+}$, whereas the amounts of 5fdC as well as 5cdC are higher in the reaction with $[Fe^{IV}\mathbf{L2}(O)]^{2+}$.

In addition to a difference in product distribution, the goal of this screening was also to find conditions leading to higher overall conversion of 5mdC. More equivalents of iron(IV)-oxido species result in a higher conversion but still the amount of oxidized products remain very low. A series of experiments was now conducted, following the impact of $[Fe^{IV}\mathbf{L1}(O)]^{2+}$ equivalents (small steps between 4 and 40 equivalents) on the conversion of 5mdC (Figure 11).

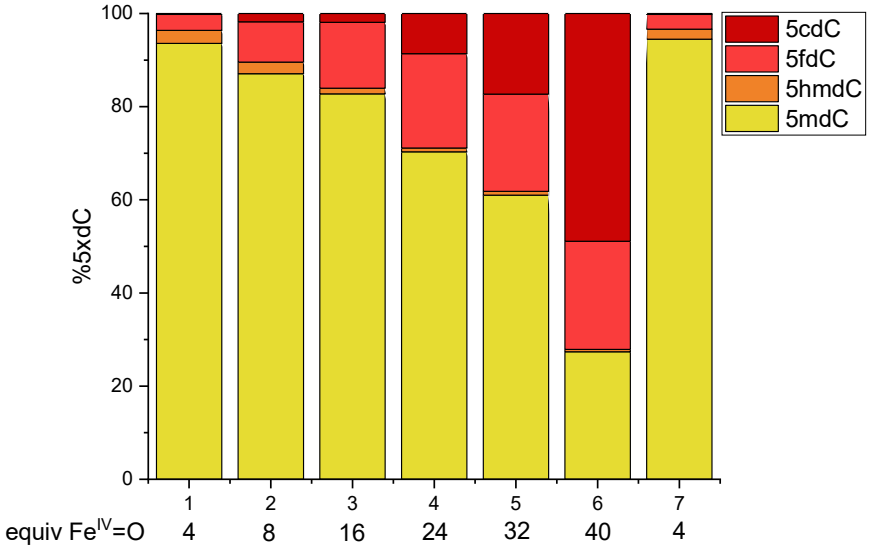

Figure 11: Amounts of 5xdC in a reaction of **oligo1** with $[Fe^{IV}\mathbf{L1}(O)]^{2+}$ after a reaction time of 1 hour. Conditions: [**oligo1**] = 0.125 mM, $[Fe^{IV}=O]$ = 0.5-5 mM, H_2O, 25 °C. Experiment 7 consists of a control measurement in iron(IV)-oxido activity performed at the end of the series of experiments. Quantification was performed by Hanife Sahin (Carell group, LMU Munich).

The overall oxidation of 5mdC increases with increasing iron(IV)-oxido equivalents. Although the iron(IV)-oxido equivalents are raised with equal intervals, the overall oxidation of 5mdC increases non-linearly and the differences vary more with higher equivalents. For example between 24 and 32 equivalents of iron(IV)-oxido complex, an

increase of 11% in overall oxidation is observed, whereas between 32 and 40 equivalents of iron(IV)-oxido complex, the overall oxidation rises to 34%.

The distribution of the oxidation products 5hmdC, 5fdC and 5cdC seems also to depend on the iron(IV)-oxido equivalents applied. 5hmdC is only part of the main products at very low equivalents. This could be expected as 5hmC with the lowest bond dissociations energy (BDE, see appendix section VII.3, Table 22 for calculated values) reacts fast and all formed 5hmdC is immediately converted to 5fdC. The 5fdC level remains quite constant at higher iron(IV)-oxido equivalents with decreasing 5mdC and increasing 5cadC level. The BDE of 5fC is slightly higher than that of 5mC. Both 5mdC and 5fdC seem to react with similar reaction rates so that the amount of 5fdC does not change significantly. This is an interesting feature as with this property, the distribution of oxidation products can be influenced by the iron(IV)-oxido equivalents. For example in a reaction carried out with 16 equivalents, 5fdC is the main species upon the oxidation products, whereas 40 equivalents afford mainly 5cadC.

The two experiments affording 5fdC as main species were repeated with both iron(IV)-oxido species ($[Fe^{IV}\mathbf{L1}(O)]^{2+}$ or $[Fe^{IV}\mathbf{L2}(O)]^{2+}$) and samples were taken over time (Figure 12).

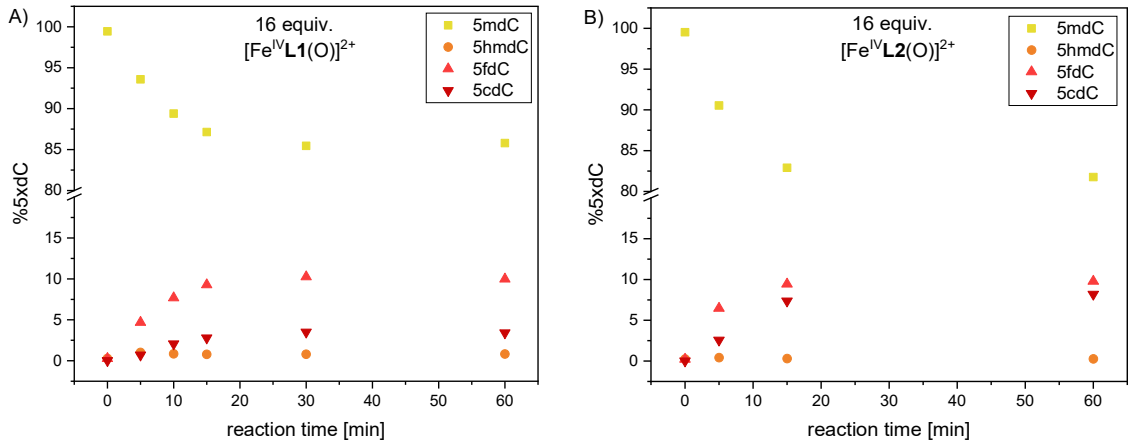

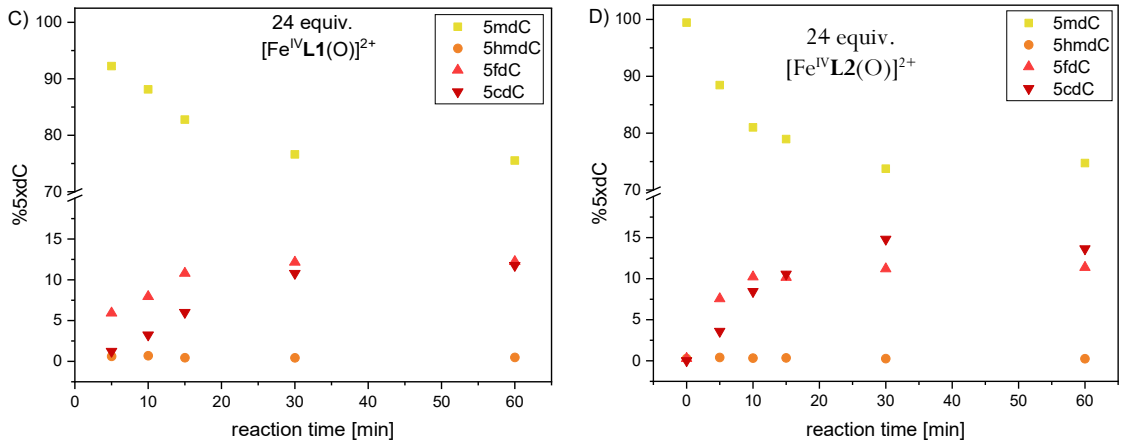

Figure 12: Amounts of 5xdC over time in a reaction of **oligo1** with A) 16 equiv. $[Fe^{IV}\mathbf{L1}(O)]^{2+}$ B) 16 equiv. $[Fe^{IV}\mathbf{L2}(O)]^{2+}$. C) 24 equiv. $[Fe^{IV}\mathbf{L1}(O)]^{2+}$ and D) 16 equiv. $[Fe^{IV}\mathbf{L2}(O)]^{2+}$. Conditions: [**oligo1**] = 0.125 mM, $[Fe^{IV}{=}O]$ = 2-3 mM, H_2O, 25 °C. Quantification was performed by Hanife Sahin (Carell group, LMU Munich).

As also previously observed, complex $[Fe^{IV}\mathbf{L2}(O)]^{2+}$ reacts faster and in contrast to the reaction with $[Fe^{IV}\mathbf{L1}(O)]^{2+}$ 5fdC and 5cdC levels are similar at the end of reaction (Figure 12A and B). More equivalents of iron(IV)-oxido complex result in higher amounts of 5cdC which now consists of the main species amongst the oxidation products. It seems that in a faster reaction (due to more reactive iron(IV)-oxido complex $[Fe^{IV}\mathbf{L2}(O)]^{2+}$ or more equivalents thereof, Figure 12B, C and D) the amounts of 5fdC and 5cdC are very similar, whereas a gap between the two species can be observed for slower reactions (Figure 12A). Therefore, it would be interesting in further experiments to decrease the reaction rate for instance by performing the reaction in lower concentrations to see whether further accumulation of 5fdC can be observed under these conditions.

Thymine-containing oligonucleotides

In future experiments, DNA which contains the nucleobase thymine (T) will also be tested as substrate for the iron(IV)-oxido complexes. As the C-H bond dissociation energy of the methyl group of thymine is lower than that of 5mC, it is expected to react faster with the iron(IV)-oxido complex.[119] To find out whether 5mC is still oxidized to a certain amount in the presence of thymine, short thymine-containing oligonucleotides were used as substrate for the iron(IV)-oxido complex.

5'- CCUUAACC[5mC]G -3' (**oligo1**)

5'- CCTUAACC[5mC]G -3' (**oligo2**)

5'- CTTTAACC[5mC]G -3' (**oligo3**)

A reference without thymine (**oligo1**), a sample containing one (**oligo2**) and three (**oligo3**) thymines were treated with six equivalents of $[Fe^{IV}\mathbf{L1}(O)]^{2+}$. A sample was taken from the reaction mixture after 30 minutes and subsequently again six equivalents of $[Fe^{IV}\mathbf{L1}(O)]^{2+}$ were added. Another sample was taken after 60 minutes. The results are presented in Figure 13.

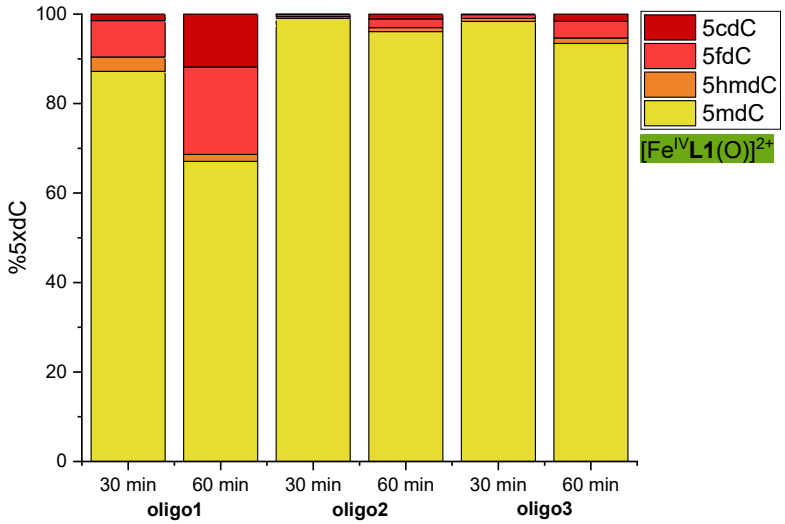

Figure 13: Amounts of 5xdC in a reaction of **oligo1**, **oligo2** and **oligo3** with $[Fe^{IV}\mathbf{L1}(O)]^{2+}$. Conditions: [**oligo**] = 0.125 mM, $[Fe^{IV}=O]$ = 0.75 mM, H_2O, 25 °C. Quantification was performed by Hanife Sahin (Carell group, LMU Munich).

Unfortunately, only very low conversion of 5mdC could be observed when thymine is present in the sample. No significant differences between **oligo2** and **oligo3** were noted in this experiment. In view of the promising results discussed above with higher conversion of 5mdC due to more equivalents of iron(IV)-oxido species, it would also be interesting here to test a significantly higher amount of $[Fe^{IV}\mathbf{L1}(O)]^{2+}$ in the reaction.

In addition to the cytosine derivatives, also the thymine (T) and 5-hydroxymethyluracil (5hmU) content was determined (Table 3) which shows that thymine is oxidized by $[Fe^{IV}\mathbf{L1}(O)]^{2+}$ as expected.

Table 3: Amounts of T and 5hmU in a reaction of **oligo2** and **oligo3** with $[Fe^{IV}\mathbf{L1}(O)]^{2+}$.

		T	**5hmU**
oligo2	30 min	90.41	9.59
	60 min	89.59	10.41
oligo3	30 min	91.82	8.18
	60 min	90.79	9.21

These experiments show that the presence of thymine residues in DNA strands seems to be problematic as their oxidation occurs faster than that of the anticipated 5mC residue. Therefore, it would be very useful to test reactivities of the corresponding RNA strands as with the presence of uracil instead of thymine, this problematic would be ruled out.

Double-stranded oligonucleotides

In the work of Schmidl, Lindlar and Korytiaková a reaction of the iron(IV)-oxido complex with double-stranded oligonucleotides revealed no significant amount of the expected oxidation products.[96] The species that could be observed in very low amounts were attributed to products from the reaction of single-stranded oligonucleotide within the mixture. This was assumed due to the very low melting temperature of 27 °C (T_m, temperature at which half of the DNA strands are present in a single-stranded state). To ensure that oligonucleotide annealing is complete, it was anticipated to shift the melting temperature towards higher temperatures avoiding the presence of single stranded **oligo1** within a reaction at room temperature. Addition of monovalent cations (e. g. Li^+, Na^+, K^+, Cs^+) leads to a slight increase of the melting temperature whereas bivalent cations (e. g. Mg^{2+}, Ca^{2+}, Ba^{2+}, Mn^{2+}) are known to increase the melting temperature even further.[120] This expectation could be realized by addition of sodium chloride or magnesium chloride. Despite of the shift of the melting temperature from 27 °C to 41 °C, it seems that there is still single stranded oligonucleotide present at room temperature as the curve does not tail out at low temperatures. This experiment was carried out with **oligo1** purchased in desalted quality, still containing impurities of 9mers and 11mers. It was therefore assumed that they may not anneal perfectly if these impurities are present.

To prove this hypothesis, the experiment was repeated with **oligo1** and **oligo1-comp** in HPLC purity (Figure 14).

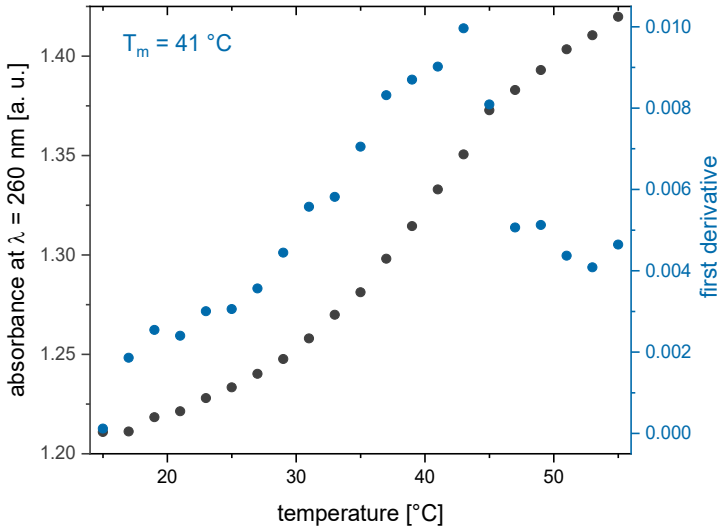

Figure 14: Plot of the absorbance of the DNA strands at 260 nm over different temperatures and first derivative of the obtained curve. Conditions: [**ds-oligo1**] = 0.125 mM, [$MgCl_2$] = 100 mM, water, T = 15-55 °C.

No difference could be observed for **oligo1** in HPLC purity compared to desalted quality. Possibly the sequence or length of **oligo1** does not favor complete annealing. This experiment could be broadened to a larger temperature range to see if at some point a completely flat development of the curve is reached and it could be tested to carry out **ds-oilgo1** experiments at lower temperatures such as 4 °C.

Nevertheless, a reaction of the iron(IV)-oxido complex with the double-stranded oligonucleotide was tested and no anticipated oxidation products could be observed. Probably, steric reasons hinder the accessibility of the methyl group by the bulky iron complex. Thus, it seems that double-stranded samples are no suitable substrate for this iron(IV)-oxido model complex. To circumvent this problem and nevertheless be able to use this complex for sequencing applications it would be more promising to focus on sequencing of RNA samples that are naturally occurring in single strands. Additionally, it can be attempted to open the strands for the time of the reaction with the iron(IV)-oxido complex for example by performing the reaction at higher temperatures.

MALDI-MS experiments

To identify possible decomposition of the oligonucleotide strand within the oxidation process, the oxidized samples were examined with matrix-assisted laser desorption ionization (MALDI) coupled with time of flight (TOF) mass spectrometry. At first, the parameters employed by Lindlar and Korytiaková[96] were repeated to ensure reproducibility of the data. The recorded spectrum (see appendix section VII.7, Figure 75) revealed identical features compared to the one depicted in the publication[96] with the only difference being the peak resolution (publication: old instrument, peak width 5-15 m/z; this work: new instrument, resolution of isotopic pattern). With the new resolution it was possible to confirm the presence of the oxidation products **oligo1**-5hmC and **oligo1**-5fC (Scheme 9).

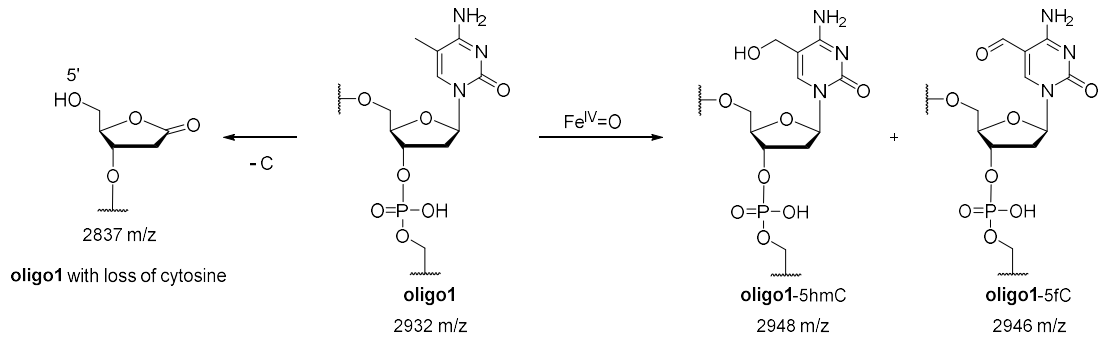

Scheme 9: Observed compounds in a reaction of **oligo1** with $[Fe^{IV}\mathbf{L1}(O)]^{2+}$ followed by MALDI-MS experiments under the conditions employed by Lindlar and Korytiaková.[96] Conditions: [**oligo1**] = 0.125 mM, $[Fe^{IV}=O]$ = 0.5 mM, H_2O, 25 °C, 20 min.

Oligo1-5cC was not detected in this experiment, which is not surprising considering the four equivalents of iron(IV)-oxido complex employed and the necessity of two equivalents of complex for one substrate oxidation. Furthermore, an observed m/z value was attributed to a decomposition product of **oligo1** resulting from the cleavage of one cytosine nucleobase. This side product has previously been proposed in the respective oxidation reaction with nucleosides instead of oligonucleotides (section III.1.1). The loss of cytosine from **oligo1** could possibly occur at the end of the oligonucleotide (which is more exposed) or at the cytidines positioned in the middle of the strand. Further m/z values have been observed that could not be attributed to specific species, eventually

indicating arbitrary oxidative bond cleavages leading to a variety of different decomposition products.

A variety of samples from **oligo1** oxidation reactions under different conditions was measured to get an idea of the amount of oligonucleotide decomposition within these reactions. An overview of the conditions and the resulting MALDI signals is given in the appendix, section VII.7, Table 25. With progressing reaction time, first unreacted **oligo1** and the corresponding oxidation products can be observed. Then they turn into unknown oxidation products (m/z higher than **oligo1**, see appendix section VII.7, Figure 76) and in the end only signals with low masses remain. Increasing the iron(IV)-oxido equivalents provokes the same result. Thus, it can be stated that with more than 4 equivalents of iron(IV)-oxido complex or reaction times longer than 20 minutes, no signal of **oligo1** or its expected oxidation products can be observed anymore. Unfortunately, these results revealed partial or complete decomposition of **oligo1** under these reaction conditions. Besides of the structures represented in Scheme 9, no further signals could be assigned.

To conclude, acceptable yield in overall conversion of 5mdC in **oligo1** into the natural metabolites was only achieved with high amounts of iron(IV)-oxido species. MALDI-MS measurements in contrast demonstrated decomposition of the oligonucleotide strand under these conditions. In this setup it will be challenging to find conditions suitable for the elimination of both problems concurrently. With modifications of the ligand system of the iron complex and possibly also immobilization on a solid support to control possible side reactions, these problems may be remedied.

Additional Q-TOF experiments

In order to work more independently it was decided to try out whether the Q-TOF instrument in our group would also be suitable for a first condition screening. Consequently, only selected samples might be analyzed and thoroughly quantified by external collaborators.

In a standard procedure, oligonucleotides were reacted with the iron(IV)-oxido complex under different reaction conditions, digested to nucleosides and analyzed with LC-MS/MS measurements. Thus, an HPLC method was developed using a mixture of all cytosine modifications including nucleosides as well as nucleobases.

An UHPLC column (C18-PFP material) was chosen and it was first developed which flow rate could be applied on this column without having a too high pressure. It was possible to increase the flow rate from 0.25 mL/min to 0.4 mL/min. Furthermore, the sample concentration was optimized for the UV trace (0.5 mM) und the mass trace (0.05 mM). The final parameters of the HPLC method are summarized in Table 4.

Table 4: Parameters applied for the final HPLC conditions.

column	ACE C18-PFP (100 x 2.1 mm)
temperature	30 °C
solvents	A: H_2O + 0.1% FA; B: MeOH + 0.1% FA
flow	0.4 mL/min
injection volume	3 µL
sample conc.	0.05 mM in water
gradient	0% B (2min) $\xrightarrow{15\ min}$ 15% B $\xrightarrow{2\ min}$ 100% B (5 min) $\xrightarrow{2\ min}$ 0% B (10 min)

Unfortunately, a significant amount of species is already detected within isocratic elution with 100% solvent A (H_2O + 0.1% FA). These absorption peaks could not be perfectly separated (Figure 15). Other columns should be tested here with longer elution pathway or different material. Additionally, the method needs to be optimized also considering the other nucleosides present in the digested reaction mixture (cytidine, guanosine, adenosine, uridine).

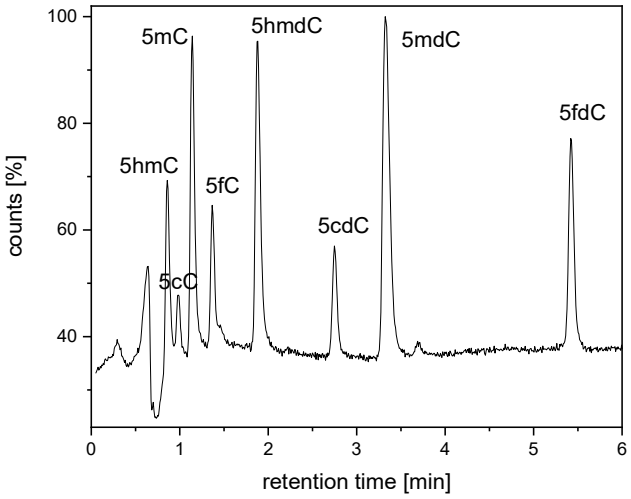

Figure 15: Excerpt of the HPLC-MS trace of a mixture of 5xdC and 5xC derivatives. Conditions: [5xdC] = [5xC] = 0.05 mM, H_2O, 30 °C.

This method with a good separation of the relevant cytosine nucleoside modifications was applied on a reaction sample of oligo1 with $[Fe^{IV}\mathbf{L1}(O)]^{2+}$ and digested by Hanife Sahin (without addition of a standard for quantification and using only DNA degradase for the digestion). The obtained HPLC-MS trace is depicted in Figure 16.

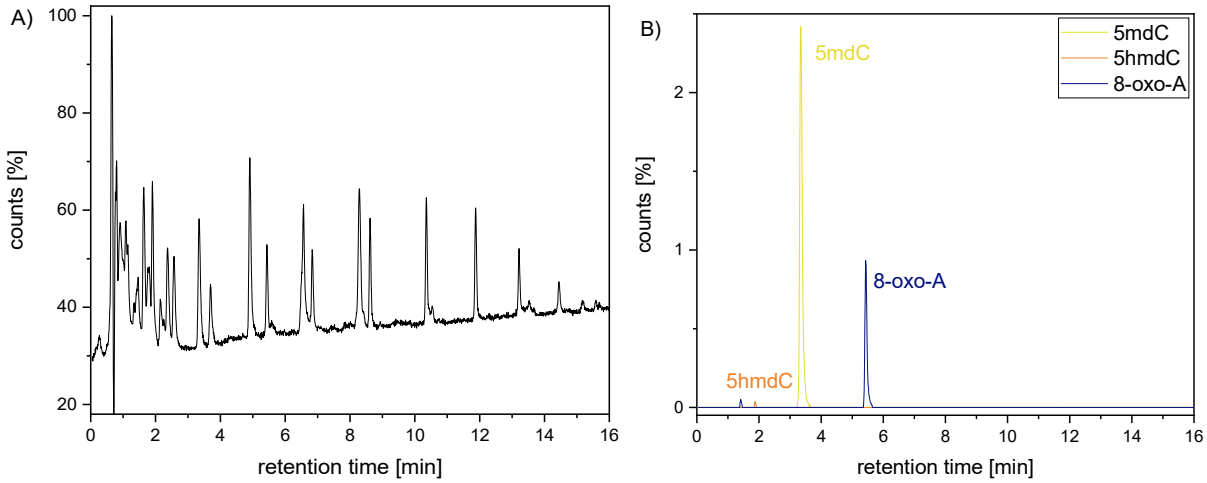

Figure 16: A) Excerpt of the HPLC MS trace of a reaction sample (reaction conditions: $[Fe^{IV}=O]$ = 0.25 mM, [**Oligo1**] = 1.00 mM, H_2O, 23 °C, 30 min) digested by Hanife Sahin. B) Extracted masses from A) for 5mdC, 5hmdC and 8-oxo-A. HPLC method as described in Table 4.

As expected, there is a variety of different species present and not all of them could be separated in this HPLC method. Mass extraction of the desired cytosine modifications showed the presence of 5mdC and a small amount of 5hmdC, whereas 5fdC and 5cdC could not be detected. A reason for no 5fdC detection might be the digestion procedure as

the missing enzyme should be responsible for 5fC cleavage in the oligonucleotide. Comparison with previously obtained results suggest similar amounts of 5hmdC and 5fdC or higher 5fdC content. In all former experiments, the 5cdC amount was very low, so its concentration might be under the detection limit here.

A huge disadvantage in this experimental setup here is the large difference in the concentration of the species present in the sample. Unfortunately, it is not possible to enable detection of species with low concentration through increase of the injection volume as the therein resulting amount of higher concentrated species is not suitable for MS-measurements.

In analogy to the previously published experiments, also here the amount of 8-oxo-guanine (possibly evolving from a side reaction between $[Fe^{IV}\mathbf{L1}(O)]^{2+}$ and guanine) was investigated and no 8-oxoG was detected. Surprisingly, a m/z value was found that could be assigned to 8-oxo-adenine, however this needs to be verified with a reference sample.

It can be stated that in the end the described method is limited by the insufficient separation of the different species present due to fast elution as well as by the large differences in concentration of the species present in this mixture. Statements about the amounts of cytidine derivatives are therefore not possible. Nevertheless, this experiment confirms the observations made from MALDI-MS measurements. In addition to the expected nucleosides cytidine with derivatives, guanosine, adenosine and uridine, also a high amount of other species presumably deriving from oxidation side reactions is present in this mixture.

To conclude, reactivity studies between the iron(IV)-oxido complex and oligonucleotide substrates showed that 5mdC is oxidized to its natural metabolites in oligonucleotides. The overall oxidation of 5mdC was increased from about 7% to the significantly higher amount of 63%. Furthermore, depending on the reaction conditions and especially the iron(IV)-oxido complex employed, the accumulation of 5fdC from all oxidation products could be achieved. In thymine-containing oligonucleotides, no significant 5mdC oxidation was

observed due to the fast oxidation of the methyl group of the thymine residue. Similarly, double-stranded oligonucleotides revealed no oxidation of 5mdC in reactions with the iron(IV)-oxido complex, possibly due to steric hindrance. A major challenge was found in the analysis of MALDI-MS measurements, revealing nearly complete decomposition of the oligonucleotide strand at longer reaction times and/or higher equivalents of iron(IV)-oxido complex. This problem certainly needs to be further addressed, although it seems challenging to find conditions combing high oxidation rates and intact oligonucleotide strands with the unmodified ligand system. Additional analyses such as MS/MS experiments could be helpful for the identification of the decomposition products to find out whether strand decomposition mainly occurs at the end or also in the middle of the strand. To reduce unwanted side reactions, iron(IV)-oxido complexes with modifications of the ligand could be tested. These could for example consist of additional moieties capable of selective coordination to the nucleobase substrate or immobilization of the complex on a solid support.

1.3 Investigations on the Reactivity of the Iron(IV)-oxido Complex Towards Single-Stranded DNA Substrates

With the hope of finding mainly decomposition at the end of the strand or methods to reduce unwanted side reactions generally, the reactivity of the synthetic iron(IV)-oxido complex towards DNA samples was investigated in a next step to test this complex for possible sequencing applications. As it was shown that in double-stranded samples no reaction with 5mdC occurred in significant amounts, single stranded-DNA samples were chosen for first reactivity studies. Luckily, also for many sequencing methods, single strands are required and it was anticipated to also carry out sequencing experiments with the reacted samples together with the group of Pascal Giehr. An overview of the sequences of all employed DNA strands can be found in the appendix, Table 21.

DNA isolation from reaction solution

Before reactivity studies were investigated, a suitable method for isolation of the DNA from the reaction solution needed to be established. For DNA analysis after reaction with the iron(IV)-oxido complex it is necessary to be able to stop the reaction at a specific time as well as to separate the reactive/reacted iron species from the reaction solution. For the previous reactions with oligonucleotides, this was accomplished by filtration over silica which retains the iron species. This method was also tested with DNA (further referred to as *method A*). The concentration of DNA in the sample after each workup method was determined by absorption measurement at 260 nm (nanodrop). Unfortunately, in the silica filtration method, some silica is washed into the sample and this falsifies the concentration measurement as silica shows slight absorption in the relevant area for DNA (260 nm). *Method A* was applied to samples without DNA (water only) and the concentration measured to get an idea of the silica background. The average of ten such experiments (*method A*, water only) is given in Table 5.

Table 5: Different methods applied for DNA isolation and corresponding concentrations found by nanodrop measurement. **DNA1-contr** was used for all DNA isolation experiments. Initial DNA concentration: 25.23 ng/µL.

experiment	**concentration**
untreated DNA	20.018 ng/µL
filtration over silica (*method A*)	7.770 ng/µL
filtration over silica (*method A*, water only)	2.624 ng/µL
magnetic beads standard procedure (*method B*)	0.138 ng/µL
magnetic beads modified procedure (*method C*)	4.140 ng/µL

It has to be noted here that the silica background varies significantly within the series of experiments with the highest value measured being 8.350 ng/µL (for all values see section VI.3, Table 15). This means that subtracting the silica background from specific DNA samples implies impreciseness and also the measured DNA concentration (*method A*) of 7.770 ng/µL might only occur from silica absorption without DNA present in the sample.

Therefore, another method was tested comprising magnetic beads that bind DNA and the remaining reaction solution can be removed. The standard procedure[121] was applied (*method B*) as well as a modified procedure (*method C*, see section VI.3 for details) suggested for short DNA strands. Unfortunately, both methods did not yield the expected concentrations (see Table 5). Eventually the applied DNA strand **DNA1-contr** is too short and does not bind to the magnetic beads.

Subsequently, an *Oligo Clean & Concentrator* kit from Zymo Research was tested. In this method, DNA is bound to a small column with the help of a special DNA binding buffer and the remaining reaction solution separated by centrifugation. After washing steps, the DNA can be re-isolated from the column with water. In a first try, **DNA1-contr** could be isolated with 61% recovery. This method will therefore be applied in further experiments.

Oxidation of 5mdC in single-stranded DNA as substrate for the iron(IV)-oxido complex

First, **DNA1** was reacted with three equivalents of $[Fe^{IV}\mathbf{L1}(O)]^{2+}$ per methyl group (5mC and T). The *Oligo Clean & Concentrator* method was applied and afforded DNA recoveries of 67-97% (see section VI.3, Table 16). The higher yield of DNA recovery compared to the first try was attributed to a change in the procedure, where water at a temperature of 40 °C was employed in the last elution step instead of room temperature. Additionally, a slightly different strand was used with **DNA1** containing one 5mdC instead of cytidine in **DNA1-contr**.

Enzymatic digestion revealed that only about 1% oxidation of 5mdC and about 6% oxidation of thymine occurred (see appendix, Table 24). The higher amount of thymine oxidation was expected from the lower BDE and previous experiments on the nucleobases.[119] Nevertheless, it is still promising that 5mdC oxidation by the synthetic model complex occurs at all given the complexity of the substrate. To get more insights into the amount of intact DNA strand or possible decomposition, MALDI-MS measurements were performed. After reaction with $[Fe^{IV}\mathbf{L1}(O)]^{2+}$, significantly broader peaks could be observed as well as the appearance of many new peaks at lower m/z values.

No signals were assigned to plausible reaction products. To exclude that the different appearance in the MADLI-MS trace of the isolated DNA after reaction was evoked by the workup procedure, the same reaction was carried out with only addition of water instead of iron(IV)-oxido compound. Also this sample was subjected to MALDI-MS analysis and the resulting spectrum (see appendix, Figure 78) revealed intact **DNA1** by comparison to a measurement of untreated **DNA1** (see appendix, Figure 77).

As the decomposition issue observed with oligonucleotides (compare section III.1.2) also seems to be a problem for DNA samples, a DNA-stabilizing buffer might be helpful. PBS buffer (phosphate-buffered saline) was chosen as it contains no compounds with functional groups that obviously react with the iron(IV)-oxido species. The stability of the reactive iron(IV)-oxido species in this buffer was tested with UV-vis measurements (Figure 17).

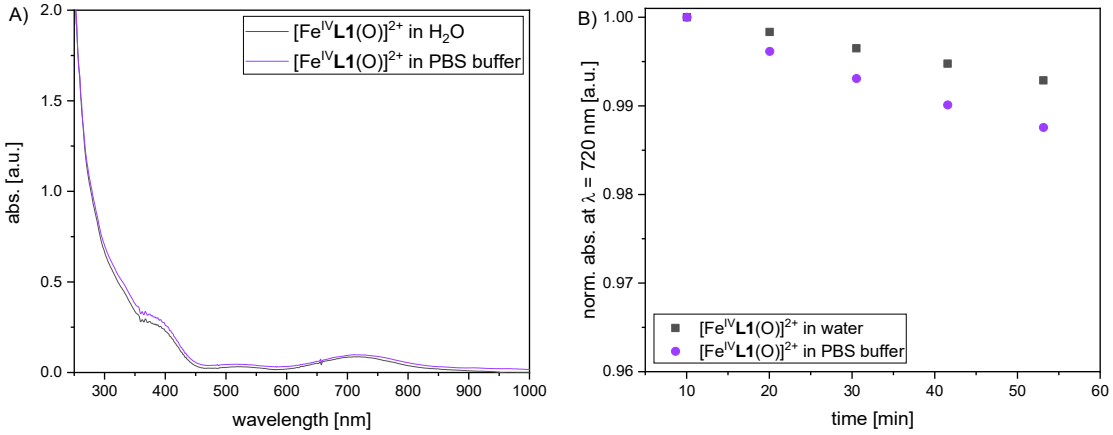

Figure 17: A) UV-vis spectrum of $[Fe^{IV}\mathbf{L1}(O)]^{2+}$ recorded in water or in phosphate-buffered saline (PBS). B) UV-vis absorption at $\lambda = 720$ nm to follow the decay of $[Fe^{IV}\mathbf{L1}(O)]^{2+}$ in water and in PBS buffer. Conditions: $[Fe^{IV}{=}O] = 1$ mM, water/PBS buffer, 25 °C.

The UV-vis spectrum of $[Fe^{IV}\mathbf{L1}(O)]^{2+}$ in PBS buffer is very similar to that recorded in water (Figure 17A). Furthermore, the absorption maximum of the iron(IV)-oxido complex in PBS buffer and in water was followed over a time of 60 min (Figure 17B). The decay of $[Fe^{IV}\mathbf{L1}(O)]^{2+}$ seems to occur faster in PBS buffer than in water, however, it is still magnitudes slower than a reaction with substrates. To assure that the iron(IV)-oxido complex is still reactive in this medium, a reaction with 5mC as substrate was carried out

in water and in PBS buffer and the absorption maximum of the iron(IV)-oxido complex followed *via* UV-vis spectroscopy (Figure 18).

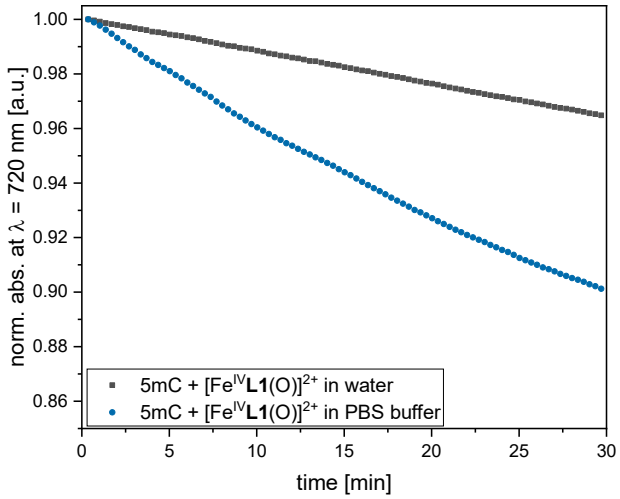

Figure 18: UV-vis absorption at λ = 720 nm in a reaction of 5mC with $[Fe^{IV}\mathbf{L1}(O)]^{2+}$ in water and PBS buffer over time. Conditions: [5mC] = $[Fe^{IV}=O]$ = 1 mM, H_2O/PBS buffer, 25 °C.

The absorption of the iron(IV)-oxido complex decreases faster in the reaction carried out in water. This may be due to decomposition in addition to the reaction or the PBS buffer as medium could also influence the reactivity by the presence of other ions in the mixture or a different pH. However, the differences in reactivities from the reaction in water and PBS buffer were considered to overall be rather small and it was therefore decided to focus on reactivity studies in PBS buffer. A series of experiments was performed varying different parameters in the reaction of **DNA1** with $[Fe^{IV}\mathbf{L1}(O)]^{2+}$ (Table 6).

Table 6: Series of reactions between **DNA1** and $[Fe^{IV}\mathbf{L1}(O)]^{2+}$ with corresponding reaction conditions.

exp	equiv. $Fe^{IV}=O$ per Me	time [min]	Temp [°C]	solvent
1	3	10	4	H_2O
2	6	10	4	H_2O
3	6	10	4	PBS buffer
4	6	10	25	H_2O
5	6	10	25	PBS buffer
6	-	-	25	H_2O (contr. without Fe)

The number of equivalents of iron(IV)-oxido complex was raised from 3 to 6 equivalents per methyl group hoping to observe more 5mdC oxidation. The reaction was carried out at room temperature (25 °C) and at 4 °C to investigate whether lower temperatures might influence the product distribution at the end of the reaction. The third variation in the reaction conditions consists of the different solvents water and PBS buffer. Ideally, the PBS buffer should stabilize the DNA sample to protect it against unwanted strand breaks and decomposition.

The products of the reaction series were analyzed *via* MALDI-MS measurements (Figure 19). Raising the number of iron(IV)-oxido equivalents results in a decrease in intensity of the peaks (Figure 19A and B). This can be attributed to higher amount of decomposition of the DNA strand due to side reactions with the iron(IV)-oxido complex.

Comparing the results from variation of the solvent, it can be stated that samples reacted in water display broad peaks with lower m/z values than expected for unreacted **DNA1**.

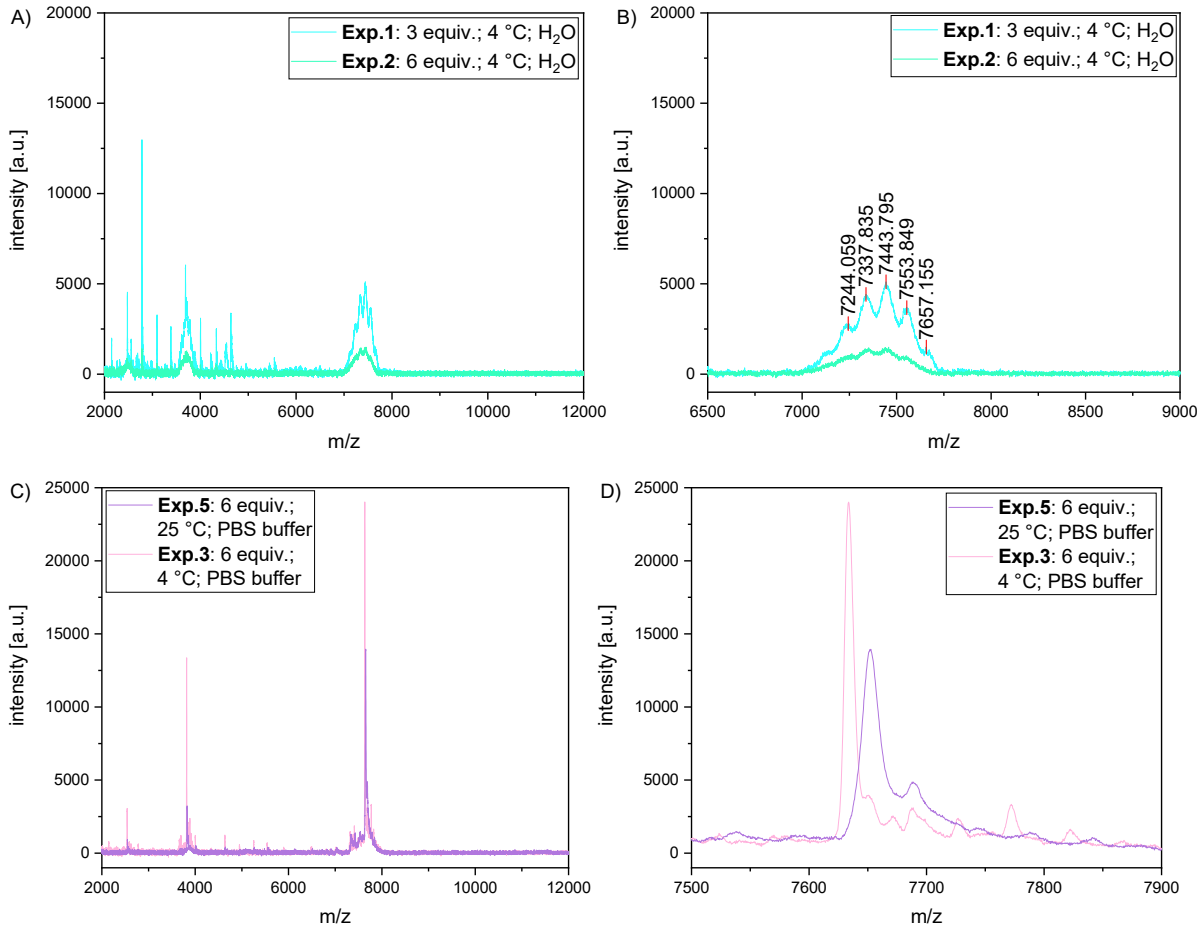

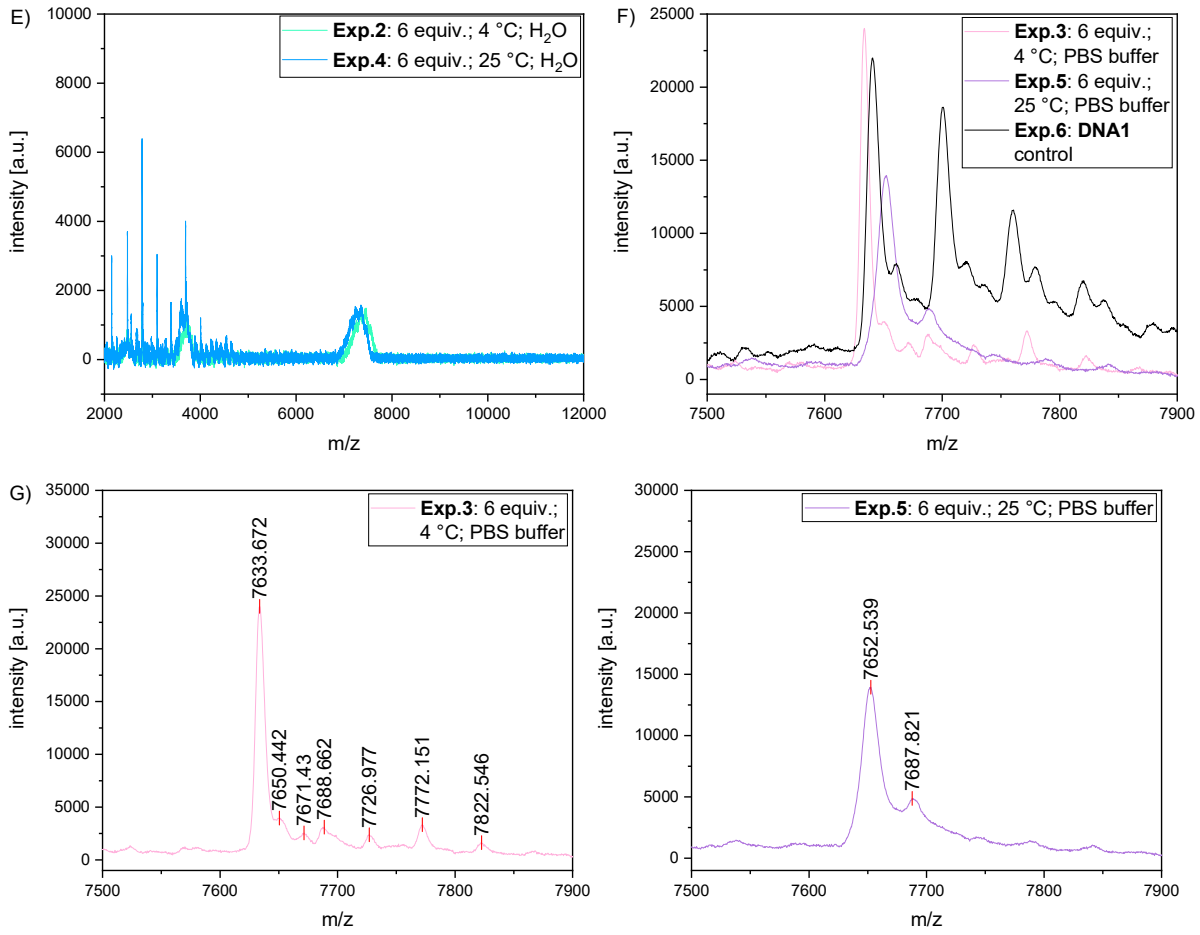

Figure 19: MALDI-MS traces of the products from reactions between **DNA1** and $[Fe^{IV}$**L1**$(O)]^{2+}$ performed under different conditions. Conditions: [**DNA1**] = 2.5 µM (1 equiv.), $[Fe^{IV}=O]$ = 60 µM (24 equiv.; 3 equiv. per methyl group) or 120 µM (48 equiv.; 6 equiv. per methyl group), H_2O or PBS buffer, 4 °C or 25 °C.

The MALDI-MS traces obtained from reactions in PBS buffer in contrast afford sharp signals (similar to the reference measurement, Figure 77, section VII.7). Furthermore, significantly less additional peaks are observed at lower m/z values, eventually indicating less unwanted decomposition of the DNA strand (Figure 19C and D). An overlay with the samples from the reaction in PBS buffer with the **DNA1** control measurements reveals no identical signals (Figure 19F). It is therefore assumed that modification of the DNA strand has occurred. Unfortunately, the peaks could not be assigned to specific species from their m/z values. The expected masses for the starting material as well as for the expected oxidation products can be found in Table 7. However, it has to be noted here that not only the oxidation of 5mdC but also of thymine residues provide the listed masses. Moreover, also a mixture of oxidized 5mdC (one residue present in **DNA1**) and thymine (seven residues present in **DNA1**) might occur, making attribution of signals to specific species

very challenging. The sample from a reaction in PBS buffer at 25 °C (Figure 19H) reveals a m/z value that could tentatively be assigned to 5fdC-modified **DNA1**. However, no starting material was detected in any of the reaction samples. This fact is surprising since a low percentage of overall 5mdC or thymine oxidation was observed.

A change in reaction temperature, however seems to have a slight impact on the outcome of the reaction. Samples from reactions in water show a small shift towards higher m/z values for lower temperatures (Figure 19E). The opposite was observed for the samples from reactions in PBS buffer (Figure 19C and D). Repetition of the reactions could show whether these slight differences really occur from the chosen reaction conditions or if they occur within the error of this procedure.

Table 7: Calculated m/z values for 5mdC-containing **DNA1** as well as for the expected oxidation products.

sample	**DNA1-5mdC**	**DNA1-5hmdC**	**DNA1-5fdC**	**DNA1-5cdC**
m/z	7639	7655	7653	7669

To conclude, it could be shown in first test reactions between **DNA1** and $[Fe^{IV}\mathbf{L1}(O)]^{2+}$ that the synthetic model complex is capable of oxidizing 5mdC in small amounts. This is a good starting point to further elaborate different reaction conditions which has due to time reasons not been done in this project so far. Two major draw-backs in this procedure have been identified that make sequencing applications challenging. The first problem is the faster oxidation of thymine residues compared to 5mdC residues. This can easily be circumvented by using the complex to modify RNA samples instead of DNA. The second challenge consists of the decomposition of the DNA strand within a reaction with the iron(IV)-oxido complex. It was shown in reactions with oligonucleotides that a high amount of iron complex is needed to achieve high oxidation rates. At the same time, oligonucleotide degradation was observed with more equivalents of iron(IV)-oxido complex. It thus remains challenging to evaluate conditions that combine both desired properties (high oxidation rate and intact strands). The usage of stabilizing buffers such as the PBS buffer to avoid DNA degradation seems to be a promising procedure that is worth

investigating in more detail. Again, the employment of RNA instead of DNA could eventually also contribute in increased stability as with the additional hydroxy group at the sugar moiety, there is already one possibility less for unwanted side reactions. Reactivity studies with RNA samples as substrate for the iron(IV)-oxido complex as well as sequencing experiments thereof would consequently be the next step in this project.

2 Application of the Iron(IV)-oxido Complex in Synthetic Epigenetics

In addition to the naturally occurring DNA modifications, a whole research field focuses on the development of synthetically modified DNA. The replacement of natural by modified nucleobases can lead to additional or improved properties of the resulting unnatural nucleic acid. Elaborated information storage possibilities in DNA as well as better understanding of the properties of natural DNA are the main goals addressed in this still growing research area. The DNA strand can be modified at the sugar unit,[122] the phosphate backbone[123] or the nucleobase subunit, leading to a variety of unnatural nucleic acids.[124] This chapter provides a short overview on the current status of nucleobase modifications and their applications.

The attachment of various functional groups to natural nucleobases can introduce new properties to DNA, thereby opening a vast area of new tools in research.[125-127] Kool and coworkers expanded the natural nucleobase by addition of a benzene ring (Chart 4A).[128-129] Their so-called size-expanded nucleobases (xDNA) still contain the motif responsible for Watson-Crick hydrogen bonding and the authors could show that their modified bases are able to selectively recognize the natural binding partner. Fully expanded xDNA helices could be obtained.[130] Interestingly, these new helices are more stable than natural DNA and more importantly, in contrast to their native counterpart, they exhibit fluorescence in aqueous buffers.[131-133] This property in combination with the ability of xDNA to interact with natural genetic systems, can eventually be exploited to use this system as biotechnological reporters for instance giving insights on specific DNA sequences.[134]

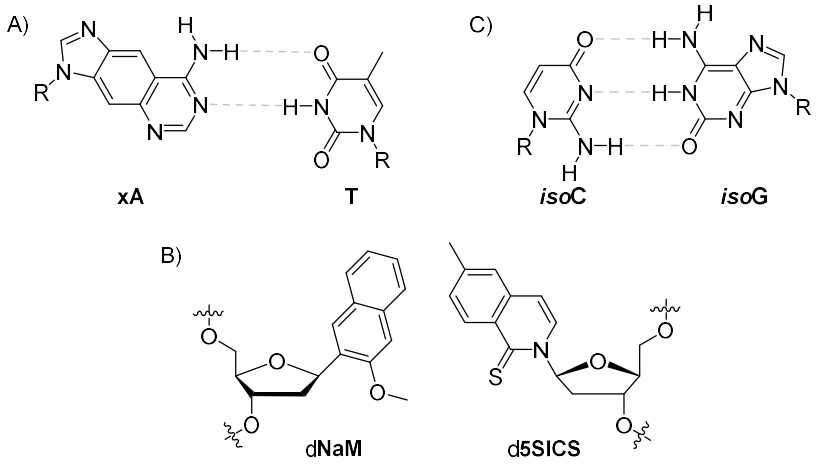

Chart 4: A) Modified base pair where adenine is replaced by the size-expanded artificial base **xA** by Kool and coworkers.[134] B) Unnatural base pair developed by Romesberg and coworkers.[135] C) The first unnatural base pair *iso*C:*iso*G developed by Benner and coworkers.[136]

A different approach was used by Romesberg and coworkers, who developed synthetic base pairs on the basis of hydrophobic and packing forces instead hydrogen bond complementarity (Chart 4B).[135] The authors managed to incorporate their unnatural base pairs into DNA and observed efficient PCR amplification. They also created semi-synthetic organisms able to store[137] and release[138] increased information.

Benner and coworkers synthesized the first unnatural base pair consisting of *iso*-cytosine and *iso*-guanine (*iso*C:*iso*G) in 1989 and incorporated it successfully into DNA/RNA (Chart 4C).[136] In 1990, Benner and coworker proposed a variety of additional structures based on size complementarity and the ability to form Watson-Crick-like base pairs *via* hydrogen bonds.[139] With their synthetic base pairs the authors were able to expand the genetic alphabet from four to six building blocks. Investigations on such artificially expanded genetic systems gained popularity in recent years,[140-145] especially the incorporation of such systems into living cells.[146-147] In 2019, Benner and coworkers managed to expand the synthetic genetic system further from six to eight building blocks, thereby significantly enhancing the possibility of information storage.[148] The resulting synthetic DNA was named "*hachimoji*" DNA ("*hachi*" = eight, "*moji*" = letters) and consists of the four canonical DNA nucleobases together with four additional synthetic nucleobases.

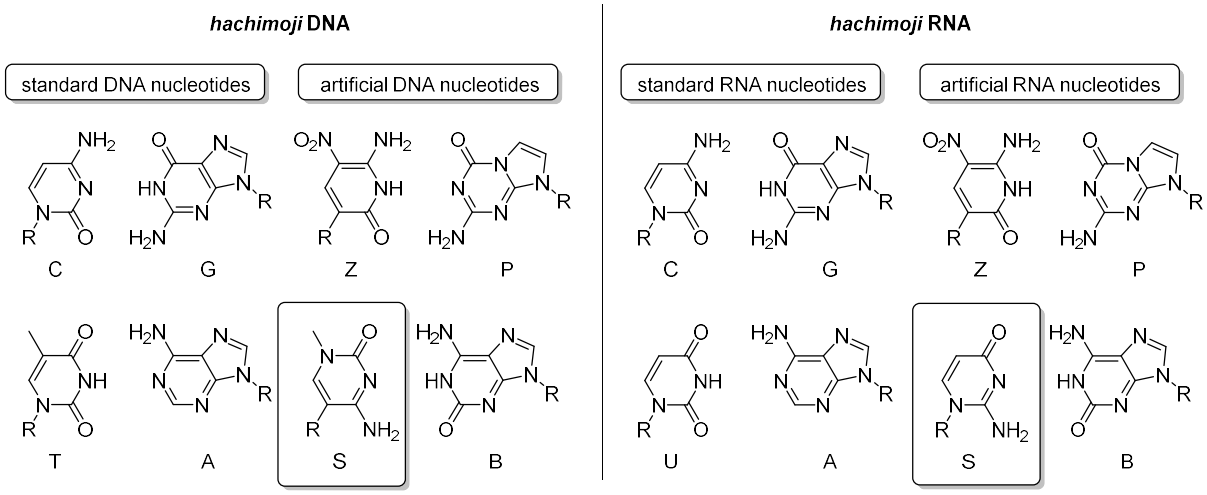

Figure 20: *Hachimoji* DNA (left) and RNA (right) developed by Benner and coworkers, consisting of the four natural nucleobases and four additional artificial nucleobases.[148] R = deoxyribose for DNA and R = ribose for RNA nucleotides. Species of particular interest for this work are highlighted.

Similar to natural DNA, this synthetic DNA is based on size- and hydrogen bond complementarity of the nucleobases and forms stable double helices. Remarkably, the authors managed to develop an RNA polymerase able to transcribe *hachimoji* DNA into RNA.[148] Especially the artificial nucleobase named "S" caught our attention due to the presence of a methyl group in the structure. Interestingly, Benner and coworkers employ to different structures "S" (highlighted in Figure 20) for the pairing with *iso*-guanine "B" in their *hachimoji* RNA compared to their *hachimoji* DNA structures. In the DNA nucleotide, the nucleobase cytosine is used but instead of the natural N^1-position, the deoxyribose moiety is connected to the nucleobase at the C^5-position whereas the original N^1-position is methylated. In analogy to the reported pseudo-uridine, this compound is further referred to as "1-methyl-pseudo-cytidine" or at the nucleobase level simply "1-methylcytosine" (1mC). In *hachimoji* RNA however, *iso*-cytosine is used instead of cytosine (Chart 5).

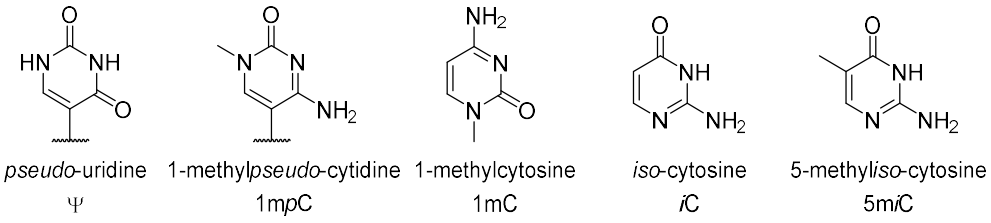

Chart 5: Selection of different synthetic nucleobases/nucleosides and the applied nomenclature.

In nature, the high density of information stored in genetic systems is even further expanded by introducing a second layer of information through epigenetics (see section I). The epigenetic DNA modifications 5mC and 5hmC are referred to as fifth and sixth letter of the genetic alphabet.[26] Oxidation of the methyl group can alter or remove these epigenetic markers, which has been studied as DNA information storage systems by the group of Balasubramanian.[149] A DNA strand containing specific modifications should afford different information ("read-outs") depending on the conditions with which it was treated. The authors propose that a 5mdC- and 5hmdC-containing DNA strand is treated A) with bisulfite and B) with potassium perruthenate and bisulfite. Sequencing of all three samples (untreated and treatment A) and B)) affords three different read-outs.[149]

Applying this method to the system studied in this work, two different methylated nucleobases are needed displaying different oxidation reactivities. In the example depicted in Figure 21, a short oxidation reaction could selectively transform only the more reactive nucleobase. Submitting the same DNA strand to longer oxidation reaction times would possibly afford complete transformation of both nucleobases. Therefore, a different read-out (from sequencing for example) would be obtained here compared to the short or no treatment. In this manner, three layers of information can be stored in one single DNA strand.

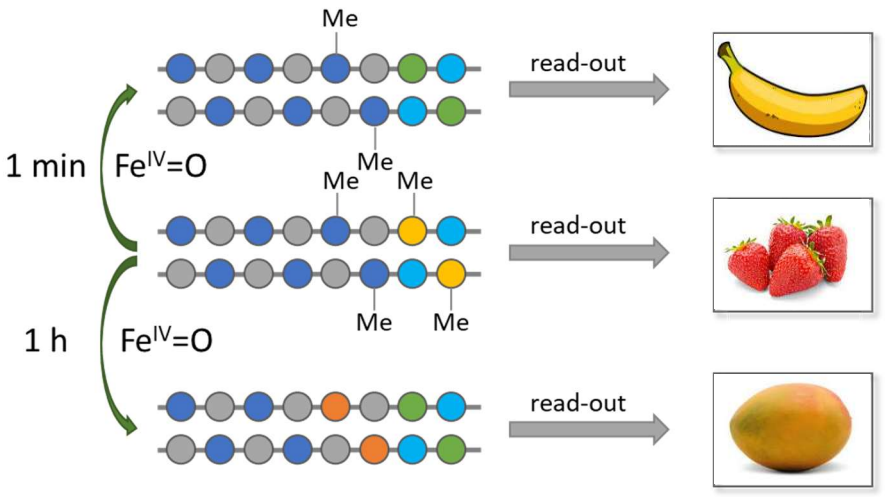

Figure 21: Three different potential read-outs are obtained from one DNA strand depending on the treatment which leads to different amounts of epigenetic markers present in the DNA strands. Inspired from Balasubramanian and coworkers.[149]

Employing methylated artificial nucleobases in the synthetic *hachimoji* DNA/RNA could allow the addition of a second layer of information, forming the completely new field of synthetic epigenetics. For this purpose, 1mC and 5-methyl*iso*-cytosine (5m*i*C, Chart 5) as well as a variety of other synthetic or natural methylated nucleobases were chosen for further studies, investigating their oxidation behavior by the iron(IV)-oxido complex established in our group.

2.1 Synthesis of *Iso*-cytosine Derivatives and Preliminary Reactivity Studies

5-Methyl*iso*-cytosine (5m*i*C) was chosen as synthetic analogue for the natural nucleobase 5mC. To test the reactivity of this substrate with the iron(IV)-oxido complex and to be able to clearly identify the formed species during the reaction, all oxidized derivatives of 5m*i*C (5-hydroxymethyl *iso*-cytosine (5hm*i*C), 5-formyl *iso*-cytosine(5f*i*C) and 5-carboxy *iso*-cytosine (5c*i*C)) should be synthesized as reference samples (Chart 6).

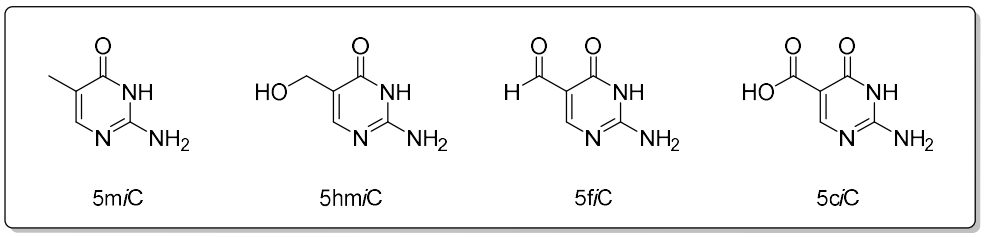

Chart 6: Anticipated target molecules for which a synthesis route should be established.

The synthesis of 5m*i*C is literature-known[150] and was already performed in this group by Caroline Kliem in her Bachelor Thesis supervised by Niko Lindlar. The pyrimidine ring is constructed in a one pot reaction and the product was isolated by filtration without further purification (Scheme 10). Unfortunately, by reproducing this reaction, it was shown by elemental analysis that a high amount of impurity (not detected by ^{1}H NMR spectroscopy) was still present in the isolated product. Different purification methods such as HPLC or amberlite purification were tested and finally the pure product could be isolated after recrystallization from water.

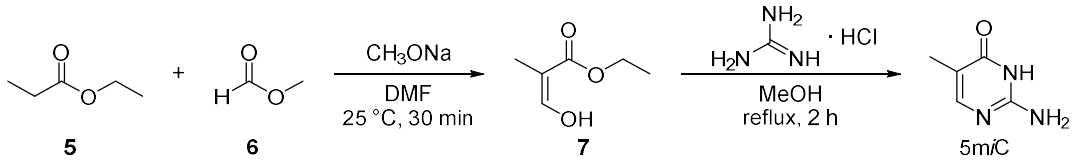

Scheme 10: Synthesis of 5m*i*C.[150]

To obtain the oxidized derivatives of 5m*i*C, Caroline Kliem tested the synthetic pathways that had been established for the corresponding 5mC compounds.[151] Unfortunately, the

desired structures could not be obtained with these methods and new synthetic routes had to be examined.

One approach to obtain 5hm*i*C consisted of a variation of the 5m*i*C synthesis procedure. The application of ethyl 3-hydroxypropanoate as starting material instead of ethyl propionate should theoretically lead directly to the desired compound 5hm*i*C. To avoid side reactions with the free hydroxy group, a protecting group should be introduced. For the protection of the alcohol functionality in the starting material, either a benzyl group or a methoxymethyl ether (MOM) were chosen as both are stable under the basic conditions needed for the reaction (Scheme 11).

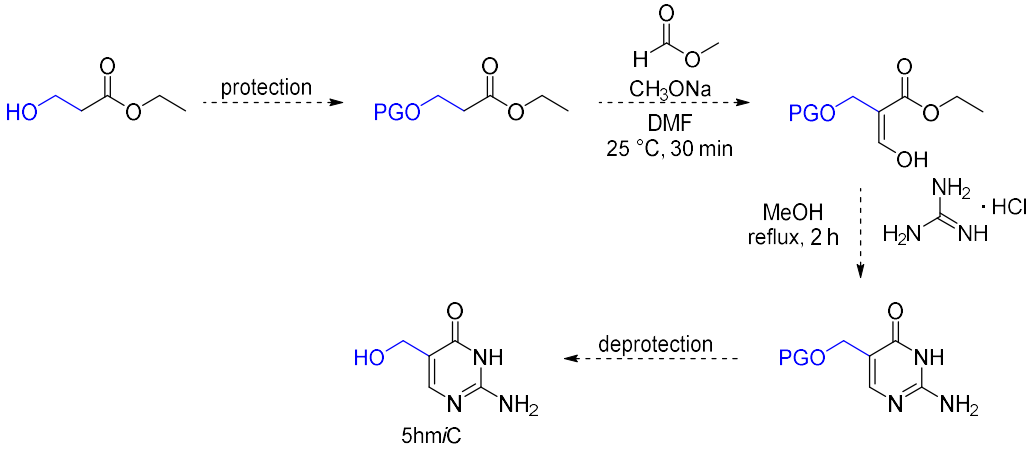

Scheme 11: Suggested reaction pathway for the synthesis of 5hm*i*C (PG = protecting group).

In a first attempt, the benzyl protection showed no conversion of the starting material after stirring at room temperature for three days, whereas the crude product of the protection using MOM ether looked promising according to ^{1}H NMR analysis. Unfortunately, flash column chromatography purification of the MOM-protected crude product led to unwanted elimination of the protecting group. The attempt of obtaining the MOM-protected 5hm*i*C in the one-pot reaction described in Scheme 11 was not successful.

Alternative synthetic approaches were examined starting from 5-carboxyethyl *iso*-cytosine (5caet*i*C) which is commercially available (Scheme 12). Alkaline hydrolysis of the ester functionality provided the 5c*i*C as a pure product in good yield (Scheme 12, I).

Although a variety of different conditions were tested, a reduction of the ester group could not be achieved (Scheme 12, II). This reaction type is commonly used for corresponding cytosine derivatives (carrying an amino group next to the ester moiety).[152] However, the ester group in 5caet*i*C seems to be extremely stable due to the proximity to a second carbonyl moiety, since all attempts to reduce the ester resulted in unreacted starting material. To turn this rather inactive group into a reactive species, it was anticipated to transform the carboxylic acid of 5caet*i*C into the corresponding acid chloride, which then would eventually be easier reduced. But even treatment with the reactive reagent thionyl chloride did not lead to any conversion of the carboxylic acid in any conditions applied.

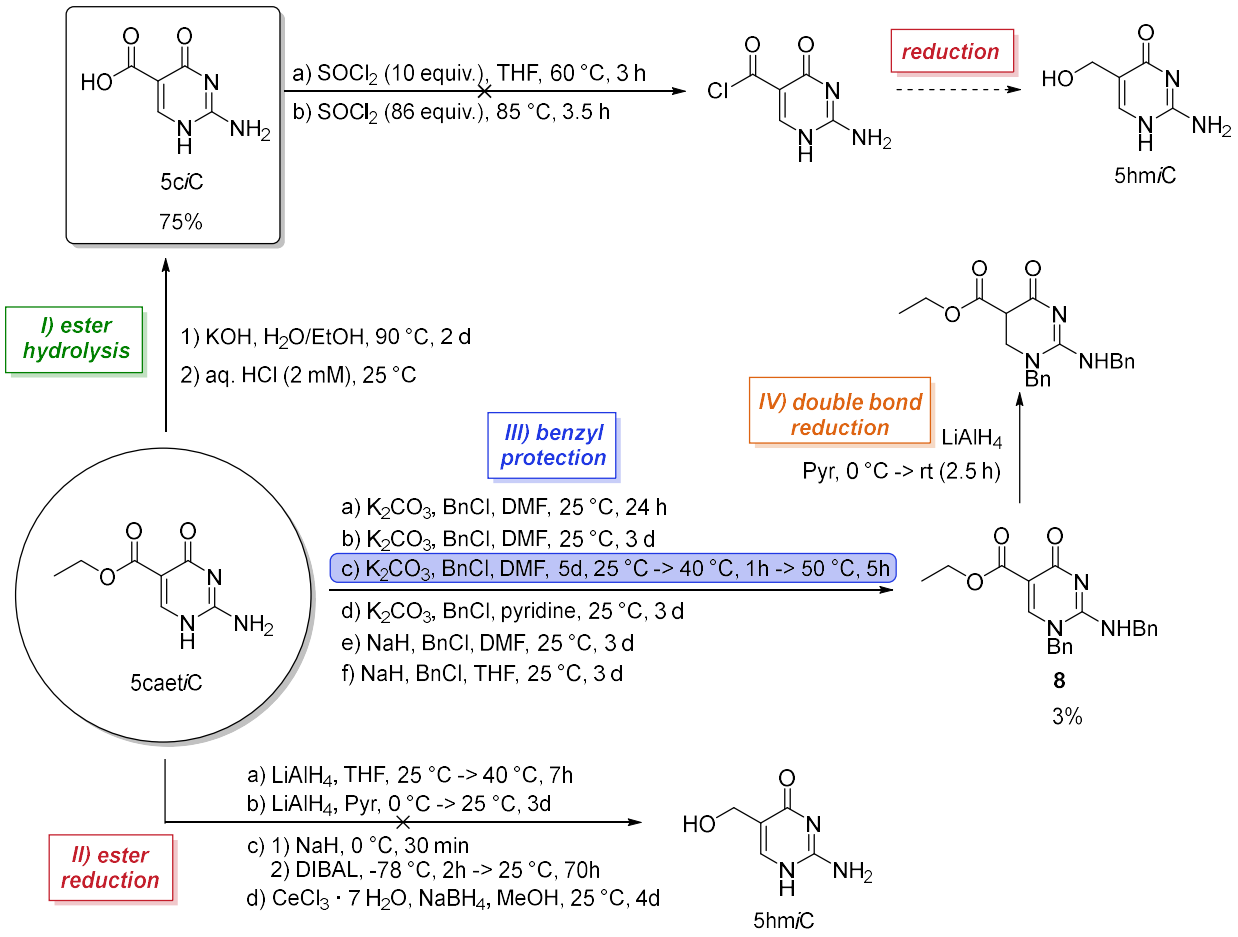

Scheme 12: Synthetic procedures tested for the generation of 5hm*i*C starting from 5caet*i*C.

The 5caet*i*C starting material as well as the outcoming reaction products exhibit very low solubility in different organic solvents but show a moderate solubility in water. This complicates the reaction progress as well as extraction workups. Therefore, a benzyl

protection reaction was carried out (Scheme 12, III). The benzyl protecting group was expected to enhance the solubility of the starting material as well as of the desired reaction product in organic solvents and to avoid possible side reactions with reactive groups.

It was expected that in this reaction the amino group in the 2-position would be the most nucleophilic position but from ^{1}H NMR spectra it can be suggested that the N^1-position with the nitrogen in the pyrimidine ring is more reactive. Nevertheless, there are several chemically very similar isomers that possibly have formed in this reaction, which complicates separation by column chromatography. The appearance of different products as well as impure mixed fractions after column chromatography affected the yield of product **8** which could only be isolated in very low yield bearing two benzyl groups.

The attempt of reducing the ester moiety of the benzyl protected 5caet*i*C **8** resulted in complete conversion of the starting material. The better solubility of the benzyl protected compound **8** in organic solvents compared to the unprotected 5caetiC might be responsible for the turnover of the starting material here. However, it turned out that instead of the desired ester reduction an unwanted reduction of the double bond occurred (Scheme 12, IV). Apparently, due to the neighboring carbonyl group a Michael Addition is the preferred reaction over the ester reduction. Similar observations were made by David Schmidl in his master thesis[153] in our group when he anticipated to reduce ester moieties in related structures derived from the nucleobase uracil (also bearing a carbonyl group next to the ester function).

As the synthesis of the oxidized 5m*i*C derivatives turned out to be more challenging than expected, it was decided to proceed further to the next project step and test the reactivity of 5m*i*C with the iron(IV)-oxido complex instead of spending more time for the synthesis of the reference compound.

The reaction of 5m*i*C with $[Fe^{IV}\mathbf{L1}(O)]^{2+}$ was monitored by UV-vis spectroscopy following the characteristic absorption maximum of the iron(IV)-oxido species at a wavelength of λ = 720 nm (Figure 22).

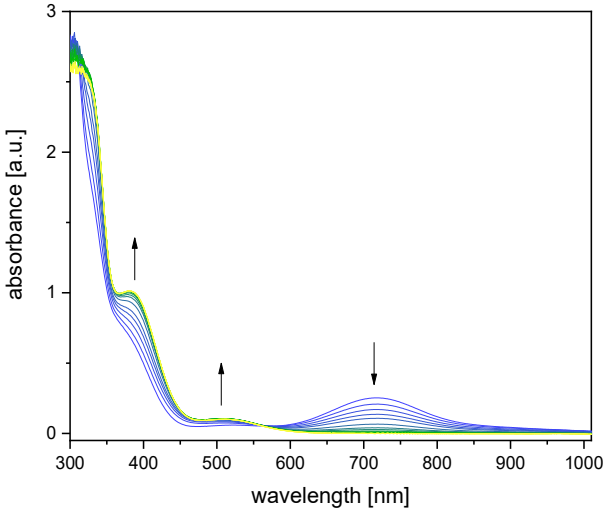

Figure 22: UV-vis spectra of the reaction of 5m*i*C with $[Fe^{IV}\mathbf{L1}(O)]^{2+}$ over 70 min. Conditions: [5m*i*C] = $[Fe^{IV}=O]$ = 1 mM, H_2O, 25 °C.

The iron(IV)-oxido absorption band is decreasing as the reactive species is consumed within the reaction progress which is completed after approximately 35 min under the applied conditions. Two new maxima at 387 nm and 511 nm are formed and the resulting spectrum shows similar features as observed with the corresponding iron(III) species (compare section IV.1.1). An isosbestic point can be observed at a wavelength of 559 nm.

To identify the respective products in this reaction, analytical HPLC analysis was performed. Thereby, two different methods were used to study this reaction. The first method included not only the detection of the UV absorption at 280 nm but also an additional low-resolution mass spectrometry analysis (for analytical HPLC method see section VI.4, method "UV+MS"). This allowed the assignment of the observed signals to the respective oxidation products, however the method required a low flow rate of 0.4 mL min^{-1} resulting in relatively long runtimes (Figure 23A). For this reason, a shorter method with only UV detection was used for kinetic measurements including a high amount of samples (Figure 23B, for analytical HPLC method see section VI.4, method "UV only"). To follow the product distribution over time, samples were taken from the reaction mixture every 5 min over a range of 70 min and subjected to analytical HPLC analysis.

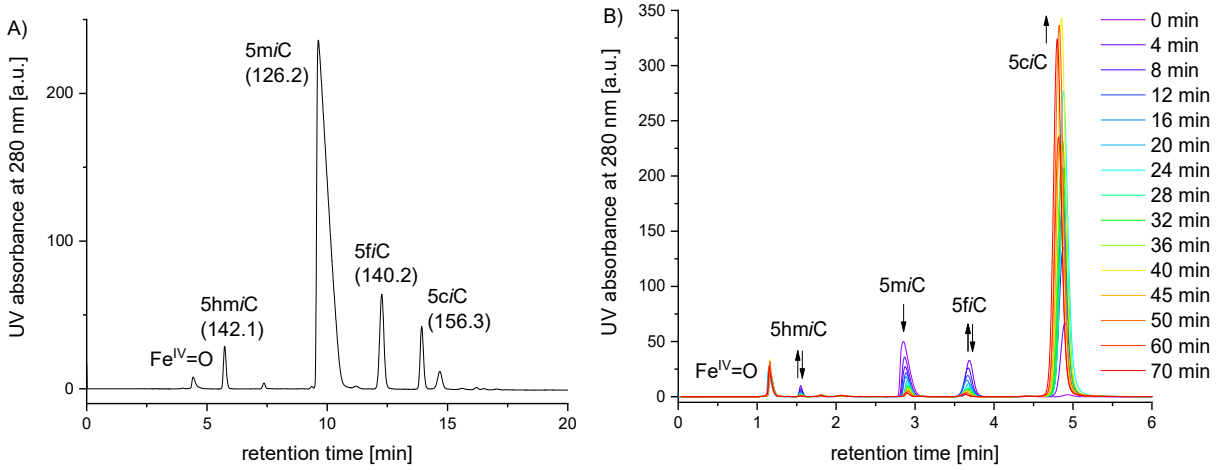

Figure 23: Analytical HPLC-trace of the reaction of 5m*i*C with $[Fe^{IV}$**L1**$(O)]^{2+}$ at A) 0 min (conditions: [5m*i*C] = 20 mM, 5m*i*C:$[Fe^{IV}$**L1**$(O)]^{2+}$ 1:5, H_2O, 25 °C, HPLC method "UV+MS") and B) over 70 min (conditions: [5m*i*C] = 2 mM, 5m*i*C: $[Fe^{IV}$**L1**$(O)]^{2+}$ 1:10, H_2O, 25 °C, HPLC method "UV only"). Assignment of the absorption peaks in B) not verified as a method without coupled mass spectrometry was used.

At an initial 5m*i*C concentration of 20 mM and five-fold stoichiometry $[Fe^{IV}$**L1**$(O)]^{2+}$, the reaction occurs in a few seconds and does not further change over time (Figure 23A). Using LC-MS analysis, 5m*i*C starting material as well as the oxidation products 5hm*i*C, 5f*i*C and 5c*i*C could be assigned to the UV absorption signals. The high amount of starting material can be explained by the presence of a side reaction (iron(II)/iron(IV) comproportionation, for more information refer to section IV.1.1) leading to the need of two equivalents of iron(IV)-oxido complex for the oxidation of one equivalent of substrate. Therefore, more equivalents of $[Fe^{IV}$**L1**$(O)]^{2+}$ might be needed for complete conversion into the last oxidation product 5c*i*C. This was achieved with ten equivalents of $[Fe^{IV}$**L1**$(O)]^{2+}$, with 5c*i*C being nearly the only species left after a reaction time of 70 min and an initial 5m*i*C concentration of 2 mM (Figure 23B). As these kinetic experiments were analyzed with a different analytical HPLC method, the UV absorption peaks shift to different retention times compared to the HPLC method with coupled mass spectrometry shown. Therefore, the different species can not be assigned unambiguously to the observed UV absorption peaks.

Without reference samples of the 5m*i*C oxidation products, no exact quantification measurement was possible. Nevertheless, the integral area against the time shows the

trends of consumption and formation of the different species within the reaction (Figure 24).

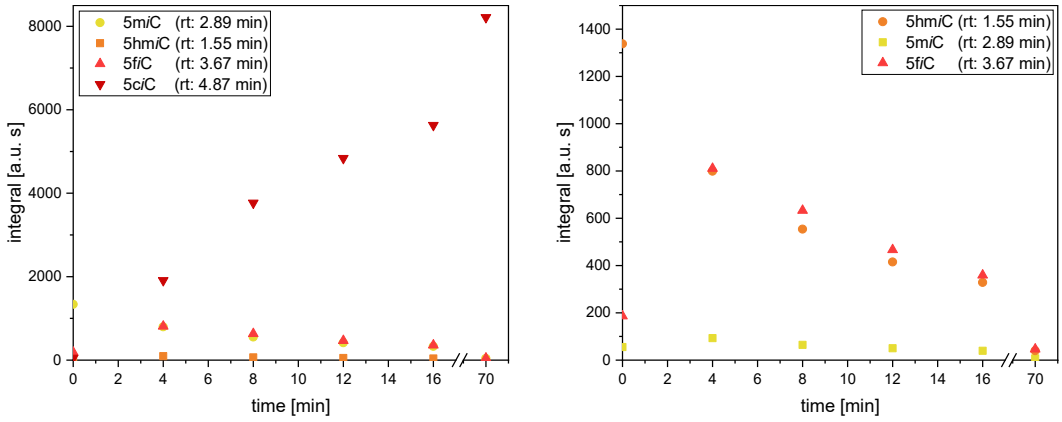

Figure 24: Representation of the integral areas of all observed UV absorption peaks at specific retention times over time (left) and detailed view (right).

The amount of 5hm*i*C is very low over the entire reaction time, indicating a faster reaction of 5hm*i*C with $[Fe^{IV}\mathbf{L1}(O)]^{2+}$ compared to 5m*i*C. The intensity of 5f*i*C increases in the first minutes and decreases then in a similar rate compared to 5m*i*C. At the end of the reaction only the last formed oxidation product 5c*i*C is present.

Although the synthesis of all oxidation products of 5m*i*C was not completely achieved, it could be shown that similarly to 5mC, also the artificial nucleobase 5m*i*C reacts with the iron(IV)-oxido complex affording all expected oxidation products. Compared to the previously investigated nucleobase 5mC, the reaction of 5m*i*C with $[Fe^{IV}\mathbf{L1}(O)]^{2+}$ occurs significantly faster. This difference in reactivity might be further exploited for example to discriminate between different methylated nucleobases and exclusively oxidize the desired species.

2.2 A Comparative Study on Different Epigenetically Relevant Nucleobase Substrates with a TET Model Iron(IV)-oxido Complex

Instead of focusing exclusively on the substrate 5m*i*C and its reaction with the iron(IV)-oxido complex, it was decided to include a variety of natural and synthetic nucleobases bearing methyl groups. The following publication[119] evolved from a cooperation in the frame of the SFB1309 with Fabian Zott from the Zipse group and compares the reactivity of these substrates with the iron(IV)-oxido complex by calculation of the corresponding reaction rates from kinetic investigations. Additional calculation of the C-H bond dissociation energies (BDEs) of the substrates results in a correlation between the theoretically expected and experimentally determined reactivities.

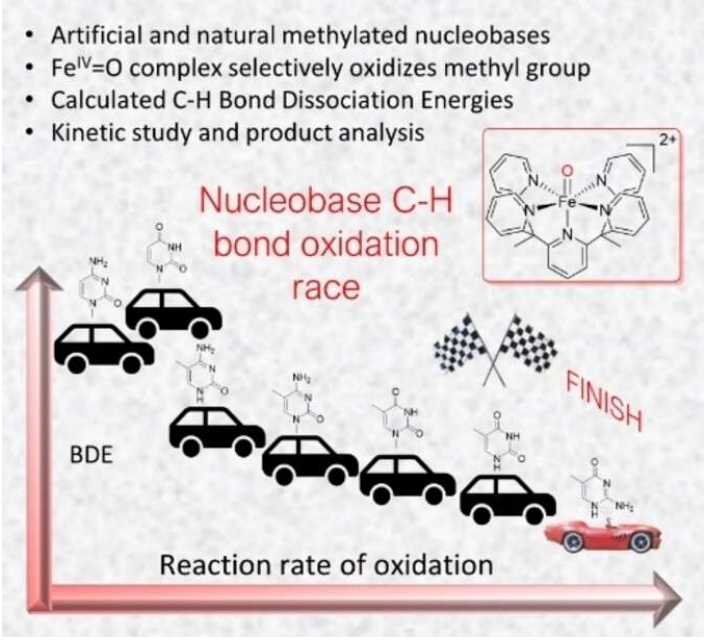

Title

TET-Like Oxidation in 5-Methylcytosine and Derivatives: A Computational and Experimental Study

Authors

Niko S.W. Jonasson, Rachel Janßen, Annika Menke, Fabian L. Zott, Hendrik Zipse and Lena J. Daumann*

Author Contribution

Niko S.W. Jonasson, Rachel Janßen, Annika Menke and Lena J. Daumann developed the project. Niko S.W. Jonasson, Rachel Janßen and Annika Menke performed the syntheses of substrates and iron complexes and were involved in the writing and review process of the manuscript. Niko S.W. Jonasson conducted the GC-MS measurements, Rachel Janßen performed the HPLC measurements and Annika Menke carried out the UV-vis kinetic investigations including reaction rate calculation as well as the correction thereof. Fabian Zott accomplished the BDE calculation, writing of the manuscript and the synthesis of 1mU. Hendrik Zipse and Lena J. Daumann supervised this project.

Licence

The manuscript as well as the supporting information are available at

https://doi.org/10.1002/cbic.202100420

The corrigendum is available at

https://doi.org/10.1002/cbic.202400445

ChemBioChem

Combining Chemistry and Biology

Chemistry Europe

European Chemical Societies Publishing

Cover Feature:

L. J. Daumann et al.

TET-Like Oxidation in 5-Methylcytosine and Derivatives: A Computational and Experimental Study

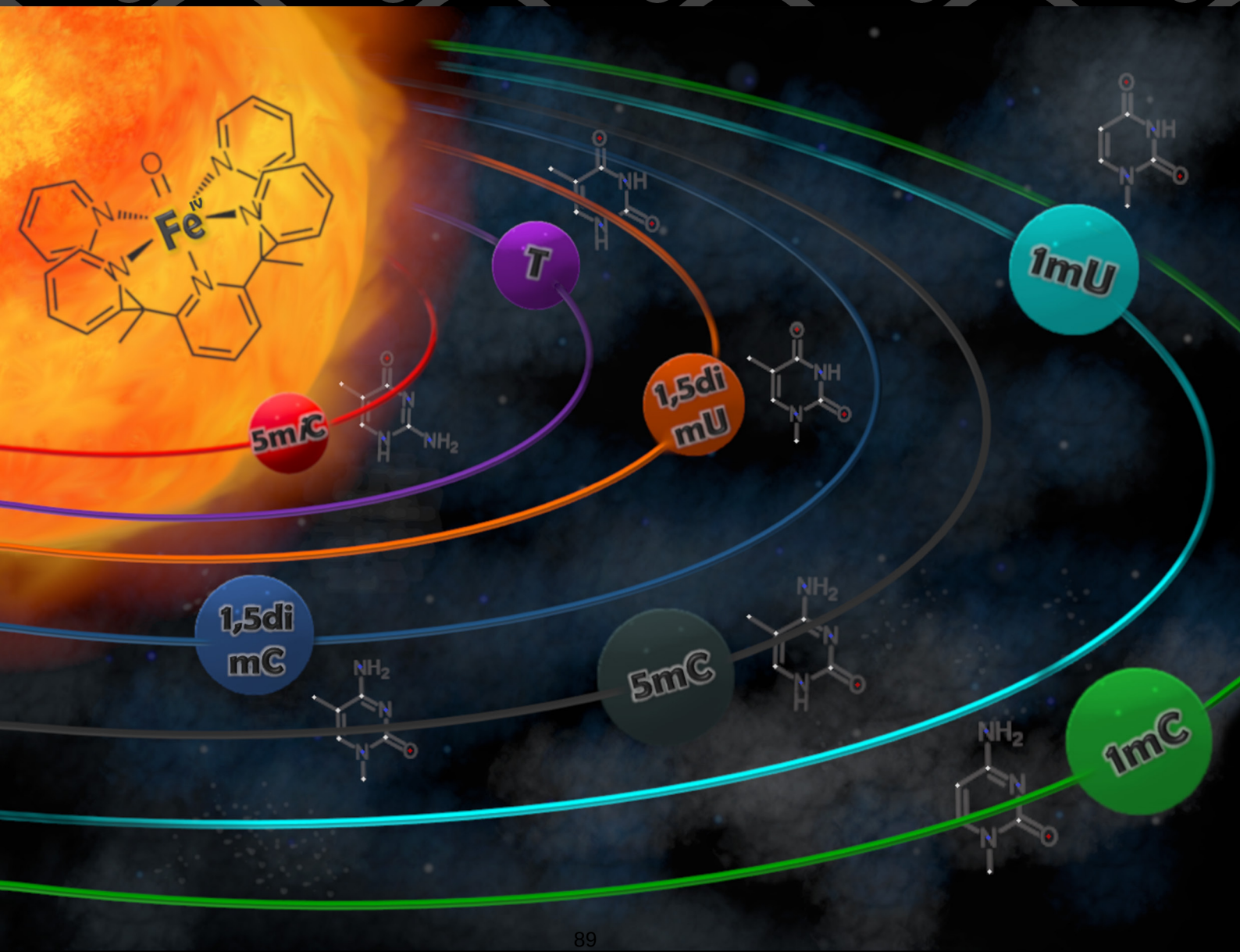

Special Collection

TET-Like Oxidation in 5-Methylcytosine and Derivatives: A Computational and Experimental Study

Niko S. W. Jonasson[+],[a] Rachel Janßen[+],[a] Annika Menke[+],[a] Fabian L. Zott,[a] Hendrik Zipse,[a] and Lena J. Daumann*[a]

The epigenetic marker 5-methylcytosine (5mC) is an important factor in DNA modification and epigenetics. It can be modified through a three-step oxidation performed by ten-eleven-translocation (TET) enzymes and we have previously reported that the iron(IV)-oxo complex $[Fe(O)(Py_5Me_2H)]^{2+}$ (**1**) can oxidize 5mC. Here, we report the reactivity of this iron(IV)-oxo complex towards a wider scope of methylated cytosine and uracil derivatives relevant for synthetic DNA applications, such as 1-methylcytosine (1mC), 5-methyl-*iso*-cytosine (5m*i*C) and thymine (T/5mU). The observed kinetic parameters are corroborated by calculation of the C–H bond energies at the reactive sites which was found to be an efficient tool for reaction rate prediction of **1** towards methylated DNA bases. We identified oxidation products of methylated cytosine derivatives using HPLC-MS and GC-MS. Thereby, we shed light on the impact of the methyl group position and resulting C–H bond dissociation energies on reactivity towards TET-like oxidation.

Introduction

Using DNA as information storage for non-biological data has experienced a considerable development in recent years.[1] DNA not only provides an immensely high density of information, but its durability allows to store information over decades and centuries.[1c] Besides the canonical nucleobases C, G, T and A, epigenetics extend the 'DNA alphabet' with the epigenetic markers 5-methylcytosine (5mC) and 5-hydroxymethylcytosine (5hmC) as fifth and sixth letter.[2] In nature, these additional nucleobases are formed by direct methylation of cytosine which causes the gene to be silenced. Oxidation of the methyl group can alter or remove the epigenetic marker and therefore introduces a second layer of information.[3] This has also been put to use in DNA information storage systems.[4] Aside from nature, using unnatural orthogonal nucleobases pairs in synthetic DNA systems has expanded the 'DNA alphabet' up to eight letters within one system, called hachimoji DNA, increasing the density of information storable in DNA even further (Figure 1A).[5] Furthermore, the synthetic nucleoside *N1*-methylpseudouridine (1mΨ, Figure 1B), which consists of a 1-methyluracil (1mU) nucleobase fragment bound at its 5 position to ribose, was used in the Covid-19 mRNA vaccines by Pfizer/BioNTech (Comirnaty, BNT162b2) and Moderna (Spikevax, mRNA-1273).[6] The use of 1mΨ in mRNA has been reported to increase protein expression compared to *pseudo*-uridine Ψ and therefore likely contributes to the high efficacy of the mentioned vaccines.[7]

Using epigenetic markers or synthetic DNA bases has increased the potential for DNA information storage, however, the idea of epigenetic manipulation of synthetic DNA bases has not been employed yet. In natural epigenetics, ten-eleven translocation (TET) enzymes are involved in the oxidation of the methyl group in 5mC. TET enzymes belong to the superfamily of iron(II)/α-KG dependent non-heme enzymes and use an iron(IV)-oxo moiety as the catalytically active species for the stepwise transformation of 5mC to 5hmC, then to 5-formylcytosine (5fC) and finally to 5-carboxycytosine (5caC). We have recently shown that a synthetic iron(IV)-oxo complex (**1**, Figure 2) is capable of performing the same reaction on nucleobase,[9] nucleoside, and even nucleotide substrates.[10] It has been shown that hydroxyl radicals are capable of oxidizing 5mC, however, in addition to hydroxylation of the methyl group yielding 5hmC and/or 5fC, oxidation of the 5,6-double bond in 5mC was observed.[11] In epigenetic sequencing applications, 5hmC is oxidized to 5fC with potassium perruthenate ($KRuO_4$). Under these conditions, 5mC is unaffected. In this work, we explored the chemistry of the biomimetic system (**1**) towards synthetic DNA bases 1mC and *iso*-cytosine (as methylated 5m*i*C) occurring in hachimoji DNA and RNA, respectively, as well as methylated uracil derivatives. We present data on the diverse reactivity of different methylated nucleobases with the biomimetic compound **1** and present calculations of C–H bond dissociation energies (BDEs) as a viable method to predict the corresponding reactivity. The obtained results open up the possibility to install methyl groups with different reactivity towards oxidation and thus tunability for reaction, as well as to

[a] *N. S. W. Jonasson,[+] R. Janßen,[+] A. Menke,[+] F. L. Zott, H. Zipse, L. J. Daumann*
Department of Chemistry,
Ludwig-Maximilians-University Munich
Butenandtstr. 5–13
81377 München (Germany)
E-mail: lena.daumann@lmu.de

[+] *These authors contributed equally to this work.*

Supporting information for this article is available on the WWW under https://doi.org/10.1002/cbic.202100420

This article is part of a joint ChemBioChem-ChemMedChem Special Collection on Chemical Epigenetics available at bit.ly/chemepi2021.

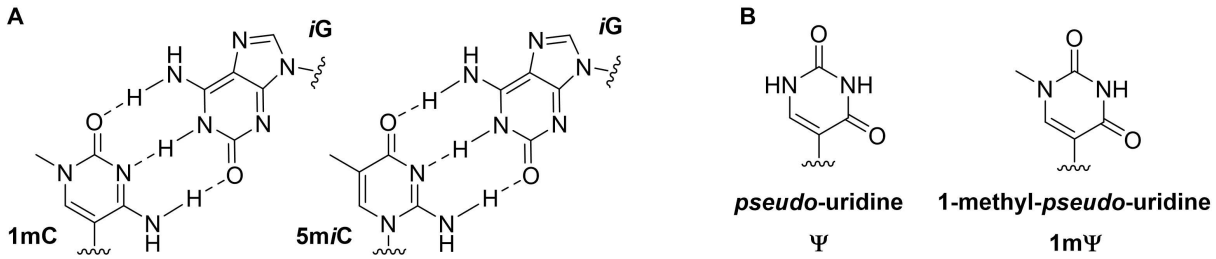

Figure 1. A) Base pairs 1-methylcytidine (1mC) – *iso*-guanosine (*i*G) and 5-methyl-*iso*-cytidine (5m*i*C) – *iso*-guanosine used in hachimoji DNA and other synthetic DNA applications.[5a,8] B) Nucleobase fragments in *pseudo*-uridine (Ψ) and 1-methyl-*pseudo*-uridine (1mΨ).

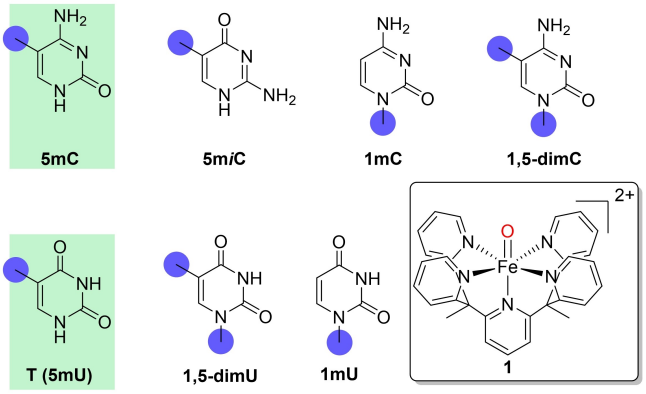

Figure 2. Methylated cytosine and uracil derivatives used in this work: 5-methylcytosine (5mC), 5-methyl-*iso*-cytosine (5miC), 1-methylcytosine (1mC), 1,5-dimethylcytosine (1,5dimC), thymine (T), 1-methyluracil (1mU), 1,5-dimethyluracil (1,5dimU). The studied methyl groups are marked with blue circles, the naturally occurring nucleobases have a green background. Used iron(IV)-oxo complex $[Fe(O)(Py_5Me_2H)]^{2+}$ (**1**) shown in rounded rectangle.

draw conclusions on the suitability of certain methylated DNA species in nature.

Results and Discussion

As substrates we used the naturally occurring 5-methylcytosine (5mC) and thymine/5-methyluracil (T/5mU) in addition to the synthetic nucleobases 5-methyl-*iso*-cytosine (5m*i*C), 1-methylcytosine (1mC), 1,5-dimethylcytosine (1,5dimC), 1-methyluracil (1mU) and 1,5-dimethyluracil (1,5dimU, Figure 2). The cytosine derivatives were also analyzed for the products formed when reacted with **1** using HPLC-MS and GC-MS. We evaluate which nucleobases could be useful for synthetic biology and epigenetics with respect to their ability to be further modified by TET enzymes and their biomimetic complexes.

UV Vis kinetics

We have previously reported that the absorbance of **1** at $\lambda =$ 718 nm can be used to measure the initial reaction rates (data points used for rate calculation: minute 1–2) and then to determine the rate constants k_S of the individual substrates with **1**.[9] To confirm this is valid for the substrates used in this work, we monitored the observed relative absorbance of each substrate: in all reactions the initial absorbance was not significantly decreased after 2 min reaction time (>85–90%), indicating that only small amounts of **1** had been consumed. The only exception with 80% of the initial absorbance of **1** was with the rapidly reacting 5m*i*C (Figures S1 and S2). As the absorption decrease was still reliably linear within the monitored timeframe (Figure 3B) we deemed this data analysis to be a suitable approximation. Additionally, we analyzed the reaction mixture of 5m*i*C and **1** after 2 min reaction time using GC-MS and found mostly unreacted 5m*i*C (see Figure S15). For all other substrates the linear consumption of **1** was observed for a much longer timeframe. We were therefore confident to monitor almost exclusively the reaction of **1** with the respective starting material and not that of any further oxidized products.

For all substrates we found a decrease of the absorbance at $\lambda = 718$ nm over the monitored time frame (Figure 3A, compare also Supporting Information Figures S1 and S2 for full UV-Vis spectra and control reactions). Using the method of initial rates, reaction rates were calculated from the observed decrease in absorbance by linear regression. We then calculated the corresponding rate constants k_S (Figure 4) using the second order rate law found by Jonasson and Daumann for the reaction of 5mC with **1**. This rate law was applied for all substrates used in this work (Eq. 1):

$$v = k_s[S][1] \quad (1)$$

where v is the observed reaction rate, $[S]$ the concentration of the substrates and $[1]$ the concentration of **1**. When the amount of **1** was varied from 1–9 equivalents, a linear dependence of the reaction rates on the amount of **1** (Figure 5) was observed for all substrates and none showed any saturation behavior (as had been previously observed for 5hmC).[9] This confirms that the chosen concentration ranges are suitable for our purposes. The linear increase in reaction rate upon increase of the added amount of **1** indicates a rate law of first order for **1** for all substrates. This agrees with our previous findings concerning the reaction of **1** with 5mC and justifies use of Eq. (1) for the calculation of k_S.[9]

The *N*-methylated substrates 1mC and 1mU reacted significantly slower than all other compounds (Figures 4 and 5). The uracil derivatives 1mU, T, and 1,5dimU reacted faster than their

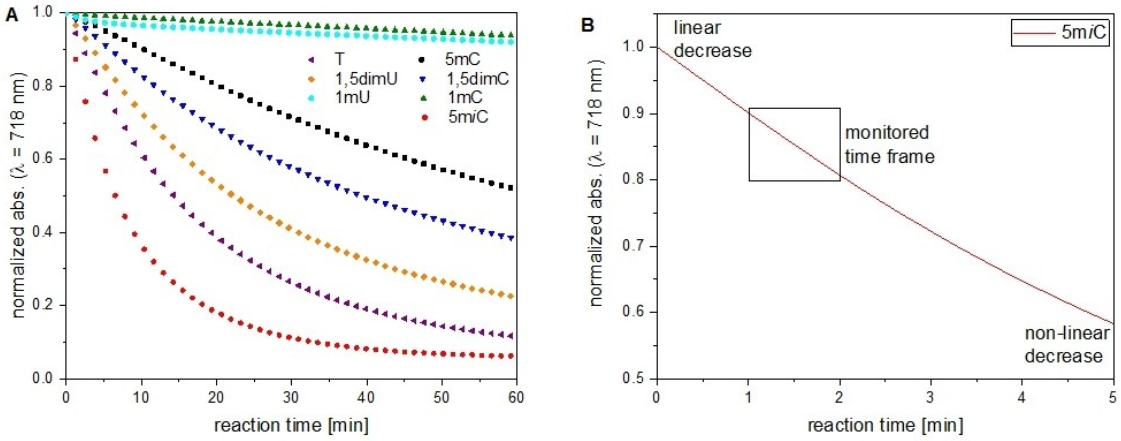

Figure 3. UV/Vis spectroscopy kinetics: A) Plot of the development of the absorbance of a series of reactions. B) Linear and non-linear decrease of the absorbance at λ = 718 nm. Conditions: [S] = 1 mM, [**1**] = 5 mM, H_2O, 30 °C.

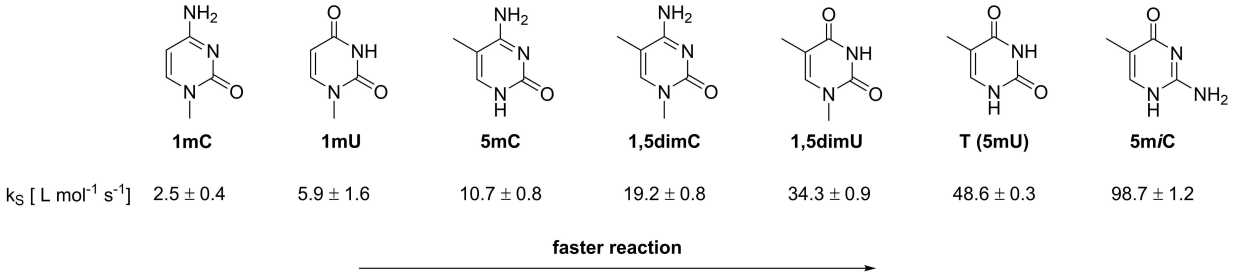

Figure 4. Observed rate constants k_S of the substrates at the following conditions: [S] = 1 mM, [**1**] = 5 mM, H_2O, 30 °C. Rate constants k_S were calculated using a second order rate equation (Eq. 1).

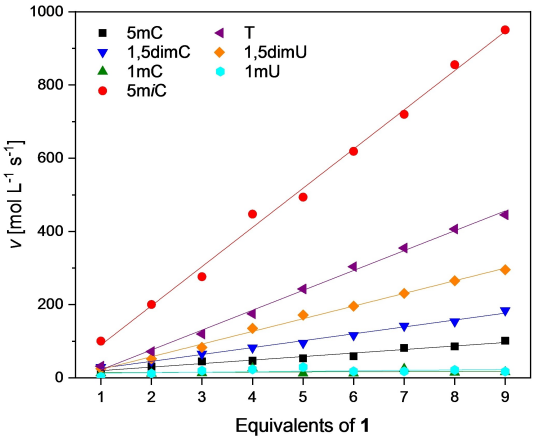

Figure 5. Plot of the measured reaction rates *v* of the reaction of **1** with nucleobase substrates. For a zoomed-in version of 5mC, 1mC, and 1,5dimC results see Supporting Information Figure S3[B]. 5mC (black squares), 5m*i*C (red dots), 1mC (green triangles), 1,5dimC (blue inverted triangles), T (purple twisted triangles), 1,5dimU (orange diamonds), and 1mU (cyan circles). Conditions: [S] = 1 mM, [**1**] = 1–9 mM, H_2O, 30 °C. The Supporting Information contains a second set of measurements for 5mC, 5m*i*C, 1mC, and 1,5dimC (Figure S3[A]).

cytosine counterparts 1mC, 5mC and 1,5dimC, respectively. When comparing mono- vs. dimethylation, a significant difference between uracil- and cytosine derived substrates was noted: The dimethylated compounds 1,5dimC and 1,5dimU showed divergent reactivity: whereas 1,5dimC reacts faster than 5mC, 1,5dimU reacts slower than its monomethylated counterpart T. We found that in the case of dimethylated substrates, reactivity can be attributed almost completely to the methyl group bound to the carbon atom at position 5 (*vide infra* for details). 5m*i*C then shows the fastest reaction rates *v* by a large margin.

Clearly, the nature of the substituents on the 1, 2, and 4 position influences the reactivity of the methyl groups present. It can be summarized that an amine group at position 4 (as in 5mC) slows the reactivity, whereas a carbonyl moiety (as in T and 1,5mU) increases it. Also, a guanidine moiety (amine substituent at position 2, as in 5m*i*C) increases reactivity compared to a urea moiety (as in 5mC or T). Methylation of the 1 position can influence the reactivity both ways: in the case of an exocyclic amine on position 4 (as in 1,5dimC), the reaction rate is increased. If, however, two carbonyl functions are present (as in 1,5dimU), the rate is decreased when the 1 position is methylated. These observations imply that the heterocyclic, conjugated ring system is capable of relaying electronic information from the substituents to the methyl groups. Effects

stemming from steric interactions and coordination of substrates and products to **1** might also influence the reactivity.

BDE calculation

In a next step, we wanted to rationalize the above described trends. As iron(IV)-oxo compounds both in synthetic[12] and enzymatic context,[13] as well as **1** in particular,[9,14] are reported to react *via* a hydrogen atom transfer from an aliphatic C–H bond (Scheme 1), BDEs are commonly believed to play an integral part concerning reaction rates.

We therefore calculated the relevant BDEs of the substrates (Figure S17). All quantum mechanics (QM) results are reported at the SMD(H_2O)/DLPNO-CCSD(T)/CBS//(U)B3LYP-D3/6-31+G-(d,p) level of theory as stated in the supporting information (for thermodynamic data see Tables S5–10).[15] A graphical representation of all aqueous phase BDE values at the relevant C–H bonds in the above-mentioned substrates is shown in Figure 6 (also compare gas phase BDE values, Figures S18–19). A significant difference in BDE values can be observed between *N1*- and *C5*-methylated compounds: methyl groups connected to another carbon atom possess BDE values of 379–387 kJ mol^{-1}, whereas the methyl groups situated on the *N1*-nitrogen atom show much higher BDEs of 413–416 kJ mol^{-1}. The BDE of 5m*i*C is somewhat lower than all other compounds, including its closest structural relatives T (ΔBDE = 3.7 kJ mol^{-1}) and 5mC (ΔBDE = 7.9 kJ mol^{-1}). The site-specific BDE values of doubly methylated compounds generally compare to their mono-methylated parent species. The aqueous phase BDE value of 1hmC is the highest of all calculated compounds at 421.0 kJ mol^{-1}, although we note that there is a substantial solvation effect on this value (see Table S2).

Comparing BDEs to observed rate constants

The calculated BDE values were found to predict reactivity of the substrates perfectly: low BDEs correspond to high rate constants k_S. The only exception from the observed flawless correlation is 1mU, which reacts slightly faster than its BDE reactivity would predict. We hypothesize that this observation is

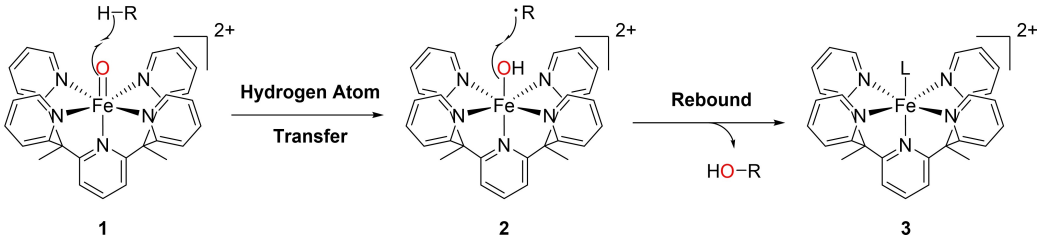

Scheme 1. Two-step reaction mechanism for **1** with aliphatic C–H bonds (indicated as R–H) as postulated by Daumann and Jonasson and Chantarojsiri et al.[9,14] The transferred oxygen atom is marked in red. L = solvent, substrate, or product molecule that completes the coordination sphere of **3**.

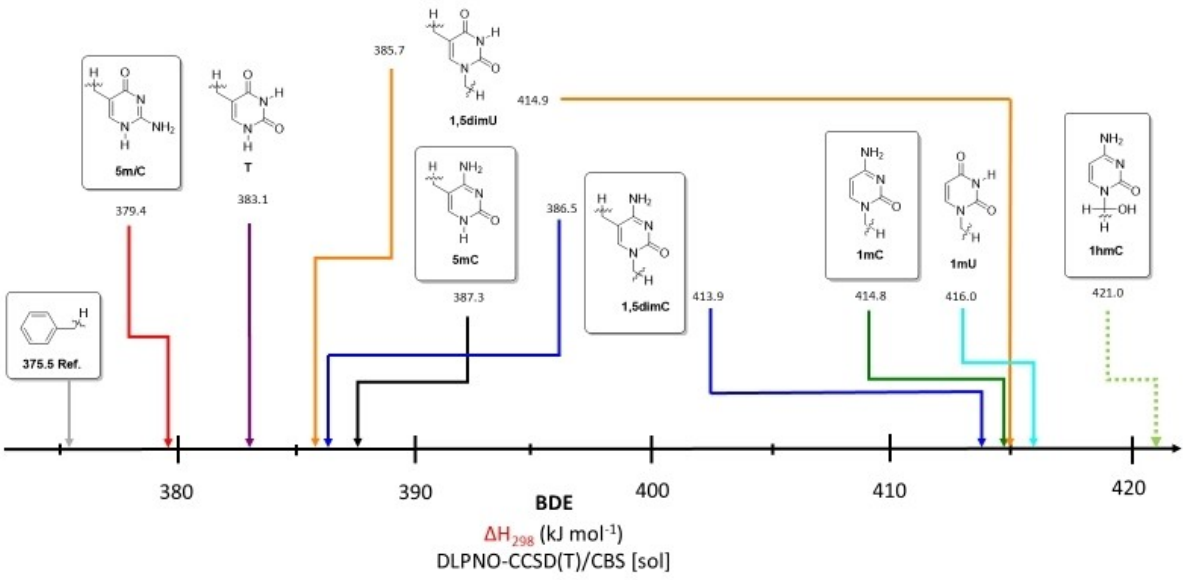

Figure 6. Aqueous phase ($\Delta H_{sol} = \Delta H_{298} + \Delta G_{solv}$) RCH_2–H bond dissociation energies (BDEs) of the relevant substrates calculated at the DLPNO-CCSD(T)/CBS level of theory. Dotted lines indicate the BDEs of molecules that were calculated but not included in experiments. For comparison of calculated BDEs of gas and aqueous phase see Figures S18–19.

due to the method of data analysis. We used the absorbance values between 1–2 min reaction time for the calculation of reaction time, however, as the reaction of 1mC and 1mU is very slow, small variations (possibly due to uncompleted mixing upon starting the experiment) influence the observed reactivity strongly. When the decrease in absorbance for 1mC and 1mU is compared for the entire length of the experiment, a very similar behavior is observed. This would fit very well with the BDEs of 1mC and 1mU being very similar at 415 and 416 kJ mol^{-1}, respectively. Nonetheless, the behavior of 1mU does fit very well within the broader trend described above, even if the data analysis is not perfectly suited to its behavior.

The correlation of BDE and k_S is in particular remarkable for the situation in the twice-methylated substrates 1,5dimC and 1,5dimU (Table 1). As described above we found that *N*-methylation increased the reaction rate in the cytosine derivative whereas the opposite was observed for the uracil derivative. This behavior is mirrored in the corresponding BDE values: the C–H bond on the carbon-bound methyl group in 1,5dimC is found to possess a lower BDE than 5mC, implying the experimentally confirmed increased reactivity. In the case of 1,5dimU a higher BDE was calculated, matching its lower reactivity compared to T.

The perfect correlation of calculated BDEs to observed reaction rates provides further evidence to corroborate the previously postulated two-step reaction pathway of **1** with aliphatic C–H bonds (Scheme 1).[9] In the first step in this mechanism, a hydrogen atom is transferred from the substrates R–Me(H) to the iron compound, generating an iron(III)-hydroxido species (**2**) and a carbon-centered radical. These species then recombine in a rebound step to form the product R–OH and an iron(II)-species (**3**). It was found that C–H abstraction/hydrogen transfer is the rate limiting step.[9]

As the hydrogen atom transfer (HAT) step involves the breaking of the C–H bond in the substrate, the BDE should determine the reaction rate. We had previously demonstrated this for both 5mC and 5hmC; in this work we expanded the substrate scope significantly to include 1mC, 1,5dimC, 5m*i*C, T, 1mU, and 1,5dimU.

When plotting the aqueous phase BDE values versus ln(k_s), a linear Bell-Evans-Polanyi correlation can be observed for 5mC, 1,5dimC, 1,5dimU, T and 5m*i*C (Figure 7). 1mC and 1mU are outliers, probably due to them being *N*-methylated instead of C-methylated as all other compounds. As mentioned previously, for the doubly methylated compounds the reactivity of the methyl group at the 5-position prevails (*vide infra* for details on how we come to this conclusion). Repeating this type of analysis with gas phase BDE(C–H) values we obtain similar results (see Figure S23), thus, we conclude that the observed correlation reflects the intrinsic properties of the studied nucleobase substrates.

Table 1. Comparison of calculated BDEs and observed reaction rates.

Substrate	BDE [kJ mol^{-1}]	k_S [L mol^{-1} s^{-1}]
1mC	414.8	2.5 ± 0.4
1mU	416.0	5.9 ± 1.6
5mC	387.3	10.7 ± 0.8
1,5dimC	386.5	19.2 ± 0.8
1,5dimU	385.7	34.4 ± 0.9
T	383.1	48.6 ± 0.3
5m*i*C	379.4	98.7 ± 1.2

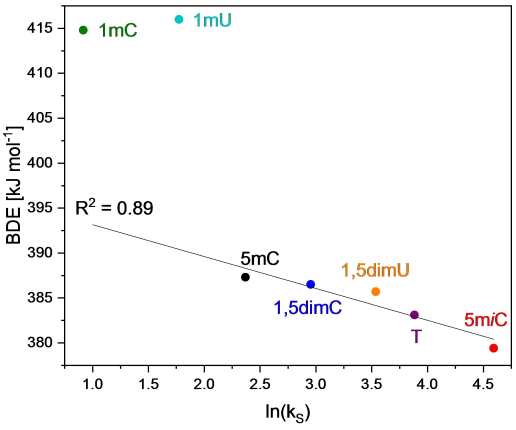

Figure 7. Plot of the calculated BDE values in aqueous phase against the observed rate constants k_s on a logarithmic scale ($R^2 = 0.891$) of the substrates 1mC, 1mU, 5mC, 1,5dimC, 1,5dimU, T, and 5m*i*C. In the case of the demethylated substrates 1,5dimC and 1,5dimU only the BDE of the carbon bound methyl groups are plotted. A similar plot of calculated BDE values in the gas phase against the observed rate constants k_s on a logarithmic scale can be found in Figure S23.

The presented data is a remarkable result, as it both provides evidence to confirm the previously postulated mechanism of **1** and shows that calculated BDEs can be reliably used to predict reaction rates for these types of substrates (in the absence of an enzyme's second coordination sphere). It is noteworthy that the reactivity of the natural nucleobase 5mC is in the middle of the observed spectrum: the *N*-methylated compounds 1mC or 1mU react significantly slower whereas 5m*i*C reacts significantly faster. This could be considered an indication on why 5mC can be considered an ideal epigenetic marker in nature: the reactivity of 5mC towards an iron(IV)-oxo moiety seems to be in a range that is both fast enough for efficient catalytic conversion by an enzyme and still slow enough to be controlled within a biological system. For example, 1mC is oxidized so slowly that even if its oxidized derivatives were stable (*vide infra*) it would not be a suitable substrate for enzymatic conversion. On the other hand, the reactivity of 5m*i*C seems to be so fast that it would be hard to control - an important factor in the delicate methylation equilibrium that is maintained by DNA methyltransferases (DNMT) and TET enzymes.[16] Whereas we do not claim that this behavior of 5mC and the other substrates towards iron(IV)-oxo species has been an evolutionary pressure resulting in the formation of 5mC epigenetics as we know it, we provide evidence that 5mC is indeed a perfect substrate for the task it performs. Regarding applications of natural and artificial methylated nucleobases in synthetic biology and DNA-based storage systems, their different reactivities could allow for additional layers of information and tunability. By incorporating two nucleobases of vastly different reactivity towards **1**, such as

1mC and 5m*i*C, into an artificial DNA strand, differentiation during oxidative sequencing could be used to drastically increase density of information.

Product Analysis (HPLC-MS/GC-MS)

We used both UHPLC-MS and GC-MS to identify the products formed in the reactions of **1** with the cytosine substrates, as these are most relevant to our research question (see Supporting Information, Table S1 and Figures S4–16). We also analyzed the product distribution of T oxidation products using GC-MS (see Figure S16).

In our recently published work on the reactivity of **1** towards 5mC we identified the oxidized derivatives 5hmC, 5fC, and 5caC, that are also formed by TET enzymes in DNA substrates, using GC-MS.[9] In this work we corroborated these results with HPLC-MS measurements (Scheme 2A). In the measurements of the reaction samples we found signals corresponding to all expected products (5hmC, 5fC, 5caC), but did also find an additional signal with a mass-to-charge ratio of 126.0622, which would correspond to 5mC. Due to the longer retention time (~13.2 min) than for the reference signal of 5mC (~7 min) but equal m/z ratio, we propose that this is a dimer of 5mC, probably formed during lyophilization (see Figures S4 and S5). In fact, a hemi-protonated dimer of 5mC (5mC-5mCH$^+$) has previously been isolated by us and was structurally characterized.[17] For reactions with 5m*i*C we found signals at m/z values corresponding to 5-hydroxymethyl *iso*-cytosine (5hm*i*C), 5-formyl *iso*-cytosine (5f*i*C), 5-carboxy *iso*-cytosine (5ca*i*C, Scheme 2B). When 5 equivalents of **1** were used, no significant difference in product distribution can be observed between the sample taken after 1 h and that taken after 24 h. This indicates that the reaction is complete after 1 h, which agrees with the observed high reaction rates and calculated low BDEs. When changing the substrate to 1mC only small amounts of cytosine (C) could be identified as a product using the standard procedure: conducting the reaction in water, filtration through silica, lyophilization, UHPLC measurement. However, traces of all oxidation products can be found using HPLC-MS when injecting samples before standard workup procedures were applied. We propose that the methyl group on 1mC is indeed oxidized to the expected products 1hmC, 1fC and 1cC, however, several pathways can lead to a quick decomposition towards cytosine. The first oxidation of 1mC leads to 1hmC which, as an hemiaminal, tends to equilibrate towards cytosine, when removing formaldehyde at reduced pressure (Scheme 2). This overall process, however, is endergonic (see Figure S21[A] and [B] and Table S3). Oxidation of 1hmC towards 1fC is proposed to be faster compared to the oxidation of 1mC, since the gas phase BDE of 1hmC is 4.3 kJ mol^{-1} lower than for 1mC. In this particular case, we observed that the gas phase BDE value represents a better estimation of the reaction trend than in solution phase. This is possibly due to formation of a cyclic hydrogen bond between the hydroxymethyl group and urea moiety (for details, please refer to Figure S20 and subsequent text). The oxidation products that follow, 1fC and 1caC, were both found to be exergonic and therefore unstable (see Scheme 2C). The calculated solution phase free energies of reaction ΔG for the

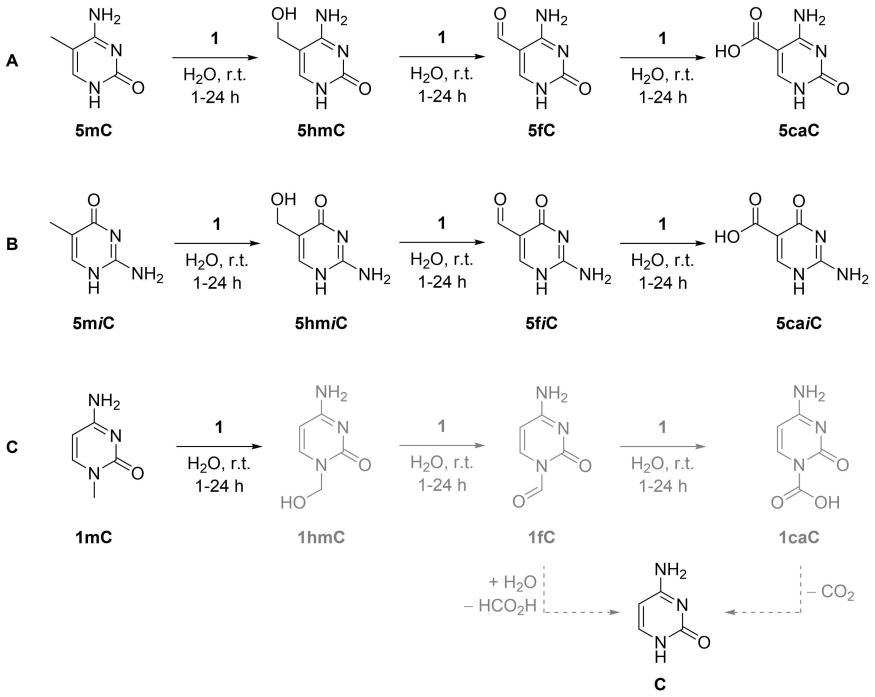

Scheme 2. Identified products in the reactions of 5mC, 5m*i*C, and 1mC with **1**. All structures in black were detected using HPLC-MS after 1 h and 24 h using both 1 and 5 equiv. of **1**, although in different ratios. 5m*i*C, 5hm*i*C and 5ca*i*C were also detected using GC-MS with 1 equiv. of **1** after 1 h. All structures in gray were detected on HPLC-MS by injection of the untreated reaction solution with 1 equiv. of **1** after 24 h and 44 h.

deformylation of 1fC is $-17.0\ kJ\,mol^{-1}$ (Figure S21[C]), for the decarboxylation of 5caC it is $-44.9\ kJ\,mol^{-1}$ (Figure S21[D]).

As a proof-of-concept for this hypothesis, free energies of reaction ΔG were calculated for the literature known deformylation of 6-hydroxymethyladenine (6hmA) and 6-formyladenine (6fA), which are oxidation products of naturally occurring 6-methyladenine (6mA) in mammalian DNA.[18] The deformylation of 6hmA towards adenine and formaldehyde is endergonic ($\Delta G_{298,H2O} = +16.5\ kJ\,mol^{-1}$, see Figure S22[B] and Table S4), while the deformylation of the following oxidative product, 6fA, is thermoneutral ($\Delta G_{298,H2O} = +1.1\ kJ\,mol^{-1}$, see Figure S22[C]). It has been reported, that 6hmA and 6fA are transient intermediates of the oxidation of 6 mA with hydrogen peroxide.[19] The aqueous phase BDE(C–H) value of 6 mA ($+396.4\ kJ\,mol^{-1}$, see Table S2) is $13.3\ kJ\,mol^{-1}$ lower than that of 6hmA ($+408.7\ kJ\,mol^{-1}$, see Table S2), which is in support of a consecutive oxidation cascade and therefore also of the proposed pathway for the oxidative demethylation of 1mC to C.

In the case of 1,5-dimC, the product composition is more convoluted, however, it matches with the expectations based on observed reaction rates and calculated BDEs (Scheme 3): in addition to the starting material we detected m/z values corresponding to 1-methyl-5-hydroxymethylcytosine (1m-5hmC), 1-methyl-5-formylcytosine (1m-5fC), and 1-methyl-5-carboxycytosine (1m-5caC). These products are expected as the carbon-bound methyl group at position 5 has a lower calculated BDE and should therefore be oxidized more readily. The observed products are also corresponding to those observed for reactions of 5mC and 5m*i*C with **1**. However, besides the oxidation products of position 5, we additionally detected both 5mC and 5caC (confirmed by m/z and retention time). We therefore propose, that for 1,5dimC hydroxylation on the 1-methyl group also occurs to some small extent, and this oxidation product then reacts to 5mC (Scheme 3), corresponding to our proposed mechanism for 1mC (Scheme 2). Similarly, 1m-5caC only offers the 1-methyl group as a substrate position for **1** to react with, so 5caC is formed *via* hydroxylation and subsequent reaction to 1m-5caC. The amounts of 1m-5hmC and 1m-5fC are too low to represent a significant target for 1-methyl-hydroxylation, therefore no 5hmC or 5fC are detected. Similarly, only small amounts of 5mC are detected and it is, as the calculated BDE values show, less readily oxidized to 5hmC and 5fC as its *N*-methylated counterpart 1,5dimC.

Conclusion

We have presented a comprehensive study of the reactivity of the biomimetic iron(IV)-oxo complex **1** towards a number of methylated cytosine and uracil substrates and compared the results to calculated BDE values. Using HPLC-MS and GC-MS we also identified the products of the reaction of **1** with the cytosine derivatives 5m*i*C, 1mC, and 1,5dimC. We also provided a reasonable explanation for the observed decomposition of oxidized 1mC derivatives 1hmC, 1fC, and 1caC by calculating deformylation and decarboxylation energy profiles and comparing these to the literature known pathway in 6hmA/6fA. In the case of 1,5dimC, combining the observed reaction rates, the calculated BDE values and the observations regarding 1mC allowed for a clear interpretation of the observed product distribution. We found that the reported reaction rates are in very good agreement with the calculated BDEs which therefore prove to be a very good predictor for the reactivity of **1** towards a broad range of methylated substrates. In summary the observed reaction rates towards **1** seemed to be dominated by the reactivity of the C-methylated part of the substrates. 5mC, T

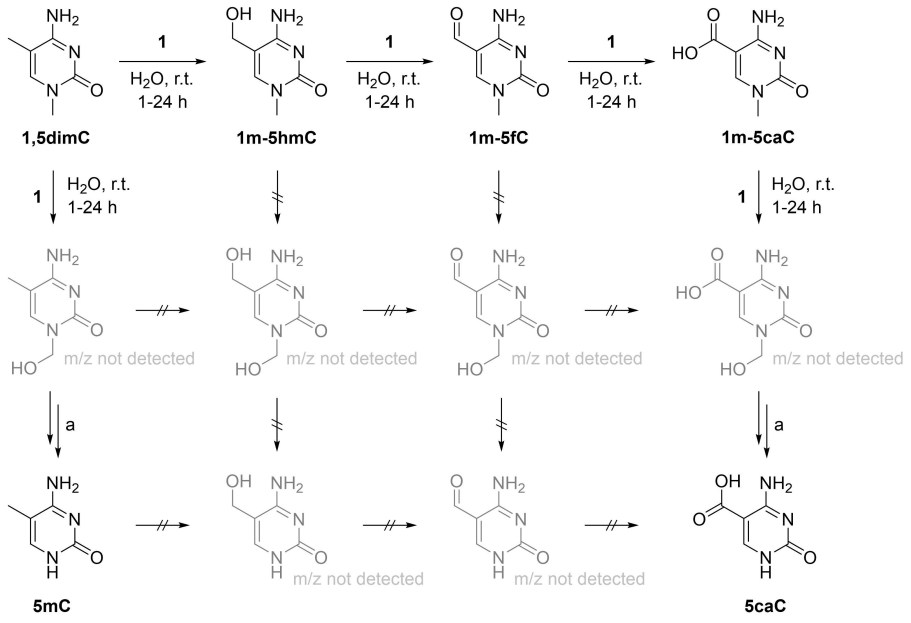

Scheme 3. Identified products in the reaction of 1,5dimC with **1**. All structures in black were detected using HPLC-MS after 1 h and 24 h using both 1 and 5 equiv. of **1**, although in different ratios. a: For this step we propose a similar reaction sequence as for 1mC (see Scheme 2).

and 5m*i*C possess a distinctly different reactivity than the solely *N*-methylated compounds 1mC and 1mU. For the compounds 1,5dimC and 1,5dimU that are both *C*-methylated and *N*-methylated, their C–H reactivity towards oxidation by **1** is mostly determined by the methyl group bound to the carbon atom. Interestingly, diverging effects were observed for *N*-methylation in 1,5-dimC and 1,5-dimU: in the case of 1,5dimC the reactivity is higher than for its mono-methylated counterpart 5mC, whereas 1,5dimU was observed to react faster than T. The observed rates also suggest that the reactivity of the 5-methyl group on the epigenetic marker 5mC is ideal to fit its purpose in a delicate equilibrium maintained by a series of enzymes. While the low reactivity of 1mU towards **1** is certainly not the reason for the stability of the corresponding nucleoside *pseudo*-methyl-uridine (1mΨ) that is used in some Covid-19 mRNA vaccines, our analysis shows that 1mUs methyl group is rather inert towards oxidation reactions. These observations can be a useful tool in predicting the possibilities of using and manipulating methylated nucleobases in synthetic biology, e.g. data storage, and further understanding the mechanisms of epigenetics.

Acknowledgements

We thank Prof. Dr. Bernhard Lippert for a sample of 1,5dimC. This work was funded by the Deutsche Forschungsgemeinschaft (DFG, German Research Foundation) – SFB 1309-325871075. N.S.W.J. thanks the Studienstiftung des Deutschen Volkes. Open Access funding enabled and organized by Projekt DEAL.

Conflict of Interest

The authors declare no conflict of interest.

Keywords: 5-methylcytosine · computational chemistry · DNA methylation · epigenetics · synthetic biology

[1] a) L. Organick, S. D. Ang, Y.-J. Chen, R. Lopez, S. Yekhanin, K. Makarychev, M. Z. Racz, G. Kamath, P. Gopalan, B. Nguyen, *Nat. Biotechnol.* **2018**, *36*, 242; b) R. Lopez, Y.-J. Chen, S. D. Ang, S. Yekhanin, K. Makarychev, M. Z. Racz, G. Seelig, K. Strauss, L. Ceze, *Nat. Commun.* **2019**, *10*, 1–9; c) L. Ceze, J. Nivala, K. Strauss, *Nat. Rev. Genet.* **2019**, *20*, 456–466.
[2] A. Hofer, Z. J. Liu, S. Balasubramanian, *J. Am. Chem. Soc.* **2019**, *141*, 6420–6429.
[3] F. R. Traube, T. Carell, *RNA Biol.* **2017**, *14*, 1099–1107.
[4] C. Mayer, G. R. McInroy, P. Murat, P. Van Delft, S. Balasubramanian, *Angew. Chem. Int. Ed.* **2016**, *55*, 11144–11148; *Angew. Chem.* **2016**, *128*, 11310–11314.
[5] a) S. Hoshika, N. A. Leal, M.-J. Kim, M.-S. Kim, N. B. Karalkar, H.-J. Kim, A. M. Bates, N. E. Watkins, H. A. SantaLucia, A. J. Meyer, *Science* **2019**, *363*, 884–887; b) S. A. Benner, A. M. Sismour, *Nat. Rev. Genet.* **2005**, *6*, 533–543.
[6] J. W. Park, P. N. Lagniton, Y. Liu, R.-H. Xu, *Int. J. Biol. Sci.* **2021**, *17*, 1446.
[7] O. Andries, S. Mc Cafferty, S. C. De Smedt, R. Weiss, N. N. Sanders, T. Kitada, *J. Controlled Release* **2015**, *217*, 337–344.
[8] A. M. Sismour, S. A. Benner, *Nucleic Acids Res.* **2005**, *33*, 5640–5646.
[9] N. S. Jonasson, L. J. Daumann, *Chem. Eur. J.* **2019**, *25*, 12091–12097.
[10] a) D. Schmidl, N. Jonasson, E. Korytiakova, T. Carell, L. Daumann, *Angew. Chem. Int. Ed.* **2021**, https://doi.org/10.1002/anie.202107277.
[11] a) M. J. Booth, M. R. Branco, G. Ficz, D. Oxley, F. Krueger, W. Reik, S. Balasubramanian, *Science* **2012**, *336*, 934–937; b) G. S. Madugundu, J. Cadet, J. R. Wagner, *Nucleic Acids Res.* **2014**, *42*, 7450–7460; c) A. Burdzy, K. T. Noyes, V. Valinluck, L. C. Sowers, *Nucleic Acids Res.* **2002**, *30*, 4068–4074.
[12] a) J. Kaizer, E. J. Klinker, N. Y. Oh, J.-U. Rohde, W. J. Song, A. Stubna, J. Kim, E. Münck, W. Nam, L. Que, *J. Am. Chem. Soc.* **2004**, *126*, 472–473; b) Y. Morimoto, J. Park, T. Suenobu, Y.-M. Lee, W. Nam, S. Fukuzumi, *Inorg. Chem.* **2012**, *51*, 10025–10036; c) A. Barbieri, O. Lanzalunga, A. Lapi, S. Di Stefano, *J. Org. Chem.* **2019**, *84*, 13549–13556; d) J. J. D. Sacramento, D. P. Goldberg, *Acc. Chem. Res.* **2018**, *51*, 2641–2652.
[13] a) J. C. Price, E. W. Barr, T. E. Glass, C. Krebs, J. M. Bollinger, *J. Am. Chem. Soc.* **2003**, *125*, 13008–13009; b) D. A. Proshlyakov, T. F. Henshaw, G. R. Monterosso, M. J. Ryle, R. P. Hausinger, *J. Am. Chem. Soc.* **2004**, *126*, 1022–1023; c) S. Kal, L. Que, *J. Biol. Inorg. Chem.* **2017**, *22*, 339–365.
[14] T. Chantarojsiri, Y. Sun, J. R. Long, C. J. Chang, *Inorg. Chem.* **2015**, *54*, 5879–5887.
[15] a) A. D. Becke, *J. Chem. Phys.* **1993**, *98*, 5648–5652; b) S. Grimme, J. Antony, S. Ehrlich, H. Krieg, *J. Chem. Phys.* **2010**, *132*, 154104; c) R. Ditchfield, W. J. Hehre, J. A. Pople, *J. Chem. Phys.* **1971**, *54*, 724; d) R. Krishnan, J. S. Binkley, R. Seeger, J. A. Pople, *J. Chem. Phys.* **1980**, *72*, 650; e) A. Altun, F. Neese, G. Bistoni, *Beilstein J. Org. Chem.* **2018**, *14*, 919–929; f) M. Saitow, U. Becker, C. Riplinger, E. F. Valeev, F. Neese, *J. Chem. Phys.* **2017**, *146*, 164105; g) F. Neese, *WIREs Comput. Mol. Sci.* **2018**, *8*, e1327; h) T. H. D. Jr., *J. Chem. Phys.* **1989**, *90*, 1007–1023; i) A. V. Marenich, C. J. Cramer, D. G. Truhlar, *J. Phys. Chem. B* **2009**, *113*, 6378–6396.
[16] a) M. V. Greenberg, D. Bourc'his, *Nat. Rev. Mol. Cell Biol.* **2019**, *20*, 590–607; b) Y. He, J. R. Ecker, *Annu. Rev. Genomics Hum. Genet.* **2015**, *16*, 55–77; c) S. Ito, L. Shen, Q. Dai, S. C. Wu, L. B. Collins, J. A. Swenberg, C. He, Y. Zhang, *Science* **2011**, *333*, 1300–1303; d) Y.-F. He, B.-Z. Li, Z. Li, P. Liu, Y. Wang, Q. Tang, J. Ding, Y. Jia, Z. Chen, L. Li, *Science* **2011**, *333*, 1303–1307.
[17] A. Menke, R. C. A. Dubini, P. Mayer, P. Rovó, L. J. Daumann, *Eur. J. Inorg. Chem.* **2021**, 30–36.
[18] a) J. Xiong, T.-T. Ye, C.-J. Ma, Q.-Y. Cheng, B.-F. Yuan, Y.-Q. Feng, *Nucleic Acids Res.* **2019**, *47*, 1268–1277; b) Y. Fu, G. Jia, X. Pang, R. Wang, X. Wang, C. Li, *Nat. Commun.* **2013**, *4*, 1798.
[19] J. Wu, H. Xiao, T. Wang, T. Hong, B. Fu, D. Bai, Z. He, S. Peng, X. Xing, J. Hu, *Chem. Sci.* **2015**, *6*, 3013–3017.

Manuscript received: August 15, 2021
Revised manuscript received: September 8, 2021
Accepted manuscript online: September 9, 2021
Version of record online: September 23, 2021

CORRIGENDUM

Correction Document for TET-Like Oxidation in 5-Methylcytosine and Derivatives: A Computational and Experimental Study

ChemBioChem., **2021**, *22*, e202100420

DOI: 10.1002/cbic.202100420

In the published calculations a mistake occurred while transferring data from the UV-vis instrument to the analysis software used (Microsoft Excel). Thereby the time format was shown correctly in graphs but not used correctly in the linear regression calculations (MS Excels RGP function) used for determining the slope values (see Figure 1).

			calculated slope	
Time [s]	Time as exported	Abs.	RGP function with time as exported	RGP function with time converted into seconds
0	00:00:00	0.3423	-4.711	-5.45E-05
7	00:00:07	0.3409		
14	00:00:14	0.3403		
21	00:00:21	0.3397		
28	00:00:28	0.3394		
35	00:00:35	0.3390		
42	00:00:42	0.3380		
49	00:00:49	0.3371		
56	00:00:56	0.3364		
63	00:01:03	0.3363		
70	00:01:10	0.3361		
77	00:01:17	0.3356		
84	00:01:24	0.3353		
91	00:01:31	0.3346		
98	00:01:38	0.3345		
105	00:01:45	0.3339		
112	00:01:52	0.3336		
119	00:01:59	0.3335		
126	00:02:06	0.3327		

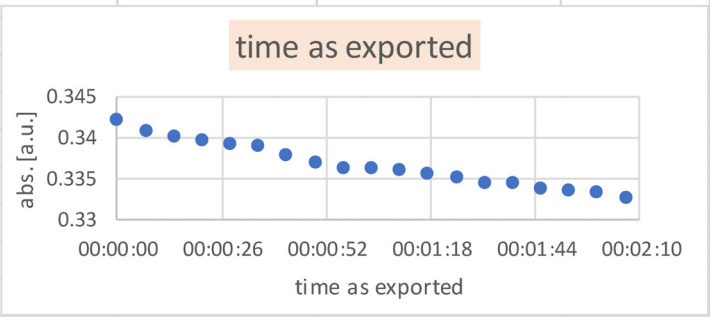

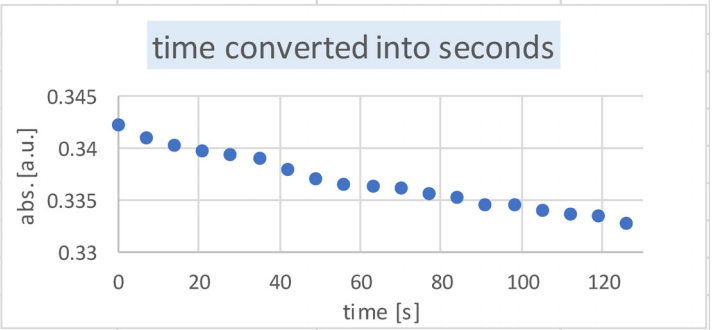

Figure 1. Illustration of the problematic data processing. The exported time format is used correctly in plotting functions and used incorrectly in linear regression calculations (MS Excel RGP function).

The corrected values and graphs are found below. The authors apologize for this oversight.

To allow for maximum transparency and reproducibility, all raw data are published alongside this corrigendum. Additionally, an overview of the exact data evaluation process is given here:

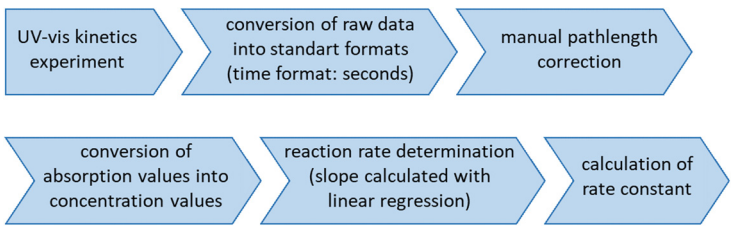

Corrigendum
doi.org/10.1002/cbic.202400445

Chemistry Europe
European Chemical Societies Publishing

Reaction rates (Figure 5):

manuscript

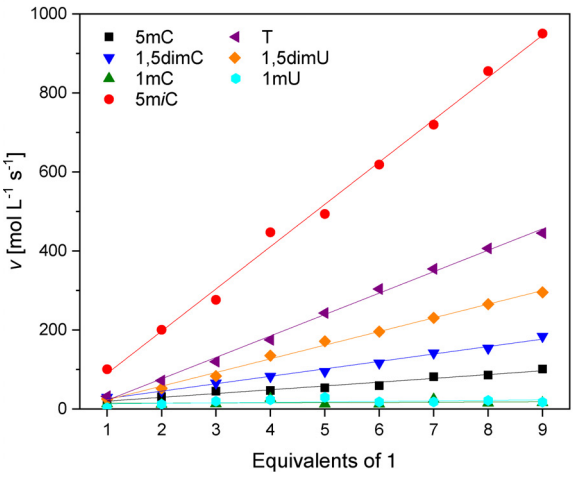

correction

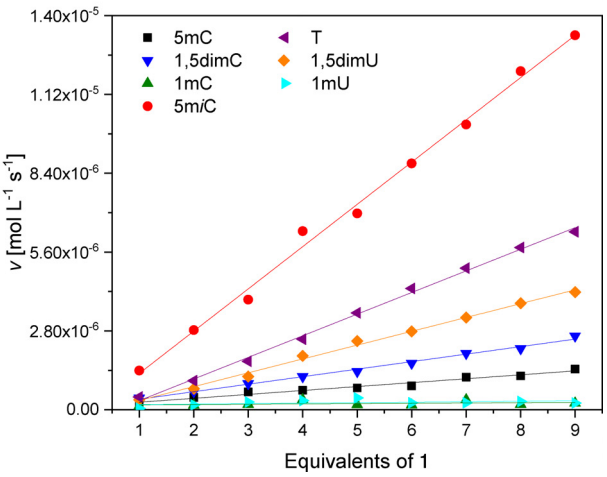

Rate constants (Figure 4):

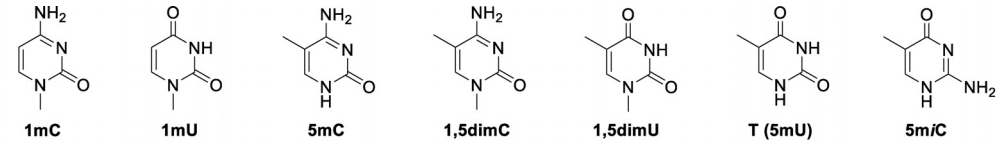

	1mC	1mU	5mC	1,5dimC	1,5dimU	T (5mU)	5m*i*C	
k_S [L mol^{-1} s^{-1}]	2.5 ± 0.4	5.9 ± 1.6	10.7 ± 0.8	19.2 ± 0.8	34.3 ± 0.9	48.6 ± 0.3	98.7 ± 1.2	*manuscript*
	0.06 ± 0.03	0.06 ± 0.02	0.18 ± 0.03	0.30 ± 0.03	0.44 ± 0.04	0.63 ± 0.08	1.44 ± 0.06	*correction*

faster reaction

Bell-Evans-Polanyi correlation (Figure 7):

manuscript

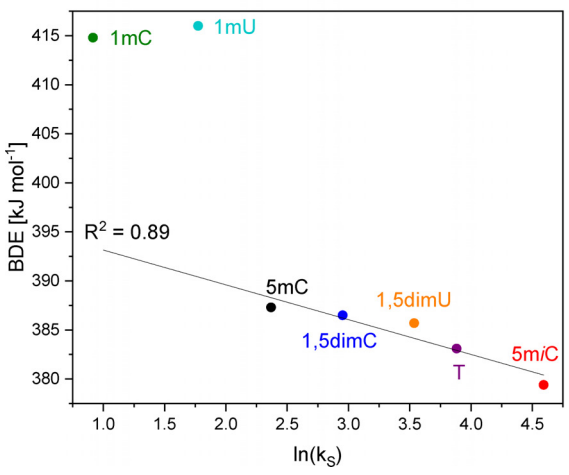

correction

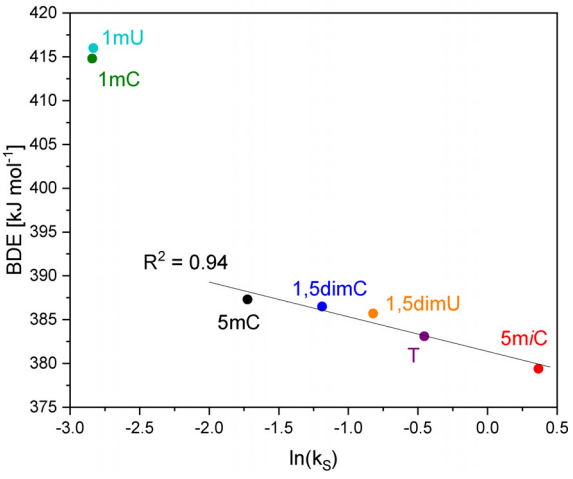

Corrigendum
doi.org/10.1002/cbic.202400445

Chemistry Europe
European Chemical Societies Publishing

Figure S23:

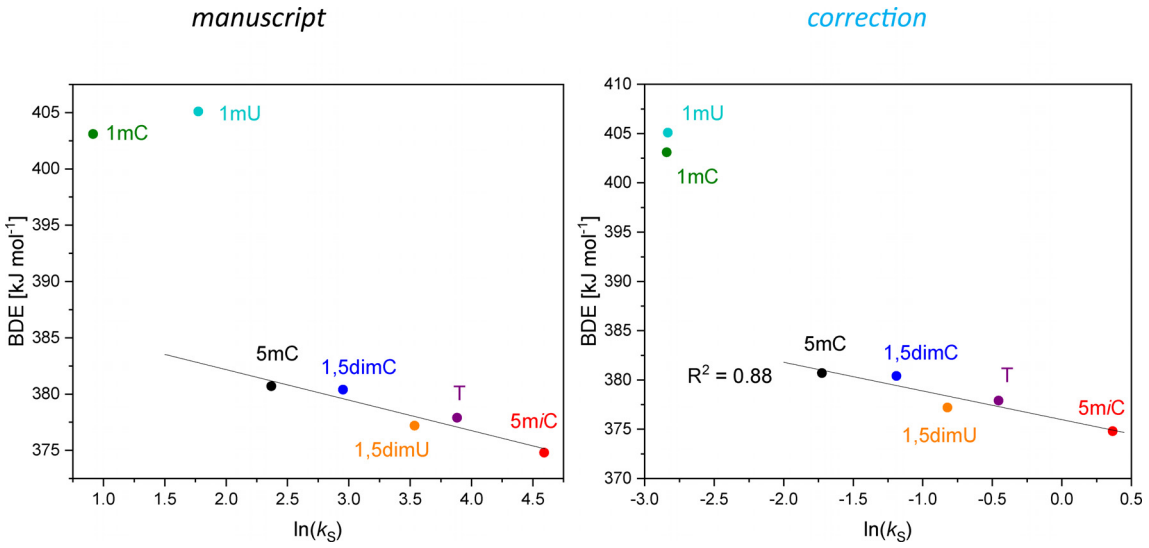

Author's comment on the change of the difference between the values of 1 mU and 1 mC:

The calculated values for 1 mC and 1 mU seem to shift significantly when the correct evaluation technique is employed in the Bell-Evans-Polanyi-plot. However, this has no influence on the statements made in the manuscript, as the conclusion is the clustering of substrates containing "C-bound" and "N-bound" methyl groups which remains unchanged.

3 Application of the Iron(IV)-oxido Complex in Mechanistic Studies on TET Enzymes: Oxidation of 5fC *via* Aldehyde *versus* Hydrate

It was previously mentioned that oxidation of 5mC, 5hmC and 5fC residues by TET enzymes does not follow the reaction rates expected from the corresponding BDE values,[95] although the hydrogen atom abstraction is mainly considered as rate-limiting in this catalytic process.[154-155] As calculated by Xu and coworkers, 5hmC (86.20 kcal mol^{-1}) displays the lowest BDE in this series, followed by 5mC (90.39 kcal mol^{-1}) and the only slightly higher BDE of 5fC (92.89 kcal mol^{-1}, an overview of all relevant BDEs is given in the appendix, section VII.3, Table 22).[95] In enzymatic catalysis however, TET enzymes show higher activity towards 5mC-containing DNA compared to 5hmC- or 5fC-containing DNA as substrates. This substrate preference was attributed to an unfavorable orientation of the abstractable hydrogen in the case of 5hmC and 5fC. Even though all three pyrimidine bases adopt almost identical conformation within the catalytic cavity,[156] the hydroxyl group of 5hmC and the formyl group of 5fC form hydrogen bonds with the secondary coordination sphere. This interaction leads to a restrained conformation preventing the abstractable hydrogens from adopting a favorable orientation, resulting in lower catalytic efficiency. In 2015, Xu and coworkers performed steady-state kinetic analyses for the oxidation of 5mC/5hmC/5fC-DNA as substrate for TET2.[95] From the obtained catalytic constant k_{cat} and Michaelis constant K_M values, free energy barriers $\Delta G^{\ddagger}$ can be obtained by applying the Michaelis-Menten equation (Table 8).

Table 8: Free energy barrier calculated from experimentally obtained kinetic values reported by Xu and coworkers ($\Delta G^{\ddagger}$(exp))[95] and free energy barrier calculated for the hydrogen abstraction step by Luo and coworkers $\Delta G^{\ddagger}$(calc)[157] for TET-mediated oxidation of the substrates 5mC/5hmC/5fC.

substrate	$\Delta G^{\ddagger}$(exp) [kcal mol^{-1}]	$\Delta G^{\ddagger}$(calc) [kcal mol^{-1}]
5mC	17.01	16.0
5hmC	17.73	18.6
5fC	17.91	27.2

In a theoretical approach of Luo and coworkers, $\Delta G^{\ddagger}$ values are calculated for all proposed steps in the catalytic cycle of TET-mediated 5mC/5hmC/5fC oxidation.[157] Their results for the hydrogen atom abstraction reaction are presented in Table 8. Comparable values in both experimental and computational approaches are obtained for 5mC and 5hmC. The values for 5fC however differ significantly. In the experimental approach, slightly higher energy barriers were obtained for 5fC than for 5hmC, whereas the calculated energy barrier for 5fC increases significantly compared to 5hmC. This difference in experimental and computational observations lead to the assumption that eventually additional so far neglected processes might play a role in this system.

One process that is surprisingly little addressed in this context in literature is the characteristic of aldehydes to form hydrates in aqueous solutions. The oxidation from 5fC to 5cC is usually described using the aldehyde form but it might potentially also occur from the corresponding hydrate species (Scheme 13).

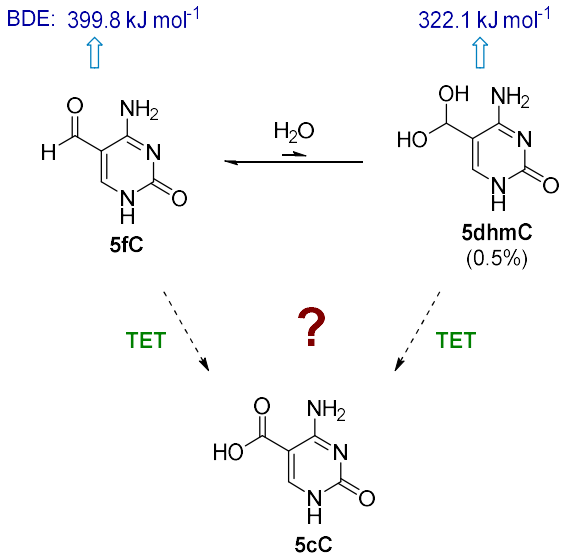

Scheme 13: TET-mediated oxidation of 5fC to 5cC occurring either *via* the aldehyde or the hydrate from. BDEs calculated by Fabian Zott (Zipse group, LMU Munich).

The geminal diol form of 5fC was detected occasionally in levels of about 0.5% *via* mass spectrometric analyses under acidic conditions.[158-159] However, no hydrate was identified in the course of an ^{1}H NMR chemical exchange study on 5fC-modified DNA strands.[160] Recent work by Zipse and coworkers provided investigations on possible systematic

manipulation of the aldehyde-hydrate equilibrium.[161] The authors found that protonation at the N^3-position under acidic condition increases the formation of the geminal diol. By quantification with ^{1}H NMR spectroscopy it was shown that in near-neutral unbuffered solutions of 5fC (nucleobase and nucleoside) in deuterated water the hydrate form was not quantifiable. When acidic conditions (about pH 3) are applied, 0.5% of the hydrate form were observed, matching the aforementioned observations from other groups. Investigating the nucleobase 5-formyluracil (5fU), already 1.3% geminal diol were detected under neutral conditions. Zipse and coworkers also conducted isotope exchange experiments in which the aldehyde species is treated with ^{18}O-labeled water under neutral conditions. The incorporation of the isotope label into the nucleobase was proven my mass spectrometric analysis, strongly suggesting a fast oxygen exchange reaction. Their work demonstrates that the aldehyde-hydrate equilibrium can be affected by environmental changes, suggesting the possibility of also stabilizing this hydrate species through hydrogen bonding interactions for instance in enzymatic catalysis. The oxidation of 5fC *via* the geminal diol displays therefore an alternative pathway that also needs to be considered.

The aim of the following project is now to further elaborate this possibility in close cooperation with the Zipse group. It was shown before that the reactivity of nucleobases correlates with their corresponding calculated BDEs in oxidation reactions with an iron(IV)-oxido complex employed in our group (section 2.2). Given the lower BDE of the diol compared to the aldehyde (Scheme 13), differences in reaction rate should be observed depending on the level of diol present in the equilibrium. The search for substrates showing structural similarity to the natural nucleobase as well as different hydrate contents afforded the compounds presented in Chart 7.

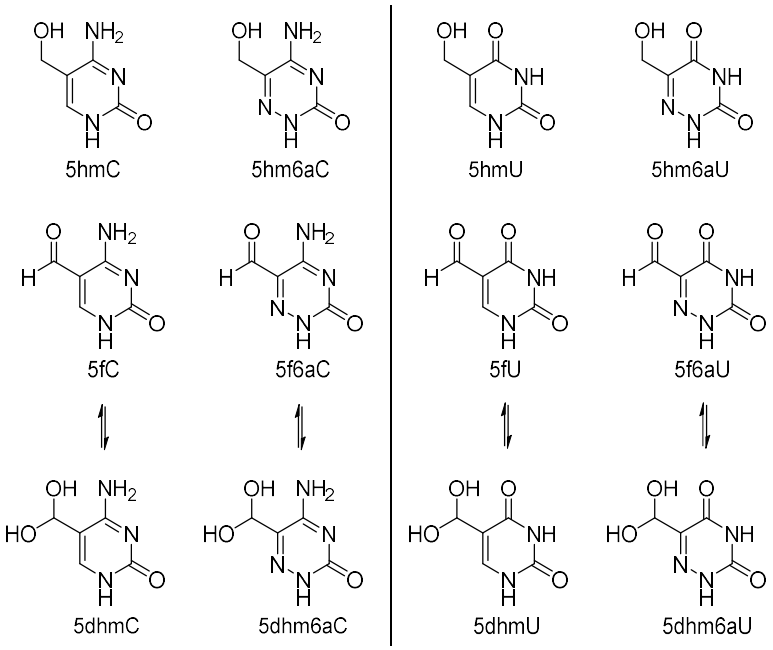

Chart 7: Chosen substrates for reactivity studies with the iron(IV)-oxido complex.

It was reported by Carell and coworkers in the synthesis of the artificial nucleoside 5-formyl-6-aza-cytidine that this compound contains about 20% of its hydrated form.[162] As described above, also uracil derivatives seem to display a small amount of hydrate. The corresponding 5-formyl-6-aza-uracil is therefore expected to even show higher amounts of hydrate compared to its cytosine counterpart. It was therefore aimed to synthesize the shown compounds and perform kinetic investigations on oxidation reactions with the iron(IV)-oxido complex. The obtained results should then be compared with the BDEs of the substrates which were calculated by Fabian Zott from the Zipse group (see appendix, section VII.3).[163]

Synthesis of the modified cytosine und uracil nucleobases

The synthesis plan towards the 6-aza derived nucleosides was developed on the basis of a synthetic procedure towards 5-formyl-6-aza cytidine published by Carell and coworkers.[162] The anticipated synthetic route towards the target molecules is depicted in Scheme 14. The standard cytosine nucleobases should be prepared following literature-known syntheses.[164] The first steps in this developed synthetic pathway are identical to the route published by Carell and coworkers. The authors introduce a protected sugar moiety

after step **c** which provides the compound with completely different properties, for instance concerning solubility.

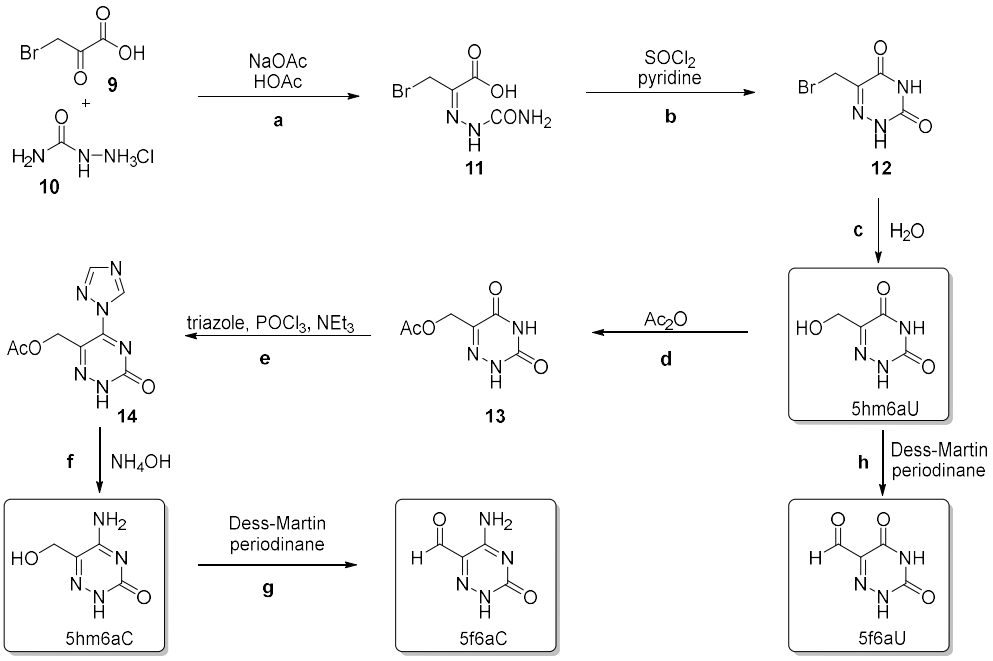

Scheme 14: Anticipated synthetic route towards the 6-aza uracil/cytosine derivatives 5hm6aC, 5f6aC, 5hm6aU and 5f6aU inspired by a published synthesis pathway towards 5-formyl-6aza-cytidine.[162]

In the first step 3-bromopyruvic acid **9** was reacted with semicarbazide hydrochloride **10** in an acidic aqueous medium (Scheme 14a, Scheme 15). The colourless product **11** precipitated from the yellowish reaction solution at 0 °C and was filtered. It was found *via* ^{1}H NMR spectroscopy that the product contained residues of acetic acid. These could be reduced by washing with higher amounts of ice-cold water and diethyl ether, however the obtained yield also decreased significantly, indicating that the product was also washed into the filtrate.

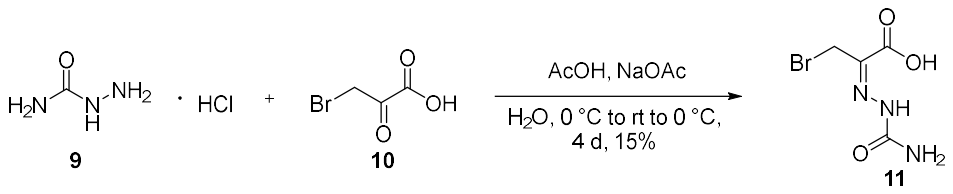

Scheme 15: Reaction procedure towards compound **11**.[162]

Alternatively, recrystallization from water was attempted. For this purpose, compound **11** was heated to reflux until complete dissolution was achieved and the solution was kept at 4 °C. As no precipitate was found after a week, the solvent was removed using a rotary evaporator, affording a brown solid. This solid however transformed into a brown foam setting free some gas, likely suggesting a decarboxylation reaction. It seems that compound **11** is not stable especially at higher temperatures and prone to decomposition but no defined reaction product could be identified with ^{1}H NMR spectroscopy. Furthermore, it was observed that the colourless compound **11** turned pinkish red upon exposure to an iron spatula. For this reason, compound **11** was only handled with plastic spatula and prepared freshly.

The next steps of the reaction cascade consist of the formation of the carbonyl chloride with thionyl chloride followed by a ring closure reaction resulting in compound **12** (Scheme 14b). Refluxing in water over night affords 5-hydroxymethyl-6-aza-uracil (5hm6aU, Scheme 14c) which was subsequently protected with an acetyl protecting group at the hydroxy moiety (compound **13**, Scheme 14d).

In order to obtain the corresponding cytosine nucleobase instead of the uracil derivative, an amination reaction needed to be performed. In the first part a 1,2,4-triazole ring should be introduced at the *C4*-carbonyl group (Scheme 14e) which should subsequently be cleaved by ammonium hydroxide to afford the aminated and deprotected species 5-hydroxymethyl-6-aza-cytosine (5hm6aC, Scheme 14f). This procedure however turned out to be more challenging than expected and will be discussed in more detail (Scheme 16).

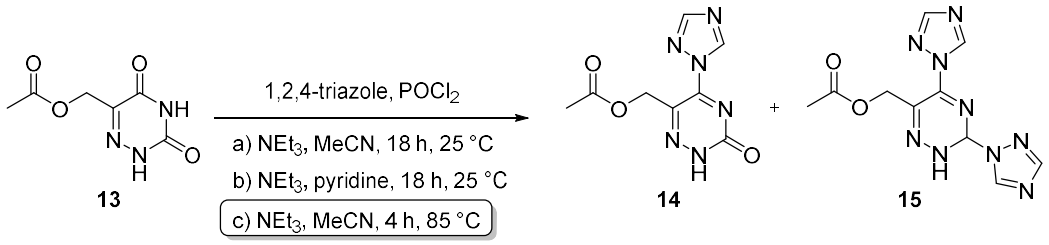

Scheme 16: Tested reaction conditions towards compound **14**. Only the conditions described in c) afforded the depicted reaction products.

In this reaction, 1,2,4-triazole and phosphoryl chloride form a reactive intermediate which abstracts the oxygen atom from the carbonyl group of compound **13**. facilitating the formation of the C-N bond towards the triazole.[165] In the literature, this reaction with the corresponding nucleoside is carried out in acetonitrile at room temperature over night.[162] Under these conditions, only traces of the desired product **14** could be observed. This was detected by direct injection mass spectrometric analysis. However, this method turned out to not always be very reliable with these kinds of compounds. Therefore, additional ^{1}H NMR spectroscopic analysis of the crude product was performed. These compounds display only few protons in general and the signals of free triazole could be distinguished from those of bound triazole. Several different species including starting material were detected and flash column chromatography did not afford the desired product. The reaction was also carried out in pyridine as solvent, affording the same result. To achieve more conversion of the starting material, the reaction temperature was raised to reflux. In this procedure, a pale orange solid precipitated which was filtered and ^{1}H NMR spectroscopy indicated the presence of a species containing two triazole residues (compound **15**, compare appendix, section VII.4.1, Figure 67). This side reaction was not reported for the corresponding nucleoside. The additional bulky sugar moiety in the nucleoside may sterically hinder the attack of the *C2*-carbonyl.[166]

After flash column chromatography of the filtrate, the pure product **14** could be obtained in a relatively low yield of 18%. A moderate reaction temperature such as 50 and 60 °C was tried to avoid the species with two triazole residues. However, no reaction occurred and only starting material was isolated. Even the reaction under reflux could not always be reproduced as somehow compound **13** seems to be very stable and harsh reaction conditions are necessary to start a reaction.

The small amount of obtained product **14** was used to further substitute the triazole moiety with an amino group. In the literature, this is proposed to be achieved by addition of concentrated ammonium hydroxide in 1,4-dioxane followed by extraction workup using dichloromethane.[162] Due to the poor solubility of compound **14** in 1,4-dioxane it was

decided to use aqueous ammonia (25%) instead. Furthermore, in contrast to the highly protected carbohydrate from the literature compound **14** was found to stay in the aqueous phase. Therefore, the aqueous solvent was removed *in vacuo* with the hope to use chromatographic purification afterwards. Analysis of the crude product by ^{1}H NMR spectroscopy revealed the presence of the deacetylated starting material still bearing the triazole group although the desired mass had been detected from the reaction mixture. A likely explanation for this observation could be the existence of an equilibrium reaction formed between the ammonia and the triazole species (Scheme 17).

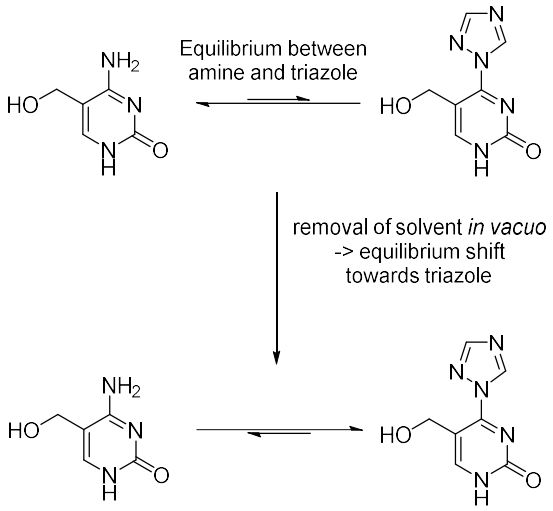

Scheme 17: Assumed equilibrium reaction between the triazole and the amine species.

In the reaction solution, triazole is substituted by ammonia but when water and ammonia are removed after the reaction the remaining triazole resubstitutes the amine group. As the reaction product as well as the reactants triazole and ammonia are all soluble in water, extraction from the reaction solution does not seem to be possible.[167] Crystallization or precipitation of the product from the reaction solution would be an elegant alternative. A first crystallization attempt from the concentrated reaction solution at 4 °C did not yield any precipitate. Nevertheless, it might still be worth conducting a more systematic research on suitable solvents provoking precipitation of the product. Due to time reasons, this could not be investigated more detailed at this point.

As alternative to the amination with triazole, a different approach was tested transforming the carbonyl group into a sulfonic acid ester[168] and subsequent amination by a reaction with a methanolic ammonia solution.[169] 2,4,6-Tri*iso*propylbenzenesulfonyl chloride (TPSCl) in conjunction with sodium hydride was applied to attach the TPS group to compound **16** (Scheme 18).

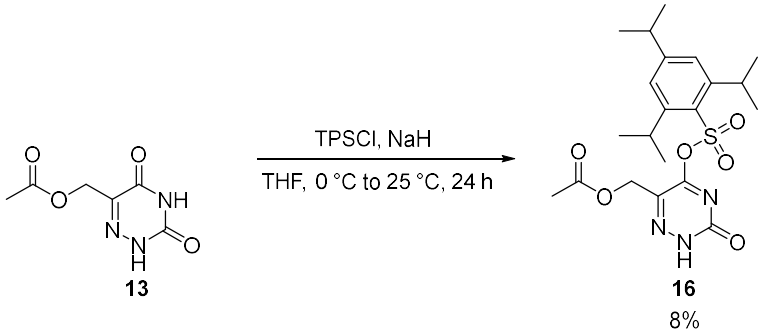

13 **16** 8%

Scheme 18: Reaction scheme towards compound **16**. TPSCl: 2,4,6-triisopropylbenzenesulfonyl chloride, THF: tetrahydrofurane.

In a first attempt, the desired compound could be obtained in a low yield of 8%. However, after flash column chromatography, the product still contained small amounts of starting material. It has to be noted here that solidification of the reaction mixture was observed at the chosen concentration probably resulting from the formed sodium chloride side product. This could prevent further reaction of the starting material which has been recovered after flash column chromatography. Due to the low amount of isolated compound **16** and time limitations the following amination reaction has not been tested. However, this approach seems to be a promising amination alternative as the bulky non-nucleophilic sulfonic acid is not expected to undergo such equilibrium reactions as proposed in the case of triazole.

Alternative synthetic strategies could aim for the reported compound 5-formyl-6-aza cytidine,[162] cleaving the glycosidic bond in an additional reaction step. This is commonly achieved in either acidic or alkaline aqueous media using reagents such as aqueous toluene-4-sulfonic acid, hydrochloric or acetic acid. Furthermore, introduction of protecting groups could be considered.[170] Zheng and coworkers for instance report the protection of

the secondary amines in the pyrimidine moieties by *para*-methoxybenzyl (PMB) protecting groups.[171] This implies further steps in the reaction cascade but simultaneously facilitates the handling of the reaction products concerning solubility in organic solvents and the possibility of applying usual workup procedures. The authors also report a Dess-Martin oxidation step from a PMB-protected 5hm6aU compound towards the respective aldehyde which might also be helpful for these studies. Further methods for amination reactions in the nucleobase context can be found in literature such as derivatization with sodium azide and subsequent palladium-catalyzed reduction[172] or transformation *via* the coupling reagent PyAOP (((7-Azabenzotriazol-1-yloxy)tripyrrolidinophosphonium hexafluoro-phosphate))[173] that can be considered as possible alternative procedures.

At this point, I was supported in the synthesis of the desired target structures by Kuangjie Liu from the Zipse group joining the project. He provided the compounds 5hmC, 5fC, 5hmU, 5hm6aU and additionally crude samples of 5fU and 5f6aU containing significant amounts of the corresponding carboxylic acid. However, due to time reasons, first experiments were carried out with the unpurified samples. It seems that the 5-hydroxymethyl uracil derivatives are surprisingly stable and harsh conditions are needed for oxidation which then result in the complete transformation into the carboxylic acid instead of the desired aldehyde. Similar challenges in the synthesis of 6-aza-cytosine derivatives were observed so that they could not be isolated so far. It was decided to run first reactivity tests towards the iron(IV)-oxido complex with the substrates available.

Reactivity study

The four uracil-derived substrates 5hmU, 5fU, 5hm6aU and 5f6aU were reacted with $[Fe^{IV}\mathbf{L1}(O)]^{2+}$ and the absorption maximum of the iron(IV)-oxido species followed over time *via* UV-vis spectroscopy (Figure 25).

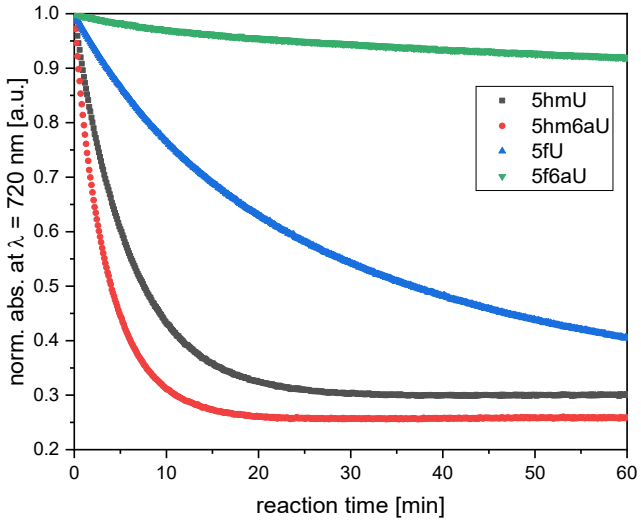

Figure 25: Absorption at $\lambda = 720$ nm in a reaction of uracil-derived substrates with $[Fe^{IV}\mathbf{L1}(O)]^{2+}$. Conditions: [substrate] = $[Fe^{IV}=O]$ = 1 mM, H_2O, 30 °C.

Unfortunately, the sample of 5f6aU turned out to mainly consist of the corresponding carboxylic acid 5c6aU, which explains why no significant reaction with the iron(IV)-oxido species was observed. The sample of 5fU however consists of an equimolar mixture of 5fU and 5cU. A reaction with the iron(IV)-oxido complex is visible in this case but due to differences in concentration, no comparison to the other species measured can be made. In the two remaining reactions, a slightly faster reaction is observed with 5hm6aU compared to its counterpart 5hmU. This result suits the expectation derived from the calculated BDEs which are depicted in Table 9.

Table 9: Overview of the calculated BDE values for the different substrates. Calculated by Fabian Zott (group of Prof. Zipse, LMU Munich).[163]

substrate	**calc. BDE [kJ mol^{-1}]**	
	formyl	**hydrate**
5hmU	360.0	-
5hm6aU	337.7	-
5fU	394.7	354.1
5f6aU	395.4	313.8

To identify the corresponding reaction products the reaction mixture was filtered over silica to stop the reaction and separate the iron species. This filtrate was lyophilized, the

remaining residue dissolved in D_2O and the mixture analyzed *via* ^1H NMR spectroscopy. An example is shown from the reaction of 5hm6aU with $[Fe^{IV}\mathbf{L1}(O)]^{2+}$ (Figure 26, see appendix section VII.4.2 for additional spectra).

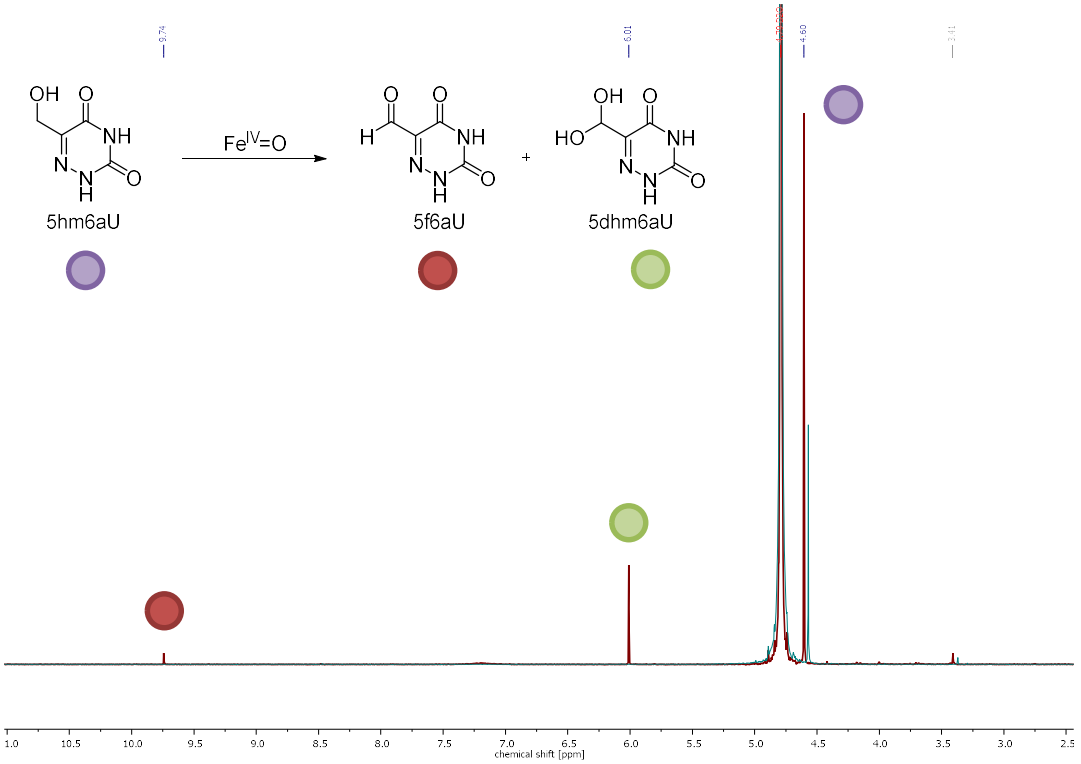

Figure 26: ^1H NMR spectra of the obtained products from a reaction of 5hm6aU with $[Fe^{IV}\mathbf{L1}(O)]^{2+}$ (red) and reference measurement of 5hm6aU (green) in D_2O at 298 K. Reaction conditions: [5hm6aU] = $[Fe^{IV}=O]$ = 5 mM, H_2O, 25 °C, 1 h.

At the end of the reaction, a high amount of starting material can still be detected. This was expected as only one equivalent of iron(IV)-oxido species was applied. A second species was formed which consists of the corresponding formyl species. Interestingly, this compound stands in an equilibrium reaction with its hydrate form 5dhm6aU. As expected from the previously observed equilibria of the species 5fU[161] and 5-formyl-6-aza cytidine (5f6adC[162]) at the applied conditions, clearly the hydrate species is the main species present (Table 10). Unfortunately, it can not be detected with this method if the carboxylic acid as oxidation product has formed as this species only contains exchangeable protons that are not visible in ^1H NMR spectra measured in D_2O. The analysis could be repeated in DMSO-d_6, however no species distribution within the formyl-hydrate equilibrium can be determined in this solvent. ^{13}C NMR measurements could also be considered but high

concentrations are required here to sufficiently resolve the signals of minor species as well. Furthermore, the compounds containing the carboxy groups show low solubility in water. This problem could be solved by the addition of a small amount of diluted aqueous sodium hydroxide solution, however this also affects the species distribution within the formyl-hydrate equilibrium which is sensitive to changes in pH.

Table 10: Species distribution in the formyl-hydrate equilibria for different species a) determined by Zipse and coworkers,[161] b) observed by Schön *et al*.[162] and c) found in this work by ^{1}H NMR spectroscopic analysis.

	aldehyde : hydrate
5fC/5fdC	99.95 : 0.05[a)]
5fU	98.7 : 1.3[a)]
5f6adC	80 : 20[b)]
5f6aU	14 : 86[c)]

To conclude, the synthesis of the nucleobase target structures turned out to be more challenging than expected. The high polarity and solubility in water complicates workup procedures and purification of the resulting products. Low reactivity of intermediates as well as low stability of some desired products was observed. Nevertheless, together with the help of Kuangjie Liu from the group of Prof. Zipse some of the desired compounds could be obtained and first reactivity tests with the iron(IV)-oxido compound conducted. These preliminary experiments show reaction rates in accordance with the respective calculated BDEs. Unfortunately, no conclusion can be drawn on the reactivity of the formyl species in regard of dependency on formyl-hydrate equilibrium due to impurities in the investigated samples.

Next steps in this project will be quantification attempts of the products from a reaction with the iron(IV)-oxido complex and the different hydroxymethyl species without the need of the synthetically challenging formyl species. For this purpose, GC-MS measurements were considered. In this procedure however, the nucleobase samples need to be derivatized prior to subjection to the instrument, for example with BSTFA (*N*,*O*-bis(trimethylsilyl)trifluoroacetamide).[94] This derivatization step is not occurring quantitatively and was not investigated for all present species probably leading to inaccurate

measurement results. Analysis *via* HPLC-MS was also considered with the advantage of no need for an additional derivatization step. This approach could only afford trends in the species distribution within the reaction as no exact quantification is possible without reference samples and the preparation of calibration curves. Addition of an unreactive standard such as uracil would be possible to achieve similar properties concerning UV absorption and ionization. Exact quantification could eventually be accomplished with NMR spectroscopy in combination with the addition of a standard (uracil). Challenges in this approach could be the low solubility of the carboxy species along with the relatively high concentration required to also resolve minor species. Furthermore, due to the necessity of separating the iron species from the reaction mixture before analysis only few data points within the reaction time can be collected. The species distribution in this reaction can be followed over time but the calculation of reaction rates with the method of initial rates can probably not be employed in this procedure.

IV. Understanding the Iron Chemistry in the Applied System

Chapter III described how the iron(IV)-oxido complex $[Fe^{IV}\mathbf{L1}(O)]^{2+}$ was established as synthetic model for the active site of TET enzymes performing a broad range of substrate reactivity studies. However, some details in these experiments remained elusive. Background reactions evolving simultaneously to substrate oxidation such as iron(II)/iron(IV) comproportionation reactions are elucidated in chapter IV. The established system is expanded by additional ligands and the resulting new iron complexes are characterized. Their properties (such as spin crossover behavior of iron(II) complexes for instance) and their reactivities towards substrates are presented.

1 Expanding the System with Additional Ligands: Characterization and Reactivity of New Iron Complexes

In addition to the ligand system Py_5Me_2 (referred to as **L1** in this work) – first synthesized by Long and coworkers in 2010[174] and established in our group - a variety of similar pentapyridyl ligands have been extensively studied in the literature.[175-179] A selection is shown in Chart 8.

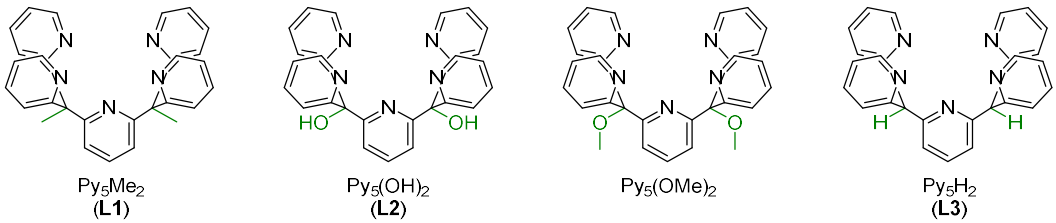

Chart 8: Selection of ligand systems used for various metal complexes.

In 1997, Stack and coworkers introduced the new ligand system $Py_5(OMe)_2$ and presented an iron(II) as well as an iron(III) complex thereof ($[Fe^{II}Py_5(OMe)_2(MeOH)](OTf)_2$ and $[Fe^{III}Py_5(OMe)_2(OMe)](OTf)_2$, respectively).[180] The iron(II) precursor was oxidized with either H_2O_2 or iodosobenzene to obtain the iron(III) species which was used as synthetic

model for the active site of lipoxygenases. These belong to the group of mononuclear non-heme iron enzymes and catalyze the oxidation of polyunsaturated fatty acids into alkyl hydroperoxides.[181-182] The rate-limiting step in this transformation is proposed to be the hydrogen atom abstraction from the substrate by an iron(III)-hydroxido species.[183-185] Stack and coworkers managed to transform the model substrate cyclohexadiene into benzol with their iron(III)-OMe species.[180] A few years later, the authors isolated the corresponding iron(III)-hydroxido complex ($[Fe^{III}Py_5(OMe)_2(OH)](CF_3SO_3)_2$ and performed reactivity studies with substrates such as 9,10-dihydroanthracene, xanthene or fluorene.[186] The $Py_5(OMe)_2$ ligand system was also used by Feringa and coworkers to develop manganese(II), iron(II) and iron(III) complexes as possible candidates for modeling oxygenases.[187]

In the synthetic pathway towards the $Py_5(OMe)_2$ ligand, $Py_5(OH)_2$ (**L2**) is obtained as intermediate which itself can serve as unique ligand. The crystal structure of this ligand has been reported in 2004[188] and metal complexes thereof have been extensively studied in the literature.[189-193] Cobalt(II) and iron(II) complexes ($[Co^{II}\mathbf{L2}Cl](BF_4)$ and $[Fe^{II}\mathbf{L2}Cl](PF_6)$, respectively) have been studied in the context of water oxidation for instance.[194-195] Furthermore, the iron(II) species $[Fe^{II}\mathbf{L2}(mecn)](ClO_4)_2$ has been examined towards its properties as anti-tumor agent.[196-197] The authors state that due to its stability against spontaneous demetallation and oxidation as well as its cytotoxity against various cancer cells this complex presents a promising candidate.

Since the family of different pentapyridyl ligands is reported to form iron(II) complexes similar to those observed with **L1** that was handled in our group, it seemed plausible that iron(IV)-oxido complexes could also be formed with other ligands of the pentapyridyl family. In addition to the aim of finding and characterizing new iron(IV)-oxido complexes, a library of complexes with different properties and reactivities can be a useful tool to perform specific desired substrate reactions.

Iron(II)/iron(IV) comproportionation reaction

In the course of substrate oxidation reactions, it was found that the formed iron(II) species reacted further with remaining iron(IV)-oxido complex, resulting in an iron(III) species (Our findings on this phenomenon are discussed in section IV.1.1). Surprisingly few examples of this reactivity are reported in literature (Scheme 19).

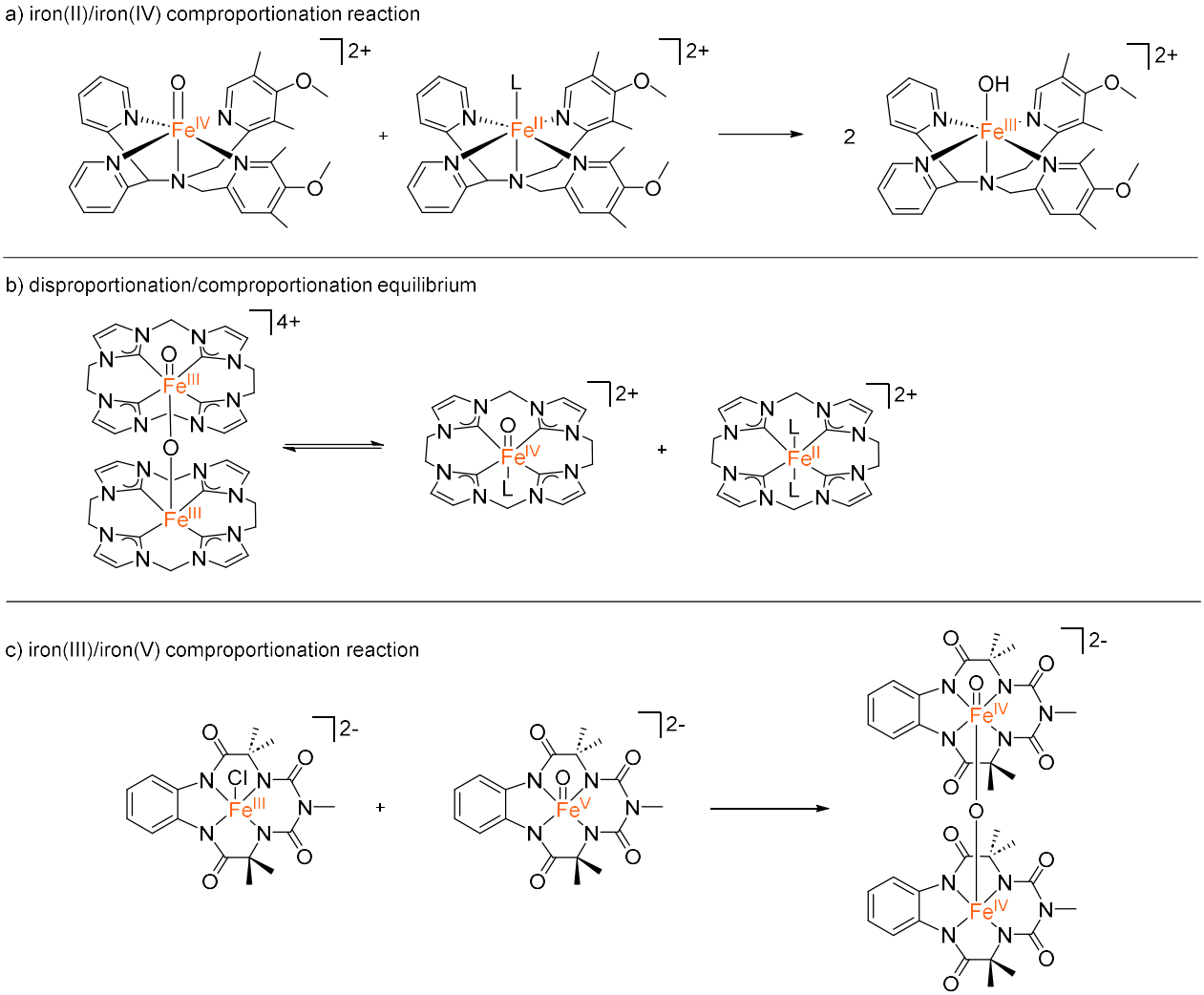

Scheme 19: Examples of comproportionation reactivity of iron complexes. A) Iron(II)/iron(IV) comproportionation presented by Maiti and coworkers,[198] B) disproportionation/comproportionation equilibrium observed by Meyer and coworkers, [199] C) iron(III)/iron(V) comproportionation reported by Gupta and coworkers.[200] L = ligand (solvent molecule).

In 2015, Maiti and coworkers reported an iron(II)/iron(IV) comproportionation reaction with mononuclear non-heme iron complexes.[198] This reactivity was observed within a substrate reactivity study of the iron(IV)-oxido compound resulting in the oxidized

substrate and an iron(II) species. The presence of this iron(II) species in the reaction mixture together with remaining iron(IV)-oxido complex led to formation of a mononuclear iron(III)-hydroxido compound (Scheme 19A). A dinuclear μ-oxo bridged iron(III) species reported by Meyer and coworkers was found to perform this reactivity in the opposite direction, resulting in a disproportionation reaction.[199] The authors observed a dis- and comproportionation equilibrium which opens the possibility to access reactive species from the Fe^{III}-O-Fe^{III} species previously considered as dead-end of the reaction (Scheme 19B).

A further example of comproportionation reactions in iron chemistry is shown in Scheme 19C. In contrast to the before discussed complexes, different oxidation states are presented here, however the overall reactivity seems to be similar. Gupta and coworkers report the reaction between iron(III) and iron(V)-oxido complexes towards a species that they tentatively assigned to a μ-oxo bridged iron(IV) compound.[200] The authors corroborated their assumption by UV-vis and ^{1}H NMR spectroscopy and monitored the comproportionation reaction following the decrease in iron(V)-oxido absorption in UV-vis spectroscopic measurements.

Since a rich iron chemistry seems to be possible in this system, the goal of this project was to elucidate background reactions that occur simultaneous to substrate oxidation with iron(IV)-oxido complexes. All iron species present in the reaction mixture should be carefully analyzed to learn more about the ligand system established in our group. Furthermore, it was anticipated to investigate additional ligands from the pentapyridyl family such as **L2** and **L3**. Formation of new iron complexes, characterization and reactivity studies thereof should be compared to the chemistry of iron complexes of the ligand system **L1**.

1.1 Investigations on Iron(II)/Iron(IV) Comproportionation Reactions and Reactivity Study with a New Iron(IV)-oxido Complex

The following manuscript[201] focuses on a comproportionation reaction between iron(II) and iron(IV) species, resulting in two equivalents of an iron(III) complex. This phenomenon was observed as a side reaction from substrate oxidation reactions with iron(IV)-oxido complexes where the herein formed iron(II) complex reacts with the remaining iron(IV)-oxido complex. Furthermore, a new iron(IV)-oxido complex with a slightly different ligand system was synthesized as well as the iron(III) complexes of both ligand systems. All new complexes were thoroughly characterized and the reactivity of the two different ligand systems compared.

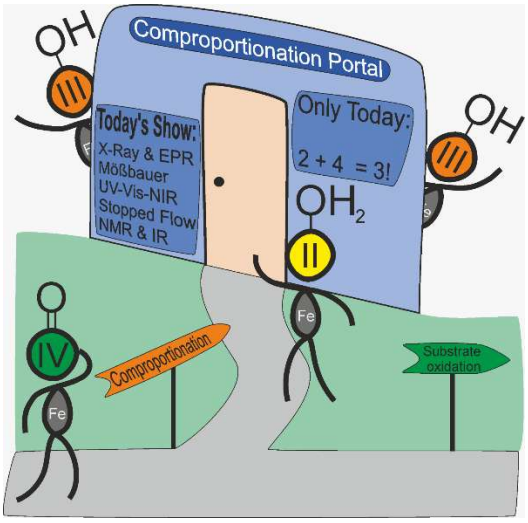

Title

Two plus Four Equals Three – Iron(II)/Iron(IV) Comproportionation as an Additional Pathway For Iron(IV)-oxido Reactions

Authors

Niko S. W. Lindlar né Jonasson, Annika Menke, Laura Senft, Andrea Squarcina, David Schmidl, Katherine Fisher, Serhiy Demeshko, Jan C. Kruse, Thomas Josephy, Peter Mayer, Jonathan Gutenthaler-Tietze, Peter Comba, Franc Meyer, Ivana Ivanović-Burmazović, Lena J. Daumann*

Author Contribution

N.S.W.L. and A.M. developed the project, accomplished the synthetic work, performed the UV-vis-NIR experiments and wrote the manuscript. L.S. carried out the HR-MS measurements as well as simulations thereof, supervised by I.I.-B.. A.S. performed cyclic voltammetry investigations and interpretations, supervised by I.I.-B.. D.S. was involved in the discovery of the comproportionation reaction and contributed in the synthesis and crystallization of $[Fe^{III}\mathbf{L1}(OH)]^{2+}$. K.F. simulated the EPR spectra. S.D. and J.C.K. performed the Mößbauer measurements, supervised by F.M.. T.J. carried out stopped-flow UV-vis-NIR measurements, supervised by P.C.. P.M. and J. G.-T. performed the X-ray measurements and solution of the crystal structures. L.J.D. coordinated and supervised the whole project.

Licence

The manuscript as well as the supporting information are available at

https://pubs.acs.org/doi/10.1021/acs.inorgchem.4c04518

Inorganic Chemistry

pubs.acs.org/IC Article

Two Plus Four Equals Three—Iron(II)/Iron(IV) Comproportionation as an Additional Pathway for Iron(IV)-Oxido Reactions

Niko S. W. Lindlar né Jonasson, Annika Menke, Laura Senft, Andrea Squarcina, David Schmidl, Katherine Fisher, Serhiy Demeshko, Jan C. Kruse, Thomas Josephy, Peter Mayer, Jonathan Gutenthaler-Tietze, Peter Comba, Franc Meyer, Ivana Ivanović-Burmazović, and Lena J. Daumann*

Cite This: *Inorg. Chem.* 2025, 64, 3719−3734 Read Online

ACCESS | Metrics & More | Article Recommendations | Supporting Information

ABSTRACT: Iron enzymes are ubiquitous in nature. In particular, enzymes with iron−oxygen cofactors as active sites perform a vast variety of reactions. Both iron(III)-hydroxido and iron(IV)-oxido species have been observed to play a catalytically active role. In order to complement biochemical investigations, a large variety of synthetic compounds using these motifs were synthesized in past decades to study and understand their inherent reactivity. One such synthetic model complex is $[Fe^{IV}(O)(Py_5Me_2)]^{2+}$, ($Py_5Me_2$ = 2,6-bis(1,1-bis(2-pyridyl)ethyl)pyridine, henceforth labeled **L1**), which was used as a model complex for epigenetically relevant iron(II)/α-ketoglutarate-dependent ten-eleven translocation 5-methylcytosine dioxygenases (TET). Additionally, $[Fe^{III}(OH)(Py_5(OH)_2)]^{2+}$ ($Py_5(OH)_2$ = pyridine-2,6-diylbis [di(pyridin-2-yl)methanol, henceforth labeled **L2**) was tested as a lipoxygenase model. We have complemented the available complexes of these related pentapyridyl complexes to include all oxidation states II−IV and performed detailed spectroscopic and spectrometric investigations. We found that iron(II) and iron(IV)-oxido compounds (cross-)comproportionate readily to form iron(III)-hydroxido species, which represents a major side reaction for model complex investigations. We also investigated the oxidative reactivity of a new iron(IV)-oxido complex.

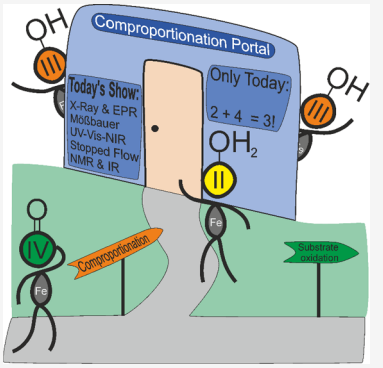

INTRODUCTION

Iron enzymes are ubiquitous in nature, and synthetic iron complexes have been used for decades to study these. In particular, iron(III)-hydroxido[1−7] and iron(IV)-oxido[8−14] complexes have been at the center of scientific interest. This is due to the involvement of these species in a multitude of enzymatic transformations. Two well-studied systems are lipoxygenases,[15−19] which contain an iron(III)-hydroxido active site, and taurine dioxygenases (TauD),[20−23] which incorporate an iron(IV)-oxido center. Both enzymes are nonheme iron dioxygenases, while TauD specifically belongs to the iron(II)/α-KG-dependent enzyme superfamily. Lipoxygenases are typically thought to abstract a hydrogen atom from the fatty acid substrate via an iron(III)-hydroxido species, yielding a radical species. This is then thought to react with molecular oxygen, which is followed by cleavage of the substrate.[17−19,24] The consensus mechanisms for TauD, on the other hand, involves the formation of an iron(IV)-oxido species, which abstracts a hydrogen atom from the substrate. This is followed by rebound hydroxylation to generate the product (Figure 1D).[20−23,25,26] Subsequent reactions might lead to demethylation, ring closure, ring expansion, desaturation, and other transformations.[27]

In synthetic (model) compounds, several pathways are observed after the initial H-atom abstraction step. A common feature in iron(III)-hydroxido chemistry is the prevalence of these compounds to form μ-O-bridged or μ−OH-dinuclear compounds.[28−30] A recent, representative example is the bispidine-based system described by Abu-Odeh et al. in 2021.[14] Using high-resolution electrospray ionization mass spectrometry (HR−ESI−MS)), the authors observed an iron(IV)-oxido species upon oxidation of $[Fe^{II}(bisp)Cl_2]$ (bisp = dimethyl 3,7-dimethyl-9-oxo-2,4-di(pyridin-2-yl)-3,7-diazabicyclo[3.3.1]nonane-1,5-dicarboxylate) with ^{s}PhIO (^{s}PhIO = 1-(*tert*-butylsulfonyl)-2-iodosylbenzene) in acetonitrile. In addition, $[(bisp)Fe^{III}-O-Fe^{III}(bisp)]^{2+}$ was also observed in MS measurements at low concentrations of the oxidant ^{s}PhIO. The emergence of this species was attributed to the second-order reaction of the iron(IV)-oxido species with

Received: October 23, 2024
Revised: December 9, 2024
Accepted: January 10, 2025
Published: February 18, 2025

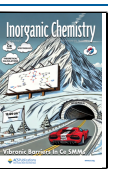

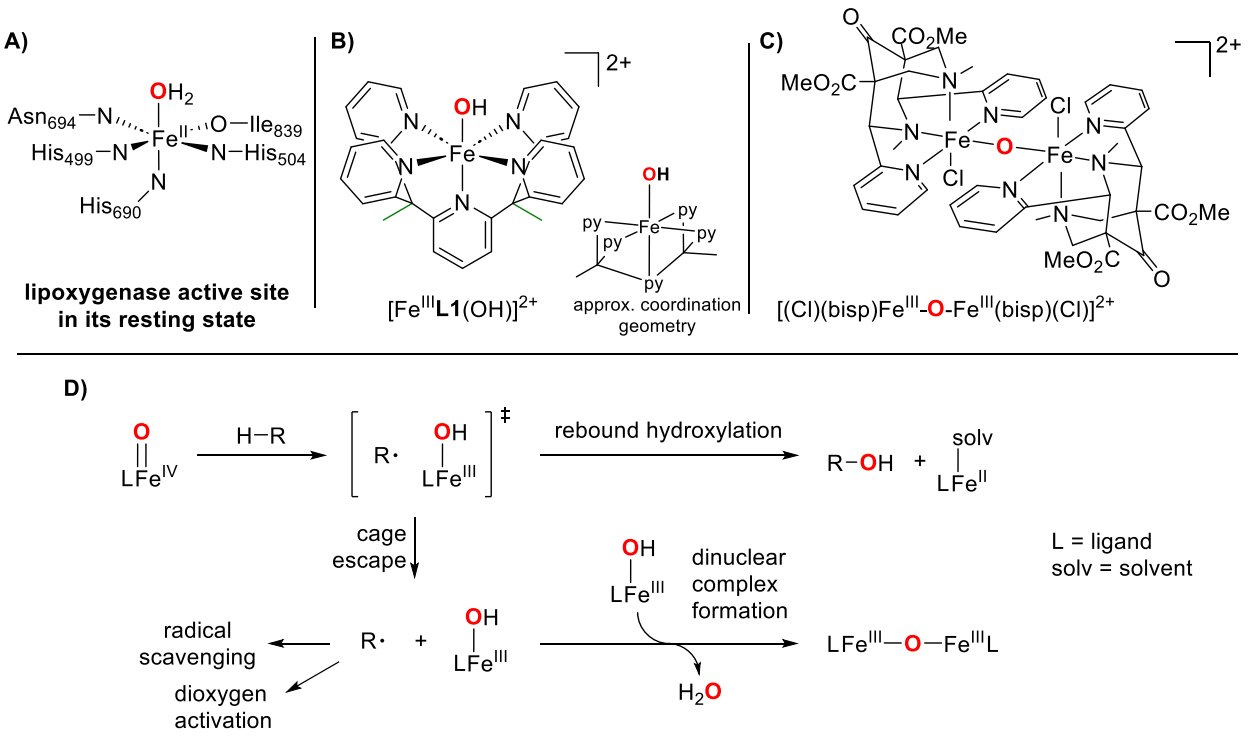

Figure 1. (A) Representation of the lipoxygenase active site in its resting state according to Minor et al.[32] (B) New iron(III)-hydroxido complex reported in this work. (C) Dinuclear iron(III)-oxido complex reported by Abu-Odeh et al.[14] (D) Proposed mechanisms for the reaction of iron(IV)-oxido species with organic substrates bearing C−H bonds: after the initial hydrogen atom transfer reaction, rebound hydroxylation leads to an iron(II) species and the hydroxylated substrate. "Escape" of the radical from the "iron cage" giving an iron(III)-hydroxido species has also been observed. This can further lead to dinuclear complex formation with another equivalent of iron complex or scavenging of the radical or reaction with O_2, depending on the conditions. Adapted from Cho et al.[33]

Chart 1. Overview of the Ligands and Corresponding Iron(II), Iron(III), and Iron(IV)-Oxido Complexes Used in This Work[a]

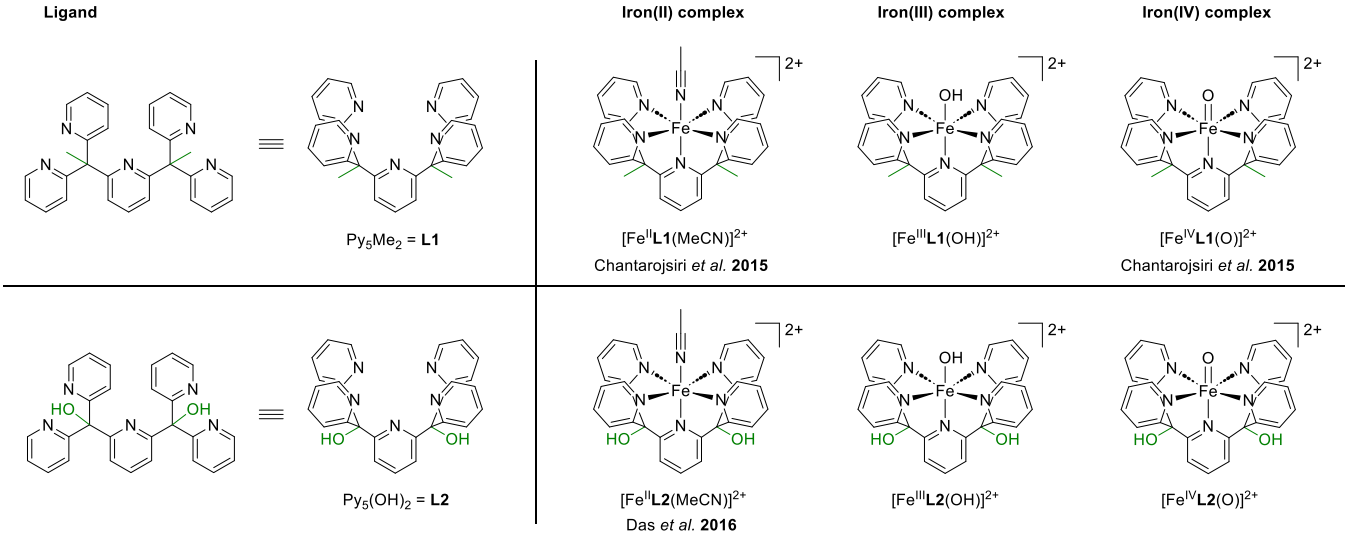

[a]Counter ions: triflate (iron(II) and iron(III) species) and cerium nitrate (iron(IV)-oxido species). Spectroscopic and spectrometric data on newly synthesized compounds can be found in the Supporting Information and is referenced when applicable. It has to be noted here that the co-ligand of the iron(II) species is exchanged in solution by solvent molecules (see Figure S14, p 18), and the nomenclature used in the paper refers to the actual species present in solution ($[Fe^{II}\mathbf{L1}/\mathbf{L2}(OH_2)]^{2+}$ in water) and not necessarily to the complex applied in the experiment.

unreacted iron(II) precursor. Other works have described similar comproportionation (or disproportionation of iron(III)) behavior, e.g., the equilibrium between a tetracarbene-coordinated μ-oxidodiiron(III) complex with its iron(IV)-oxido and iron(II) derivatives.[31]

In addition to several dinuclear iron(III) complexes with terminal hydroxido ligands,[34−36] several mononuclear iron(III) complexes have been described in the literature.[2,5−7,37] However, the isolation, especially of iron(III)-hydroxido species, is often complicated, for example, by their tendency to form μ-oxido-bridged diiron(III) species as discussed above.

https://doi.org/10.1021/acs.inorgchem.4c04518
Inorg. Chem. 2025, 64, 3719−3734

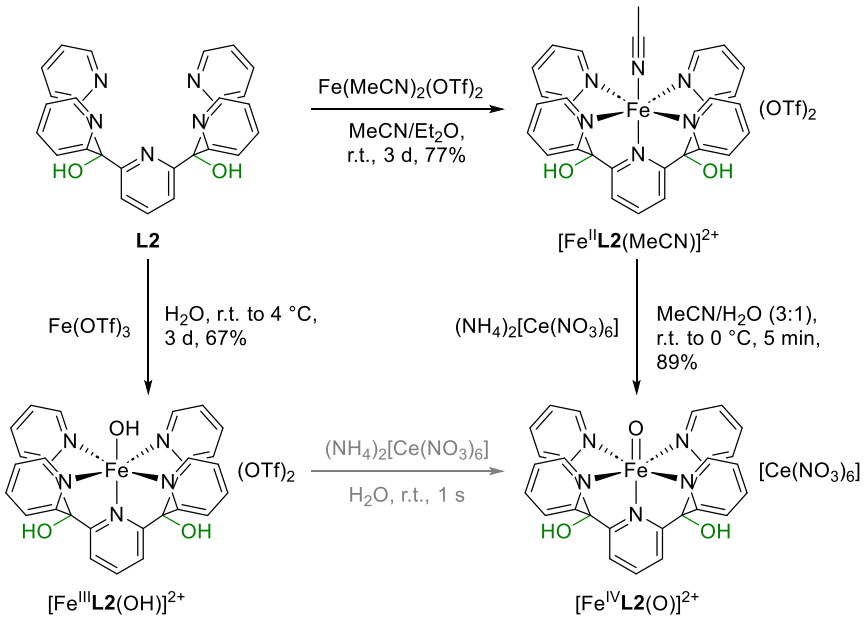

Figure 2. Synthesis of iron complexes $[Fe^{II}\mathbf{L2}(MeCN)]^{2+}$, $[Fe^{III}\mathbf{L2}(OH)]^{2+}$, and $[Fe^{IV}\mathbf{L2}(O)]^{2+}$ from ligand **L2** according to (modified) literature procedures.[3,8,9]

The reported examples of mononuclear iron(III)-hydroxido complexes often consist of ligand systems similar to those employed in this work. In the present work, we report the synthesis and isolation of two new mononuclear, low-spin iron(III)-hydroxido complexes and present their X-ray structures as well as EPR, Mössbauer, and UV−vis−NIR spectra.

In our previous work, we studied the iron(IV)-oxido complex $[Fe^{IV}\mathbf{L1}(O)]^{2+}$ as a functional model for the epigenetically relevant iron(II)/α-ketoglutarate-dependent enzyme TET (ten-eleven translocation 5-methyl-cytosine dioxygenase).[9−11] This complex was first described by Chantarojsiri et al. in 2015.[8] It is capable of hydroxylating organic compounds such as ethylbenzene sulfonic acid (EBS) and the biologically more relevant 5-methyl cytosine (5mC)[9]/5-methyl cytidine (5mdC) as well as oligonucleotides containing 5mC.[10] In the present work, we report the synthesis and isolation of a new iron(IV)-oxido complex including the corresponding Mössbauer and UV−vis−NIR spectra as well as a preliminary reactivity study.

RESULTS AND DISCUSSION

In this work, the repertoire of known iron complexes containing pentapyridyl ligands of the Py5-type was expanded. Two complete series of iron(II), iron(III), and iron(IV) species of the Py_5Me_2 and $Py_5(OH)_2$ ligand systems are presented here, including two new mononuclear iron(III)-hydroxido and a new iron(IV)-oxido species. All synthesized compounds were characterized using electron paramagnetic resonance (EPR), Mössbauer, and UV−vis−NIR spectroscopy as well as cyclic voltammetry and ultrahigh-resolution low-temperature mass spectrometry (cryo-UHR−MS). In addition, a comparative reactivity study containing several substrates with C−H bonds was performed. Chart 1 shows the ligands and iron complexes as well as the nomenclature applied in this work.

Characterization of New Iron Complexes and Comparison of the Two Ligand Systems. When analyzing reaction mixtures of $[Fe^{IV}\mathbf{L1}(O)]^{2+}$ with an epigenetically relevant substrate (5-methyl cytosine, 5mC or 5-methyl-deoxycytidine, 5mdC) in previous studies,[9,10] we found significant amounts of the iron(III) species $[Fe^{III}\mathbf{L1}(OH)]^{2+}$. This was attributed to a side reaction consisting of an iron(II)/iron(IV) comproportionation reaction (vide infra for detailed discussion) that prompted us to synthesize and characterize this mononuclear iron(III)-hydroxido complex.

The series of iron complexes for both ligand systems **L1** and **L2** (Chart 1) was synthesized, and various spectroscopic and spectrometric techniques as well as cyclic voltammetry were applied for a thorough characterization of the new iron complexes and for comparison studies among the different iron species. Here, a short overview of the syntheses is presented; synthetic details can be found at the end of this article.

Synthesis. Py_5Me_2 (**L1**) was synthesized according to a modified literature procedure,[8] as previously described in our report on iron(IV)-oxido complex $[Fe^{IV}\mathbf{L1}(O)]^{2+}$ as a functional model for TET enzymes.[9] Complexes $[Fe^{II}\mathbf{L1}(MeCN)]^{2+}$ and $[Fe^{IV}\mathbf{L1}(O)]^{2+}$ were then synthesized according to literature procedures.[8] Complex $[Fe^{III}\mathbf{L1}(OH)]^{2+}$ was prepared by suspending a finely ground powder of **L1** in pure water and adding iron(III) triflate ($Fe(OTf)_3$). The solution immediately turned a deep, dark red. Crystals of the iron(III)-hydroxido compound formed in a filtered aqueous solution at 4 °C after 1 day. A similar iron(III)-hydroxido[2] as well as an iron(III)-methoxido[1] species has been described before by Goldsmith et al. with a ligand system bearing methoxy instead of methyl/hydroxy groups (2,6-bis(bis(2-pyridyl)methoxymethane)pyridine). The authors obtained this complex by reacting the corresponding iron(II) species with iodosylbenzene.

Ligand $Py_5(OH)_2$ (**L2**) was synthesized according to a modified literature procedure (Figure 2).[2] $[Fe^{II}\mathbf{L2}(MeCN)](OTf)_2$ was then synthesized using the same procedures as for the corresponding iron(II) complex of **L1** ($[Fe^{II}\mathbf{L1}(MeCN)](OTf)_2$) that had previously been published by Chantarojsiri et al.[8] In 2016, Das et al. published their results on water

https://doi.org/10.1021/acs.inorgchem.4c04518
Inorg. Chem. 2025, 64, 3719−3734

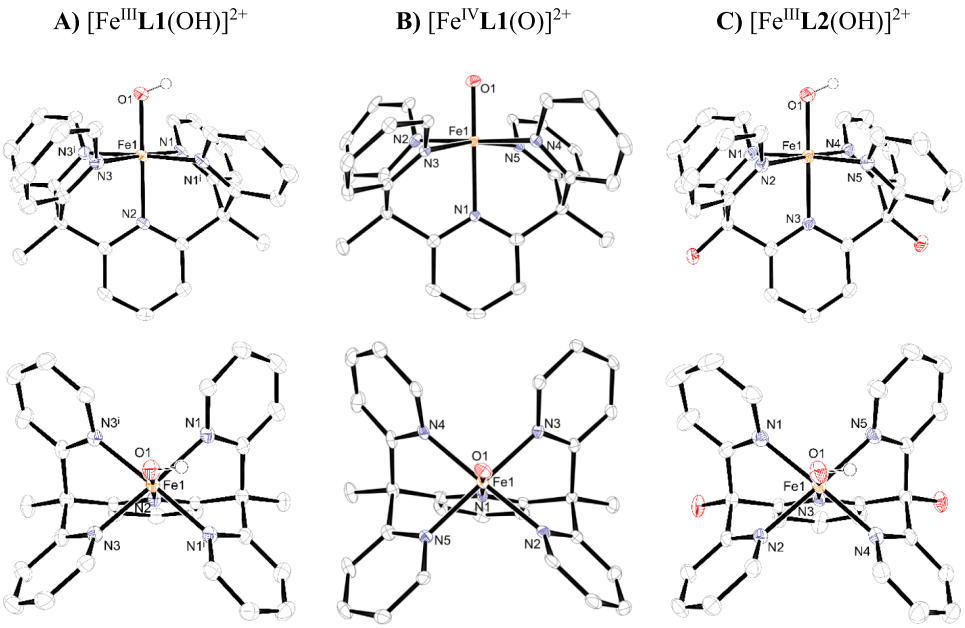

Figure 3. (A) Graphical representation of the crystal structures of $[Fe^{III}\mathbf{L1}(OH)]^{2+}$. Ellipsoids are drawn at 50% probability; hydrogen atoms, the counterion (OTf^-), and one cocrystallized water molecule were omitted for clarity. A full structure can be found in the Supporting Information, p 50. (B) Graphical representation of the crystal structure of $[Fe^{IV}\mathbf{L1}(O)]^{2+}$, taken from Rasheed et al.[13] Ellipsoids are drawn at 50% probability, and hydrogen atoms and the counterion ($[Ce(NO_3)_6]^{2-}$) were omitted for clarity. (C) Graphical representation of the crystal structure used for X-ray crystallography of $[Fe^{III}\mathbf{L2}(OH)]^{2+}$. Ellipsoids are drawn at 50% probability; hydrogen atoms, counterions (OTf^-), and two cocrystallized water molecules were omitted for clarity. A full structure can be found in the Supporting Information, p 54.

oxidation using an iron-**L2** system.[3] Upon addition of ceric(IV) ammonium nitrate to $[Fe^{II}\mathbf{L2}(MeCN)](BF_4)_2$, the authors observed a band at λ = 730 nm in UV−vis−NIR spectroscopy, which they attributed to the formation of an iron(IV)-oxido species. The authors, however, could not isolate this compound. Applying the conditions published by Chantarojsiri et al.,[8] i.e., oxidation of $[Fe^{II}\mathbf{L2}(MeCN)](OTf)_2$ in an acetonitrile/water mixture using 5.3 equiv of ceric(IV) ammonium nitrate, we were able to isolate $[Fe^{IV}\mathbf{L2}(O)][Ce(NO_3)_6]$ as a green powder. Synthesis of $[Fe^{III}\mathbf{L2}(OH)]^{2+}$ was performed in the same way as that for $[Fe^{III}\mathbf{L1}(OH)]^{2+}$ (vide supra).

Characterization by X-ray Crystallography. The cations $[Fe^{II}\mathbf{L1}(MeCN)]^{2+}$ and $[Fe^{IV}\mathbf{L1}(O)]^{2+}$ are known in the literature and corroborated by our own measurements (not shown; refer to the Supporting Information, p 48ff for crystallographic details including a table containing relevant bond lengths and angles and a comparison with published data). A structural study of $[Fe^{IV}\mathbf{L1}(O)]^{2+}$ using X-ray crystallography (Figure 3B) and ^{1}H NMR spectroscopy was published in 2019 by Rasheed et al.[13] In this work, single crystals of $[Fe^{IV}\mathbf{L1}(O)]^{2+}$ suitable for X-ray crystallography were also obtained from an aqueous solution of $[Fe^{IV}\mathbf{L1}(O)]^{2+}/CeCl_3$ (1:3). Crystals of the iron(III)-hydroxido compound $[Fe^{III}\mathbf{L1}(OH)]^{2+}$ formed both after evaporation of water from a reaction mixture of $[Fe^{IV}\mathbf{L1}(O)]^{2+}$ with 5-methyl cytosine (used in this work, Figure 3A) and in a filtered aqueous solution of ligand **L1** and iron(III)triflate at 4 °C after 1 day (the obtained structure is identical, not shown).

A crystal structure of $[Fe^{II}\mathbf{L2}(MeCN)]^{2+}$ was reported in the literature[3]; however, no details were provided due to the poor quality of the crystals. We were able to obtain crystals of $[Fe^{II}\mathbf{L2}(MeCN)]^{2+}$ in good quality by diffusing diethyl ether into an acetonitrile solution of $[Fe^{II}\mathbf{L2}(MeCN)]^{2+}$ at room temperature. A comparison with $[Fe^{II}\mathbf{L1}(MeCN)]^{2+}$ showed that almost identical parameters were obtained for both complexes (refer to the Supporting Information, p 48 for relevant bond length and angle values and p 52 for a full structure of $[Fe^{II}\mathbf{L2}(MeCN)]^{2+}$).

Crystals of $[Fe^{III}\mathbf{L2}(OH)]^{2+}$ were obtained in an aqueous solution at 4 °C (Figure 3C). Comparing the bond lengths in $[Fe^{III}\mathbf{L1}(OH)]^{2+}$ and $[Fe^{III}\mathbf{L2}(OH)]^{2+}$, the iron−oxygen bond in $[Fe^{III}\mathbf{L2}(OH)]^{2+}$ was found to be slightly longer than in $[Fe^{III}\mathbf{L1}(OH)]^{2+}$ (1.81 vs 1.79 Å, respectively), as were the iron−nitrogen bonds (averaged: 2.01 vs 2.00 Å, respectively). Apart from these minor discrepancies, the structures exhibit a high degree of similarity (refer to the Supporting Information, p 48 for relevant bond length and angle values).

A comparison of the crystallographic data obtained for $[Fe^{III}\mathbf{L1}(OH)]^{2+}$ with the literature-known data[5,8,13] for $[Fe^{II}\mathbf{L1}(OH_2)](BF_4)_2$ and $[Fe^{IV}\mathbf{L1}(O)]^{2+}$ (compare Figure 4A,B) shows a shorter iron−oxygen bond length with increasing oxidation state. Similarly, the iron atom "moves" out of the coordinative plane of the four equatorial pyridine donors, which also lengthens the iron−nitrogen bond of the axial pyridine moiety (Figure 4B).

In the literature, similar bond lengths were observed for chemically similar nonheme iron(IV) complexes, e.g, $[Fe^{IV}(O)(5Me_2N4Py)](ClO_4)_2$ (1.654 Å)[13] or $[Fe^{IV}(O)(Bn\text{-}tpen)]^{2+}$ (1.616 Å)[38] and also in the nonheme iron enzyme taurine dioxygenase TauD (1.646 Å).[39] For the iron−nitrogen bond trans to the iron−oxygen bond, also similar values have been reported for related complexes such as $[Fe^{IV}(O)(5Me_2N4Py)](ClO_4)_2$ (2.042 Å)[13] and $[Fe^{IV}(O)(Bn\text{-}tpen)]^{2+}$ (2.112 Å).[38] The observed iron−oxygen bond lengths in the two newly synthesized iron(III)-hydroxido complexes (~1.80 Å) are similar to or shorter than what has been reported for other iron(III)-hydroxido complexes (1.880 Å,[40]

https://doi.org/10.1021/acs.inorgchem.4c04518
Inorg. Chem. 2025, 64, 3719−3734

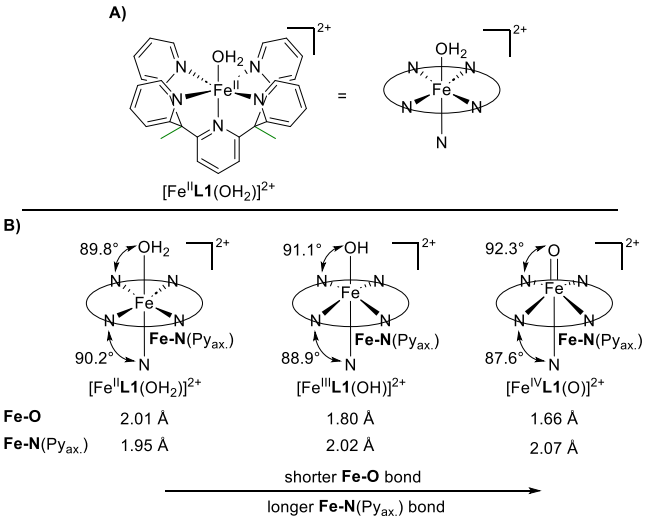

Figure 4. (A) Simplified graphical representation of the coordination environment of the iron(II) central ion in $[Fe^{II}\mathbf{L1}(OH_2)](BF_4)_2$. (B) Graphical representation of the changes in coordination geometry between $[Fe^{II}\mathbf{L1}(OH_2)]^{2+}$, $[Fe^{III}\mathbf{L1}(OH)]^{2+}$, and $[Fe^{IV}\mathbf{L1}(O)]^{2+}$ including selected bond lengths. Data for $[Fe^{II}\mathbf{L1}(OH_2)](BF_4)_2$ and $[Fe^{IV}\mathbf{L1}(O)]^{2+}$ were taken from the literature.[8] Additional angles and bond lengths are provided in the Supporting Information, p 48.

1.876 Å,[41] or 1.872 Å[42]). This is expected, as in the complexes discussed herein, no hydrogen bonding interactions take place that might elongate the iron−oxygen bond.

Characterization by Mössbauer Spectroscopy. The Mössbauer spectra (Figure 5) of the newly synthesized complexes $[Fe^{III}\mathbf{L1}(OH)]^{2+}$, $[Fe^{II}\mathbf{L2}(MeCN)]^{2+}$, $[Fe^{III}\mathbf{L2}(OH)]^{2+}$, and $[Fe^{IV}\mathbf{L2}(O)]^{2+}$ correspond well to the assigned oxidation and spin states. All complexes of L1 are low-spin (iron(II): $S = 0$; iron(III): $S = 1/2$; and iron(IV): $S = 1$), as expected for the iron(II) and iron(IV) states from the literature.[8] For all three complexes of **L2**, both isomer shift and quadrupole splitting parameters are nearly identical to those of the complexes of **L1**, showing only a small influence of the ligand periphery on the electronic structure around the iron atom. Detailed information as well as Mössbauer spectra of the literature-known species $[Fe^{II}\mathbf{L1}(MeCN)]^{2+}$ and $[Fe^{IV}\mathbf{L1}(O)]^{2+}$ are provided in the Supporting Information, p 47. The isomer shift and quadrupole splitting values we observed for the iron(IV)-oxido complex $[Fe^{IV}\mathbf{L2}(O)]^{2+}$ are in the same range of what is commonly observed in the literature for similar complexes, e.g., $[Fe^{IV}(O)(N4Py^{2PhF2})]^{2+}$ (δ = 0.03 mm s^{-1}, ΔE_Q = 0.54 mm s^{-1}),[43] $[Fe^{IV}(O)(TMG_3tren)]^{2+}$ (δ = 0.09 mm s^{-1}, ΔE_Q = −0.29 mm s^{-1}),[44] or $Fe^{IV}(O)(TMG_2dien)(MeCN)]^{2+}$ (δ = 0.08 mm s^{-1}, ΔE_Q = 0.58 mm s^{-1}).[45] Especially, the low isomer shift is typical for an iron(IV)-oxo complex. The observed isomer shifts for the newly synthesized iron(III)-hydroxido complexes are also in agreement with values found in the literature, e.g., $[Fe^{III}H_3buea(OH)]^-$ (δ = 0.32 mm s^{-1}), whereas the observed quadrupole splitting differs from what is reported for this complex (ΔE_Q = −0.82 mm s^{-1}), which is unsurprising, considering the different ligand geometries.[46]

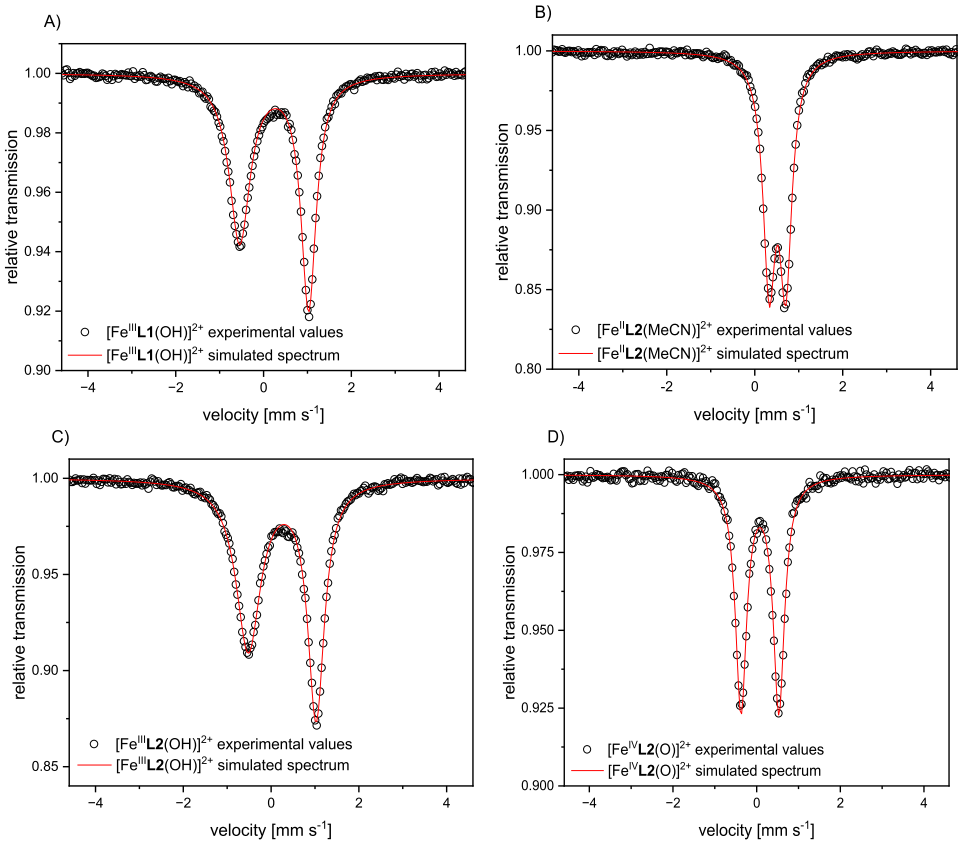

Figure 5. Experimentally obtained solid-state and simulated Mössbauer spectra and values of (A) $[Fe^{III}\mathbf{L1}(OH)](OTf)_2$ (δ = 0.24 mm s^{-1}, ΔE_Q = 1.57 mm s^{-1}), (B) $[Fe^{II}\mathbf{L2}(MeCN)](OTf)_2$ (δ = 0.52 mm s^{-1}, ΔE_Q = 0.38 mm s^{-1}), (C) $[Fe^{III}\mathbf{L2}(OH)](OTf)_2$ (δ = 0.25 mm s^{-1}, ΔE_Q = 1.54 mm s^{-1}), and (D) $[Fe^{IV}\mathbf{L2}(O)][Ce(NO_3)_6]$ (δ = 0.08 mm s^{-1}, ΔE_Q = 0.35 mm s^{-1}). Mössbauer spectra were measured at 80 K.

https://doi.org/10.1021/acs.inorgchem.4c04518
Inorg. Chem. 2025, 64, 3719−3734

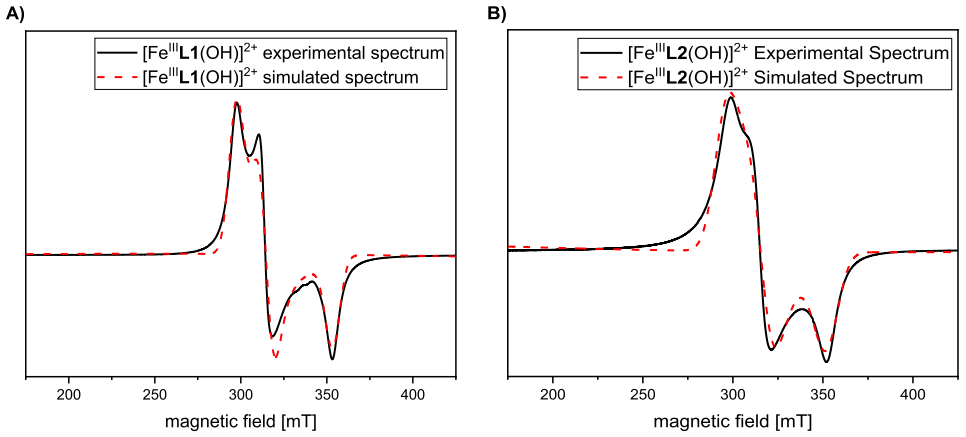

Figure 6. Experimentally obtained solid-state and simulated EPR spectra of (A) $[Fe^{III}\mathbf{L1}(OH)]^{2+}$ (g = 2.32, 2.19, and 1.95) and (B) $[Fe^{III}\mathbf{L2}(OH)]^{2+}$ (g = 2.33, 2.18, 1.96). EPR spectra were measured at 298 K in X-band at 9.649818 and 9.649704 GHz, respectively; for more experimental details please refer to the Supporting Information, p 4.

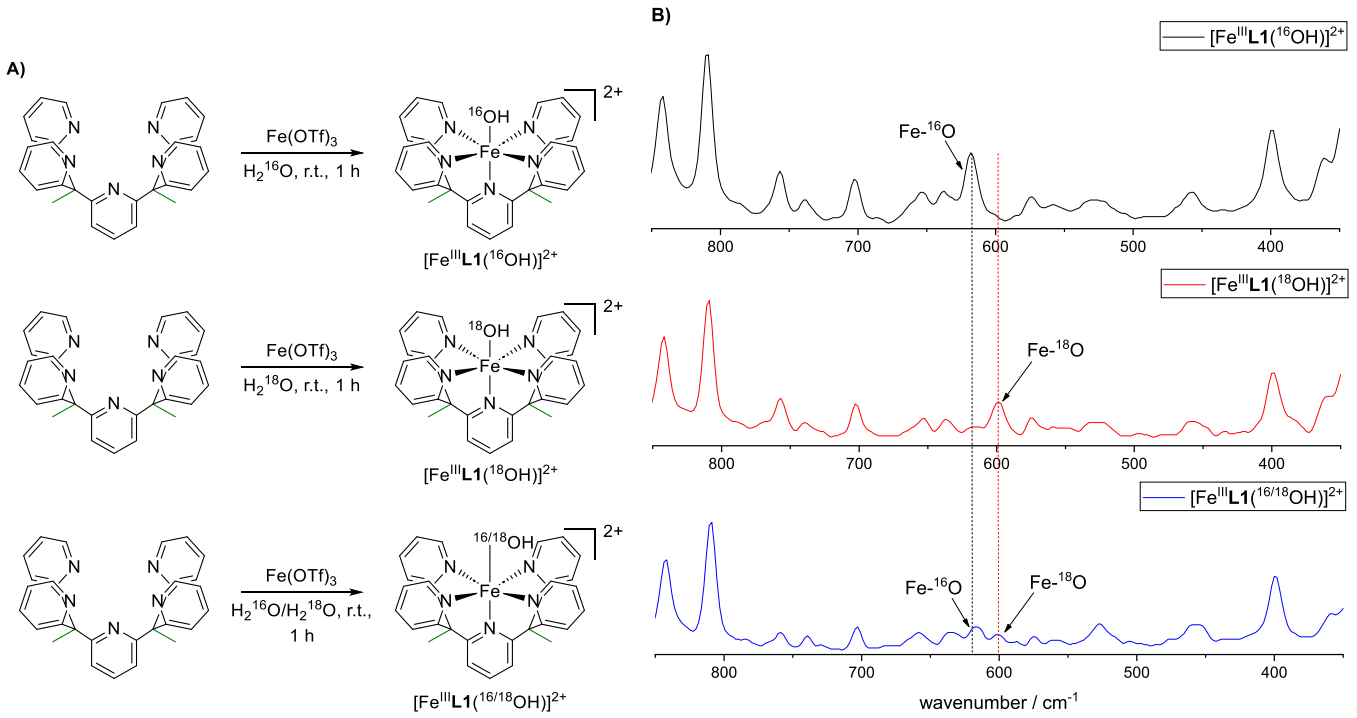

Figure 7. (A) Synthesis of different derivatives of $[Fe^{III}\mathbf{L1}(OH)]^{2+}$ from **L1**: $[Fe^{III}\mathbf{L1}(^{16}OH)](OTf)_2$, $[Fe^{III}\mathbf{L1}(^{18}OH)](OTf)_2$, and a mixture of $[Fe^{III}\mathbf{L1}(^{18/16}OH)](OTf)_2$. (B) Excerpts of solid-state Raman spectra of the corresponding derivatives of $[Fe^{III}\mathbf{L1}(OH)]^{2+}$, the respective signal corresponding to the Fe−^{16}O or Fe−^{18}O bond is indicated.

Having observed the **L2**-based complexes in low-spin electron configurations is so far remarkable, as oxygen-free conditions were used in literature syntheses—a common precaution in the case of high-spin iron complexes. Additionally, a low stability was observed in the literature for $[Fe^{IV}\mathbf{L2}(O)]^{2+}$, which could have also indicated a high-spin state.[3] This was, however, not corroborated by our Mössbauer measurement—even though the samples were handled under ambient conditions for prolonged periods of time.

Characterization of the Iron(III)-Hydroxido Complexes by EPR. The assignment of a low-spin iron(III)-hydroxido species was confirmed by EPR analysis (Figure 6) and subsequent simulation of the assigned low-spin iron(III)-hydroxido compounds. The observed spectra, as well as the observed g values, were qualitatively and quantitatively similar to related complexes previously described in the literature ($[Fe^{III}(PY5)(OMe)]^{2+}$: g = 2.25, 2.17, 1.96 and $[Fe^{III}(PY5)(OH)]^{2+}$: g = 2.30, 2.18, 1.94[2]; PY5 = 2,6-bis(bis(2-pyridyl)-methoxymethane)pyridine).

Characterization by High-Resolution Mass Spectrometry and Raman Spectroscopy. All iron species were characterized as aqueous solutions with cryo high-resolution mass spectrometry (not shown; please refer to the Figures S53−S58, p 36ff). Regarding the iron(III) species $[Fe^{III}(\mathbf{L1})(OH)]^{2+}$ or $[Fe^{III}(\mathbf{L2})(OH)]^{2+}$, no hints of any bridged diiron(III) complexes have been observed, and no $[Fe^{III}(\mathbf{L1})(OH_2)]^{3+}$ or $[Fe^{III}(\mathbf{L2})(OH_2)]^{3+}$ species as potential intermediate were detected. In addition to the expected signals, other minor species could be observed for complexes with the ligand system **L2**, which were assigned to species such as $[Fe^{III}(\mathbf{L2}-$

https://doi.org/10.1021/acs.inorgchem.4c04518
Inorg. Chem. 2025, 64, 3719−3734

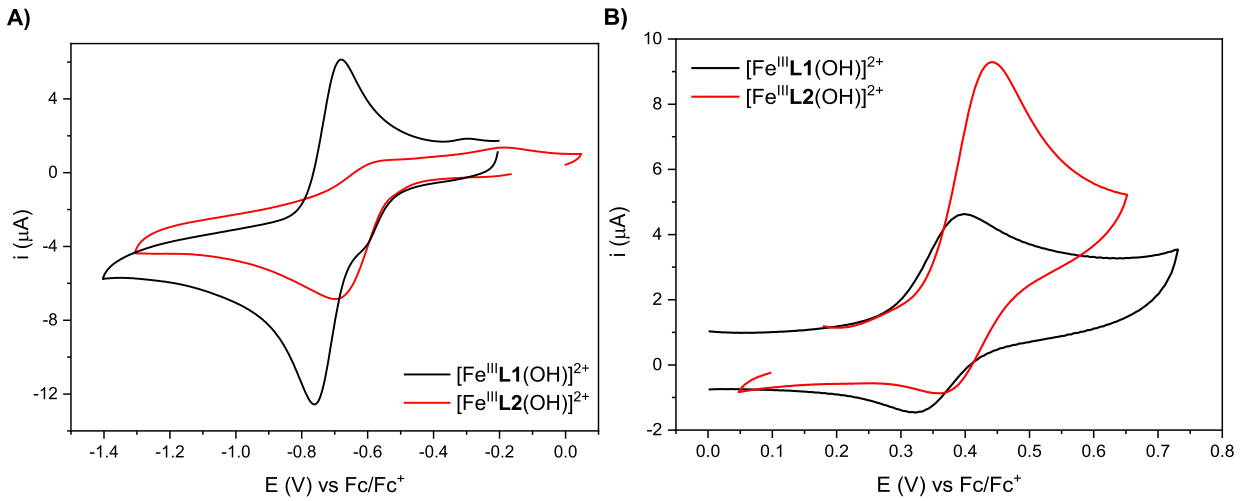

Figure 8. Comparison between the cyclic voltammograms of $[Fe^{III}\mathbf{L1}(OH)]^{2+}$ and $[Fe^{III}\mathbf{L2}(OH)]^{2+}$ (1 mM) in acetonitrile ($[TBAPF_6]$ = 0.1 M) in reductive (A) and oxidative (B) scans at 100 mV/s. For additional cyclic voltammograms, please refer to the Figures S34−S50, p 29ff.

H)(OH)]$^{2+}$, $[Fe^{III}(\mathbf{L2}\text{-}2H)(OH)]^{2+}$, or dinuclear species $[Fe^{II}(\mathbf{L2}\text{-}2H)]_2^{2+}$. This was attributed to a species in which one or both of the two hydroxy groups of **L2** are deprotonated and likely coordinate to the iron center, probably displacing one of the equatorial pyridine moieties.

We then also synthesized the ^{18}O-labeled derivative of $[Fe^{III}\mathbf{L1}(OH)]^{2+}$ (Figure 7A, middle reaction) as well as a mixture of $[Fe^{III}\mathbf{L1}(^{16/18}OH)]^{2+}$ (Figure 7A, lower reaction). We confirmed the successful integration of the ^{18}O label by Raman spectroscopy (Figure 7B). When direct-injection mass spectrometry of these compounds was measured, only the species containing the ^{16}OH group could be detected. This observation was attributed to an immediate exchange of the hydroxyl group in water. The exchange occurred even when dried solvents were used under strict inert gas conditions (not shown).

Characterization by UV−Vis−NIR Spectroscopy. The series of complexes was also characterized by UV−vis−NIR spectroscopy (Figures S31 and S32, p 27f). The UV−vis−NIR spectra of complexes $[Fe^{II}\mathbf{L2}(OH_2)]^{2+}$, $[Fe^{III}\mathbf{L2}(OH)]^{2+}$, and $[Fe^{IV}\mathbf{L2}(O)]^{2+}$ are similar to the respective spectra of $[Fe^{II}\mathbf{L1}(OH_2)]^{2+}$, $[Fe^{III}\mathbf{L1}(OH)]^{2+}$, and $[Fe^{IV}\mathbf{L1}(O)]^{2+}$ and correspond well to those found in the literature.[47,48] The absorption maxima at about 350 to 450 nm of the iron(II) species show the highest intensity, with extinction coefficients of ε = 5932/4190 L mol^{-1} cm^{-1} for $[Fe^{II}\mathbf{L1}/\mathbf{L2}(OH_2)]^{2+}$ (λ = 450 nm, water, 25 °C), which can be attributed to a metal-to-ligand charge transfer, which has been observed regularly in literature for iron(II) complexes with pyridine-derived ligands.[1−3,8] $[Fe^{IV}\mathbf{L2}(O)]^{2+}$ shows an absorption band at λ = 730 nm, which is a typical range for S = 1 iron(IV)-oxido species.[8,14,34,42−44]

Characterization by Cyclic Voltammetry. The redox properties of the iron(II) and iron(III) complexes (1 mM) have been addressed by cyclic voltammetry (CV) experiments, performed both in acetonitrile (using tetrabutylammonium hexafluorophosphate, $[TBAPF_6]$ = 0.1 M as the supporting electrolyte) and in aqueous solution (using potassium nitrate, $[KNO_3]$ = 0.1 M as the supporting electrolyte).

In oxidative scan mode in acetonitrile, both iron(II) complexes present a reversible wave: at 657 mV (vs Fc^+/Fc, ΔE = 85 mV) and 663 mV (vs Fc^+/Fc, ΔE = 76 mV) for $[Fe^{II}\mathbf{L1}(MeCN)]^{2+}$ and $[Fe^{II}\mathbf{L2}(MeCN)]^{2+}$, respectively. These processes are associated with the iron(III)/iron(II) redox couple (Figures S34−S38, p 29f).[8] The analogous redox potential for the two iron(II) centers suggests a negligible effect associated with the change of the peripheral methyl group with a hydroxy group.[3]

Moving to the iron(III) complexes $[Fe^{III}\mathbf{L1}(OH)]^{2+}$ and $[Fe^{III}\mathbf{L2}(OH)]^{2+}$, the presence of a negatively charged hydroxy group directly coordinated to the iron(III) center (instead of acetonitrile) drastically shifts the potentials of the iron(III)/iron(II) redox couples, −720 mV (vs Fc^+/Fc, ΔE = 80 mV) and E_c^1 = −698 mV (vs Fc^+/Fc), respectively (Figure 8A). Contrary to what was previously observed for $[Fe^{II}\mathbf{L1}(MeCN)]^{2+}$ and $[Fe^{II}\mathbf{L2}(MeCN)]^{2+}$,[3,8,47,48] $[Fe^{III}\mathbf{L1}(OH)]^{2+}$ and $[Fe^{III}\mathbf{L2}(OH)]^{2+}$ present marked differences. The iron(III) reduction in $[Fe^{III}\mathbf{L2}(OH)]^{2+}$ is shifted to a more positive potential (approximately 60 mV), and more importantly, the reoxidation process becomes irreversible (Figure 8A, see also Figure S40). When the scan rates were increased, a minor wave at approximately −400 mV was also observed (Figure S41). Even if the overall process remains irreversible, this suggests a fast ligand reorganization occurring after electron transfer (ET). In oxidative scan mode, a new reversible wave has also been detected for $[Fe^{III}\mathbf{L1}(OH)]^{2+}$ at 361 mV (vs Fc^+/Fc, ΔE = 76 mV), attributed to the iron(IV)/iron(III) redox couple (Figure 8B). $[Fe^{III}\mathbf{L2}(OH)]^{2+}$ presents a similar iron(IV)/iron(III) oxidation potential E_a^2 = 442 mV, but the process is again irreversible (Figure 8B). Interestingly, when the scan rate is gradually increased (Figure S43), a shift from the initial irreversible wave (100 mV/s) to a quasi-reversible process (ΔE = 100 mV, 600 mV/s) was observed. This behavior suggests a reversible ET followed by a slow chemical reaction involving the electrochemically generated $[Fe^{IV}\mathbf{L2}(O)]^{2+}$,[49] thus indicating a lower stability of $[Fe^{IV}\mathbf{L2}(O)]^{2+}$ compared with $[Fe^{IV}\mathbf{L1}(O)]^{2+}$. At higher potentials, an unresolved irreversible wave at ca. 1.30 V has also been observed and attributed to a ligand-based oxidation (refer to the Figures S36, S44, and S45).

This suggests how the coordinated OH group in $[Fe^{III}\mathbf{L1}(OH)]^{2+}$ and $[Fe^{III}\mathbf{L2}(OH)]^{2+}$ not only contributes to shifting the iron(III)/iron(II) redox couple to a more positive potential but also allows access to the iron(IV)-oxido

https://doi.org/10.1021/acs.inorgchem.4c04518
Inorg. Chem. 2025, 64, 3719−3734

state, which is not possible in the absence of an O-donor (see $[Fe^{II}\mathbf{L1}(MeCN)]^{2+}$ and $[Fe^{II}\mathbf{L2}(MeCN)]^{2+}$ Figures S37 and S38). In addition, the nature of the side CH_3/OH groups seems not to affect the iron redox couple, even if it does impact the stability of the iron(IV) intermediate, as stated above.

In unbuffered aqueous media ($[KNO_3]$ = 0.1 M), $[Fe^{III}\mathbf{L1}(OH)]^{2+}$ presents a quasi-reversible wave in reduction at −6 mV (vs Ag/AgCl, ΔE = 144 mV, Figure S46), approximately 300 mV lower in comparison with the potential reported in the literature for the iron(II)−OH_2 species.[8] An additional minor oxidation wave was observed upon reduction at a potential of approximately 0.20 V (Figures S46 and S47), which was not observed in acetate-buffered solution. Under the same experimental conditions, $[Fe^{III}\mathbf{L2}(OH)]^{2+}$ presents a completely different behavior: in the reductive scan, no waves attributable to the presence of an iron(III) center have been observed (Figure S48). In the oxidative scan, a quasi-reversible wave at 372 mV (vs Ag/AgCl, ΔE = 111 mV, Figure S49) attributable to the iron(III)/iron(II) redox couple has been observed without the appearance of any additional wave at higher potentials (Figure S50). This suggests the formation of a new iron(II) species from $[Fe^{III}\mathbf{L2}(OH)]^{2+}$ under the conditions applied here. This finding prompted us to further study the behavior of this species in solution (vide infra), as we were confident to have obtained a solid iron(III) sample in the first place, as confirmed by EPR and Mössbauer spectroscopy as well as X-ray crystallography.

We also investigated the effects of pH changes on the observed potentials of the iron(III)/iron(II) couple of $[Fe^{III}\mathbf{L1}(OH)]^{2+}$ and $[Fe^{II}\mathbf{L2}(OH_2)]^{2+}$. Instead of using the iron(II) species $[Fe^{II}\mathbf{L1}(OH_2)]^{2+}$, as had been done previously in the literature,[8] we used the iron(III)-hydroxido species $[Fe^{III}\mathbf{L1}(OH)]^{2+}$ to investigate complexes of **L1**. We found a linear decrease with a slope value of −59 mV/pH, indicating a proton-coupled electron transfer (Figure 9, PCET). In the case

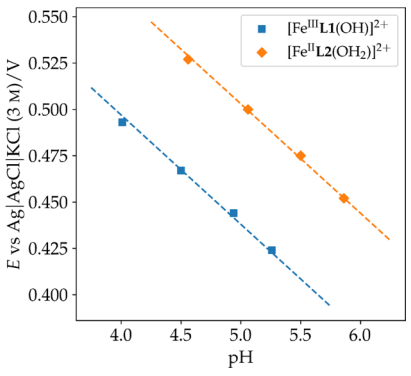

Figure 9. Pourbaix diagram of $[Fe^{III}\mathbf{L1}(OH)]^{2+}$ (blue squares) and $[Fe^{II}\mathbf{L2}(OH_2)]^{2+}$ (orange diamonds). The slope values of both lines are −59 mV/pH, which indicates a proton-coupled electron transfer (PCET) and was reported for **L1** in the literature.[8]

of **L2**, we used the iron(II) complex $[Fe^{II}\mathbf{L2}(OH_2)]^{2+}$ due to its higher stability under prolonged measurements compared with the respective iron(III)-hydroxido complex. The measured values are shifted to higher potentials; however, the slope value is identical at −59 mV/pH, also indicating PCET, as has been described in the literature for **L1** and other related ligands.[2,8,50]

Iron(II)/Iron(IV) Comproportionation. Based on the mechanism proposed for heme and nonheme enzymes containing iron(IV)-oxido moieties and their reactions with C−H bonds,[2,8,12,13] we had proposed this iron(III)-hydroxido species as the intermediate in the reaction of $[Fe^{IV}\mathbf{L1}(O)]^{2+}$ with organic substrates containing C−H groups in our previous work.[9] In this mechanism, a hydrogen atom is transferred from the organic substrate R-H to the iron(IV)-oxido moiety in a hydrogen atom transfer reaction (HAT). This step yields the iron(III)-hydroxido species, $[Fe^{III}\mathbf{L1}(OH)]^{2+}$, as well as a carbon-centered radical R·. These species can then recombine in a reaction often referred to as "rebound" to form the product and an iron(II) species in water $[Fe^{II}\mathbf{L1}(OH_2)]^{2+}$ (Figure 10A). This mechanism resembles the consensus mechanism for the oxidation of biological substrates by iron(II)/α-ketoglutarate-dependent enzymes, of which superfamily the previously mentioned TET enzymes are a member.[20−23,26,51,52]

Surprised by the large amounts of $[Fe^{III}\mathbf{L1}(OH)]^{2+}$ present in the reaction mixture of $[Fe^{IV}\mathbf{L1}(O)]^{2+}$and 5mC (Figure 11) after complete reaction, we searched for different pathways that might lead to the formation of this iron(III)-hydroxido species.

For synthetic nonheme iron complexes, several other mechanisms and pathways are discussed in addition to rebound: cage escape[33] and the formation of a dinuclear complex, as mentioned in the introduction,[14] are two representatives. Also, comproportionation of iron(II)/iron(IV) species has been described in the literature, although mostly as a minor side note.[14,31,53] In the case of the complexes studied in this work, we found that the comproportionation reaction of $[Fe^{II}\mathbf{L1}(OH_2)]^{2+}$ with $[Fe^{IV}\mathbf{L1}(O)]^{2+}$ gave $[Fe^{III}\mathbf{L1}(OH)]^{2+}$ in a quantitative yield. The UV−vis−NIR spectrum of an equimolar mixture of $[Fe^{II}\mathbf{L1}(OH_2)]^{2+}$ and $[Fe^{IV}\mathbf{L1}(O)]^{2+}$ appears to have identical features compared to the spectrum of a $[Fe^{III}\mathbf{L1}(OH)]^{2+}$ reference sample (Figure 12). This observation was also confirmed by cryo-UHR−MS (refer to Figure S59, p 43). Whereas Gosh et al.[29] and Rana et al.[53] reported on the comproportionation of biuret-amide and N4Py-based systems, respectively, Cho et al. ruled out comproportionation when studying $[Fe^{IV}(O)(Bn\text{-}TPEN)]^{2+}$ (Bn-TPEN = *N*-benzyl-*N*,*N*′,*N*′-tris(2-pyridylmethyl)ethane-1,2-diamine). In this work, we report on another example of the comproportionation of iron(IV)-oxido and iron(II) compounds as a pathway for synthetic nonheme iron(IV)-oxido complexes.

As a result, we decided to study this behavior in more detail and chose to include the iron complexes of the structurally similar ligand **L2** in this analysis. We found that not only $[Fe^{II}\mathbf{L1}(OH_2)]^{2+}$ and $[Fe^{IV}\mathbf{L1}(O)]^{2+}$ but also $[Fe^{II}\mathbf{L2}(OH_2)]^{2+}$ and $[Fe^{IV}\mathbf{L2}(O)]^{2+}$ show comproportionation behavior—as well as the cross-reactions of $[Fe^{II}\mathbf{L1}(OH_2)]^{2+}$ with $[Fe^{IV}\mathbf{L2}(O)]^{2+}$ and $[Fe^{II}\mathbf{L2}(OH_2)]^{2+}$ with $[Fe^{IV}\mathbf{L1}(O)]^{2+}$, the latter two giving a mixture of $[Fe^{III}\mathbf{L1}(OH)]^{2+}$ and $[Fe^{III}\mathbf{L2}(OH)]^{2+}$. The iron(II) species $[Fe^{II}\mathbf{L1}(OH_2)]^{2+}$ and $[Fe^{II}\mathbf{L2}(OH_2)]^{2+}$ as well as the iron(IV)-oxido complexes $[Fe^{IV}\mathbf{L1}(O)]^{2+}$ and $[Fe^{IV}\mathbf{L2}(O)]^{2+}$ do not react with each other; both reactions were observed to yield a mixture of the respective starting materials.

To gain a deeper insight into this reactivity, these individual comproportionation reactions were followed by stopped-flow UV−vis−NIR kinetics (Figure 13). The presence of both iron(II) and iron(IV)-oxido complexes was measured at the respective absorption maxima ($[Fe^{II}\mathbf{L1}(OH_2)]^{2+}$/

https://doi.org/10.1021/acs.inorgchem.4c04518
Inorg. Chem. 2025, 64, 3719−3734

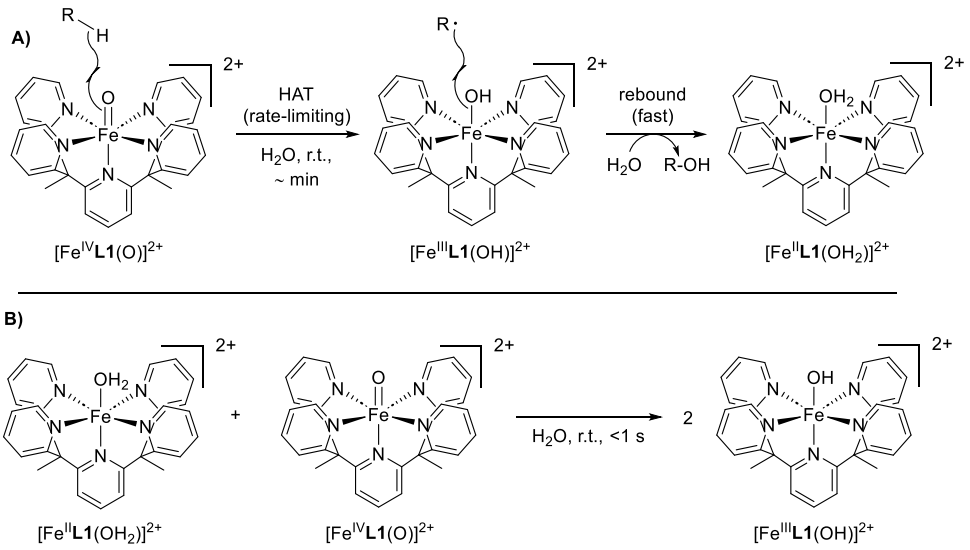

Figure 10. (A) Proposed mechanism for the reaction of $[Fe^{IV}\mathbf{L1}(O)]^{2+}$ with an organic substrate R-H that contains a C−H bond via hydrogen atom transfer (HAT) and subsequent rebound.[9] (B) Observed comproportionation reaction of the iron(II) complex $[Fe^{II}\mathbf{L1}(OH_2)]^{2+}$ and the iron(IV)-oxido complex $[Fe^{IV}\mathbf{L1}(O)]^{2+}$ to yield iron(III)-hydroxido species $[Fe^{III}\mathbf{L1}(OH)]^{2+}$.

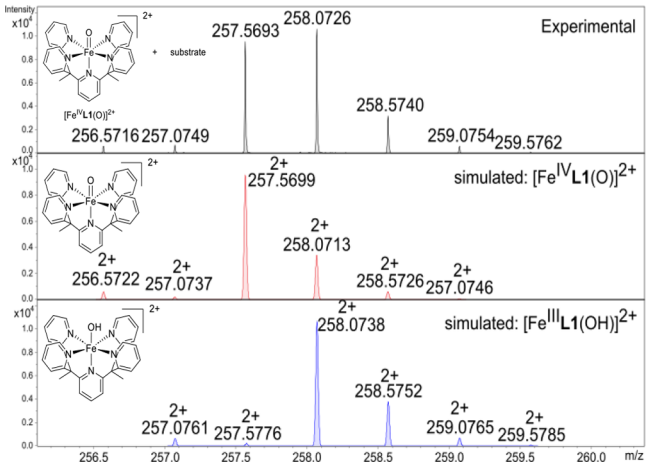

Figure 11. Excerpt of a cryo-UHR−MS spectrum of the reaction mixture of $[Fe^{IV}\mathbf{L1}(O)]^{2+}$ with an organic substrate (5-methyl cytosine, 5mC) as well as simulated mass spectra of $[Fe^{IV}\mathbf{L1}(O)]^{2+}$ (red, middle spectrum) and $[Fe^{III}\mathbf{L1}(OH)]^{2+}$ (blue, lower spectrum).

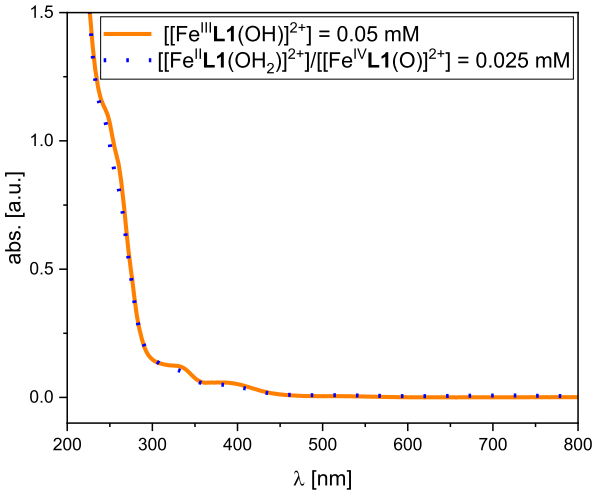

Figure 12. Excerpt of a UV−vis−NIR spectrum of the comproportionation reaction of $[Fe^{II}\mathbf{L1}(OH_2)]^{2+}$ and $[Fe^{IV}\mathbf{L1}(O)]^{2+}$ (blue dotted line) as well as a reference spectrum of $[Fe^{III}\mathbf{L1}(OH)]^{2+}$ (orange solid line) in water at room temperature. A graph also containing $[Fe^{II}\mathbf{L1}(OH_2)]^{2+}$ and $[Fe^{IV}\mathbf{L1}(O)]^{2+}$ as reference can be found in the Supporting Information, p 27 (Figure S30).[8]

$[Fe^{II}\mathbf{L2}(OH_2)]^{2+}$: λ = 450 nm, $[Fe^{IV}\mathbf{L1}(O)]^{2+}$: λ = 720 nm, and $[Fe^{IV}\mathbf{L2}(O)]^{2+}$: λ = 730 nm).

A comparison of the decreasing absorption of both iron(II) and iron(IV)-oxido species over time suggests a bimolecular reaction of both complexes (not shown; please refer to the Figure S4, p 10). Using the same analytical kinetics we applied to study the reaction of $[Fe^{IV}\mathbf{L1}(O)]^{2+}$ with organic substrates in our previous work,[11] we obtained rate constants in the order of 1.5−4.2 × 10^4 L mol^{-1} s^{-1} (refer to the Supporting Information, p 9f for detailed calculations.) These values are 4−6 orders of magnitude larger than those observed for $[Fe^{IV}\mathbf{L1}(O)]^{2+}$ with a variety of substrates bearing alkyl groups, both the ones tested in this work (vide infra) and in our previous work.[11]

The stopped-flow UV−vis−NIR measurements were repeated in deuterated water, and the same linear regression calculations were performed. A kinetic isotope effect (KIE) was observed in the range of 1.9 to 5.6, which would suggest a proton transfer to be the rate-limiting step in this reaction. Interestingly, this isotope effect seems to be more pronounced in comproportionation reactions involving iron complexes with the ligand system **L2**. A comparison of all conducted measurements in water or deuterated water is provided in the Figures S4−S6, p 11ff.

Substrate Oxidation by Iron(IV)-Oxido Species. In the next step, we wanted to confirm the oxidative capabilities of $[Fe^{IV}\mathbf{L2}(O)]^{2+}$ and compare the reactivities of the two different ligand systems in substrate oxidation processes. Therefore, complexes $[Fe^{IV}\mathbf{L1}(O)]^{2+}$ and $[Fe^{IV}\mathbf{L2}(O)]^{2+}$ were reacted with selected substrates chosen on the basis of the work of Chantarojsiri et al.[8] (Chart 2). Due to the high reactivity of the iron(IV)-oxido complexes toward organic substrates, no organic buffers could be used. Due to solubility issues in phosphate buffer, pure water was chosen. The pH value after the addition of all components was measured at

https://doi.org/10.1021/acs.inorgchem.4c04518
Inorg. Chem. 2025, 64, 3719−3734

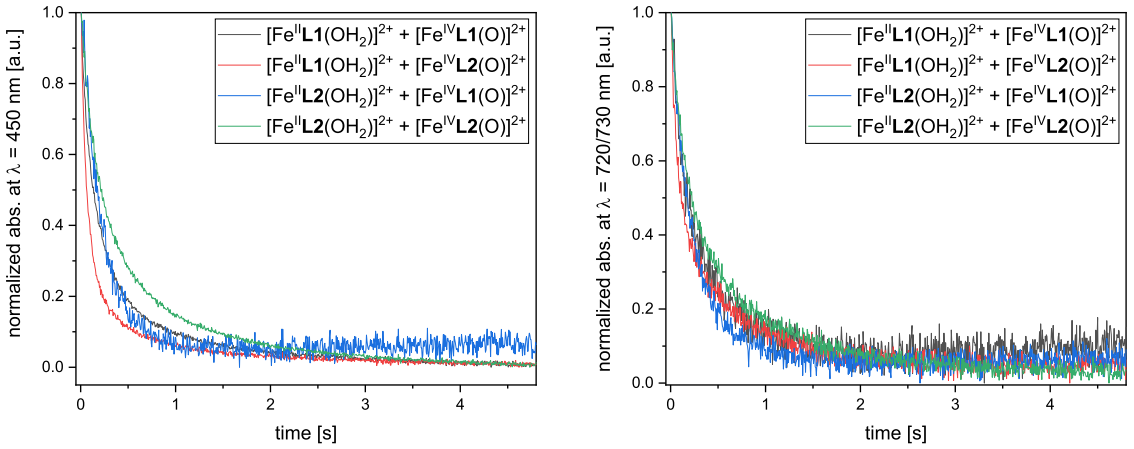

Figure 13. Equimolar reaction of iron(II) and iron(IV)-oxido species followed by stopped-flow UV−vis−NIR spectroscopy at the respective absorption band (iron(II): λ = 450 nm; iron(IV): λ = 720/730 nm). Conditions: [[Fe^{II}**L1**$(OH_2)]^{2+}$ or [Fe^{II}**L2**$(OH_2)]^{2+}$] = [[Fe^{IV}**L1**$(O)]^{2+}$ or [Fe^{IV}**L2**$(O)]^{2+}$] = 0.5 mM, H_2O, 25 °C.

Chart 2. Overview of Substrates (S) Tested in the Reactivity Study

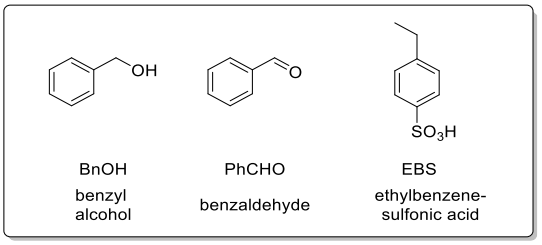

4.77 ± 0.10 at the beginning of the reaction and found to decrease to 4.68 during the reaction (refer to the Figure S2, p 7 for details).

The reaction was followed with UV−vis−NIR spectroscopy at the characteristic iron(IV)-oxido absorption band (λ = 720 nm for [Fe^{IV}**L1**$(O)]^{2+}$ and λ = 730 nm for [Fe^{IV}**L2**$(O)]^{2+}$), which decreases during the reaction as the iron(IV)-oxido species is consumed (Figure 14A). The reaction rates were calculated using the method of initial rates. The newly synthesized [Fe^{IV}**L2**$(O)]^{2+}$ reacts slightly faster with the substrates benzyl alcohol (10.94 L mol^{-1} s^{-1}) and ethylbenzenesulfonic acid (16.75 L mol^{-1} s^{-1}) than the literature-known compound [Fe^{IV}**L1**$(O)]^{2+}$ (7.40 and 11.99 L mol^{-1} s^{-1}, respectively). In the case of benzaldehyde, no significant difference in reaction rates could be observed (2.08 L mol^{-1} s^{-1} for [Fe^{IV}**L2**$(O)]^{2+}$ and 2.77 L mol^{-1} s^{-1} for [Fe^{IV}**L1**$(O)]^{2+}$; Figure 14B). The faster reaction of both iron complexes with benzyl alcohol as the substrate compared to benzaldehyde is in accordance with the reactivity expected from the corresponding C−H bond dissociation energies of the substrates (83.0 kcal mol^{-1} for benzyl alcohol[S4] and 89.3 kcal mol^{-1} for benzaldehyde[S5]). Hydrogen atom transfer occurs faster with lower BDE, and this observation supports the reaction mechanism proposed in Figure 10.

To ensure that substrate oxidation occurred, the products after the reaction with the iron(IV)-oxido species were identified by ^{1}H NMR spectroscopy. In the case of benzyl alcohol and benzaldehyde, this was accomplished by extracting the aqueous reaction mixture with deuterated chloroform, leaving the remaining iron species in the aqueous layer. As

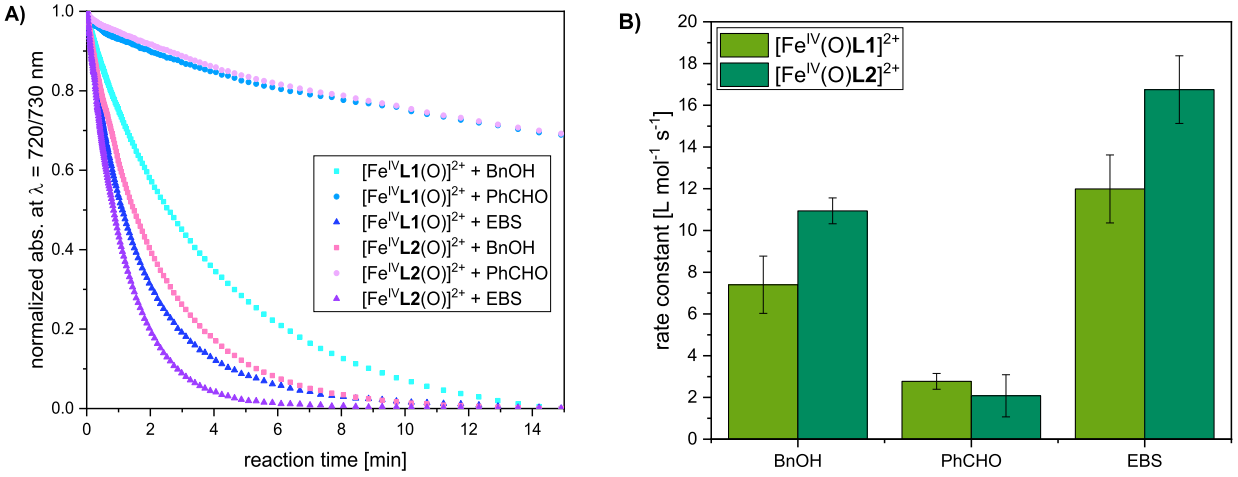

Figure 14. (A) Reaction of [Fe^{IV}**L1**$(O)]^{2+}$ and [Fe^{IV}**L2**$(O)]^{2+}$ with different substrates monitored by UV−vis−NIR absorption at λ = 720 nm ([Fe^{IV}**L1**$(O)]^{2+}$) or λ = 730 nm ([Fe^{IV}**L2**$(O)]^{2+}$) and (B) calculated rate constants for these reactions (refer to the literature[T1] and the Supporting Information, p 7 for calculation method, exact values, and comparison with corresponding BDE values). Conditions: [[Fe^{IV}**L1**$(O)]^{2+}$/[Fe^{IV}**L2**$(O)]^{2+}$] = [*S*] = 0.5 mM, H_2O, rt. The experiments were conducted in triplicate and averaged.

https://doi.org/10.1021/acs.inorgchem.4c04518
Inorg. Chem. 2025, 64, 3719−3734

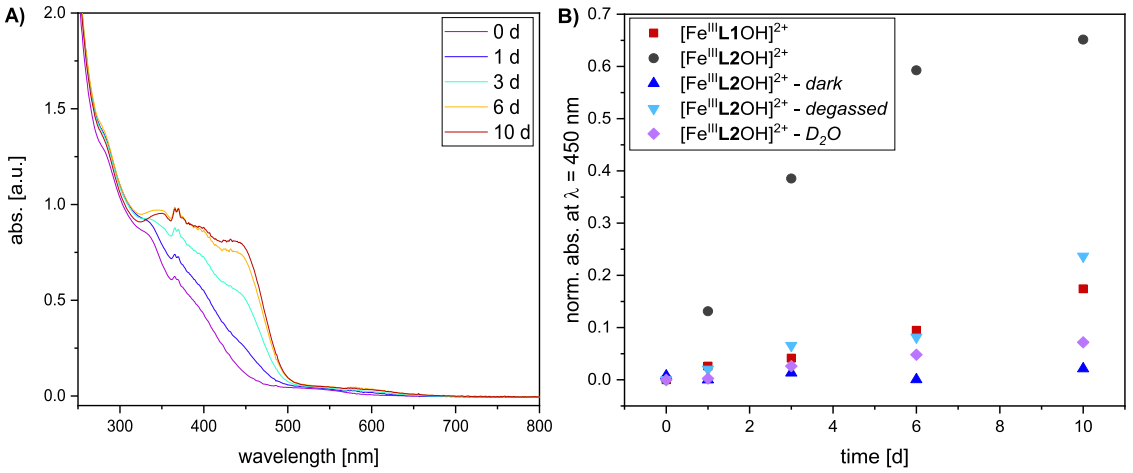

Figure 15. (A) UV−vis−NIR spectra of $[Fe^{III}\mathbf{L2}(OH)]^{2+}$ in aqueous solution under ambient conditions and exposed to light after different times and (B) absorbance of $[Fe^{III}\mathbf{L1}(OH)]^{2+}$ and $[Fe^{III}\mathbf{L2}(OH)]^{2+}$ at λ = 450 nm over time. Conditions: $[[Fe^{III}\mathbf{L1}(OH)]^{2+}$ or $[Fe^{III}\mathbf{L2}(OH)]^{2+}] = 0.5$ mM, H_2O, 25 °C. Additional spectra are provided in the Figure S33, p 28.

expected, benzyl alcohol was first converted into benzaldehyde, which reacted further to benzoic acid (Figures S15−S18). As the substrate ethylbenzenesulfonic acid (EBS) remained in the aqueous layer, this method could not be applied here. To separate the formed products from the iron species present, the yellowish reaction mixture was filtered over silica. The yellow iron species remained on the silica, and the clear filtrate was analyzed with ^{1}H NMR spectroscopy (Figures S27 and S28). In addition to the EBS starting material, two new species could be observed, which were attributed to the hydroxylated (4-(1-hydroxyethyl)benzenesulfonic acid) and carbonylated (4-acetylbenzenesulfonic acid) derivative of EBS. LC−MS measurements support this assumption (Figures S64 and S65, p 46). Control reactions with the corresponding iron(II) or iron(III) species revealed no oxidation of the substrates under the applied conditions (please refer to the Figures S19−S26 and S29, p 21ff). The results presented herein show that the complex with **L2** is a suitable model system for further investigations of iron-dependent nonheme enzymes, just as $[Fe^{IV}\mathbf{L1}(O)]^{2+}$ has been used in recent years as a model system.[9−11] The observed difference in reaction rates with organic substrates might offer intriguing possibilities for differential oxidation of several substrates in the same reaction mixture, depending on the added iron catalyst, mimicking complex enzyme mixtures in living cells.

Iron(III) to Iron(II) Conversion. Puzzled by the detection of iron(II) species upon the application of iron(III) species in some cyclic voltammetry experiments, a possible reduction of iron(III) under the applied conditions was assumed. To test the stability of the iron(III) species in aqueous solution, UV−vis−NIR spectra of $[Fe^{III}\mathbf{L1}(OH)]^{2+}$ and $[Fe^{III}\mathbf{L2}(OH)]^{2+}$ were recorded at certain time intervals (see Figure 15).

The UV−vis−NIR spectra show that when $[Fe^{III}\mathbf{L2}(OH)]^{2+}$ is stored in aqueous solution at ambient conditions, a new absorption band is formed after some time (Figure 15A). The higher intensity and position of this new absorption band (about λ = 450 nm) suggest the formation of the corresponding iron(II) species. To test this hypothesis, a sample of $[Fe^{III}\mathbf{L2}(OH)]^{2+}$ in water was kept under ambient conditions for 5 weeks, the solvent was removed, and the sample was subjected to Mössbauer measurements. The spectra revealed that 37% of the iron(III) species has been converted into an iron(II) species (not shown; please refer to the Figure S67, p 47). The parameters of the newly observed species are similar but not identical to the iron(II)/iron(III) reference samples (see Table S6, p 47), and this slight difference is attributed to the assumed presence of water as a co-ligand for the iron(II) species (instead of acetonitrile) and possible ligand oxidation for both species. The complex with the other ligand system $[Fe^{III}\mathbf{L1}(OH)]^{2+}$ showed similar behavior, but the transformation occurred significantly slower (Figure 15B).

To learn more about this process, three different aqueous solutions of $[Fe^{III}\mathbf{L2}(OH)]^{2+}$ were prepared (a) with exclusion of light, (b) under a nitrogen atmosphere using degassed water, and (c) under ambient conditions but using deuterated water. Light exclusion led to no conversion to iron(II) species over the investigated time, and with the exclusion of oxygen, the transformation started slower and not immediately (Figure 15B). As no other suitable reaction partner is present in the reaction mixture, we assume that in combination with the reduction from iron(III) to iron(II) species, oxidation of the ligand occurs. It seems that light is required to start this oxidation process, which indicates the involvement of one-electron processes. This has been described previously in the literature, e.g., a tpena-based iron(III) complex (tpena = *N*,*N*,*N*′-tris(2-pyridylmethyl)ethylendiamine-*N*′-acetate) was reported to photolytically release CO_2 in a one-electron reduction to the respective iron(II) complex with a radical present on the ligand.[56] Then, traces of oxygen seem to be sufficient for the conversion to occur. When $[Fe^{III}\mathbf{L2}(OH)]^{2+}$ is dissolved in deuterated water instead of water under ambient conditions, no conversion into the iron(II) species is observed over the investigated time (Figure 15B), suggesting that proton transfer also seems to play a role in this transformation process.

These findings show that after the comproportionation of iron(II) and iron(IV) species, the resulting iron(III) compound seems not to be the final product in this complex mixture. Even though magnitudes of dimensions lie between the reaction rates of these two different processes (seconds for the comproportionation and days/weeks for iron(III) to iron(II) conversion), it appears that, in the end, the most stable species is an iron(II) complex under the conditions applied here.

https://doi.org/10.1021/acs.inorgchem.4c04518
Inorg. Chem. 2025, 64, 3719−3734

CONCLUSIONS

In this work, we presented a comprehensive overview of the iron(II), iron(III)-hydroxido, and iron(IV)-oxido chemistry of two pentapyridyl ligands, **L1** and **L2**. With the exception of $[Fe^{IV}\mathbf{L2}(O)]^{2+}$, we provided a full set of X-ray structures for all three oxidation states for both ligands, including the relatively rare low-spin iron(III)-hydroxido complexes, $[Fe^{III}\mathbf{L1}(OH)]^{2+}$ and $[Fe^{III}\mathbf{L2}(OH)]^{2+}$. We complemented these X-ray structures with further structural investigations using Mössbauer, EPR, as well as UV−vis−NIR and IR spectroscopy, and the electrochemistry of the iron compounds was studied with cyclic voltammetry investigations. Additionally, UV−vis−NIR kinetic analysis of the reactivity of the iron(IV)-oxido compounds, $[Fe^{IV}\mathbf{L1}(O)]^{2+}$ and $[Fe^{IV}\mathbf{L2}(O)]^{2+}$, toward a series of substrates was performed. Thereby, we could establish a structure−function relationship between the methyl group in **L1**-derived compounds and the hydroxyl group in **L2**-derived compounds. The comproportionation reaction of iron(II) compounds $[Fe^{II}\mathbf{L1}(OH_2)]^{2+}$ and $[Fe^{II}\mathbf{L2}(OH_2)]^{2+}$ with iron(IV)-oxido complexes $[Fe^{IV}\mathbf{L1}(O)]^{2+}$ and $[Fe^{IV}\mathbf{L2}(O)]^{2+}$ was confirmed using UV−vis−NIR spectroscopy and high-resolution mass spectrometry. This finding is especially relevant for the bioinorganic chemistry of these complexes, as it shows that iron model systems of enzymes do undergo significant side reactions.

EXPERIMENTAL SECTION

Synthesis of 2,2′-(ethane-1,1′diyl)dipyridine (1). According to a modified literature procedure,[57] a flame-dried flask was charged with 2-ethylpyridine (6.27 mL, 5.88 g, 54.84 mmol, 2.1 equiv) under an inert atmosphere (nitrogen) and 50 mL of absolute tetrahydrofuran and then cooled to −78 °C. When a solution of *n*-butyl lithium (2.5 M in hexane, 20.80 mL, 52.01 mmol, 2.0 equiv) was added dropwise, the solution turned deep red. The mixture was stirred for 60 min at −78 °C, and then 2-fluoropyridine (2.21 mL, 2.50 g, 25.8 mmol, 1.0 equiv) was added dropwise; the solution was stirred at −78 °C for an additional 10 min, and the cooling bath was removed. The reaction mixture was allowed to warm to room temperature and then stirred at room temperature for 3 h. Next, 30 g of ice was added slowly, at which point the mixture turned yellow. An additional 30 mL of Milli-Q grade water was added, and the solution was stirred vigorously for 10 min. The layers were separated, and the aqueous layer was extracted with dichloromethane (3 × 50 mL). The combined organic layers were dried over anhydrous magnesium sulfate, and the solvents were removed in vacuo to yield a yellow to orange oil as the crude product. Excess 2-ethylpyridine was removed under reduced pressure to yield product 1 as a yellow to orange oil in 84% yield (3.79 g). R_F = 0.23 (silica, UV, 80% ethyl acetate - hexanes). **^{1}H NMR** (400.0 MHz, $CDCl_3$, 295 K): δ = 8.55 (ddd, J = 4.9 Hz, J = 1.9 Hz, J = 0.9 Hz, 2H), 7.60 (td, J = 7.7 Hz, J = 1.8 Hz, 2H), 7.28 (dd, J = 7.9 Hz, J = 1.0 Hz, 2H), 7.11 (ddd, J = 7.5 H, J = 4.9 Hz, J = 1.2 Hz, 2H), 4.48 (q, J = 7.2 Hz, 2H), 1.76 (d, J = 7.2 Hz, 3H) ppm. **^{13}C NMR** (100.0 MHz, $CDCl_3$, 295 K): δ = 163.9, 149.3, 136.6, 122.5, 121.5, 49.9, 19.8 ppm. NMR data are in accordance with the literature.[57] **HR−MS (ESI):** Calculated for $C_{12}H_{13}N_2$ $[M + H]^+$: 185.10787 *m/z*; Found: 185.10723 *m/z*.

Synthesis of L1. According to a modified literature procedure,[8,9] a flame-dried flask was charged with **1** (2.00 g, 10.9 mmol, 3.0 equiv), 36 mL of absolute 1,4-dioxane under an inert atmosphere (nitrogen), and 4 mL of absolute tetrahydrofuran and cooled to 0 °C. When a solution of *n*-butyl lithium (2.5 M in hexane, 4.34 mL, 10.9 mmol, 3.0 equiv) was added, the solution turned dark red. The solution was stirred for 45 min at 0 °C, at which time 2,6-dichloropyridine (535.5 mg, 3.62 mmol, 1.0 equiv) was added all at once. The reaction mixture was allowed to warm to room temperature and then heated to reflux for 60 h (bath temperature 105 °C). When the solution had turned from deep red to light brown and thin-layer chromatography showed no change during a time span of 6 h, the mixture was allowed to cool to room temperature. Then, 20 mL of water was added, and the mixture was extracted with dichloromethane (3 × 70 mL). The combined organic layers were then dried over anhydrous magnesium sulfate, and the solvents were removed in vacuo. Afterward, 40 mL of methanol was added, and the solvents were removed in vacuo to remove residual 1,4-dioxane. A deep red oil was obtained as the crude product. Diethyl ether was added until a yellow precipitate began to form, which was filtered off, washed with diethyl ether (1 × 10 mL), and dried to yield the product **L1** as a yellow solid in 91% yield. R_F = 0.10 (silica, UV, 80% ethyl acetate - hexanes). **^{1}H NMR** (400.0 MHz, $CDCl_3$, 295 K): δ = 8.51 (ddd, J = 4.8 Hz, J = 1.9 Hz, J = 0.9 Hz, 4H), 7.54 (t, J = 7.9 Hz, 1H), 7.39 (ddd, J = 8.1 Hz, J = 7.5 Hz, J = 1.9 Hz, 4H), 7.05 (d, J = 7.9 Hz, 2H) 7.04 (ddd, J = 7.5 Hz, J = 4.8 Hz, J = 1.1 Hz, 4H), 6.84 (dt, J = 8.0 Hz, J = 1.0 Hz, 4H), 2.21 (s, 6H) ppm. **^{13}C NMR** (100.0 MHz, $CDCl_3$, 295 K): δ = 166.2, 166.3, 148.5, 136.8, 135.6, 124.1, 121.0, 120.0, 60.1, 26.8 ppm. NMR data are in accordance with the literature.[8] **HR−MS (ESI)**: Calculated for $C_{29}H_{26}N_5$ $[M + H]^+$: 444.21882 *m/z*; Found: 444.21811 *m/z*. **IR (thin film)**: $\nu\sim$ = 3053, 2992, 1566, 1466, 1428, 1365, 1293, 1153, 1102, 1078, 1067, 1046, 991, 962, 903, 875, 799, 786, 768, 752, 699, 654 cm^{-1}.

Synthesis of $[Fe^{II}\mathbf{L1}(MeCN)](OTf)_2$. According to a modified literature procedure,[8,9] ligand **L1** (300.0 mg, 0.679 mmol, 1.0 equiv) was dissolved in 15 mL of acetonitrile under a nitrogen atmosphere. Iron(II)bis(acetonitrile)bis(triflate) (294.9 mg, 0.679 mmol, 1.0 equiv) was added as a solid, turning the solution deep red. The mixture was then stirred for an additional 5 min, and then diethyl ether was diffused into the solution under ambient conditions to give the product $[Fe^{II}\mathbf{L1}(MeCN)](OTf)_2$ as brown crystals in 91% yield (516.0 mg). **^{1}H NMR** (400.0 MHz, CD_3CN, 295 K): δ = 9.81 (d, J = 5.9 Hz, 4H), 8.03 (s, 3H), 7.93 (d, J = 3.8 Hz, 8H), 7.54 (m, 4H), 2.75 (s, 6H), 1.96 (s, 3H) ppm. **^{13}C NMR** (100.0 MHz, CD_3CN, 295 K): δ = 165.0, 163.0, 158.2, 140.1, 139.7, 124.3, 123.8, 122.1, 118.3, 55.7, 24.2 ppm. NMR data is in accordance with the literature.[8] **HR−MS (ESI)**: Calculated for $C_{30}H_{25}F_3FeN_5O_3S$ $[Fe(\mathbf{L1})(MeCN)(OTf)]^+$: 648.09796 *m/z*; Found: 648.09648 *m/z*. Calculated for $C_{31}H_{28}FeN_6$ $[Fe(\mathbf{L1})(MeCN)]^{2+}$: 270.08625 *m/z*; Found: 270.08562 *m/z*. **Elemental Analysis**: Calculated for $C_{33}H_{28}F_6FeN_6O_6S_2$: C 47.27, H 3.37, N 10.02, S 7.65; Found: C 47.03, H 3.33, N 9.94, S 7.86. **IR (thin film)**: $\nu\sim$ = 1598, 1469, 1442, 1415, 1281, 1251, 1225, 1149, 1070, 1028, 865, 791, 761, 702 cm^{-1}.

Synthesis of $[Fe^{II}\mathbf{L1}(OH_2)](BF_4)_2$. According to a modified literature procedure,[8] ligand **L1** (90.0 mg, 0.190 mmol, 1.0 equiv) was dissolved in 4.0 mL of acetone. Hexaqua iron(II) bis(tetrafluoroborate) (64.2 mg, 0.190 mmol, 1.0 equiv) was dissolved in 0.5 mL of water and then added to the solution of the ligand, turning the solution red-brown. The mixture was stirred for 5 min, and then diethyl ether was diffused into the solution to give the product $[Fe^{II}\mathbf{L1}(OH_2)](OTf)_2$ as a red-brown powder in 73% yield (100.0 mg). **HR−MS (ESI)**: Calculated for $C_{29}H_{25}FFeN_5$ $[Fe(\mathbf{L1})(F)]^+$: 518.14434 *m/z*; Found: 518.14454 *m/z*. Calculated for $C_{31}H_{28}FeN_6$ $[Fe(\mathbf{L1})(MeCN)]^{2+}$: 270.08625 *m/z*; Found: 270.05525 *m/z*. Calculated for $C_{31}H_{28}FeN_6$ $[Fe(\mathbf{L1})]^{2+}$: 249.5730 *m/z*; Found: 249.5730 *m/z*. **Elemental Analysis**: Calculated for $C_{29}H_{27}B_2F_8FeN_5O$: C 50.41, H 3.94, N 10.15.; Found: C 50.43, H 3.80, N 10.11. **IR (thin film)**: $\nu\sim$ = 3398, 1653, 1597, 1465, 1442, 1412, 1390, 1283, 1069, 993, 863, 768 cm^{-1}.

Synthesis of $[Fe^{III}\mathbf{L1}(OH)](OTf)_2$. Ligand **L1** (1.00 g, 2.25 mmol, 1.0 equiv) was suspended in 40 mL of water. Iron(III) triflate (1.51 mg, 3.00 mmol, 1.3 equiv) was added as a solid. The mixture turned orange-red upon mixing; the mixture was sonicated for 1 h at 40 °C which led to a color change to deep red. Additional iron(III) triflate (0.56 g, 1.11 mmol, 0.8 equiv) was added, and the mixture was sonicated briefly. The mixture was filtered through a sintered glass frit, and sodium triflate (775.0 mg, 4.50 mmol) was added as a solid to the filtrate. The mixture was stored at 4 °C for 3 days. The formed crystals were washed with water and dried in vacuo to give $[Fe^{III}\mathbf{L1}(OH)](OTf)_2$ (no yield determined). The precipitate

https://doi.org/10.1021/acs.inorgchem.4c04518
Inorg. Chem. 2025, 64, 3719−3734

obtained from filtering was collected and recrystallized from water (40 °C) to give $[Fe^{III}\mathbf{L1}(OH)](OTf)_2 \times 2\ H_2O$ (no yield determined). **HR–MS (ESI)**: Calculated for $C_{29}H_{26}FeN_5O$ $[Fe\mathbf{L1}(OH)]^{2+}$: 258.07434 *m/z*; Found: 258.07355 *m/z*. **Elemental Analysis**: Calculated for $C_{31}H_{26}F_6FeN_5O_7S_2$: C 45.71, H 3.22, N 8.60, S 7.87. Found: C 44.17, H 3.36, N 8.07, S 7.78. Calculated for $C_{31}H_{30}F_6FeN_5O_9S_2$ $(Fe^{III}\mathbf{L1}(OH)](OTf)_2 \times 2H_2O)$: C 43.78, H 3.56, N 8.23, S 7.54. Found: C 43.53, H 3.42, N 8.06, S 7.99. **IR (thin film)**: $\nu\sim$ = 3424, 3091, 1657, 1599, 1462, 1447, 1390, 1256, 1224, 1154, 1103, 1026, 914, 868, 847, 782, 764, 742, 664 cm^{-1}.

Synthesis of $[Fe^{IV}\mathbf{L1}(O)][Ce(NO_3)_6]$. According to a modified literature procedure,[8,9] $[Fe^{II}\mathbf{L1}(MeCN)](OTf)_2$ (100 mg, 0.119 mmol, 1.0 equiv) was dissolved in 1.5 mL of 3:1 acetonitrile:water. Cerium(IV) ammonium nitrate (347.1 mg, 0.633 mmol, 5.3 equiv) was added as a solid, and the mixture was sonicated for 60 s. As a pale green precipitate began to form, the reaction mixture was placed in an ice bath to complete the precipitation. The solid was collected on a sintered glass frit, washed with 1.5 mL of ice cold 3:1 acetonitrile:water, and dried in vacuo to yield product $[Fe^{IV}\mathbf{L1}(O)][Ce(NO_3)_6]$ as a pale green solid (107.2 mg, 87%). **Elemental Analysis**: Calculated for $C_{29}H_{25}CeFeN_{11}O_{19}$: C 33.90, H 2.45, N 14.99. Found: C 33.81, H 2.58, N 15.20. **ICP-OES**: Fe: 52.3 mg/g ≙ 0.937 mmol/g; Ce: 131.5 mg/g ≙ 0.939 mmol/g; Molecular ratio of Fe:Ce = 1:1. **IR (thin film)**: $\nu\sim$ = 1600, 1496, 1277, 1033, 864, 822, 804, 784, 760, 742 cm^{-1}. **UV–vis-NIR (H_2O)**: λ = 720 nm (ε = 277 l mol^{-1} cm^{-1}).

Synthesis of Pyridine-2,6-diylbis(pyridin-2-ylmethanone) (2). According to a modified literature procedure,[2] a flame-dried flask was charged with 2-bromo pyridine (2.62 mL, 4.25 g, 26.88 mmol, 3.0 equiv), and 100 mL of absolute tetrahydrofuran was added. After cooling the mixture to −78 °C, a solution of *n*-butyl lithium (2.5 M in hexanes, 10.75 mL, 1.72 g, 26.88 mmol, 3.0 equiv) was added dropwise, resulting in a color change to yellowish brown. The mixture was stirred at −78 °C for 10 min, and then a solution of 1-(6-(1,1-dipyridin-2-yl)ethyl)pyridin-2-yl)ethan-1-one (0.224 M in tetrahydrofuran, 40.0 mL, 2.0 g, 8.96 mmol, 1.0 equiv) was added dropwise; the solution's color slowly changed to a very dark green. The reaction was stirred at −78 °C for 40 min; then, 50 mL methanol was added slowly to quench the reaction. The mixture was allowed to warm to room temperature, 100 mL of aqueous hydrochloric acid (3 M) was added, and the organic solvents were removed via rotary evaporation (90 mbar at 40 °C). The mixture was transferred to a separatory funnel. Additional 10 mL of aqueous hydrochloric acid (3 M) was added, and the mixture was washed with dichloromethane (2 × 25 mL); this organic layer was discarded. The aqueous layer was basified to pH 12 with an aqueous solution of sodium hydroxide (19 M) and extracted with dichloromethane (3 × 100 mL). These combined organic layers were dried over anhydrous magnesium sulfate, and the solvents were removed in vacuo to yield the crude product. Recrystallization at room temperature from acetone/diethyl ether gave pure product **2** as a colorless crystalline solid in 67% yield (1.74 g). R_F = 0.13 (silica, UV, 10% triethyl amine, 50% ethyl acetate, 40% hexanes). **^{1}H NMR** (400.0 MHz, $CDCl_3$, 295 K): δ = 8.75 (ddd, *J* = 4.7 Hz, *J* = 1.7 Hz, *J* = 0.9 Hz, 2H), 8.31 (d, *J* = 8.0 Hz, 2H), 8.19 (dt, *J* = 7.9 Hz, *J* = 1.1 Hz, 2H), 8.11 (dd, *J* = 8.2 Hz, *J* = 7.4 Hz, 1H), 7.79 (td, *J* = 7.8 Hz, *J* = 1.8 Hz, 2H), 7.45 (ddd, *J* = 7.6 Hz, *J* = 4.7 Hz, *J* = 1.2 Hz, 2H) ppm. NMR data are in accordance with the literature.[2] **HR–MS** (ESI): Calculated for $C_{17}H_{12}N_3O_2$ $[M + H]^+$: 290.09295 *m/z*; Found: 290.09271 *m/z*.

Synthesis of L2. According to a modified literature procedure,[2] a flame-dried flask was charged with 2-bromo pyridine (0.36 mL, 0.58 g, 3.66 mmol, 2.12 equiv), and 80 mL of absolute tetrahydrofuran was added. After the mixture was cooled to −78 °C, a solution of *n*-butyl lithium (2.5 M in hexanes, 1.49 mL, 0.24 g, 3.72 mmol, 2.15 equiv) was added dropwise, resulting in a color change to yellowish brown. The mixture was stirred at −78 °C for 10 min, and then a solution of **2** (57.5 mM in tetrahydrofuran/1,4-dioxane (4:1), 30.0 mL, 0.5 g, 1.73 mmol, 1.0 equiv) was added dropwise, and the solution's color changed first to red and then to a very dark green. The reaction was stirred at −78 °C for 60 min, then allowed to warm to room temperature. When LC–MS confirmed complete consumption of **2**, 50 mL of methanol was added slowly to quench the reaction. Then, 100 mL of aqueous hydrochloric acid (3 M) was added, the organic solvents were removed via rotary evaporation (90 mbar @ 40 °C), and the mixture was transferred to a separatory funnel. An additional 10 mL of aqueous hydrochloric acid (3 M) was added, and the mixture was washed with dichloromethane (2 × 25 mL); this organic layer was discarded. The aqueous layer was basified to pH 12 with an aqueous solution of sodium hydroxide (19 M) and extracted with dichloromethane (3 × 100 mL). These combined organic layers were dried over anhydrous magnesium sulfate, and the solvents were removed in vacuo to yield the crude product. Recrystallization at room temperature from acetone/diethyl ether gave the pure product **L2** as a colorless solid in a 38% yield (290.0 mg). R_F = 0.04 (silica, UV, 10% methanol, 90% dichloromethane) **^{1}H NMR** (400.0 MHz, $CDCl_3$, 295 K): δ = 8.49 (ddd, *J* = 4.9 Hz, *J* = 1.8 Hz, *J* = 1.0 Hz, 4H), 7.73–7.71 (m, 3H), 7.52 (ddd, *J* = 8.0 Hz, *J* = 7.3 Hz, *J* = 1.8 Hz, 4H), 7.44 (dt, *J* = 8.0 Hz, *J* = 1.1 Hz, 4H), 7.17–7.13 (m, 6H) ppm. NMR data are in accordance with the literature.[2] **HR–MS (ESI)**: Calculated for $C_{27}H_{22}N_5O_2$ $[M + H]^+$: 448.17735 *m/z*; Found: 448.17693 *m/z*.

Synthesis of $[Fe^{II}\mathbf{L2}(MeCN)](OTf)_2$. According to a modified literature procedure,[8,9] ligand **L2** (51.0 mg, 0.114 mmol, 1.0 equiv) was dissolved in 2.55 mL of acetonitrile. Iron(II)bis(acetonitrile)bis-(triflate) (49.7 mg, 0.114 mmol, 1.0 equiv) was added as a solid, turning the solution deep red. The mixture was then stirred for an additional 5 min, and then diethyl ether was diffused into the solution under ambient conditions to give the product $[Fe^{II}\mathbf{L2}(MeCN)](OTf)_2 \times H_2O$ as brown crystals in 77% yield (80.0 mg). **^{1}H NMR** (400.0 MHz, CD_3CN, 295 K): δ = 9.73 (d, *J* = 5.8 Hz, 4H, H_{Py}), 8.17 (m, 5H, H_{Py}/H-2/H-3), 7.98 (ddd, *J* = 8.1 Hz, *J* = 7.4 Hz, *J* = 1.4 Hz, 4H, H_{Py}), 7.56 (ddd, *J* = 7.4 Hz, *J* = 5.8 Hz, *J* = 1.5 Hz, 4H, H_{Py}), 6.85 (s, 2H, O*H*), 1.96 (s, 3H, CH_3CN) ppm. **^{13}C NMR** (100.0 MHz, CD_3CN, 295 K): δ = 164.5 ($C_{Py\text{-}quart}$), 163.1 (C-1), 158.1 (C_{Py}), 140.7 (C-2), 140.0 (C_{Py}), 124.9 (C_{Py}), 122.4 (C_{Py}), 121.0 (C-3), 80.7 (C-4) ppm. **HR–MS (ESI)**: Calculated for $C_{30}H_{25}F_3FeN_5O_3S$ $[Fe\mathbf{L2}(OTf)]^+$: 652.05649 *m/z*; Found: 652.05432 *m/z*. **Elemental Analysis**: Calculated for $C_{33}H_{30}F_6FeN_6O_7S_2$ $([Fe^{II}\mathbf{L2}(MeCN)](OTf)_2 \times H_2O)$: C 43.27, H 3.05, N 9.77, S 7.45. Found: C 43.25, H 3.12, N 9.79, S 7.91. **IR (thin film)**: $\nu\sim$ = 3288, 1738, 1603, 1469, 1444, 1373, 1276, 1244, 1224, 1157, 1096, 1028, 887, 800, 762, 712, 661 cm^{-1}. **UV–vis-NIR (MeCN)**: λ = 347 nm (ε = 5315 l mol^{-1} cm^{-1}); λ = 420 nm (ε = 5415 l mol^{-1} cm^{-1}).

Synthesis of $[Fe^{III}\mathbf{L2}(OH)](OTf)_2$. A scintillation vial was charged with finely ground **L2** (200.0 mg, 0.447 mmol, 1.0 equiv) and 1.1 mL of water. Iron(III) triflate (247.3 mg, 0.492 mmol, 1.1 equiv) was added, and the suspension was mixed by pumping of an Eppendorf pipet. The mixture was sonicated for 60 s, shaken, and again sonicated for 60 s, resulting in a dark red suspension. The mixture was then syringe-filtered (PTFE, 0.45 μm) to give a clear red-orange solution. This was placed in a fridge at 4 °C for 3 days until dark red crystals had formed. The supernatant was removed, and the crystals were washed with water (2 × 0.5 mL, brief sonication) and subsequently dried in vacuo to give the pure product $[Fe^{III}\mathbf{L2}(OH)](OTf)_2$ as brown crystals (67%). **HR–MS** (EI): Calculated for $C_{27}H_{22}FeN_5O_3$ $[Fe\mathbf{L2}(OH)]^{2+}$: 260.0536 *m/z*; Found: 260.0548 *m/z*. **Elemental Analysis**: Calculated for $C_{29}H_{24}F_6FeN_5O_{10}S_2$ $[Fe\mathbf{L2}(OH)](OTf)_2 \times H_2O$: C 41.64, H 2.89, N 8.37, S 7.67. Found: C 41.71, H 2.92, N 8.24, S 7.94. **IR (thin film)**: $\nu\sim$ = 3450, 3264, 1739, 1604, 1458, 1445, 1364, 1278, 1243, 1222, 1152, 1097, 1027, 927, 810, 795, 766, 741, 675, 662 cm^{-1}.

Synthesis of $[Fe^{IV}\mathbf{L2}(O)][Ce(NO_3)_6]$. According to a modified literature procedure,[8,9] $[Fe^{II}\mathbf{L2}(MeCN)](OTf)_2$ (80 mg, 0.950 mmol, 1.0 equiv) was dissolved in 1.2 mL of 3:1 acetonitrile:water. Cerium(IV) ammonium nitrate (276.4 mg, 0.504 mmol, 5.3 equiv) was added as a solid, and the mixture was sonicated for 60 s. As a pale green precipitate began to form, the reaction mixture was placed in the refrigerator at 4 °C to complete the precipitation. The solid was collected via centrifugation (600 rpm), washed with 10.5 mL of ice cold 3:1 acetonitrile: water, and dried in vacuo to yield product

https://doi.org/10.1021/acs.inorgchem.4c04518
Inorg. Chem. 2025, 64, 3719−3734

$[Fe^{IV}L2(O)][Ce(NO_3)_6]$ as a pale green solid (89%). **Elemental Analysis**: Calculated for $C_{27}H_{23}CeFeN_{11}O_{22}$ ($[Fe^{IV}L2(O)][Ce(NO_3)_6] \times H_2O$): C 30.90, H 2.21, N 14.68. Found: C 30.71, H 2.54, N 15.05. **HR−MS** (ESI): Calculated for $C_{27}H_{21}FeN_5O_3$ $[Fe^{IV}L2(O)]^{2+}$: 259.5497 *m/z*; Found: 259.5492 *m/z*. **IR (thin film)**: $\nu\sim$ = 1605, 1504, 1463, 1278, 1170, 1098, 1029, 830, 805, 780, 763, 742, 661, 626, 614 cm^{-1}. **UV−vis-NIR (H_2O)**: λ = 720 nm (ε = 292 l mol^{-1} cm^{-1}).

Reaction Rate Determination via UV−Vis−NIR Spectroscopy. Benzyl alcohol, benzaldehyde, and ethylbenzenesulfonic acid were used as substrates. An aqueous solution of $[Fe^{IV}L1(O)]^{2+}$ or $[Fe^{IV}L2(O)]^{2+}$ (25 μL, 10 mM, 1 equiv) was diluted with water (450 μL), and this mixture was added to a 500 μL cuvette with an aqueous solution of the substrate (25 μL, 10 mM, 1 equiv). Measurements were started immediately after addition, and spectra were recorded over a time period of 15 min. The method of initial rates was applied to calculate the reaction rate constants. The obtained absorption values were converted to concentrations using the Lambert−Beer Law. The therefore needed extinction coefficient was obtained by recording UV−vis−NIR spectra of the complexes in different concentrations and applying linear regression on a plot of absorbance against concentration (ε = 277.2 L mol^{-1} cm^{-1} for $[Fe^{IV}L1(O)]^{2+}$ and ε = 291.6 L mol^{-1} cm^{-1} for $[Fe^{IV}L2(O)]^{2+}$). Reaction rates were obtained by linear regression of the decreasing concentrations and transformed into rate constants. For results, refer to Table S2, p 7.

Product Identification via ^{1}H NMR Spectroscopy−BnOH and PhCHO. All aqueous solutions were prepared in deuterated water. Benzyl alcohol and benzaldehyde were used as substrates. A solution of the substrate in deuterated water (400 μL, 10 mM, 1 equiv) was mixed with a solution of $[Fe^{IV}L1(O)]^{2+}$ or $[Fe^{IV}L2(O)]^{2+}$ in deuterated water (400 μL, 10 mM, 1 equiv) and reacted for 30 min at 25 °C. A solution of deuterated hydrochloric acid in deuterated water (400 μL, 2 mM) was added, and the reaction solution was extracted with deuterated chloroform (2 × 400 μL). The combined organic phases were transferred into an NMR tube, and a ^{1}H NMR spectrum was recorded.

Product Identification via ^{1}H NMR Spectroscopy−EBS. A solution of ethylbenzylsulfonic acid (EBS) in deuterated water (500 μL, 10 mM, 1 equiv) was mixed with a solution of $[Fe^{IV}L1(O)]^{2+}$ or $[Fe^{IV}L2(O)]^{2+}$ in deuterated water (500 μL, 10 mM, 1 equiv) and reacted for 30 min at 25 °C. The reaction mixture was filtered over silica (1 mL syringe equipped with cotton and silica filled to the 0.5 mL mark). The colorless filtrate was transferred into an NMR tube, and a ^{1}H NMR spectrum recorded.

■ ASSOCIATED CONTENT

Supporting Information

The Supporting Information is available free of charge at https://pubs.acs.org/doi/10.1021/acs.inorgchem.4c04518.

General methods and materials, synthetic procedures, additional ^{1}H and ^{13}C NMR spectra, UV−vis-NIR spectra, cyclic voltammograms, stopped-flow UV−vis data (CSV), cryo UHR−MS spectra, LC−MS data, Mössbauer spectra, crystallographic information, and EPR spectra (TXT, DSC, and DTA) (PDF)

Raw data excluding mass spectrometry (ZIP)

Cryo high resolution mass spectrometry (ZIP)

Accession Codes

Deposition Numbers 2314071, 2314072, and 2320855 contain the supplementary crystallographic data for this paper. These data can be obtained free of charge via the joint Cambridge Crystallographic Data Centre (CCDC) and Fachinformationszentrum Karlsruhe Access Structures service.

■ AUTHOR INFORMATION

Corresponding Author

Lena J. Daumann − *Department of Chemistry, Ludwig-Maximilians-University Munich, 81377 München, Germany; Mathematisch Naturwissenschaftliche Fakultät, Lehrstuhl für Bioanorganische Chemie, Heinrich-Heine-Universität, 40225 Düsseldorf, Germany;* orcid.org/0000-0003-2197-136X; Email: lena.daumann@hhu.de

Authors

Niko S. W. Lindlar né Jonasson − *Department of Chemistry, Ludwig-Maximilians-University Munich, 81377 München, Germany; Department of Chemistry, University of Zurich, 8057 Zurich, Switzerland;* orcid.org/0000-0002-6034-6164

Annika Menke − *Department of Chemistry, Ludwig-Maximilians-University Munich, 81377 München, Germany*

Laura Senft − *Department of Chemistry, Ludwig-Maximilians-University Munich, 81377 München, Germany*

Andrea Squarcina − *Department of Chemistry, Ludwig-Maximilians-University Munich, 81377 München, Germany;* orcid.org/0000-0003-1770-586X

David Schmidl − *Department of Chemistry, Ludwig-Maximilians-University Munich, 81377 München, Germany; Department of Chemical and Pharmaceutical Sciences, London Metropolitan University, London N7 8DB, U.K.;* Present Address: Department of Chemistry, University of Cambridge, Lensfield Road, Cambridge CB2 1EW, U.K

Katherine Fisher − *Department of Chemistry, Ludwig-Maximilians-University Munich, 81377 München, Germany; Department of Chemical and Pharmaceutical Sciences, London Metropolitan University, London N7 8DB, U.K.;* orcid.org/0000-0002-2716-561X

Serhiy Demeshko − *Institute of Inorganic Chemistry, Georg-August-Universität Göttingen, 37077 Göttingen, Germany*

Jan C. Kruse − *Institute of Inorganic Chemistry, Georg-August-Universität Göttingen, 37077 Göttingen, Germany;* orcid.org/0009-0003-5564-8090

Thomas Josephy − *Institute of Inorganic Chemistry, Ruprecht-Karls-Universität Heidelberg, 69120 Heidelberg, Germany*

Peter Mayer − *Department of Chemistry, Ludwig-Maximilians-University Munich, 81377 München, Germany*

Jonathan Gutenthaler-Tietze − *Department of Chemistry, Ludwig-Maximilians-University Munich, 81377 München, Germany*

Peter Comba − *Institute of Inorganic Chemistry, Ruprecht-Karls-Universität Heidelberg, 69120 Heidelberg, Germany;* orcid.org/0000-0001-7796-3532

Franc Meyer − *Institute of Inorganic Chemistry, Georg-August-Universität Göttingen, 37077 Göttingen, Germany;* orcid.org/0000-0002-8613-7862

Ivana Ivanović-Burmazović − *Department of Chemistry, Ludwig-Maximilians-University Munich, 81377 München, Germany*

Complete contact information is available at: https://pubs.acs.org/10.1021/acs.inorgchem.4c04518

Author Contributions

The manuscript was written through contributions of all authors. All authors have given approval to the final version of the manuscript. N.S.W.L. and A.M. developed the project, accomplished the synthetic work, performed the UV−vis-NIR experiments, and wrote the manuscript. L.S. carried out the

UHR−MS measurements as well as simulations thereof, supervised by I.I.-B. A.S. performed cyclic voltammetry investigations and interpretations, supervised by I.I.-B. D.S. was involved in the discovery of the comproportionation reaction and contributed in the synthesis and crystallization of $[Fe^{III}\mathbf{L1}(OH)]^{2+}$. K.F. simulated the EPR spectra. SD and J.C.K. performed the Mössbauer measurements and J.C.K. accomplished cyclic voltammetry investigations and interpretation concerning the pourbaix diagram, supervised by F.M., T.J. carried out stopped-flow UV−vis-NIR measurements, supervised by P.C., P.M. and J. G.-T. performed the X-ray measurements and solution of the crystal structures. L.J.D. coordinated and supervised the whole project. N.S.W.L. and A.M. contributed equally to this work.

Funding

This work was funded by the Deutsche Forschungsgemeinschaft (DFG, German Research Foundation)−SFB 1309-325871075 and FOR 5215 in the framework of the Research Unit "Bioinspired Oxidation Catalysis with Iron Complexes" (BioOxCat). N.S.W.L. thankfully acknowledges support by the Studienstiftung des deutschen Volkes and the Joachim-Herz-Foundation. J.C.K. acknowledges support by the Fonds der Chemischen Industrie (Kekulé fellowship).

Notes

The authors declare no competing financial interest.

■ ACKNOWLEDGMENTS

A.M. thanks Jan Prohaska and Sophie Falkai for their work in this project. N.S.W.L. wishes to thank Katharina Scholz and Hannah Wilken for their help in this project.

■ REFERENCES

(1) Goldsmith, C. R.; Jonas, R. T.; Stack, T. D. P. C-H bond activation by a ferric methoxide complex: modeling the rate-determining step in the mechanism of lipoxygenase. *J. Am. Chem. Soc.* **2002**, *124* (1), 83−96.

(2) Goldsmith, C. R.; Stack, T. D. P. Hydrogen atom abstraction by a mononuclear ferric hydroxide complex: insights into the reactivity of lipoxygenase. *Inorg. Chem.* **2006**, *45* (15), 6048−6055.

(3) Das, B.; Orthaber, A.; Ott, S.; Thapper, A. Iron Pentapyridyl Complexes as Molecular Water Oxidation Catalysts: Strong Influence of a Chloride Ligand and pH in Altering the Mechanism. *ChemSusChem* **2016**, *9* (10), 1178−1186.

(4) Gupta, R.; Borovik, A. S. Monomeric Mn III/II and Fe III/II Complexes with Terminal Hydroxo and Oxo Ligands: Probing Reactivity via O−H Bond Dissociation Energies. *J. Am. Chem. Soc.* **2003**, *125* (43), 13234−13242.

(5) Mukherjee, J.; Lucas, R. L.; Zart, M. K.; Powell, D. R.; Day, V. W.; Borovik, A. S. Synthesis, structure, and physical properties for a series of monomeric iron(III) hydroxo complexes with varying hydrogen-bond networks. *Inorg. Chem.* **2008**, *47* (13), 5780−5786.

(6) Drummond, M. J.; Ford, C. L.; Gray, D. L.; Popescu, C. V.; Fout, A. R. Radical Rebound Hydroxylation Versus H-Atom Transfer in Non-Heme Iron(III)-Hydroxo Complexes: Reactivity and Structural Differentiation. *J. Am. Chem. Soc.* **2019**, *141* (16), 6639−6650.

(7) Ching, W.-M.; Zhou, A.; Klein, J. E. M. N.; Fan, R.; Knizia, G.; Cramer, C. J.; Guo, Y.; Que, L. Characterization of the Fleeting Hydroxoiron(III) Complex of the Pentadentate TMC-py Ligand. *Inorg. Chem.* **2017**, *56* (18), 11129−11140.

(8) Chantarojsiri, T.; Sun, Y.; Long, J. R.; Chang, C. J. Water-Soluble Iron(IV)-Oxo Complexes Supported by Pentapyridine Ligands: Axial Ligand Effects on Hydrogen Atom and Oxygen Atom Transfer Reactivity. *Inorg. Chem.* **2015**, *54* (12), 5879−5887.

(9) Jonasson, N. S. W.; Daumann, L. J. 5-Methylcytosine is Oxidized to the Natural Metabolites of TET Enzymes by a Biomimetic Iron(IV)-Oxo Complex. *Chem.—Eur. J.* **2019**, *25* (52), 12091−12097.

(10) Schmidl, D.; Jonasson, N. S. W.; Korytiaková, E.; Carell, T.; Daumann, L. J. Biomimetic Iron Complex Achieves TET Enzyme Reactivity*. *Angew. Chem., Int. Ed.* **2021**, *60* (39), 21457−21463.

(11) Jonasson, N. S. W.; Janßen, R.; Menke, A.; Zott, F. L.; Zipse, H.; Daumann, L. J. TET-Like Oxidation in 5-Methylcytosine and Derivatives: A Computational and Experimental Study. *ChemBioChem.* **2021**, *22* (23), 3333−3340.

(12) Puri, M.; Que, L. Toward the synthesis of more reactive S = 2 non-heme oxoiron(IV) complexes. *Acc. Chem. Res.* **2015**, *48* (8), 2443−2452.

(13) Rasheed, W.; Fan, R.; Abelson, C. S.; Peterson, P. O.; Ching, W.-M.; Guo, Y.; Que, L. Structural implications of the paramagnetically shifted NMR signals from pyridine H atoms on synthetic nonheme FeIV = O complexes. *J. Biol. Inorg. Chem.* **2019**, *24* (4), 533−545.

(14) Abu-Odeh, M.; Bleher, K.; Johnee Britto, N.; Comba, P.; Gast, M.; Jaccob, M.; Kerscher, M.; Krieg, S.; Kurth, M. Pathways of the Extremely Reactive Iron(IV)-oxido complexes with Tetradentate Bispidine Ligands. *Chemistry−A. European Journal* **2021**, *27* (44), 11377−11390.

(15) Pistorius, E. K.; Axelrod, B. Iron, an Essential Component of Lipoxygenase. *J. Biol. Chem.* **1974**, *249* (10), 3183−3186.

(16) *Active Oxygen in Biochemistry*; Valentine, J. S.; Foote, C. S.; Greenberg, A.; Liebman, J. F., Eds.; Springer US, 1995.

(17) Andreou, A.; Feussner, I. Lipoxygenases - Structure and reaction mechanism. *Phytochemistry* **2009**, *70* (13−14), 1504−1510.

(18) Gaffney, B. J. EPR Spectroscopic Studies of Lipoxygenases. *Chem.—Asian J.* **2020**, *15* (1), 42−50.

(19) Schilstra, M. J.; Veldink, G. A.; Vliegenthart, J. F. The dioxygenation rate in lipoxygenase catalysis is determined by the amount of iron (III) lipoxygenase in solution. *Biochem.* **1994**, *33* (13), 3974−3979.

(20) Price, J. C.; Barr, E. W.; Glass, T. E.; Krebs, C.; Bollinger, J. M. Evidence for hydrogen abstraction from C1 of taurine by the high-spin Fe(IV) intermediate detected during oxygen activation by taurine:alpha-ketoglutarate dioxygenase (TauD). *J. Am. Chem. Soc.* **2003**, *125* (43), 13008−13009.

(21) Price, J. C.; Barr, E. W.; Tirupati, B.; Bollinger, J. M.; Krebs, C. The first direct characterization of a high-valent iron intermediate in the reaction of an alpha-ketoglutarate-dependent dioxygenase: a high-spin FeIV complex in taurine/alpha-ketoglutarate dioxygenase (TauD) from Escherichia coli. *Biochemistry* **2003**, *42* (24), 7497−7508.

(22) Proshlyakov, D. A.; Henshaw, T. F.; Monterosso, G. R.; Ryle, M. J.; Hausinger, R. P. Direct detection of oxygen intermediates in the non-heme Fe enzyme taurine/alpha-ketoglutarate dioxygenase. *J. Am. Chem. Soc.* **2004**, *126* (4), 1022−1023.

(23) Price, J. C.; Barr, E. W.; Hoffart, L. M.; Krebs, C.; Bollinger, J. M. Kinetic dissection of the catalytic mechanism of taurine:alpha-ketoglutarate dioxygenase (TauD) from Escherichia coli. *Biochem.* **2005**, *44* (22), 8138−8147.

(24) Matsui, K. Green leaf volatiles: hydroperoxide lyase pathway of oxylipin metabolism. *Curr. Opin. Plant Biol.* **2006**, *9* (3), 274−280.

(25) Jasniewski, A. J.; Que, L. Dioxygen Activation by Nonheme Diiron Enzymes: Diverse Dioxygen Adducts, High-Valent Intermediates, and Related Model Complexes. *Chem. Rev.* **2018**, *118* (5), 2554−2592.

(26) Krebs, C.; Price, J. C.; Baldwin, J.; Saleh, L.; Green, M. T.; Bollinger, J. M. Rapid freeze-quench 57Fe Mössbauer spectroscopy: monitoring changes of an iron-containing active site during a biochemical reaction. *Inorg. Chem.* **2005**, *44* (4), 742−757.

(27) Islam, M. S.; Leissing, T. M.; Chowdhury, R.; Hopkinson, R. J.; Schofield, C. J. 2-Oxoglutarate-Dependent Oxygenases. *Annu. Rev. Biochem.* **2018**, *87*, 585−620.

(28) Tagliapietra, M.; Squarcina, A.; Hickey, N.; De Zorzi, R.; Geremia, S.; Sartorel, A.; Bonchio, M. Hydrogen Evolution by FeIII Molecular Electrocatalysts Interconverting between Mono and Di-

https://doi.org/10.1021/acs.inorgchem.4c04518
Inorg. Chem. 2025, 64, 3719−3734

Nuclear Structures in Aqueous Phase. *ChemSusChem* **2017**, *10* (22), 4430−4435.
(29) Ghosh, S. K.; Rath, S. P. A remarkably bent diiron(III)-μ-hydroxo bisporphyrin: unusual stabilization of two spin states of iron in a single molecular framework. *J. Am. Chem. Soc.* **2010**, *132* (51), 17983−17985.
(30) Tanase, S.; Bouwman, E.; Long, G. J.; Shahin, A. M.; Mills, A. M.; Spek, A. L.; Reedijk, J. Acid-Base Self-Assembly Chemistry and Hydrogen Bonding Interactions Resulting in the Formation of a Tetranuclear Aggregate Containing Four Crystallographically Non-Equivalent Fe III Centers. *Eur. J. Inorg. Chem.* **2004**, *2004* (23), 4572−4578.
(31) Cordes Née Kupper, C.; Morganti, M.; Klawitter, I.; Schremmer, C.; Dechert, S.; Meyer, F. Disproportionation Equilibrium of a μ-Oxodiiron(III) Complex Giving Rise to C-H Activation Reactivity: Structural Snapshot of a Unique Oxoiron(IV) Adduct. *Angew. Chem., Int. Ed.* **2019**, *58* (32), 10855−10858.
(32) Minor, W.; Steczko, J.; Stec, B.; Otwinowski, Z.; Bolin, J. T.; Walter, R.; Axelrod, B. Crystal structure of soybean lipoxygenase L-1 at 1.4 A resolution. *Biochem.* **1996**, *35* (33), 10687−10701.
(33) Cho, K.-B.; Wu, X.; Lee, Y.-M.; Kwon, Y. H.; Shaik, S.; Nam, W. Evidence for an alternative to the oxygen rebound mechanism in C-H bond activation by non-heme Fe(IV)O complexes. *J. Am. Chem. Soc.* **2012**, *134* (50), 20222−20225.
(34) Horn, A.; Vencato, I.; Bortoluzzi, A. J.; Hörner, R.; Silva, R. A. N.; Spoganicz, B.; Drago, V.; Terenzi, H.; de Oliveira, M. C. B.; Werner, R.; Haase, W.; Neves, A. Synthesis, crystal structure and properties of dinuclear iron(III) complexes containing terminally coordinated phenolate/H_2O/OH−groups as models for purple acid phosphatases: efficient hydrolytic DNA cleavage. *Inorg. Chim. Acta* **2005**, *358* (2), 339−351.
(35) Bernhardt, P. V.; Bosch, S.; Comba, P.; Gahan, L. R.; Hanson, G. R.; Mereacre, V.; Noble, C. J.; Powell, A. K.; Schenk, G.; Wadepohl, H. An Approach to More Accurate Model Systems for Purple Acid Phosphatases (PAPs). *Inorg. Chem.* **2015**, *54* (15), 7249−7263.
(36) Zimmermann, T. P.; Limpke, T.; Orth, N.; Franke, A.; Stammler, A.; Bögge, H.; Walleck, S.; Ivanovic-Burmazovic, I.; Glaser, T. Two Unsupported Terminal Hydroxido Ligands in a μ-Oxo-Bridged Ferric Dimer: Protonation and Kinetic Lability Studies. *Inorg. Chem.* **2018**, *57* (16), 10457−10468.
(37) Kripli, B.; Sólyom, B.; Speier, G.; Kaizer, J. Stability and Catalase-Like Activity of a Mononuclear Non-Heme Oxoiron(IV) Complex in Aqueous Solution. *Molecules* **2019**, *24* (18), 3236.
(38) Yeh, C.-C. G.; Hörner, G.; de Visser, S. P. Computational Study on O−O Bond Formation on a Mononuclear Non-Heme Iron Center. *Eur. J. Inorg. Chem.* **2020**, *2020* (27), 2573−2581.
(39) Rohde, J.; In, J.; Lim, M. H.; Brennessel, W. W.; Bukowski, M. R.; Stubna, A.; Münck, E.; Nam, W.; Que, L. Crystallographic and Spectroscopic Characterization of a Nonheme Fe(IV)═O Complex. *Science* **2003**, *299*, 1037−1039.
(40) Yadav, V.; Gordon, J. B.; Siegler, M. A.; Goldberg, D. P. Dioxygen-Derived Nonheme Mononuclear FeIII(OH) Complex and Its Reactivity with Carbon Radicals. *J. Am. Chem. Soc.* **2019**, *141* (26), 10148−10153.
(41) Ogo, S.; Wada, S.; Watanabe, Y.; Iwase, M.; Wada, A.; Harata, M.; Jitsukawa, K.; Masuda, H.; Einaga, H. Synthesis, Structure, and Spectroscopic Properties of [Feiii(tnpa)(OH)(PhCOO)]ClO4: A Model Complex for an Active Form of Soybean Lipoxygenase-1. *Angew. Chem., Int. Ed.* **1998**, *37* (15), 2102−2104.
(42) Ogo, S.; Yamahara, R.; Roach, M.; Suenobu, T.; Aki, M.; Ogura, T.; Kitagawa, T.; Masuda, H.; Fukuzumi, S.; Watanabe, Y. Structural and spectroscopic features of a cis (hydroxo)-Fe(III)-(carboxylato) configuration as an active site model for lipoxygenases. *Inorg. Chem.* **2002**, *41* (21), 5513−5520.
(43) Sahu, S.; Quesne, M. G.; Davies, C. G.; Dürr, M.; Ivanović-Burmazović, I.; Siegler, M. A.; Jameson, G. N. L.; de Visser, S. P.; Goldberg, D. P. Direct observation of a nonheme iron(IV)-oxo complex that mediates aromatic C-F hydroxylation. *J. Am. Chem. Soc.* **2014**, *136* (39), 13542−13545.
(44) England, J.; Martinho, M.; Farquhar, E. R.; Frisch, J. R.; Bominaar, E. L.; Münck, E.; Que, L. A synthetic high-spin oxoiron(IV) complex: generation, spectroscopic characterization, and reactivity. *Angew. Chem., Int. Ed.* **2009**, *48* (20), 3622−3626.
(45) England, J.; Guo, Y.; van Heuvelen, K. M.; Cranswick, M. A.; Rohde, G. T.; Bominaar, E. L.; Münck, E.; Que, L. A more reactive trigonal-bipyramidal high-spin oxoiron(IV) complex with a cis-labile site. *J. Am. Chem. Soc.* **2011**, *133* (31), 11880−11883.
(46) Gupta, R.; Lacy, D. C.; Bominaar, E. L.; Borovik, A. S.; Hendrich, M. P. Electron paramagnetic resonance and Mössbauer spectroscopy and density functional theory analysis of a high-spin Fe(IV)-oxo complex. *J. Am. Chem. Soc.* **2012**, *134* (23), 9775−9784.
(47) Boniolo, M.; Hossain, M. K.; Chernev, P.; Suremann, N. F.; Heizmann, P. A.; Lyvik, A. S. L.; Beyer, P.; Haumann, M.; Huang, P.; Salhi, N.; Cheah, M. H.; Shylin, S. I.; Lundberg, M.; Thapper, A.; Messinger, J. Water Oxidation by Pentapyridyl Base Metal Complexes? A Case Study. *Inorg. Chem.* **2022**, *61* (24), 9104−9118.
(48) Boniolo, M.; Chernev, P.; Cheah, M. H.; Heizmann, P. A.; Huang, P.; Shylin, S. I.; Salhi, N.; Hossain, M. K.; Gupta, A. K.; Messinger, J.; Thapper, A.; Lundberg, M. Electronic and geometric structure effects on one-electron oxidation of first-row transition metals in the same ligand framework. *Dalton Trans.* **2021**, *50* (2), 660−674.
(49) Elgrishi, N.; Rountree, K. J.; McCarthy, B. D.; Rountree, E. S.; Eisenhart, T. T.; Dempsey, J. L. A Practical Beginner's Guide to Cyclic Voltammetry. *J. Chem. Educ.* **2018**, *95* (2), 197−206.
(50) Jonas, R. T.; Stack, T. D. P. C−H Bond Activation by a Ferric Methoxide Complex: A Model for the Rate-Determining Step in the Mechanism of Lipoxygenase. *J. Am. Chem. Soc.* **1997**, *119* (36), 8566−8567.
(51) Hu, L.; Lu, J.; Cheng, J.; Rao, Q.; Li, Z.; Hou, H.; Lou, Z.; Zhang, L.; Li, W.; Gong, W.; Liu, M.; Sun, C.; Yin, X.; Li, J.; Tan, X.; Wang, P.; Wang, Y.; Fang, D.; Cui, Q.; Yang, P.; He, C.; Jiang, H.; Luo, C.; Xu, Y. Structural insight into substrate preference for TET-mediated oxidation. *Nature* **2015**, *527* (7576), 118−122.
(52) Hanauske-Abel, H. M.; Günzler, V. A stereochemical concept for the catalytic mechanism of prolylhydroxylase: applicability to classification and design of inhibitors. *J. Theor. Biol.* **1982**, *94* (2), 421−455.
(53) Rana, S.; Dey, A.; Maiti, D. Mechanistic elucidation of C-H oxidation by electron rich non-heme iron(IV)-oxo at room temperature. *Chem. Commun.* **2015**, *51* (77), 14469−14472.
(54) Xie, J.; Lo, P.-K.; Lam, C.-S.; Lau, K.-C.; Lau, T.-C. A hydrogen-atom transfer mechanism in the oxidation of alcohols by FeO42- in aqueous solution. *Dalton Trans.* **2018**, *47* (1), 240−245.
(55) Pelucchi, M.; Cavallotti, C.; Cuoci, A.; Faravelli, T.; Frassoldati, A.; Ranzi, E. Detailed kinetics of substituted phenolic species in pyrolysis bio-oils. *React. Chem. Eng.* **2019**, *4* (3), 490−506.
(56) Wegeberg, C.; de Aguirre, A.; Maseras, F.; McKenzie, C. J. Photosynthesis of a Dihydroimidazopyridine Chelate Shines Light on the Reactions of a Photoactivated Iron(III) Complex with O_2. *Inorg. Chem.* **2020**, *59* (22), 16281−16290.
(57) Cong, J.; Kinschel, D.; Daniel, Q.; Safdari, M.; Gabrielsson, E.; Chen, H.; Svensson, P. H.; Sun, L.; Kloo, L. Bis(1,1-bis(2-pyridyl)ethane)copper(i/ii) as an efficient redox couple for liquid dye-sensitized solar cells. *J. Mater. Chem. A* **2016**, *4* (38), 14550−14554.

1.2 Synthesis and Characterization of Complexes with Ligand System L3

To expand the library of iron complexes, a third ligand (**L3**) was introduced bearing a hydrogen at the methine group. The synthesis of this ligand has previously been published in 2004 by Dyker and coworkers[202] and recently again by Wang *et al.*.[203] However, to the best of our knowledge, no metal complex has been reported with this ligand so far.

Ligand synthesis

For the synthesis of **L3**, the pathway proposed by Dyker and coworkers[202] was chosen, which is depicted with slight modifications in Scheme 20.

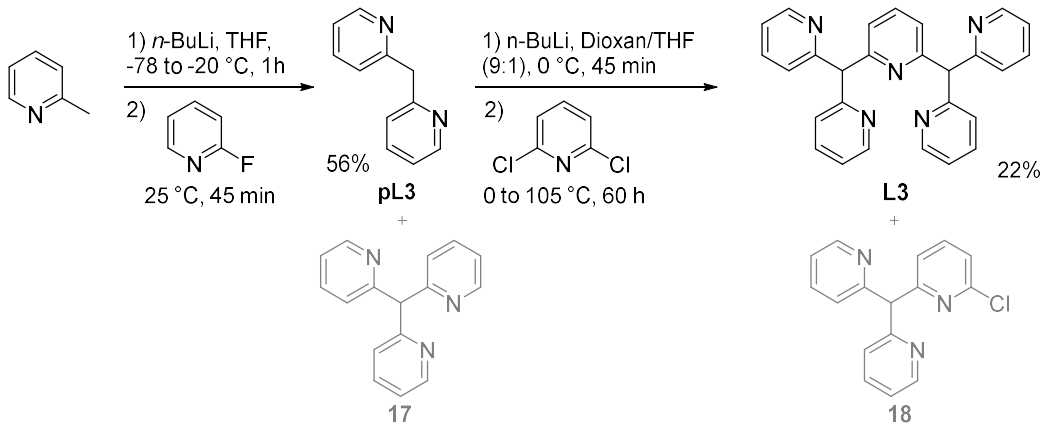

Scheme 20: Synthetic pathway towards ligand **L3** after a modified procedure presented by Dyker and coworkers.[202]

According to the literature, 2-fluoropyridine is added to lithiated 2-methylpyridine at -20 °C in the first synthesis step and the reaction mixture is refluxed.[202] However, it was found that under these conditions a mixture of the desired ligand precursor **pL3** and the side product **17** formed. **17** was isolated from the mixture and characterized with NMR spectroscopy as well as low-resolution mass spectrometry. Unfortunately, it was challenging to isolate pure **pL3** from the mixture as the solid **17** is readily soluble in **pL3** (oil) and separation by flash column chromatography is challenging. Pure **pL3** was obtained by adapting the reaction conditions. The reaction temperature was decreased from reflux to room temperature and the reaction progress was followed every ten minutes. As soon as traces of **17** were detected, the reaction was quenched as the separation of **pL3** from the

starting materials is more comfortable (they are removed *in vacuo*) than from the side product **17**.

In the second step of the synthesis, Dyker and coworkers used 2,6-difluoropyridine in conjunction with the lithiated **pL3** (6 equivalents) and the mixture is refluxed for 45 min.[202] Applying these conditions and refluxing for 24 h only afforded unreacted starting material. As the desired ligand **L3** shows high structural similarity to the previously established ligand **L1**, a synthetic route analogous to that towards **L1** was tested. In this procedure, 2,6-dichloropyridine and 3.0 equivalents of **pL3** are used and the reaction mixture is refluxed for 60 h.[91, 94] This attempt afforded the desired compound **L3**, however in this step a side product was also formed in significant amounts. This could be attributed to a species **18** at which only one of the two chlorides of 2,6-dichloropyridine had reacted. Flash column chromatography did not achieve successful separation of the two species. The attempt of performing the reaction again with compound **18** as starting material did not yield higher amounts of **L3**. The amount of side product **18** forming could be reduced by using 6 equivalents of the precursor **pL3** as initially proposed by Dyker and coworkers.[202] Pure **L3** was obtained in 22% yield, however this reaction still lacks reproducibility concerning the amount of side product **18** formed.

Synthesis of iron complexes

Following the synthetic procedure towards complex $[Fe^{II}\mathbf{L1}(mecn)](OTf)_2$ established in our group,[94] the corresponding iron(II) complex with **L3** was obtained (Scheme 21). The species $[Fe^{II}\mathbf{L3}(mecn)](OTf)_2$ was confirmed by crystal structure analysis and the data is in accordance with previously obtained parameters (see appendix, section VII.11, Table 28 for comparison of all crystallographic information acquired in this work).

It has to be noted here, that if a sample of **L3** containing impurities (presumably of side product **18**) was employed in this reaction, single crystal analysis afforded only the desired complex $[Fe^{II}\mathbf{L3}(mecn)](OTf)_2$. ^{1}H NMR spectra of the isolated crystals however also displayed impurities. The impurity also seems to coordinate the iron(II) ion and co-

crystallizes with the desired complex. To exclude that the additional observed species can be attributed to a form of isomerism of the complex, ^{1}H NMR spectra were recorded at different temperatures (appendix, section VII.4.3, Figure 72). If different isomers were present in the sample, it was expected that the intensities of the signals varied with the temperature, shifting the equilibrium of the isomer transformation. This phenomenon was not observed but another interesting feature appeared: with increasing temperature, the well-defined NMR signals of $[Fe^{II}\mathbf{L3}(mecn)](OTf)_2$ transformed into very broad signals. This observation was attributed to a temperature-induced spin crossover behavior of this complex leading to a paramagnetic species. A more detailed investigation and discussion thereof can be found in section IV.2.

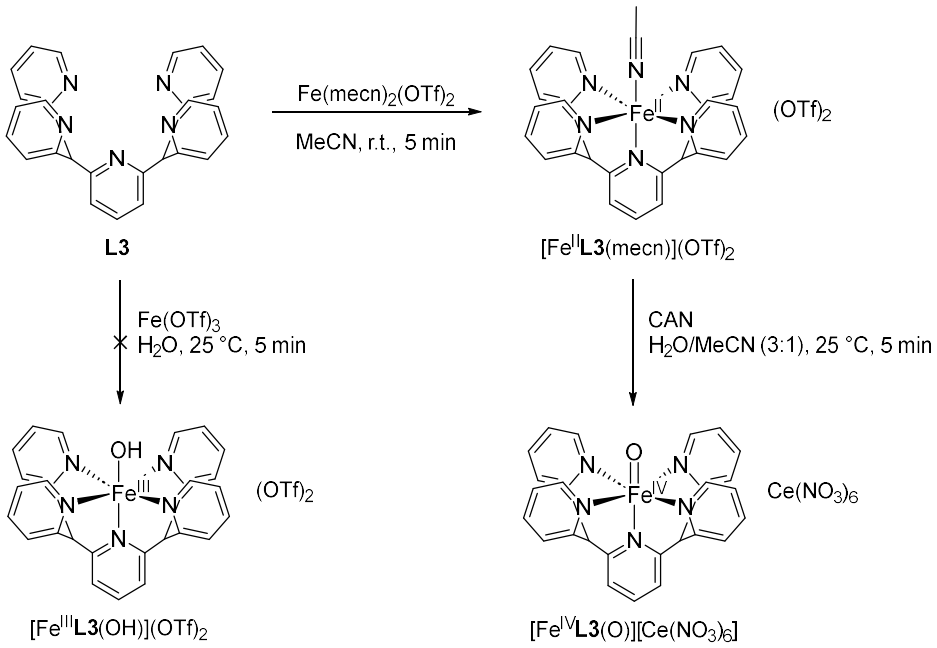

Scheme 21: Reaction pathway towards the iron complexes $[Fe^{II}\mathbf{L3}(mecn)](OTf)_2$, $[Fe^{III}\mathbf{L3}(OH)](OTf)_2$ and $[Fe^{IV}\mathbf{L3}(O)][Ce(NO_3)_6]$ based on the synthetic approaches established in our group for the respective complexes with ligand systems **L1** and **L2**.[94, 201] CAN: cerium(IV) ammonium nitrate; OTf: triflate.

As a next step in this project, it was investigated whether the corresponding iron(IV)-oxido complex could be formed and isolated from the iron(II) precursor. For this attempt, the synthetic procedure established in our group was applied (Scheme 21).[94] Complex $[Fe^{IV}\mathbf{L3}(O)][Ce(NO_3)_6]$ was obtained as a pale green solid and confirmed by elemental analysis as well as UV-vis spectroscopy displaying an absorption band at 730 nm that is characteristic for iron(IV)-oxido complexes.

To complete the series of iron complexes in this ligand system analogous to the systems **L1** and **L2**, the synthesis of the iron(III) species $[Fe^{III}\mathbf{L3}(OH)](OTf)_2$ was attempted. Following the procedures[201] developed in section IV.1.1 did not afford the desired compound as no solid crystallized or precipitated from the reaction mixture (Scheme 21). However, due to time limitations, no further condition screenings were performed for this reaction and it might still be possible to obtain the iron(III)-hydroxido complex by adapting for example the crystallization procedure.

Reactivity of the iron(IV)-oxido complex

To test the reactivity of the new iron(IV)-oxido complex towards substrates, the cerium ion needed to be removed in order to avoid unwanted substrate oxidation by that species. This was accomplished by following the established procedure in which cerium fluoride is precipitated by addition of ammonium fluoride under basic conditions.[94] Analogous to the complexes of ligand systems **L1** and **L2**, a pale green aqueous solution was obtained with **L3**. However, this solution quickly changed its color from green to orange/yellow within a minute indicating decay of the iron(IV)-oxido species. This assumption was confirmed by following the characteristic iron(IV)-oxido absorption over time with UV-vis spectrometric analysis before and after the anion exchange procedure (Figure 27).

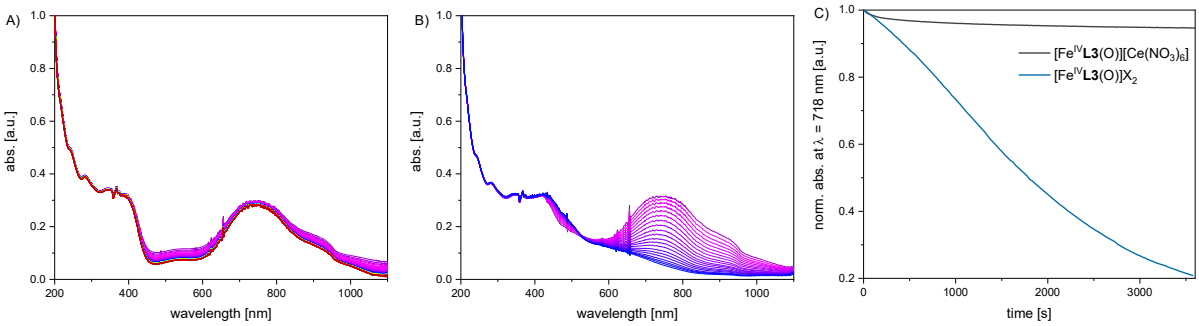

Figure 27: UV-vis spectra of $[Fe^{IV}\mathbf{L3}(O)]^{2+}$ with A) cerium(IV) nitrate and B) X^- (= F^-/$(OH)^-$/$(NO_3)^-$) as anion over two hours. C) UV-vis absorbance of both species at λ = 718 nm. Conditions: $[Fe^{IV}{=}O]$ = 10 mM, H_2O, 25 °C.

It can be deduced from the experiment that $[Fe^{IV}\mathbf{L3}(O)][Ce(NO_3)_6]$ is stable in a similar time frame to the complexes $[Fe^{IV}\mathbf{L1}/\mathbf{L2}(O)][Ce(NO_3)_6]$. After anion exchange however, the iron(IV)-oxido absorption decreases rapidly. This is a very interesting observation as

the ligand system does not seem to be the only influence on iron(IV)-oxido stability but also the anion or metal salts present as well as changes in pH play a significant role. Experiments at different pH values or screening of further anions might be worth investigating to elaborate a method stabilizing this complex in solution without the cerium(IV) nitrate anion. ICP measurements show no cerium content after the anion exchange process.

Cryo-HR-MS experiments were performed to characterize the synthesized iron complexes and to investigate whether the iron(II)/iron(IV) comproportionation reaction as described in section IV.1.1 also occurs in this **L3** ligand system. Samples of $[Fe^{II}\mathbf{L3}(mecn)](OTf)_2$, $[Fe^{IV}\mathbf{L3}(O)][Ce(NO_3)_6]$ and equimolar mixtures thereof were analyzed. The resulting spectrum of sample $[Fe^{IV}\mathbf{L3}(O)][Ce(NO_3)_6]$ together with simulated spectra is shown in Figure 28.

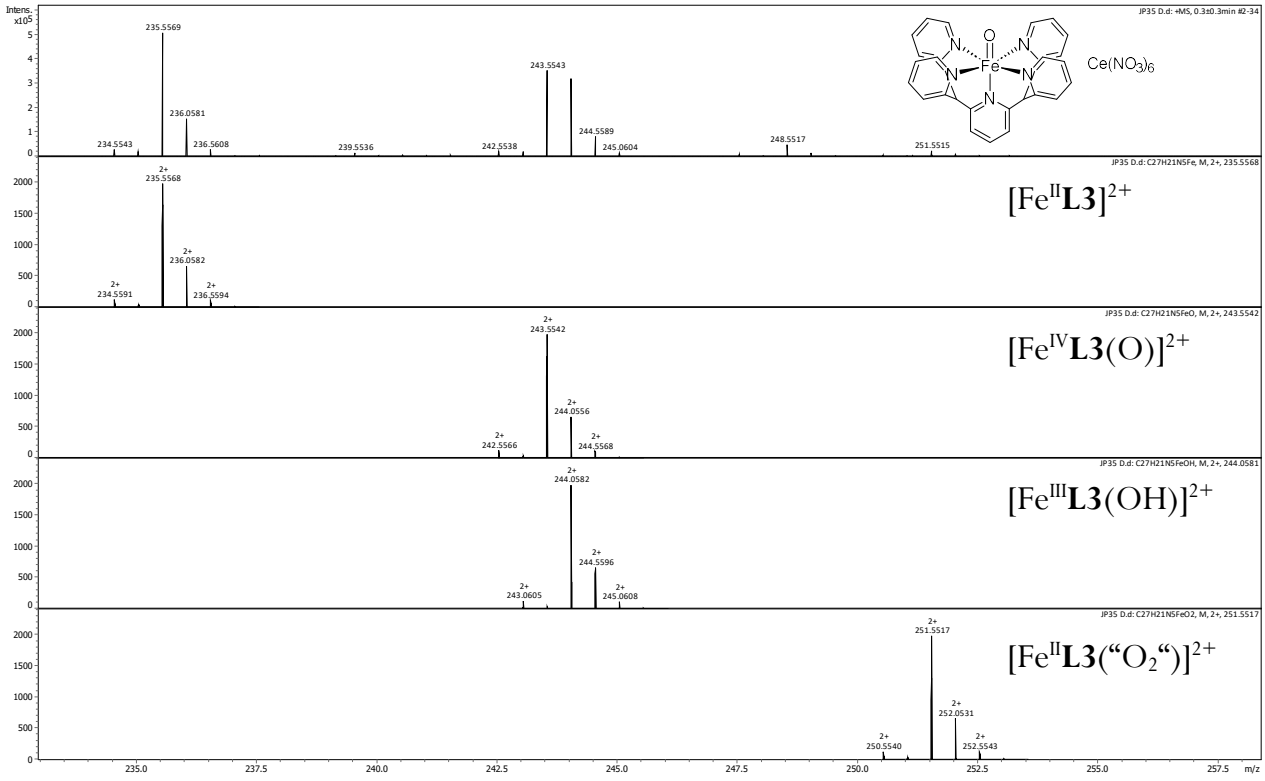

Figure 28: Experimentally obtained HR-MS spectrum of $[Fe^{IV}\mathbf{L3}(O)][Ce(NO_3)_6]$ as well as simulated spectra. Measurements and simulations were performed by Laura Senft (Ivanović-Burmazović group, LMU Munich). Conditions: $[Fe^{IV}{=}O]$ = 0.005 mM, H_2O, 5 °C.

The iron(IV)-oxido complex could be identified in the HR-MS spectrum. Additional signals were attributed to the corresponding iron(II) and iron(III)-hydroxido species. The presence of these two compounds hint towards a decay of the iron(IV)-oxido complex during measurement. The detection of the iron(III)-hydroxido species is of special interest as it indicates that this compound can be formed even though synthesis attempts have not been successful yet. Furthermore, it can be assumed that also in this ligand system an iron(II)/iron(IV) comproportionation reaction occurs forming the iron(III)-hydroxido species. An overview of the conducted experiments and the species detected by cryo-HR-mass spectrometry is given in Table 11.

Table 11: Observed species from cryo-HR-MS measurements. Species marked with a bold **x** seem to be the main species in the spectra. Measurements and simulations were performed by Laura Senft (Ivanović-Burmazović group, LMU Munich). All spectra can be found in the appendix, section VII.10.

measured compounds	**observed species**			
	Fe^{II}	**Fe^{III}-OH**	**Fe^{IV}=O**	**others**
$[Fe^{II}$**L3**$(mecn)](OTf)_2$	**x**	x	x	Fe^{II}-O_2, Fe^{II}-OTf
$[Fe^{IV}$**L3**$(O)][Ce(NO_3)_6]$	**x**	x	**x**	Fe^{II}-O_2
$[Fe^{II}$**L3**$(mecn)](OTf)_2$ + $[Fe^{IV}$**L3**$(O)][Ce(NO_3)_6]$	**x**	**x**	x	Fe^{II}-O_2

Interestingly, all three iron complexes seem to be present in the sample of the iron(II) compound (compare appendix, Figure 83). This is a surprising result as oxidation of this kind of species usually does not occur spontaneously but rather strong oxidants are required. In addition to the expected iron complexes, another signal was detected that might be attributed to an iron(II)-dioxygen species. To get more insight into this reactivity, repetitions of this experiment with samples enriched with oxygen or under inert conditions could be interesting.

To conclude, a new iron(II) complex was introduced with ligand system **L3** displaying interesting features such as possible spin crossover activities (more details are provided in

the following section IV.2). This iron(II) precursor was successfully oxidized to form a new iron(IV)-oxido complex. However, a fast decay was observed after removal of the cerium(IV) nitrate anion suggesting a higher reactivity of this complex compared to its **L1**/**L2** counterparts. To employ this species in substrate investigations, a stabilization method for instance by the presence of other species or by changes in the pH needs to be established.

2 Spin Crossover Properties of Iron(II) Complexes

While working with iron(II) species with ligand system **L3**, it was observed that ^{1}H NMR spectra at higher temperatures exhibit paramagnetic properties. This observation was attributed to possible temperature-induced spin flip behavior. A short insight into the field of spin crossover (SCO) properties of transition metal complexes related to the research of our group is given in the following.

Octahedral transition metal complexes with d^4-d^7 configuration can be present either in a high spin (HS) or low spin (LS) state, depending on the ligand field strength of the corresponding ligands. In compounds displaying SCO properties the spin state can be interconverted by external stimuli such as temperature variation, light irradiation or change in pressure.[204-205] This phenomenon was first described by Cambi and coworkers in 1931 where a series of tris(*N*,*N*-disubstituted-dithiocarbamate)iron(III) complexes was investigated.[206-207] More than thirty years later, the first example of thermal SCO behavior on iron(II) complexes ($[Fe(phen)_2(NCS)_2]$, phen = 1,10-phenanthroline, SCN^- = thiocyanate) was presented.[208] Since then, a multitude of complexes undergoing spin transitions have been reported.[209-215] In particular, numerous iron(II) complexes have been investigated, most of them possessing a N^6 coordination sphere.[216-219] The spin transition of octahedral iron(II) complexes is visualized in Figure 29.

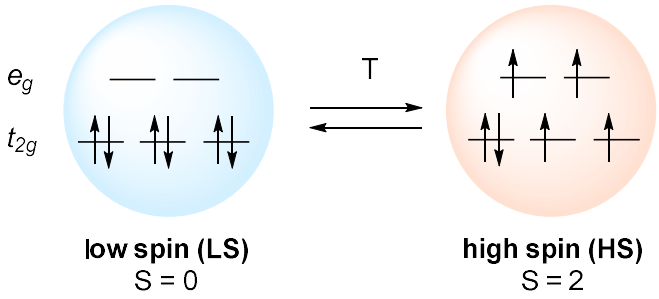

Figure 29: Transition between LS and HS states of octahedral iron(II) complexes induced by a change in temperature.

Usually, this alteration in the electronic configuration of the central metal ion leads to a change in physical properties of the compounds.[220-222] This can be observed for example

in crystal structure analysis since the transfer of electrons from non-bonding into antibonding orbitals weakens the Fe-N bonds and results in longer bond lengths. Furthermore, SCO properties are commonly accompanied by color changes of the compounds. The frequently observed intense charge-transfer absorption bands are more pronounced in HS complexes compared to LS complexes. Temperature-dependent UV-vis spectroscopy is therefore a regularly used tool to study SCO behavior.[223-228]

The change in physical properties upon SCO allows a wide range of applications in the fields of information storage, chemical sensors, display technology and molecular switches amongst others.[229-231] For these applications, the compounds ideally feature a $T_{1/2}$ (temperature at which 50% of the complex completed spin transition) near room temperature, a wide hysteresis loop and abrupt spin transitions.[221]

Recent work of Liu and coworkers[218] for instance showed an iron(II) complex displaying SCO properties that was coupled to a so-called aggregation-induced emission luminogen (AIEgen). The switch from LS to HS state of the iron(II) complex at higher temperatures lead to a significant increase in the Fe-N bond lengths. This change induced a five-fold increase in luminescence intensity of the AIEgen compound. This process is illustrated in Figure 30. The authors were also able to observe the change in spin state by temperature-dependent UV-vis spectroscopy.

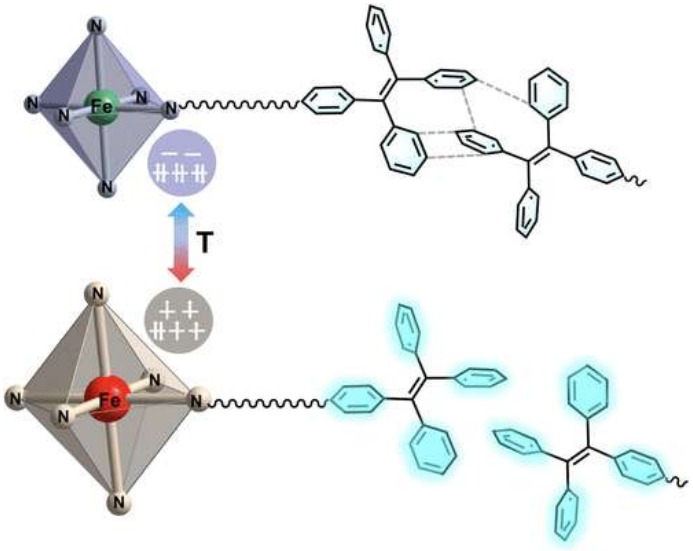

Figure 30: Schematic illustration of SCO responsive aggregation-induced emission luminogens (AIEgens) by SCO-tuned intermolecular interactions. The grey dashed lines represent the intermolecular contact interactions. Figure taken from reference.[218]

Iron(II) complexes with SCO activity have also been reported with ligand systems that are commonly used in our group. The most interesting complexes related to our work are depicted in Chart 9.

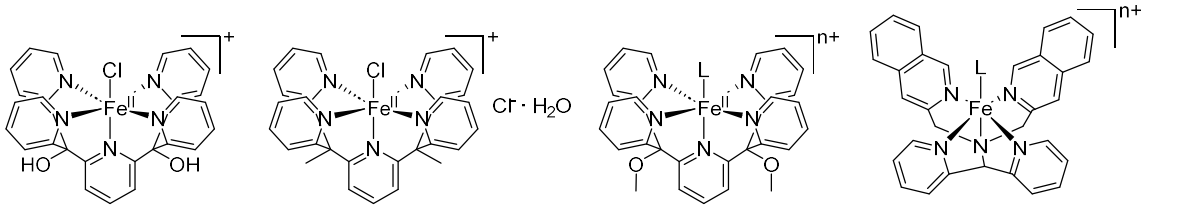

Chart 9: Overview of selected reported iron(II) complexes with SCO properties.[79, 191, 232-233]

In 2020, Messinger and coworkers discovered that the iron(II) complex $[Fe^{II}\mathbf{L2}Cl]^+$ was able to perform spin transition from HS to LS at low temperatures[232] although it was assumed before that chloride ligands provoke only HS state due to their weak-field ligand property. The SCO transition of this complex could be upshifted to temperatures near room temperature (Tao and coworkers) by the replacement of the electron-withdrawing hydroxyl groups with electron-donating methyl groups in the ligand.[233]

In addition to changes in the pentapyridyl ligand backbone, the nature of the axial ligand also has an enormous impact on the spin state of the complex. In the work of Hedman and coworkers, chloride as weak-field ligand led to HS complexes, whereas the strong-field ligand acetonitrile generated a LS complex.[191] Ligands with intermediate strength such as azide or methanol resulted in complexes that undergo spin transition. In the case of methanol, no complete SCO to the LS configuration was achieved. Temperature-dependent UV-vis spectroscopy revealed an increase in intensity of the iron(II) ligand-to-metal charge-transfer band at lower temperatures.

Similar observations were made by Nordlander and coworkers investigating an iron(II) complex with a quinoline-substituted pentadentate ligand.[79] A chloride, fluoride or water co-ligand led to the HS complex and acetonitrile in contrast generated a complex with SCO properties.

Since previous literature described the ligand systems used in our group as perfect candidates for investigations on SCO behavior, the aim was to have a closer look at these properties. The already characterized iron(II) complexes from our group as well as additional newly synthesized complexes with the established ligand systems but differing in the co-ligand at the axial position should be examined.

2.1 Synthesis and Characterization of Iron(II) Complexes

Based on these observations from the literature, it was decided to investigate the SCO properties of a series of iron(II) complexes (Chart 10) with variations in the pentapyridyl ligand backbone (bringing different electronic properties into the system) as well as with different co-ligands. Their ligand field strength (position in the spectrochemical series) seems to be a determining factor for HS or LS complexes. Acetonitrile was chosen as a rather strong-field co-ligand tending to form LS complexes and water as well as methanol with intermediate ligand field strength were expected to form HS complexes or mixed state complexes. Together with the changes in the ligand backbone, it was anticipated to

confirm these expectations experimentally and eventually discover species that display a complete spin crossover around room temperature.

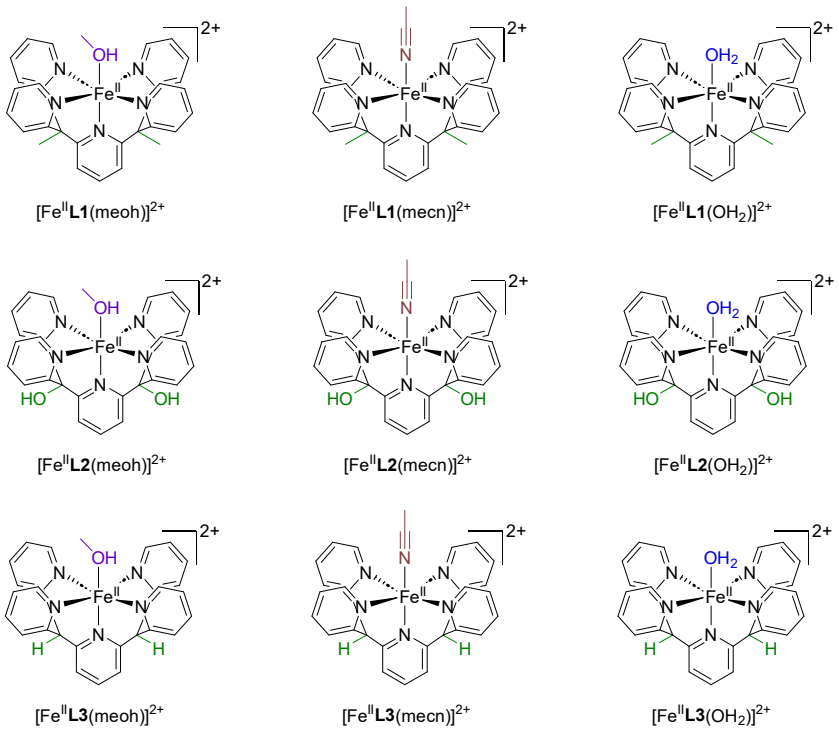

Chart 10: Overview of iron(II) complexes planned for investigations on spin crossover properties. All complexes should be synthesized with triflate as anion.

*Acetonitrile complexes [Fe^{II}**L1**/**L2**/**L3**(mecn)](OTf)$_2$*

The complexes bearing an acetonitrile co-ligand were synthesized following the procedures described before (section VI.2).[94] The ligands were suspended in acetonitrile and addition of iron(II) triflate resulted in complex formation which was isolated through crystallization by diffusion of diethyl ether into the reaction solution (Scheme 22).

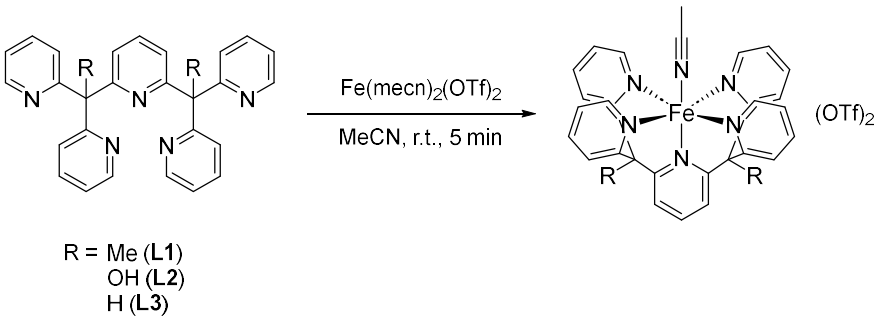

Scheme 22: Synthetic pathway towards the complexes [Fe^{II}**L1**/**L2**/**L3**(mecn)](OTf)$_2$.

Crystals in sufficient quality for crystal structure analysis could be obtained for all three ligand systems (see appendix, section VII.11). Complex $[Fe^{II}\mathbf{L3}(mecn)]^{2+}$ was also characterized by Mößbauer spectroscopy (Figure 31).

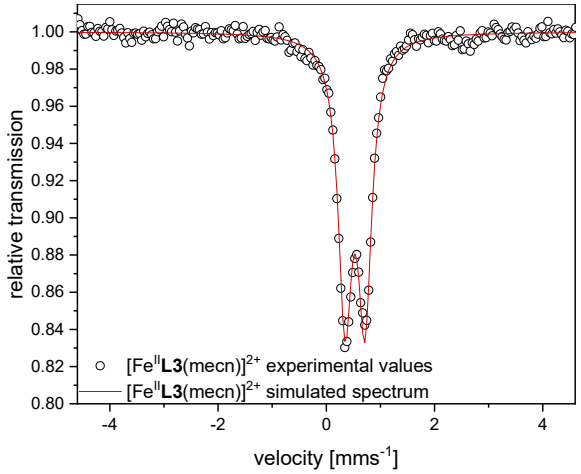

Figure 31: Experimentally obtained solid-state and simulated Mössbauer spectra of $[Fe^{II}\mathbf{L3}(mecn)]^{2+}$. Mössbauer spectra were acquired at 80 K. Measurement and simulation performed by Jan Kruse (group of Franc Meyer, Göttingen).

Similar to the previously characterized complexes $[Fe^{II}\mathbf{L1}(mecn)]^{2+}$ and $[Fe^{II}\mathbf{L2}(mecn)]^{2+}$ (section IV.1.1), this complex is present as a low-spin S = 0 iron(II) species with an isomeric shift of $\delta = 0.53$ mm s^{-1} and a quadrupole splitting of $\Delta E_Q = 0.37$ mm s^{-1}. A comparison of all Mößbauer data acquired in this work can be found in the appendix, Table 27.

The three acetonitrile complexes were also objected to analysis by IR spectroscopy. A comparison of the resulting spectra is depicted in Figure 32. All three complexes exhibit very similar features. An almost identical sharp band can be found at a wavenumber of 1025 cm^{-1} and a second well-pronounced band is located at approximately 1125 cm^{-1} with slight shifts depending on the compound. In a range between 1210 and 1280 cm^{-1}, three signals are observed with the middle one being the most intense at approximately 1225 cm^{-1}.

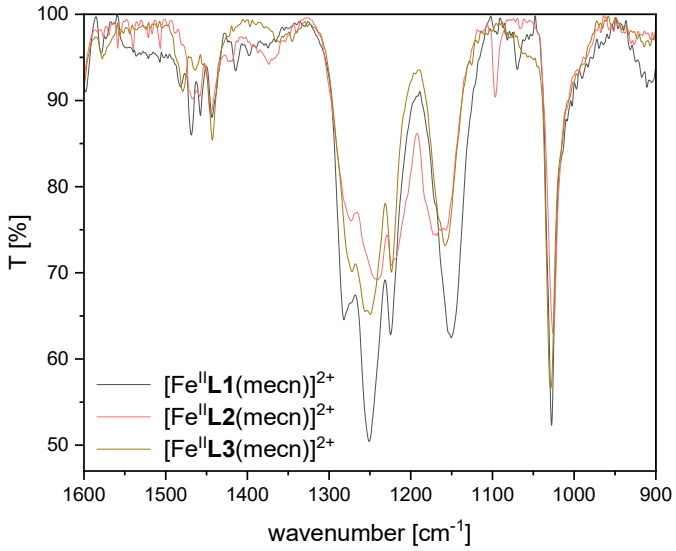

Figure 32: Detailed view of IR spectra of the complexes $[Fe^{II}$**L1**/**L2**/**L3**$(mecn)](OTf)_2$. Full spectra can be found in the appendix, Figure 79.

Aqua complexes $[Fe^{II}$***L1*** */* ***L2*** */* ***L3****$(OH_2)](OTf)_2$

It is assumed that in solution, a quick exchange of the co-ligand occurs. A solution of $[Fe^{II}$**L1**$(mecn)]^{2+}$ in water should therefore result in the corresponding aqua complex. This assumption was corroborated by ^{1}H NMR spectra showing identical peaks for the complexes $[Fe^{II}$**L1**$(mecn)]^{2+}$ and $[Fe^{II}$**L1**$(OH_2)]^{2+}$ in D_2O (except for the free acetonitrile signal, see section IV.1.1). It was therefore anticipated to obtain the desired aqua complexes by dissolving the corresponding acetonitrile complexes in water (Scheme 23).

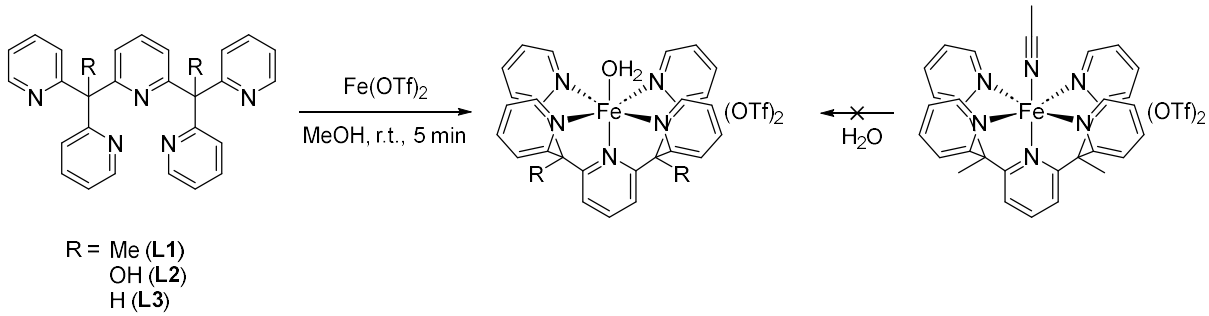

Scheme 23: Synthetic pathway towards the complexes $[Fe^{II}$**L1**/**L2**/**L3**$(OH_2)](OTf)_2$. Only the complex with **L1** could be unambiguously identified.

Unexpectedly, crystallization of the complex from this solution afforded the acetonitrile complex. Although the co-ligand exchange is occurring in solution, crystallization seems to be preferred with acetonitrile as co-ligand.

The desired complex with ligand **L1** could be isolated in a reaction of **L1** with iron(II) triflate in methanol at ambient conditions. It was anticipated to form the methanol complex in this procedure, however the aqua complex seems to be preferably formed from the amount of water present in the non-dry methanol. Complex $[Fe^{II}\mathbf{L1}(OH_2)]^{2+}$ could be characterized by crystal structure analysis (see appendix, section VII.11) as well as by Mößbauer spectroscopy (Figure 33).

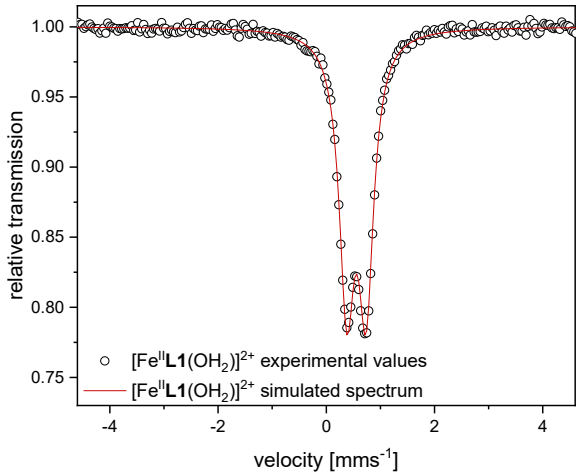

Figure 33: Experimentally obtained solid-state and simulated Mössbauer spectra of $[Fe^{II}\mathbf{L1}(OH_2)]^{2+}$. Mössbauer spectra were acquired at 80 K. Measurement and simulation performed by Jan Kruse (group of Franc Meyer, Göttingen).

Similar to the before characterized iron(II) complexes, this complex is present as a low-spin S = 0 iron(II) species with an isomeric shift of $\delta = 0.56$ mm s^{-1} and a quadrupole splitting of $\Delta E_Q = 0.36$ mm s^{-1}. A comparison of all Mößbauer data acquired in this work can be found in the appendix, Table 27.

The synthesis of complexes $[Fe^{II}\mathbf{L2}(OH_2)]^{2+}$ and $[Fe^{II}\mathbf{L3}(OH_2)]^{2+}$ did not yield any crystals suitable for crystal structure analysis. The solvent was evaporated and the isolated green/yellow solids were analyzed with IR spectroscopy.

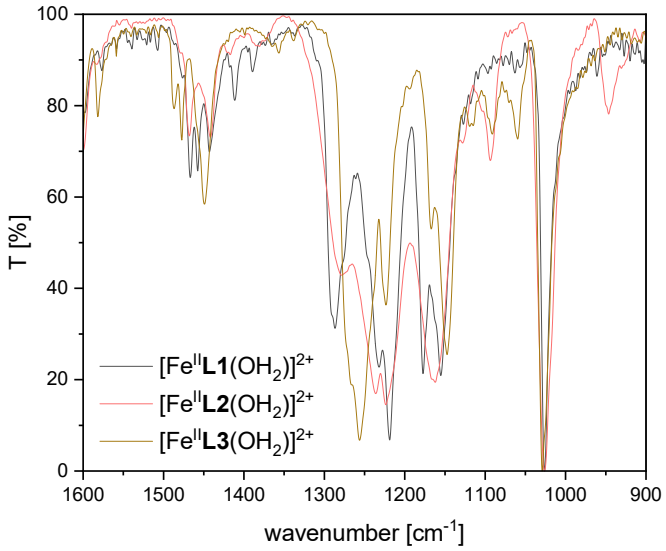

Figure 34: Detailed view of IR spectra of the complexes $[Fe^{II}$**L1**/**L2**/**L3**$(OH_2)](OTf)_2$. Full spectra can be found in the appendix, Figure 80.

Compared to the corresponding acetonitrile complexes which exhibited distinct similarities in the spectra (Figure 32), the aqua complexes feature more differences in the spectra such as shifts of the signals in wavenumber or intensity. All spectra display the pronounced signal at approximately 1025 cm^{-1} that also has been observed in the spectra of acetonitrile complexes (Figure 32). A direct comparison of the acetonitrile and aqua complexes of **L1** ($[Fe^{II}$**L1**$(mecn)]^{2+}$ and $[Fe^{II}$**L1**$(OH_2)]^{2+}$) can be found in the appendix, Figure 81. Since only the structure of complex $[Fe^{II}$**L1**$(OH_2)]^{2+}$ has been confirmed by crystal structure analysis in this series, it was hoped that similarities in the IR spectra would corroborate the suggested structures for the other two ligand systems. However, an unequivocal assignment of the complexes without known references on the basis of the recorded IR spectra is not possible.

*Methanol complexes $[Fe^{II}$**L1**/**L2**/**L3**$(MeOH)](OTf)_2$*

To avoid the formation of aqua complexes, the synthesis of the methanol species was performed under nitrogen atmosphere using dry methanol as solvent (Scheme 24).

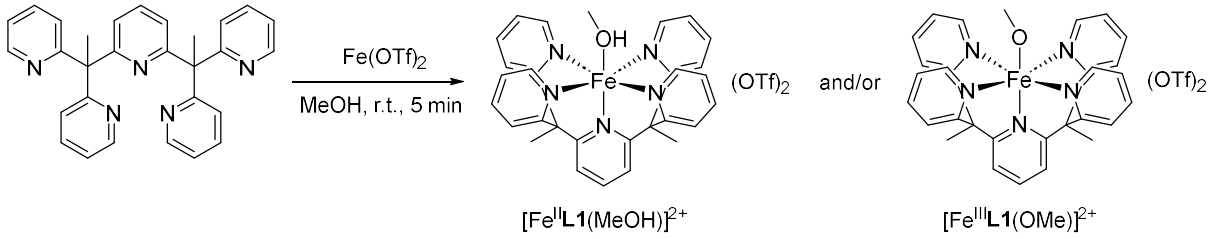

Scheme 24: Synthetic pathway towards the anticipated complex $[Fe^{II}\mathbf{L1}(MeOH)](OTf)_2$.

Crystals suitable for crystal structure analysis could be obtained by diffusion of *tert*-butyl methyl ether into the reaction solution. Surprisingly, an iron(III)-methanolate species was obtained instead of the expected iron(II)-methanol complex. This could be stated from the obtained Fe-O bond length (1.80 Å) compared to our previous findings and to the literature (2.04 Å for Fe(II)-MeOH and 1.78 Å for Fe(III)-OMe in a similar ligand system).[180] An overview of important bond lengths acquired from crystal structures in this work is given in the appendix, Table 28.

Interestingly, UV-vis spectra of the obtained crystals rather showed features expected for an iron(II) species from intensity as well as the position of the absorption maxima. The question arose whether the isolated crystals display a mixture of iron(II) and iron(III) species and only the iron(III) species was picked by chance for crystal structure analysis. However, a transformation from the isolated iron(III) species to an iron(II) species in solution could also be a possibility. Unfortunately, the presence of iron(III) would not be visible in a UV-vis spectrum together with an iron(II) species as the high absorption of the latter would superimpose all iron(III) absorption.

To compare the behavior of the species as a solid and in solution, EPR spectra of the isolated crystals were recorded as a solid and in solution (Figure 35).

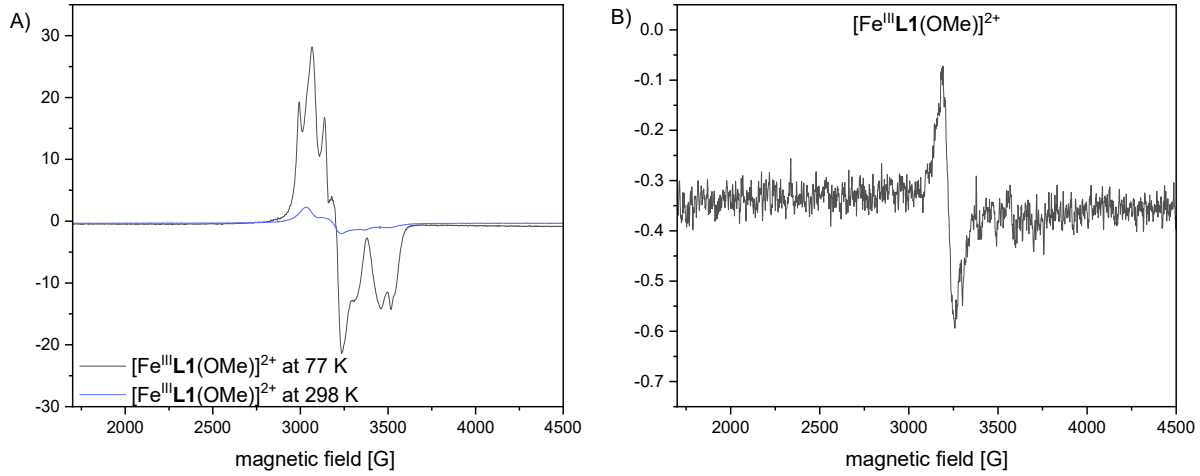

Figure 35: A) EPR spectra of the solid $[Fe^{II}\mathbf{L1}(MeOH)]^{2+}$ and/or $[Fe^{III}\mathbf{L1}(OMe)]^{2+}$ recorded at 77 K and room temperature. B) EPR spectra of a saturated solution of $[Fe^{II}\mathbf{L1}(MeOH)]^{2+}$ and/or $[Fe^{III}\mathbf{L1}(OMe)]^{2+}$ in methanol recorded at room temperature.

No signal was expected for the presumably diamagnetic iron(II) species but the unpaired electron of the iron(III) species should be visible similar to our previously detected iron(III) complexes (section IV.1.1). The isolated crystals measured as a solid provided a signal at room temperature which became more defined and intense recorded at 77 K (Figure 35A) and was comparable to our previous measurements, thus confirming the presence of the iron(III) complex. The measurement in solution however, turned out to be more challenging than expected as limited solubility of the complex afforded only signals in very low intensity and resolution. It can not be differentiated whether this low intensity results from the low amount of complex in solution or from a conversion of the iron(III) into the iron(II) species in solution.

For further characterization of the oxidation state, Mößbauer measurements were conducted on the isolated crystals (Figure 36).

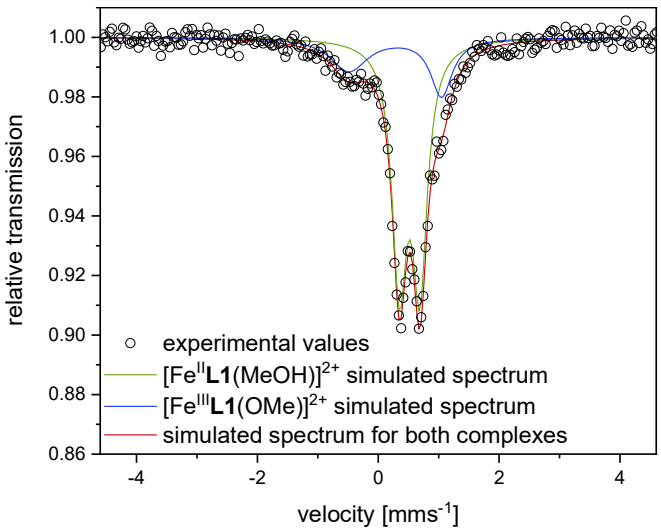

Figure 36: Experimentally obtained solid-state and simulated Mößbauer spectra of $[Fe^{II}\mathbf{L1}(MeOH)]^{2+}$ and/or $[Fe^{III}\mathbf{L1}(OMe)]^{2+}$ recorded at 80 K. Measurement and simulation performed by Jan Kruse (group of Franc Meyer, Göttingen).

These measurements revealed that these isolated crystals are composed of a mixture of an iron(II) species (74%) and an iron(III) species (26%). The obtained values for isomeric shift and quadrupole splitting for the assumed complex $[Fe^{II}\mathbf{L1}(MeOH)]^{2+}$ are nearly identical to those observed for $[Fe^{II}\mathbf{L1}(mecn)]^{2+}$ (see appendix Table 27 for a comparison of all acquired Mößbauer data). For $[Fe^{III}\mathbf{L1}(OMe)]^{2+}$ an iron(III) low spin ($S = ½$) state is confirmed with similar parameters as obtained for the iron(III)-hydroxido complex $[Fe^{III}\mathbf{L1}(OH)]^{2+}$.

It can be assumed from the Mößbauer data that the synthetic procedure where ligand **L1** is mixed with iron(II) triflate in dry methanol under nitrogen atmosphere (Scheme 24) somehow evokes partly oxidation of the iron(II) metal ion and affords complexes in an iron(II)/iron(III) mixture. The iron(III) species could be identified by crystal structure analysis and the iron(II) species is proposed to present complex $[Fe^{II}\mathbf{L1}(MeOH)]^{2+}$ analogous to the before synthesized iron(II) complexes. The compound that is in contrary reduced in this process could not be identified. Interestingly, the synthesis of a similar iron(II) complex bearing a methanol co-ligand has been previously reported by Stack and coworkers.[180] The authors isolated the complex $[Fe^{II}(Py_5(OMe)_2(MeOH)](OTf)_2$ from a 1:1 mixture of the ligand and iron(II) triflate in methanol. Despite of the structural

similarity of both ligands from the pentapyridyl family, the additional methoxy group in $Py_5(OMe)_2$ seems to favor the formation of the respective iron(II)-methanol complex. The corresponding syntheses with ligand systems **L2** and **L3** were not accomplished due to time reasons but are definitely interesting for future investigations.

2.2 Spin Crossover Properties of Iron(II) Complexes

The now available iron(II) complexes (Chart 11) were then investigated in terms of spin crossover activity.

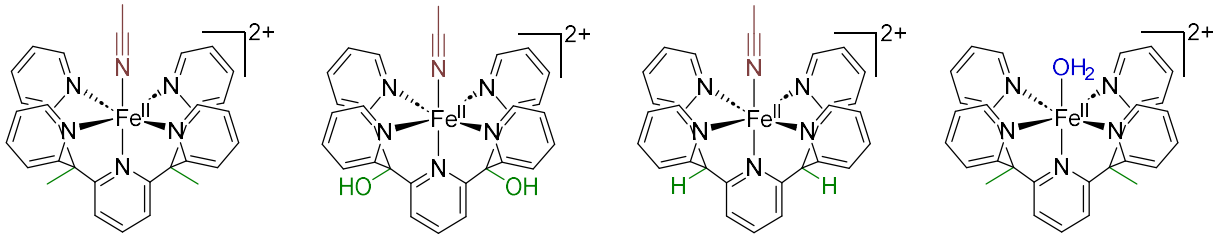

Chart 11: Overview of iron(II) complexes for spin crossover investigations. All complexes bear triflate as anion.

Temperature-dependent UV-vis spectroscopy, temperature-dependent ^{1}H NMR spectroscopy as well as SQUID measurements were chosen to follow eventual spin transitions related to a change in temperature.

Temperature-dependent UV-vis spectroscopy

The characteristic absorption bands for iron(II) complexes with similar ligand systems is attributed to ligand-centered π-π* transitions (about 270 nm) and metal-to-ligand charge transfers (MLCT, about 340 nm).[85, 223-228] These transitions are more pronounced in high spin complexes. A temperature-dependent change of spin state should therefore be visible in UV-vis spectroscopic analysis (high spin at higher temperatures leading to lower UV-vis intensities) and was often observed and described in the literature before.[234]

All complexes were measured over a temperature range from 10 °C to 70 °C and isopropanol was chosen as solvent for all complexes due to consistency and as it was assumed that no exchange of the co-ligand would occur (Figure 37).

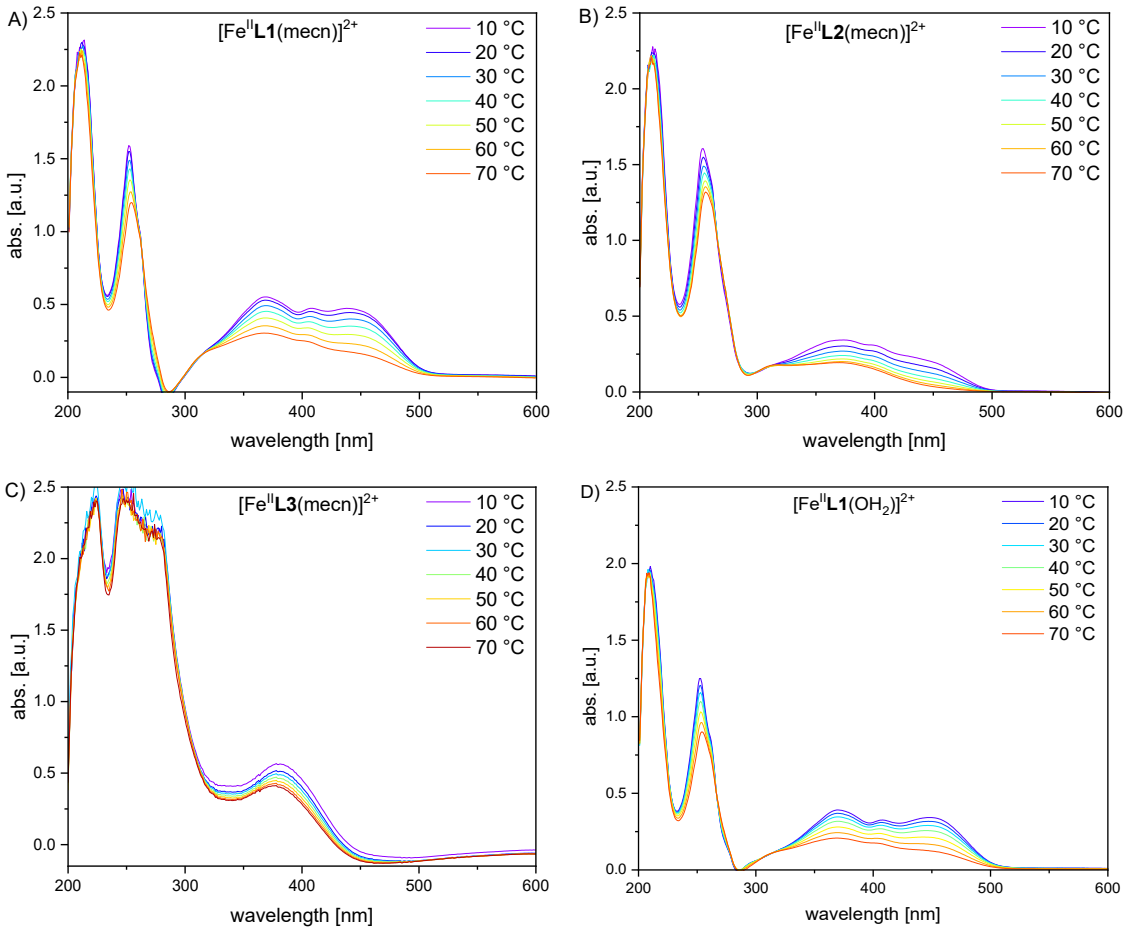

Figure 37: UV-vis spectra of the complexes A) [Fe^{II}**L1**(mecn)]$^{2+}$ and B) [Fe^{II}**L2**(mecn)]$^{2+}$ C) [Fe^{II}**L3**(mecn)]$^{2+}$ and D) [Fe^{II}**L1**(OH$_2$)]$^{2+}$ in isopropanol (0.1 mM (A, B, D) and 0.5 mM (C)) recorded between 10 °C and 70 °C.

All four investigated complexes display a change in the UV-vis spectra upon temperature variation; the intensity of the absorption band decreases with increasing temperature. This observation is in accordance with the literature and hints towards a transition from low spin towards high spin with higher temperatures.

Comparing the three complexes with acetonitrile as co-ligand ([Fe^{II}**L1**(mecn)]$^{2+}$, [Fe^{II}**L2**(mecn)]$^{2+}$ and [Fe^{II}**L3**(mecn)]$^{2+}$), it can be stated that the complex with **L1** shows the highest intensities of the absorption bands whereas the absorption of the complex with **L2** is significantly lower. The absorption of the complex with **L3** was barely visible at the

chosen concentration and therefore was measured at higher concentration (0.5 mM instead of 0.1 mM). Assumably, this complex already displays a significant amount of HS state even at low temperatures which decreases the intensity in absorption. This assumption also explains the observed smaller change in absorption of this complex over the investigated temperature range. Furthermore, the absorption band at approximately 450 nm is less pronounced in $[Fe^{II}\mathbf{L2}(mecn)]^{2+}$ and not visible in $[Fe^{II}\mathbf{L3}(mecn)]^{2+}$. From this observation it can be assumed that the amount of high spin state in the complexes rises from **L1** < **L2** < **L3** at the temperatures investigated. It would be interesting here to test lower temperatures (especially for investigations on $[Fe^{II}\mathbf{L3}(mecn)]^{2+}$) which unfortunately was not possible in this experimental setup.

In a comparison of the different co-ligands acetonitrile and water within the same basic ligand **L1** ($[Fe^{II}\mathbf{L1}(mecn)]^{2+}$ and $[Fe^{II}\mathbf{L1}(OH_2)]^{2+}$), the shape of the UV-vis spectra is very similar. The intensity of the absorption of the complex with water as co-ligand is slightly lower than with acetonitrile. Therefore, water as co-ligand seems to provoke a high spin state more than acetonitrile. This observation is in accordance with the literature and the expectations drawn from the spectrochemical series, where acetonitrile as a strong field ligand is known to preferably generate low spin complexes compared to water with intermediate ligand field strength.

Temperature-dependent ^1H NMR spectroscopy

To corroborate these findings with more analytical investigations, the complexes were investigated with ^1H NMR spectroscopy at varying temperatures. In the LS state, the iron(II) complexes exhibit no unpaired electrons and common NMR features are obtained measuring these diamagnetic species. With occurring spin transitions into the HS state, the complexes transform into paramagnetic compounds which alter the NMR signals, for instance resulting in broadening and shifting of the signals. The transition between LS and HS complexes should therefore be visible in ^1H NMR spectroscopy. Due to consistency reasons, all complexes were measured in acetone-d_6 (assuming no exchange of the co-ligand) which allows investigation of a temperature range from -80 to 40 °C. The obtained

spectra for $[Fe^{II}\mathbf{L1}(OH_2)]^{2+}$ are depicted in Figure 38 and the spectra of the remaining complexes can be found in the appendix, section VII.4.3.

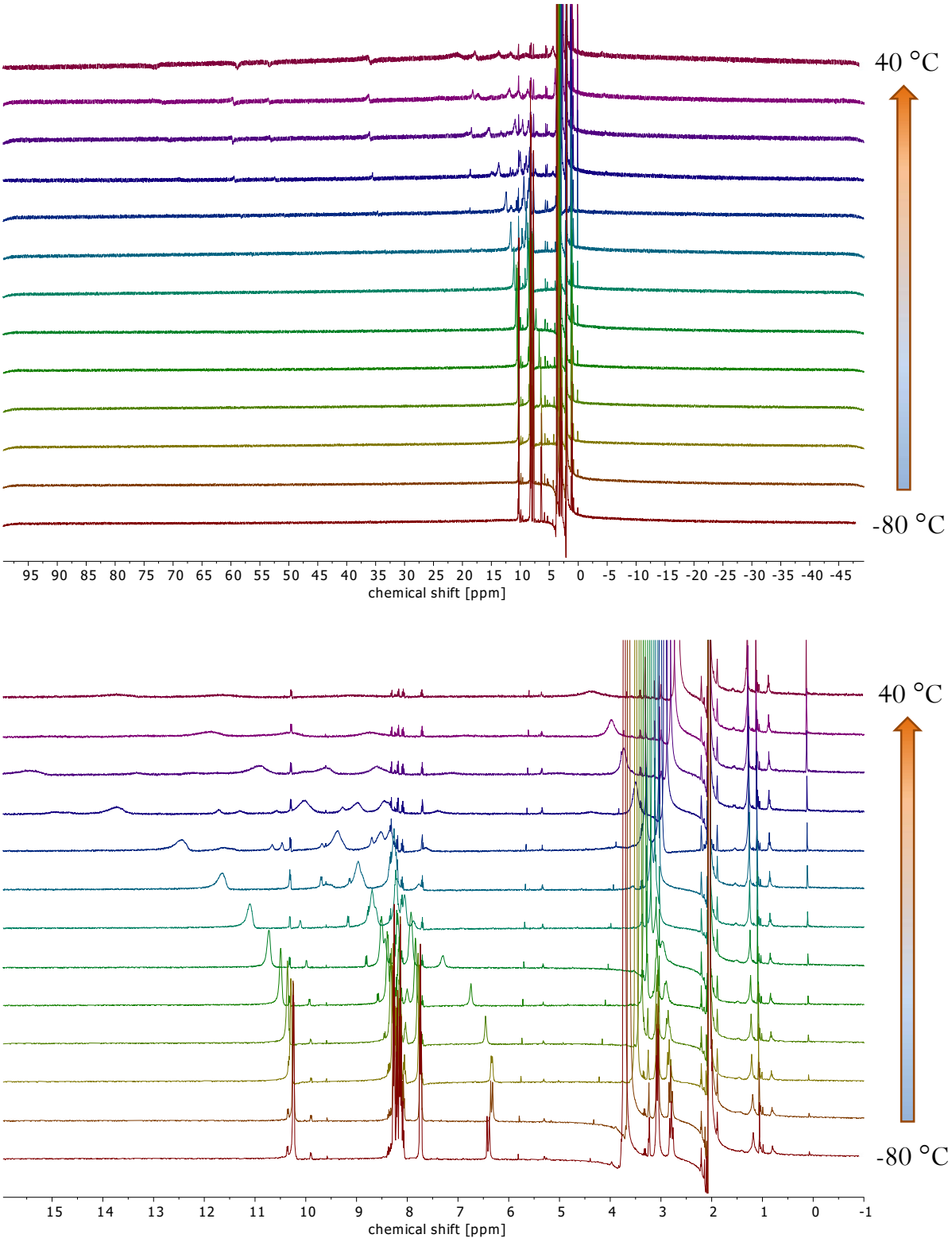

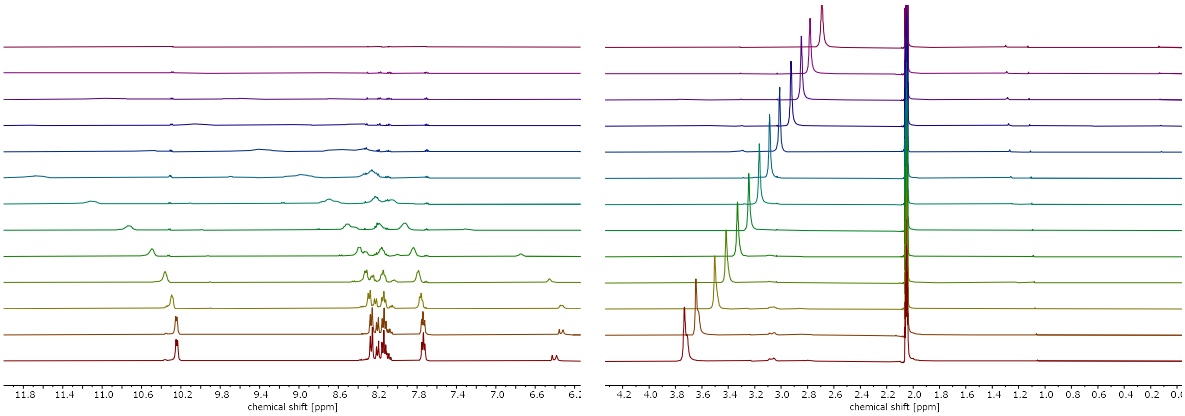

Figure 38: Complete ^{1}H NMR spectra and detailed views of $[Fe^{II}\mathbf{L1}(OH_2)]^{2+}$ recorded between -80 °C and 40 °C in acetone-d_6.

At low temperatures, only sharp signals were detected, indicating the presence of a complex completely in LS state. With raising temperature, the intensity of these signals decreased significantly. Simultaneously, new broad signals appeared in a chemical shift range of -4 to 73 ppm which can be attributed to the formation of the paramagnetic species. In the case of $[Fe^{II}\mathbf{L1}(OH_2)]^{2+}$, both spin states seem to be present at the highest investigated temperature of 40 °C. Unfortunately, the nature of the broad paramagnetic NMR signals does not allow exact determination of the LS-HS ratio. Still, the main species present at low/high temperature and the temperature at which the first paramagnetic signals appeared was approximately estimated. An overview is given in Table 12.

Table 12: Main species at low/high temperature and temperature at which the first paramagnetic signals appeared approximately estimated from obtained ^{1}H NMR spectra for the complexes $[Fe^{II}\mathbf{L1}(mecn)]^{2+}$, $[Fe^{II}\mathbf{L2}(mecn)]^{2+}$, $[Fe^{II}\mathbf{L3}(mecn)]^{2+}$ and $[Fe^{II}\mathbf{L1}(OH_2)]^{2+}$.

	$[Fe^{II}\mathbf{L1}(mecn)]^{2+}$	$[Fe^{II}\mathbf{L2}(mecn)]^{2+}$	$[Fe^{II}\mathbf{L3}(mecn)]^{2+}$	$[Fe^{II}\mathbf{L1}(OH_2)]^{2+}$
low T (-80 °C)	LS	LS	LS + HS	LS
SCO start	ca -50 °C	ca -60 °C	ca -80 °C	ca -40 °C
high T (40 °C)	LS (+ HS)	(LS +) HS	HS	LS + HS

In the series of acetonitrile complexes, more HS amount at lower temperatures was found for **L2** compared to **L1**. The complex with **L3** already exhibits HS features at low temperatures and no diamagnetic signals were detected at high temperatures. Comparing

the influence of the two different co-ligands acetonitrile and water in ligand system **L1**, slightly more HS species seems to be present at higher temperatures in the case of the aqua complex. These observations are in line with the findings from UV-vis spectroscopic analysis.

It has to be noted here that some minor signals have been found in all NMR spectra recorded in acetone-d_6 that were not attributed to specific species and were not observed in the respective spectrum for compound characterization. The acetonitrile complexes have been characterized in CD_3CN at room temperature (see appendix, section VII.4.1), characterization of $[Fe^{II}\mathbf{L2}(mecn)]^{2+}$ in D_2O however, only afforded paramagnetic signals (see appendix, Figure 73). This can be explained by the exchange of the co-ligand depending on the respective solvent. The assumption of no coordination of acetone-d_6 is corroborated by the slightly different spectra obtained for the complexes $[Fe^{II}\mathbf{L1}(mecn)]^{2+}$ and $[Fe^{II}\mathbf{L1}(OH_2)]^{2+}$. With solely acetone as co-ligand, identical spectra for the two complexes were expected. However, partially exchange of the co-ligand by the solvent can not be completely excluded. It would be helpful here to repeat the temperature-dependent NMR study in the solvent that displays the co-ligand to avoid unwanted exchange. However, measurement in different solvents allows different temperature ranges and in the case of the water complexes, investigations below 10 °C are not possible.

Magnetic measurements (SQUID)

Information on the magnetic susceptibility of the compounds over a broad temperature range from 0 to 400 K should be acquired with superconducting quantum interference device (SQUID) measurements. These are performed by Serhiy Demeshko from the group of Franc Meyer. Due to time limitations on the instrument, only one complex of the series was chosen for a first measurement that exhibited the most prominent color change upon cooling with liquid nitrogen. The resulting SQUID spectrum of $[Fe^{II}\mathbf{L2}(mecn)]^{2+}$ is shown in Figure 39.

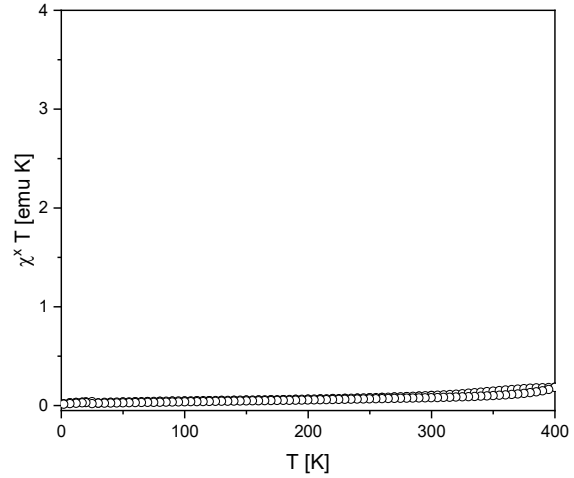

Figure 39: Experimentally obtained SQUID spectrum of $[Fe^{II}\mathbf{L2}(mecn)]^{2+}$. SQUID spectrum was acquired between 0 K and 400 K. Measurement performed by Serhiy Demeshko (group of Franc Meyer, Göttingen).

Surprisingly, no spin transition could be observed in the measurement although both UV-vis and NMR spectroscopy afforded evidence for this process to occur. However, both spectroscopic methods do not reveal any ratios of LS or HS species. The presence of LS and HS compounds at 40 °C was stated from NMR spectroscopy for $[Fe^{II}\mathbf{L2}(mecn)]^{2+}$. The therein observed paramagnetic signals may only be provoked by traces of the HS complex, leading to the merely visible change in magnetic susceptibility between 300 and 400 K. Moreover, the different results obtained from SQUID analysis compared to other spectroscopic methods may also be explained by sample preparation. A solid sample of $[Fe^{II}\mathbf{L1}(OH_2)]^{2+}$ was measured in SQUID analysis and for UV-vis as well as NMR investigations, a solution of $[Fe^{II}\mathbf{L1}(OH_2)]^{2+}$ in isopropanol or acetone-d_6, respectively, was used. Since the solvent can have a large impact on the spin state, it is possible that compound $[Fe^{II}\mathbf{L1}(OH_2)]^{2+}$ shows different properties in solution than as a solid. It would be interesting to compare this finding with SQUID measurements of the other investigated complexes, especially $[Fe^{II}\mathbf{L3}(mecn)]^{2+}$ seems to be a promising candidate as for this species, no LS was detected in the NMR spectrum at 40 °C.

Crystal structure analysis

In iron(II) high spin complexes, the Fe-N bonds from the iron centre to the ligand are weakened by the transfer of electrons from the non-bonding into the antibonding

orbitals.[235] This is reflected by the resulting longer bond lengths observed in crystal structure analysis. Table 13 shows a comparison of two low spin iron complexes (iron(II) and iron(III)) newly characterized in this work with similar complexes from the literature that exist in the high spin state (iron(II) and iron(III)).

Table 13: Selected bond lengths in single crystals of complexes from this work as well as from the literature (a),[236] b)[180]) for comparison reasons together with their respective spin state. $Py_{eq.}$ = pyridines in the equatorial plane, $Py_{ax.}$ = axial pyridine. For values involving equatorial pyridines the average value is provided.

complex	**spin state**	**Fe-N**(Py_{eq})	**Fe-N**(Py_{ax})
$[Fe^{II}$**L1**$(OH_2)](OTf)_2$	LS	2.00 Å	1.96 Å
$[Fe^{II}Py_5(OMe)_2(MeOH)](OTf)_2$[a)]	HS	2.18 Å	2.10 Å
$[Fe^{III}$**L1**$(OMe)](OTf)_2$	LS	2.02 Å	2.02 Å
$[Fe^{III}Py_5(OMe)_2(OMe)](OTf)_2$[b)]	HS	2.17 Å	2.15 Å

Regarding the two iron(II) complexes, a significant increase in Fe-N bond lengths is found in the HS-iron(II) complex $[Fe^{II}Py_5(OMe)_2(MeOH)](OTf)_2$ compared to the shown LS-iron(II) complex. The same phenomenon is observed in the case of the HS-/LS-iron(III) species. In this example, the only difference between the two complexes is the ligand $Py_5(OMe)_2$ *versus* Py_5Me_2 (**L1**). As shortly described in the introduction of this chapter, investigations on spin crossover properties of iron(II) complexes in the $Py_5(OMe)_2$ ligand system with a variety of different co-ligands (such as MeOH, OH_2, MeCN, pyridine, chloride, benzyl, azide, methanolate, phenylate or cyanate) have been presented in the literature.[191, 237] The comparison of the described complexes with newly synthesized complexes from ligand system **L1** and **L2** would be very interesting.

To conclude, the synthesis of two new iron(II) complexes was accomplished in this project. Compound $[Fe^{II}$**L1**$(OH_2)](OTf)_2$ was thoroughly characterized using crystal structure analysis as well as UV-vis, IR and Mößbauer spectroscopy. The second newly isolated species $[Fe^{III}$**L1**$(OMe)](OTf)_2$ was confirmed by crystal structure analysis, however UV-vis, EPR and Mößbauer spectroscopy indicated a mixture of iron(II) and iron(III)

complexes. As the synthesis of the complexes with methanol as co-ligand turned out to be more challenging than expected, further investigations will focus on the synthesis of the aqua complexes of **L2** and **L3**. The SCO properties of the available complexes ($[Fe^{II}$**L1**/**L2**/**L3**$(mecn)]^{2+}$ and $[Fe^{II}$**L1**$(OH_2)]^{2+}$) were studied using temperature-dependent UV-vis and ^{1}H NMR spectroscopy. Both methods revealed changes in the spectra that were attributed to a spin transition from LS to HS with higher temperatures for all complexes. As shown in Figure 40, the amount of HS complex depends on the ligand (**L1** < **L2** < **L3**) and on the co-ligand (mecn < OH_2).

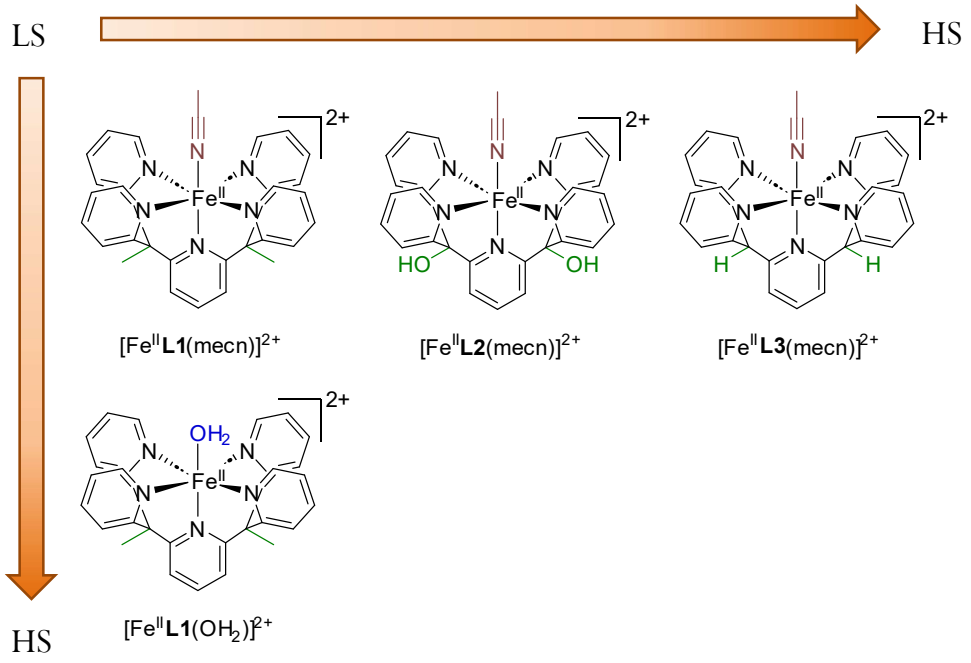

Figure 40: Alignment of the investigated complexes based on the estimated amount of LS/HS complex observed in temperature-dependent ^{1}H NMR spectroscopy.

Further current investigations will focus on the synthesis of the aqua complexes with **L2** and **L3** to complete the series. The spin crossover behavior of all obtained species will be analyzed and complemented by SQUID measurements.

V. SUMMARY AND OUTLOOK

This work comprises a comprehensive study on synthetic iron(IV)-oxido complexes focusing on substrate reactivity studies and on understanding as well as expanding this system followed by suggestions of possible applications in different processes. The results from the different approaches are shortly summarized in the following.

Approaching Natural Substrates of TET Enzymes

The iron(IV)-oxido complex $[Fe^{IV}\mathbf{L1}(O)]^{2+}$ has previously been established as a functional model of TET enzymes in our group and the reactivity has been tested with the substrate 5-methylcytosine.[94] In addition to the nucleobase, investigations on the deoxyribonucleoside as well as first studies on 5-methylcytosine-containing oligonucleotides have also been conducted.[96] It could be shown in this work that comparable to the corresponding deoxyribonucleoside, 5-methylribocytidine can also be oxidized to its natural metabolites 5-hydroxymethylribocytidine, 5-formylribocytidine and 5-carboxyribocytidine. The product distribution was monitored over the reaction time by HPLC-MS analysis.

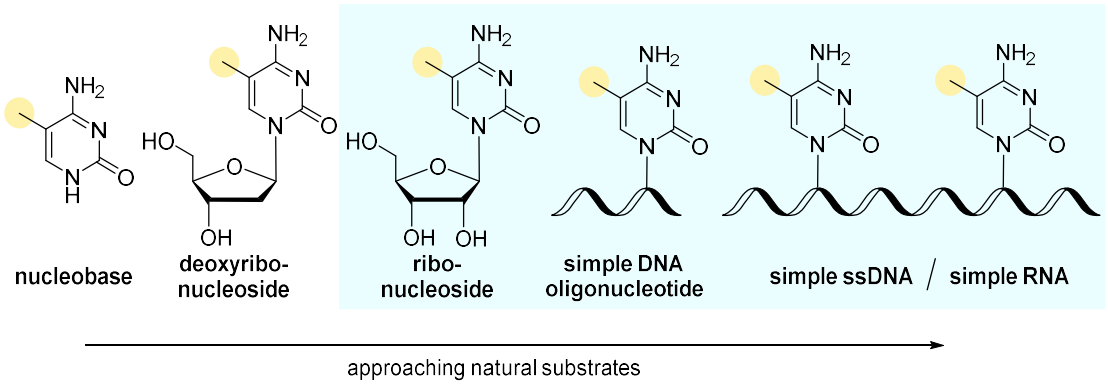

Chart 12: Model substrates for reaction with the synthetic iron(IV)-oxido model complex. Substrate complexity increases from the simple nucleobase towards single-stranded DNA. Substrates investigated in this work are highlighted.

Reactivity studies on 5-methylcytosine-containing oligonucleotides were further elaborated. Compared to the former studies, the overall oxidation of 5-methylcytidine in

oligonucleotides was increased from approximately 7% to 63% and depending on the reaction conditions, selective accumulation of 5-formyldeoxycytidine was achieved. Unfortunately, MALDI-MS experiments revealed significant oligonucleotide decomposition under these conditions. First reactions between 5-methylcytosine-containing single-stranded DNA and $[Fe^{IV}\mathbf{L1}(O)]^{2+}$ showed small conversion, preferred oxidation of thymine residues and partial decomposition of the DNA strand. The DNA sample can possibly be stabilized in buffered systems (promising first results were achieved with phosphate buffered saline) and the use of this complex for more selective oxidation of RNA samples containing uracil instead of thymine would be very interesting.

Application of the Iron(IV)-oxido Complex in Synthetic Epigenetics

The reactivity of various natural and artificial methylated nucleobases with $[Fe^{IV}\mathbf{L1}(O)]^{2+}$ was investigated. The reaction rates were determined experimentally from time-resolved UV-vis spectroscopy and could be correlated to the calculated bond dissociation energies of the substrates. These findings further confirm the proposed oxidation mechanism in which the hydrogen atom abstraction is considered the rate-limiting step. These results emerging from a close cooperation with the Zipse group were published in 2021 (Figure 41).

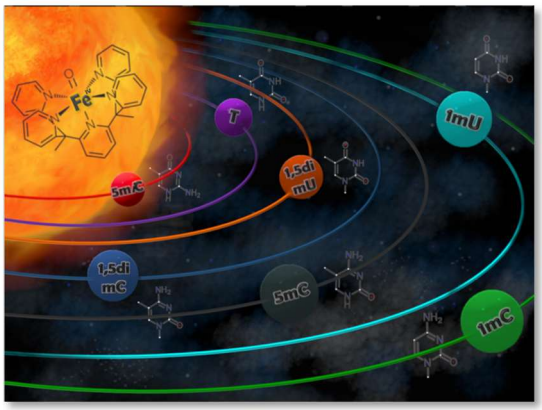

Figure 41: Cover feature of the publication from our cooperation with the Zipse group.[119]

Application of the Iron(IV)-oxido Complex in Mechanistic Studies on TET Enzymes: Oxidation of 5fC via Aldehyde versus Hydrate

To address the question whether oxidation of 5-formylcytidine occurs through the aldehyde or the corresponding hydrate form in enzymatic catalysis, a variety of target molecules was considered. Different amounts of hydrate form and close similarity to the natural substrate were important features which were found in 6-aza-derived nucleosides. The synthesis of all desired substrates, however, turned out to be very challenging. Preliminary reactivity studies were performed with the available compounds. Together with the Zipse group, different synthetic approaches towards the remaining structures are currently under investigation and quantification methods *via* ^{1}H NMR spectroscopy to identify the species distributions over time within a reaction of the substrates with the iron(IV)-oxido complex will be developed.

Expanding the System with Additional Ligands: Characterization and Reactivity of New Iron Complexes

Two additional ligands from the pentapyridyl family were introduced and new iron complexes synthesized and characterized. The new iron(IV)-oxido species $[Fe^{IV}\mathbf{L2}(O)]^{2+}$ and $[Fe^{IV}\mathbf{L3}(O)]^{2+}$ were obtained and their reactivity compared to the previously established system (**L1**). An iron(II)/iron(IV) comproportionation reaction was identified as important side reaction and studied with stopped-flow UV-vis spectroscopy and HR-MS analysis. The thereby forming mononuclear iron(III)-hydroxido species ($[Fe^{III}\mathbf{L1}/\mathbf{L2}(OH)]^{2+}$) could also be synthetically isolated, completing the series of iron(II), iron(III) and iron(IV) complexes for two ligand systems. The main part of this study was presented in a manuscript that was submitted together with our cooperation partners (groups of Prof. Ivanović-Burmazović, Prof. Meyer and Prof. Comba, Scheme 25).[201]

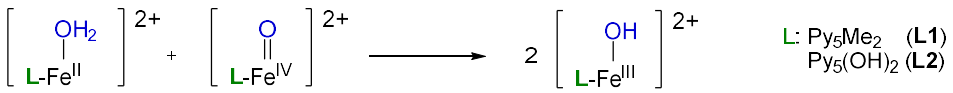

Scheme 25: Schematic representation of the iron(II)/iron(IV) comproportionation reaction, investigated for the two ligand systems Py_5Me_2 (**L1**) and $Py_5(OH)_2$ (**L2**).

Spin Crossover Properties of Iron(II) Complexes

In the course of the investigations on the new complex $[Fe^{II}\mathbf{L3}(mecn)]^{2+}$, a spin crossover towards paramagnetic species at higher temperatures was detected. To closer examine this phenomenon, the synthesis and characterization of a series of iron(II) complexes with three pentapyridyl ligands and different co-ligands (acetonitrile, water and methanol) was attempted. The spin crossover property of the obtained species was investigated with temperature-dependent ^{1}H NMR and UV-vis spectroscopy. Ligand system **L3** showed the highest amount of high spin and the aqua co-ligand induced the presence of slightly more high spin species compared to acetonitrile as co-ligand. The synthesis and characterization of additional iron(II) complexes as well as the study of their spin crossover properties are currently further investigated.

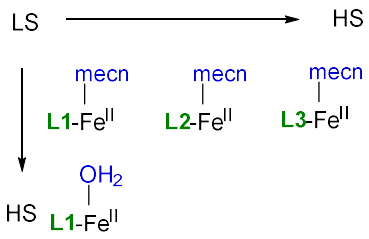

Figure 42: Observed trends in investigations of spin crossover properties of different iron(II) complexes.

VI. EXPERIMENTAL PART

1 Methods and Materials

General experimental methods

Chemicals were purchased from commercial sources (Sigma Aldrich, ABCR, Acros Organics, Alfa Aesar, TCI Chemicals, Oakwood Chemicals) or the LMU Munich chemical supply and used without further purification except for dichloromethane, diethyl ether and hexanes. The solvents were purchased from the LMU Munich chemical supply and distilled once under reduced pressure prior to use.

All organic syntheses were carried out in flame-dried glassware under a positive pressure of nitrogen gas and magnetically stirred if not stated otherwise. Air- and moisture-sensitive chemicals and absolute solvents were transferred via stainless-steel cannula or syringe. Organic solutions were concentrated by rotary evaporation at 40 °C. Analytical thin layer chromatography (TLC) was performed on pre-coated (silica gel, 0.25 mm, 60 Å pore-size, 230–400 mesh, Merck KGA) aluminum plates or which were impregnated with a fluorescent indicator (254 nm). TLC plates were visualized by exposure to ultraviolet light.

All manipulations concerning iron complexes and substrate reactions were carried out under ambient conditions if not stated otherwise.

MilliQ grade water (pH = 5.5) was used for all experiments, received through deionization and subsequent filtration by a Millipore® Synergy® UV system from Merck (Darmstadt, Germany).

Analytical methods

^{1}H NMR and **^{13}C NMR** spectra were recorded, unless otherwise stated, at room temperature on Jeol ECP 270 (400MHz), Jeol ECX 400 (400MHz) and Bruker Avance III

(400MHz) operating at 400MHz for proton nuclei and 100MHz for carbon nuclei. ^{1}H chemical shifts are reported in δ units relative to $CDCl_3$ (δ_H = 7.26), MeOD-*d4* (δ_H = 3.30), CD_3CN (δ_H = 1.93), acetone-*d6* (δ_H = 3.31), D_2O (δ_H = 4.79), DMF-*d7* (δ_H = 8.03) or DMSO-*d6* (δ_H = 2.50). ^{13}C chemical shifts are given in δ units relative to $CDCl_3$ (central line of triplet: δ_C = 77.0), MeOD-*d4* (δ_C = 49.0), CD_3CN (δ_C = 1.30), D_2O with 5% dioxane (δ_C = 67.2). The following abbreviations were used: s = singlet, d = doublet, t = triplet, dd = doublet of doublet, dt = doublet of triplet, m = multiplet. Coupling constants are given in Hertz. The software used for data processing was MNova Version 12.0.4. Two-dimensional correlation spectroscopy (COSY), heterobinuclear single quantum correlation (HSQC) and heterobinuclear multiple bond connectivity (HMBC) experiments were used to assign each signal in the spectra.

Electrospray Ionization Mass Spectrometry (ESI-MS) and electron ionization mass spectroscopy (EI-MS) measurements for characterization of organic compounds and complexes was carried out by Dr. Werner Spahl at the department of chemistry. ESI spectra were recorded with a Thermo Finnigan LTQ FT Ultra Fourier Transform Ion Cyclotron Resonance mass spectrometer with acetonitrile/water as the carrier solvent. Samples were dissolved in dichloromethane, methanol, or water prior to measurement at concentrations of ~0.1 mg/ml.

Electron Ionization Mass Spectrometry (EI-MS) spectra were recorded with a Thermo Q Exactive GC, a Thermo Finnigan MAT 95 or a Jeol MStation mass spectrometer. ESI and EI experiments were carried out by Dr. Werner Spahl at the department of chemistry.

Further, **Cryospray-Ionization Mass Spectrometry (CSI-MS)** measurements of iron complexes and comproportionation reactions were performed on an UHR-TOF Bruker Daltonik (Bremen, Germany) maXis plus, an ESI-quadrupole time-of-flight (qToF) mass spectrometer capable of a resolution of at least 60.000 (FWHM), which was coupled to a Bruker Daltonik Cryospray unit. Detection was in positive ion mode; the source

voltage was 3.5 kV, and the flow rate was 240 µl/hour. The temperature of the spray gas (N_2) and the temperature of the dry gas (N_2) to aid solvent removal were both kept at 5 °C. The mass spectrometer was calibrated prior to every experiment *via* direct infusion of Agilent ESI-TOF low concentration tuning mixture, which provided an m/z range of singly charged peaks up to 2700 Da in both ion modes. Processing of the obtained spectra was done with Bruker DataAnalysis 5.2. Samples were prepared by dissolving the iron complexes in water at concentrations of c = 5 mM. Then, the samples were either diluted directly to a concentration of c = 1 mM for pure compounds or reaction with another iron complex in a 1:1 ratio, resulting in a concentration of c = 2.5 mM. These samples were then diluted to a concentration of c = 1 mM prior to CSI-MS measurement.

FT-Infrared Spectroscopy (IR) was carried out with a JASCO FT/IR-460Plus with an ATR Diamond Plate. Spectra Manager Version 2 from JASCO was used for Data processing.

Elemental Microanalyses (EA) (C, H, N) were performed with a vario EL element analyzer.

X-ray crystallographic data collection and structure elucidation was performed by Dr. Peter Mayer at the Chemistry Department of the Ludwig-Maximilians University Munich. The X-ray intensity data were collected on a Bruker D8 Venture TXS system equipped with a multilayer mirror optics monochromator and a Mo Kα rotating-anode X-ray tube (Λ = 0.71073 Å). The frames were integrated with the Bruker SAINT software package using a narrow-frame algorithm[238]. Data were corrected for absorption effects using the Multi-Scan method (SADABS)[239]. The structure was solved and refined using the Bruker SHELXTL Software Package.[240]

UV-Vis Spectroscopy measurements were either conducted with an Agilent Cary 60 UV-Vis with Peltier Element or with an Agilent 8453 Diode Array Spectrophotometer with stirred, thermostatted cuvette holder. 10 mm quartz suprasil cuvettes from Hellma were used unless noted otherwise.

Solid samples were measured on a Cary 500 Scan UV-Vis-NIR-Spectrophotometer with a Labsphere DRA-CA-5500 photometer sphere. The *Kubelka-Munk* function (eq. 2) was used to translate the measured diffuse reflection into data, which can be compared to absorption experiments. Highly colored samples were diluted with $BaSO_4$ in order to keep the diffuse reflectance above at least 60% at all times.

$$\frac{K}{S} = \frac{(1-R)^2}{2R} \qquad (2)$$

(R = remission; K = absorption coefficient; R = scattering coefficient)

Stopped-flow measurements were performed with a SFM-4000/S stopped flow mixer from Bio-Logic Science Instruments. The UV-vis spectra were recorded by using a Tidas MCS UV/NIR from J&M Analytik AG.

EPR Spectroscopy measurements were performed using a BRUKER EMXNano X-band (9.5 GHz) spectrometer at room temperature. All 1D continuous wave (CW) EPR experiments were conducted using a microwave power of 1.0 mW. Modulation amplitudes and frequencies of 0.4 mT and 100 kHz were used, respectively. A time constant of 1.28 ms and a sweep time of 10 min were also used.

For **centrifugation**, a Heraeus Megafuge 8R Benchtop Centrifuge with swinging bucket was used.

A Christ Alpha 1-2 LDplus **Lyophilisator** (LYO) was used to remove residual water from the products.

For **GC-MS** measurements an Agilent 7920 GC coupled to an Agilent 5970 EI mass spectrometer was used equipped with a silica capillary column (30 m x 0.25 mm) coated with cross-linked 5% phenyl/95% methylpolysiloxane. The injector temperature was set to 280 °C and the temperature of the ion source 230 °C.

General derivatization and measurement procedure for GC-MS Samples: Each sample was suspended in acetonitrile, BSTFA was added and the mixture was shaken at 70 °C for

30 min. The samples were syringe filtered (PTFE, 0.45 µm) and injected onto the aforementioned GC-MS instrument. The initial oven temperature was 80 °C, held there for 2 min, ramped to 240 °C at 5 K/min and then held there for 20 min.

Inductively coupled plasma optical emission spectroscopy (ICP-OES) was conducted by the central analysis department on a VARIAN-VISTA instrument with an autosampler. To sample solutions, 0.15 ml of concentrated nitric acid (69%, Aristar for trace analysis by VWR®) were added and the mixture incubated at 105 °C. After being allowed to cool to room temperature, the samples were diluted with MilliQ® grade water to a total volume of 5.0 ml. The measurements were then conducted on a Varian® ICP OES Vista Pro RL and repeated a total of three times for 10 s; each after a stabilization period of 45 s. For the measurement of the iron content the wavelengths 234 nm, 238 nm, 239 nm, and 259 nm were used while 380 nm, 407 nm, 418 nm, and 447 nm were used to determine the cerium content.

Cyclic voltammetry measurements were performed using an Autolab instrument with a PGSTAT 204 potentiostat. A three-electrode arrangement was employed consisting of a glassy carbon disk working electrode (A = 0.07 cm^2) (Metrohm), a platinum counter electrode (Metrohm) and a silver wire (Metrohm) as reference electrode. Potentials were referred to a Fc/Fc^+ redox couple, in acetonitrile and to an Ag/AgCl/(3 M KCl) reference electrode in water. Prior to each experiment, the working electrode was polished with 1 µm alumina, rinsed with deionized water and wiped with a paper tissue. In a typical experiment, a 1 mM solution of the iron compound in acetonitrile or water, with 0.1 M $TEAPF_6$ or KNO_3 respectively as support electrolyte was purged with nitrogen and then analyzed.

HPLC traces were recorded on an Agilent 1260 Infinity II HPLC system, equipped with a flexible quaternary pump (G7104C), a vialsampler with heatable column compartment (G7129C) and a multi-wavelength detector (G7165A). An ACE C-18/PFP column (150×4.6mm; 5 µm; 100 Å) was used with a binary solvent system grading from 100% A/0% B to 99% A/1% B over 18 min (A: 0.1% TFA in H2O; B: 0.1% TFA in MeCN).

In the case of the oligonucleotide experiments, nucleosides of interest were quantified using the stable isotope dilution technique.[241] Internal standards (isotopically labelled 5mdC*, 5hmdC*, 5fdC*, 5cadC*, and 8-oxo-dG*) were added to a sample and the samples were then digested using Degradase Plus from Zymo Research, and subsequently measured on a tandem **UHPLC-MS/MS** system (UHPLC system: Agilent Technologies, model no. 1290 Infinity II LC; MS system: Triple quadrupole LC/MS system with iFunnel technology (Agilent Technologies, model no. 6490)). The exact method was described here.[241] The sample data were analyzed by Quantitative MassHunter Software from Agilent. Nucleosides dC and dG were quantified using the signal of the UV-trace with known calibration curves.[241]

MALDI Mass Spectra were recorded on a Bruker Autoflex maX time-of-flight mass spectrometer equipped with a nitrogen laser (λ =337 nm). The oligonucleotides (2-3 µL) were desalted on a 0.025 µm VSWP filter (Millipore) and co-crystallized in a 3-hydroxypicolinic acid matrix (HPA, 1 µL).

Mößbauer spectra were recorded using an alternating constant acceleration Wissel Mößbauer spectrometer operated in the transmission mode, equipped with a ^{57}Co source in a rhodium matrix and a Janis closed-cycle He cryostat. Simulated Lorentzian doublet spectra were fitted to the experimental data using the program mf2.SL.[242]

Temperature-dependent **magnetic susceptibility** measurements were carried out with a Quantum-Design MPMS3 SQUID magnetometer equipped with a 7 Tesla magnet in the range from 400 to 2.0 K at a magnetic field of 0.5 T. The powdered sample was contained in a polycarbonate capsule and fixed in a non-magnetic sample holder. Each raw data file for the measured magnetic moment was corrected for the diamagnetic contribution of the sample holder and the polycarbonate capsule. The molar susceptibility data were corrected for the diamagnetic contribution.

Flash column chromatography was performed by the Interchim PuriFlash PF420. Self-Packed columns were used, with Silica gel 60 (40-63 µm) from Merck as stationary phase. As eluent, the solvent mixtures mentioned in the specific experiments were used.

ESI-LRMS/LC-ESI-LRMS measurements were performed on an Agilent 1100 SL system (G1313A ALS, G1316A COLCOM, G1316A VWD, G1312A Bin Pump) coupled to a Bruker Daltonik HCTultra PTM Discovery system (ESI mode), used either with a thermo scientific Hypersil GOLD™ column (50 mm × 2. mm, 3 µm) or *via* direct-injection. As eluent system either a mixture of water/acetonitrile with 0.1% formic acid or water/methanol with 0.1% formic acid was used. The flow rate was 0.4 mL/min. As detection wavelength either 210 nm, 254 nm, 399 nm or 400 nm was used.

2 Synthetic Procedures

2.1 Syntheses Involving Ligand L1

Synthesis of **pL1**

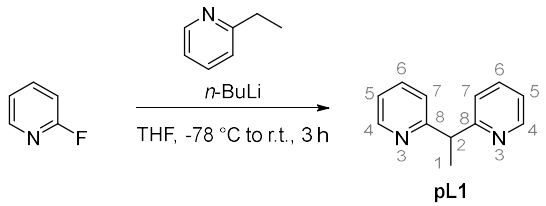

According to a modified literature procedure.[243]

2-ethylpyridine (6.27 mL, 5.88 g, 54.84 mmol, 2.1 equiv.) was dissolved in dry tetrahydrofuran (50 mL) under inert atmosphere (nitrogen) and cooled to −78 °C. A solution of *n*-butyl lithium (2.5 M in hexane, 20.80 mL, 52.01 mmol, 2.0 equiv.) was added dropwise turning the solution red. After stirring the reaction mixture for 60 min at −78 °C, 2-fluoropyridine (2.21 mL, 2.50 g, 25.8 mmol, 1.0 equiv.) was added dropwise and the solution stirred at −78 °C for an additional 10 min. The reaction mixture was allowed to warm to room temperature and then stirred at room temperature for 3 h. Ice (30 g) was added slowly and additional MilliQ grade water (30 mL) was added, and the mixture stirred for 10 min. The layers were separated, and the aqueous layer was extracted with dichloromethane (3 x 50 mL). The combined organic layers were dried over anhydrous magnesium sulfate and the solvents removed *in vacuo*. Excess 2-ethylpyridine was removed under reduced pressure overnight to yield the product **pL1** as an orange oil (3.79 g, 84%).

^{1}H NMR (400.0 MHz, $CDCl_3$, 295 K): δ = 8.55 (ddd, J = 4.9 Hz, J = 1.9 Hz, J = 0.9 Hz, 2H, *H-4*), 7.60 (td, J = 7.7 Hz, J = 1.8 Hz, 2H, *H-6*), 7.28 (dd, J = 7.9 Hz, J = 1.0 Hz, 2H, *H-7*), 7.11 (ddd, J = 7.5 H, J = 4.9 Hz, J = 1.2 Hz, 2H, *H-5*), 4.48 (q, J = 7.2 Hz, 2H, *H-2*), 1.76 (d, J = 7.2 Hz, 3H, *H-1*) ppm.

^{13}C NMR (100.0 MHz, $CDCl_3$, 295 K): δ = 163.9 (*C-8*), 149.3 (*C-4*), 136.6 (*C-6*), 122.5 (*C-7*), 121.5 (*C-5*), 49.9 (*C-2*), 19.8 (*C-1*) ppm.

HR-MS (ESI): calc. for $C_{12}H_{13}N_2$ $[M+H]^+$: 185.10787 m/z; found: 185.10723 m/z.

Synthesis of **L1**

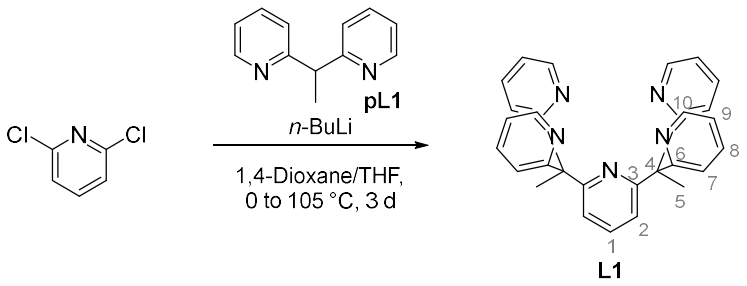

According to a modified literature procedure.[91]

pL1 (2.00 g, 10.9 mmol, 3.0 equiv.) was dissolved in dry 1,4-dioxane (36 mL) under inert atmosphere (nitrogen) and dry tetrahydrofuran (4 mL) and cooled to 0 °C. A solution of *n*-butyl lithium (2.5 M in hexane, 4.34 mL, 10.9 mmol, 3.0 equiv.) was added and the solution turned red. The mixture was stirred for 45 min at 0 °C, then 2,6-dichloropyridine (535.5 mg, 3.62 mmol, 1.0 equiv.) was added. The reaction mixture was allowed to warm to room temperature and then heated to reflux (105 °C) for 60 hours. The mixture was allowed to cool to room temperature and water (20 mL) was added. The solution was extracted with dichloromethane (3 x 70 mL), the combined organic layers were dried over anhydrous magnesium sulfate and the solvents removed *in vacuo*. Methanol (40 mL) was added, and the solvents removed *in vacuo* to remove residual 1,4-dioxane. Diethyl ether was added until a yellow precipitate began to form which was filtered, washed with diethyl ether (1 x 10 mL) and dried to yield the product **L1** as a yellow solid (91%).

^{1}H NMR (400.0 MHz, $CDCl_3$, 295 K): δ = 8.51 (ddd, J = 4.8 Hz, J = 1.9 Hz, J = 0.9 Hz, 4H, *H-10*), 7.54 (t, J = 7.9 Hz, 1H, *H-1*), 7.39 (ddd, J = 8.1 Hz, J = 7.5 Hz, J = 1.9 Hz, 4H, *H-8*), 7.05 (d, J = 7.9 Hz, 2H, *H-2*) 7.04 (ddd, J = 7.5 Hz, J = 4.8 Hz, J = 1.1 Hz, 4H, *H-7*), 6.84 (dt, J = 8.0 Hz, J = 1.0 Hz, 4H, *H-9*), 2.21 (s, 6H, *H-5*) ppm.

^{13}C NMR (100.0 MHz, $CDCl_3$, 295 K): δ = 166.2 (*C-6*), 166.3 (*C-3*), 148.5 (*C-10*), 136.8 (*C-8*), 135.6 (*C-1*), 124.1 (*C-9*), 121.0 (*C-2*), 120.0 (*C-7*), 60.1 (*C-4*), 26.8 (*C-5*) ppm.

HR-MS (ESI): calc. for $C_{29}H_{26}N_5$ $[M+H]^+$: 444.21882 m/z; found: 444.21811 m/z.

IR (thin film): $\tilde{\nu}$ = 3053, 2992, 1566, 1466, 1428, 1365, 1293, 1153, 1102, 1078, 1067, 1046, 991, 962, 903, 875, 799, 786, 768, 752, 699, 654 cm^{-1}.

Synthesis of $[Fe^{II}\mathbf{L1}(mecn)](OTf)_2$

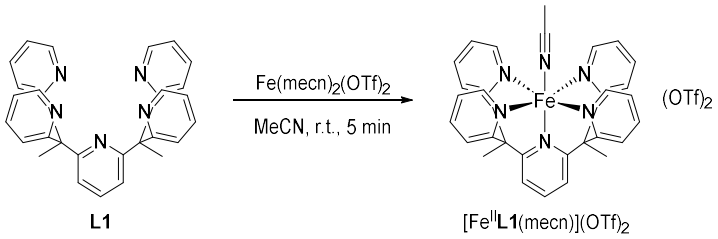

According to a modified literature procedure.[91]

Ligand **L1** (300.0 mg, 0.679 mmol, 1.0 equiv.) was suspended in acetonitrile (15 mL). Iron(II)bis(acetonitrile)bis(triflate) (294.9 mg, 0.679 mmol, 1.0 equiv.) was added, turning the solution deep red. The mixture was then stirred for 5 min and then diethyl ether was diffused into the solution to give the product $[Fe^{II}\mathbf{L1}(mecn)](OTf)_2$ as red-brown crystals (516.0 mg, 91%).

^{1}H NMR (400.0 MHz, CD_3CN, 295 K): δ = 9.81 (d, J = 5.9 Hz, 4H), 8.03 (s, 3H), 7.93 (d, J = 3.8 Hz, 8H), 7.54 (m, 4H), 2.75 (s, 6H), 1.96 (s, 3H) ppm.

^{13}C NMR (100.0 MHz, CD_3CN, 295 K): δ = 165.0, 163.0, 158.2, 140.1, 139.7, 124.3, 123.8, 122.1, 118.3, 55.7, 24.2 ppm.

HR-MS (ESI): calc. for $C_{30}H_{25}F_3FeN_5O_3S$ $[Fe(\mathbf{L1})(mecn)(OTf)]^+$: 648.09796 m/z; found: 648.09648 m/z. calc. for $C_{31}H_{28}FeN_6$ $[Fe(\mathbf{L1})(mecn)]^{2+}$: 270.08625 m/z; found: 270.08562 m/z.

Elemental Analysis: calc. for $C_{33}H_{28}F_6FeN_6O_6S_2$: C, 47.27; H, 3.37; N, 10.02; S, 7.65. found: C, 47.03; H, 3.33; N, 9.94; S, 7.86.

IR (thin film): $\tilde{\nu}$ = 1598, 1469, 1442, 1415, 1281, 1251, 1225, 1149, 1070, 1028, 865, 791, 761, 702 cm^{-1}.

UV-vis (H_2O, 25 °C): absorption maxima at λ = 220, 260, 370, 450 nm.

ε (λ = 450 nm): 5932.4 L mol^{-1} cm^{-1}.

Synthesis of $[Fe^{II}\mathbf{L1}(mecn)](OTf)_2$

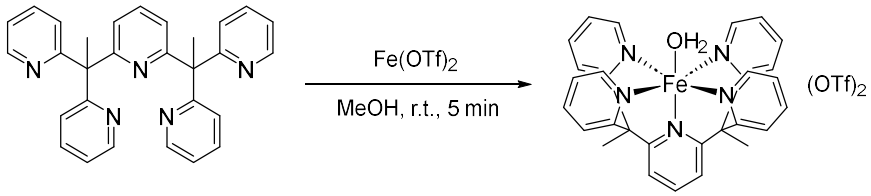

L1 $[Fe^{II}\mathbf{L1}(OH_2)](OTf)_2$

Ligand **L1** (50.2 mg, 0.113 mmol. 1.0 equiv.) was suspended in methanol (2.5 mL) under ambient conditions and iron(II)bis(triflate) (40.06 mg, 0.113 mmol, 1.0 equiv.) was added as a solid. The reaction mixture was stirred for 10 min at room temperature and then diethyl ether was diffused into the solution under ambient conditions to give the product (79.10 mg, 0.096 mmol, 86%) as black crystals.

^{1}H NMR (400 MHz, acetone-d_6, 293 K): δ = 8.32 (d, J = 8.0 Hz, 5H), 8.19 (d, J = 7.7 Hz, 5H), 8.08 (td, J = 8.4, 7.9, 1.5 Hz, 5H), 7.73 – 7.68 (m, 5H), 3.73 (s, 2H), , 2.08 (d, J = 1.1 Hz, 6H) ppm.

IR (thin film): $\tilde{\nu}$ = 1597, 1471, 1469, 1439, 1409, 1389, 1289, 1233, 1219, 1278, 1154, 1028, 861, 802, 764 cm^{-1}.

UV-vis (H_2O, 25 °C): absorption maxima at λ = 210, 260, 370, 460 nm.

Compound confirmed by crystal structure analysis (section VII.11).

This experiment was part of the research internship of Antonia Goldhammer, conducted under my supervision.

Synthesis of $[Fe^{II}\mathbf{L1}(OH)](OTf)_2$

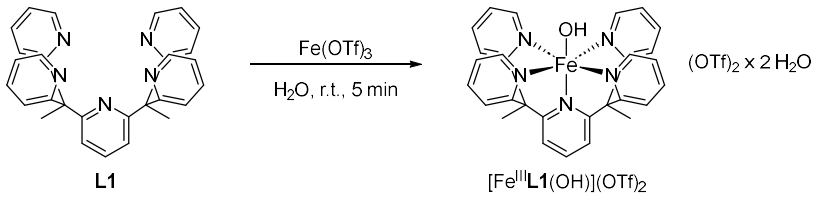

Ligand **L1** (1.00 g, 2.25 mmol, 1.0 equiv.) was suspended in water (40 mL). Iron(III) triflate (1.51 mg, 3.00 mmol, 1.3 equiv.) was added. The mixture turned red upon mixing, and was sonicated for 1 h at 40 °C. The mixture was filtered through a syringe filter (PTFE 0.45 µm) and stored at 4 °C for 3 days. The formed crystals were washed with water and dried *in vacuo* to give $[Fe^{III}\mathbf{L1}(OH)](OTf)_2$ x 2 H_2O (no yield determined).

HR-MS (ESI): calc. for $C_{29}H_{26}FeN_5O$ $[Fe\mathbf{L1}(OH)]^{2+}$: 258.07434 m/z; found: 258.07355 m/z.

Elemental Analysis: calc. for $C_{31}H_{26}F_6FeN_5O_7S_2$: C, 45.71; H, 3.22; N, 8.60; S, 7.87. found: C, 44.17; H, 3.36; N, 8.07; S, 7.78.

IR (thin film): $\tilde{\nu}$ = 3424, 3091, 1657, 1599, 1462, 1447, 1390, 1256, 1224, 1154, 1103, 1026, 914, 868, 847, 782, 764, 742, 664 cm^{-1}.

Compound confirmed by crystal structure analysis (section **Fehler! Verweisquelle konnte nicht gefunden werden.**).

Synthesis of $[Fe^{IV}\mathbf{L1}(O)][Ce(NO_3)_6]$

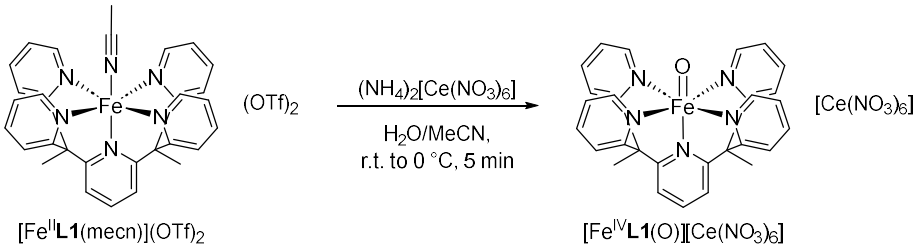

According to a modified literature procedure.[91]

$[Fe^{II}\mathbf{L1}(mecn)](OTf)_2$ (100 mg, 0.119 mmol, 1.0 equiv.) was dissolved in a 3:1 acetonitrile:water mixture (1.5 ml). Cerium(IV) ammonium nitrate (347.1 mg, 0.633 mmol, 5.3 equiv.) was added as a solid and the mixture sonicated for 60 s. A green precipitate formed and the reaction mixture was placed in an ice bath for 10 min. The solid was collected on a sintered glass frit, washed with an ice cold 3:1 acetonitrile:water mixture (1.5 mL) and dried *in vacuo* to yield product $[Fe^{IV}\mathbf{L1}(O)][Ce(NO_3)_6]$ as a green solid (107.2 mg, 87%).

Elemental Analysis: calc. for $C_{29}H_{25}CeFeN_{11}O_{19}$: C, 33.90; H, 2.45; N, 14.99. found: C, 33.81; H, 2.58; N, 15.20.

ICP-OES:

Fe: 52.3 mg/g ≙ 0.937 mmol/g

Ce: 131.5 mg/g ≙ 0.939 mmol/g

Molecular ratio of Fe:Ce = 1:1

IR (thin film): $\tilde{\nu}$ = 1600, 1496, 1277, 1033, 864, 822, 804, 784, 760, 742 cm^{-1}.

UV-vis (H_2O, 25 °C): absorption maxima at λ = 720 nm.

ε (λ = 720 nm): 277 L mol^{-1} cm^{-1}.

Compound confirmed by crystal structure analysis (section **Fehler! Verweisquelle konnte nicht gefunden werden.**).

2.2 Syntheses Involving Ligand L2

Synthesis of **pL2**

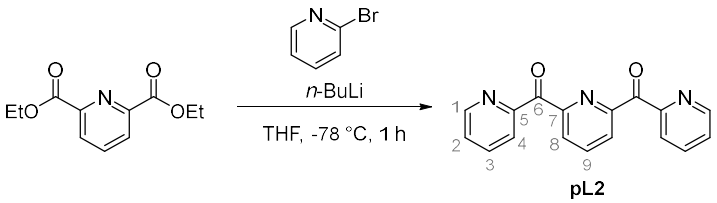

According to a modified literature procedure.[186]

A flame-dried flask was charged with 2-bromo pyridine (2.62 mL, 4.25 g, 26.88 mmol, 3.0 equiv.) in dry tetrahydrofuran (100 mL). After cooling the mixture to −78 °C, a solution of *n*-butyl lithium (2.5 M in hexanes, 10.75 mL, 1.72 g, 26.88 mmol, 3.0 equiv.) was added dropwise, resulting in a color change to brown. The mixture was stirred at −78 °C for 10 min and then a solution of 1-(6-(1,1-dipyridin-2-yl)ethyl)pyridin-2-yl)ethan-1-one (0.224 M in tetrahydrofuran, 40.0 mL, 2.0 g, 8.96 mmol, 1.0 equiv.) was added dropwise, turning the solution to a very dark green. The reaction was stirred at −78 °C for 40 min, then methanol (50 mL) were added slowly to quench the reaction. The mixture was allowed to warm to room temperature, of aqueous hydrochloric acid (3 M, 100 mL) were added, and organic solvents removed. Additional of aqueous hydrochloric acid (3 M, 10 mL) were added, and the mixture washed with dichloromethane (2 x 25 mL), this organic layer was discarded. The aqueous layer was carefully basified to pH 12 with an aqueous solution of sodium hydroxide (19 M) and extracted with dichloromethane (3 x 100 mL). These combined organic layers were dried over anhydrous magnesium sulfate and the solvents removed *in vacuo*. Recrystallization at room temperature from acetone/diethyl ether afforded the product **pL2** as a colorless crystalline solid (1.74 g, 67%).

^{1}H NMR (400.0 MHz, $CDCl_3$, 295 K): δ = 8.75 (ddd, J = 4.7 Hz, J = 1.7 Hz, J = 0.9 Hz, 2H, *H-1*), 8.31 (d, J = 8.0 Hz, 2H, *H-8*), 8.19 (dt, J = 7.9 Hz, J = 1.1 Hz,

2H, *H-4*), 8.11 (dd, J = 8.2 Hz, J = 7.4 Hz, 1H, *H-9*), 7.79 (td, J = 7.8 Hz, J = 1.8 Hz, 2H, *H-3*), 7.45 (ddd, J = 7.6 Hz, J = 4.7 Hz, J = 1.2 Hz, 2H, *H-2*) ppm.

^{13}C NMR (100.0 MHz, CD_3CN, 295 K): δ = 191.91 (*C-6*), 153.77 (*C-7*), 153.54 (*C-5*), 149.35 (*C-1*), 137.91 (*C-9*), 136.57 (*C-3*), 127.54 (*C-8*), 126.52 (*C-2*), 126.21 (*C-4*) ppm.

HR-MS (ESI): calc. for $C_{17}H_{12}N_3O_2$ $[M+H]^+$: 290.09295 m/z; found: 290.09271 m/z.

Elemental Analysis: calc. for $C_{17}H_{11}N_3O_2$: C, 70.58; H, 3.83; N, 14.53. found: C, 70.09; H, 3.70; N, 14.11.

Synthesis of **L2**

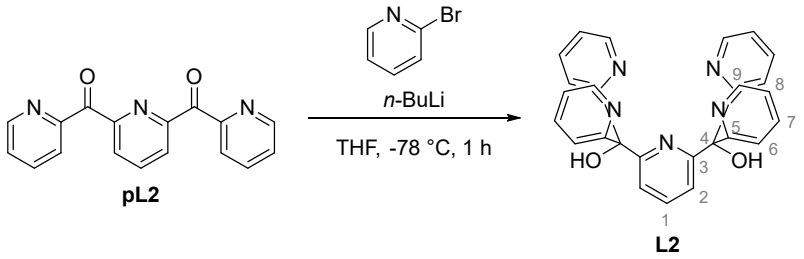

According to a modified literature procedure.[186]

2-bromo pyridine (0.36 mL, 0.58 g, 3.66 mmol, 2.12 equiv.) was dissolved in dry tetrahydrofuran (80 mL) under nitrogen atmosphere. After cooling the mixture to −78 °C, a solution of *n*-butyl lithium (2.5 M in hexanes, 1.49 mL, 0.24 g, 3.72 mmol, 2.15 equiv.) was added dropwise, resulting in a color change to brown. The mixture was stirred at −78 °C for 10 min and then a solution of **pL2** (57.5 mM in tetrahydrofuran/1,4-dioxane (4:1), 30.0 mL, 0.5 g, 1.73 mmol, 1.0 equiv.) was added dropwise, turning the solution to a dark green. The reaction was stirred at −78 °C for 60 min, then allowed to warm to room temperature. When LC-MS confirmed complete consumption of **pL2**, methanol (50 mL) was added slowly to quench the reaction. Then aqueous hydrochloric acid (3 M, 100 mL) was added and the organic solvents removed. Additional aqueous hydrochloric acid (3 M, 10 mL) was added, and the mixture washed with dichloromethane (2 x 25 mL), this organic layer was discarded. The aqueous layer was carefully basified to pH 12 with an aqueous solution of sodium hydroxide (19 M) and extracted with dichloromethane (3 x 100 mL). These combined organic layers were dried over anhydrous magnesium sulfate and the solvents removed *in vacuo*. Recrystallization at room temperature from acetone/diethyl ether gave the product **L2** as a colorless solid (290.0 mg, 38%).

^{1}H NMR (400.0 MHz, $CDCl_3$, 295 K): δ = 8.49 (ddd, J = 4.9 Hz, J = 1.8 Hz, J = 1.0 Hz, 4H, *H-9*), 7.72 (d, J = 1.4 Hz, 1H, *H-1*), 7.52 (ddd, J = 8.0 Hz, J = 7.4 Hz, J = 1.8 Hz, 4H, *H-7*), 7.44 (dt, J = 8.0 Hz, J = 1.1 Hz, 4H, *H-8*), 7.17-7.13 (m, 6H, *H-2*, *H-6*) ppm.

^{13}C NMR (100.0 MHz, CD_3CN, 295 K): δ = 162.63 (*C-5*), 147.56 (*C-9*), 136.21 (*C-7*), 123.55 (*C-8*), 122.51 (*C-2*), 122.32 (*C-6*), 120.65 (*C-1*), 77.48 (*C-4*) ppm.

HR-MS (ESI): calc. for $C_{27}H_{22}N_5O_2$ $[M+H]^+$: 448.17735 m/z; found: 448.17693 m/z.

Elemental Analysis: calc. for $C_{27}H_{21}N_5O_2$: C, 72.47; H, 4.73; N, 15.65. found: C, 71.49; H, 4.60; N, 15.24.

Synthesis of $[Fe^{II}\mathbf{L2}(mecn)](OTf)_2$

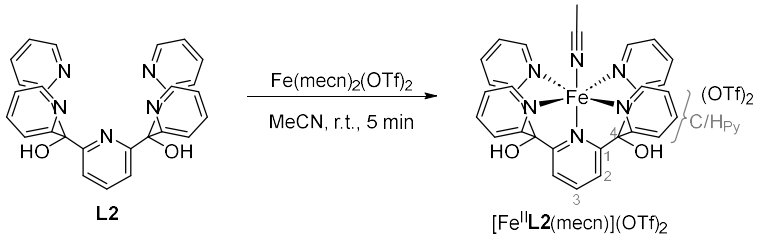

According to a modified literature procedure.[91]

Ligand **L2** (51.0 mg, 0.114 mmol, 1.0 equiv.) was suspended in acetonitrile (2.55 mL). Iron(II)bis(acetonitrile)bis(triflate) (49.7 mg, 0.114 mmol, 1.0 equiv.) was added as a solid, turning the solution deep red. The mixture was then stirred for an additional 5 min and then diethyl ether was diffused into the solution under ambient conditions to give the product $[Fe^{II}\mathbf{L2}(mecn)](OTf)_2$ as red crystals (80.0 mg, 77%).

^{1}H NMR (400.0 MHz, CD_3CN, 295 K): δ = 9.73 (d, J = 5.8 Hz, 4H, H_{Py}), 8.17 (m, 5H, H_{Py}/H-2/H-3), 7.98 (ddd, J = 8.1 Hz, J = 7.4 Hz, J = 1.4 Hz, 4H, H_{Py}), 7.56 (ddd, J = 7.4 Hz, J = 5.8 Hz, J = 1.5 Hz, 4H, H_{Py}), 6.85 (s, 2H, O*H*), 1.96 (s, 3H, CH_3CN) ppm.

^{13}C NMR (100.0 MHz, CD_3CN, 295 K): δ = 164.5 ($C_{Py\text{-}quart}$), 163.1 (C-1), 158.1 (C_{Py}), 140.7 (C-2), 140.0 (C_{Py}), 124.9 (C_{Py}), 122.4 (C_{Py}), 121.0 (C-3), 80.7 (C-4) ppm.

HR-MS (ESI): calc. for $C_{30}H_{25}F_3FeN_5O_3S$ $[Fe\mathbf{L2}(OTf)]^+$: 652.05649 m/z; found: 652.05432 m/z.

Elemental Analysis: calc. for $C_{33}H_{30}F_6FeN_6O_7S_2$ ($[Fe^{II}\mathbf{L2}(mecn)](OTf)_2$ x H_2O): C, 43.27; H, 3.05; N, 9.77; S, 7.45. **f**ound: C, 43.25; H, 3.12; N, 9.79; S, 7.91.

IR (thin film): $\tilde{\nu}$ = 3288, 1738, 1603, 1469, 1444, 1373, 1276, 1244, 1224, 1157, 1096, 1028, 887, 800, 762, 712, 661 cm^{-1}.

UV-vis (H_2O, 25 °C): absorption maxima at λ = 220, 260, 370, 450 nm.

ε (λ = 450 nm): 4190 L mol^{-1} cm^{-1}.

Compound confirmed by crystal structure analysis (section **Fehler! Verweisquelle konnte nicht gefunden werden.**).

Synthesis of $[Fe^{III}\mathbf{L2}(OH)](OTf)_2$

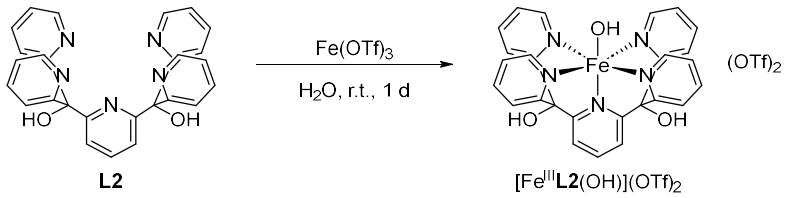

Finely ground **L2** (200.0 mg, 0.447 mmol, 1.0 equiv.) was suspended in water (1.1 mL). Iron(III) triflate (247.3 mg, 0.492 mmol, 1.1 equiv.) was added and the mixture was sonicated for 60 s, shaken, and again sonicated for 60 s resulting in a orange-red suspension. The mixture was then syringe-filtered (PTFE, 0.45 µm) to give a clear orange solution. This was placed in a fridge at 4 °C for 3 d until dark red crystals had formed. The supernatant was removed, the crystals washed with water (2 x 0.5 mL, brief sonication) and subsequently dried *in vacuo* to give the pure product $[Fe^{III}\mathbf{L2}(OH)](OTf)_2$ as brown crystals (no yield determined).

HR-MS (EI): calc. for $C_{27}H_{22}FeN_5O_3$ $[Fe\mathbf{L2}(OH)]^{2+}$: 260.0536 m/z; found: 260.0548 m/z.

Elemental Analysis: calc. for $C_{29}H_{24}F_6FeN_5O_{10}S_2$ $[Fe\mathbf{L2}(OH)](OTf)_2$ x H_2O: C, 41.64; H, 2.89; N, 8.37; S, 7.67. **f**ound: C, 41.71; H, 2.92; N, 8.24; S, 7.94.

IR (thin film): $\tilde{\nu}$ = 3450, 3264, 1739, 1604, 1458, 1445, 1364, 1278, 1243, 1222, 1152, 1097, 1027, 927, 810, 795, 766, 741, 675, 662 cm^{-1}.

Compound confirmed by crystal structure analysis (section **Fehler! Verweisquelle konnte nicht gefunden werden.**).

Synthesis of $[Fe^{IV}\mathbf{L2}(O)][Ce(NO_3)_6]$

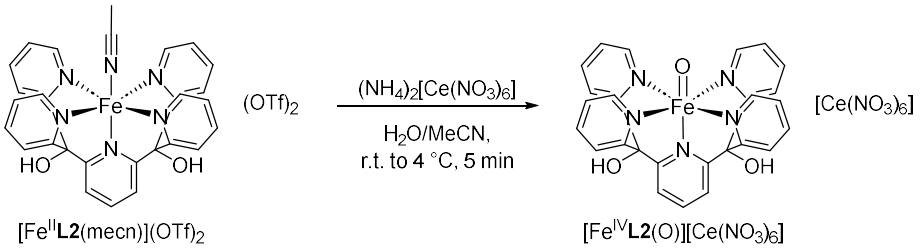

According to a modified literature procedure.[91]

$[Fe^{II}\mathbf{L2}(mecn)](OTf)_2$ (80 mg, 0.950 mmol, 1.0 equiv.) was dissolved in a 3:1 acetonitrile:water mixture (1.2 mL). Cerium(IV) ammonium nitrate (276.4 mg, 0.504 mmol, 5.3 equiv.) was added as a solid and the mixture sonicated for 60 s. As a pale green precipitate began to form the reaction mixture was placed on ice for 10 min. The solid was collected *via* filtration, washed with ice cold 3:1 acetonitrile:water (1.2 mL) and dried *in vacuo* to yield product $[Fe^{IV}\mathbf{L2}(O)][Ce(NO_3)_6]$ as a pale green solid (no yield determined).

Elemental Analysis: calc. for $C_{27}H_{23}CeFeN_{11}O_{22}$ (M x H_2O): C, 30.90; H, 2.21; N, 14.68. **f**ound: C, 30.71; H, 2.54; N, 15.05.

HR-MS (ESI)**:** calc. for $C_{27}H_{21}FeN_5O_3$ $[Fe^{IV}\mathbf{L2}(O)]^{2+}$: 259.5497 m/z; found: 259.5492 m/z.

IR (thin film): $\tilde{\nu}$ = 1605, 1504, 1463, 1278, 1170, 1098, 1029, 830, 805, 780, 763, 742, 661, 626, 614 cm^{-1}.

UV-vis (H_2O, 25 °C): absorption maxima at λ = 730 nm.

ε (λ = 730 nm): 292 L mol^{-1} cm^{-1}.

2.3 Syntheses Involving Ligand L3

Synthesis of **pL3**

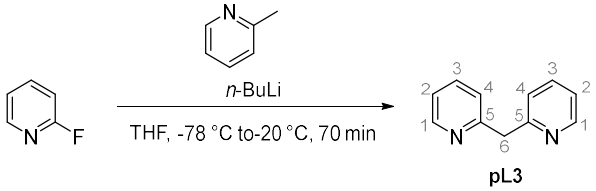

According to a modified literature procedure.[202]

A flame-dried SCHLENK flask was charged with 2-methylpyridine (3.73 g, 3.95 mL, 40.00 mmol, 2.0 equiv.) in dry tetrahydrofuran (40 mL) and then cooled to -78 °C. *n*-Butyl lithium (2.5 M in hexane, 16 mL, 40.00 mmol, 2.0 equiv.) was added dropwise. The reaction mixture was stirred for 70 min at -78 °C and then allowed to warm to -20 °C. 2-Fluoropyridine (1.72 mL, 20.00 mmol, 1.0 equiv.) was added to the reaction and the mixture was stirred at room temperature for 30 min and then hydrolyzed with ice (40 g). The aqueous layer was extracted with dichloromethane (3 x 50 mL) and the combined organic layers were dried over anhydrous sodium sulfate. The solvent was evaporated to afford **pL3** (3818 mg, 22.43 mmol, 56%) as a brown oil.

^{1}H NMR (400 MHz, $CDCl_3$, 295 K): δ = 8.55 (dd, J = 4.9, 1.9 Hz, 2H, *H-1*), 7.60 (td, J = 7.7, 1.9 Hz, 2H, *H-3*), 7.26 (dt, J = 7.8, 1.1 Hz, 2H, *H-4*), 7.12 (ddd, J = 7.5, 4.9, 1.2 Hz, 2H, *H-2*), 4.34 (s, 2H, *H-6*) ppm.

^{13}C NMR (101 MHz, $CDCl_3$, 295 K) δ = 159.6 (*C-5*), 149.6 (*C-1*), 136.7 (*C-3*), 123.7 (*C-4*), 121.6 (*C-2*), 47.5 (*C-6*) ppm.

HR-MS (EI): calc. for $C_{11}H_{10}N_2$ [M]: 170.0844 m/z; found: 170.0793 m/z.

Elemental Analysis: calc. for $C_{11}H_{10}N_2$: N, 16.46; C, 77.62; H, 5.92. found: N, 15.94; C, 75.39; H, 5.81.

This experiment was part of the research internship of Jan Prohaska and Antonia Goldhammer, conducted under my supervision.

Synthesis of **L3**

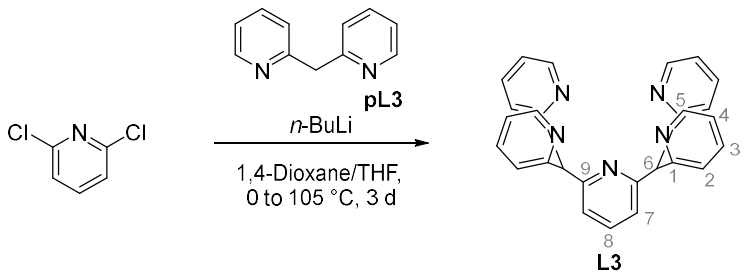

According to a modified literature procedure.[91, 202]

A SCHLENK flask was charged with the precursor (1.50 g, 8.81 mmol, 1.0 equiv.) in 1,4-dioxane/tetrahydrofuran (9:1, 36 mL, 4 mL) and then cooled to 0 °C. *n*-Butyl lithium (2.5 M in hexane, 3.53 mL, 8.81 mmol, 1.0 equiv.) was added dropwise. The reaction mixture was stirred at 0 °C for 2 h and then 2,6-dichloropyridine (430 mg, 2.91 mmol, 0.33 equiv.) was added as a solid and the reaction was heated to reflux for 60 h and was then allowed to cool to room temperature. Water (30 mL) was added, and the aqueous layer extracted with dichloromethane (3 x 80 mL). The combined organic layers were dried over sodium sulfate. Methanol (40 mL) was added and subsequently removed, the crude product was recrystallized from diethyl ether to obtain ligand **L3** (796 mg, 1.93 mmol, 22%) as slightly yellow crystals.

^{1}H NMR (400 MHz, $CDCl_3$, 295 K) δ = 8.53 (ddd, J = 4.9, 1.9, 0.9 Hz, 4H, *H-1*), 7.58 (t, J = 7.7 Hz, 1H, *H-8*), 7.50 (td, J = 7.7, 1.9 Hz, 4H, *H-3*), 7.19 (t, J = 8.1 Hz, 6H, H-7, *H-4*), 7.10 (ddd, J = 7.5, 4.9, 1.2 Hz, 4H, *H-2*), 5.92 (s, 2H, *H-6*) ppm.

^{13}C NMR (101 MHz, $CDCl_3$, 295 K) δ = 161.6 (*C-5*), 160.4 (*C-9*), 149.3 (*C-1*), 137.4 (*C-8*), 136.3 (*C-3*), 124.3 (*C-4*), 122.3 (*C-7*), 121.6 (*C-2*), 64.1 (*C-6*) ppm.

HR-MS (ESI): calc. for $C_{27}H_{22}N_5$ [M+H]: 415.19172 m/z; found: 416.27003 m/z.

Elemental Analysis: calc. for $C_{27}H_{21}N_5$: N, 16.86; C, 78.05; H, 5.09. found: N, 16.60; C, 77.58; H, 5.19.

Compound confirmed by crystal structure analysis (section VII.11).

This experiment was part of the research internship of Jan Prohaska and Antonia Goldhammer, conducted under my supervision.

Synthesis of $[Fe^{II}\mathbf{L3}(mecn)](OTf)_2$

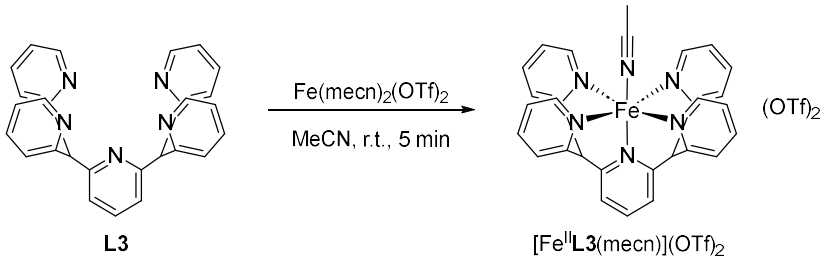

According to a modified literature procedure.[91]

Ligand **L3** (50.3 mg, 0.121 mmol, 1.0 equiv.) was suspended in acetonitrile (2.5 mL), then iron(II)bis(acetonitrile)bis(triflate) (47.82 mg, 0.121 mmol, 1.0 equiv.) was added. The reaction mixture was stirred for 10 min at room temperature and then methyl tert-butyl ether was diffused into the solution under ambient conditions to give the product (80.0 mg, 0.980 mmol, 82%) as deep red crystals.

^{1}H NMR (400 MHz, acetone-d_6, 293 K) δ = 8.30 (ddd, J = 7.2, 3.1, 1.5 Hz, 5H), 8.10 – 7.99 (m, 5H), 7.79 (dd, J = 9.0, 5.0 Hz, 5H), 7.17 (s, 5H), 5.62 (m, 2H), 3.12 (s, 2H), 2.09 (s, 1H), 1.12 (s, 6H) ppm.

HR-MS (ESI): calc. for $C_{27}H_{21}FeN_5^{2+}$ $[M]^{2+}$: 471.1141, found: 471.1126 m/z.

IR (thin film): $\tilde{\nu}$ = 1602, 1479, 1442, 1252, 1223, 1151, 1028, 762 cm^{-1}.

UV-vis (H_2O, 25 °C): absorption maxima at λ = 220, 260, 390 nm.

Compound confirmed by crystal structure analysis (section VII.11).

This experiment was part of the research internship of Jan Prohaska and Antonia Goldhammer, conducted under my supervision.

Synthesis of $[Fe^{IV}\mathbf{L3}(O)][Ce(NO_3)_6]$

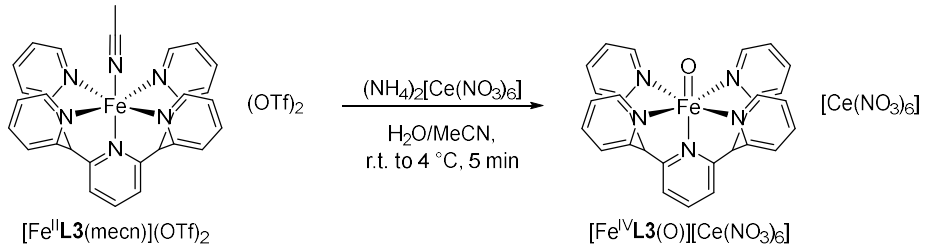

$[Fe^{II}\mathbf{L3}(mecn)](OTf)_2$ (29 mg, 0.036 mmol, 1.0 equiv.) was dissolved in a 3:1 acetonitrile:water mixture (44 µL). Cerium(IV) ammonium nitrate (103.6 mg, 0.189 mmol, 5.3 equiv.) was added as a solid and the mixture sonicated for 60 s. As a pale green precipitate began to form the reaction mixture was placed on ice for 10 min. The solid was collected *via* filtration, washed with ice cold 3:1 acetonitrile:water (44 µL) and dried *in vacuo* to yield product $[Fe^{IV}\mathbf{L3}(O)][Ce(NO_3)_6]$ as a pale green solid (no yield determined).

HR-MS (ESI): calc. for $C_{27}H_{21}FeN_5O^{2+}$ $[M]^{2+}$: 487.1090, found: 487.1084 m/z.

UV-vis (H_2O, 25 °C): absorption maxima at $\lambda = 730$ nm.

This experiment was part of the research internship of Jan Prohaska, conducted under my supervision.

2.4 Syntheses of Substrates and Substrate Precursors

Synthesis of **2**

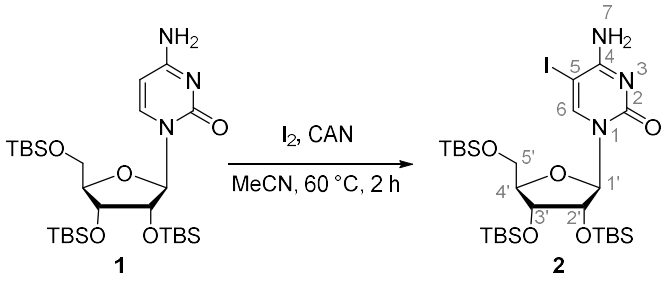

According to a modified literature procedure.[244]

Silyl-protected cytidine **1** (1.36 g, 2.32 mmol, 1.00 equiv.) was dissolved in anhydrous acetonitrile (110 mL) followed by the addition of iodine (1.30 g, 5.11 mmol, 2.20 equiv.) and ceric ammonium nitrate (2.80 g, 5.11 mmol, 2.20 equiv.). The resulting dark red reaction mixture was heated to 60 °C under exclusion of light for 3.5 h. The reaction was allowed to cool to 21 °C and the brown suspension was slowly poured into a mixture of saturated aqueous sodium bicarbonate solution (150 mL) and aqueous sodium thiosulfate solution (1.0 M, 100 mL). Acetonitrile was evaporated from the resulting slightly yellow suspension and ethyl acetate (150 mL) was added. After the separation of the layers, the aqueous layer was extracted with ethyl acetate (3×80 mL). All organic layers were washed with saturated aqueous sodium chloride solution (80 mL) and then dried over magnesium sulfate. The filtrate obtained after filtration was concentrated *in vacuo*. Purification of the obtained yellow solid followed by flash column chromatography (2% to 4% to 5% methanol in dichloromethane) to afford silyl-protected 5-iodocytidine **2** (1.01 g, 1.42 mmol, 61%) as a colorless solid.

^{1}H NMR (400 MHz, $CDCl_3$, 295 K): δ = 8.06 (s, 1H; *H-6*), 6.81 (s, 1H; *H-7a*), 5.97 (d, J = 4.5Hz, 1H; *H-1'*), 5.50 (s, 1H; *H-7b*), 4.16 – 4.05 (m, 2H; *H-2'*, *H-4'*), 4.03 – 3.94 (m, 2H; *H-3'*, *H-5'a*), 3.76 (dd, J = 11.6, 2.3 Hz, 1H; *H-5'b*), 0.99 (s, 9H; *TBS*), 0.90 (s,

9H; *TBS*), 0.88 (s, 9H; *TBS*), 0.19 (s, 3H; *TBS*), 0.19 (s, 3H; *TBS*), 0.07 (s, 3H; *TBS*), 0.06 (s, 3H; *TBS*), 0.06 (s, 3H; *TBS*), 0.05 (s, 3H; *TBS*) ppm.

^{13}C NMR (101 MHz, $CDCl_3$, 295 K): δ = 163.3 (*C-4*), 154.8 (*C-2*), 147.2 (*C-6*), 89.3 (*C-1'*), 84.9 (*C-4'*), 77.3 (*C-5*), 76.4 (*C-2'*), 71.4 (*C-3'*), 62.6 (*C-5'*), 26.6 (*TBS*), 26.0 (*TBS*), 26.0 (*TBS*), 18.9 (*TBS*), 18.2 (*TBS*), 18.1 (*TBS*), −4.1 (*TBS*), −4.3 (*TBS*), −4.5 (*TBS*), −4.6 (*TBS*), −4.6 (*TBS*), −4.9 ppm.

HR-MS (ESI): calc. for $(C_{27}H_{55}IN_3O_5Si_3)^+$ $[M+H]^+$: 712.2489, found: 712.2498 m/z.

Elemental Analysis: calc. for $C_{27}H_{54}IN_3O_5Si_3$: C, 45.55; H, 7.98; N, 5.90; found: C, 45.38; H, 7.88; N, 5.91.

This experiment was part of the research internship of Maya Brown, conducted under my supervision.

Synthesis of **4**

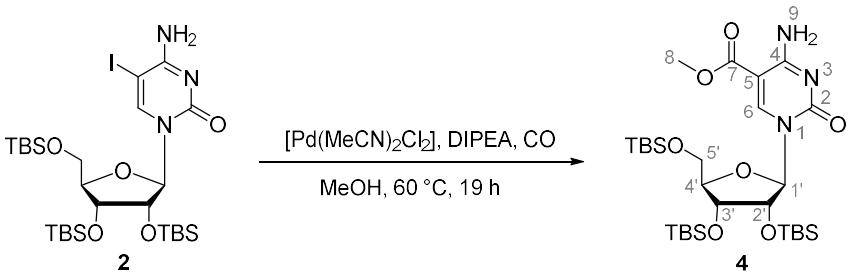

According to a modified literature procedure.[158]

The following reaction was carried out in an high-pressure autoclave under argon atmosphere. Silyl-protected iodocytidine **2** (500 mg, 0.702 mmol, 1.00 equiv.) and bis(acetonitrile)palladium dichloride (9.11 mg, 35.12 µmol, 0.050 equiv.) were dissolved in an- hydrous methanol (8.33 mL) under argon atmosphere in the autoclave. Flushing of the autoclave with carbon monoxide gas (3.5 bar) occurred while stirring the reaction solution. After 10 min the pressure was released. After achieving carbon monoxide saturation of the reaction solution by repeating the flushing procedure two more times, the autoclave was filled with carbon monoxide gas (3.5 bar) and the reaction mixture was heated to 60 °C. The addition of a solution of *N*,*N*-di-*iso*-propylethylamine (244.68 µL, 1.40 mmol, 2.0 equiv.) in anhydrous methanol (282 µL) followed *via* syringe in one portion. The reaction was allowed to cool to 21 °C after 19 h and the pressure was released. The reaction was transferred to a 50 mL flask and the autoclave was washed with ethyl acetate (10 mL). The orange-black suspension was diluted with ethyl acetate and filtered through a plug of silica. The filter cake was washed with ethyl acetate (ca. 1000 mL) repeatedly and the filtrate was concentrated *in vacuo*. The resulting orange solid was purified by flash column chromatography (0% to 2% to 5% methanol in dichloromethane) to afford silyl-protected 5-methoxycarbonylcytidine **4** (363.5 mg, 0.564 mmol, 80%) as a light yellow powder.

^{1}H NMR (400 MHz, $CDCl_3$, 295 K): δ = 8.50 (s, 1H; *H-6*), 7.94 (d, *J* = 4.4 Hz, 1H; *H-9a*), 5.96 (d, *J* = 4.7 Hz, 1H; *H-1'*), 5.89 (s, 1H; *H-9b*), 4.23 (t, *J* = 4.5 Hz, 1H; *H-2'*),

4.12 (m, 1H; *H-4'*), 3.98 – 3.90 (m, 2H; *H-3'*, *H-5'a*), 3.84 (s, 3H; *H-8*), 3.76 (dd, J = 11.5, 4.0 Hz, 1H; *H-5'b*), 0.95 (s, 9H; *TBS*), 0.90 (s, 9H; *TBS*), 0.88 (s, 9H; *TBS*), 0.14 (s, 3H; *TBS*), 0.13 (s, 3H; *TBS*), 0.07 (s, 3H; *TBS*), 0.06 (s, 3H; *TBS*), 0.05 (s, 3H; *TBS*), 0.04 (s, 3H; *TBS*) ppm.

^{13}C NMR (101 MHz, $CDCl_3$, 295 K): δ = 165.4 (*C-7*), 163.1 (*C-4*), 153.9 (*C-2*), 148.2 (*C-6*), 95.7 (*C-5*), 90.2 (*C-1'*), 85.3 (*C-4'*), 76.1 (*C-2'*), 72.0 (*C-3'*), 63.4 (*C-5'*), 52.2 (*C-8*), 26.2 (*TBS*), 26.0 (*TBS*), 26.0 (*TBS*), 18.2 (*TBS*), 18.1 (*TBS*), 18.1 (*TBS*), −4.1 (*TBS*), −4.3 (*TBS*), −4.6 (*TBS*), −4.6 (*TBS*), −5.1 (*TBS*), −5.3(*TBS*) ppm.

HR-MS (ESI): calc. for $(C_{29}H_{58}N_3O_7Si_3)^+$ $[M+H]^+$: 644.3577, found: 644.3581 m/z.

Elemental Analysis: calc. for $C_{29}H_{57}N_3O_7Si_3$: C, 54.08; H, 8.92; N, 6.52; found: C, 53.99; H, 8.81; N, 6.42.

This experiment was part of the research internship of Maya Brown, conducted under my supervision.

Synthesis of 5crC

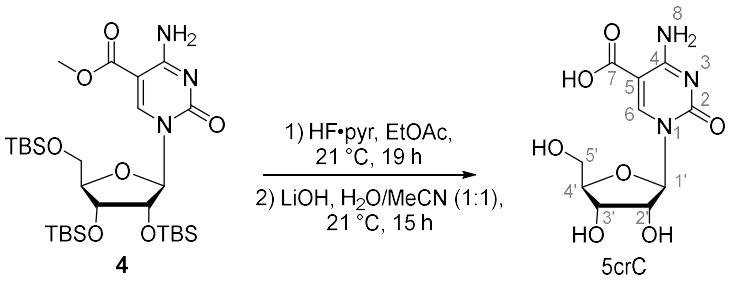

According to a modified literature procedure.[152]

In a plastic tube open to air silyl-protected methyl ester **4** (363.50 mg, 0.564 mmol, 1.00 equiv.) was suspended in anhydrous ethyl acetate (16.97 mL) and hydrogen fluoride pyridine complex (70 wt% HF, 153.98 µL, 8.47 mmol, 15 equiv.) was added slowly *via* an Eppendorf-pipette resulting in a clear solution. After 22 h 20 min, the reaction was cooled to 0 °C and the careful addition of methoxytrimethylsilane (2.49 mL, 18.06 mmol, 32 equiv.) followed *via* syringe. The reaction was allowed to slowly warm to 21 °C. After 5 h, the suspension was diluted with methanol (35.8 mL) and all volatiles were removed *in vacuo*. Complete conversion was expected to continue the reaction. The resulting yellowish solid was dissolved in a mixture of water and acetonitrile (1:1, 239.14 mL) open to air, following the addition of lithium hydroxide (162.16 mg, 6.77 mmol, 12.0 equiv.). After 16 h 55 min, the solution was brought to pH 3 by the dropwise addition of 2.0 M hydrochloric acid and all volatiles were removed *in vacuo*. The resulting tan solid was purified by HPLC (see Section 5.2.6) to afford 5-carboxycytidine 5crC (9.8 mg, 34.1 µmol, 6% over two steps) as a colorless solid.

^{1}H NMR (400 MHz, DMSO-d_6, 295 K): δ = 8.95 (s, 1H; *H-6*), 5.76 (d, *J* = 3.2 Hz, 1H; *H-1'*), 4.00 (dd, *J* = 4.6, 3.3 Hz, 1H; *H-2'*), 3.97 – 3.86 (m, 2H; *H-3'*, *H-4'*), 3.71 (dd, *J* = 12.0, 2.6 Hz, 1H; *H-5'a*), 3.56 (dd, *J* = 12.1, 2.8 Hz, 1H; *H-5'b*) ppm.

^{13}C NMR (101 MHz, DMSO-d_6, 295 K): δ = 166.4 (*C-7*), 163.0 (*C-4*), 152.9 (*C-2*), 149.1 (*C-6*), 95.8 (*C-5*), 90.1 (*C-1'*), 84.2 (*C-4'*), 74.5 (*C-2'*), 68.8 (*C-3'*), 60.2 (*C-5'*) ppm.

HR-MS (ESI): calc. for $(C_{10}H_{14}N_3O_7)^+$ $[M+H]^+$: 288.0826, found: 288.0829 m/z.

Elemental Analysis: calc. for $C_{10}H_{13}N_3O_7$: C, 41.82; H, 4.56; N, 14.63; found: C, 38.69; H, 4.48; N, 12.78.

This experiment was part of the research internship of Maya Brown, conducted under my supervision.

Synthesis of **3**

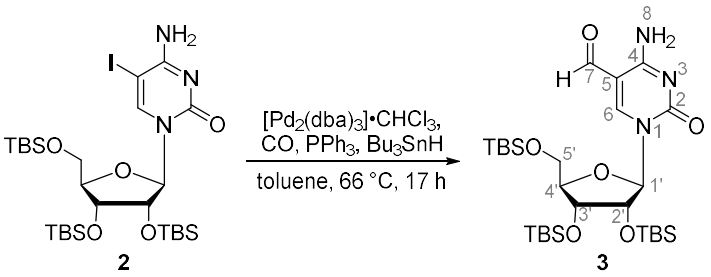

According to a modified literature procedure.[169]

In a high-pressure autoclave, 5-iodocytidine **2** (500 mg, 0.702 mmol, 1.00 equiv.), $[Pd_2(dba)_3]$ chloroform adduct (72.7 mg, 0.070 mmol, 0.100 equiv.) as well as triphenylphosphine (110 mg, 0.421 mmol, 0.600 equiv.) were dissolved in anhydrous toluene (21 mL) under argon atmosphere. After flushing the autoclave with carbon monoxide gas (3.5 bar) while stirring the reaction solution, pressure was released when 10 min had passed. Achieving carbon monoxide saturation of the reaction solution was done by flushing the autoclave two more times with carbon monoxide. The autoclave was then saturated with carbon monoxide gas (3.5 bar) again and the reaction was started by heating the mixture to 60 °C. Over a period of 16 h a dropwise addition of a solution of tributyltin hydride (0.3 mL, 0.842 mmol, 1.2 equiv.) in anhydrous toluene (0.3 mL) *via* syringe (0.060 mL per hour) occurred. The pressure dropped to 30 PSI over the course of the night and the temperature rose to 66 °C. After 17 h from the start of the tributyltin hydride addition, the reaction was allowed to cool to 40 °C and the pressure was released. The reaction was then allowed to further cool to 21 °C. The dilution of the obtained greenish black suspension was done with ethyl acetate (10 mL) and filtered through a plug of silica. Concentration *in vacuo* followed after washing the filter cake with ethyl acetate (400 mL). An orange solid was obtained and purified by flash column chromatography (25% to 50% ethyl acetate in hexanes) to afford silyl-protected 5-formylcytidine **3** (410 mg, 0.668 mmol, 95%) as a colorless solid.[245]

^{1}H NMR (400 MHz, $CDCl_3$, 295 K): δ = 9.52 (s, 1H; *H-7*), 8.62 (s, 1H; *H-6*), 8.16 (s, 1H; *H-8a*), 5.94 (s, 1H; *H-8b*), 5.87 (d, *J* = 2.5 Hz, 1H, *H-1'*), 4.20 (dd, *J* = 4.1, 2.5 Hz, 1H; *H-2'*), 4.17 (dt, *J* = 6.8, 2.1 Hz, 1H; *H-4'*), 4.15 – 4.08 (m, 1H, *H-5'a*), 3.98 (dd, *J* = 6.7, 4.1 Hz, 1H; *H-3'*), 3.82 (dd, *J* = 11.9, 2.0 Hz, 1H; *H-5'b*), 0.97 (s, 9H; *TBS*), 0.91 (s, 9H; *TBS*), 0.90 (s, 9H; *TBS*), 0.17 (s, 3H; *TBS*), 0.17 (s, 3H; *TBS*), 0.13 (s, 3H; *TBS*), 0.11 (s, 3H; *TBS*), 0.07 (s, 3H; *TBS*), 0.06 (s, 3H; *TBS*) ppm.

^{13}C NMR (101 MHz, $CDCl_3$, 295 K): δ = 187.6 (*C-7*), 162.9 (*C-4*), 153.9 (*C-2*), 153.7 (*C-6*), 105.8 (*C-5*), 91.1 (*C-1'*), 84.3 (*C-4'*), 76.9 (C-2'), 70.2 (*C-3'*), 62.0 (*C-5'*), 26.8 (*TBS*), 26.3 (*TBS*), 26.3 (*TBS*), 19.3 (*TBS*), 18.5 (*TBS*), 18.5 (*TBS*), −3.5 (*TBS*), −3.7 (*TBS*), −4.1 (*TBS*), −4.5 (*TBS*), −4.6 (*TBS*), −4.9 (*TBS*) ppm.

HR-MS (ESI): calc. for $(C_{28}H_{56}N_3O_6Si_3)^+$ $[M+H]^+$: 614.3471, found: 614.3479 m/z.

Elemental Analysis: calc. for $C_{28}H_{55}N_3O_6Si_3$: C, 54.77; H, 9.03; N, 6.84; found: C, 55.23; H, 9.08; N, 6.16.

This experiment was part of the research internship of Maya Brown, conducted under my supervision.

Synthesis of 5-methyl*iso*cytosine (5m*i*C)

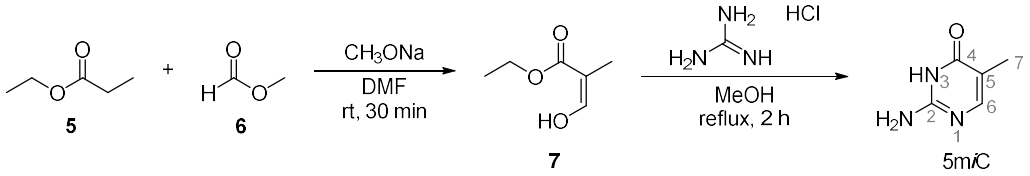

According to a modified literature procedure.[150]

Ethyl propionate (4.50 mL, 3.98 g, 38.97 mmol, 1.50 equiv.) was added to a solution of sodium methoxide (2.82 g, 52.20 mmol, 2.01 equiv.) and dimethylformamide (4 mL) under nitrogen atmosphere. Methyl formate (1.60 mL, 1.57 g, 26.11 mmol, 1.01 equiv.) was added to the mixture over a period of one hour, resulting in a slight foaming. The solution was stirred for 30 min at room temperature. A solution of guanidine hydrochloride (2.49 g, 26.07 mmol, 1.00 equiv.) in methanol (9.2 mL) was added rapidly and the mixture was refluxed (bath temperature 95°C) for 2 hours. The suspension was allowed to cool and when it reached 30 °C it was filtered through a sintered glass frit. The filter cake was discarded, and the pH of the filtrate was adjusted to 6 with concentrated hydrochloric acid, resulting in a colorless precipitate. The mixture was kept at 4°C for 30 min, filtered off through a sintered glass frit, washed with methanol and recrystallized in water. The precipitate was filtered, washed with water and dried *in vacuo* to yield the product as a colorless solid (684.4 mg, 21%).

^{1}H NMR (400 MHz, DMSO-*d6*): δ = 10.90 (br. s., 1H, *H-3*), 7.39 (q, *J* = 1.4 Hz, 1H, *H-6*), 6.33 (s, 2H, *2-NH$_2$*), 1.74 (d, *J* = 1.1 Hz, 3H, *H-7*) ppm.

Elemental Analysis: calc. for $C_5H_7N_3O$: C, 47.99; H, 5.64; N, 33.58. Found: C, 47.93; H, 5.86; N, 33.48.

HR-MS (ESI): calc. for $C_5H_8N_3O$ $[M+H^+]^+$ 126.06619; found 126.06631 m/z.

Synthesis of ethyl 3-(methoxymethoxy)propanoate

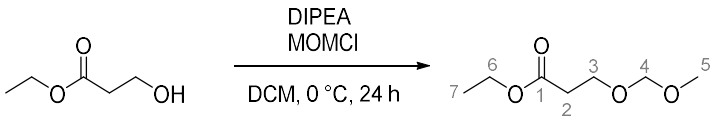

Ethyl 3-hydroxypropanoate (90.9 µL, 100 mg, 847 µmol, 1.0 equiv.) was suspended in dry dichloromethane (10 mL) under nitrogen atmosphere. The mixture was cooled to 0 °C and *N*,*N*-diisopropylamine (576 µL, 438 mg, 3.39 mmol, 4.0 equiv.) was added. After addition of chloromethyl methyl ether (258 µL, 273 mg, 3.39 mmol, 4.0 equiv.), the reaction mixture was stirred at 22 °C for 24 hours. Saturated aqueous ammonium chloride solution (10 mL), ethyl acetate (20 mL) and water (20 mL) were added, the layer separated and the aqueous layer was extracted with ethyl acetate (3×20 mL). The combined organic layers were washed with saturated aqueous sodium chloride solution (20 mL) and dried over magnesium sulfate. The dried solution was filtered and the filtrate was concentrated *in vacuo* to afford the crude product as a yellow solid (88 mg, 543 µmol, 64%).

^{1}H NMR (400 MHz, $CDCl_3$): δ = 4.63 (s, 2H; *H-4*), 4.17 (q, *J* = 7.1 Hz, 2H; *H-6*), 3.81 (t, *J* = 6.3 Hz, 2H; *H-3*), 3.36 (s, 3H; *H-5*), 2.60 (t, *J* = 6.3 Hz, 2H; *H-2*), 1.27 (t, *J* = 7.1 Hz, 3H; *H-7*) ppm.

This corresponds to the crude product and no further analytic measurements were conducted as attempted purification lead to decomposition of the product.

Synthesis of 5-carboxy-*iso*-cytosine (5c*i*C)

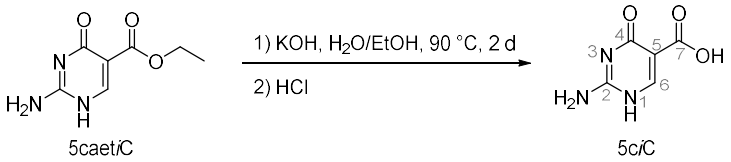

Ethyl 2-amino-4-hydroxypyrimidine-5-carboxylate (5caet*i*C) (100.0 mg, 546.0 µmol, 1.0 equiv.) and potassium hydroxide (61.26 mg, 1.09 mmol, 2.0 equiv.) were dissolved in a 1:1 mixture of water and ethanol (10 mL) and refluxed (oil bath temperature: 90 °C) for 28 hours. Aqueous HCl (2 M, 3 mL) was added, resulting in a colorless precipitate which was filtered, washed with water and dried *in vacuo*. The product was obtained as a colorless solid (63.1 mg, 406.8 µmol, 75%).

^{1}H NMR (400.0 MHz, DMSO-d_6): δ = 8.41 (s, 1H, *H-6*) ppm.

HR-MS (ESI): calc. for $C_5H_6N_3O_3$ $[M+H]^+$: 156.04092; found: 156.04048 m/z.
Calc. for $C_5H_4N_3O_3$ $[M-H]^-$: 154.02581; found: 154.02574 m/z

IR (thin film): $\tilde{\nu}$ = 3299.1, 1682.1, 1645.0, 1575.0, 1511.0, 1455.0, 1386.6, 1330.6, 1199.0, 1150.81, 823.5, 800.3, 728.0, 676.4, 668.2, 657.1 cm^{-1}.

Elemental Analysis: calc. for $C_5H_5N_3O_3$: C, 38.72; H, 3.25; N, 27.09. found: C, 37.44; H, 3.28; N, 25.82.

Synthesis of N^1,N^2-dibenzyl-5caet*i*C

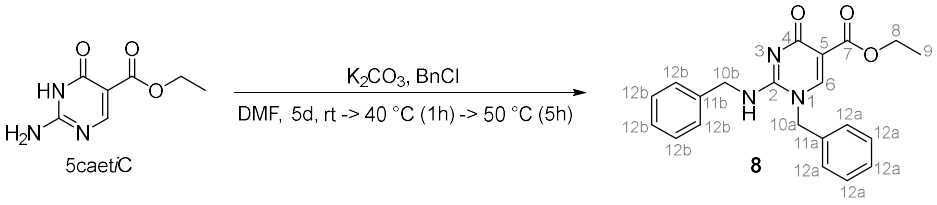

5caet*i*C (200.0 mg, 1.09 µmol, 1.0 equiv.) was suspended in dry dimethylformamide (10 mL) and potassium carbonate (755 mg, 5.46 µmol, 5.0 equiv.) was added in one portion. After 5 min, benzyl chloride (276 mg, 2.18 µmol, 2.0 equiv.) was added dropwise and the reaction mixture was stirred at room temperature for 5 days, heated to 40 °C for one hour and stirred at 50 °C for 4 hours. Ethyl acetate (20 mL) and water (15 mL) were added and the aqueous phase was extracted with ethyl acetate (3 x 5 mL). The combined organic phases were dried over sodium sulfate, filtered and the solvent was removed in vacuo. Column chromatography (silica, 100% dichloromethane grading to 98% dichloromethane, 2% methanol) afforded the product as a colorless solid (13.4 mg, 3%).

^{1}H NMR (400.0 MHz, DMSO-d_6, 295 K): δ = 8.41 (s, 1H, *H-6*), 7.37-7.08 (m, 10H, *H-11*), 5.26 (s, 2H, *H-10*), 4.61 (d, *J* = 5.6 Hz, 2H, *H-10*), 4.14 (q, *J* = 7.1 Hz, 2H, *H-8*), 1.22 (t, *J* = 7.1 Hz, 3H, *H-9*) ppm.

^{13}C NMR (400.0 MHz, DMSO-d_6, 295 K): δ = 164.1, 160.5, 158.2, 156.1, 138.5, 135.2, 128.5, 128.2, 128.2, 127.6, 127.2, 126.8, 126.8, 126.4, 103.4, 59.4, 44.5, 42.6, 14.3 ppm.

Synthesis of **11**

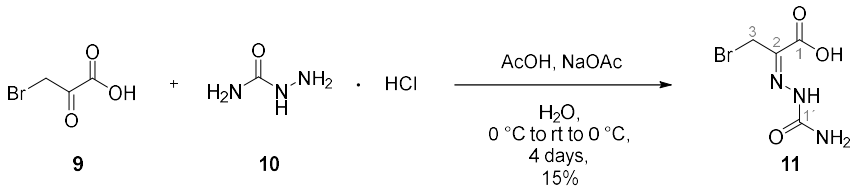

According to a modified literature procedure.[162]

3-Bromopyruvic acid (4.56 g, 27.29 mmol, 1.0 equiv.) was dissolved in water (4.5 mL) and glacial acetic acid (13.5 mL) in an Erlenmeyer flask and cooled to 0 °C. In a second Erlenmeyer flask, sodium acetate (2.915 g, 35.53 mmol, 1.3 equiv.) was dissolved in water (22.5 mL) and semicarbazide hydrochloride (3.04 g, 27.29 mmol, 1.0 equiv.) was added. The second solution was poured onto the first solution at 0 °C and the mixtre was stored at room temperature for 4 days. The white precipitation was filtered, washed using water at 0 °C (3 x 20 mL) and diethyl ether at 0 °C (2 x 20 mL) and dried under *hv*. The product was again washed using water at 0 °C (3 x 10 mL) and diethyl ether at 0 °C (1 x 10 mL) and dried under *hv*, yielding 3-bromopyruvic acid semicarbazone **11** (930 mg, 4.15 mmol, 15%) as a mixture of (E)- and (Z)-isomers and colorless solid.

^{1}H NMR (400 MHz, DMSO-d_6, 295 K): δ = 10.56 (s, 1H, *NH*), 4.58 (s, 2H, *H-3*) ppm.

^{13}C NMR (101 MHz, DMSO-d_6, 295 K): δ = 163.5 (s, *C-1*), 155.6 (s, *C-1'*), 132.5 (s, *C-2*), 32.9 (s, *C-3*) ppm.

This experiment was part of the research internship of Domenic Mayer, conducted under my supervision.

Synthesis of 5hm6aU

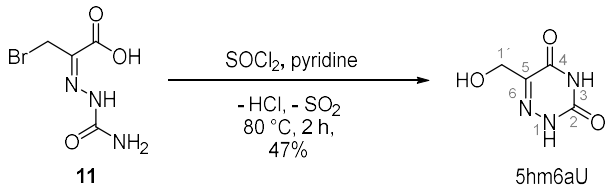

According to a modified literature procedure.[162]

3-Bromopyruvic acid semicarbazone **11** (751.0 mg, 3.352 mmol, 1.0 equiv.) was suspended in thionyl dichloride (25.5 mL, 41.82 g, 351.5 mmol) under nitrogen atmosphere and one drop of pyridine was added. The reaction mixture was refluxed at 80 °C for 120 min, allowed to cool to room temperature, filtered through Celite and washed with dichloromethane (5 mL). After concentrating the solution to roughly 6 mL, crystallization of the filtrate for 4 days at 0 °C resulted in a beige/yellow precipitate, which was filtered and dissolved in 10 mL dichloromethane. It was then concentrated *in vacuo* and dried under *hv*. The dry solid was dissolved in water (12 mL) and refluxed at 110 °C for 18 h. After cooling to room temperature, the solvent was removed in vacuo and the solid was resuspended in 10 mL water. Removing the solvent again and drying the product under hv yielded 5-hydroxymethyl-6-azauracil (227.0 mg, 1.59 mmol, 47%) as a yellowish solid.

^{1}H NMR (400 MHz, DMSO-d_6, 295 K): δ = 12.15 (s, 1H, *H-1*), 11.92 (s, 1H, *H-3*), 4.25 (s, 2H, *H-1'*) ppm.

^{13}C NMR (101 MHz, DMSO-d_6, 295 K): δ = 156.7 (s, *C-4*), 149.5 (s, *C-2*), 144.3 (s, *C-5*), 58.0 (s, *C-1'*) ppm.

Elemental Analysis: calc. for C4H5N3O3: N, 29.36; C, 33.57; H, 3.52; found: N, 7.92; C, 32.84; H, 3.11.

This experiment was part of the research internship of Domenic Mayer, conducted under my supervision.

Synthesis of **13**

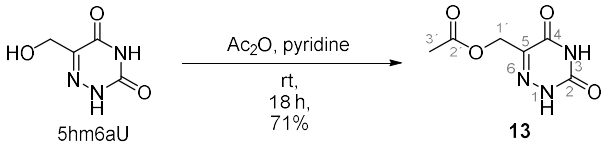

5hm6aU (646.3 mg, 4.516 mmol, 1.0 equiv.) was dissolved in dry pyridine (25 mL) under nitrogen atmosphere. Acetic anhydride (1.72 mL, 18.20 mmol, 4.0 equiv.) was added and the reaction mixture was stirred at room temperature for 18 h. The reaction then was quenched using absolute ethanol (10 mL) and the solvents were removed *in vacuo*. The pyridine was co-distilled using toluene (2 x 20 mL). Silica flash column chromatography was used twice (dichloromethane / methanol (0 → 5%); dichloromethane / methanol (0 → 2%)) to purify the product, yielding 5-methylacetate-6-azauracil **13** (597.6 mg, 3.228 mmol, 71%) as a white solid.

^{1}H NMR (400 MHz, DMSO-d_6, 295 K): δ = 12.35 (s, 1H, *H-1*), 12.09 (s, 1H, *H-3*), 4.86 (s, 2H, *H-1'*), 2.04 (s, 3H, *H-3'*) ppm.

^{13}C NMR (101 MHz, DMSO-d_6, 295 K): δ = 169.7 (s, *C-2'*), 156.4 (s, *C-4*), 149.3 (s, *C-2*), 139.71 (s, *C-5*), 59.8 (s, *C-1'*), 20.5 (s, *C-3'*) ppm.

This experiment was part of the research internship of Domenic Mayer, conducted under my supervision.

Synthesis of **14**

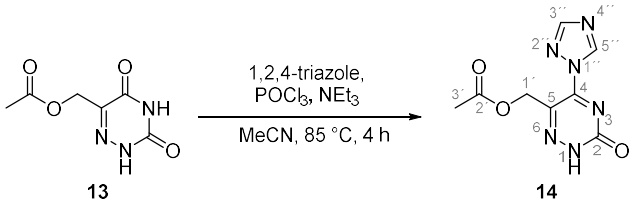

13 14

In a heat-dried Schlenk flask under nitrogen atmosphere 1,2,4-triazole (128.8 mg, 1.865 mmol, 6.9 equiv.) was dissolved in dry acetonitrile (6 mL) and the solution was cooled to 0 °C. Phosphoryl chloride (57.9 µL, 0.621 mmol, 2.3 equiv.) and 15 min later triethylamine (262 µL, 1.890 mmol, 7.0 equiv.) were added dropwise. After 30 min, the suspension was allowed to warm to room temperature and after 30 more minutes **13** (50.1 mg, 0.271 mmol, 1.0 equiv.) was added. After stirring at room temperature for 2 h, the reaction mixture was refluxed at 85 °C for 4 h, resulting in a brownish suspension. The reaction was quenched with water (170 µL) leading to a clear solution, which was stored at 0 °C over night. After 15 h, the solution was decanted separating it from the formed solid. The solvent was removed *in vacuo*, the resulting solid dissolved in water (3 mL) and stirred over night at room temperature. The solvent was removed under hv and the product was purified by silica flash column chromatography (dichloromethane / methanol (0 → 10 %)) yielding **14** (11.34 mg, 0.048 mmol, 18%).

^{1}H NMR (400 MHz, DMSO-d_6): δ = 9.12 (s, 1H, *H-3''*), 8.14 (s, 1H, *H-5''*), 5.00 (s, 2H, *H-1'*), 2.05 (s, 3H, *H-3'*) ppm.

^{13}C NMR (101 MHz, DMSO-d_6): δ = 171.1 (s, *C-2'*), 156.3 (s, *C-4*), 154.3 (s, *C-3''*), 152.2 (s, *C-5''*), 150.5 (*C-2*), 143.3 (s, *C-5*), 62.1 (*C-1'*), 20.7 (*C-3'*) ppm.

This experiment was part of the research internship of Domenic Mayer, conducted under my supervision.

3 Oligonucleotide and DNA Reactions

MilliQ water was applied for all oligonucleotide reactions and RNAse-free water was used for DNA experiments.

Reaction of oligonucleotides with iron(IV)-oxido complexes: example

An aqueous solution of *in situ* prepared $[Fe^{IV}\mathbf{L1}(O)]^{2+}$ (30 µL, 1 mM, 4 equiv.) was given to an aqueous solution of **Oligo1** (30 µL, 0.25 mM, 1 equiv.) in an 1.5 mL reaction tube and shaken at 25 °C. After 1 hour, a sample (50 µL) was taken from the reaction mixture, filtered through silica (1 mL syringe filled with cotton in the bottom and silica up to the 0.3 mL mark), washed with water (2 x 400 µL) and dried by lyophilization. The residue was resuspended in water (500 µL), syringe-filtered (PTFE 0.2) and given to Hanife Sahin from the Carell group for enzymatic digestion and mass spectrometric analysis.

Melting temperature of double stranded oligonucleotides

To an aqueous solution of the two complementary DNA strands **O1** (6.25 µL, 1 mM, 1 equiv.), **O1-comp** (6.25 µL, 1 mM, 1 equiv.) in HPLC-grade quality and water (12.5 µL) an aqueous solution of magnesium chloride (25 µL, 200 mM) was added, and the mixture was incubated in a pre-heated shaker for 5 min at 95 °C. The mixture was allowed to cool to room temperature slowly and then a sample (25 µL) was taken from the mixture, diluted with an aqueous solution of magnesium chloride (475 µL, 200 mM) and transferred into a 500 µL cuvette. UV Vis spectra were recorded at different temperatures from 15 °C to 55 °C in intervals of 2 °C.

Compatibility of magnetic beads with iron(IV)-oxido complex

To an aqueous solution of *in situ* prepared **C3** (2 mM, 50 µL) a sample of RNAClean XP magnetic beads was added (90 µL) and the mixture extensively mixed by pipette pumping. The mixture was placed on a magnet (SPRIstand magnetic tube rack) for 5 min and the slightly brown solution was aspired (*S1*). 70% ethanol (500 µL) was added and then aspired again without mixing with the magnetic beads. This was repeated two times (*S2-4*). Water

(50 µL) was added, the solution mixed by pipette pumping, placed on the magnet for 5 min and the solution aspired (*S5*). The iron content of all solutions (*S1-5*) was determined *via* ICP-MS measurements.

Table 14: Iron content of all samples determined by ICP-MS analysis.

	S1	*S2*	*S3*	*S4*	*S5*
iron content	0.49 µg/mL	<LOD	<LOD	<LOD	<LOD

DNA isolation with magnetic beads

To a 50 µL sample solution in water, 90 µL of a solution of magnetic beads (RNACleanXP) was added and mixed by extensive pipette pumping. The mixture was placed next to a magnet (SPRIstand magnetic tube rack) for 5 min. The colorless solution was discarded and 500 µL of 70% ethanol was added. After short incubation the solution was discarded again and this procedure was repeated three times. 50 µL of water were added, mixed by pipette pumping and again placed next to the magnet. The colorless solution was collected and sample concentration determined with nanodrop measurements.

Modification: a 1:1:1 mixture of sample, magnetic beads and isopropanol was employed.

DNA isolation with Zymo Research Oligo Clean &Concentrator kit

An aqueous solution of **DNA1-contr** (3 µL, 100 µM) was diluted with water (47 µL). *Oligo Binding Buffer* (100 µL) and ethanol (400 µL, 100%) were added and mixed by pipette pumping. The sample was transferred into a column (*Zymo-Spin IC Column*) in a collection tube and centrifuged (1 min, 10000 xg, 25 °C). The flow-through was discarded, *DNA Wash Buffer* (750 µL) added to the column and centrifuged (1 min, 10000 xg, 25 °C). The flow-through was discarded and the column transferred into an 1.5 mL eppendorff tube. Water (15 µL, 40 °C) was added and centrifuged (1 min, 10000 xg, 25 °C). Nanodrop measurements showed 61% recovery of **DNA1-contr**.

DNA isolation: determination of the silica background

Experiment 1: An 1 mL syringe was filled with silica up to the 0.3 mL mark. Water (50 µL) was filtered through the silica and washed with water (2 x 400 µL). The filtrate was lyophilized, the resulting residue resuspended in water (200 µL) and filtered (PTFE 0.2 µm). This procedure was performed ten times with ten different silica-syringes. The silica background was determined with nanodrop measurements.

Experiment 2: This experiment was conducted as described in experiment 1, with the only difference that water filtration occurred with the same silica-syringe for 6 times.

Table 15: Results from concentration measurement with nanodrop instrument.

sample	**concentration [ng/µL]**			
	a	**b**	**c**	**average**
1-1	1.742	1.944	1.712	1.799
1-2	2.359	2.400	4.408	3.056
1-3	2.153	2.364	2.286	2.268
1-4	8.350	2.185	2.052	4.196
1-5	2.070	2.169	1.857	2.032
1-6	2.283	4.696	2.444	3.141
1-7	2.252	2.247	2.361	2.287
1-8	2.761	2.521	2.638	2.640
1-9	2.593	2.451	2.499	2.514
1-10	2.078	2.460	2.384	2.307
			average	**2.624**

sample	**concentration [ng/µL]**			
	a	**b**	**c**	**average**
2-1	5.199	9.922	5.181	6.767
2-2	5.065	1.754	0.990	2.603
2-3	1.358	0.195	1.715	1.089
2-4	0.562	0.917	0.530	0.670
2-5	1.174	0.476	5.631	2.427
	-	-		
2-6	0.278	0.189	0.347	-0.040

Reaction of DNA strands with iron(IV)-oxido complexes: example

An aqueous solution of *in situ* prepared $[Fe^{IV}\mathbf{L1}(O)]^{2+}$ (26.2 µL, 120 µM, 24 equiv.) was given to an aqueous solution of **DNA1** (26.2 µL, 5.0 µM, 1 equiv.) in an 1.5 mL reaction tube and shaken at 25 °C for 30 min. A sample (50 µL) was taken from the reaction mixture and **DNA1** isolation was accomplished with the *Zymo Research Oligo Clean & Concentrator* procedure.

Table 16: Nanodrop results from a reaction of **DNA1** with $[Fe^{IV}\mathbf{L1}(O)]^{2+}$.

exp.	time [min]	conc [ng/µL] a	b	c	average	conc [µM]	expected conc [µL]	recovery
1	5	63.0	62.1	67.1	64.1	8.4	12.5	67%
2	10	70.3	69.9	71.3	70.5	9.2	12.5	74%
3	15	93.5	91.8	93.8	93.1	12.2	12.5	97%
4	60	83.8	86.2	87.8	85.9	11.2	12.5	90%

4 Iron(IV)-oxido Reactivity Studies

*Reaction of ribonucleoside 5mrC with $[Fe^{IV}$**L1**$(O)]^{2+}$ followed by analytical HPLC measurements*

Stock solutions (3 mg mL^{-1} in water) of ribonucleosides (5mrC, 5hmrC, 5frC, 5crC) and nucleobases (5mC, 5hmC, 5fC, 5cC) were used. For the determination of the retention times of the reference samples *via* analytical HPLC measurements, the parameters provided in Table 17 were applied. A mixture of all eight reference samples was measured in different concentrations (Table 18) to achieve calibration curves (Figure 43) allowing the quantification of all species during the reaction with the iron(IV)-oxido complex.

For the reaction of 5mrC with the iron(IV)-oxido complex, a freshly prepared aqueous solution of $[Fe^{IV}$**L1**$(O)]^{2+}$ (1.6 mL, 17.5 mg, 17.1 µmol, 5 equiv.) was added to a solution of 5mrC (1.6 mL, 823 µg, 3.2 µmol, 1 equiv.) in water and stirred at 25 °C for 70 min. Directly after addition and every 5 min, a sample (200 µL) was taken from the reaction mixture, filtered over silica (2 mL syringe equipped with cotton and silica filled to the 1.5 mL mark) and washed with water (2x3 mL and 1x1 mL). The filtrate was lyophilized and the residue resuspended in water (400 µL). The samples were vortexed, centrifuged (25 °C, 4000 rpm, 2.5 min) and the collected supernatant syringe-filtered (PTFE 0.45 µm) and subjected to analytical HPLC analysis.

Table 17: Detailed information of the applied analytical HPLC method for the separation of the cytidine and cytosine derivatives.

column	ACE® C18-PFP(150×4.6mm;5µm)
column temperature [°C]	30.0
eluent (A/B)	H_2O + 0.1% FA/MeOH + 0.1% FA
eluent flow [mL min^{-1}]	1.500
eluent gradient	from 100/0 to 99.7/0.3 in 5 min, to 90/10 in 5 min, to 0/100 in 1 min, hold for 6 min, to 100/0 in 1 min, hold for 7 min (total run time 24 min)
monitored λ_{abs} [nm]	280
sample concentration [mg mL^{-1}]	0.3
injection volume [µL]	5

Table 18: Dilution series of a mixture of all reference samples in water.

sample	1	2	3	4	5	6	7	8	9
conc. [mg mL^{-1}]	99.0	75.0	62.5	49.8	24.8	12.4	6.2	3.1	1.2

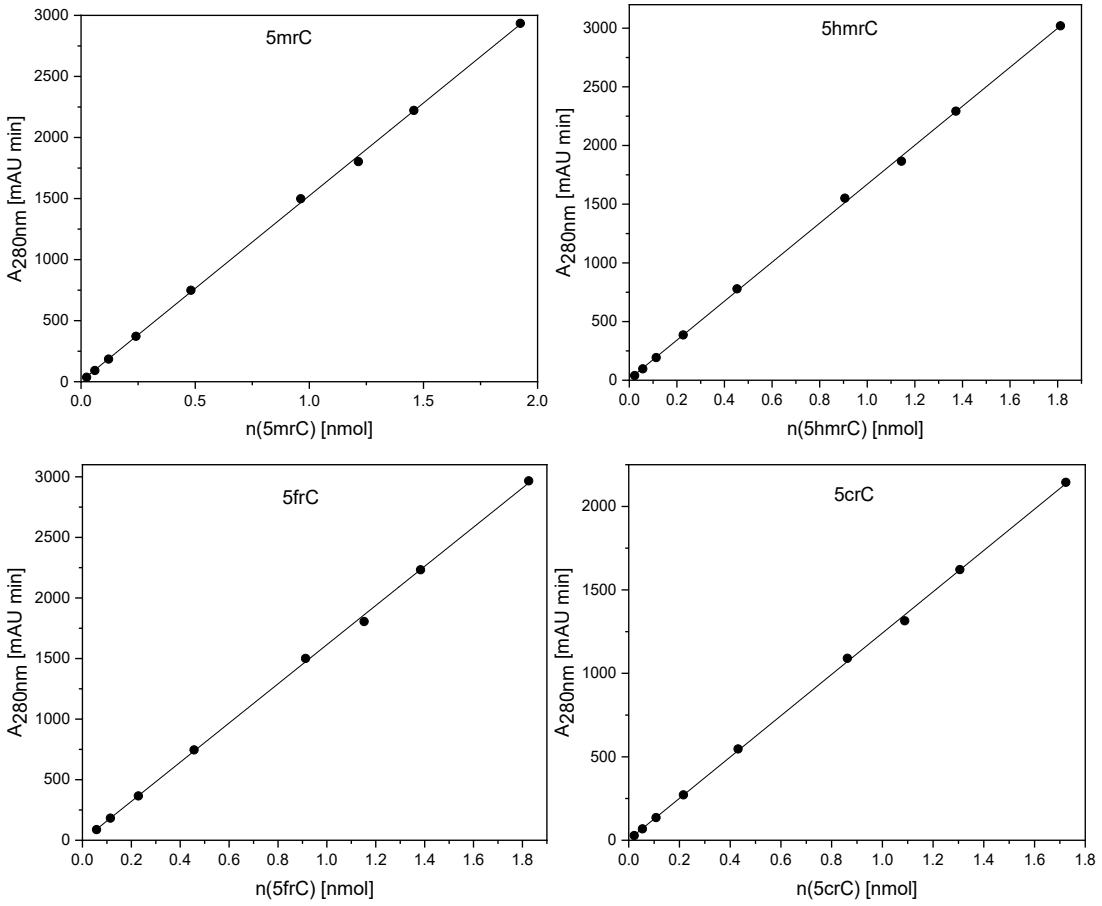

Figure 43: Calibration curves for the ribonucleosides 5mrC, 5hmrC, 5frC and 5crC for quantification of these nucleosides after a reaction with the iron(IV)-oxido complex.

Reaction of iron(IV)-oxido complexes with substrates followed via analytical HPLC measurements

A freshly prepared aqueous solution of $[Fe^{IV}$**L1**/**L2**$(O)]^{2+}$ (10 mM, 1.60 mL, 5 equiv.) was added to a solution of substrate in water (20 mM, 1.60 mL, 1.0 equiv.) and stirred at 22 °C for 70 min. Just after the addition as well as every 5 min, a sample (200 µL) was taken from the reaction mixture, filtered through silica and washed with water (2x3.50 mL). All filtrates were lyophilized resulting in a colorless solid residue which was then resuspended in water (400 µL), vortexed, filtered and subjected to analytical HPLC analysis either with

or without coupled low-resolution mass spectrometry (view Table 19 for detailed information on HPLC parameters).

Table 19: Parameters for analytical HPLC analysis monitored by UV absorption at 280 nm and coupled mass spectrometry (FA = formic acid).

	UV only	**UV + MS**
column	ACE C18-PFP (150 x 4.6 mm; 5 µm)	
T	30 °C	
solvents	A: H_2O + 0.1% FA; B: MeOH + 0.1% FA	
flow	0.4 mL/min	1.5 mL/min
injection volume	7 µL	5 µL
gradient	0% B $\xrightarrow{5\text{ min}}$ 0.3% B $\xrightarrow{5\text{ min}}$ 10% B $\xrightarrow{1\text{ min}}$ 100% B (4 min) $\xrightarrow{1\text{ min}}$ 0% B	0% B $\xrightarrow{10\text{ min}}$ 10% B (10 min) $\xrightarrow{1\text{ min}}$ 100% B (5 min) $\xrightarrow{1\text{ min}}$ 0% B

Product identification via ^{1}H NMR spectroscopy in a reaction of substrates with iron(IV)-oxido complexes

To an aqueous solution of substrate (500 µL, 10 mM, 1 equiv.) a freshly prepared aqueous solution of iron(IV)-oxido complex (500 µL, 10 mM, 1 equiv.) was added. The mixture was shaken for one hour at 25 °C and then filtered over silica (3 mL syringe equipped with cotton and silica filled to the 2 mL mark), washed with water (2 x 1 mL) and the filtrate lyophilized. The residue was redissolved in D_2O (500 µL) and a ^{1}H NMR spectrum recorded.

*Stability of $[Fe^{IV}$**L1**/**L2**$(O)]^{2+}$ at higher temperatures*

In a 1 mL cuvette, an aqueous solution of $[Fe^{IV}$**L1**/**L2**$(O)]^{2+}$ (1 mL, 1 mM, freshly prepared) was incubated at 95 °C for 60 min and UV Vis spectra were recorded every 60 s.

VII. APPENDIX

1 Nomenclature

All compounds employed in this thesis are listed here with the corresponding nomenclature.

ligands and ligand precursors

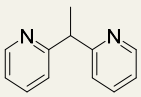

pL1

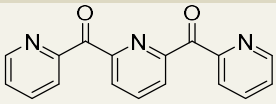

pL2

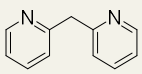

pL3

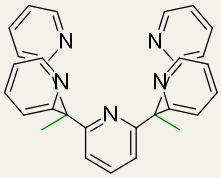

L1

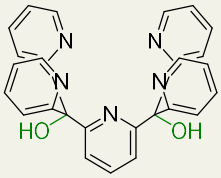

L2

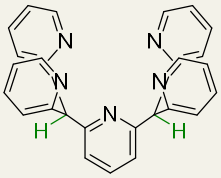

L3

iron complexes

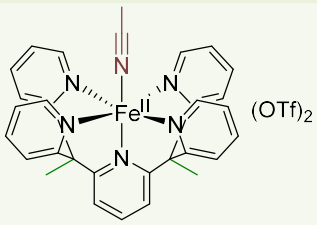

$[Fe^{II}\mathbf{L1}(mecn)](OTf)_2$

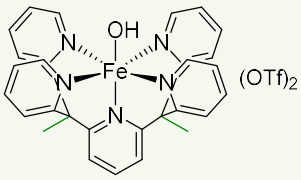

$[Fe^{III}\mathbf{L1}(OH)](OTf)_2$

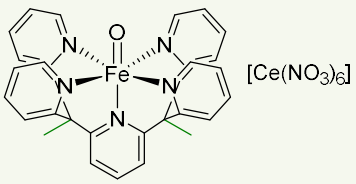

$[Fe^{IV}\mathbf{L1}(O)][Ce(NO_3)_6]$

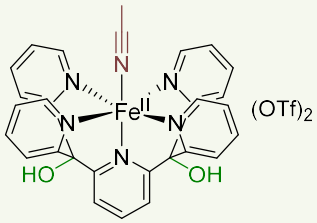

$[Fe^{II}\mathbf{L2}(mecn)](OTf)_2$

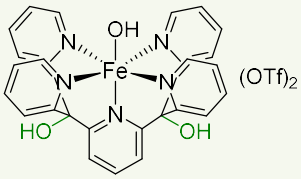

$[Fe^{III}\mathbf{L2}(OH)](OTf)_2$

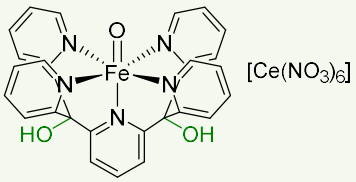

$[Fe^{IV}\mathbf{L2}(O)][Ce(NO_3)_6]$

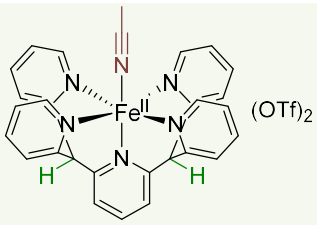

$[Fe^{II}\mathbf{L3}(mecn)](OTf)_2$

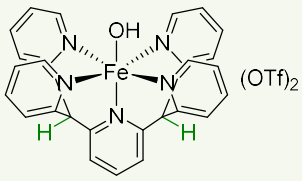

$[Fe^{III}\mathbf{L3}(OH)](OTf)_2$

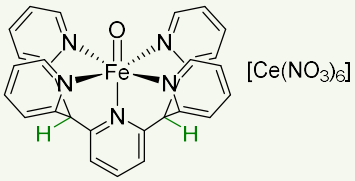

$[Fe^{IV}\mathbf{L3}(O)][Ce(NO_3)_6]$

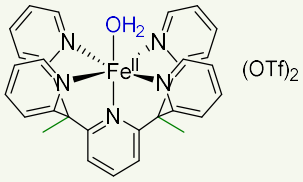

$[Fe^{II}\mathbf{L1}(OH_2)](OTf)_2$

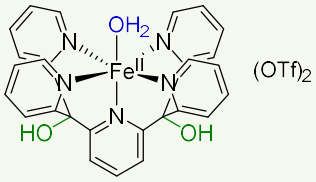

$[Fe^{II}\mathbf{L2}(OH_2)](OTf)_2$

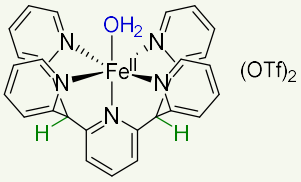

$[Fe^{II}\mathbf{L3}(OH_2)](OTf)_2$

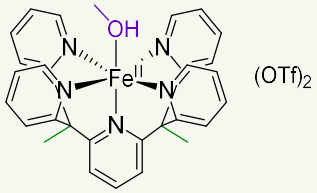

$[Fe^{II}\mathbf{L1}(meoh)](OTf)_2$

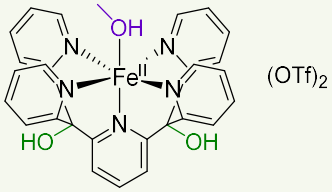

$[Fe^{II}\mathbf{L2}(meoh)](OTf)_2$

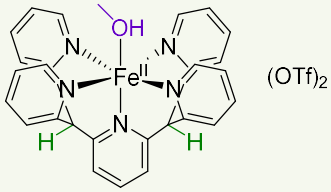

$[Fe^{II}\mathbf{L3}(meoh)](OTf)_2$

DNA nucleobases and nucleosides

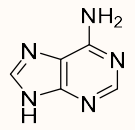

A
adenine

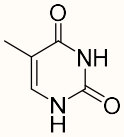

T
thymine

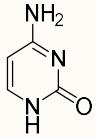

C
cytosine

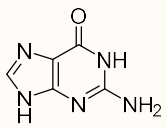

G
guanine

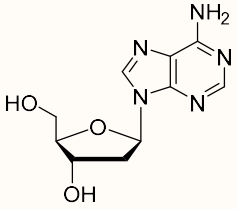

dA
2'-
deoxyadenosine

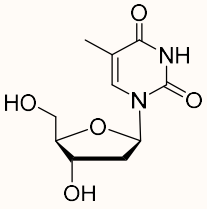

dT
2'-
deoxythymidine

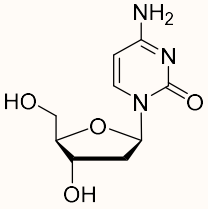

dC
2'-
deoxycytidine

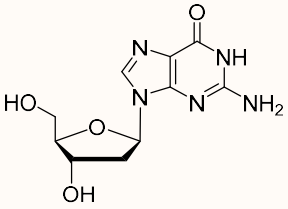

dG
2'-deoxyguanosine

substrates

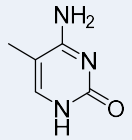

5mC
5-methylcytosine

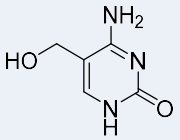

5hmC
5-hydroxy-
methylcytosine

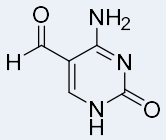

5fC
5-formylcytosine

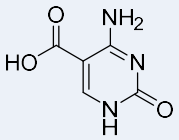

5cC
5-carboxycytosine

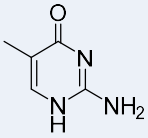

5m*i*C

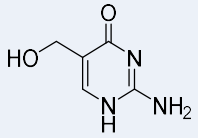

5hm*i*C

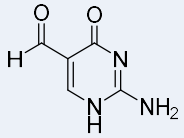

5f*i*C

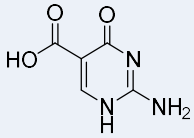

5c*i*C

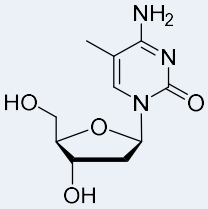

5mdC

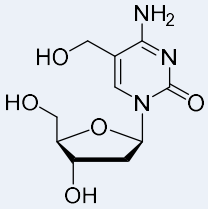

5hmdC

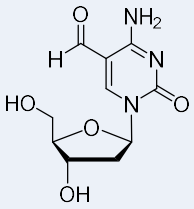

5fdC

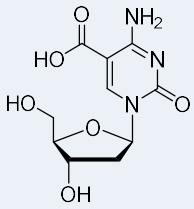

5cdC

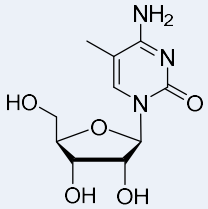

5mrC

5hmrC

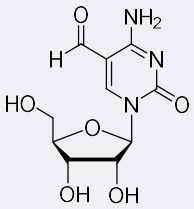

5frC

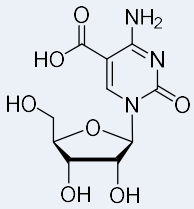

5crC

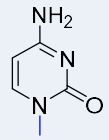

1mC

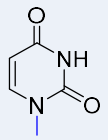

1mU

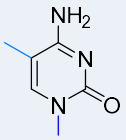

1,5dimC

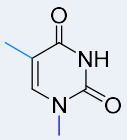

1,5dimU

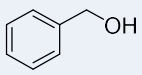

BnOH

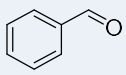

PhCHO

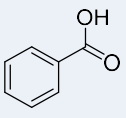

PhCOOH

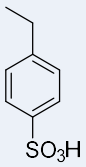

EBS

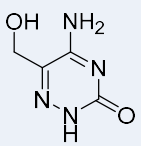

5hm6aC

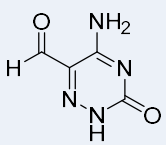

5f6aC

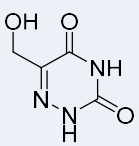

5hm6aU

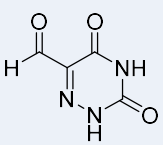

5f6aU

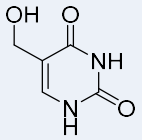

5hmU

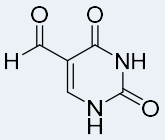

5fU

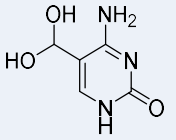

5dhmC

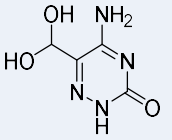

5dhm6aC

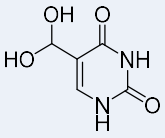

5dhmU

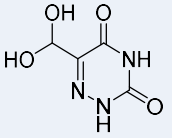

5dhm6aU

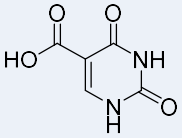

5cU

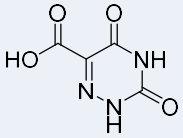

5c6aU

other compounds or intermediates

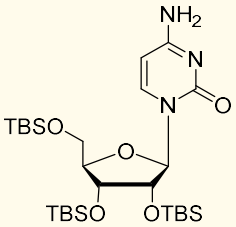

1

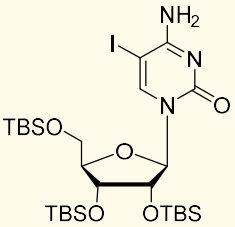

2

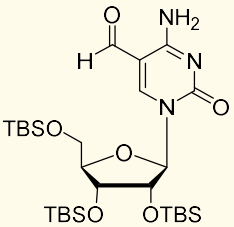

3

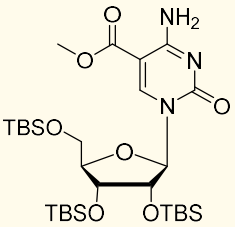

4

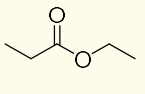

5

6

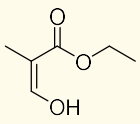

7

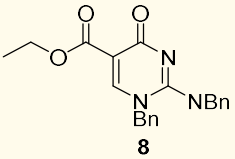

8

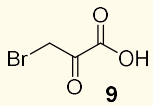

9

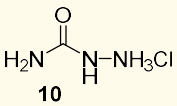

10

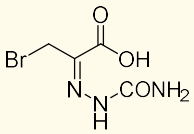

11

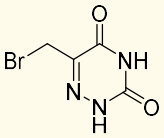

12

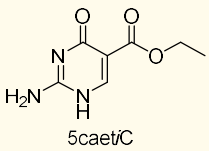

5caetiC

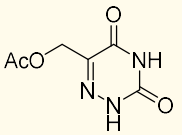

13

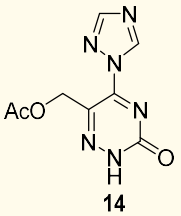

14

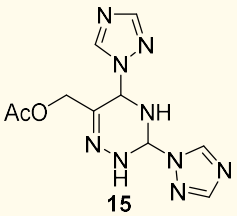

15

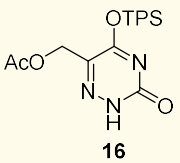

16

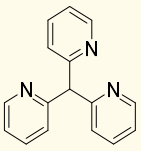

17

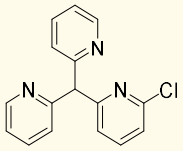

18

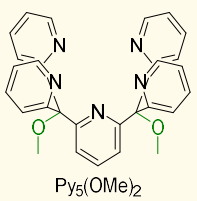

$Py_5(OMe)_2$

Table 20: Nomenclature and Sequence of single stranded DNA oligonucleotides used in this work.

name	sequence
oligo1	5'- CCUUAACC[5mC]G -3'
oligo2	5'- CCTUAACC[5mC]G -3'
oligo3	5'- CTTTAACC[5mC]G -3
oligo1-comp	5'- CGGGAAUUAAGG 3'

Table 21: Nomenclature and important data (molar weight, number of 5mC and thymine residues) of all DNA strands applied in this work.

name	M [g/mol]	Nb 5mdC	Nb dT
DNA1	7639	1	7
	5'-gtc att gct atg atc a5g aac aac t-3'		
DNA1-contr	7625	-	7
	5'-gtc att gct atg atc acg aac aac t-3		
DNA2	43296	2	46
	5'-taa taa atg ttt gcg gtt tgc aat tga ttc aaa ttc aag 5ga aat aat aat atg tat caa agc ata cgt taa atc tat aag tct aaa tat cgt cgt agt cga taa cta taa tac aag ttg tt5 gtg atc ata gca atg ac-3'		
DNA2-contr	43268	-	46
	5'-taa taa atg ttt gcg gtt tgc aat tga ttc aaa ttc aag cga aat aat aat atg tat caa agc ata cgt taa atc tat aag tct aaa tat cgt cgt agt cga taa cta taa tac aag ttg ttc gtg atc ata gca atg ac-3'		
DNA3	43186	2	52
	5'-aat taa tgt tag ctt tct tgc ggt ttg att ata tga ttc aaa tat aag cga aat atc aaa ata tgt aac gac gat acg ata aat cta tat gtc ttc ata tt5 gtt tat tag tca tgt cat tgc tat gat ca5 gaa caa ct-3'		
DNA3-contr	43158	-	52
	5'-aat taa tgt tag ctt tct tgc ggt ttg att ata tga ttc aaa tat aag cga aat atc aaa ata tgt aac gac gat acg ata aat cta tat gtc ttc ata ttc gtt tat tag tca tgt cat tgc tat gat cac gaa caa ct-3'		

2 Abbreviations

1,5-dimC	1,5-dimethylcytosine
1,5-dimU	1,5-dimathyluracil
1mC	1-methylcytosine
1mU	1-methyluracil
5cC	5-carboxycytosine
5fC	5-formylcytosine
5gmC	β-glycosyl-5-hydroxymethylcytosine
5hmC	5-hydroxymethylcytosine
5mC	5-methylcytosine
A	adenine
a.u.	arbitrary units
Ac	acetyl
aq.	aqueous
asp	aspartate
BDE	bond dissociation energy
BER	base excision repair
BS-Seq	bisulfate sequencing
BSTFA	*N*,*O*-bis(trimethylsilyl)trifluoroacetamide
Bu	butyl
C	cytosine
calc.	calculated
CAN	cerium(IV) ammonium nitrate
conc.	concentrated
COSY	correlation spectroscopy
CpG	(2'-deoxy)cytidine-phosphate-(2'-deoxy)guanosine
CSI-MS	cryospray-ionization mass spectrometry
CV	cyclic voltammetry
d	days or doublet
dA	2'-deoxyadenosine
dC	2'-deoxyadcytidine
dG	2'-deoxyguanosine
DIPEA	di*iso*propyl ethyl amine
DMF	dimethylformamide
DNA	deoxyribonucleic acid
DNMT	DNA methyltransferase

dT	2'-deoxythymidine
EA	elemental analysis
EI-MS	electron ionization mass spectrometry
EM-Seq	enzymatic methylation sequencing
EPR	electron paramagnetic resonance
equiv.	equivalents
ESI-MS	electrospray ionization mass spectrometry
Et	ethyl
Et_2O	diethyl ether
EtOAc	ethyl acetate
FA	formic acid
FT IR	fourier-transform infrared
G	guanine
GC-MS	gas chromatography mass spectrometry
h	hours
HAT	histone transferase
HAT	histone acetyltransferase or hydrogen atom transfer
HDAC	histone deacetylase
HDM	histone demethylase
his	histidine
HMBC	heteronuclear multiple-bond correlation spectroscopy
HMQC	heteronuclear multiple quantum correlation spectroscopy
HMT	histone methyltransferase
HPLC	high performance liquid chromatography
HR	high resolution
HS	high spin
hv	high vacuum
Hz	hertz (frequency)
ICP-OES	inductively-coupled plasma optical emission spectroscopy
IR	infrared
J	coupling constant in Hz (NMR)
kcal	kilocalories
L	ligand
LC	liquid chromatography
LR	low resolution
LS	low spin
m	multiplet or meter
MALDI	matrix-assisted laser desorption ionization

Me	methyl
MeCN	acetonitrile
mecn	acetonitrile (ligand)
MeOH	methanol
meoh	methanol (ligand)
min	minutes
MLCT	metal to ligand charge transfer
MOM	methoxymethyl ether
MS	mass spectrometry
n-BuLi	*n*-butyllithium
NGS	next generation sequencing
nm	nanometer
NMR	nuclear magnetic resonance
ONT-Seq	oxford nanopore technology
OTf	triflate ($F_3CSO_3^-$)
oxBS-Seq	oxidative bisulfate sequencing
PBS	phosphate-buffered saline
PG	protecting group
ppm	parts per million
Pr	propyl
py	pyridine (ligand)
q	quartet
RNA	ribonucleic acid
rt	room temperature
S	spin; substrate
s	singlet
SAH	*S*-adenosyl homocysteine
SAM	*S*-adenosyl methionine
SCO	spin crossover
SMRT-Seq	single molecules real-time sequencing
SQUID	superconducting quantum interference device
SUMO	
t	triplet
T	thymine
TAB-seq	TET-assisted bisulfite sequencing
TAPS	TET-assisted pyridine borane sequencing
TAPSβ	TAPS with βGT protection sequencing

TauD	taurine/α-keto glutarate dioxygenase
TDG	thymine glycosylase
TET	ten-eleven translocation methylcytosine dioxygenase
TFA	trifluoroacetic acid
TGS	third generation sequencing
THF	tetrahydrofuran
thf	tetrahydrofuran (ligand)
TLC	thin layer chromatography
TOF	time of flight
TPSCl	2,4,6-triisopropylbenzenesulfonyl chloride
U	uracil
UDP	uridine diphosphate
UV-vis	ultra violet/visible (irradiation)
α-KG	α-ketoglutarat/2-oxyglutarat
βGT	β-glycosyltransferase
δ	chemical shift in ppm (NMR)
λ	wavelength

3 Overview of BDEs

Table 22: C-H bond dissociation energies (BDEs) for 5mC, 5hmC and 5fC calculated by Xu and coworkers[95] at 298.15 K (CBS-QB3, CPCM) and for T, calculated by Zipse and coworkers.[161]

	5mC	5hmC	5fC	T
BDE [kcal mol^{-1}]	90.4	86.2	92.9	91.6
BDE [kJ mol^{-1}]	378.2	360.7	388.7	383.1

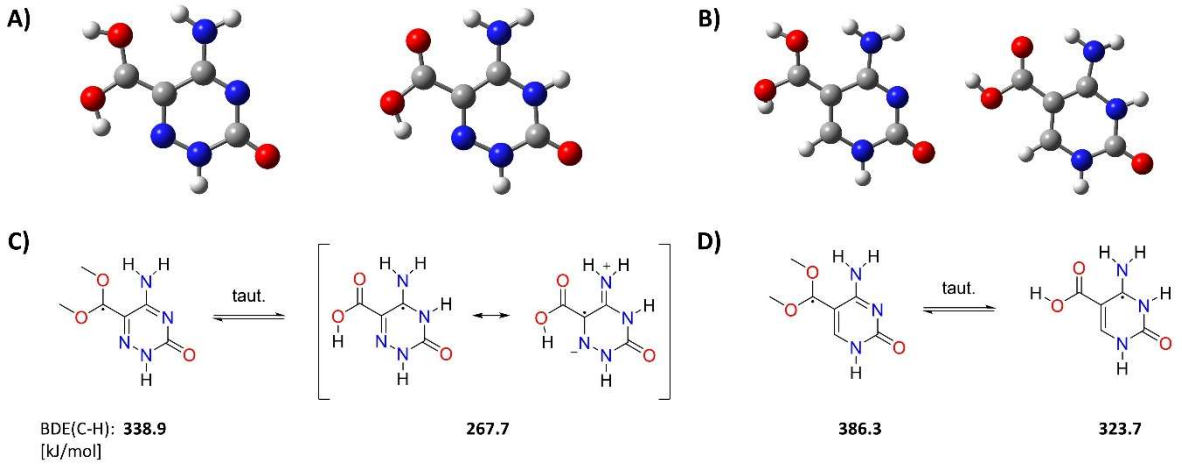

Figure 44: Rationalization of radical stabilization for tautomeric forms: A) and B) lowest energy conformer for both tautomeric radicals of 5dhmaC and 5dhmC; C) Tautomerization and captodative effect of 5dhmaC; D) Tautomerization of 5dhmC (Displayed with aqueous phase BDE(C-H) energies for the best conformer at the DLPNO-CCSD(T)/CBS level of theory; compare with value in brackets, Figure 45.[163]

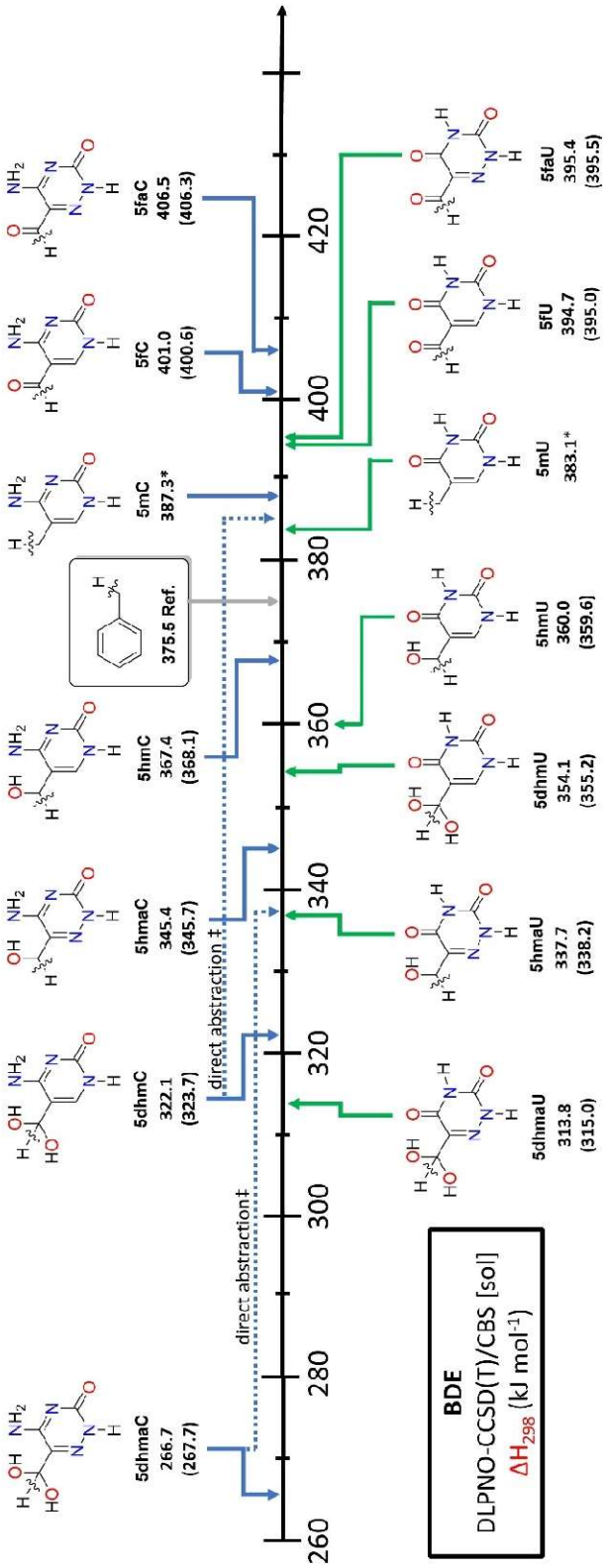

Figure 45: Boltzmann averaged aqueous phase ($\Delta H_{sol} = \Delta H_{298} + \Delta G_{solv}$) RCH_2-H bond dissociation energies (BDEs) calculated at the DLPNO-CCSD(T)/CBS level of theory. The BDE values of thymine (**5mU**) and 5-methylcytosine (**5hmC**) marked with an asterisk are taken from earlier studies.[119] (‡ direct abstraction: BDE(C-H) without tautomeric proton shift, explained in Figure 44).[163]

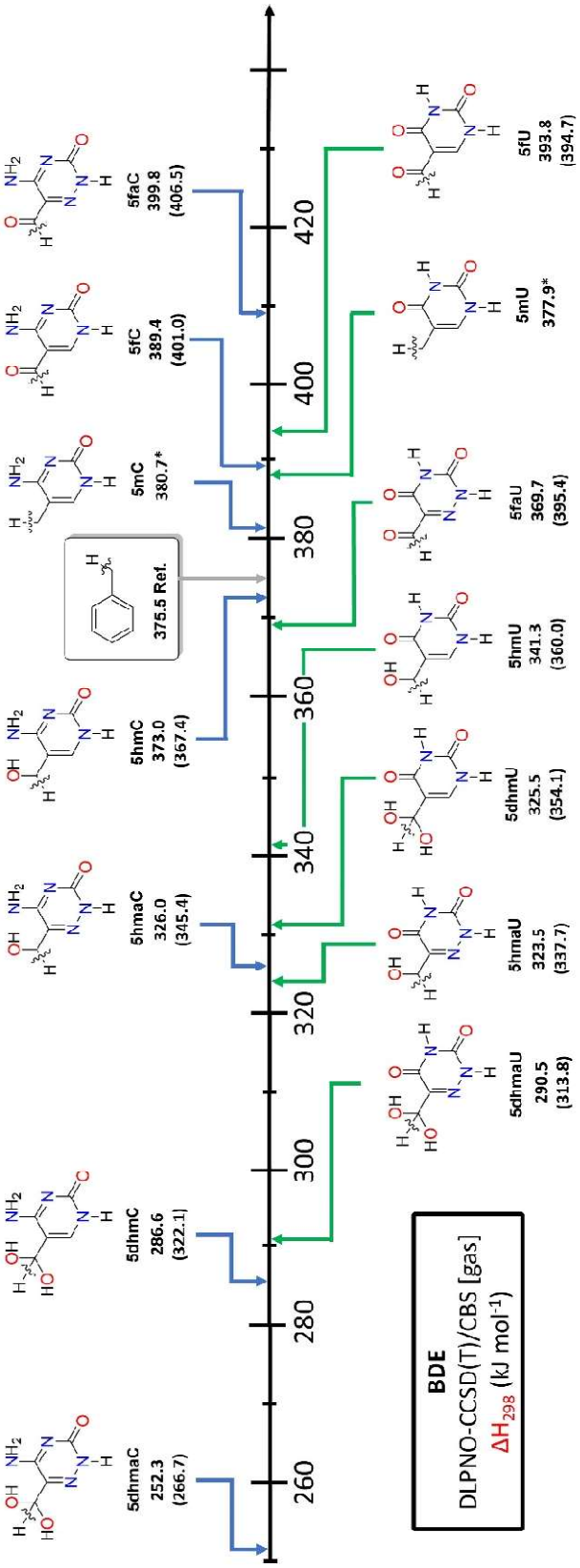

Figure 46: Boltzmann averaged gas phase (ΔH_{gas}) RCH_2-H bond dissociation energies (BDEs) calculated at the DLPNO-CCSD(T)/CBS level of theory.[161] The BDE value of thymine (**5mU**) and 5-methylcytosine (**5mC**) marked with an asterisk are taken from earlier studies.[119]

4 NMR Spectra

4.1 Compound Characterization

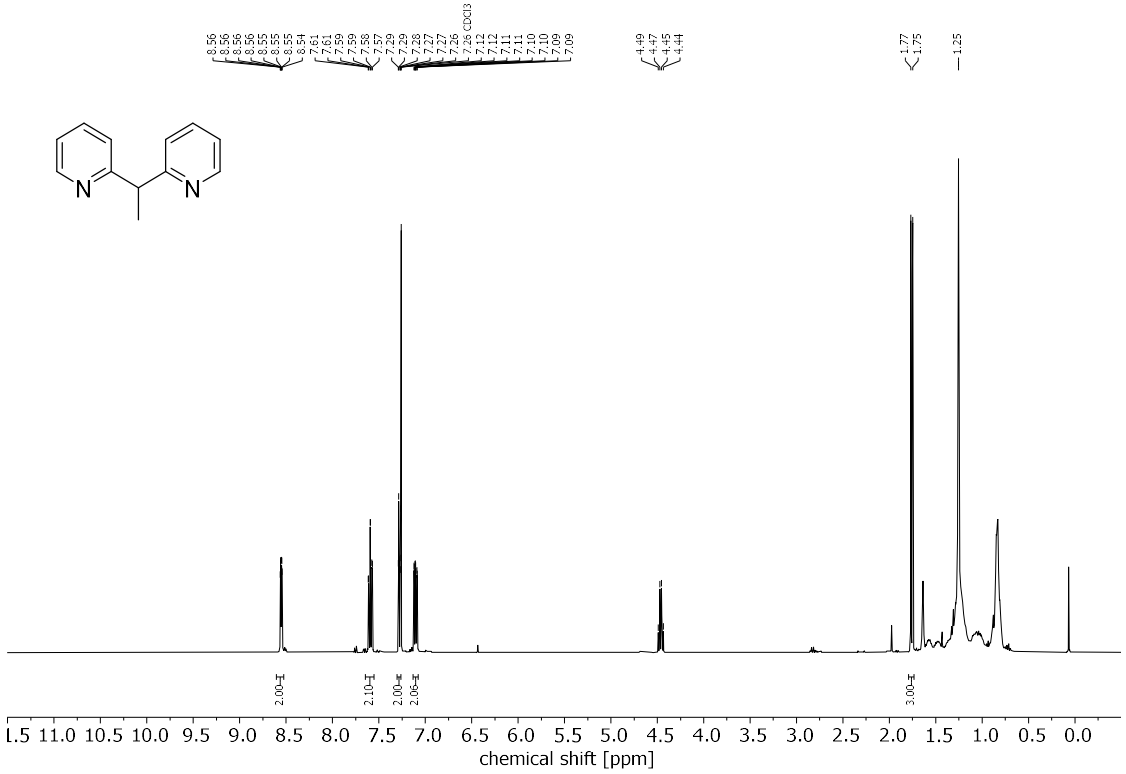

Figure 47: ^{1}H NMR spectrum of **pL1** ($CDCl_3$, 400 MHz, 295 K).

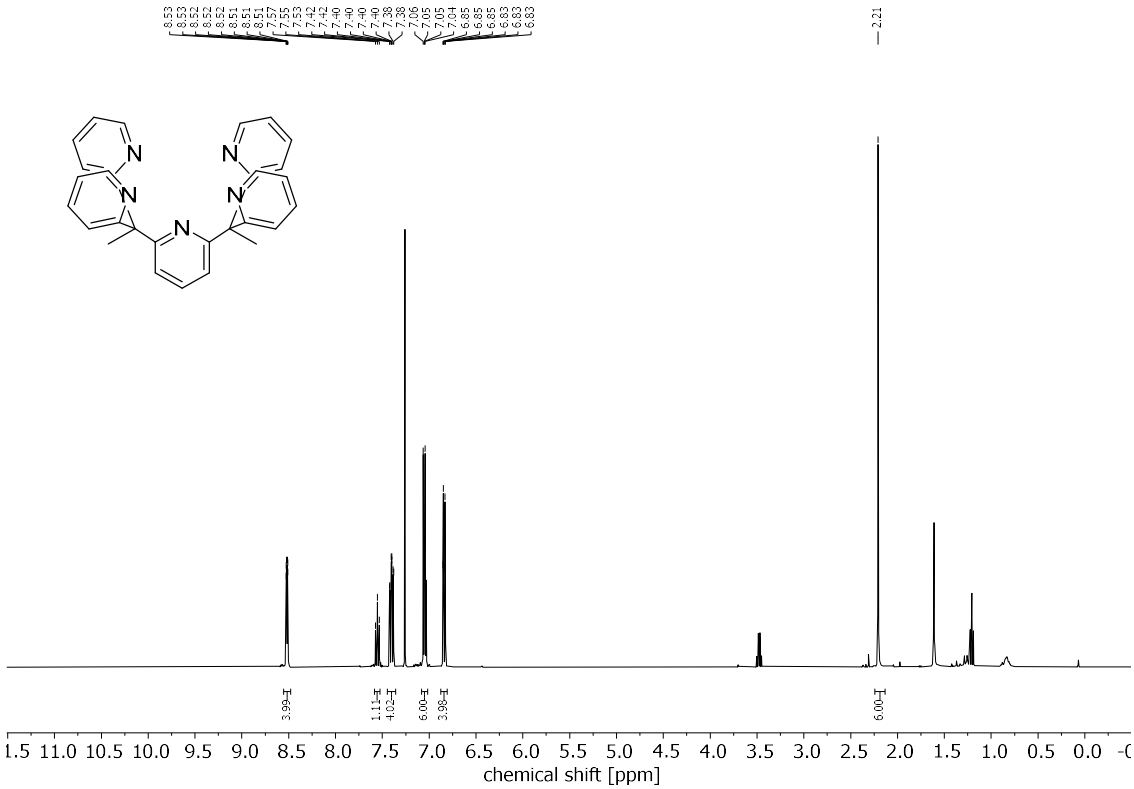

Figure 48: ^{1}H NMR spectrum of **L1** ($CDCl_3$, 400 MHz, 295 K).

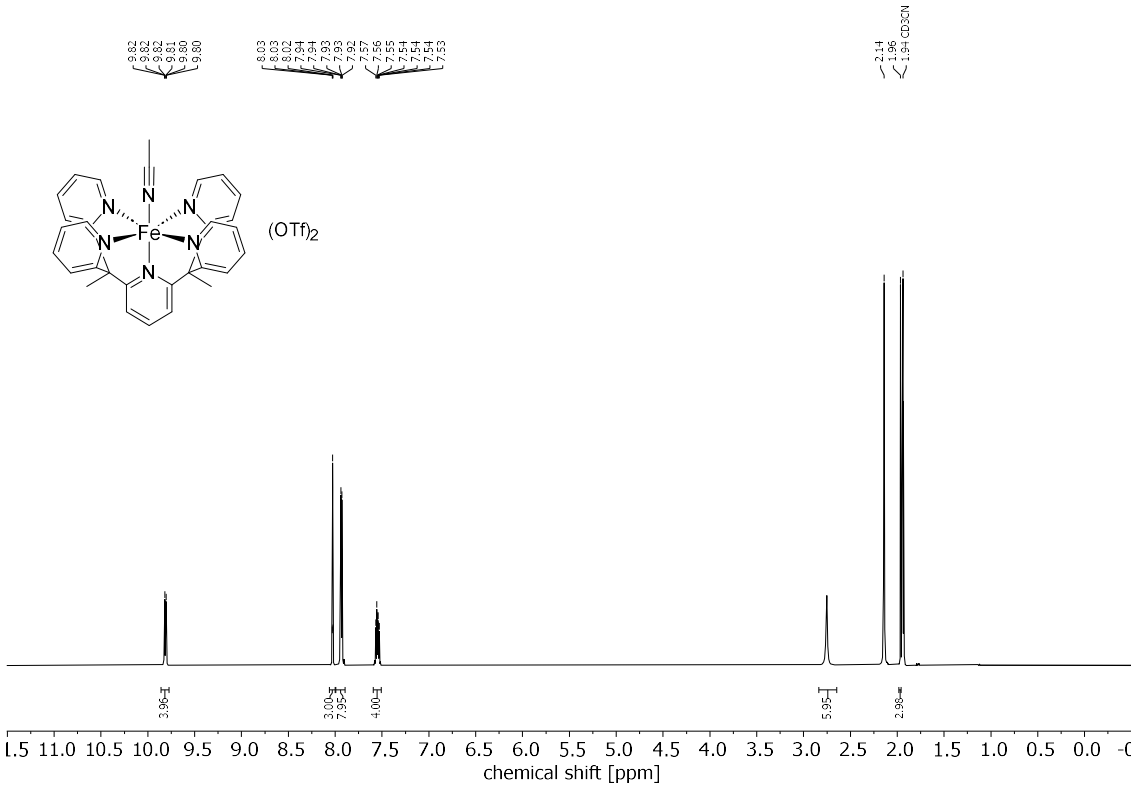

Figure 49: ^{1}H NMR spectrum of [Fe^{II}**L1**(mecn)](OTf)$_2$ (CD_3CN, 400 MHz, 295 K).

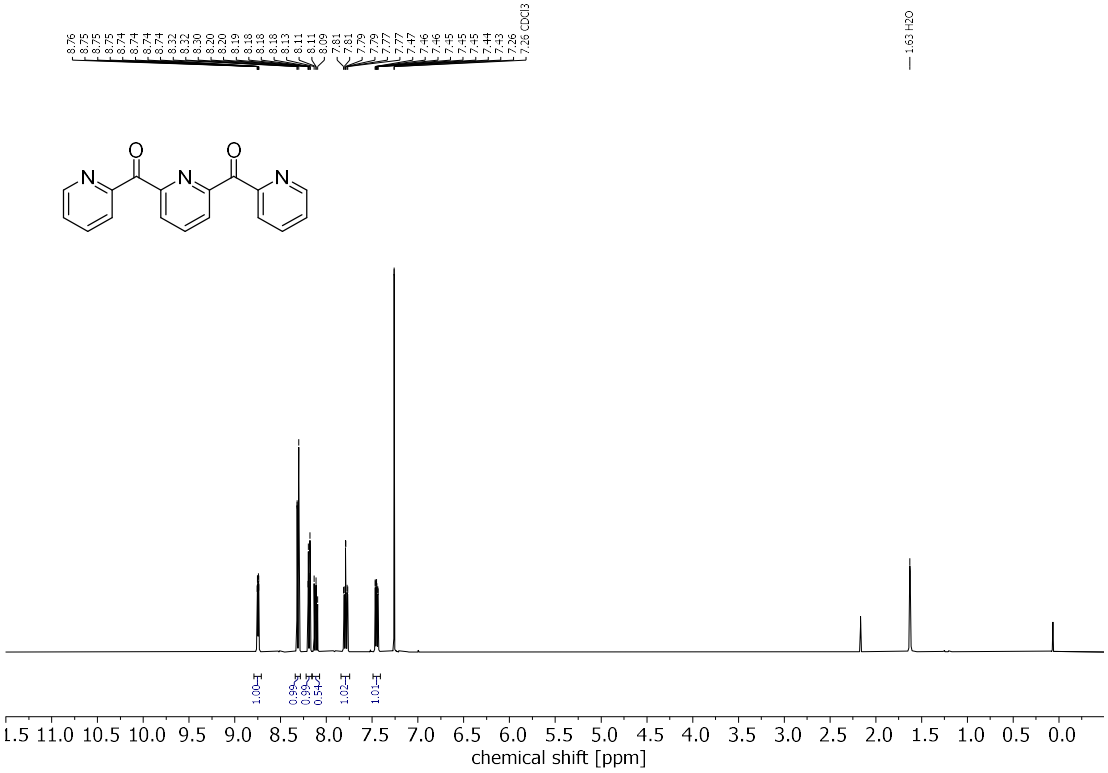

Figure 50: ^{1}H NMR spectrum of **pL2** ($CDCl_3$, 400 MHz, 295 K).

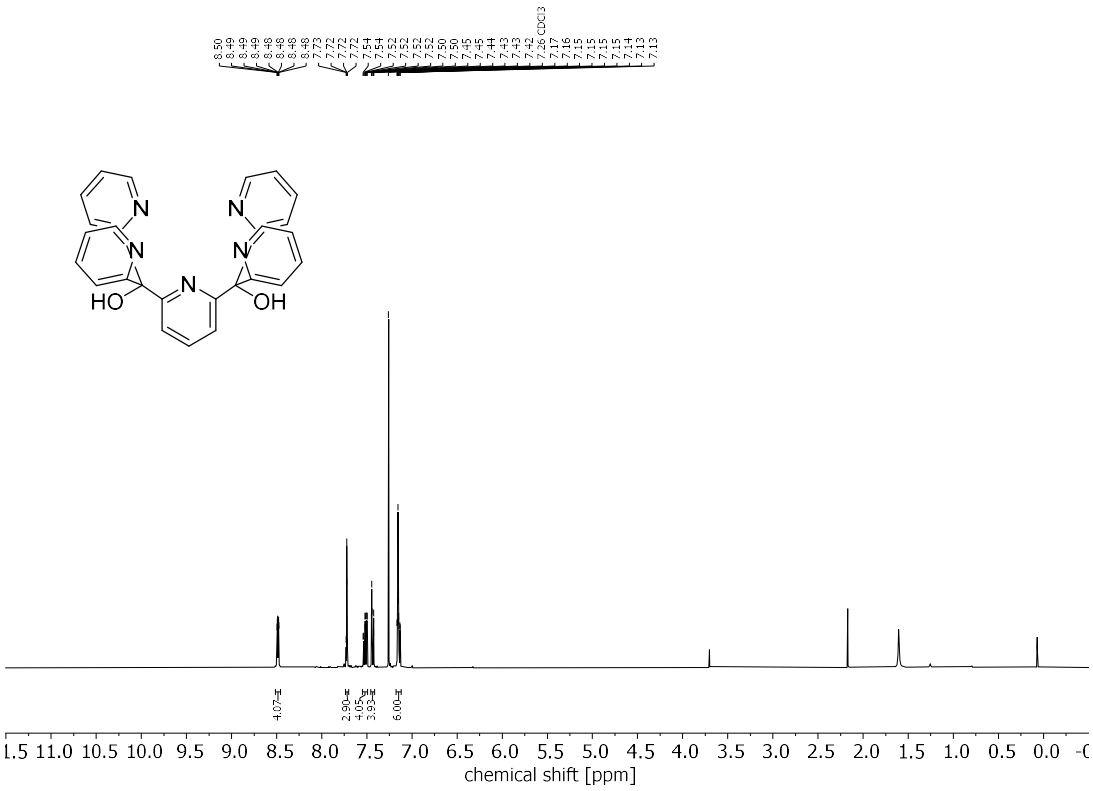

Figure 51: ^{1}H NMR spectrum of **L2** ($CDCl_3$, 400 MHz, 295 K).

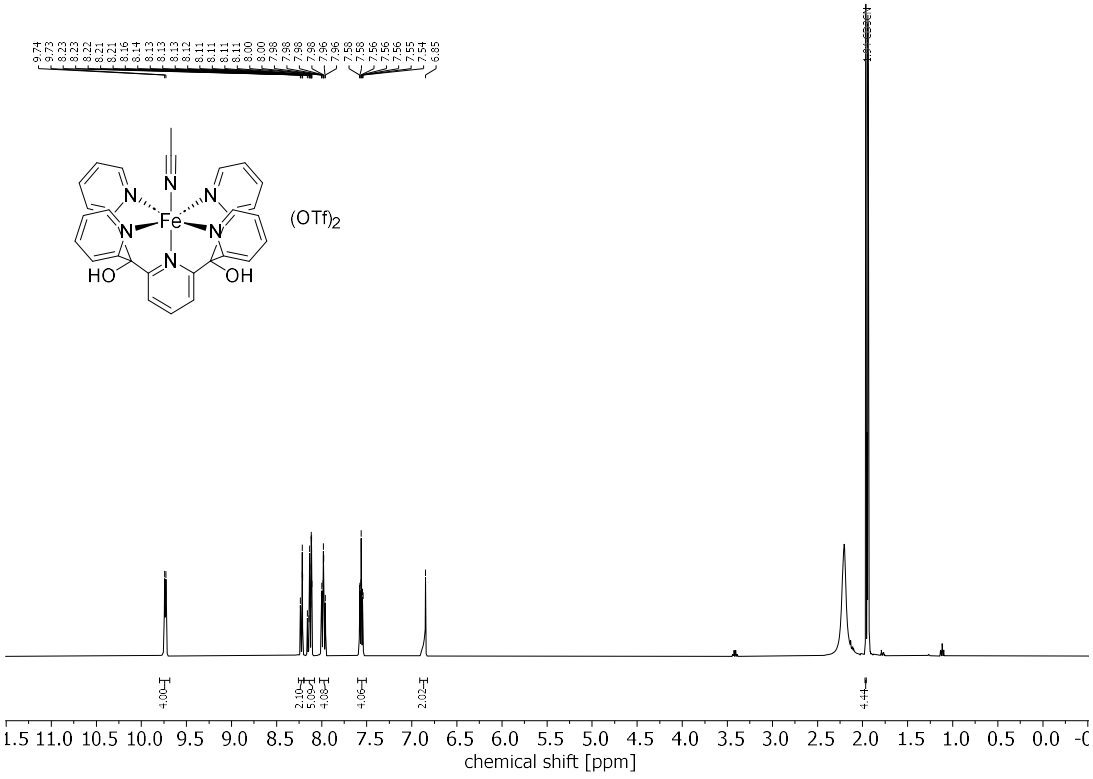

Figure 52: ^{1}H NMR spectrum of [Fe^{II}**L1**(mecn)]$(OTf)_2$ (CD_3CN, 400 MHz, 295 K).

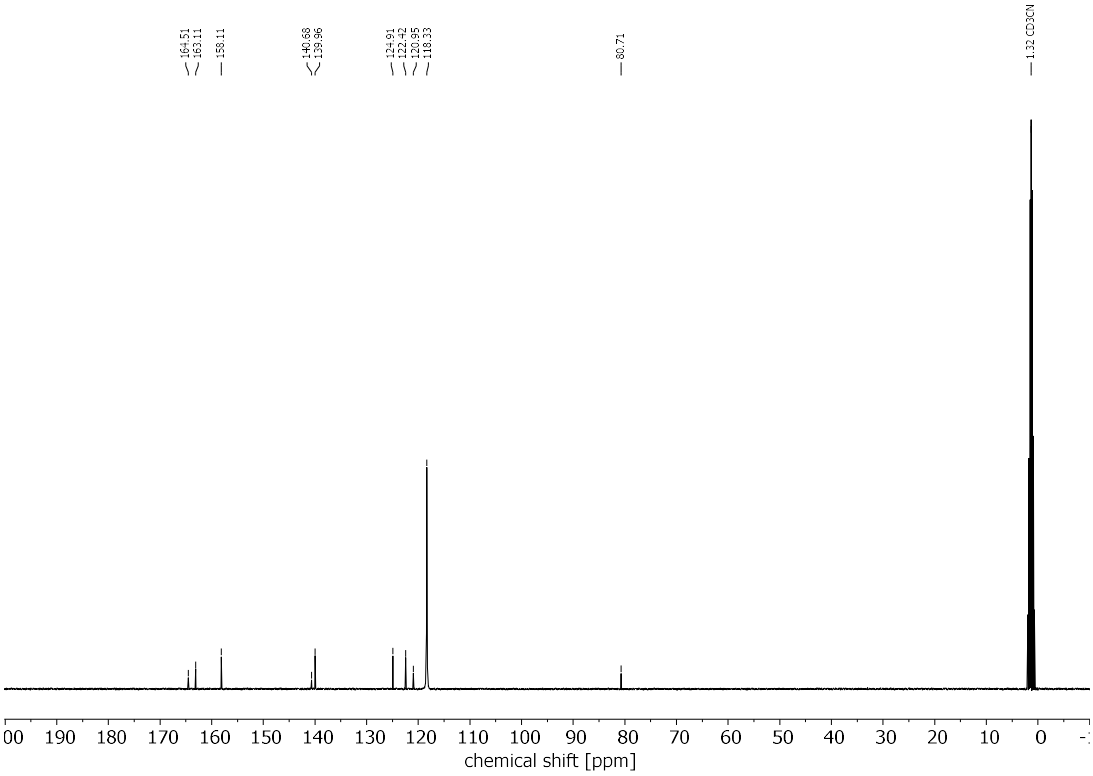

Figure 53: ^{13}C NMR spectrum of [Fe^{II}**L1**(mecn)](OTf)$_2$ (CD_3CN, 101 MHz, 295 K).

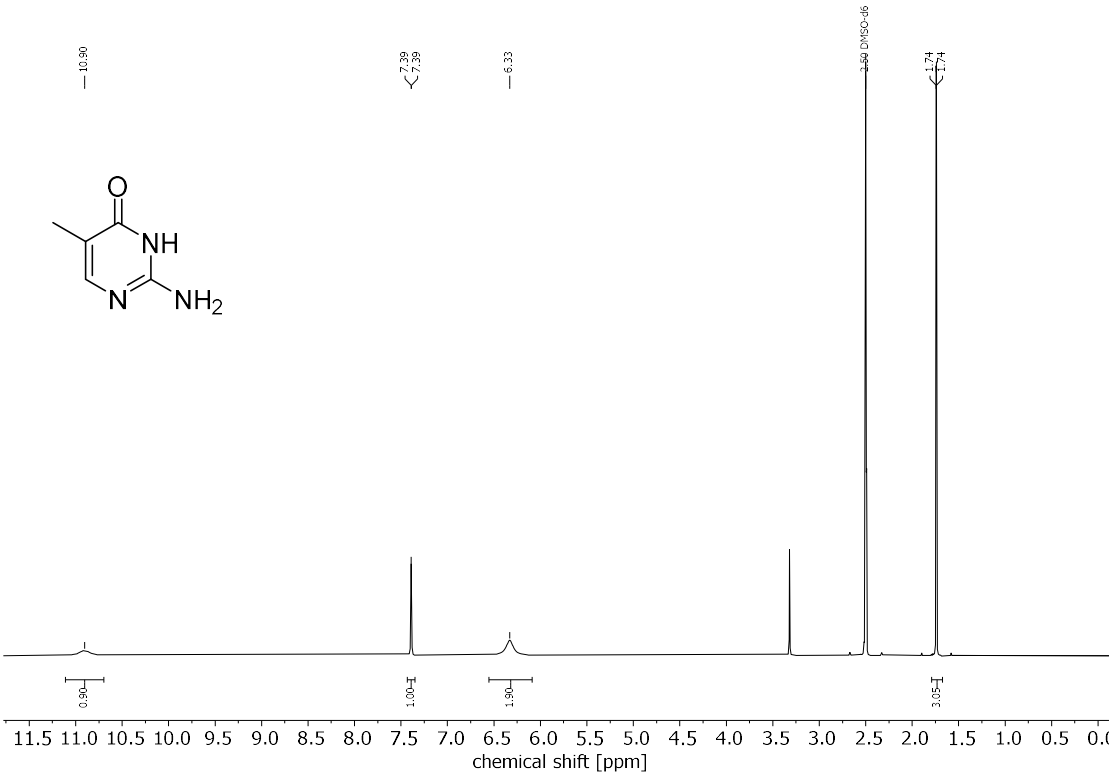

Figure 54: ^{1}H NMR spectrum of 5m*i*C (DMSO-d_6, 400 MHz, 295 K).

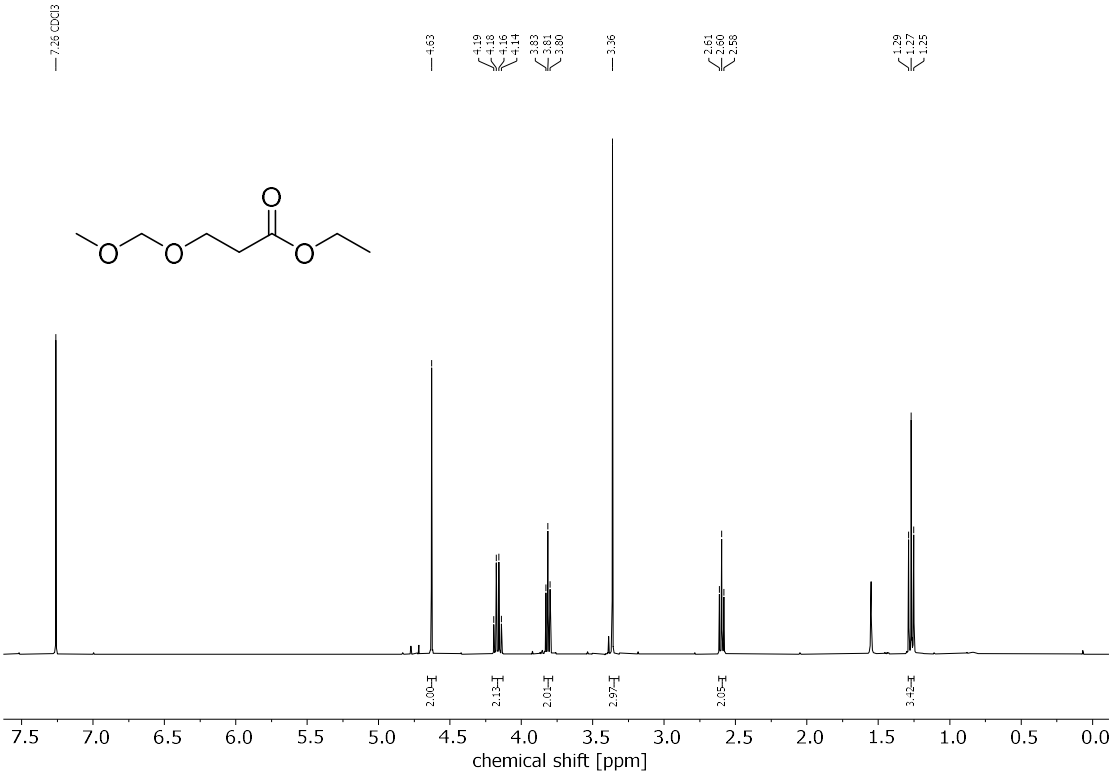

Figure 55: ^{1}H NMR spectrum of ethyl 3-(methoxymethoxy)propanoate ($CDCl_3$, 400 MHz, 295 K).

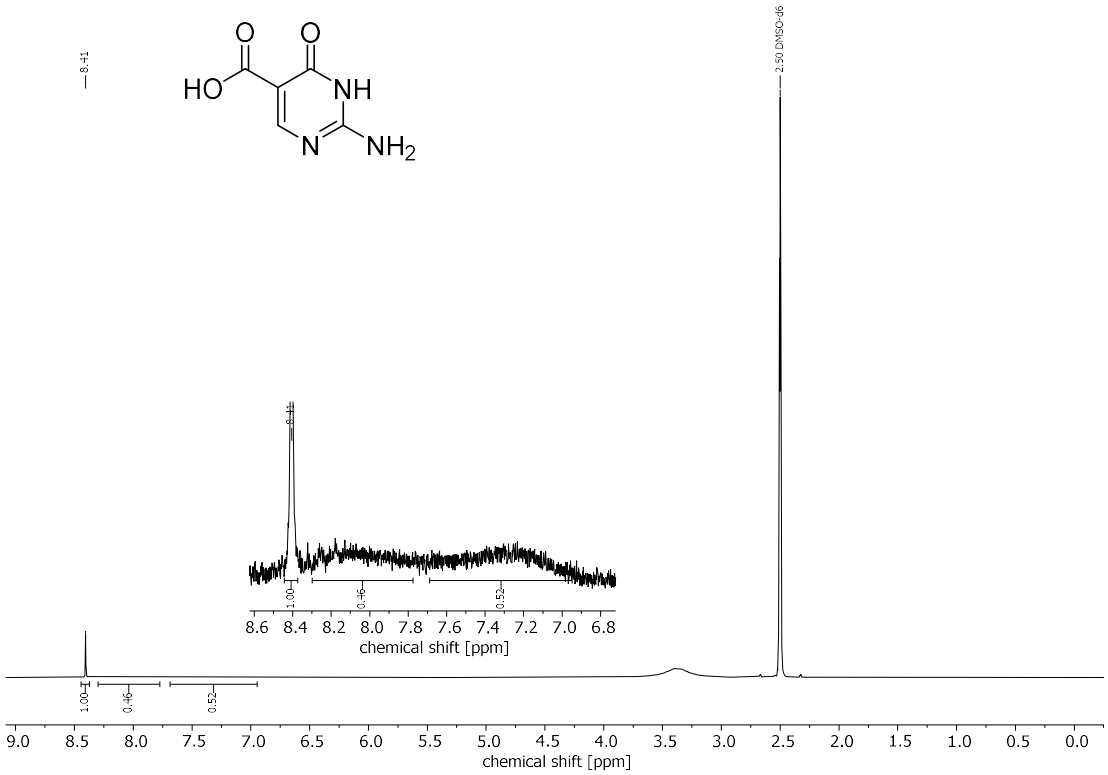

Figure 56: ^{1}H NMR spectrum of 5c*i*C (DMSO-d_6, 400 MHz, 295 K).

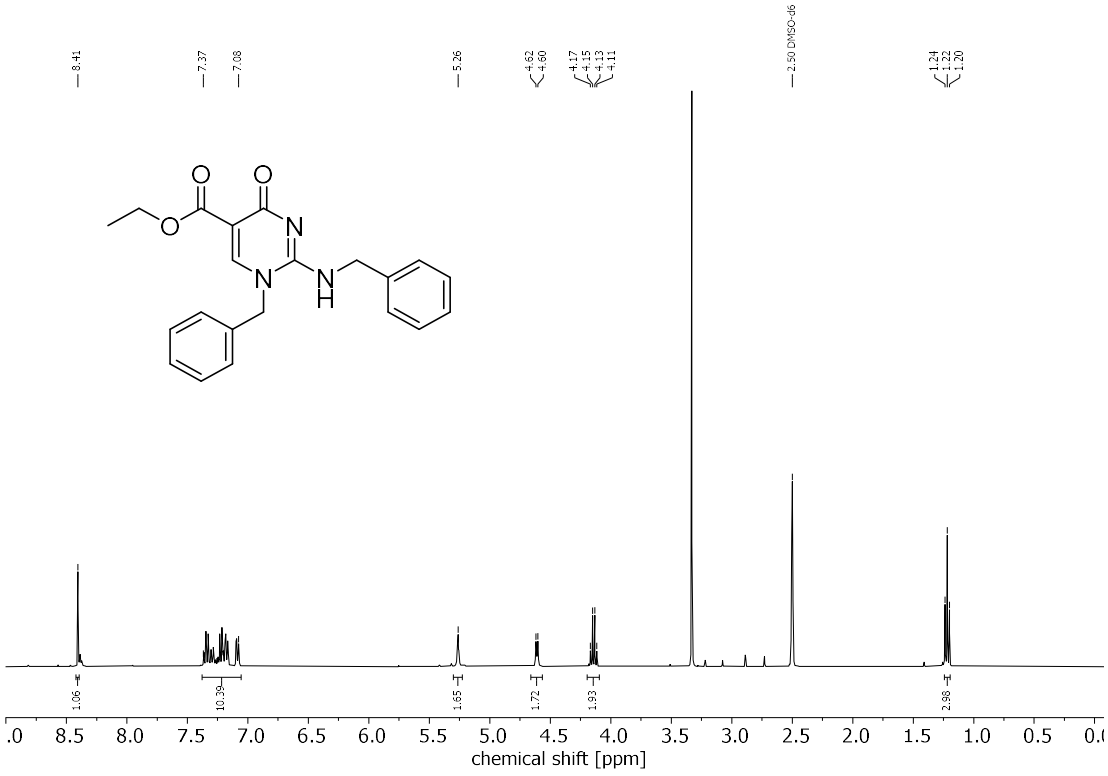

Figure 57: ^{1}H NMR spectrum of compound **8** (DMSO-d_6, 400 MHz, 295 K).

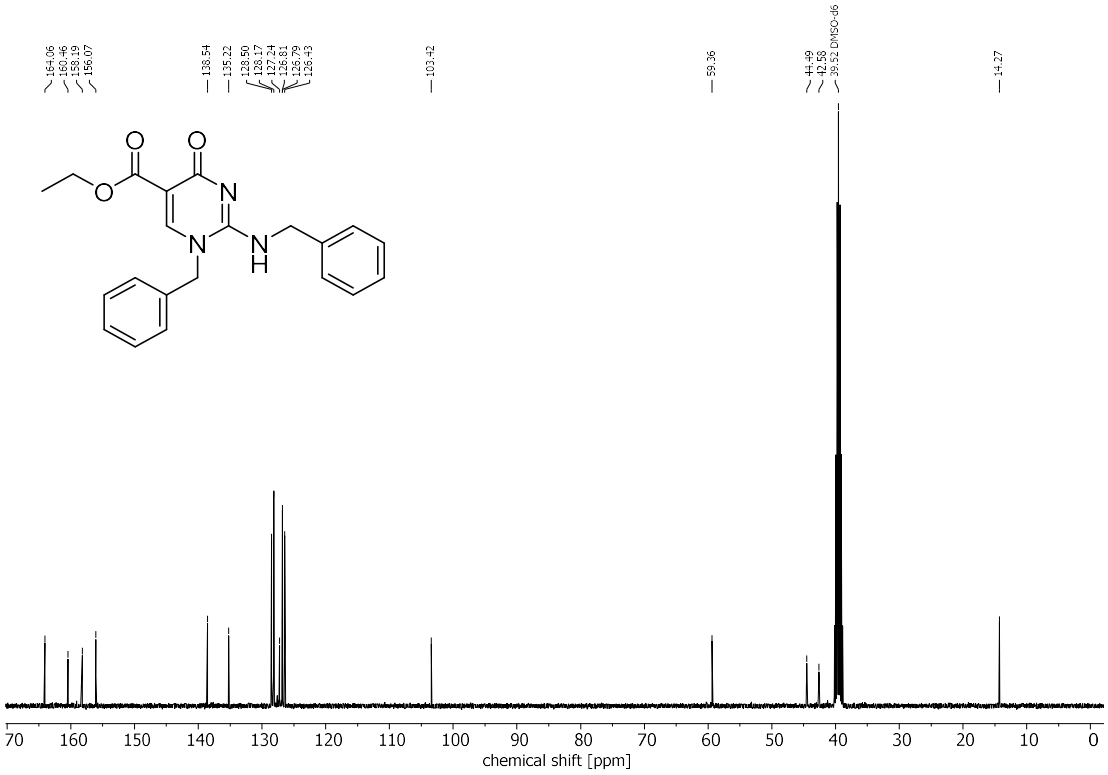

Figure 58: ^{13}C NMR spectrum of compound **8** (DMSO-d_6, 101 MHz, 295 K).

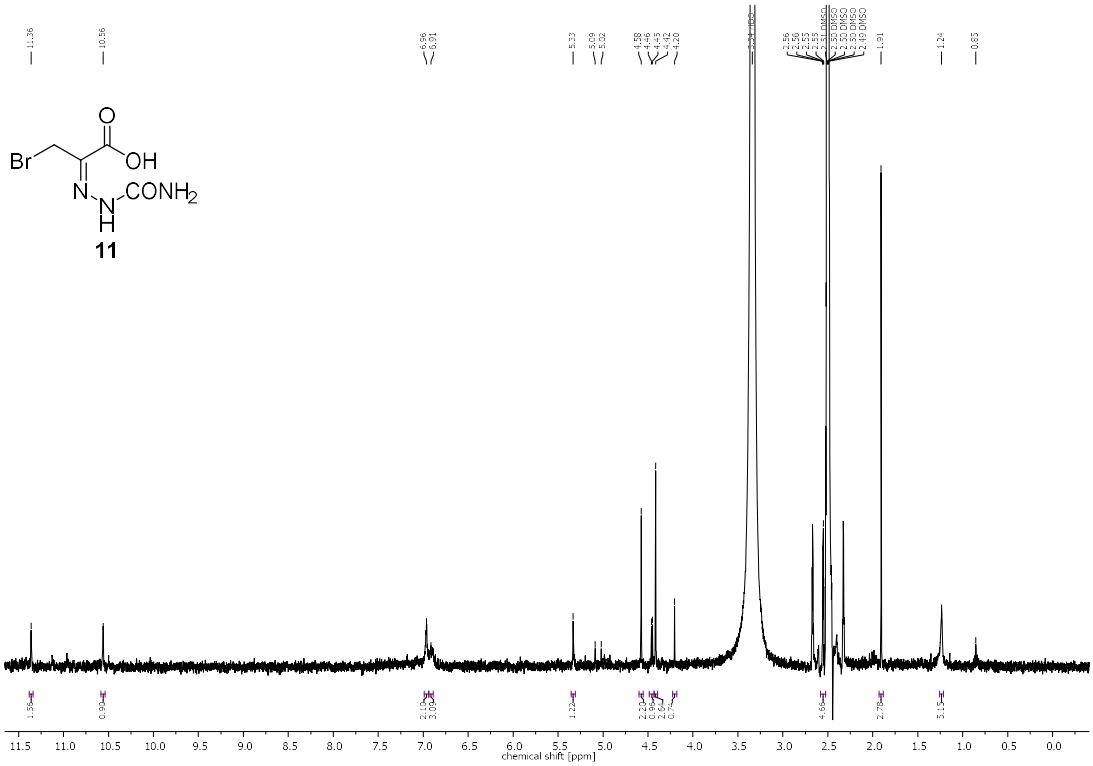

Figure 59: ^{1}H-NMR spectrum of compound **11** (DMSO-d_6, 400 MHz, 295 K).

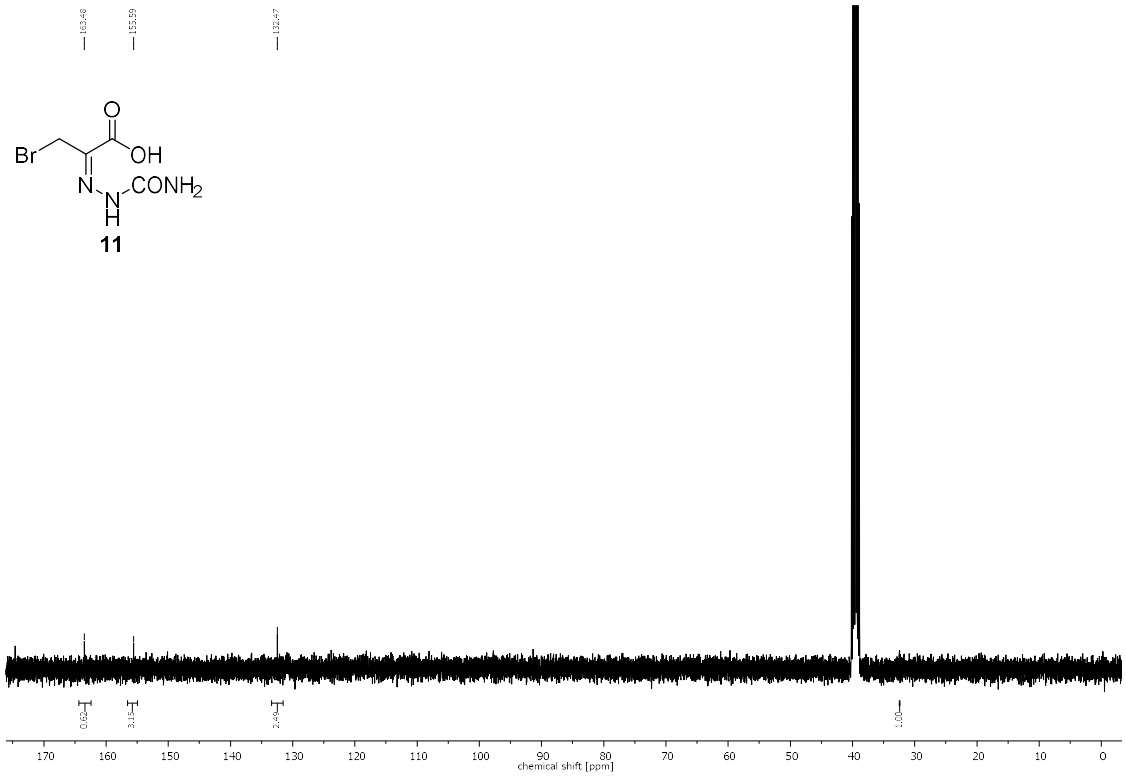

Figure 60: ^{13}C-NMR spectrum of compound **11** (DMSO-d_6, 101 MHz, 295 K).

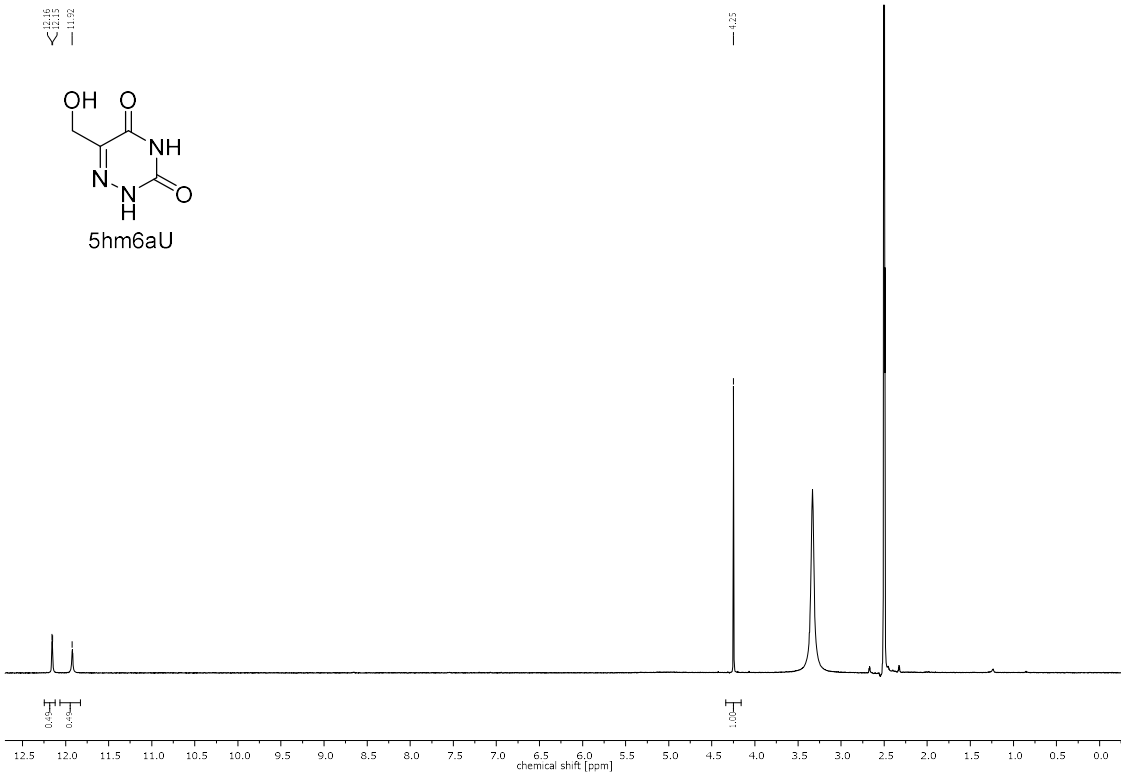

Figure 61: ^{1}H-NMR spectrum of 5hm6aU (DMSO-d_6, 400 MHz, 295 K).

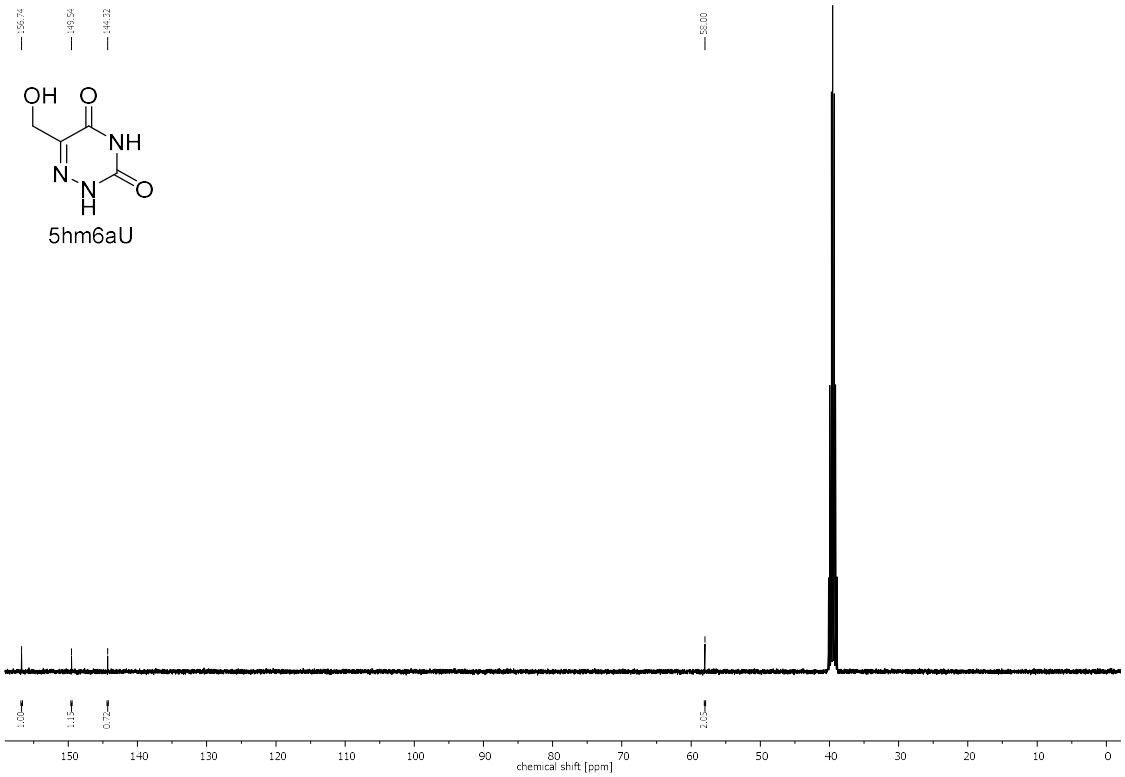

Figure 62: ^{13}C-NMR spectrum of 5hm6aU (DMSO-d_6, 101 MHz, 295 K).

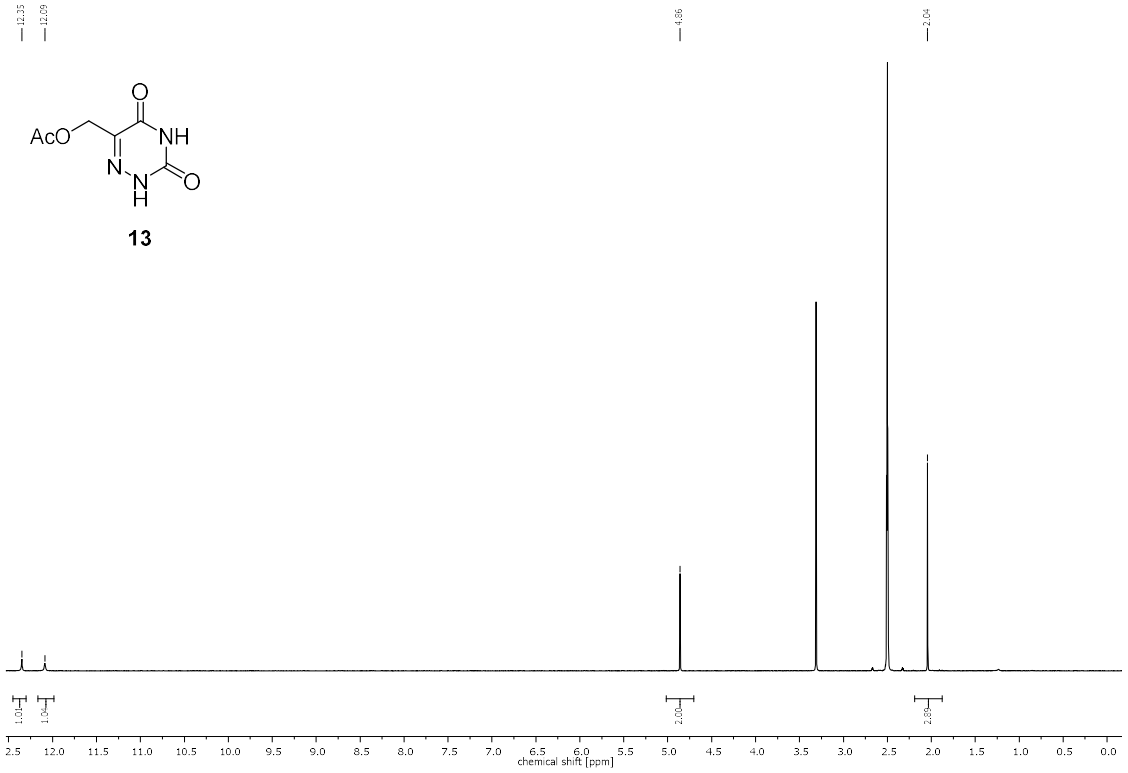

Figure 63: ^{1}H-NMR spectrum of compound **13** in (DMSO-d_6, 400 MHz, 295 K).

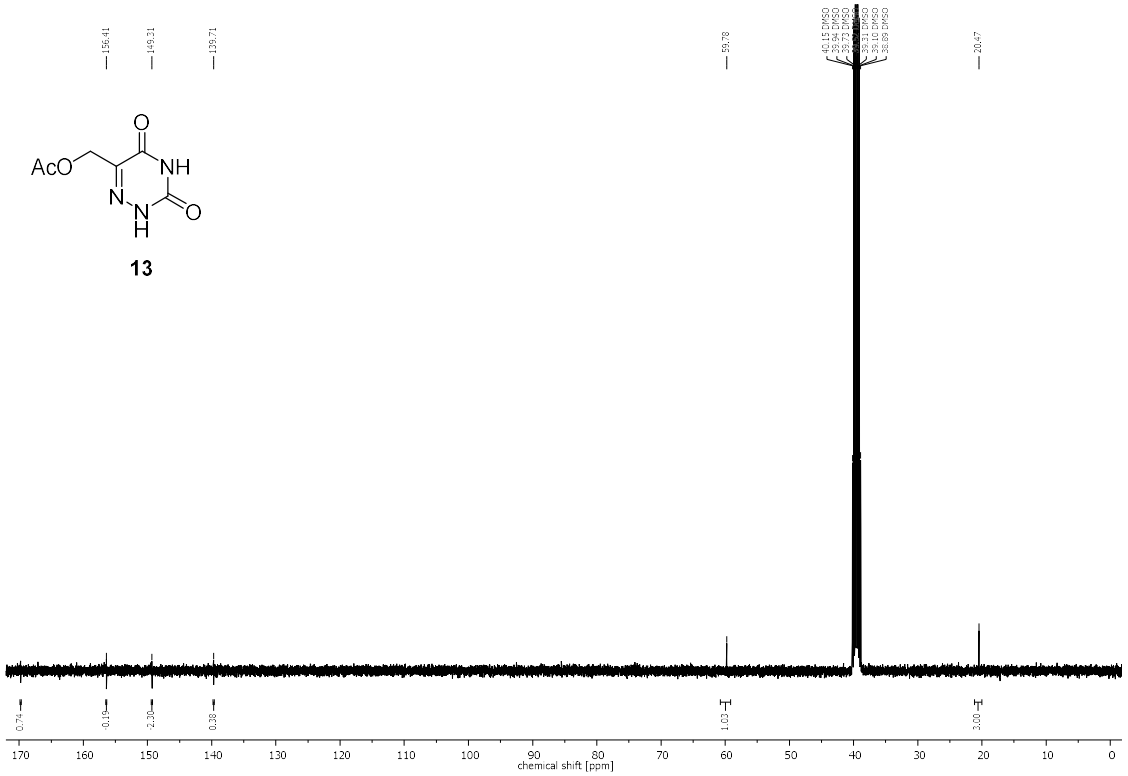

Figure 64: ^{13}C-NMR spectrum of compound **13** (DMSO-d_6, 101 MHz, 295 K).

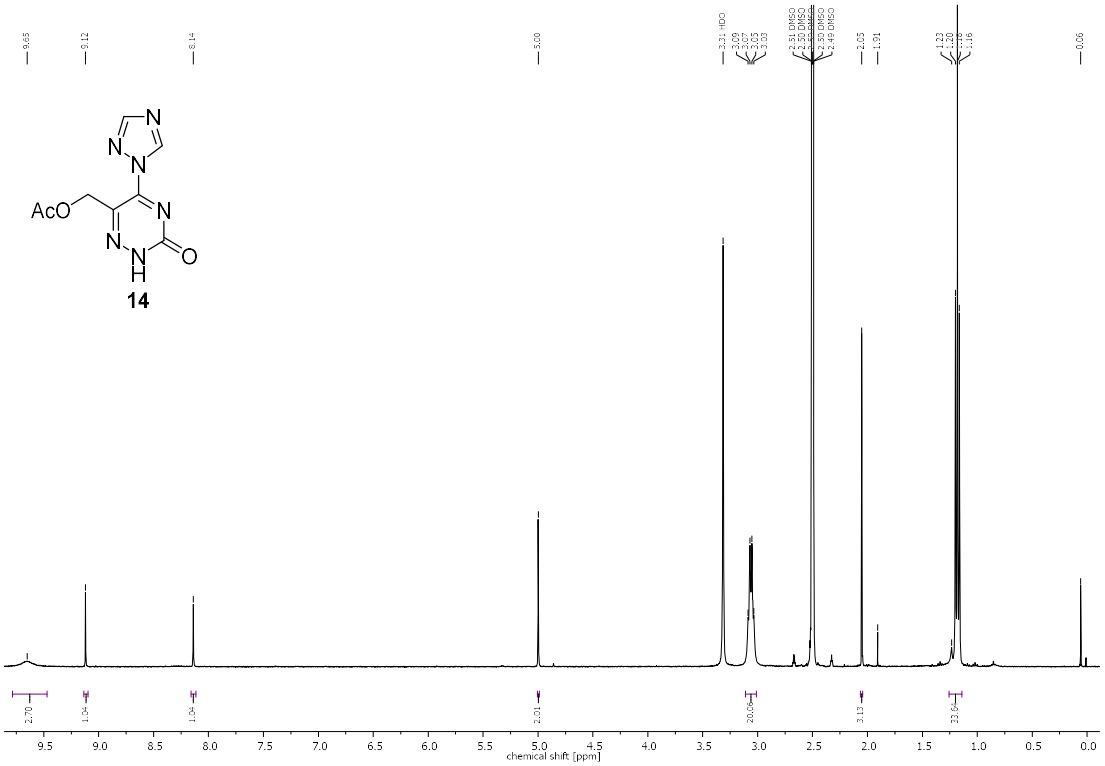

Figure 65: ^{1}H-NMR spectrum of **14** (DMSO-d_6, 400 MHz, 295 K).

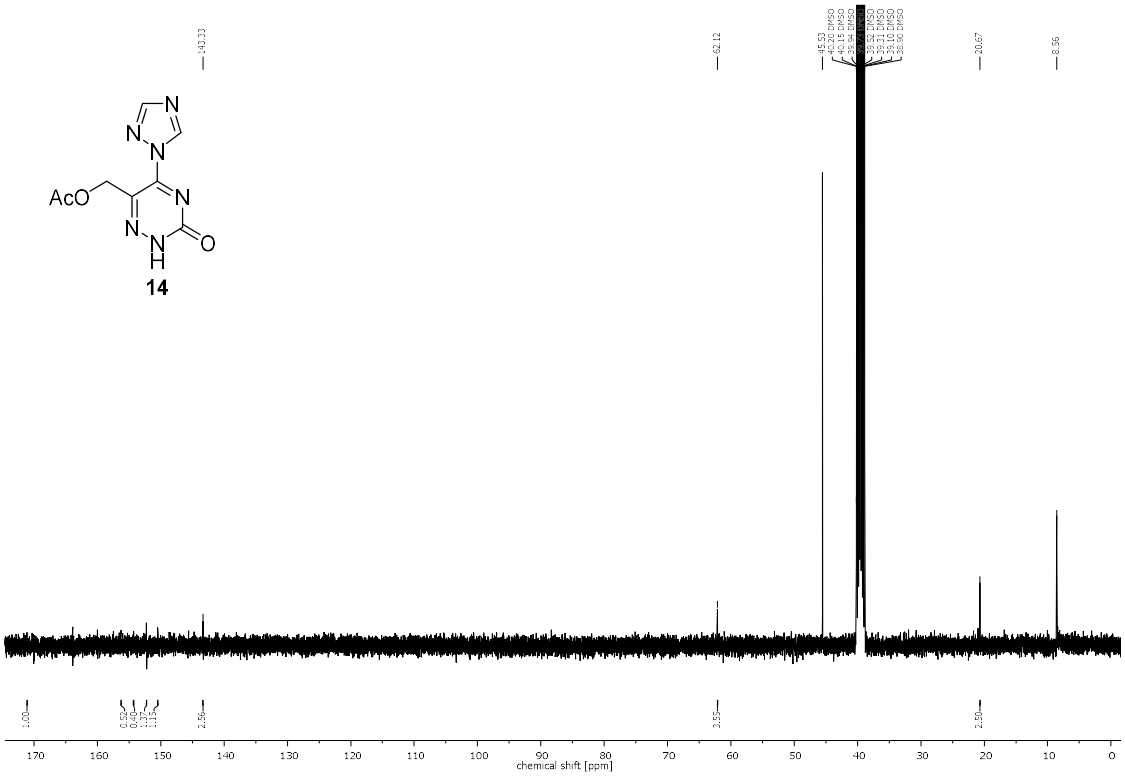

Figure 66: ^{13}C-NMR spectrum of compound **4** (DMSO-d_6, 101 MHz, 295 K).

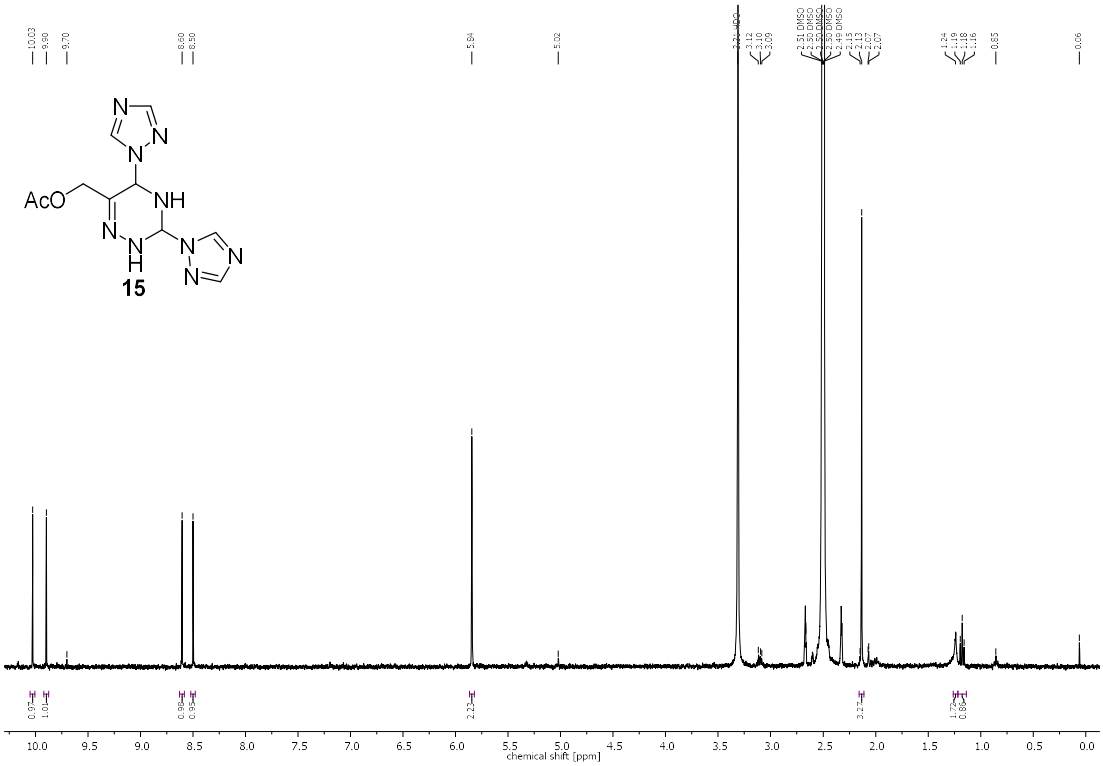

Figure 67: ^{1}H-NMR spectrum of **15** (DMSO-d_6, 400 MHz, 295 K).

4.2 Product Identification

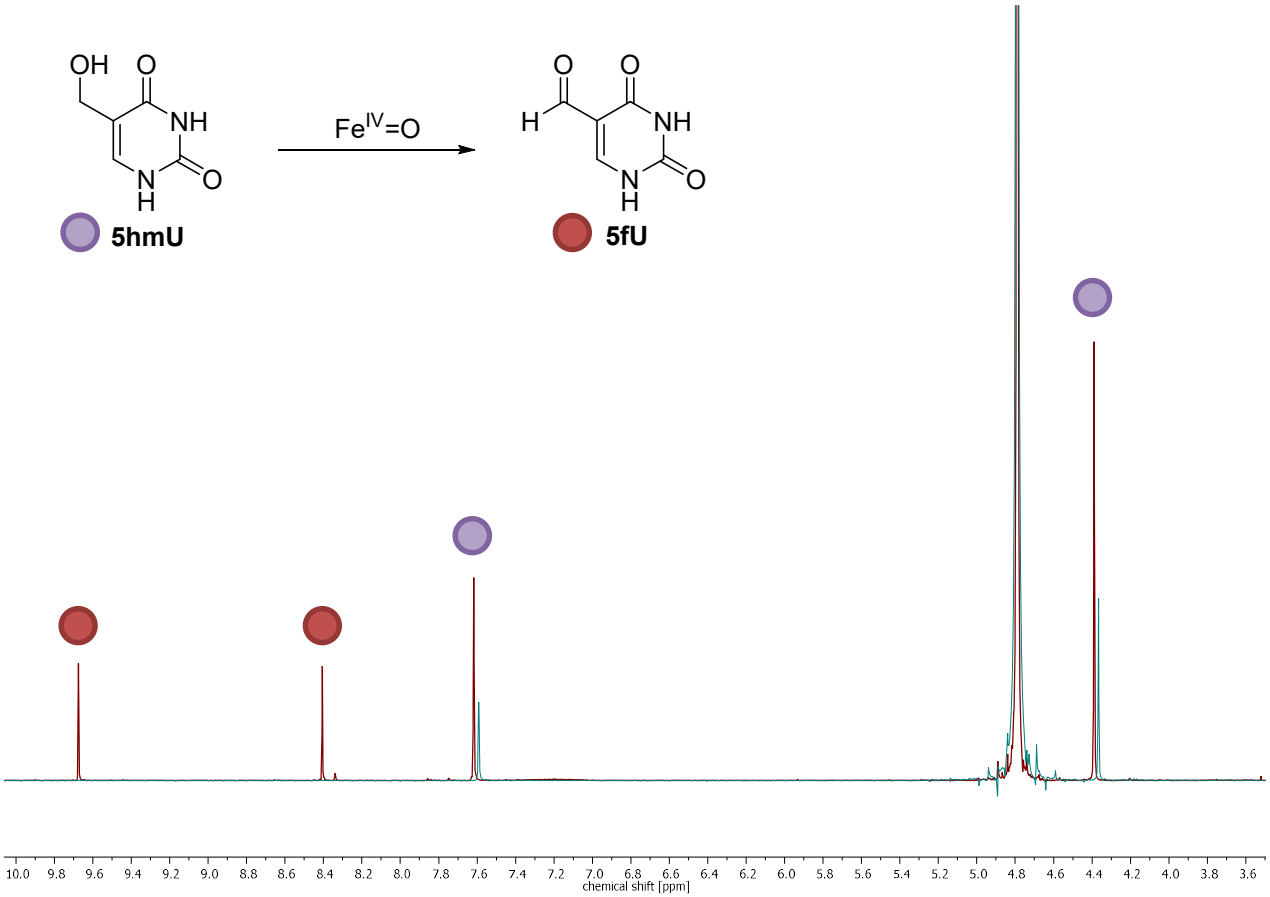

Figure 68: ^{1}H NMR spectra of the obtained products from a reaction of 5hmU with $[Fe^{IV}\mathbf{L1}(O)]^{2+}$ (red) and reference measurement of 5hmU (green) in D_2O at 298 K. Reaction conditions: [5hm6aU] = $[Fe^{IV}=O]$ = 5 mM, H_2O, 25 °C, 1 h.

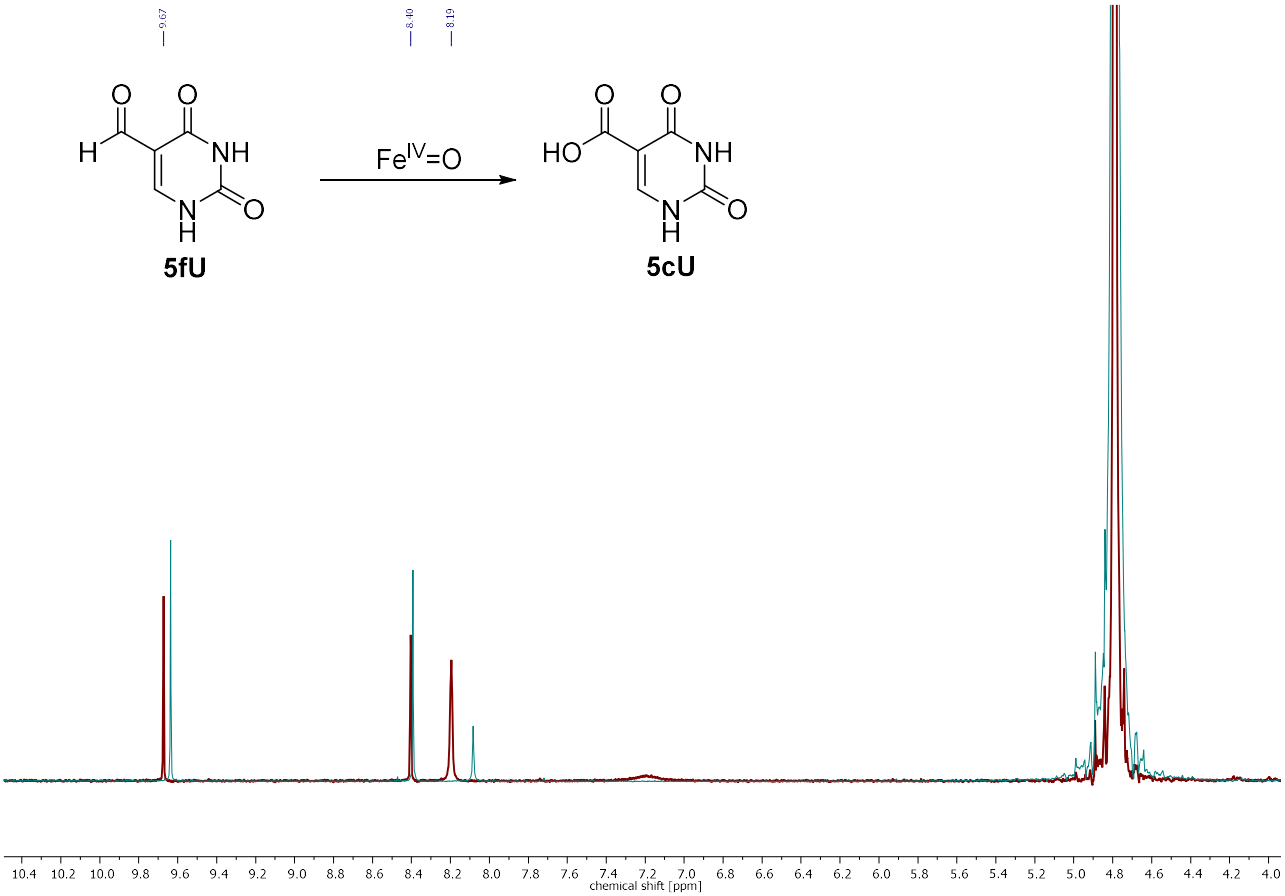

Figure 69: ^{1}H NMR spectra of the obtained products from a reaction of 5fU with $[Fe^{IV}\mathbf{L1}(O)]^{2+}$ (red) and reference measurement of 5fU (green) in D_2O at 298 K. It was found that the 5fU sample contained about equimolar amounts of the respective carboxylic acid 5cU. Reaction conditions: [5hm6aU] = $[Fe^{IV}=O]$ = 5 mM, H_2O, 25 °C, 1 h.

4.3 Spin Crossover Properties Followed by Temperature-dependent ^{1}H NMR Spectroscopy

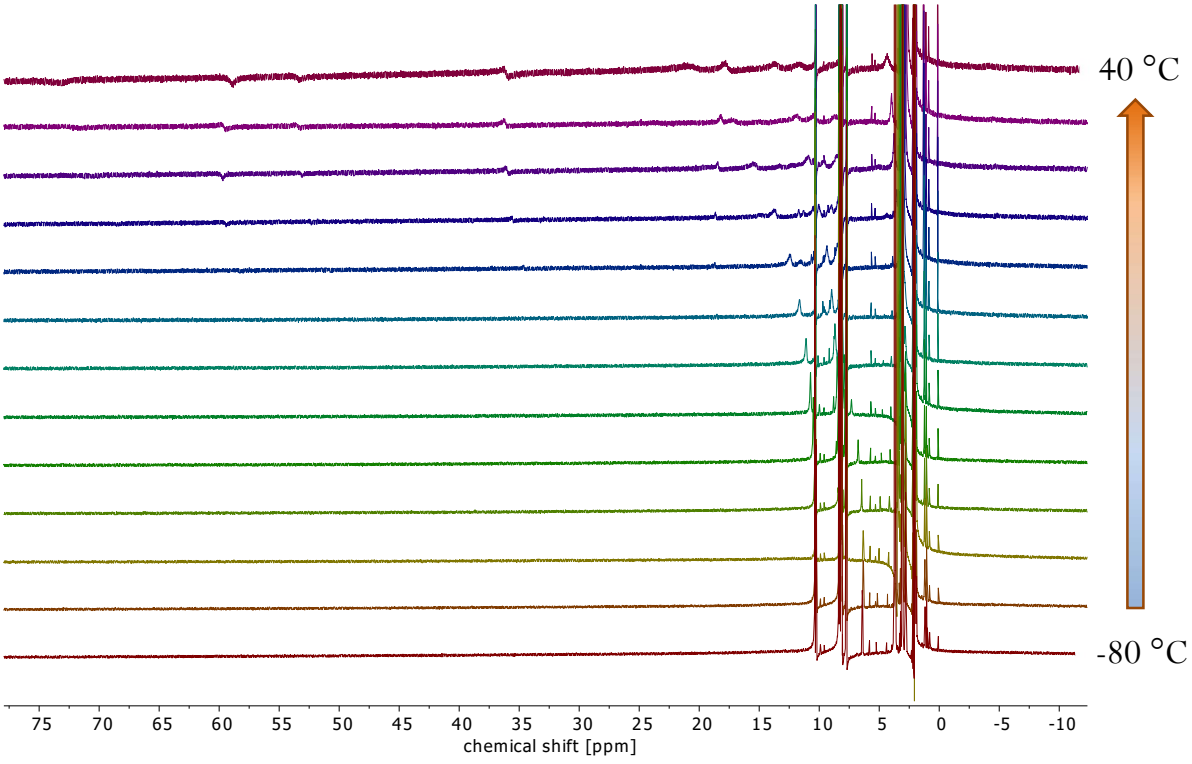

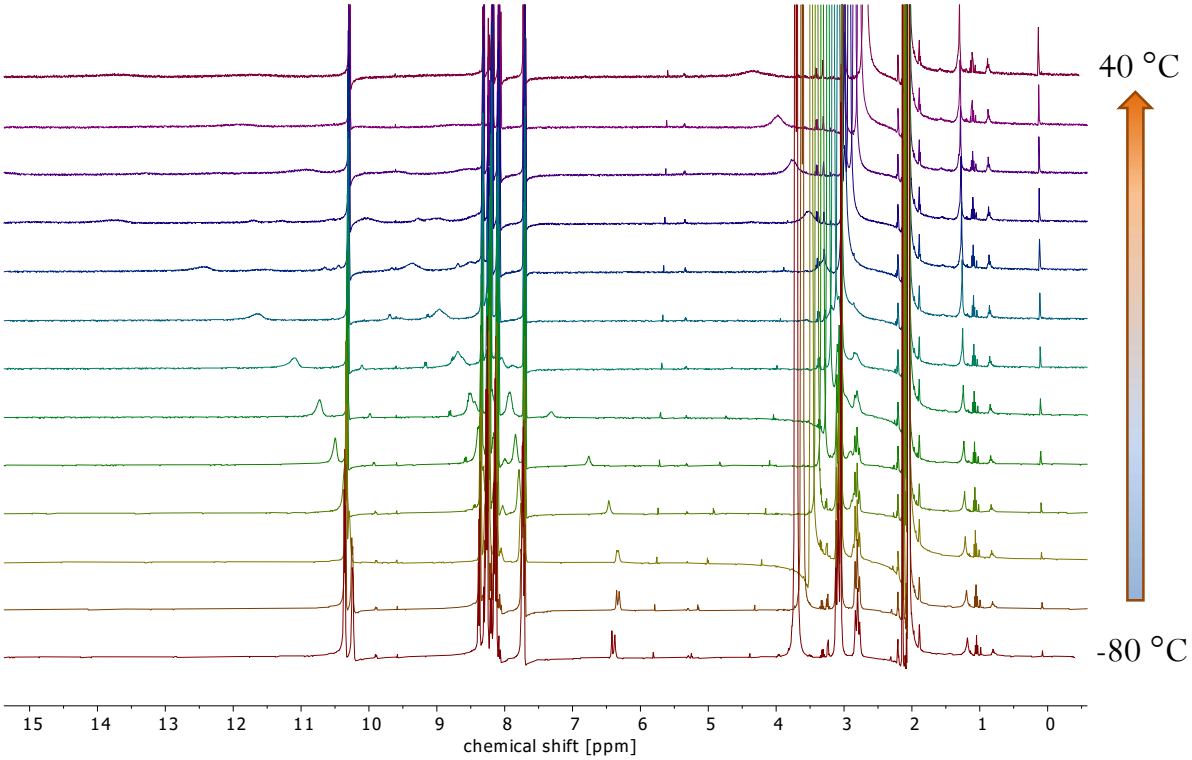

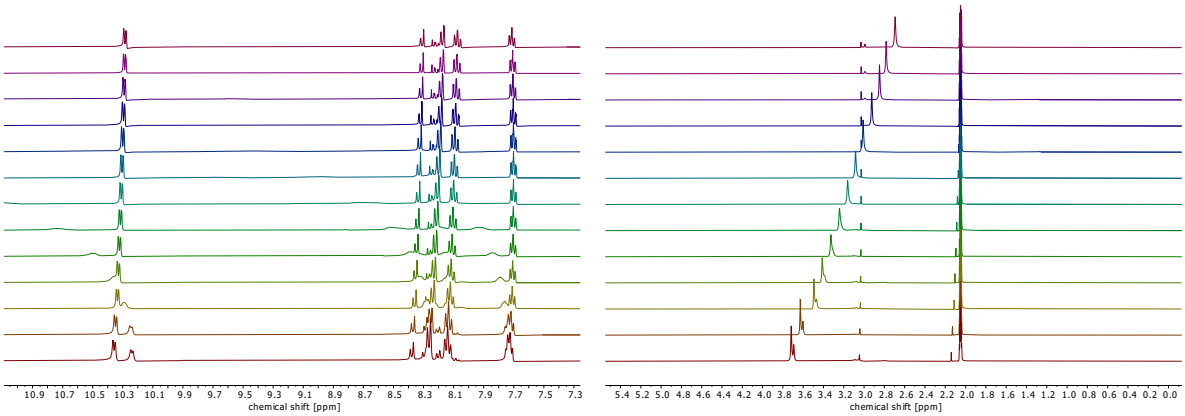

Figure 70: Complete ^{1}H NMR spectra and detailed views of $[Fe^{II}\mathbf{L1}(mecn)]^{2+}$ recorded between -80 °C and 40 °C in acetone-d_6.

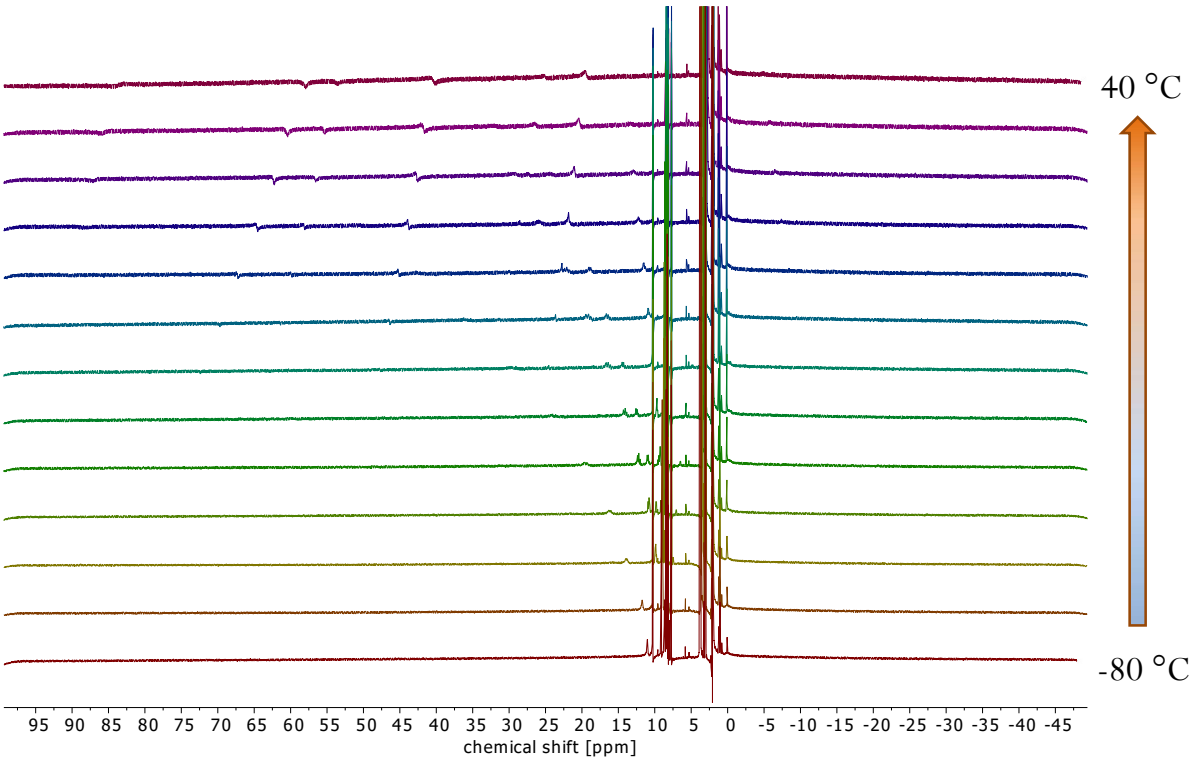

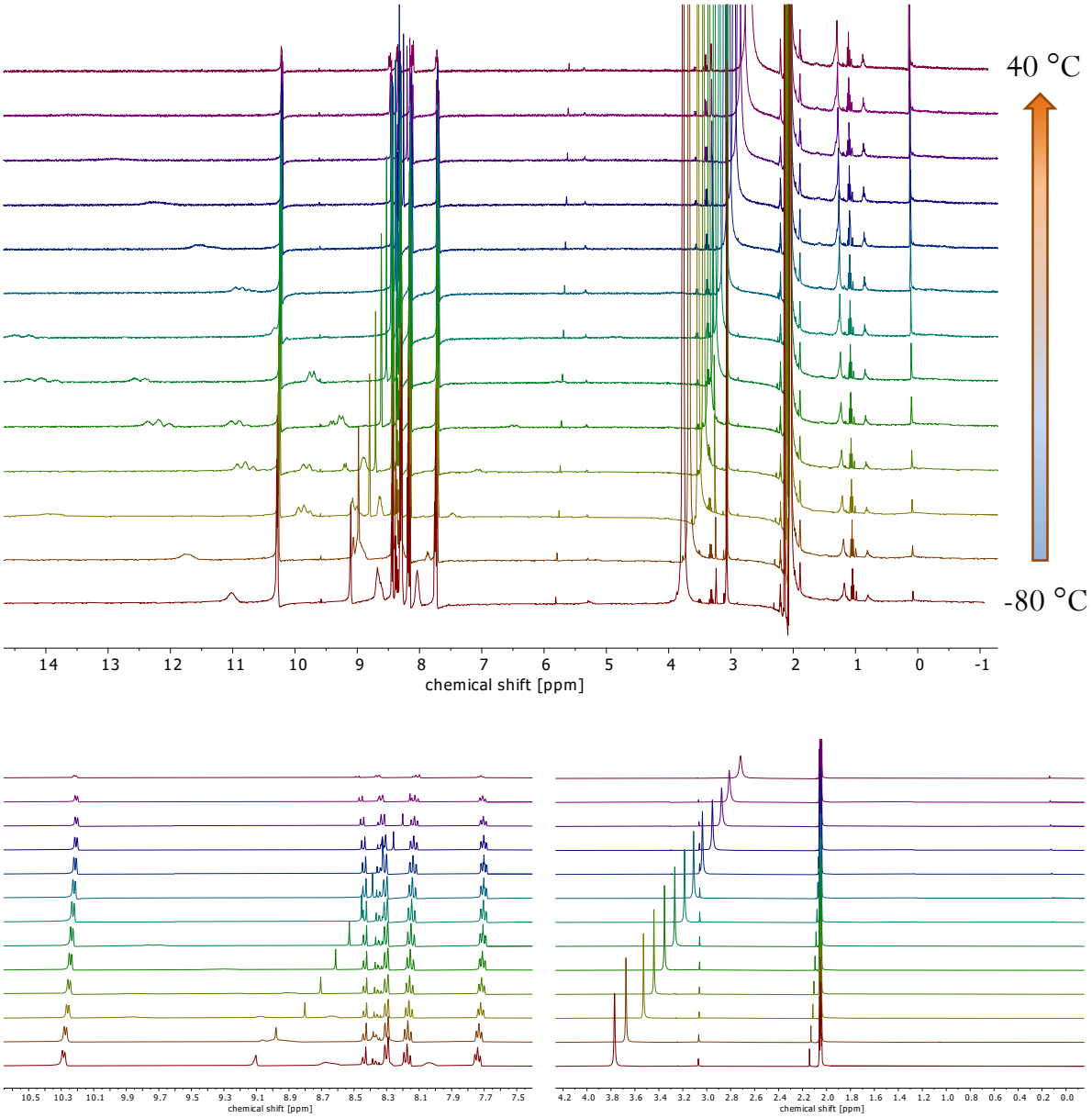

Figure 71: Complete ^{1}H NMR spectra and detailed views of $[Fe^{II}\mathbf{L2}(mecn)]^{2+}$ recorded between -80 °C and 40 °C in acetone-d_6.

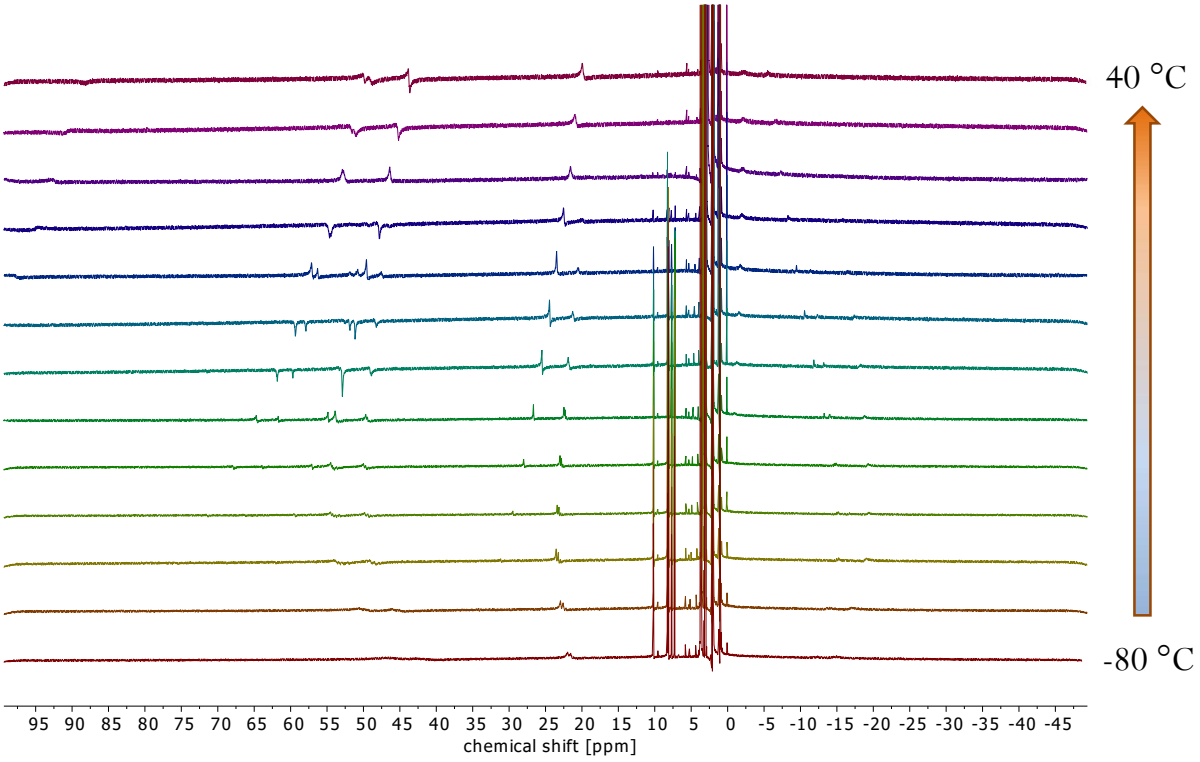
40 °C
-80 °C
95 90 85 80 75 70 65 60 55 50 45 40 35 30 25 20 15 10 5 0 -5 -10 -15 -20 -25 -30 -35 -40 -45
chemical shift [ppm]

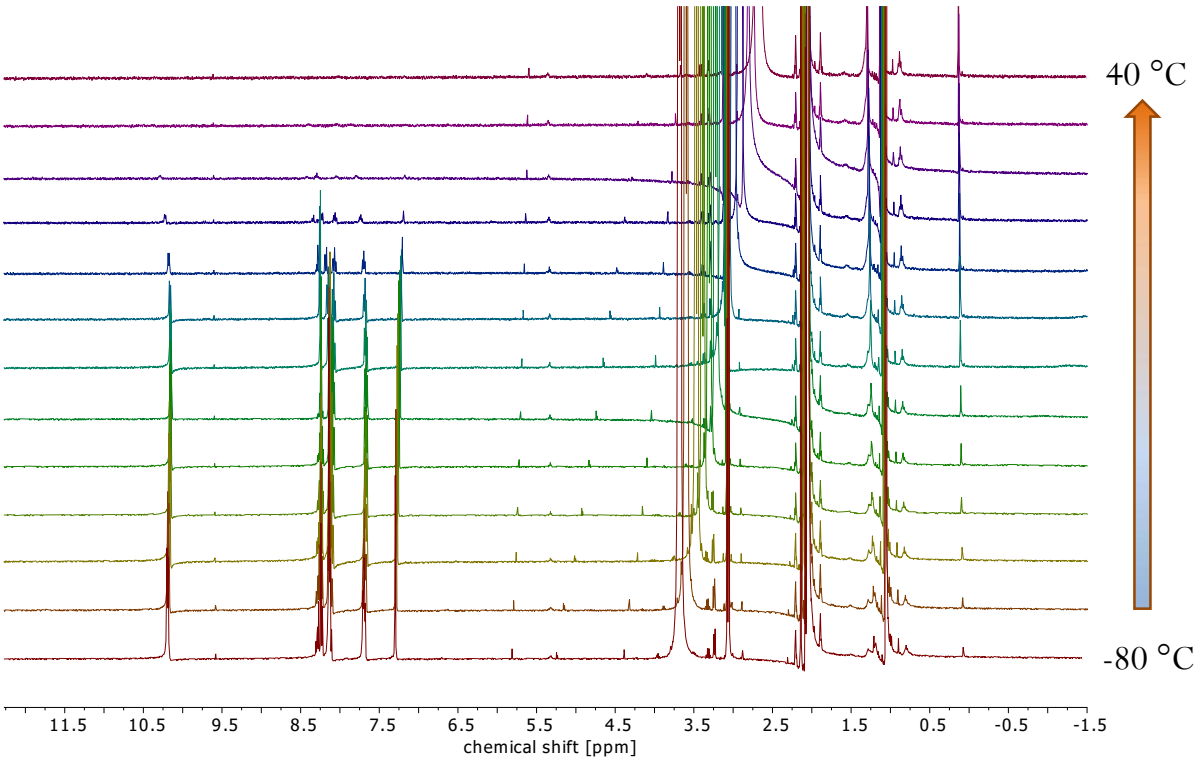
40 °C
-80 °C
11.5 10.5 9.5 8.5 7.5 6.5 5.5 4.5 3.5 2.5 1.5 0.5 -0.5 -1.5
chemical shift [ppm]

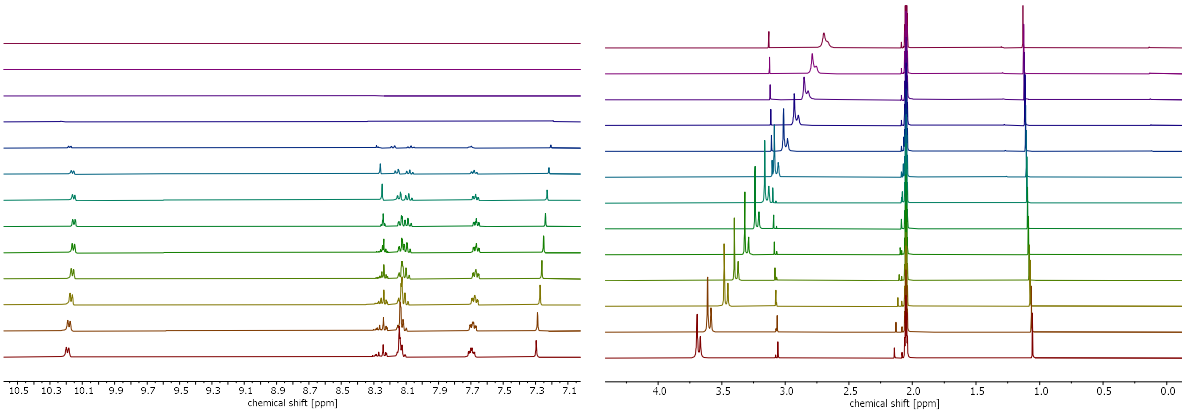

Figure 72: Complete ^{1}H NMR spectra and detailed views of [Fe^{II}**L3**(mecn)]$^{2+}$ recorded between -80 °C and 40 °C in acetone-d_6.

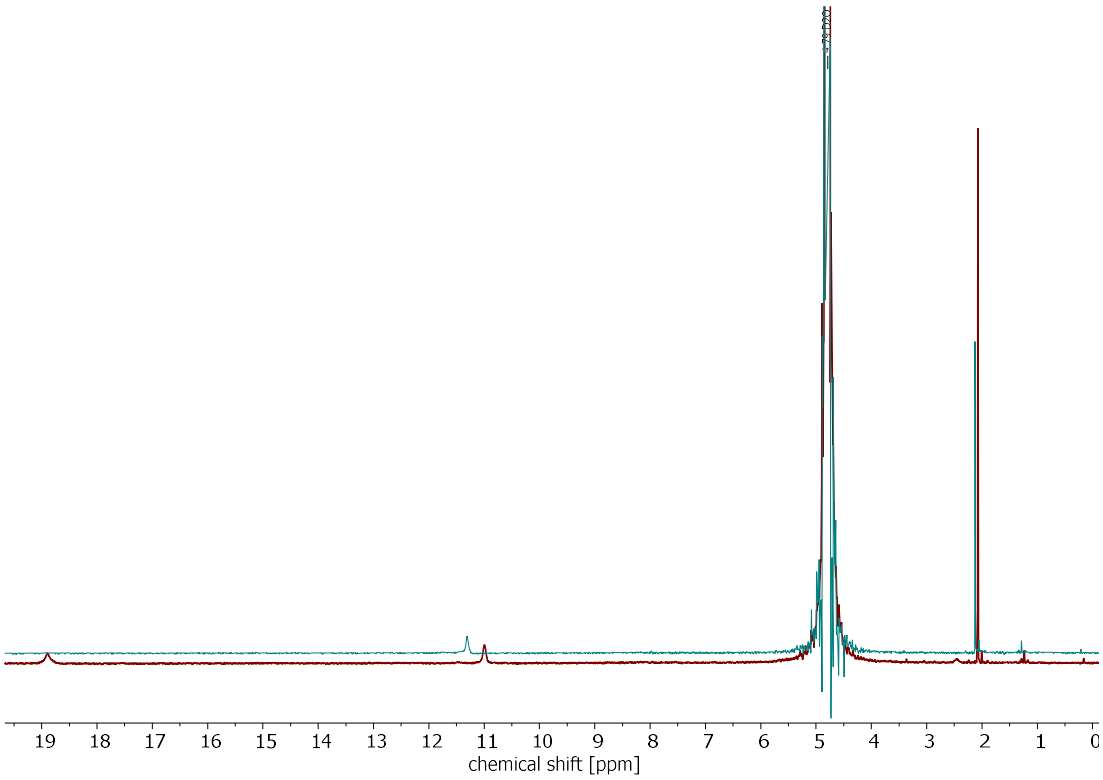

Figure 73: ^{1}H NMR spectra of [Fe^{II}**L2**(mecn)]$^{2+}$ in deuterated water. Green: measurement at 30 °C, red: measurement at 26 °C after previous heating to 60 °C.

5 UV-vis Spectra

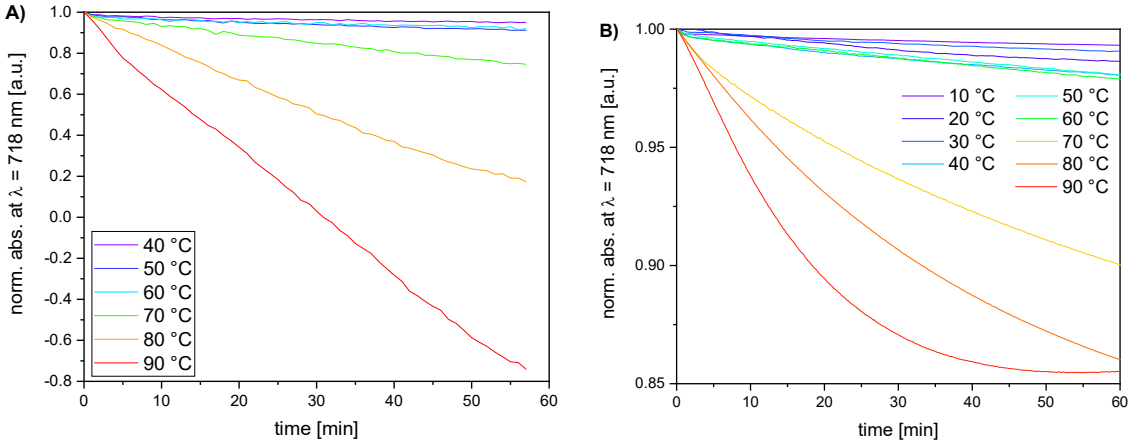

Figure 74: UV-vis absorbance (718 nm) of **A)** $[Fe^{IV}\mathbf{L1}(O)]^{2+}$ and **B)** $[Fe^{IV}\mathbf{L2}(O)]^{2+}$ at different temperatures over time. Conditions: $[[Fe^{IV}\mathbf{L1}/\mathbf{L2}(O)]^{2+}]$ = 1 mM, H_2O, 10-90 °C.

6 UHPLC-MS/MS Data

Table 23: Amount of 5xdC over time from a reaction of $[Fe^{IV}\mathbf{L1}(O)]^{2+}$ or $[Fe^{IV}\mathbf{L2}(O)]^{2+}$ with **oligo1**. Conditions shown at the bottom. Quantification was performed by Hanife Sahin (Carell group, LMU Munich).

$[Fe^{IV}\mathbf{L1}(O)]^{2+}$	$[Fe^{IV}\mathbf{L2}(O)]^{2+}$
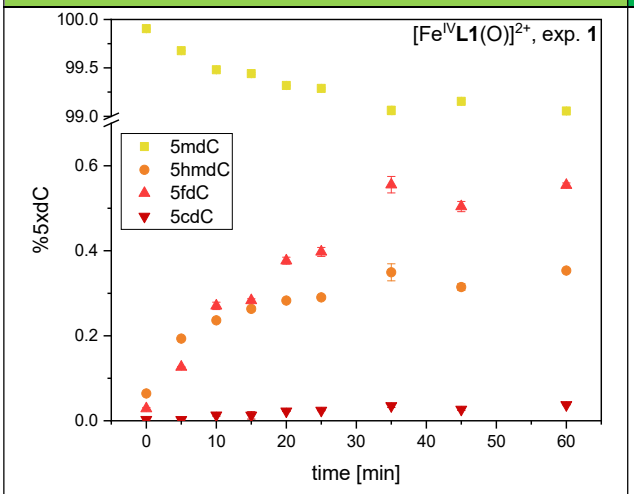	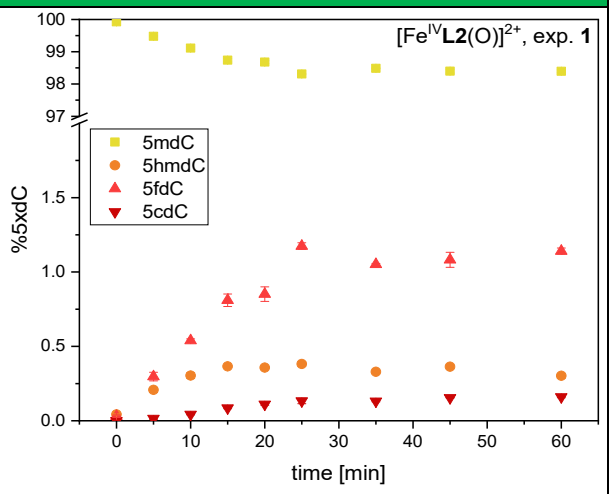
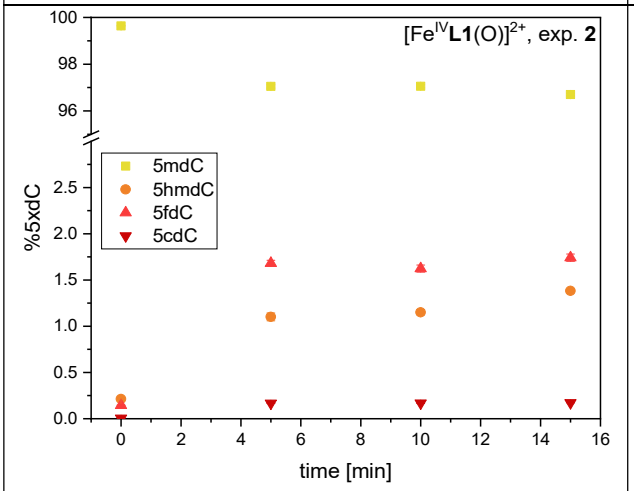	*not measured*
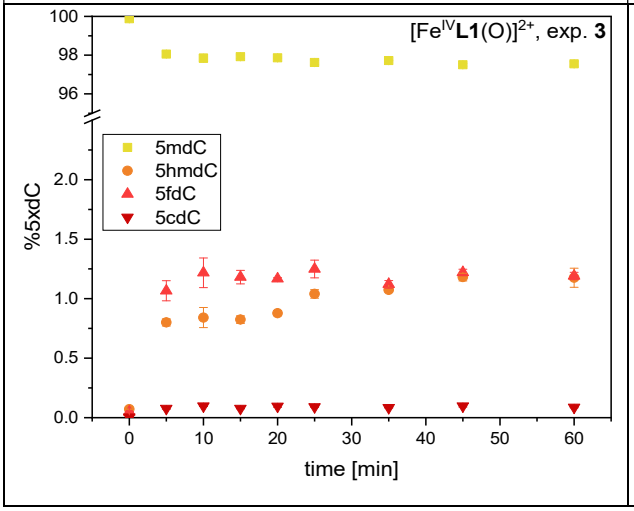	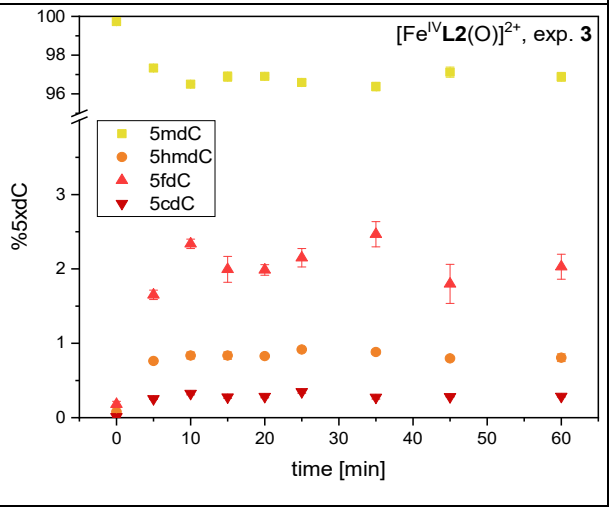

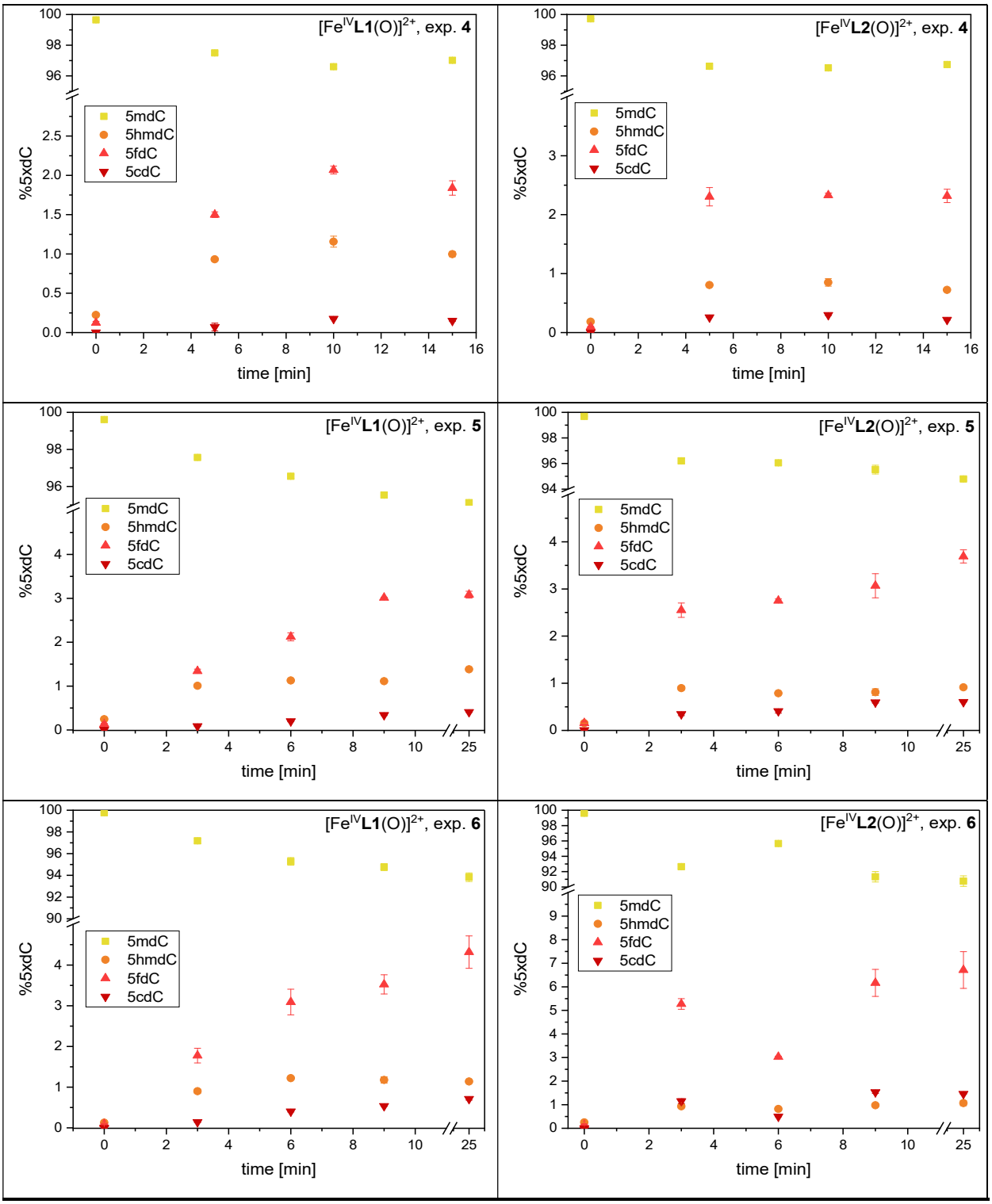

Exp.	1	2	3	4	5	6
[oligo1] [mM]	0.125	0.125	0.05	0.5	0.125	0.125
Temperature [° C]	4	40	23	23	23	23
equiv. Fe^{IV}=O	4 equiv.	4 equiv.	4 equiv.	4 equiv.	6 equiv.	8 equiv.

Table 24: Amounts of 5xdC and 5xU resulting from a reaction of **DNA1** with $[Fe^{IV}\mathbf{L1}(O)]^{2+}$.

sample	time	%5mdC	%5hmdC	%5fdC	%5cadC	%5hmU	%dT
1	5 min	98.77	0.23	0.95	0.05	6.20	93.80
2	10 min	98.73	0.22	0.99	0.06	5.81	94.19
3	15 min	98.83	0.21	0.90	0.06	6.74	93.26
4	60 min	98.71	0.23	1.00	0.06	6.10	93.90

7 MALDI-MS Data

Table 25: Overview of the conducted oligonucleotide oxidation experiments. A and B in the sample name refer to the employed iron(IV)-oxido species $[Fe^{IV}\mathbf{L1}(O)]^{2+}$ and $[Fe^{IV}\mathbf{L2}(O)]^{2+}$, respectively. 5mdC refers to observed unreaction 5mdC-containing oligonucleotide and 5xdC refers to observed oligonucleotides containing 5hmdC, 5fdC or 5cdC; a star at 5xdC implies other (unidentified) oxidation products. Other observed masses that could be attributed to a reasonable structure are highlighted in grey.

sample	oligo	observed MALDI signals			conditions	
		5mdC	5xdC	other masses	Fe equiv.	time [min]
1A	Oligo1	x	x	2814, 2823, 2836, 2859, 2874	4	20
2A	Oligo1	x	*	776, 931, 1092, 2836	4	30
3A	Oligo1	x	-	671, 738, 899, 1060, 1540, 1854	12	30
4A	Oligo2	x	-	738, 822, 899	12	30
5A	Oligo3	(x)	-	738, 819, 921, 1076	12	30
6A	Oligo1	-	-	690, 770, 931, 1086	4	60
7A	Oligo1	-	-	662, 769, 931, 1092	8	60
8A	Oligo1	-	-	671, 738, 899, 1060, 1540, 1854	16	60
9A	Oligo1	-	-	671, 738, 899, 1060	24	60
10A	Oligo1	-	-	671, 738, 899, 1060	32	60
11A	Oligo1	-	-	671, 738, 899, 1060	40	60
12A	Oligo1	x	*	770, 1466, 1541, 2836	4	60
13A	Oligo1	x	*	662, 738, 802	16	0
14A	Oligo1	x	-	770, 1540, 1854	16	5
15A	Oligo1	(x)	-	738, 770, 899	16	10
16A	Oligo1	-	-	770, 931, 1086	16	15
17A	Oligo1	-	-	738, 899	16	30
18A	Oligo1	-	-	738, 802, 899, 1061	16	60
19A	Oligo1	-	-	738, 899	24	0
20A	Oligo1	x	-	738, 899, 1541	24	5
21A	Oligo1	-	-	738, 899	24	10
22A	Oligo1	-	-	738, 899, 1060	24	15
23A	Oligo1	-	-	738, 899, 1060, 1200, 1361	24	30
24A	Oligo1	-	-	738, 899, 1060, 1432, 1541	24	60
25B	Oligo1	x	-	738, 770, 1466, 1541	4	60
26B	Oligo1	x	*	738, 770, 1466	16	0
27B	Oligo1	-	-	738, 899	16	5
28B	Oligo1	-	-	738, 899, 1070	16	30
29B	Oligo1	-	-	738, 899, 1086, 1541	16	60
30B	Oligo1	x	*	738, 899, 1466, 2836	24	0
31B	Oligo1	(x)	-	738, 899, 1541, 1854	24	5
32B	Oligo1	-	-	770, 947, 1086, 1402	24	10
33B	Oligo1	-	-	738, 899, 1060, 1362	24	15
34B	Oligo1	-	-	738, 899	24	30
35B	Oligo1	-	-	738, 899, 1070	24	60

Table 26: Overview of the expected masses of **oligo1** with different 5xdC modifications.

modified oligonucleotide	**oligo1-5mdC**	**oligo1-5hmdC**	**oligo1-5fdC**	**oligo1-5cadC**
expected mass	2932.5 m/z	2948.5 m/z	2946.5 m/z	2962.5 m/z

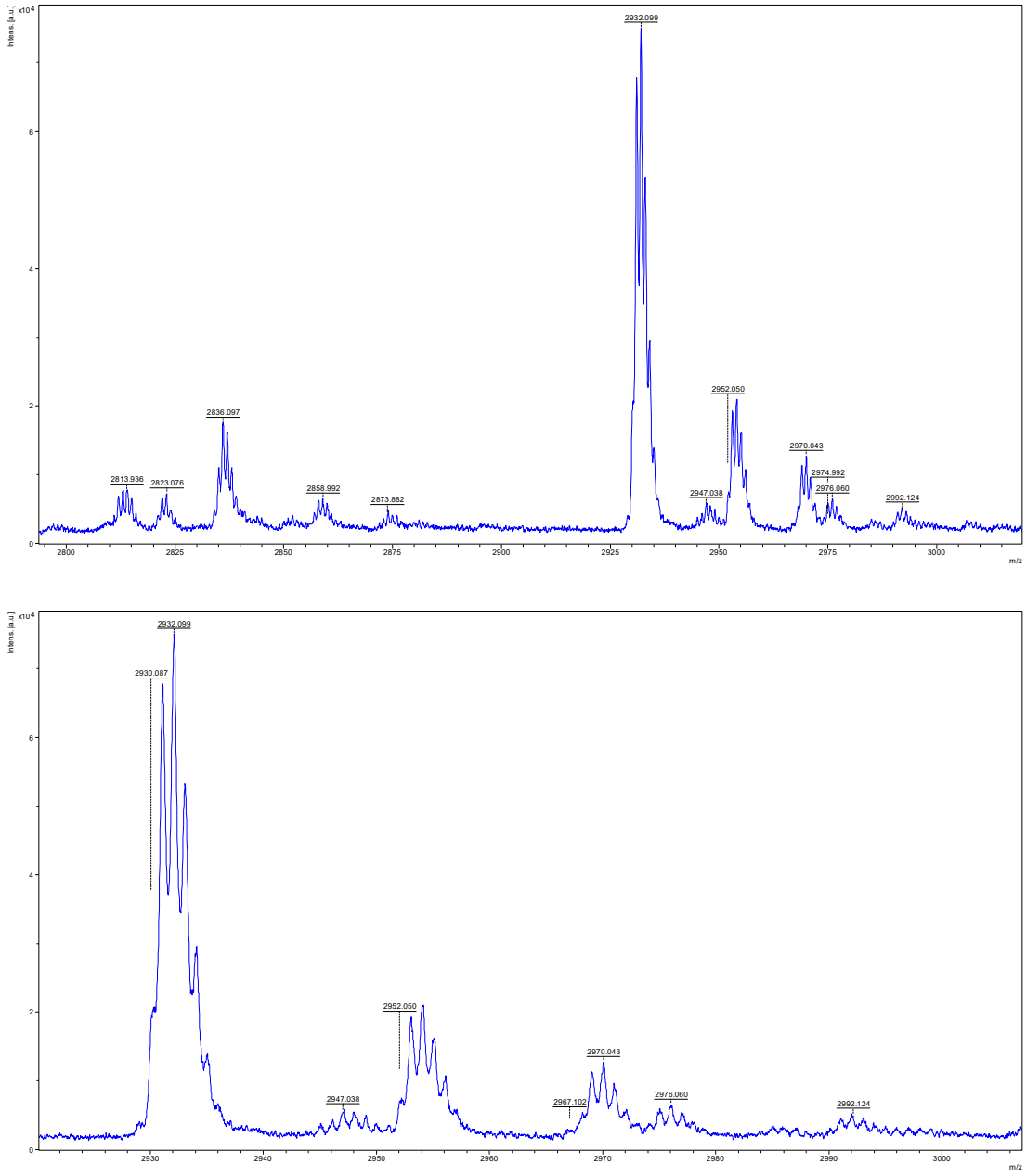

Figure 75: MALDI-MS trace of a reaction of **oligo1** with 4 equiv. of $[Fe^{IV}\mathbf{L1}(O)]^{2+}$ after 20 min reaction time (top: complete spectrum, bottom: exerpt).

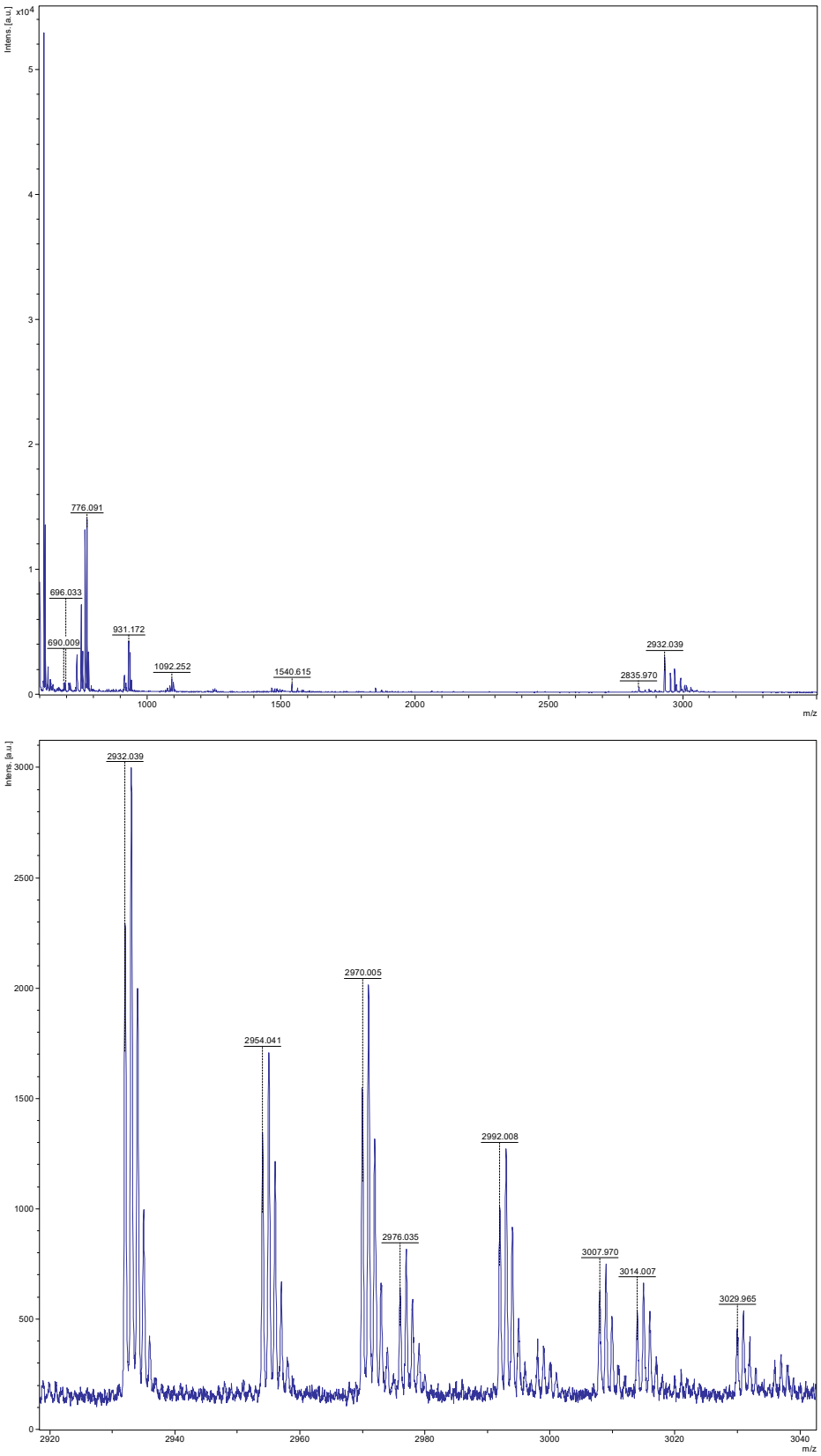

Figure 76: MALDI-MS trace of a reaction of **oligo1** with 4 equiv. of $[Fe^{IV}\mathbf{L1}(O)]^{2+}$ after 30 min reaction time (top: complete spectrum, bottom: exerpt).

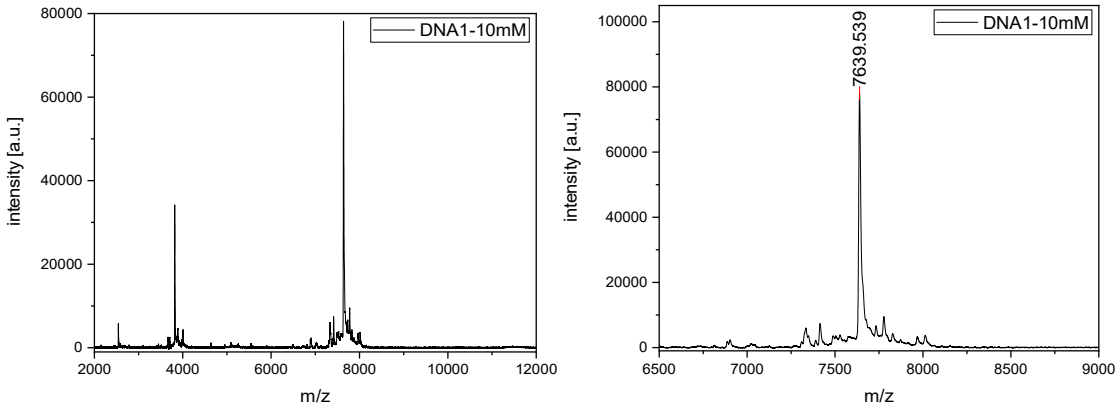

Figure 77: MALDI-MS trace (complete and detailed view) of untreated **DNA1** as reference sample. Conditions: [**DNA1**] = 10 mM, H_2O, 25 °C.

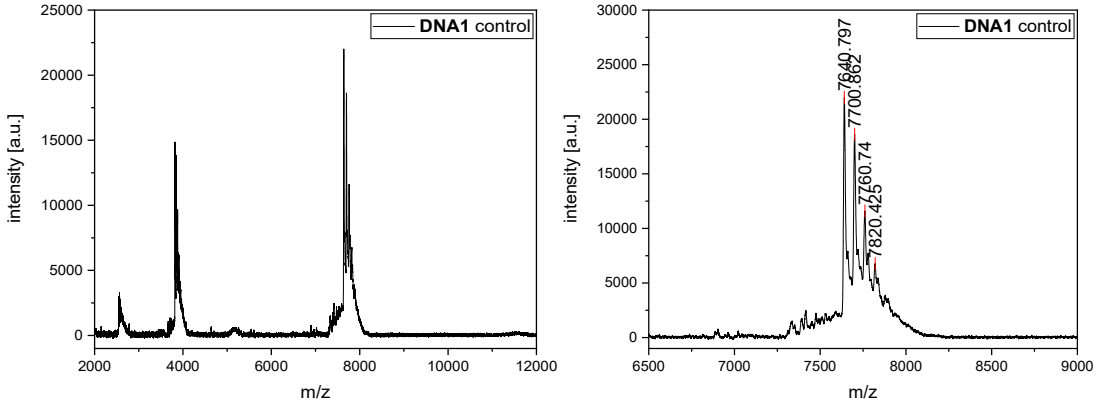

Figure 78: MALDI-MS trace (complete and detailed view) of a control measurement of **DNA1** treated as reaction sample with water instead of iron(IV)-oxido complex. Conditions: [**DNA1**] = 4.2 µM, H_2O, 25 °C.

8 Mößbauer Data

Table 27: Sum formula, oxidation state, assigned spin values as well as isomeric shift δ and quadrupole splitting ΔE_Q values for the iron complexes analysed by Mößbauer spectroscopy. Mößbauer data were aquired by Jan Kruse and Serhiy Demeshko (Meyer group, Göttingen).

Sum formula	Oxidation state	Spin S	δ [mm s^{-1}]	ΔE_Q [mm s^{-1}]
$[Fe^{II}$**L1**(mecn)$]^{2+}$	+ II	0	0.51	0.34
$[Fe^{III}$**L1**(OH)$]^{2+}$	+ III	½	0.24	1.57
$[Fe^{IV}$**L1**(O)$]^{2+}$	+ IV	1	0.07	0.80
$[Fe^{II}$**L2**(mecn)$]^{2+}$	+ II	0	0.52	0.38
$[Fe^{III}$**L2**(OH)$]^{2+}$	+ III	½	0.25	1.54
$[Fe^{IV}$**L2**(O)$]^{2+}$	+ IV	1	0.08	0.91
$[Fe^{II}$**L1**$(OH_2)]^{2+}$	+ II	0	0.56	0.36
$[Fe^{II}$**L3**(mecn)$]^{2+}$	+ II	0	0.53	0.37
$[Fe^{III}$**L2**(OH)$]^{2+}$ (after 33 d in H_2O)	+ II	0	0.57	0.35
	+ III	½	0.30	1.46
$[Fe^{III}$**L1**(OMe)$]^{2+}$	+ III	½	0.28	1.53
$[Fe^{II}$**L1**(MeOH)$]^{2+}$ (?)	+ II	0	0.52	0.34

9 Infrared Spectroscopy Data

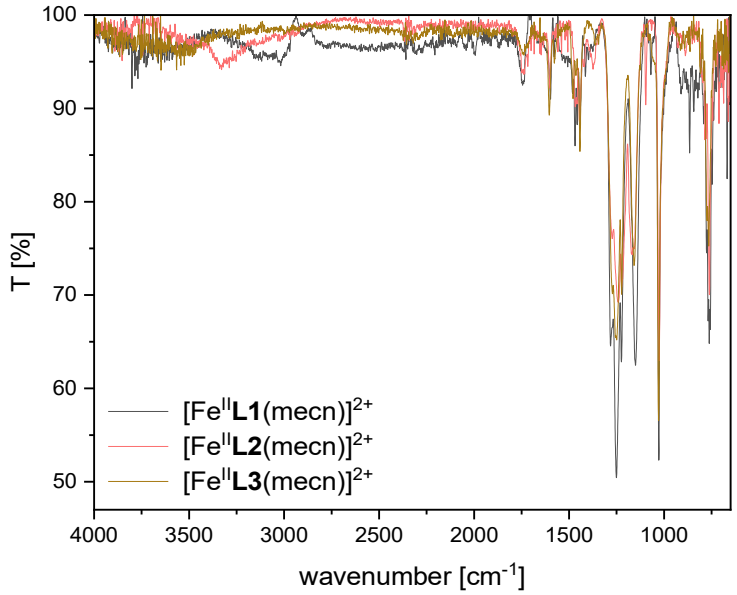

Figure 79: Full IR spectra of the complexes [Fe^{II}**L1**/**L2**/**L3**(mecn)](OTf)$_2$.

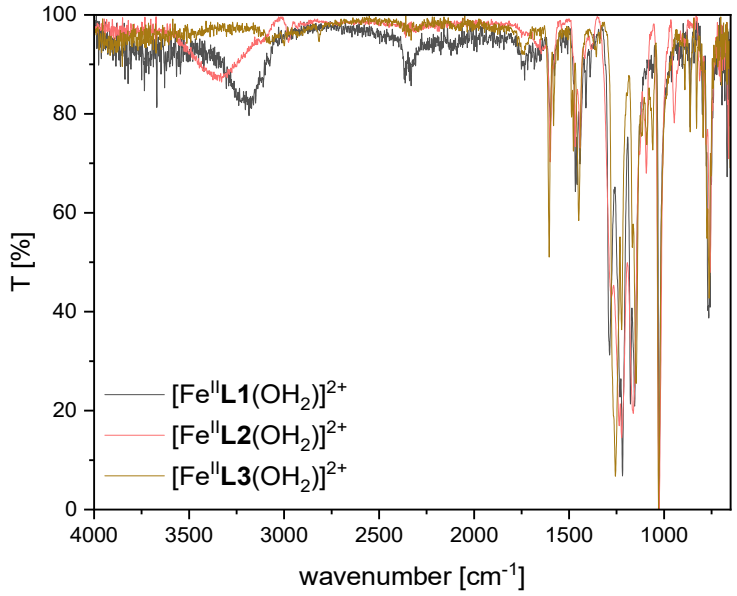

Figure 80: Full IR spectra of the complexes [Fe^{II}**L1**/**L2**/**L3**(OH$_2$)](OTf)$_2$.

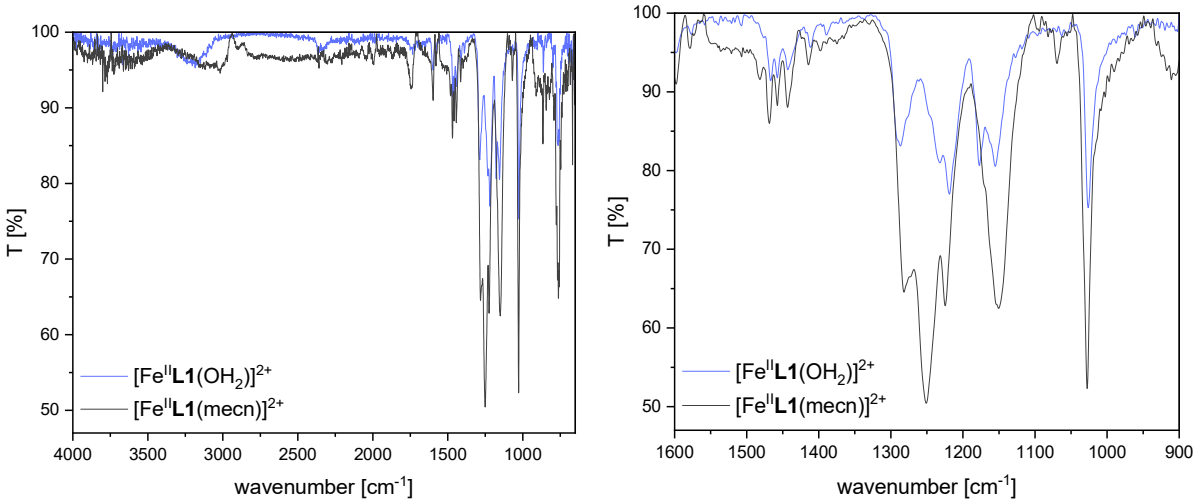

Figure 81: Full IR spectra (left) and detailed view (right) of the complexes and $[Fe^{II}\mathbf{L1}(mecn)](OTf)_2$ $[Fe^{II}\mathbf{L1}(OH_2)](OTf)_2$.

10 Cryo-HR-MS Data

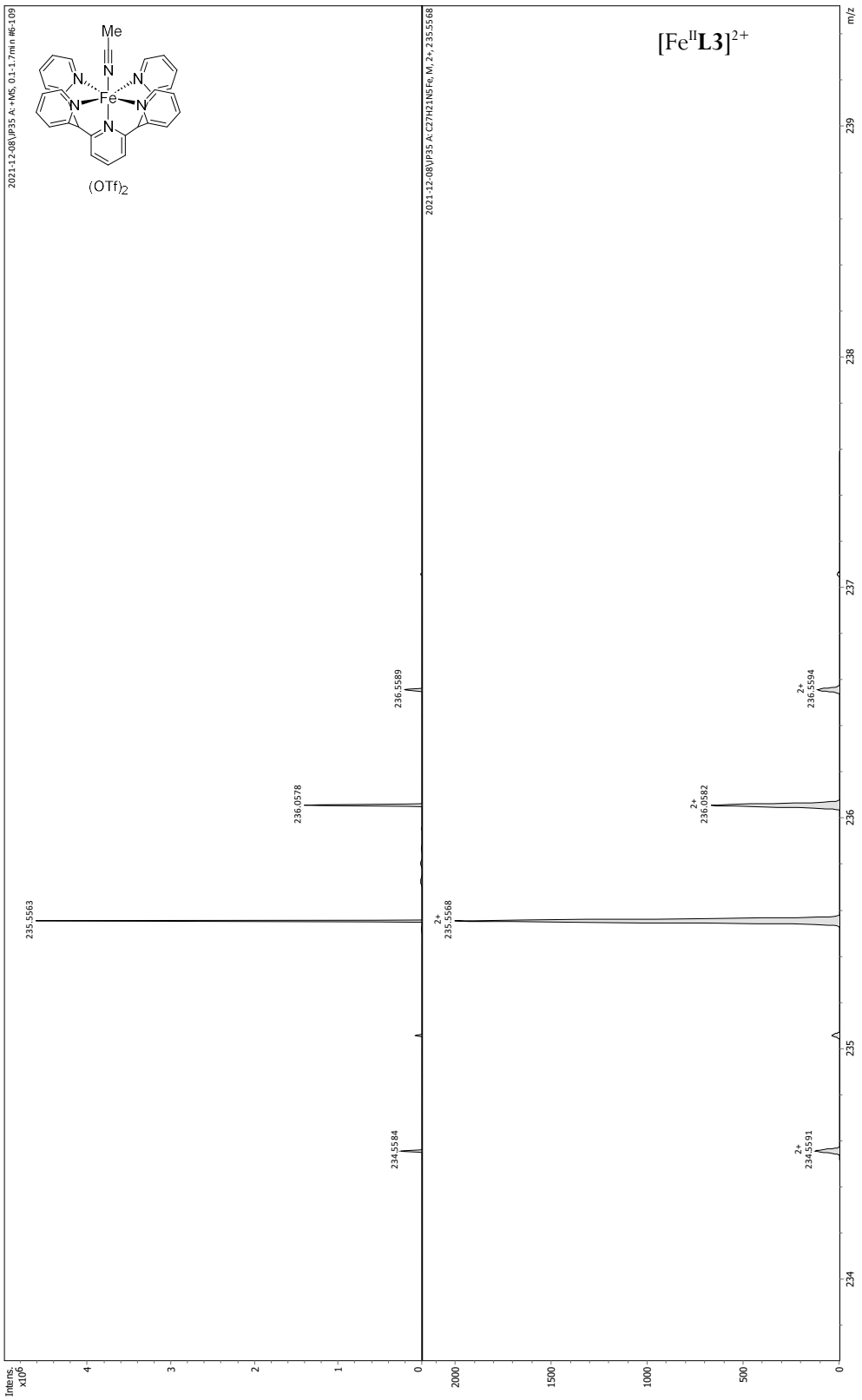

Figure 82: Experimentally obtained HR-MS spectrum of $[Fe^{II}\mathbf{L3}(mecn)](OTf)_2$ as well as simulated spectra. Measurements and simulations were performed by Laura Senft (Ivanović-Burmazović group, LMU Munich). Conditions: $[Fe^{II}] = 0.005$ mM, H_2O, 5 °C.

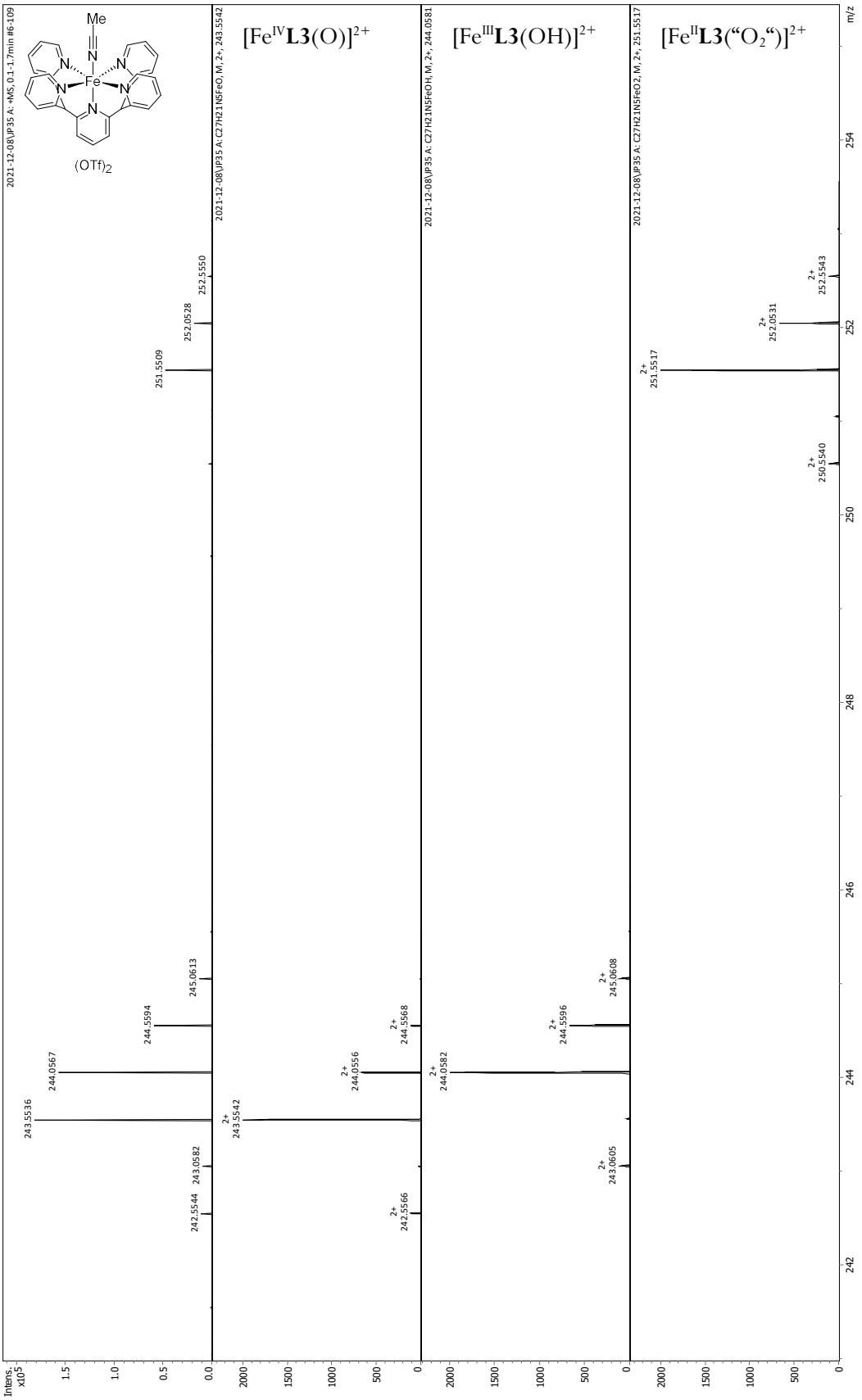

Figure 83: Experimentally obtained HR-MS spectrum of $[Fe^{II}\mathbf{L3}(mecn)](OTf)_2$ as well as simulated spectra. Measurements and simulations were performed by Laura Senft (Ivanović-Burmazović group, LMU Munich). Conditions: $[Fe^{II}] = 0.005$ mM, H_2O, 5 °C.

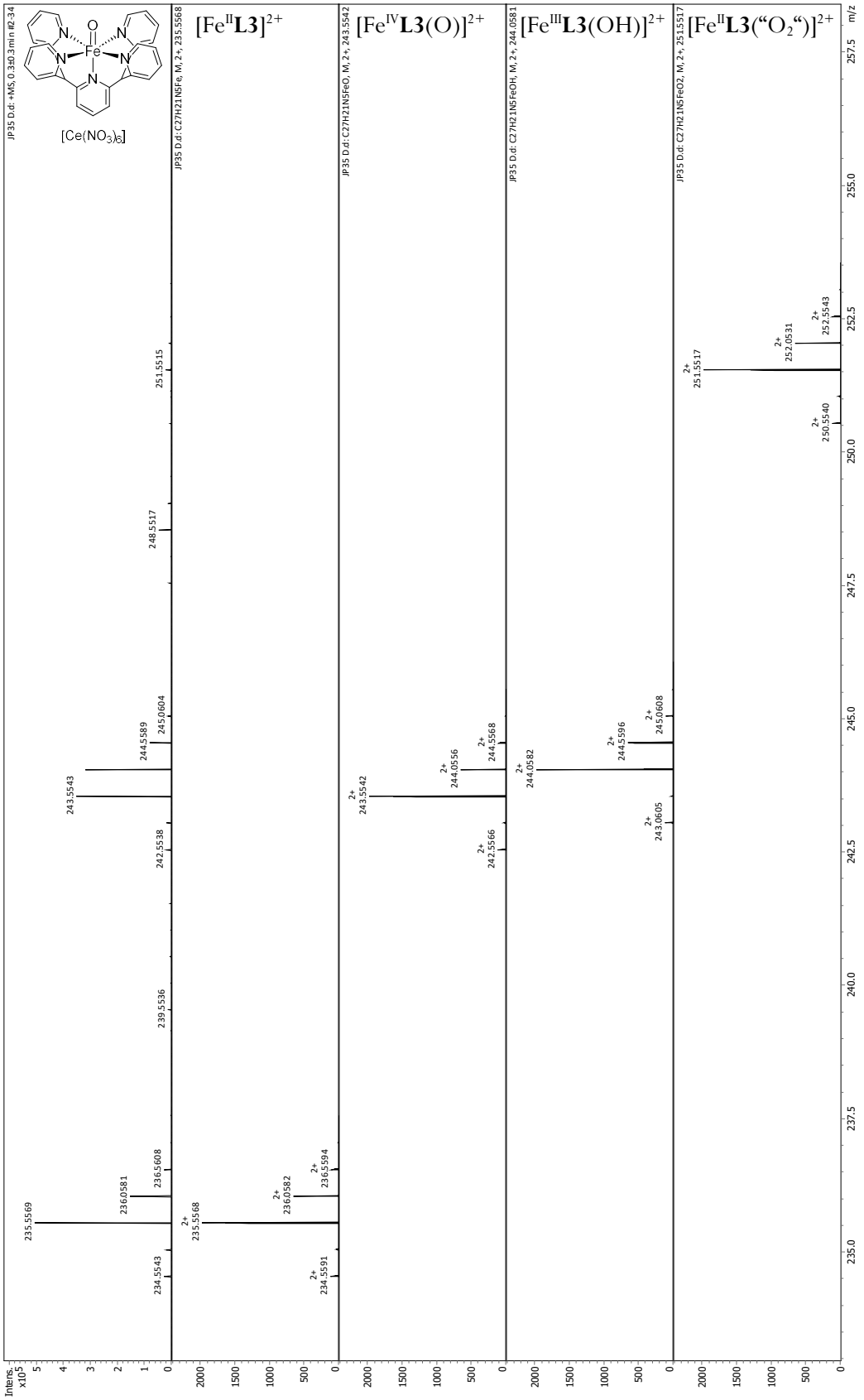

Figure 84: Experimentally obtained HR-MS spectrum of $[Fe^{IV}\mathbf{L3}(O)][Ce(NO_3)_6]$ as well as simulated spectra. Measurements and simulations were performed by Laura Senft (Ivanović-Burmazović group, LMU Munich). Conditions: $[Fe^{IV}=O]$ = 0.005 mM, H_2O, 5 °C.

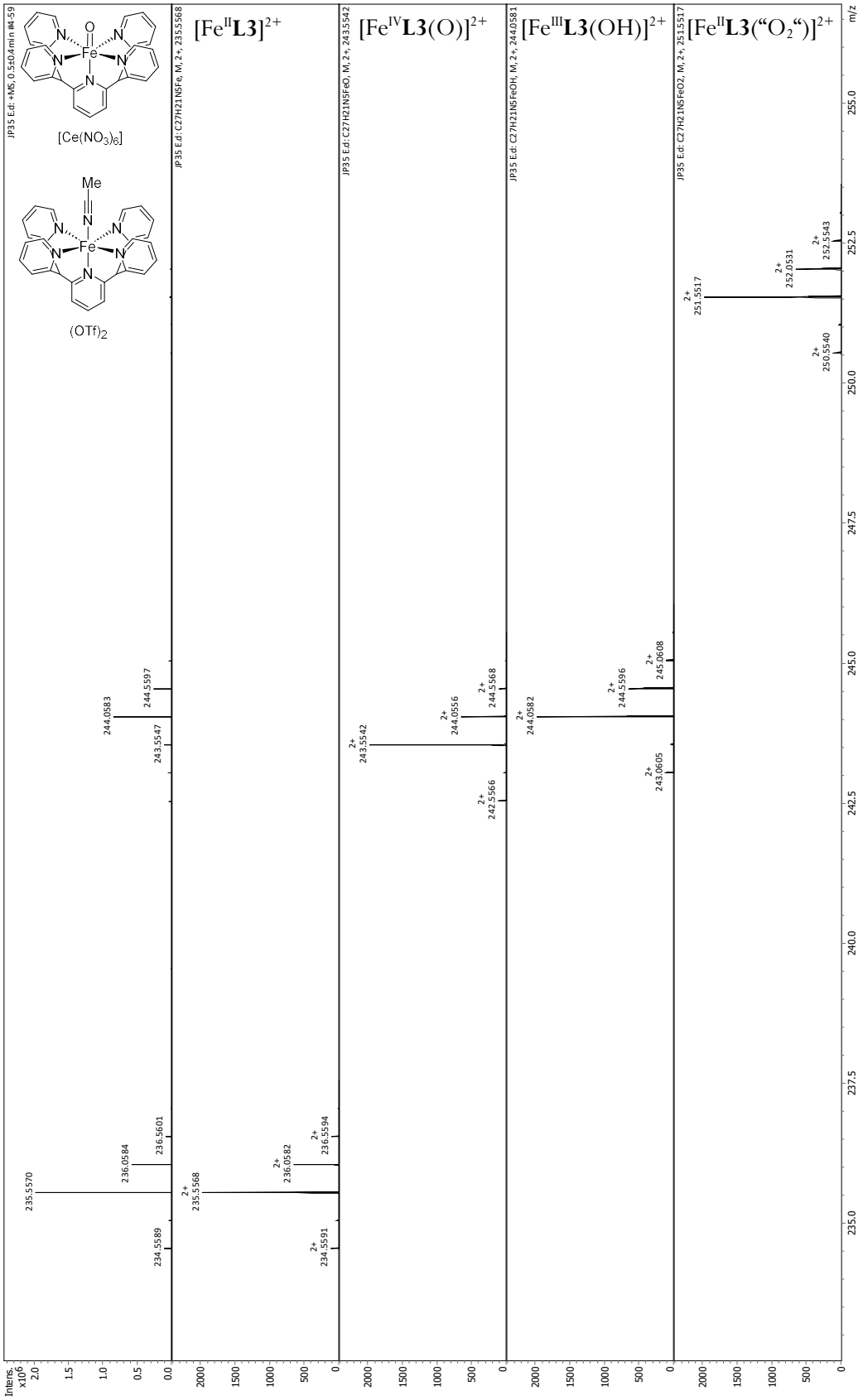

Figure 85: Experimentally obtained HR-MS spectrum of an equimolar mixture of $[Fe^{IV}\mathbf{L3}(O)][Ce(NO_3)_6]$ and $[Fe^{II}\mathbf{L3}(mecn)](OTf)_2$ as well as simulated spectra. Measurements and simulations were performed by Laura Senft (Ivanović-Burmazović group, LMU Munich). Conditions: $[Fe^{IV}{=}O] = [Fe^{II}] = 0.0025$ mM, H_2O, 5 °C.

11 Crystallographic Information

Table 28: Selected bond lengths in single crystals of complexes from this work as well as from the literature for comparison reasons. $Py_{eq.}$ = pyridines in the equatorial plane, $Py_{ax.}$ = axial pyridine. For values involving equatorial pyridines the average value is provided. The determined spin state is a) high spin and b) low spin. New complexes are highlighted in blue.

complex	**Fe-X_{ax}**	**Fe-N(Py_{eq})**	**Fe-N(Py_{ax})**
$[Fe^{II}$**L1**$(mecn)](OTf)_2$[a), [91, 201]]	1.94 Å (X: $NCCH_3$)	2.01 Å	1.97 Å
$[Fe^{II}$**L1**$(OH_2)](OTf)_2$[a)]	1.99 Å (X: OH_2)	2.00 Å	1.96 Å
$[Fe^{II}$**L1**$(OH_2)](BF_4)_2$[a), [91]]	2.01 Å (X: OH_2)	2.01 Å	1.95 Å
$[Fe^{II}$**L2**$(mecn)](OTf)_2$[a), [201]]	1.94 Å (X: $NCCH_3$)	2.01 Å	1.99 Å
$[Fe^{II}$**L3**$(mecn)](OTf)_2$[a)]	1.94 Å (X: $NCCH_3$)	2.01 Å	1.99 Å
$[Fe^{II}Py_5(OMe)_2(MeOH)](OTf)_2$[b), [236]]	2.04 Å (X: OHMe)	2.18 Å	2.10 Å
$[Fe^{III}$**L1**$(OH)](OTf)_2$[a), [201]]	1.79 Å (X: OH)	2.00 Å	2.03 Å
$[Fe^{III}$**L1**$(OMe)](OTf)_2$[a)]	1.80 Å (X: OMe)	2.02 Å	2.02 Å
$[Fe^{III}$**L2**$(OH)](OTf)_2$[a), [201]]	1.81 Å (X: OH)	2.01 Å	2.02 Å
$[Fe^{III}Py_5(OMe)_2(OMe)](OTf)_2$[b), [180]]	1.78 Å (X: OMe)	2.17 Å	2.15 Å
$[Fe^{IV}$**L1**$(O)][Ce(NO_3)_6$[a), [201, 246]]	1.66 Å (X: O)	2.00 Å	2.07 Å

Crystallographic details for **L3**

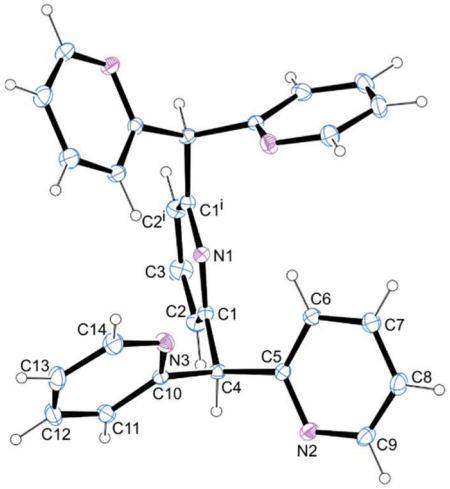

net formula	$C_{27}H_{21}N_5$
M_r/g mol^{-1}	415.49
crystal size/mm	0.100 × 0.070 × 0.050
T/K	173.(2)
radiation	MoKα
diffractometer	'Bruker D8 Venture TXS'
crystal system	monoclinic
space group	'C 1 2 1'
a/Å	15.9497(12)
b/Å	7.2580(5)
c/Å	12.1206(9)
α/°	90
β/°	130.848(2)
γ/°	90
V/Å^3	1061.38(14)
Z	2
calc. density/g cm^{-3}	1.300
μ/mm^{-1}	0.079
absorption correction	Multi-Scan
transmission factor range	0.92–1.00
refls. measured	7172
R_{int}	0.0234
mean σ(I)/I	0.0270
θ range	3.276–27.099
observed refls.	2241
x, y (weighting scheme)	0.0405, 0.3764
hydrogen refinement	constr

Flack parameter	0.5
refls in refinement	2319
parameters	146
restraints	1
$R(F_{obs})$	0.0330
$R_w(F^2)$	0.0838
S	1.068
shift/error$_{max}$	0.001
max electron density/e Å^{-3}	0.158
min electron density/e Å^{-3}	−0.149

Crystallographic details for [Fe^{II}**L3**(mecn)]$(OTf)_2$

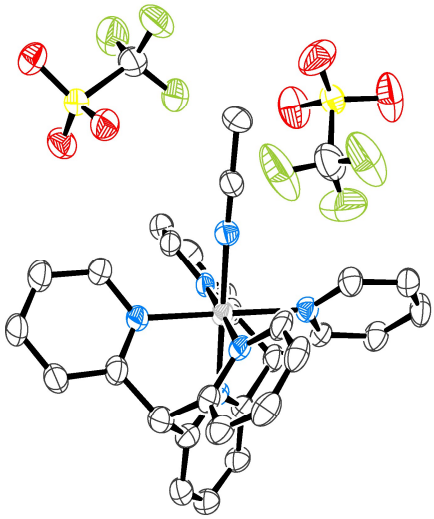

Identification code	6
Empirical formula	$C_{31}H_{24}N_6O_6F_6S_2Fe$
Formula weight	810.52
Temperature	298(2) K
Wavelength	0.71073 Å
Crystal system	Triclinic
Space group	P-1
Unit cell dimensions	a = 11.2105(5) Å a= 98.977(5)°.
	b = 14.5335(8) Å b= 100.271(4)°.
	c = 23.4129(13) Å g = 110.432(5)°.
Volume	3417.4(3) $Å^3$
Z	538976256
Density (calculated)	1.575 Mg/m^3
Absorption coefficient	0.649 mm^{-1}
F(000)	1648
Crystal size	0.30 x 0.18 x 0.18 mm3
Theta range for data collection	1.592 to 26.371°.
Index ranges -	13<=h<=14, -18<=k<=18, -29<=l<=29
Reflections collected	49482
Independent reflections	13957 [R(int) = 0.0857]
Completeness to theta = 25.242°	100.0 %
Absorption correction	Semi-empirical from equivalents
Max. and min. transmission	1.00000 and 0.82863
Refinement method	Full-matrix least-squares on F^2
Data / restraints / parameters	13957 / 0 / 939
Goodness-of-fit on F2	1.015

Final R indices [I>2sigma(I)]	R1 = 0.0928, wR2 = 0.2021
R indices (all data)	R1 = 0.1634, wR2 = 0.2464
Extinction coefficient	n/a
Largest diff. peak and hole	1.959 and -0.530 e.Å^{-3}

X-ray measurement and solution of the crystal structure was performed by Jonathan Gutenthaler-Tietze.

Crystallographic details for $[Fe^{II}\mathbf{L1}(OH_2)](OTf)_2$

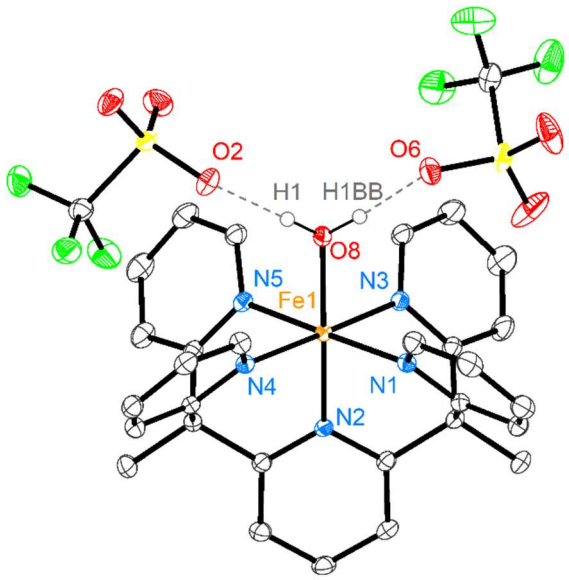

Identification code	rx290_a	
Empirical formula	$C_{31}H_{27}F_6FeN_5O_7S_2$	
Formula weight	815.54	
Temperature	243(2) K	
Wavelength	0.71073 Å	
Crystal system	Triclinic	
Space group	*P*–1	
Unit cell dimensions	a = 11.0250(4) Å	a= 82.533(2)°.
	b = 12.4310(3) Å	b= 88.484(2)°.
	c = 13.0782(3) Å	g = 66.295(3)°.
Volume	1626.59(9) Å^3	
Z	2	
Density (calculated)	1.665 Mg/m^3	
Absorption coefficient	0.684 mm^{-1}	
F(000)	832	
Crystal size	0.134 x 0.105 x 0.105 mm^3	
Theta range for data collection	2.018 to 30.508°.	
Index ranges	-15<=h<=15, -17<=k<=17, -18<=l<=18	
Reflections collected	33104	
Independent reflections	9933 [R(int) = 0.0299]	
Completeness to theta = 25.242°	99.9 %	
Absorption correction	Semi-empirical from equivalents	
Max. and min. transmission	1.00000 and 0.97282	
Refinement method	Full-matrix least-squares on F^2	

Data / restraints / parameters	9933 / 0 / 477
Goodness-of-fit on F^2	1.018
Final R indices [I>2sigma(I)]	R1 = 0.0356, wR2 = 0.0817
R indices (all data)	R1 = 0.0486, wR2 = 0.0876
Extinction coefficient	n/a
Largest diff. peak and hole	0.518 and -0.585 e.$Å^{-3}$

X-ray measurement and solution of the crystal structure was performed by Jonathan Gutenthaler-Tietze.

Crystallographic details for [Fe^{III}**L1**(OMe)](OTf)$_2$

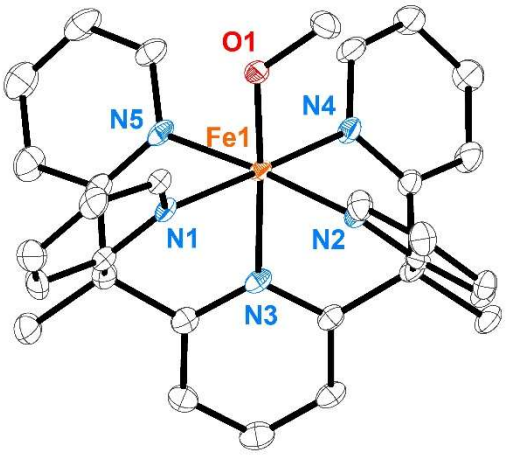

Identification code	rx313_a	
Empirical formula	$C_{32}H_{28}F_6FeN_5O_7S_2$	
Formula weight	828.56	
Temperature	223(2) K	
Wavelength	0.71073 Å	
Crystal system	Triclinic	
Space group	*P*–1	
Unit cell dimensions	a = 8.9242(2) Å	a= 115.323(4)°.
	b = 20.0762(10) Å	b= 94.428(3)°.
	c = 20.9540(9) Å	g = 94.247(3)°.
Volume	3359.4(3) $Å^3$	
Z	4	
Density (calculated)	1.638 Mg/m^3	
Absorption coefficient	0.664 mm^{-1}	
F(000)	1692	
Crystal size	0.170 x 0.062 x 0.030 mm^3	
Theta range for data collection	1.876 to 26.371°.	
Index ranges	-11<=h<=11, -25<=k<=25, -26<=l<=26	
Reflections collected	52479	
Independent reflections	13735 [R(int) = 0.0674]	
Completeness to theta = 25.242°	100.0 %	
Absorption correction	Semi-empirical from equivalents	
Max. and min. transmission	1.00000 and 0.88252	
Refinement method	Full-matrix least-squares on F^2	

Data / restraints / parameters	13735 / 0 / 961
Goodness-of-fit on F^2	1.023
Final R indices [I>2sigma(I)]	R1 = 0.0538, wR2 = 0.1153
R indices (all data)	R1 = 0.0922, wR2 = 0.1328
Extinction coefficient	n/a
Largest diff. peak and hole	0.907 and -0.459 e.$Å^{-3}$

X-ray measurement and solution of the crystal structure was performed by Jonathan Gutenthaler-Tietze.

12 Research Communication as Part of this Thesis

12.1 Publications

1) Niko S. W. Lindlar né Jonasson, Annika Menke, Laura Senft, Andrea Squarcina, David Schmidl, Katherine Fisher, Serhiy Demeshko, Jan C. Kruse, Thomas Josephy, Peter Mayer, Jonathan Gutenthaler-Tietze, Peter Comba, Franc Meyer, Ivana Ivanović-Burmazović, Lena J. Daumann* Two plus Four Equals Three – Iron(II)/Iron(IV) Comproportionation as an Additional Pathway For Iron(IV)-oxido Reactions, **2024**, *submitted to Inorg. Chem.*

2) David Schmidl, Niko S.W. Jonasson, Annika Menke, Sabine Schneider, Lena J. Daumann* Spectroscopic and *in vitro* Investigations of Fe^{2+}/α-Ketoglutarate-dependent Enzymes Involved in Nucleic Acid Repair and Modification, *ChemBioChem* **2022**, *23*, e202100605.

3) Niko S.W. Jonasson, Rachel Janßen, Annika Menke, Fabian L. Zott, Hendrik Zipse, Lena J. Daumann*, TET-like Oxidation in 5-Methylcytosine and Derivatives: A Computational and Experimental Study, *ChemBioChem* **2021**, *22*, 3333-3340.

cover article

4) Annika Menke, Romeo C.A. Dubini, Peter Mayer, Petra Rovó and Lena J. Daumann* Formation of Cisplatin Adducts with the Epigenetically-relevant Nucleobase 5-Methylcytosine, accepted, *Eur. J. Inorg. Chem.* **2020**.

VIP (very important paper), **cover article** and included in a special collection "metals in medicine"

This publication was not part of the thesis but developed in the same group. Last experiments as well as writing and review processes were accomplished during PhD time.[247]

5) H. Lumpe, A. Menke, C. Haisch, P. Mayer, A. Kabelitz, K. V. Yusenko, A. G. Buzanich, T. Block, R. Pöttgen, F. Emmerling, L. J. Daumann* The Earlier the Better: Structural Analysis and Separation of Lanthanides with Pyrroloquinoline Quinone *Chem. Eur. J.* **2020**, *26*, 10133-10139.

cover article and highlighted on different news sites: phys.org, miragenews.com, LMU

This publication was not part of the thesis but developed in the same group and presented in a conference during PhD time.[248]

12.2 Oral Presentations

1) Koordinationschemie-Treffen (KCT) Innsbruck, Februar 2024: *Two plus four equals three – iron(II)/iron(IV) comproportionation reactions and iron(IV)-oxido reactivity studies*.
2) Paris-Munich Epigenetics Symposium Munich, June 2023: *Modelling TET Enzyme Reactivity with Synthetic Iron(IV)-oxido Complexes and a Variety of Epigenetically Relevant Substrates*.
3) IRTG 1309 Journal Club, August 2020: *Synthetic Epigenetics – Pseudo and iso Methyl-Cytosine*.

12.3 Poster Presentations

1) Symposium on Advanced Biological Inorganic Chemistry (SABIC) Kolkata, January 2024: *Two plus four equals three – iron(II)/iron(IV) comproportionation reactions and iron(IV)-oxido reactivity studies*.

2) SFB conference Ettal, September 2023: *TET-Like Oxidation in 5-Methylcytosine and Derivatives: A Computational and Experimental Study*.
3) Koordinationschemie-Treffen (KCT) Jena, September 2022: *TET-Like Oxidation in 5-Methylcytosine and Derivatives: A Computational and Experimental Study*.
4) European Biologic Inorganic Chemistry Conference (EuroBIC) Grenoble, July 2022: *TET-Like Oxidation in 5-Methylcytosine and Derivatives: A Computational and Experimental Study*.
5) Koordinationschemie-Treffen (KCT) Freiburg, March 2020: *Cofactor Pyrroloquinoline Quinone Shows a Preferential Coordination for Early Lanthanides*.

VIII. REFERENCES

[1] J. D. Watson, F. H. Crick, *Nature* **1953**, *171*, 737-738.
[2] F. H. Crick, in *Symp Soc Exp Biol, Vol. 12*, **1958**, p. 8.
[3] F. Crick, *Nature* **1970**, *227*, 561-563.
[4] G. Felsenfeld, *Cold Spring Harb. perspect. biol.* **2014**, *6*, a018200.
[5] C. Dupont, D. R. Armant, C. A. Brenner, in *Seminars in reproductive medicine, Vol. 27*, © Thieme Medical Publishers, **2009**, pp. 351-357.
[6] S. L. Berger, T. Kouzarides, R. Shiekhattar, A. Shilatifard, *Genes Dev.* **2009**, *23*, 781-783.
[7] E. Niederberger, E. Resch, M. J. Parnham, G. Geisslinger, *Nat. Rev. Neurol.* **2017**, *13*, 434-447.
[8] C. R. Clapier, B. R. Cairns, *Annu. Rev. Biochem* **2009**, *78*, 273-304.
[9] E. J. Yoo, Y. K. Jang, M. A. Lee, P. Bjerling, J. B. Kim, K. Ekwall, R. H. Seong, S. Dai Park, *Biochem. Biophys. Res. Commun.* **2002**, *295*, 970-974.
[10] T. Jenuwein, C. D. Allis, *Science* **2001**, *293*, 1074-1080.
[11] D. Y. Lee, J. J. Hayes, D. Pruss, A. P. Wolffe, *Cell* **1993**, *72*, 73-84.
[12] B. D. Strahl, C. D. Allis, *Nature* **2000**, *403*, 41-45.
[13] A. Bird, *Nature* **2007**, *447*.
[14] T. Kouzarides, *Cell* **2007**, *128*, 693-705.
[15] T. Sexton, G. Cavalli, *Cell* **2015**, *160*, 1049-1059.
[16] A. Breiling, F. Lyko, *Epigenetics Chromatin* **2015**, *8*, 1-9.
[17] P. A. Jones, *Nat. Rev. Genet,* **2012**, *13*, 484-492.
[18] R. Lister, M. Pelizzola, R. H. Dowen, R. D. Hawkins, G. Hon, J. Tonti-Filippini, J. R. Nery, L. Lee, Z. Ye, Q.-M. Ngo, *nature* **2009**, *462*, 315-322.
[19] S. Feng, S. J. Cokus, X. Zhang, P.-Y. Chen, M. Bostick, M. G. Goll, J. Hetzel, J. Jain, S. H. Strauss, M. E. Halpern, *Proc. Natl. Acad. Sci.* **2010**, *107*, 8689-8694.
[20] A. Zemach, I. E. McDaniel, P. Silva, D. Zilberman, *Science* **2010**, *328*, 916-919.
[21] D. Schübeler, *Nature* **2015**, *517*, 321-326.
[22] Z. D. Smith, A. Meissner, *Nat. Rev. Genet,* **2013**, *14*, 204-220.
[23] T. Baubec, D. Schübeler, *Curr. Opin. Genet. Dev.* **2014**, *25*, 85-92.
[24] R. J. Klose, A. P. Bird, *Trends Biochem. Sci* **2006**, *31*, 89-97.
[25] R. M. Kohli, Y. Zhang, *Nature* **2013**, *502*, 472-479.
[26] A. Hofer, Z. J. Liu, S. Balasubramanian, *J. Am. Chem. Soc.* **2019**, *141*, 6420-6429.
[27] S. Ito, L. Shen, Q. Dai, S. C. Wu, L. B. Collins, J. A. Swenberg, C. He, Y. Zhang, *Science* **2011**, *333*, 1300-1303.
[28] S. Ito, A. C. D'Alessio, O. V. Taranova, K. Hong, L. C. Sowers, Y. Zhang, *Nature* **2010**, *466*, 1129-1133.
[29] T. Carell, M. Q. Kurz, M. Müller, M. Rossa, F. Spada, *Angew. Chem. Int. Ed.* **2018**, *57*, 4296-4312.
[30] Y. Feng, N.-B. Xie, W.-B. Tao, J.-H. Ding, X.-J. You, C.-J. Ma, X. Zhang, C. Yi, X. Zhou, B.-F. Yuan, *CCS Chem.* **2021**, *3*, 994-1008.
[31] N. Penn, R. Suwalski, C. O'riley, K. Bojanowski, R. Yura, *Biochem. J* **1972**, *126*, 781-790.
[32] S. Kriaucionis, N. Heintz, *Science* **2009**, *324*, 929-930.
[33] G. Ficz, M. R. Branco, S. Seisenberger, F. Santos, F. Krueger, T. A. Hore, C. J. Marques, S. Andrews, W. Reik, *Nature* **2011**, *473*, 398-402.

[34] C. G. Spruijt, F. Gnerlich, A. H. Smits, T. Pfaffeneder, P. W. Jansen, C. Bauer, M. Münzel, M. Wagner, M. Müller, F. Khan, *Cell* **2013**, *152*, 1146-1159.
[35] O. Yildirim, R. Li, J.-H. Hung, P. B. Chen, X. Dong, L.-S. Ee, Z. Weng, O. J. Rando, T. G. Fazzio, *Cell* **2011**, *147*, 1498-1510.
[36] M. Mellén, P. Ayata, S. Dewell, S. Kriaucionis, N. Heintz, *Cell* **2012**, *151*, 1417-1430.
[37] M. Iurlaro, G. Ficz, D. Oxley, E.-A. Raiber, M. Bachman, M. J. Booth, S. Andrews, S. Balasubramanian, W. Reik, *Genome Biol.* **2013**, *14*, 1-11.
[38] T. Pfaffeneder, F. Spada, M. Wagner, C. Brandmayr, S. K. Laube, D. Eisen, M. Truss, J. Steinbacher, B. Hackner, O. Kotljarova, *Nat. Chem. Biol.* **2014**, *10*, 574-581.
[39] S. Cortellino, J. Xu, M. Sannai, R. Moore, E. Caretti, A. Cigliano, M. Le Coz, K. Devarajan, A. Wessels, D. Soprano, *Cell* **2011**, *146*, 67-79.
[40] Y.-F. He, B.-Z. Li, Z. Li, P. Liu, Y. Wang, Q. Tang, J. Ding, Y. Jia, Z. Chen, L. Li, *Science* **2011**, *333*, 1303-1307.
[41] L. Zhang, W. Chen, L. M. Iyer, J. Hu, G. Wang, Y. Fu, M. Yu, Q. Dai, L. Aravind, C. He, *J. Am. Chem. Soc.* **2014**, *136*, 4801-4804.
[42] D. Schmidl, N. S. Lindlar né Jonasson, A. Menke, S. Schneider, L. J. Daumann, *ChemBioChem* **2022**, *23*, e202100605.
[43] R. H. Holm, P. Kennepohl, E. I. Solomon, *Chem. Rev.* **1996**, *96*, 2239-2314.
[44] C. E. Valdez, Q. A. Smith, M. R. Nechay, A. N. Alexandrova, *Acc. Chem. Res.* **2014**, *47*, 3110-3117.
[45] T. D. Bugg, *Tetrahedron* **2003**, *59*, 7075-7101.
[46] L. Que Jr, R. Y. Ho, *Chem. Rev.* **1996**, *96*, 2607-2624.
[47] M. Sono, M. P. Roach, E. D. Coulter, J. H. Dawson, *Chem. Rev.* **1996**, *96*, 2841-2888.
[48] S. Shima, R. K. Thauer, *Chem. Rec.* **2007**, *7*, 37-46.
[49] C. Zirngibl, R. Hedderich, R. Thauer, *FEBS Lett.* **1990**, *261*, 112-116.
[50] J. W. Peters, W. N. Lanzilotta, B. J. Lemon, L. C. Seefeldt, *Science* **1998**, *282*, 1853-1858.
[51] S. Albracht, E.-G. Graf, R. Thauer, *FEBS Lett.* **1982**, *140*, 311-313.
[52] C. Leblanc, H. Vilter, J.-B. Fournier, L. Delage, P. Potin, E. Rebuffet, G. Michel, P. Solari, M. Feiters, M. Czjzek, *Coord. Chem. Rev.* **2015**, *301*, 134-146.
[53] E. De Boer, Y. Van Kooyk, M. Tromp, H. Plat, R. Wever, *Biochim. Biophys. Acta, Protein Struct. Mol. Enzymol.* **1986**, *869*, 48-53.
[54] X. Engelmann, I. Monte-Pérez, K. Ray, *Angew. Chem. Int. Ed.* **2016**, *55*, 7632-7649.
[55] K. Ray, F. F. Pfaff, B. Wang, W. Nam, *J. Am. Chem. Soc.* **2014**, *136*, 13942-13958.
[56] T. M. Makris, K. von Koenig, I. Schlichting, S. G. Sligar, *J. Inorg. Biochem.* **2006**, *100*, 507-518.
[57] I. G. Denisov, T. M. Makris, S. G. Sligar, I. Schlichting, *Chem. Rev.* **2005**, *105*, 2253-2278.
[58] E. G. Kovaleva, J. D. Lipscomb, *Nat. Chem. Biol.* **2008**, *4*, 186-193.
[59] A. Karlsson, J. V. Parales, R. E. Parales, D. T. Gibson, H. Eklund, S. Ramaswamy, *Science* **2003**, *299*, 1039-1042.
[60] D. T. Gibson, *Science* **1968**, *161*, 1093-1097.
[61] J. Chen, W. Song, Y.-M. Lee, W. Nam, B. Wang, *Coord. Chem. Rev.* **2023**, *477*, 214945.
[62] M. Szaleniec, A. M. Wojtkiewicz, R. Bernhardt, T. Borowski, M. Donova, *Appl. Microbiol. Biotechnol.* **2018**, *102*, 8153-8171.
[63] H. Hanauske-Abel, V. Günzler, *J. Theor. Biol.* **1982**, *94*, 421-455.
[64] J. C. Price, E. W. Barr, T. E. Glass, C. Krebs, J. M. Bollinger, *J. Am. Chem. Soc.* **2003**, *125*, 13008-13009.

[65] D. A. Proshlyakov, T. F. Henshaw, G. R. Monterosso, M. J. Ryle, R. P. Hausinger, *J. Am. Chem. Soc.* **2004**, *126*, 1022-1023.
[66] J. M. Bollinger Jr, J. C. Price, L. M. Hoffart, E. W. Barr, C. Krebs, *Eur. J. Inorg. Chem.* **2005**, *2005*, 4245-4254.
[67] S.-K. Lee, J. C. Nesheim, J. D. Lipscomb, *J. Biol. Chem.* **1993**, *268*, 21569-21577.
[68] S. K. Lee, B. G. Fox, W. A. Froland, J. D. Lipscomb, E. Munck, *J. Am. Chem. Soc.* **1993**, *115*, 6450-6451.
[69] R. Banerjee, Y. Proshlyakov, J. D. Lipscomb, D. A. Proshlyakov, *Nature* **2015**, *518*, 431-434.
[70] R. Banerjee, J. C. Jones, J. D. Lipscomb, *Annu. Rev. Biochem* **2019**, *88*, 409-431.
[71] C. E. Tinberg, S. J. Lippard, *Acc. Chem. Res.* **2011**, *44*, 280-288.
[72] J.-U. Rohde, J.-H. In, M. H. Lim, W. W. Brennessel, M. R. Bukowski, A. Stubna, E. Münck, W. Nam, L. Que Jr, *Science* **2003**, *299*, 1037-1039.
[73] M. R. Bukowski, K. D. Koehntop, A. Stubna, E. L. Bominaar, J. A. Halfen, E. Münck, W. Nam, L. Que Jr, *Science* **2005**, *310*, 1000-1002.
[74] Y. M. Lee, S. N. Dhuri, S. C. Sawant, J. Cho, M. Kubo, T. Ogura, S. Fukuzumi, W. Nam, *Angew. Chem. Int. Ed.* **2009**, *48*, 1803-1806.
[75] J. England, Y. Guo, K. M. Van Heuvelen, M. A. Cranswick, G. T. Rohde, E. L. Bominaar, E. Münck, L. Que Jr, *J. Am. Chem. Soc.* **2011**, *133*, 11880-11883.
[76] J. P. Bigi, W. H. Harman, B. Lassalle-Kaiser, D. M. Robles, T. A. Stich, J. Yano, R. D. Britt, C. J. Chang, *J. Am. Chem. Soc.* **2012**, *134*, 1536-1542.
[77] S. Meyer, I. Klawitter, S. Demeshko, E. Bill, F. Meyer, *Angew. Chem.* **2013**, *125*, 935-939.
[78] M. A. Dedushko, M. B. Greiner, A. N. Downing, M. Coggins, J. A. Kovacs, *J. Am. Chem. Soc.* **2022**, *144*, 8515-8528.
[79] S. Munshi, A. Sinha, S. Yiga, S. Banerjee, R. Singh, M. K. Hossain, M. Haukka, A. F. Valiati, R. D. Huelsmann, E. Martendal, R. Peralta, F. Xavier, O. F. Wendt, T. K. Paine, E. Nordlander, *Dalton Trans.* **2022**, *51*, 870-884.
[80] P. Comba, G. Nunn, F. Scherz, P. H. Walton, *Faraday Discuss.* **2022**, *234*, 232-244.
[81] S. Chatterjee, T. K. Paine, *Acc. Chem. Res.* **2023**, *56*, 3175-3187.
[82] J. T. Groves, T. E. Nemo, R. S. Myers, *J. Am. Chem. Soc.* **1979**, *101*, 1032-1033.
[83] D. C. Lacy, R. Gupta, K. L. Stone, J. Greaves, J. W. Ziller, M. P. Hendrich, A. Borovik, *J. Am. Chem. Soc.* **2010**, *132*, 12188-12190.
[84] S. A. Wilson, J. Chen, S. Hong, Y.-M. Lee, M. Clémancey, R. Garcia-Serres, T. Nomura, T. Ogura, J.-M. Latour, B. Hedman, *J. Am. Chem. Soc.* **2012**, *134*, 11791-11806.
[85] A. C. I. Prat, T. Corona, T. Parella, X. Ribas and M. Costas,, *Inorg. Chem.* **2013**, *52*, 9229.
[86] J. Kaizer, E. J. Klinker, N. Y. Oh, J.-U. Rohde, W. J. Song, A. Stubna, J. Kim, E. Münck, W. Nam, L. Que, *J. Am. Chem. Soc.* **2004**, *126*, 472-473.
[87] O. Pestovsky, S. Stoian, E. L. Bominaar, X. Shan, E. Münck, L. Que Jr, A. Bakac, *Angew. Chem. Int. Ed.* **2005**, *44*, 6871-6874.
[88] L. Que Jr, M. Puri, *Bull. Jpn. Soc. Coord. Chem.* **2016**, *67*, 10-18.
[89] A. N. Biswas, M. Puri, K. K. Meier, W. N. Oloo, G. T. Rohde, E. L. Bominaar, E. Münck, L. Que Jr, *J. Am. Chem. Soc.* **2015**, *137*, 2428-2431.
[90] Y. Li, R. Singh, A. Sinha, G. C. Lisensky, M. Haukka, J. Nilsson, S. Yiga, S. Demeshko, S. J. Gross, S. Dechert, *Inorg. Chem.* **2023**, *62*, 18338-18356.
[91] T. Chantarojsiri, Y. Sun, J. R. Long, C. J. Chang, *Inorg. Chem.* **2015**, *54*, 5879-5887.
[92] D. Kass, T. Corona, K. Warm, B. Braun-Cula, U. Kuhlmann, E. Bill, S. Mebs, M. Swart, H. Dau, M. Haumann, *J. Am. Chem. Soc.* **2020**, *142*, 5924-5928.

[93] W. Zhu, N. Sharma, Y.-M. Lee, M. E. El-Khouly, S. Fukuzumi, W. Nam, *Inorg. Chem.* **2023**, *62*, 4116-4123.
[94] N. S. Jonasson, L. J. Daumann, *Chem. Eur. J.* **2019**, *25*, 12091-12097.
[95] L. Hu, J. Lu, J. Cheng, Q. Rao, Z. Li, H. Hou, Z. Lou, L. Zhang, W. Li, W. Gong, *Nature* **2015**, *527*, 118-122.
[96] D. Schmidl, N. S. Jonasson, E. Korytiaková, T. Carell, L. J. Daumann, *Angew. Chem. Int. Ed.* **2021**, *60*, 21457-21463.
[97] D. Palit, S. Kundu, P. K. Pain, R. Sarma, D. Manna, *Inorg. Chem.* **2023**.
[98] T. J. Collins, R. D. Powell, C. Slebodnick, E. S. Uffelman, *J. Am. Chem. Soc.* **1991**, *113*, 8419-8425.
[99] G. R. Warner, M. R. Mills, C. Enslin, S. Pattanayak, C. Panda, T. K. Panda, S. S. Gupta, A. D. Ryabov, T. J. Collins, *Chem. Eur. J.* **2015**, *21*, 6226-6233.
[100] J. Shendure, S. Balasubramanian, G. M. Church, W. Gilbert, J. Rogers, J. A. Schloss, R. H. Waterston, *Nature* **2017**, *550*, 345-353.
[101] T. Hu, N. Chitnis, D. Monos, A. Dinh, *Hum. Immunol.* **2021**, *82*, 801-811.
[102] T. Wang, C. E. Loo, R. M. Kohli, *Mol. Metab.* **2022**, *57*, 101314.
[103] J. C. Venter, M. D. Adams, E. W. Myers, P. W. Li, R. J. Mural, G. G. Sutton, H. O. Smith, M. Yandell, C. A. Evans, R. A. Holt, *science* **2001**, *291*, 1304-1351.
[104] S. Nurk, S. Koren, A. Rhie, M. Rautiainen, A. V. Bzikadze, A. Mikheenko, M. R. Vollger, N. Altemose, L. Uralsky, A. Gershman, *Science* **2022**, *376*, 44-53.
[105] F. Sanger, A. R. Coulson, *J. Mol. Biol.* **1975**, *94*, 441-448.
[106] F. Sanger, S. Nicklen, A. R. Coulson, *Proc. Natl. Acad. Sci.* **1977**, *74*, 5463-5467.
[107] K. V. Voelkerding, S. A. Dames, J. D. Durtschi, *Clin. Chem.* **2009**, *55*, 641-658.
[108] M. Frommer, L. E. McDonald, D. S. Millar, C. M. Collis, F. Watt, G. W. Grigg, P. L. Molloy, C. L. Paul, *Proc. Natl. Acad. Sci.* **1992**, *89*, 1827-1831.
[109] M. J. Booth, T. W. Ost, D. Beraldi, N. M. Bell, M. R. Branco, W. Reik, S. Balasubramanian, *Nat. Protoc.* **2013**, *8*, 1841-1851.
[110] M. Yu, G. C. Hon, K. E. Szulwach, C.-X. Song, P. Jin, B. Ren, C. He, *Nat. Protoc.* **2012**, *7*, 2159-2170.
[111] R. Vaisvila, V. C. Ponnaluri, Z. Sun, B. W. Langhorst, L. Saleh, S. Guan, N. Dai, M. A. Campbell, B. S. Sexton, K. Marks, *Genome Res.* **2021**, *31*, 1280-1289.
[112] D. Deamer, M. Akeson, D. Branton, *Nat. Biotechnol.* **2016**, *34*, 518-524.
[113] J. Eid, A. Fehr, J. Gray, K. Luong, J. Lyle, G. Otto, P. Peluso, D. Rank, P. Baybayan, B. Bettman, *Science* **2009**, *323*, 133-138.
[114] H. Wu, Y. Zhang, *Cell* **2014**, *156*, 45-68.
[115] S. Ardui, A. Ameur, J. R. Vermeesch, M. S. Hestand, *Nucleic Acids Res.* **2018**, *46*, 2159-2168.
[116] M. Jain, H. E. Olsen, B. Paten, M. Akeson, *Genome Biol.* **2016**, *17*, 1-11.
[117] G. Hu, A. Katuwawala, K. Wang, Z. Wu, S. Ghadermarzi, J. Gao, L. Kurgan, *Nat. Commun.* **2021**, *12*, 4438.
[118] Y. Liu, P. Siejka-Zielińska, G. Velikova, Y. Bi, F. Yuan, M. Tomkova, C. Bai, L. Chen, B. Schuster-Böckler, C.-X. Song, *Nat. Biotechnol.* **2019**, *37*, 424-429.
[119] N. S. Jonasson, R. Janßen, A. Menke, F. L. Zott, H. Zipse, L. J. Daumann, *ChemBioChem* **2021**, *22*, 3333-3340.
[120] S.-i. Nakano, M. Fujimoto, H. Hara, N. Sugimoto, *Nucleic Acids Res.* **1999**, *27*, 2957-2965.
[121] C. Beckman, *RNAClean XP, In Vitro Produced RNA and cDNA Purification, Instruction for Use, PN: C63085AA* **2020**.
[122] A. Eschenmoser, *Angew. Chem. Int. Ed.* **2011**, *50*, 12412-12472.
[123] Z. Huang, K. C. Schneider, S. A. Benner, *J. Org. Chem.* **1991**, *56*, 3869-3882.

[124] P. Nie, Y. Bai, H. Mei, *Molecules* **2020**, *25*, 3483.
[125] P. Sandin, L. M. Wilhelmsson, P. Lincoln, V. E. Powers, T. Brown, B. Albinsson, *Nucleic Acids Res.* **2005**, *33*, 5019-5025.
[126] I. S. Hong, M. M. Greenberg, *J. Am. Chem. Soc.* **2005**, *127*, 3692-3693.
[127] G. H. Clever, C. Kaul, T. Carell, *Angew. Chem. Int. Ed.* **2007**, *46*, 6226-6236.
[128] N. J. Leonard, A. G. Morrice, M. A. Sprecker, *J. Org. Chem.* **1975**, *40*, 356-363.
[129] H. Liu, J. Gao, S. R. Lynch, Y. D. Saito, L. Maynard, E. T. Kool, *Science* **2003**, *302*, 868-871.
[130] H. Liu, J. Gao, E. T. Kool, *J. Am. Chem. Soc.* **2005**, *127*, 1396-1402.
[131] J. Gao, H. Liu, E. T. Kool, *J. Am. Chem. Soc.* **2004**, *126*, 11826-11831.
[132] N. J. Leonard, M. A. Sprecker, A. G. Morrice, *J. Am. Chem. Soc.* **1976**, *98*, 3987-3994.
[133] F. Godde, J.-J. Toulmé, S. Moreau, *Biochem.* **1998**, *37*, 13765-13775.
[134] A. T. Krueger, E. T. Kool, *J. Am. Chem. Soc.* **2008**, *130*, 3989-3999.
[135] D. A. Malyshev, Y. J. Seo, P. Ordoukhanian, F. E. Romesberg, *J. Am. Chem. Soc.* **2009**, *131*, 14620-14621.
[136] C. Switzer, S. E. Moroney, S. A. Benner, *J. Am. Chem. Soc.* **1989**, *111*, 8322-8323.
[137] Y. Zhang, J. L. Ptacin, E. C. Fischer, H. R. Aerni, C. E. Caffaro, K. San Jose, A. W. Feldman, C. R. Turner, F. E. Romesberg, *Nature* **2017**, *551*, 644-647.
[138] E. C. Fischer, K. Hashimoto, Y. Zhang, A. W. Feldman, V. T. Dien, R. J. Karadeema, R. Adhikary, M. P. Ledbetter, R. Krishnamurthy, F. E. Romesberg, *Nat. Chem. Biol.* **2020**, *16*, 570-576.
[139] J. A. Piccirilli, S. A. Benner, T. Krauch, S. E. Moroney, S. A. Benner, *Nature* **1990**, *343*, 33-37.
[140] S. C. Johnson, C. B. Sherrill, D. J. Marshall, M. J. Moser, J. R. Prudent, *Nucleic Acids Res.* **2004**, *32*, 1937-1941.
[141] P. Ball, *Nature* **2004**, *431*, 624-627.
[142] W. W. Gibbs, *Sci. Am.* **2004**, *290*, 74-81.
[143] L. Organick, S. D. Ang, Y.-J. Chen, R. Lopez, S. Yekhanin, K. Makarychev, M. Z. Racz, G. Kamath, P. Gopalan, B. Nguyen, *Nat. Biotechnol.* **2018**, *36*, 242-248.
[144] L. Ceze, J. Nivala, K. Strauss, *Nat. Rev. Genet,* **2019**, *20*, 456-466.
[145] L. C. Meiser, B. H. Nguyen, Y.-J. Chen, J. Nivala, K. Strauss, L. Ceze, R. N. Grass, *Nat. Commun.* **2022**, *13*, 352.
[146] J. Bain, C. Switzer, R. Chamberlin, S. A. Benner, *Nature* **1992**, *356*, 537-539.
[147] C. Yu, A. A. Henry, F. E. Romesberg, P. G. Schultz, *Angew. Chem.* **2002**, *114*, 3997-4000.
[148] S. Hoshika, N. A. Leal, M.-J. Kim, M.-S. Kim, N. B. Karalkar, H.-J. Kim, A. M. Bates, N. E. Watkins Jr, H. A. SantaLucia, A. J. Meyer, S. DasGupta, J. A. Piccirilli, A. D. Ellington, J. SantaLucia Jr, M. M. Georgiadis, S. A. Benner, *Science* **2019**, *363*, 884-887.
[149] C. Mayer, G. R. McInroy, P. Murat, P. Van Delft, S. Balasubramanian, *Angew. Chem. Int. Ed.* **2016**, *55*, 11144-11148.
[150] P. Stoss, E. Kaes, G. Eibel, U. Thewalt, *J. Heterocycl. Chem.* **1991**, *28*, 231-236.
[151] J. P. Patel, M. L. Sowers, J. L. Herring, J. A. Theruvathu, M. R. Emmett, B. E. Hawkins, K. Zhang, D. S. DeWitt, D. S. Prough, L. C. Sowers, *Chem. Res. Toxicol.* **2015**, *28*, 2352-2363.
[152] B. Steigenberger, S. Schiesser, B. Hackner, C. Brandmayr, S. K. Laube, J. Steinbacher, T. Pfaffeneder, T. Carell, *Org. Lett.* **2013**, *15*, 366-369.
[153] D. Schmidl, Ludwig-Maximilians University (Munich), **2020**.
[154] J. C. Price, E. W. Barr, B. Tirupati, J. M. Bollinger, C. Krebs, *Biochem.* **2003**, *42*, 7497-7508.

[155] S. Sinnecker, N. Svensen, E. W. Barr, S. Ye, J. M. Bollinger Jr, F. Neese, C. Krebs, *J. Am. Chem. Soc.* **2007**, *129*, 6168-6179.
[156] L. Hu, Z. Li, J. Cheng, Q. Rao, W. Gong, M. Liu, Y. G. Shi, J. Zhu, P. Wang, Y. Xu, *Cell* **2013**, *155*, 1545-1555.
[157] J. Lu, L. Hu, J. Cheng, D. Fang, C. Wang, K. Yu, H. Jiang, Q. Cui, Y. Xu, C. Luo, *Phys. Chem. Chem. Phys.* **2016**, *18*, 4728-4738.
[158] T. Pfaffeneder, B. Hackner, M. Truß, M. Münzel, M. Müller, C. A. Deiml, C. Hagemeier, T. Carell, *Angew. Chem. Int. Ed.* **2011**, *50*, 7008.
[159] M. Tahiliani, K. P. Koh, Y. Shen, W. A. Pastor, H. Bandukwala, Y. Brudno, S. Agarwal, L. M. Iyer, D. R. Liu, L. Aravind, *Science* **2009**, *324*, 930-935.
[160] R. C. Dubini, A. Schön, M. Müller, T. Carell, P. Rovo, *Nucleic Acids Res.* **2020**, *48*, 8796-8807.
[161] F. L. Zott, V. Korotenko, H. Zipse, *ChemBioChem* **2022**, *23*, e202100651.
[162] A. Schön, E. Kaminska, F. Schelter, E. Ponkkonen, E. Korytiaková, S. Schiffers, T. Carell, *Angew. Chem. Int. Ed.* **2020**, *59*, 5591-5594.
[163] F. L. Zott, H. Zipse, *unpublished results* **2024**.
[164] R. H. Hudson, Y. Liu, F. Wojciechowski, *Can. J. Chem.* **2007**, *85*, 302-312.
[165] M. C. Pirrung, L. Fallon, D. C. Lever, S. W. Shuey, *J. Org. Chem.* **1996**, *61*, 2129-2136.
[166] R. J. De Pasquale, *Ind. Eng. Chem. Res.* **1978**, *17*, 278-286.
[167] J. K. Shneine, Y. H. Alaraji, *Spectrosc.* **2016**, *9*, 9c.
[168] M. Münzel, D. Globisch, T. Brückl, M. Wagner, V. Welzmiller, S. Michalakis, M. Müller, M. Biel, T. Carell, *Angew. Chem. Int. Ed.* **2010**, *31*, 5375-5377.
[169] D. Globisch, M. Münzel, M. Müller, S. Michalakis, M. Wagner, S. Koch, T. Brückl, M. Biel, T. Carell, *PloS one* **2010**, *5*, e15367.
[170] S. A. Lenz, J. D. Kohout, S. D. Wetmore, *J. Phys. Chem. B* **2016**, *120*, 12795-12806.
[171] J. Zhou, J. Zhu, M. Zheng, (Ed.: e. (Shanghai)), China, **2021**.
[172] K. Ciszweski, L. Celewicz, K. Golankiewicz, *Synth.* **1995**, *1995*, 777-779.
[173] X.-A. Zheng, H.-S. Huang, R. Kong, W.-J. Chen, S.-S. Gong, Q. Sun, *Tetrahedron* **2018**, *74*, 7095-7101.
[174] B. Bechlars, D. M. D'alessandro, D. M. Jenkins, A. T. Iavarone, S. D. Glover, C. P. Kubiak, J. R. Long, *Nat. Chem.* **2010**, *2*, 362-368.
[175] A. L. Feig, S. J. Lippard, *Chem. Rev.* **1994**, *94*, 759-805.
[176] E. J. Sundstrom, X. Yang, V. S. Thoi, H. I. Karunadasa, C. J. Chang, J. R. Long, M. Head-Gordon, *J. Am. Chem. Soc.* **2012**, *134*, 5233-5242.
[177] L. Wang, L. Duan, R. B. Ambre, Q. Daniel, H. Chen, J. Sun, B. Das, A. Thapper, J. Uhlig, P. Dinér, *J. Catal.* **2016**, *335*, 72-78.
[178] D. J. Wasylenko, R. D. Palmer, E. Schott, C. P. Berlinguette, *Chem. Commun.* **2012**, *48*, 2107-2109.
[179] E. Deponti, A. Luisa, M. Natali, E. Iengo, F. Scandola, *Dalton Trans.* **2014**, *43*, 16345-16353.
[180] R. T. Jonas, T. Stack, *J. Am. Chem. Soc.* **1997**, *119*, 8566-8567.
[181] B. Samuelsson, S.-E. Dahlen, J. Å. Lindgren, C. A. Rouzer, C. N. Serhan, *Science* **1987**, *237*, 1171-1176.
[182] H. W. Gardner, *Biochim. Biophys. Acta, Lipids Lipid Metab.* **1991**, *1084*, 221-239.
[183] J. De Groot, G. Veldink, J. Vliegenthart, J. Boldingh, R. Wever, B. Van Gelder, *Biochim. Biophys. Acta* **1975**, *377*, 71-79.
[184] M. J. Schilstra, G. A. Veldink, J. F. Vliegenthart, *Biochem.* **1994**, *33*, 3974-3979.
[185] M. J. Nelson, *J. Am. Chem. Soc.* **1988**, *110*, 2985-2986.
[186] C. R. Goldsmith, T. D. P. Stack, *Inorg. Chem.* **2006**, *45*, 6048-6055.

[187] M. E. De Vries, R. M. La Crois, G. Roelfes, H. Kooijman, A. L. Spek, R. Hage, B. L. Feringa, *Chem. Commun.* **1997**, 1549-1550.
[188] J. J. Görlitz, P. Nielsen, H. Toftlund, A. D. Bond, *Acta Crystallogr. Sect. Sect. E: Struct. Rep. Online* **2004**, *60*, o1319-o1320.
[189] M. Boniolo, P. Chernev, M. H. Cheah, P. A. Heizmann, P. Huang, S. I. Shylin, N. Salhi, M. K. Hossain, A. K. Gupta, J. Messinger, *Dalton Trans.* **2021**, *50*, 660-674.
[190] A. L. Raithel, T.-Y. Kim, K. C. Nielsen, R. J. Staples, T. W. Hamann, *Sustain. Energy Fuels* **2020**, *4*, 2497-2507.
[191] D. J. Rudd, C. R. Goldsmith, A. P. Cole, T. D. P. Stack, K. O. Hodgson, B. Hedman, *Inorg. Chem.* **2005**, *44*, 1221-1229.
[192] Y. Sun, J. P. Bigi, N. A. Piro, M. L. Tang, J. R. Long, C. J. Chang, *J. Am. Chem. Soc.* **2011**, *133*, 9212-9215.
[193] S. Ohzu, T. Ishizuka, H. Kotani, T. Kojima, *Chem. Commun.* **2014**, *50*, 15018-15021.
[194] B. Das, A. Orthaber, S. Ott, A. Thapper, *Chem. Commun.* **2015**, *51*, 13074-13077.
[195] B. Das, A. Orthaber, S. Ott, A. Thapper, *ChemSusChem* **2016**, *9*, 1178-1186.
[196] E. L.-M. Wong, G.-S. Fang, C.-M. Che, N. Zhu, *Chem. Commun.* **2005**, 4578-4580.
[197] W. L. Kwong, C. N. Lok, C. W. Tse, E. L. M. Wong, C. M. Che, *Chem. Eur. J.* **2015**, *21*, 3062-3072.
[198] S. Rana, A. Dey, D. Maiti, *Chem. Commun.* **2015**, *51*, 14469-14472.
[199] C. Cordes, M. Morganti, I. Klawitter, C. Schremmer, S. Dechert, F. Meyer, *Angew. Chem. Int. Ed.* **2019**, *58*, 10855-10858.
[200] M. Ghosh, K. K. Singh, C. Panda, A. Weitz, M. P. Hendrich, T. J. Collins, B. B. Dhar, S. Sen Gupta, *J. Am. Chem. Soc.* **2014**, *136*, 9524-9527.
[201] N. S. Lindlar né Jonasson, A. Menke, L. Senft, A. Squarcina, D. Schmidl, K. Fisher, S. Demeshko, J. C. Kruse, T. Josephy, P. Mayer, J. Gutenthaler-Tietze, P. Comba, F. Meyer, I. Ivanović-Burmazović, L. J. Daumann, *manuscript submitted to Inorganic Chemistry* **2024**.
[202] G. Dyker, O. Muth, *Eur. J. Org. Chem.* **2004**, *2004*, 4319-4322.
[203] H. Wang, N. Wu, J. Zheng, C. Zheng, D. Wang, *Mendeleev Commun.* **2020**, *30*, 100-102.
[204] P. Gütlich, Y. Garcia, H. A. Goodwin, *Chem. Soc. Rev.* **2000**, *29*, 419-427.
[205] K. Bairagi, O. Iasco, A. Bellec, A. Kartsev, D. Li, J. Lagoute, C. Chacon, Y. Girard, S. Rousset, F. Miserque, *Nat. Commun.* **2016**, *7*, 12212.
[206] L. Cambi, A. Gagnasso, *Atti. Accad. Naz. Lincei* **1931**, *13*, 809-813.
[207] L. Cambi, L. Szegö, *Ber. Dtsch. Chem. Ges.* **1931**, *64*, 2591-2598.
[208] W. Baker Jr, H. Bobonich, *Inorg. Chem.* **1964**, *3*, 1184-1188.
[209] N. Ortega-Villar, A. Y. Guerrero-Estrada, L. Pineiro-Lopez, M. C. Muñoz, M. Flores-Alamo, R. Moreno-Esparza, J. A. Real, V. M. Ugalde-Saldivar, *Inorg. Chem.* **2015**, *54*, 3413-3421.
[210] P. Gütlich, J. Jung, *J. Mol. Struct.* **1995**, *347*, 21-38.
[211] E. König, R. Schnakig, G. Ritter, W. Irler, B. Kanellakopulos, B. Powietzka, *Inorg. Chim. Acta* **1979**, *35*, 239-248.
[212] P. Gütlich, A. Hauser, *Coord. Chem. Rev.* **1990**, *97*, 1-22.
[213] C. Atmani, F. El Hajj, S. Benmansour, M. Marchivie, S. Triki, F. Conan, V. Patinec, H. Handel, G. Dupouy, C. J. Gómez-García, *Coord. Chem. Rev.* **2010**, *254*, 1559-1569.
[214] R. W. Hogue, S. Singh, S. Brooker, *Chem. Soc. Rev.* **2018**, *47*, 7303-7338.
[215] S. Brooker, *Chem. Soc. Rev.* **2015**, *44*, 2880-2892.
[216] X.-H. Zhao, S.-L. Zhang, D. Shao, X.-Y. Wang, *Inorg. Chem.* **2015**, *54*, 7857-7867.
[217] Z.-S. Yao, Z. Tang, J. Tao, *Chem. Commun.* **2020**, *56*, 2071-2086.

[218] C. Yi, Y.-S. Meng, L. Zhao, N.-T. Yao, Q. Liu, W. Wen, R.-X. Li, Y.-Y. Zhu, H. Oshio, T. Liu, *CCS Chem.* **2022**, 1-10.
[219] N. Amin, S. Said, M. Salleh, A. Afifi, N. Ibrahim, M. Hasnan, M. Tahir, N. Hashim, *Inorg. Chim. Acta* **2023**, *544*, 121168.
[220] O. Kahn, C. J. Martinez, *Science* **1998**, *279*, 44-48.
[221] O. Sato, *Nat. Chem.* **2016**, *8*, 644-656.
[222] H. Chen, H. H. Yang, T. Frauhammer, H. You, Q. Sun, P. Nagel, S. Schuppler, A. B. Gaspar, J. A. Real, W. Wulfhekel, *Small* **2023**, *19*, 2300251.
[223] A. E. Thorarinsdottir, A. I. Gaudette, T. D. Harris, *Chem Sci* **2017**, *8*, 2448-2456.
[224] I. Bernal, I. M. Jensen, K. B. Jensen, C. J. McKenzie, H. Toftlund, J.-P. Tuchagues, *J. Chem. Soc., Dalton Trans.* **1995**, 3667-3675.
[225] V. Balland, F. Banse, E. Anxolabéhère-Mallart, M. Nierlich, J.-J. Girerd, **2003**, 2529-2535.
[226] J. England , G. J. P. Britovsek, N. Rabadia , A. J. P. White, *Inorg. Chem.* **2007**, 3752.
[227] H. C. Börzel, P.; Hagen, K. S.; Lampeka, Y. D.; Lienke, A.; Linti, G.; Merz, M.; Pritzkow, H.; Tsymbal, L. V., *Inorg Chem Acta* **2002**, *337*, 407-419.
[228] P. Mialana, A. Nivorojkine, G. Pratviel, L. Azeḿa, M. Slany, F. Godde, A. Simaan, F. Banse, T. Kargar-Grisel, G. Bouchoux, J. Sainton, O. Horner, J. Guilhem, L. Tchertanova, B. Meunier, J.-J. Girerd, *Inorg Chem* **1999**, *38*, 1085-1092.
[229] J. Zhao, S. Ji, W. Wu, W. Wu, H. Guo, J. Sun, H. Sun, Y. Liu, Q. Li, L. Huang, *RSC Adv.* **2012**, *2*, 1712-1728.
[230] N. A. Smith, P. J. Sadler, *Philos. Trans. A, Math. Phys. Eng. Sci.* **2013**, *371*, 20120519.
[231] M. Alipour, T. Izadkhast, *PCCP* **2020**, *22*, 9388-9404.
[232] M. Boniolo, S. I. Shylin, P. Chernev, M. H. Cheah, P. A. Heizmann, P. Huang, N. Salhi, K. Hossain, A. Thapper, M. Lundberg, J. Messinger, *Chem. Commun.* **2020**, *56*, 2703-2706.
[233] J. Wang, Y. Li, R.-J. Wei, Z. Tang, Z.-S. Yao, J. Tao, *Inorg. Chem.* **2023**.
[234] F. Milocco, F. de Vries, H. S. Siebe, S. Engbers, S. Demeshko, F. Meyer, E. Otten, *Inorg Chem* **2021**, *60*, 2045-2055.
[235] E. Collet, P. Guionneau, *C. R. Chim.* **2018**, *21*, 1133-1151.
[236] C. R. Goldsmith, R. T. Jonas, T. D. P. Stack, *J. Am. Chem. Soc.* **2002**, *124*, 83-96.
[237] C. R. Goldsmith, R. T. Jonas, A. P. Cole, T. D. P. Stack, *Inorg. Chem.* **2002**, *41*, 4642-4652.
[238] A. Bruker, B. SAINT, *Acta Crystallogr. Sect. C: Cryst. Struct. Commun.* **2015**, *71*, 3-8.
[239] A. Bruker, *Bruker AXS Inc., Madison, Wisconsin, USA*.
[240] G. M. Sheldrick, *Acta Crystallogr. Sect. C: Struct. Chem.* **2015**, *71*, 3-8.
[241] F. R. Traube, S. Schiffers, K. Iwan, S. Kellner, F. Spada, M. Müller, T. Carell, *Nat. Protoc.* **2019**, *14*, 283-312.
[242] E. Bill, *Mfit* **2008**, Max-Planck Institute for Chemical Energy Conversion, Mühlheim/Ruhr, Germany.
[243] J. Cong, D. Kinschel, Q. Daniel, M. Safdari, E. Gabrielsson, H. Chen, P. H. Svensson, L. Sun, L. Kloo, *J. Mater. Chem. A* **2016**, *4*, 14550-14554.
[244] I. N. Michaelides, N. Tago, B. Viverge, T. Carell, *Chem. Eur. J.* **2017**, *23*, 15894-15898.
[245] D. Schmidl, Master Thesis thesis, Ludwig-Maximilians Universität München **2020**.
[246] W. Rasheed, R. Fan, C. S. Abelson, P. O. Peterson, W.-M. Ching, Y. Guo, L. Que Jr, *J. Biol. Inorg. Chem.* **2019**, *24*, 533-545.
[247] A. Menke, R. C. Dubini, P. Mayer, P. Rovó, L. J. Daumann, *Eur. J. Inorg. Chem.* **2021**, *2021*, 30-36.
[248] H. Lumpe, A. Menke, C. Haisch, P. Mayer, A. Kabelitz, K. V. Yusenko, A. Guilherme Buzanich, T. Block, R. Pöttgen, F. Emmerling, *Chem. Eur. J.* **2020**, *26*, 10133-10139.